NREL
NATIONAL RENEWABLE ENERGY LABORATORY

Turbulence-Turbine Interaction: The Basis for the Development of the TurbSim Stochastic Simulator

N.D. Kelley

NREL is a national laboratory of the U.S. Department of Energy, Office of Energy Efficiency & Renewable Energy, operated by the Alliance for Sustainable Energy, LLC.

Technical Report
NREL/TP-5000-52353
November 2011

Contract No. DE-AC36-08GO28308

NREL
NATIONAL RENEWABLE ENERGY LABORATORY

Turbulence-Turbine Interaction: The Basis for the Development of the TurbSim Stochastic Simulator

N.D. Kelley

Prepared under Task No(s). WE11.0311

National Renewable Energy Laboratory
1617 Cole Boulevard
Golden, Colorado 80401
303-275-3000 • www.nrel.gov

Technical Report
NREL/TP-5000-52353
November 2011

Contract No. DE-AC36-08GO28308

NOTICE

Available electronically at http://www.osti.gov/bridge

Available for a processing fee to U.S. Department of Energy
and its contractors, in paper, from:

U.S. Department of Energy
Office of Scientific and Technical Information
P.O. Box 62
Oak Ridge, TN 37831-0062
phone: 865.576.8401
fax: 865.576.5728
email: mailto:reports@adonis.osti.gov

Available for sale to the public, in paper, from:

U.S. Department of Commerce
National Technical Information Service
5285 Port Royal Road
Springfield, VA 22161
phone: 800.553.6847
fax: 703.605.6900
email: orders@ntis.fedworld.gov
online ordering: http://www.ntis.gov/help/ordermethods.aspx

Cover Photos: (left to right) PIX 16416, PIX 17423, PIX 16560, PIX 17613, PIX 17436, PIX 17721

Printed on paper containing at least 50% wastepaper, including 10% post consumer waste.

Acknowledgments

This work is currently supported by the U.S. Department of Energy (DOE) under contract no. DE-AC36-08GO28308. The author acknowledges the continued support of this research by the DOE Office of Wind and Hydropower Technologies and its predecessors from the embryonic stage of this research in 1989 through the present. The author specifically acknowledges Jack Cadogan for his continued support of this work over the years and more recently Mark Higgins for his patience in the production of this final report.

The author particularly acknowledges Ed McKenna's outstanding contributions to this research for more than 20 years. Without Ed's unwavering personal loyalty and superior instrumentation, planning, and field operations expertise, we would never have been able to obtain the information that has been crucial in developing our understanding of how turbulence affects wind turbines. The support of David Jager and George Scott over the years is acknowledged and greatly appreciated.

The author recognizes Bonnie Jonkman's outstanding technical support of this work. Without Bonnie's mathematical and programming skills, we would not been able to apply many of the sophisticated and state-of-the art analysis techniques that proved so useful. And the TurbSim turbulence simulator code would not be as comprehensive and useful as it is if it were not for her dedication and programming expertise.

A very productive collaboration with Herbert Sutherland of Sandia National Laboratories helped put the impact of turbulence on the material properties of wind turbine structural components on a firm technical basis.

Thanks go to Fort Felker of the National Wind Technology Center (NWTC) for his much appreciated and critical support.

The author also thanks Yelena Pichugina of the University of Colorado and the National Oceanic and Atmospheric Administration and Pat Moriarty of the NWTC for their discussions and very valuable comments.

Acronyms

AGL	above ground level
ANOVA	analysis of variance
ART	Advanced Research Turbine
BM	bending moment
CART2, CART3	Controls Advanced Research Turbine – Two Blades, Three Blades
CoRA	Colorado Research Associates
CRR	critical Richardson number stability range
CRRH	critical Richardson number stability range high
CS	coherent structure
CTKE	coherent turbulent kinetic energy
CWT	continuous wavelet transform
DNS	direct numerical simulation
DOE	U.S. Department of Energy
DOF	degrees of freedom
DWT	discrete wavelet transform
ESRL	Environmental Systems Research Laboratory (NOAA)
ETM	Extreme Turbulence Model (IEC)
FIR	finite impulse response
GE Wind	General Electric Wind Energy
GP_LLJ	TurbSim Great Plains Low-Level Jet Spectral Model
GWI	gravity wave instability
HAWT	horizontal axis wind turbine
HRDL	high-resolution Doppler lidar
IEC	International Electrotechnical Commission
IECKAI	TurbSim IEC Kaimal spectral model
IECVKM	TurbSim IEC von Kârmân spectral model
IMU	inertial measurement unit
IQR	Interquartile range
K-H	Kelvin-Helmholtz (other than KHI)
KHI	Kelvin-Helmholtz Instability
KHTEST	TurbSim severe turbulence option
LES	large-eddy simulation
LIST	Long-Term Inflow and Structural Test Program
LLJ	low-level jet stream
LLLJP	Lamar Low-Level Jet Project
LOESS	locally weighted regression
LST	local standard time
ML	mixed layer portion of PBL
MLR	multiple linear regression

M-O	Monin-Obukhov
MSL	mean sea level
NACA	National Advisory Committee for Aeronautics
NASA	National Aeronautics and Space Administration
NCAR	National Center for Atmospheric Research
NOAA	National Oceanic and Atmospheric Administration
NREL	National Renewable Energy Laboratory
NTM	Normal Turbulence Models as specified by the IEC (Kaimal, von Kârmân, or Mann)
NWP	Normal Wind Profile (IEC)
	National Wind Technology Center
NWTCUP	TurbSim NWTC spectral model
PBL	planetary boundary layer
PDF	probability density function
RL	residual layer portion of PBL
PRTD	platinum resistance temperature detector
SGS	subgrid scale
SL	surface layer portion of PBL
SMOOTH	TurbSim Rise homogeneous terrain spectral model
SNL	Sandia National Laboratories
SNLWIND	Paul Veers' original turbulence simulation code
SNLWIND-3D	NREL update of SNLWIND inflow turbulence simulation code
STC0*x*	stability class where *x* = 1 to 5
TKE	turbulent kinetic energy
UTC	Coordinated Universal Time
VAWT	vertical axis wind turbine
WF_xxx	TurbSim wind farm spectral models: xxx = UPW, 07D, or 14D
WindPACT	Wind Partnership for Advanced Component Technologies
WRF	Weather Research and Forecasting Model

Nomenclature

Atmospheric Variables

$\tau(z)$	mean shear stress profile, $\tau(z) = \rho_o(z)\left[\overline{u'w'(z)}\right]$
$\sigma_{u,}\ \sigma_1$	streamwise or longitudinal wind component standard deviation
σ_v	crosswind or lateral wind speed component standard deviation
σ_w	vertical wind speed component standard deviation
σ_T	temperature standard deviation
σ_{U_H}	horizontal wind speed standard deviation
τ_o	surface shear stress
θ_v	virtual potential temperature (θ corrected for moisture)
σ_w	vertical wind speed standard deviation
c_p	specific heat of air at constant pressure
c	perturbation phase speed
c_{nU}	Chebyshev polynomial coefficients for low-level jet U-component
$c_{n\theta}$	Chebyshev polynomial coefficients for low-level jet wind direction
Coh_{ij_x}	Coherence function
ε	turbulence viscous dissipation rate
E_T	total turbulent kinetic energy (TKE), $E_T = 1/2(u'^2 + v'^2 + w'^2)$
E_{iso}	isotropic turbulent kinetic energy, $E_{iso} = E_T - E_{coh}$
$E_{coh,}\ CTKE$	coherent turbulent kinetic energy
f	reduced frequency, $f = nz/U$
g	gravity acceleration
I_{hub}	hub-height turbulence intensity, $I_{hub} = \sigma_{U_H} / \overline{U}_H$
IAT	coherent turbulent structure event interarrival time
k	wavenumber, $k = 2\pi / \lambda$
κ	von Kârmân constant (~0.4)
$L_{M\text{-}O}$	Monin-Obukhov length, $L = -u_*^3\theta / kgQ_o$
L_b	buoyancy length scale, $L_b = \sigma_w / N_{buoy}$
n	cyclic frequency (Hz)
$N\ or\ N_{buoy}$	Brunt-Väisälä (buoyancy) frequency, $N_{buoy}^2 = (g/\overline{\theta})(\partial\theta/\partial z)$
$N(t)$	number of events in a Poisson counting process
N_{coh}	number of coherent turbulent structures found in a 10-minute record
p	atmospheric pressure
p_o	reference atmospheric pressure (typically 1000 hectopascals (hPa, millibars [mb])
$pkCTKE$	peak coherent turbulent kinetic energy, peak E_{coh}
θ	potential temperature, $\theta = T(1000/p)^{.286}$
α	power law shear exponent, $\alpha = \ln(U_2/U_1)/\ln(z_2/z_1)$
Q_o	surface heat flux
Ri	gradient Richardson number, $Ri = g/\overline{\theta}(\partial\theta/\partial z)/(\partial\overline{U}/\partial z)^2$
Ri_c	critical Richardson number, Ri = +0.25

Ri_{TL}	turbine layer gradient Richardson number stability parameter
Ri_f	flux Richardson number
r_{ij}	cross-correlation coefficient
$S(f)$	power spectral density
STC	stability class
T	sensible absolute temperature
T_v	virtual absolute temperature
T_{coh}	total length of coherent turbulent structures in 10-minute record
t	time
u	streamwise wind component
u_*	mean friction velocity or shearing stress, $u_* = \sqrt{\left|\overline{u'w'}\right|}$
u_{*D}	mean local u_* value across rotor disk layer
u'	streamwise eddy turbulence component
U_H	Horizontal wind speed, $U_H = \sqrt{u^2 + v^2}$
$\overline{U}_H$	mean U_H
v	crosswind or lateral wind component
v'	crosswind or lateral eddy turbulence component
w	vertical wind component
w'	vertical eddy turbulence component
$u'w', u'v', v'w'$	Reynolds stress components
$w'E$	vertical flux (transport) of turbulent kinetic energy (TKE)
$w'E_{coh}$	vertical flux (transport) of coherent turbulent kinetic energy
$w'T'$	buoyancy flux
x	coordinate in the direction of the mean wind
y	coordinate perpendicular to the mean wind in the horizontal plane
z	height coordinate
z_i	mixed layer (ML) depth
z_o	surface roughness length
ρ	air density
λ	wavelength, Poisson rate parameter
z/L	Monin-Obukhov stability parameter
z/L_D	Mean z/L value across turbine disk layer
ω_x	streamwise component of vorticity
ω_y	crosswind or lateral component of vorticity
ω_z	vertical component of vorticity
H	helicity, $H = 1/2(u_i \cdot \omega_i)$, where i = 1,2,3

Turbine-Related Variables

C_T	rotor thrust coefficient
D	turbine rotor diameter
DEL	damage equivalent load
EBM	blade root edgewise bending moment
FBM	blade root flapwise bending moment
$M_{p\text{-}p}$	alternating bending moment peak-to-peak loads or stress cycles

N_{cyc}	number of blade loading cycles
β_1	flapwise high-loading tail distribution exponential shape parameter
γ_2	edgewise high-loading tail distribution extreme value shape parameter

Executive Summary

Introduction

Analyses of the performance of the range of prototype wind turbines developed under the Federal Wind Program in the 1970s and early 1980s found that the structural fatigue damage sustained while operating in a wide range of environments far exceeded original design estimates. These excessive loads were attributed to the impact of atmospheric turbulence. More recently, with the return of turbine sizes and capacities at or exceeding those of the earlier multimegawatt prototypes, many of the same issues have resurfaced. Current designs do incorporate many of the lessons learned from the earlier generations. But they also tend to be more structurally flexible, and they are being installed and operated at greater heights above the ground. Even though the availability of today's design tools has given the designers of the current generation of turbines a distinct advantage over their predecessors, the increased heights have introduced new challenges. As an example, turbines now operate deeper into the atmospheric boundary layer, where the turbulence characteristics can be significantly different from those closer to the ground.

This combination of taller turbines with more flexible rotors and towers operating in turbulent conditions that are not as well understood is contributing to much higher than anticipated maintenance and repair costs and is associated with lower energy production. Statistical studies of wind farm productivity and operating costs with the currently installed fleet of turbines have shown a systemic power underproduction coupled with the need for more maintenance and repairs. Turbine availability has been estimated to account for almost half of this deficit, of which the downtime for repairs is a major constituent. The cumulative nature of the turbine lifetime trend in operating costs strongly suggests that the target operating environments for turbine design are somehow deficient (i.e., critical turbulent conditions are either being missed entirely or inadequately accommodated during design). In this report we document evidence of this and offer the turbine designer an expanded tool that resolves many of these shortcomings.

Approach

In 1989, the Wind Technology Group at the National Renewable Energy Laboratory (NREL) began a program, sponsored by the U.S. Department of Energy (DOE), to develop a physical understanding of the role of atmospheric turbulence in the dynamic response of wind turbines. The program's first objective was to develop a detailed understanding of the physics governing the interaction of atmospheric turbulence and the dynamic loading induced on turbine components. The next step was to quantify that interaction in terms of the dominant turbulence scaling parameters and their influence on the structural response and corresponding fatigue damage to wind turbine components. This is best accomplished by simultaneously measuring microscale characteristics (time and space scales of wind field motions smaller than the turbine rotor diameter); turbulence entering the rotor; and the dynamic loading response of key turbine components such as the blades, drivetrain, and tower.

Between 1989 and 2000, two major field experiments were conducted to collect and analyze this type of information. We took measurements of operating turbines at a multirow wind farm in San Gorgonio, California (California wind farm) and at the National Wind Technology Center (NWTC) near Boulder, Colorado. In addition, we extended our knowledge of the factors controlling turbulence-induced response by looking at a planned wind farm at a high-altitude site

in the Great Plains, near Lamar in southeastern Colorado (the Lamar Low-Level Jet Project, or LLLJP). The greatest wind resource in the United States resides in the Great Plains and much of it (particularly during the warmer months) results from the presence of frequent nocturnal low-level jets (LLJs).

To examine the synchronized time series of the turbine blade root loads and the three turbulence velocity components, we took measurements at the California wind farm and the NWTC with a hub-height upstream sonic anemometer or an array of sonic anemometers.

Analyzing the field measurement campaigns gave us detailed insights into the turbulence characteristics that had the greatest impact on turbine dynamic loads and fatigue accumulation. Building on the groundbreaking work of Paul Veers of Sandia National Laboratories (SNL), we used this information to develop a stochastic turbulent inflow simulation (called TurbSim) that incorporates these critical flow characteristics.

TurbSim runs simulations based on the International Electrotechnical Commission (IEC) Kaimal and von Kârmân Normal Turbulence Models (NTMs), as well as a spectral model for smooth, homogenous terrain developed at the Risø National Laboratory. In this report, however, we discuss the background and development of the site-specific spectral models representing turbulent conditions in and near the California wind farm, the NWTC, and the LLLJP site. These site-specific models are based on direct measurements taken at each location.

With nocturnal LLJ streams and their strong vertical shears occurring frequently at the Great Plains site, including them in TurbSim was a primary objective of the measurement campaign there. To accomplish this, we made measurements of vertical profiles of wind speed and direction up to 500 m and collected data from a 120-m tower. A midrange acoustic wind profiler (sodar) was operated during the peak jet season to obtain characteristic jet profiles of wind speed and direction. Smoothed combined velocity and direction profiles derived from the tower and sodar were fitted with Chebyshev polynomials for a range of LLJ heights from 70 to 480 m in 20-m increments. We arrived at a specific profile variation by scaling the Chebyshev coefficients with independent variables derived from the tower measurements.

Report Objectives

In this report we discuss three major topics. First, we summarize our understanding of the role atmospheric turbulence plays in the dynamic response of wind turbines and the associated loading, along with its contribution to fatigue damage accumulation in key structural components. Next, we describe the atmospheric dynamics responsible for creating the turbulent conditions that can be the most detrimental to wind turbines. Finally, we briefly summarize the process in which the scaling was developed and incorporated into the turbulence spectral models that are available in TurbSim for the California wind farm, the NWTC, and the LLLJP.

Results

We summarize our results in three categories: the characterization of the turbine cyclic stress loading and its scaling relationships to inflow turbulence parameters; the atmospheric processes and conditions that influence these parameters; and the stochastic simulation of the turbulent inflow that incorporates critical flow structures.

Loading Characteristics and Their Relationships with Turbulence Scaling Parameters

We found the following:

- The probability of the most damaging blade root cyclic stresses was very highly correlated with the vertical dynamic stability of the atmospheric layer (expressed by the gradient Richardson number parameter *Ri*) measured from the ground to the top of the turbine rotor and the mean friction velocity or shearing stress (u_*) within the layer occupied by the rotor.
- The most damaging fatigue loads occur within the weakly stable range of $+0.01 \leq Ri < +0.05$, with the maximum damage at a value of $Ri = +0.02$. The mean friction velocity u_* also reached a maximum within this same stability range.
- Similar correlations were found for two 65-kW turbines operating deep within the 41-row California wind farm and a 600-kW turbine operated at the NWTC, suggesting a universality of such correlations.
- The sonic anemometer measurements revealed that the loads and the velocity components were associated with spatially and temporally organized or coherent turbulent structures or patches that were embedded in and moving with the basic or background wind flow. Such coherent structures occurred most frequently and were most intense within the stability range of $+0.01 \leq Ri < +0.05$. This correlated well with our findings that the greatest fatigue damage takes place within the same range. The turbine loads scale very well with a parameter we define as coherent turbulent kinetic energy, or E_{coh}.
- Our initial attempt to simulate such turbine responses using a non-neutral expanded version of Veers' original SNLWIND simulator called SNLWIND-3D, which included all three turbulent velocity components, was not completely successful. Although we were able to reproduce the body of the observed cyclic load distributions, the simulation did not include the few very large loads needed to match the observed fatigue damage.

Atmospheric Processes That Influence Turbine Dynamic Loading

After we were unable to adequately reproduce the largest loading cycles in our simulation, we found that the simulation was not reproducing the most intense coherent turbulent structures seen in the natural flow. These structures, which were responsible for creating the largest cyclic loads, were missing in our inflow simulation even when the stability condition was specified within the critical *Ri* range discussed previously. The atmospheric instabilities that take place within this critical stability range offered a clue to the source of this discrepancy. We found the following:

- Kelvin-Helmholtz Instability (KHI) taking place within and above the turbine rotor disk is ultimately responsible for the fewer but more damaging loads observed within the narrow stability range.
- KHI transports energy from the mean background flow into intense coherent turbulent structures called billows that have a finite life span and grow and decay over a matter of minutes.

- The fastest rate of billow formation and growth with the widest range of eddy sizes is initiated by a turbulent perturbation in the upstream flow.
- A high-resolution computer simulation of the life cycle of a stationary Kelvin-Helmholtz (K-H) billow as the turbine inflow revealed that the largest turbine loads occur after the billow rolls over and begins to break down into smaller, coherent vortical structures.
- Under these weakly stable conditions the limited buoyancy damping constrains the size of the largest eddy sizes in the coherent structure, which can be expressed as the buoyancy length scale, L_b.
- The largest turbine loads generally occur when L_b is the same or slightly larger than the turbine rotor disk diameter.
- Kinetic energy can be coherently transferred from the buoyancy-damped oscillating turbulent motions within coherent structures into the lightly damped modal frequencies of turbine blades and then into the remainder of the turbine structure.
- Such organized spectral energy transfers or fluxes result in a phase-coherent summation of the amplitudes of the corresponding vibratory modes into a large load excursion. Put simply, a coherent turbulence excitation elicits a coherent aeroelastic response.
- The KHI process is highly nonlinear and cannot be adequately reproduced using the Fourier inversion technique used in SNLWIND and SNLWIND-3D.

Stochastic Simulation of Turbulent Inflows Containing Coherent Structures

Because the Fourier inversion technique used to replicate the velocity field in the TurbSim Program cannot be used to simulate the coherent structures, The structures generated by the KHI process had to be incorporated into the velocity time series of the background flow created by the Fourier inversion of the target turbulence frequency spectrum. This is more or less the way the process takes place in natural flows—the K-H billows are superimposed on the background flow while being fed from it. Eventually the strong vertical mixing created by the billow breakdown completely smears out any vestiges of the unstable perturbation into the background flow.

To include coherent structures in TurbSim simulations, we

- Extracted a number of self-contained excerpts of full 3-D, nondimensional coherent velocity structures from available high-resolution K-H billow computer simulations
- Inserted versions of these structures into the TurbSim-simulated velocity time series that had been scaled based on the boundary conditions of the specific simulation
- Chose total length and peak intensities of the structures randomly based on actual measurements at the California wind farm, at the NWTC, and at the LLLJP site; the characteristics of the coherent structures were scaled based on the specific boundary conditions of the simulation
- Set the locations of coherent events within a record according to Poisson distribution based on the measured values of the event occurrence rate or interarrival time that was also scaled by the boundary conditions of the specific simulation.

Conclusions

In this report we present the following major conclusions:

- When a turbine rotor ingests coherent structures or turbulent patches, generated large load excursions and fatigue damage often result.
- Turbulent kinetic energy can be transported into the blade structure from these coherent structures that is then propagated through the root attachments into the drivetrain and the remaining structure where it is dissipated.
- With the advent of increasingly taller towers and much larger and more flexible rotors, this vibratory energy flux process has most likely become more influential in creating fatigue damage throughout the turbine structure.
- Coherent turbulent kinetic energy created locally within the rotor disk and externally transported into it is a major contributor to increased turbine fatigue damage.
- KHI, which is associated with the stable atmospheric boundary layer, is most likely the dominant atmospheric process responsible for creating the coherent turbulent conditions.
- There is a narrow but critical range of vertical dynamic stability where the largest damaging loads arise and typically occur within specific periods of the diurnal cycle.
- The flows beneath Great Plains nocturnal LLJs contain coherent turbulent structures but often of a somewhat lesser intensity than those seen in the California wind farm and at the NWTC. The diurnal occurrence was similar to what we found in the wind farm and at the NWTC. Jets higher than the maximum height of turbine rotors were often responsible for significant downward fluxes (transport) of coherent turbulent energy similar to those seen in the lee flows downwind of mountain terrain.
- The dearth of large loading events in turbine simulations using the TurbSim predecessor SNLWIND-3D was a result of the linear process of the Fourier inversion used to create velocity time series from specified frequency spectra. The most intense coherent structures result from the nonlinear KHI process. We solved this issue by inserting coherent structures, which had been generated by high-resolution numerical models that retained the nonlinearities, into the simulated background velocity fields.
- We performed limited statistical validations of the stochastic wind field generated by the TurbSim code for the NWTC and LLLJP environments and found them to be in reasonable agreement.

We believe that the TurbSim site-specific spectral models give the turbine designer realistic emulations of the true full-field turbulent inflows seen at each site, particularly within the critical stability range. As a result, we encourage turbine designers to use one of the available multibody dynamic codes with the NREL AeroDyn aerodynamics module as the interface to TurbSim simulations.

Contents

List of Figures

List of Tables

1.0 Introduction

Between 1975 and 1985, the U.S. Department of Energy (DOE) either directly sponsored or supported the development of a series of utility-scale wind turbines ranging in generating capacity from 200 kW to 4 MW. This work was conducted under the auspices of the Federal Wind Program. The Lewis (now Glenn) Research Center of the National Aeronautics and Space Administration (NASA) managed the utility-scale turbine development program for DOE in which a series of horizontal axis wind turbine (HAWT) prototypes with increasing generating capacity were designed, constructed, and operated by several contractors, including Westinghouse, General Electric, and Boeing Engineering and Construction.

The "MOD" series of turbines developed under the Federal Wind Program included the 200-kW MOD-0A, the 2-MW MOD-1, the 2.5-MW MOD-2, and the 3.2-MW MOD-5B prototypes. The Hamilton-Standard Division of United Technologies, with support from DOE and NASA, developed a prototype 4-MW turbine (WTS-4) for the U.S. Bureau of Reclamation as a "system verification unit." The performance of this turbine was evaluated as a potential component in the integration of large-scale wind power generation with the existing hydropower system in the western United States. At the same time, Sandia National Laboratories (SNL), also under the sponsorship of the Federal Wind Program, was developing a series of utility-scale vertical axis wind turbine (VAWT) prototypes that culminated in a 600-kW prototype design with an equatorial diameter of 34 m.

Although significant knowledge was gained from this range of turbine designs, only one of the original prototypes was produced commercially. Westinghouse constructed fifteen 600-kW turbines that were largely based on the MOD-0A prototype. These were installed on the northeast coast of the Hawaiian island of Oahu. The DOE/NASA 3.2-MW Boeing MOD-5B prototype was also installed nearby. Both turbines suffered chronic underproduction issues with significant numbers of faults and failures that occurred predominately at night. The MOD-5B also experienced serious structural loading issues when the normally onshore and upsloping winds reversed and descended from the higher terrain to the west and southwest (downslope winds known locally as Kona winds). These particular wind conditions induced unacceptable vibration levels in the turbine structure, and the turbine then had to be shut down. During the same period, an unrelated commercial wind farm consisting of small 17.5-kW and 20-kW turbines installed on high terrain near the northernmost point of the island of Hawaii was suffering a significant numbers of failures that occurred exclusively at night.

Analyses of the performance of these prototype turbines found that the structural fatigue damage they sustained during their operation in various environments far exceeded the original design estimates in virtually all cases. These excessive loads were attributed to the impact of atmospheric turbulence.

As turbine sizes have grown and turbines with capacities at or exceeding the earlier multimegawatt prototypes have been constructed, many of the issues seen with the earlier designs have reappeared. Although the current generation of turbines was designed keeping in mind the earlier problems, today's more structurally flexible and taller turbines are now penetrating deeper into the planetary boundary layer. This has led to much higher than anticipated maintenance and repair costs and reduced capacity factors. Statistical studies of the

productivity and operating costs of the current fleet of wind farms have shown systemic power underproduction exacerbated by the higher than expected maintenance and repair costs. Turbine availability is estimated to account for almost half of this loss, of which downtime for repairs are a major constituent. The cumulative nature of the turbine lifetime trend in maintenance and repair costs strongly suggests that the environments used to design wind turbines are deficient. We offer evidence in this report that critical turbulent conditions are either being missed or inadequately applied when new turbine designs are being developed, which is contributing to current performance issues.

1.1 Inflow Turbulence and Turbine Response Research

In 1989, the Wind Technology Group at the National Renewable Energy Laboratory (NREL) began a DOE-sponsored program to develop a physical understanding of the role of atmospheric turbulence in the dynamic response of wind turbines. The initial objective was to gain a detailed understanding of the physics of the interaction of atmospheric turbulence and the resulting dynamic loading induced on turbine components. The next step was to quantify that interaction with the dominant turbulence scaling parameters and their influence on the structural response and corresponding fatigue damage to wind turbine components. This is best accomplished by simultaneously measuring the microscale characteristics (time and space scales of wind field motions smaller than the turbine rotor diameter) of the turbulence as it enters the turbine rotor and the resulting dynamic loading response of key turbine components such as the blades, drivetrain, and tower.

1.2 Field Measurements of Turbine-Turbulence Interactions

Such valuable information was collected and analyzed during two major field experiments conducted on operating turbines between 1989 and 2000. The purpose of the field experiments was to identify the inflow turbulence characteristics associated with the greatest dynamic response, which was therefore creating the largest fatigue loads. The analysis of these two field measurement campaigns gave us detailed insight into the turbulence characteristics. We used this information when developing the TurbSim stochastic turbulence simulator code and made sure to include the inflow conditions responsible for the most damage. Our research has been built on the foundation of Paul Veers' pioneering stochastic turbulence simulation work at SNL.

During June, July, and August of 1989 we took continuous turbulence measurements from the two 50-m (164-ft) met towers installed upwind and downwind of a 41-row wind farm consisting of almost 1,000 turbines located east of San Gorgonio Pass in Southern California (California wind farm). The following year and over the same period we collected the first time-synchronized inflow turbulence and dynamic response data from two adjacent 65-kW wind turbines located in Row 37 of this same wind farm. The second major turbulence-turbine interaction experiment took place in 1999–2000 at the National Wind Technology Center (NWTC) near Boulder, Colorado, using a 600- kW two-bladed upwind turbine operating in the natural but energetic turbulent flow identified with this site. This experiment was unique in that the inflow to the turbine was measured by five ultrasonic anemometers/thermometers mounted as a planar array upwind of the turbine rotor. The spacing of these anemometers was the same as the rotor height and diameter.

1.3 San Gorgonio Pass Wind Farm Experiment

In 1989 we entered into a cooperative agreement with the large wind farm operator SeaWest. The agreement allowed us to make turbine dynamics and turbulence measurements at their San Gorgonio wind farm near Palm Springs, California. SeaWest made two Micon 65/13 turbines on Row 37 available to NREL, enabling us to compare the performance of a set of newly designed rotor blades (NREL thin airfoil) on one turbine with a neighboring machine equipped with a set of refurbished original equipment (AeroStar) blades (see Tangler et al. [1991] for details).

1.3.1 The Turbines and Local Inflow Instrumentation

The Micon 65/13 turbine is an upwind, three-bladed machine that is stall regulated with a hub height of 23 m. Both turbines had a rotor speed of 48 rpm and an induction-type generator (65/13 kW). Table 1-1 summarizes the Micon 65/13 turbine specifications. Figure 1-1 illustrates the measurement layout.

Table 1-1. SeaWest Micon 65/13 Turbine Specifications

Characteristic	AeroStar Rotor Equipped	NREL Rotor Equipped
Rotor diameter	16.0 m	17.0 m
Blade length	7.4 m	7.9 m
Airfoils	NACA 4415-24	S806A, S805A,S807[a]
Blade weight	363-386 kg	286 kg
Peak power	70 kW @ 15.2 m s^{-1}	65 kW @ 12.5 m s^{-1}

[a]Source: Tangler and Somers (1995)
NACA = National Advisory Committee for Aeronautics

Each turbine had an extensive and identical complement of instrumentation, including strain gauges to measure out-of-plane (flapwise) and in-plane (edgewise) blade root bending loads on each blade, tower bending loads at several locations, and orthogonal low-speed shaft bending loads. Force-balance, two-axis accelerometers installed in the turbine nacelles measured the vibration environment and thrust loads parallel and lateral to the low-speed shafts. A local 31-m met tower (shown in Figure 1-1) was installed 1.5 rotor diameters upwind of and between the two turbines. It was equipped with three levels of propeller vane anemometers over the height range defined by turbine rotor disks, an ultrasonic anemometer/thermometer near hub height, mechanically aspirated platinum resistance temperature measurements near the surface and at the top of the tower, and barometric pressure measurements using a digital micro barometer at a 2-m height. Figure 1-2 displays the measured power curves for the two Micon turbines derived from the available data.

Sources: (a) James Tangler, NREL; (b) and (c) Warren Gretz, NREL

Figure 1-1. Row 37 of California wind farm: (a) looking downwind at the two test turbines (AeroStar rotor-equipped on the left, NREL rotor-equipped on the right) with the upstream met tower; (b) looking upstream (westward) from Row 37 at sunset; (c) looking north with NREL data trailer at Row 38

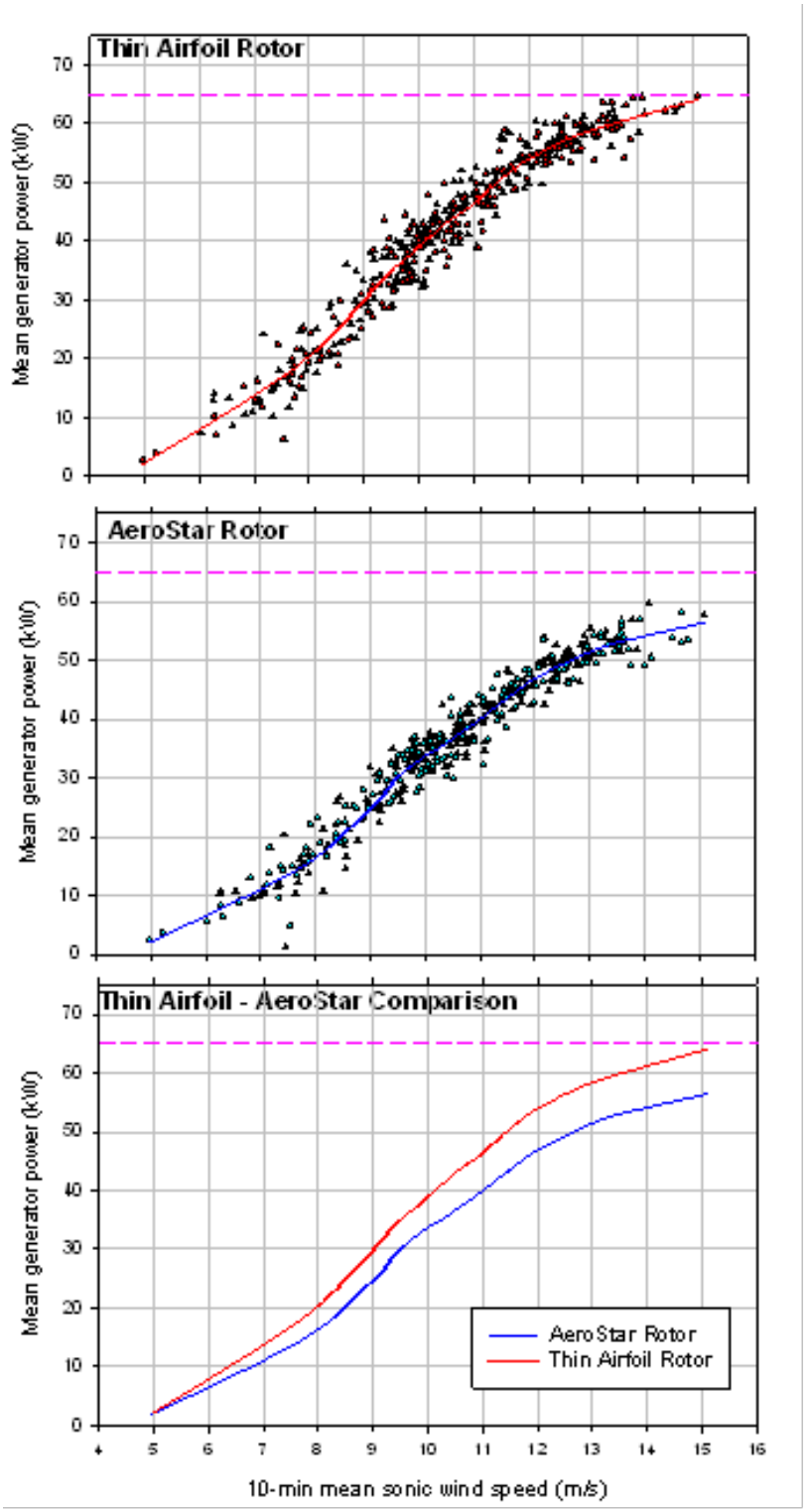

Figure 1-2. California wind farm Micon 65/13 turbine power curves

1.3.2 The Upwind and Downwind Met Towers

SeaWest also supported NREL in installing two 50-m (167-ft) meteorological measurement towers upwind of Row 1 and downwind of Row 41 at the wind farm. Figure 1-3 depicts the general area surrounding the wind farm and the location of the 50-m towers used in 1989. The flow emanating from San Gorgonio Pass to the west is channeled into the wind farm by the higher terrain on each side. Two side-by-side test turbines on Row 37 were employed in the 1990 experiment. Each 50-m tower up and downwind was equipped with the following:

- A three-axis ultrasonic anemometer mounted at the nominal wind farm turbine hub height of 23 m
- Three levels of very sensitive wind speed and direction sensors
- Platinum resistance temperature sensors at 5- and 50-m heights
- A lithium chloride/platinum resistance temperature detector (LiCl/PRTD) dew point temperature sensor at 5 m
- Barometric pressure at a height of 2 m.

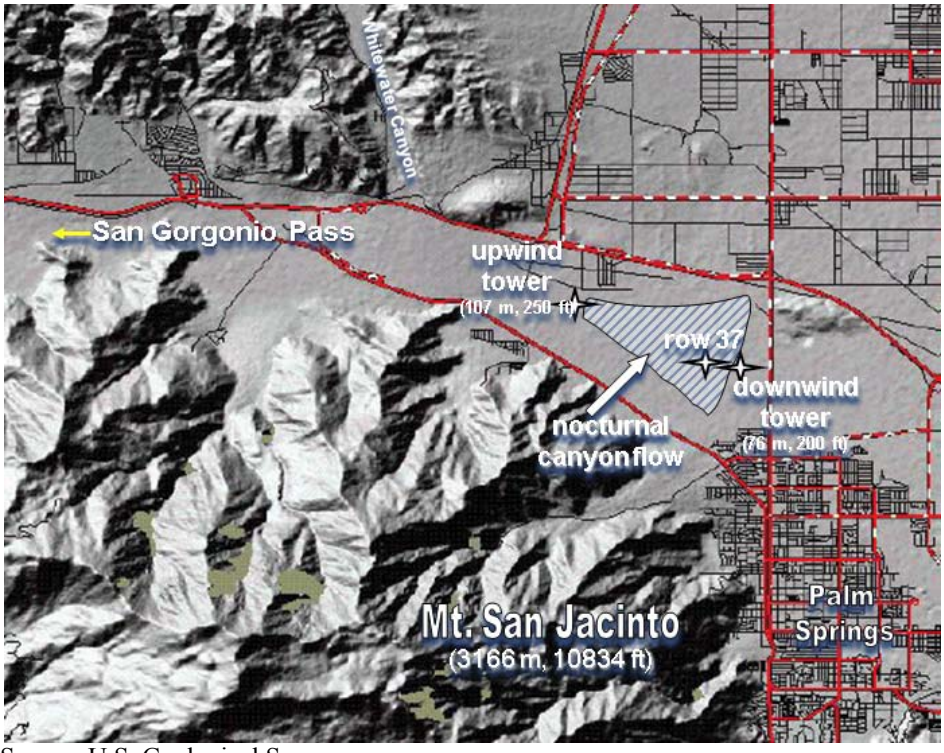

Source: U.S. Geological Survey

Figure 1-3. Terrain characteristics surrounding California wind farm. The approximate shape of the farm is shown with the locations of the upwind and downwind 50-m met towers and the two test turbines at Row 37.

1.3.3 Synopsis of San Gorgonio Wind Characteristics

The primary wind season in the San Gorgonio Pass area is between April and September, when the largest temperature difference exists between the marine air over the Pacific Ocean to the west and the hot, dry air over the Mohave and Sonoran deserts to the east. This air temperature/density difference is responsible for the development of a strong horizontal pressure gradient as cooler, denser air accelerates through the pass toward the low pressure over the desert that results from intense convectional heating. Wind speeds east of the pass tend to peak from July through early August, when the desert surface temperatures reach a maximum and produce the continuous convectional heating, which maintains a consistent low pressure over the entire diurnal period. East of the pass, where the wind farm is located, the wind speeds often decrease significantly in the middle of the day (between 1000 and 1500 local time). This wind pattern results from strong rising air currents associated with the intense midday convectional heating. These currents are a barrier to the western flows entering the wind farm. During the 2-year span of these experiments, the turbines on the western side of the wind farm often operated in light westerly winds and those in the easternmost few rows faced in the opposite direction due to the southeasterly flow there. In between, the winds were often calm or at least well below cut-in speed, so little or no power was being generated in this portion of the wind farm. This was true of the two turbines being tested at Row 37. Figure 1-4 shows the diurnal variation of the hourly percentiles of the hub-height mean wind speed ($\overline{U}_H$) measured at Row 37 during the experiment.

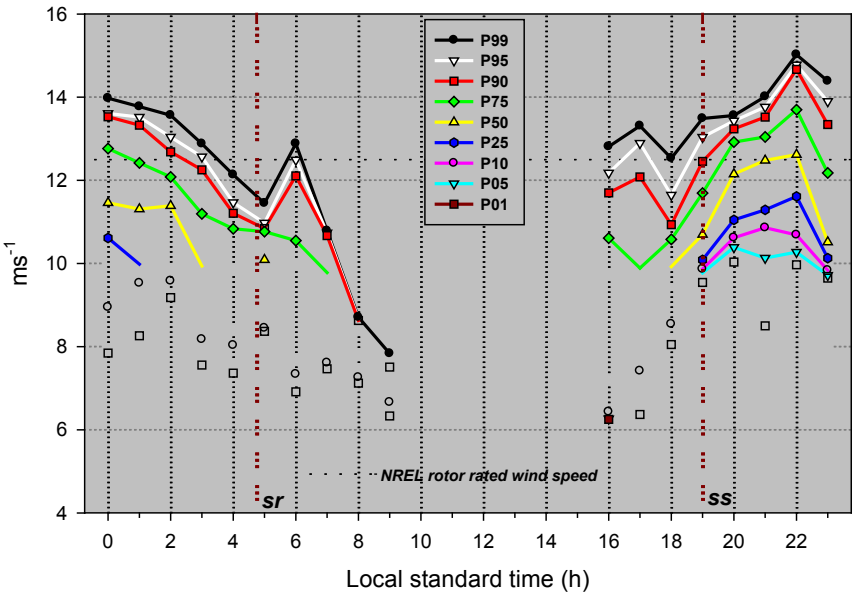

Figure 1-4. Diurnal variation of hourly percentiles of hub-height mean wind speed $\overline{U}_H$ (distributions from test of Micon 65/13 turbines at Row 37 of wind farm in 1990. The rated wind speed for the Micon 65/13 turbine with the NREL rotor is shown as a horizontal dashed line. Local sunrise (*sr*) and sunset (*ss*) for mid-July 1990 are shown as vertical dash-dot-dotted lines. The strongest winds typically occurred around 2200 local standard time (LST).

1.4 NWTC Experiments

We had the opportunity in 1999–2000 to extend the work begun with the two California Micon turbines using the 600-kW Advanced Research Turbine (ART) installed at the NWTC. It was part of the Long-Term Inflow and Structural Test (LIST) Program performed in collaboration with SNL. Though somewhat smaller in comparison with the commercial turbines being installed at the time, the ART was large enough to study the turbine dynamic response from the spatial turbulent inflow into a rotor that was twice the size of the Micon turbines. Although not exposed to an internal flow field within a multirow wind farm, the NWTC's natural turbulence characteristics are known to be very energetic because of the strong, turbulent downslope winds from the Front Range of the Colorado Rocky Mountains to the west.

The size of the ART allowed us to construct an upwind planar array of ultrasonic anemometers/thermometers and other instrumentation scaled to the turbine rotor diameter to measure the spatial aspects of the turbulent inflow. SNL constructed a similar array in upwind of a modified Micon turbine (referred to as a Micon 65/13M) that was installed at a Great Plains site near Bushland, Texas, as another element of the LIST Program (Sutherland 2002).

1.4.1 The ART

The ART is a Westinghouse WWG-0600 600-kW turbine that was constructed in the early 1980s and originally installed and operated on the island of Oahu in Hawaii before being relocated to the NWTC. During the LIST experiment it was operated in its original configuration as a two-blade, upwind machine with a 42-m-diameter rotor. It incorporated a synchronous generator and full span pitch control to regulate power and maintain a constant rotational speed of 43 rpm. The power generating range was from 6.3 m s^{-1} at cut-in to 22.3 m s^{-1} at cutout with rated power attained at 12.8 m s^{-1} . The turbine has since been retrofitted with a three-blade rotor, powerful electric blade pitch actuators, variable speed power regulation, and a highly programmable digital control system for use in advanced controls research. It is now referred as the Controls Advanced Research Turbine 3 (CART3). A second nearby Westinghouse turbine had been previously modified for variable speed controls research with the original two-blade configuration, and it is referred to as the CART2.

Figure 1-5 shows the NWTC and the locations of the ART and the CART2 as they existed during the LIST experiment (1999–2000). A schematic representation of the upwind planar measurement array is shown at its approximate position upwind of the ART. The immediate upwind fetch is relatively flat and homogenous with the surface elevation increasing slightly in the nominal prevailing wind direction towards the west boundary of the NWTC site. El Dorado Canyon is shown on the upper left. The flow out of this canyon has a significant influence on the wind conditions at the NWTC.

Source: NREL PIX 12586

Figure 1-5. NWTC, location of the ART, and approximate position of upwind planar array of five sonic anemometers and other meteorological instrumentation

1.4.2 A Synopsis of NWTC Wind Conditions

The NWTC sits along the mountain–plains interface immediately east of the Front Range Mountains, as shown in Figure 1-6. The elevations of the mountaintops along the Continental Divide about 40 km to the west average 3,800 m (12,500 ft) above mean sea level (MSL). The elevation of the NWTC property is 1,841 m (6,040 ft), a drop of more than 2,200 m (6,500 ft) from the highest terrain to the west. El Dorado Canyon channels high speed flows descending in the lee of the mountains onto the property (see Banta et al. 1995). Figure 1-7 displays an east-west cross section through Boulder of the predicted flow over the Front Range Mountains and a moderate downslope event to their lee. The location of the NWTC is approximately shown immersed in the warmer, drier, and stronger wind flow near the ground. The wind arrows also indicate the significant downward wind component at the foot of the mountains.

The winds associated with the downslope flows at the NWTC have a distinct pulsating characteristic: the wind speeds can vary over a very wide range in a few minutes. In addition to being very gusty, these winds contain high levels of turbulent energy. Based on 9 years of record, Figure 1-8a shows the distributions of streamwise turbulence intensity ($\sigma_1 / \overline{U}$) as a function of the 80-m mean wind speed. The width of the box corresponds to the 25% and 75% quartiles. The solid black indicates the median and the solid red the mean. The length of the whiskers represents the P10 and P90 percentiles and the filled circles represent the observations less than P05 and greater than P95 (outliers). The specified relationships between turbulence intensity and mean hub-height wind speed for the three International Electrotechnical Commission (IEC) turbulence classes (A, B, and C; see IEC [2005]) are also shown. The turbulence intensities near typical rated wind speeds (11–13 m s^{-1}) are often significantly greater than even the most turbulent IEC Class A. Figure 1-8b plots the distributions of the standard deviation of the streamwise wind component.

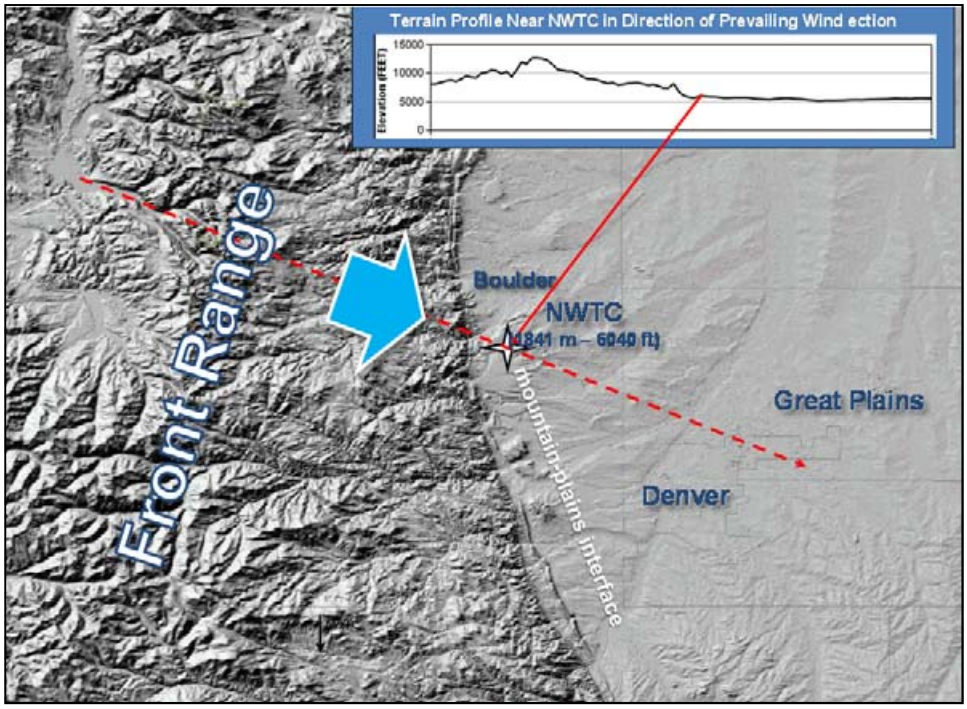

Source: U.S. Geological Survey

Figure 1-6. Topography upwind of NWTC. The inset shows the topography cross section along the prevailing wind direction (dashed line).

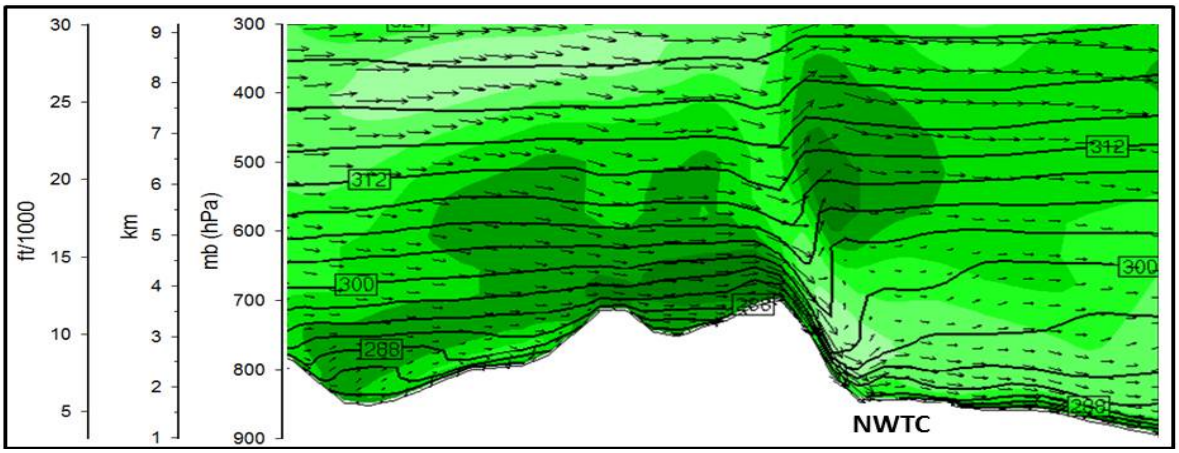

Source: Courtesy of the Research Applications Laboratory of the National Center for Atmospheric Research

Figure 1-7. East-west vertical cross section through Boulder, Colorado, from 20-km resolution Weather Research and Forecasting (WRF) model operational prediction for 1500 GMT on January 13, 2011. The arrows parallel the wind flow and their length is proportional to the speed. The solid lines indicate the potential temperature. The shaded areas represent relative humidity, with the highest values in darkest green. The approximate position of the NWTC is shown. A moderate downslope wind event is forecast with warmer and drier air being brought down by the indicated winds.

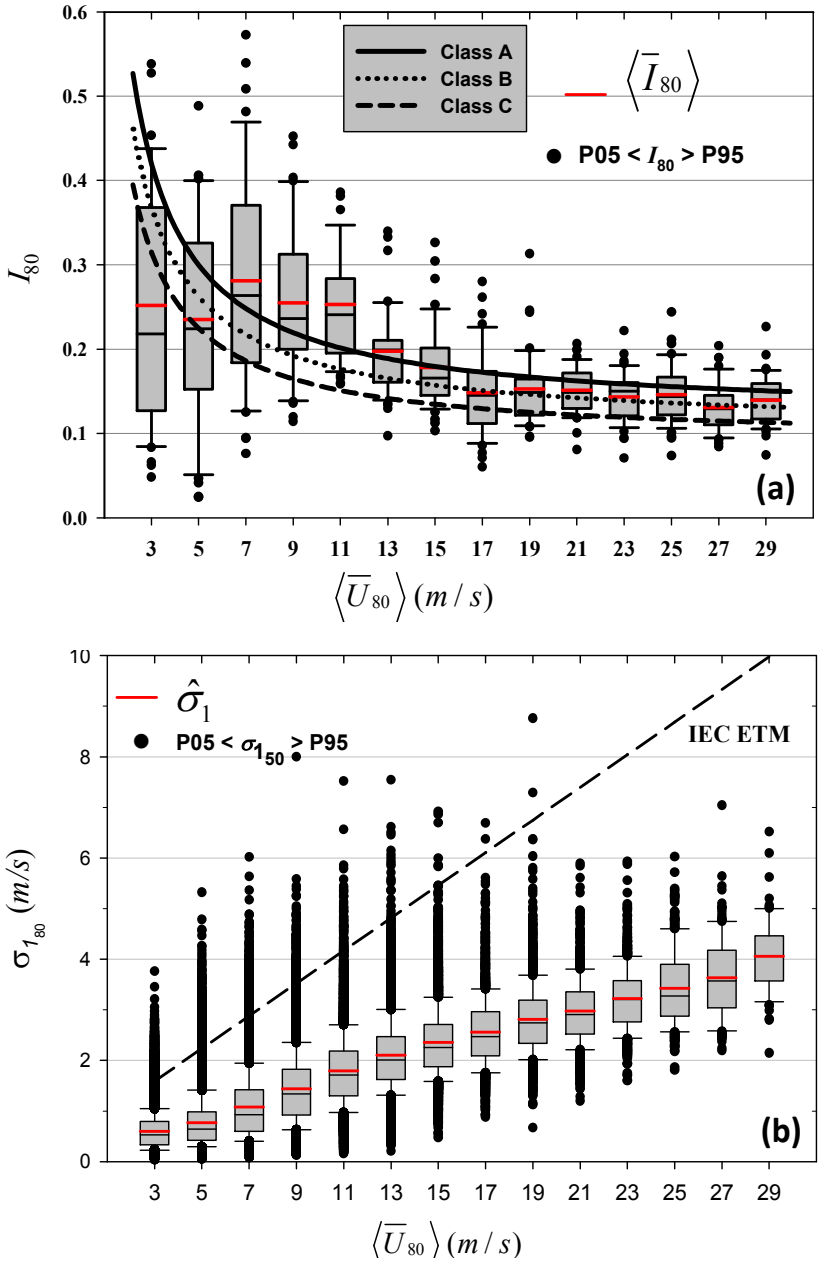

Figure 1-8. Observed NWTC box-plot probability distributions of 80-m (a) turbulence intensity, I_{80}, and (b) *U*-component standard deviation, σ_1 or σ_u

In this figure, filled circles represent the observations less than P05 and greater than P95 (outliers). To demonstrate the severity of this site, the specified relationship between σ_1 (σ_u) and the hub-height mean winds for the IEC Extreme Turbulence Model (ETM) is also plotted in this

figure. Below mean wind speeds of about 17 m s^{-1}, an increasing number of events exceed the ETM criteria.

1.4.3 ART Upwind Planar Inflow Measurement Array

To obtain information about the spatial aspects of the turbulent inflow that was not readily apparent in the measurements on the California Micon 65/13 turbines, we constructed the planar array of five ultrasonic anemometers/thermometers on the three towers shown in Figure 1-9. The array was installed perpendicular to the prevailing wind direction (292 degrees) 65 m (213 ft) upwind of the ART rotor plane. The ultrasonic anemometers/thermometers were three-axis Kaijo Model DAT-600s, which have a 10-Hz measurement bandwidth and velocity and temperature maximum resolutions of 0.002 m s^{-1} and 0.003°C, respectively. In addition to the ultrasonic anemometers, cup anemometers and wind vanes were installed at three heights on the central tower, along with PRTDs in both absolute and differential configurations, a digital microbarometer for measuring surface barometric pressure, and an LiCl/PRTD hygrometer for measuring the surface dew point temperature. All data channels were recorded at 40 samples per second. During post-processing, all but the sonic anemometer velocity and temperature measurements were smoothed to one sample per second.

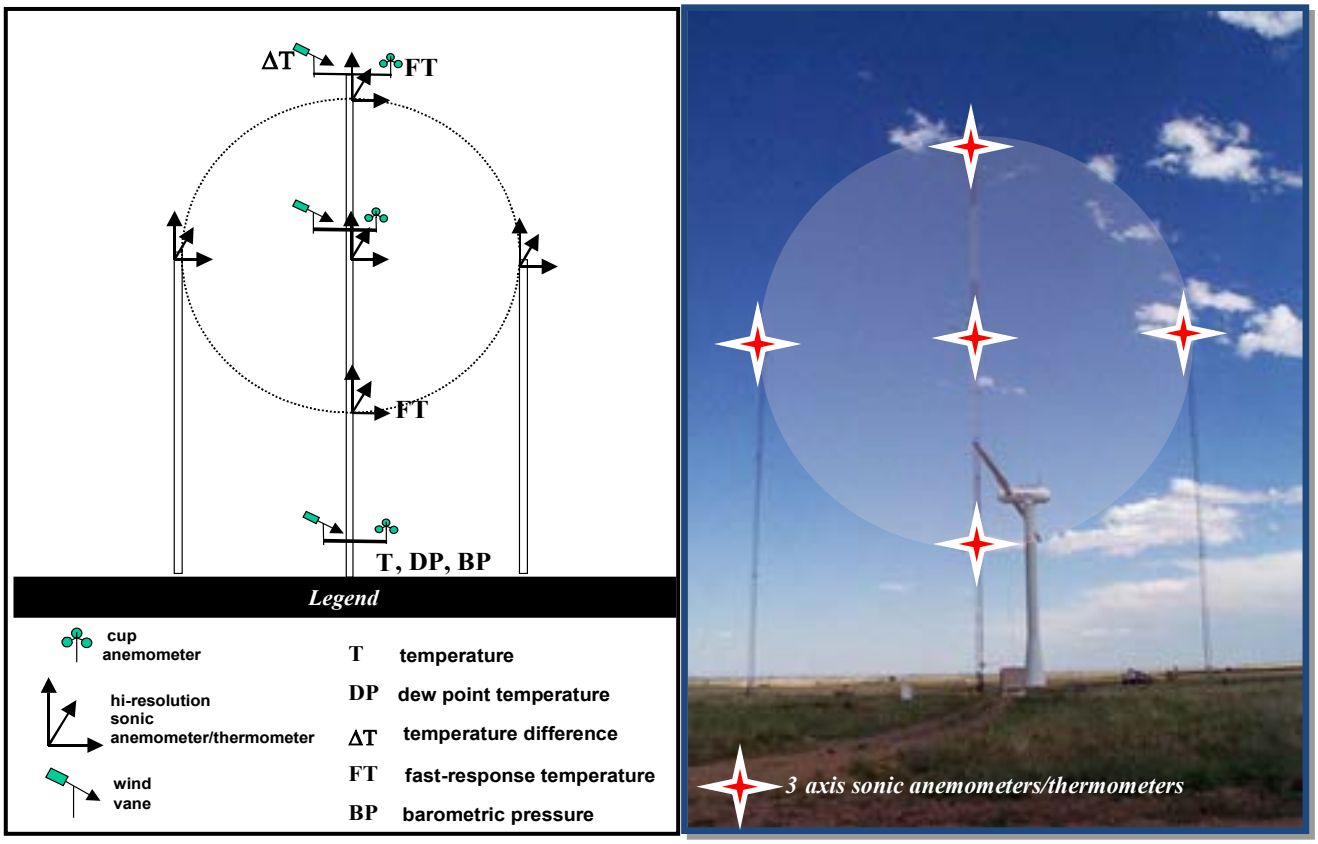

Photo source: N. Kelley, NREL

Figure 1-9. Upwind planar measurement array used for measuring turbulent inflow to NWTC ART. The maximum and minimum heights were 58 and 15 m, with the left, center, and lateral measurements at the hub height of 37 m and spaced 21 m apart. The array was located 65 m upwind of the turbine rotor plane.

1.5 The Lamar Low-Level Jet Program (LLLJP)

The LLLJP, although not using an operating wind turbine as did the California wind farm and NWTC experiments, was performed to obtain detailed information about the turbulence conditions in the atmospheric layer beneath nocturnal low-level jet streams (LLJs), a portion of which would be occupied by 106 Enron (now GE) 1.5-MW wind turbines. The LLLJP was established in the late summer of 2001 as joint effort between the NWTC and Enron Wind. NREL's purpose was to gather the information that we used to develop the Great Plains Low-Level Jet (GP_LLJ) spectral model in NREL's TurbSim.

Enron installed a 120-m (400-ft) met tower at the site of a planned wind farm development about 32 km (20 miles) south of Lamar, Colorado, in southern Prowers County. NREL instrumented that tower with several levels of sensitive instrumentation to measure the turbulence environment. Continuous, high-speed turbulence data collection took place during the stable boundary layer hours of 1600 to 0800 LST between March 2002 and March 2003. In addition, NREL installed an acoustic wind profiler or sodar nearby to locate and quantify low-level jets seen over the site and correlate that information with turbulence data collected on the tower. It was operated during the primary low-level jet season of May through November 2002. A collaborative program with the National Oceanic and Atmospheric Administration's Environmental Systems Research Laboratory (NOAA/ESRL) using high-resolution Doppler lidar (HRDL) in conjunction with the NREL tower-based measurements and the sodar was conducted during the first 2 weeks of September 2003. The LLLJP site is situated on a high plateau south of the Arkansas River Basin. Figure 1-10a shows the regional and local topography overviews surrounding the experimental site. Locally, as illustrated in Figure 1-11, the terrain is flat and homogenous but with more complex elements to the west and north (Figure 1-10b).

1.5.1 LLLJP Measurements

At the LLLJP site, the base of the 120-m (400-ft) tower is at an elevation of 1,357 m (4,451 ft) above MSL. Views of the site and the tower-mounted instrumentation, in Figures 1-11 and 1-12, show three-axis sonic anemometers/thermometers installed at heights of 54, 67, 85, and 116 m (177, 220, 279, and 380 ft). To measure wind speed and direction, cup anemometers and highly damped direction vanes were mounted at 3, 52, and 113 m (10, 171, and 419 ft).

Absolute air temperatures derived from PRTDs were measured at heights of 3, 52, and 113 m with temperature differences measured between 52 and 83 m (272 ft) and between 83 and 113 m. All temperature measurements were acquired with four-wire PRTDs placed within mechanically aspirated radiation shields.

Dew point temperatures were measured at 3, 52, 85, and 113 m with LiCl/PRTD dew point hygrometers. Barometric pressure was measured at a height of 3 m using a digital microbarometer pressure transducer that was connected to an external omnidirectional sampling head on the exterior of the building. A Scintec MFAS acoustic wind profiler or sodar was installed and operated 109 m (358 ft) southwest of the tower base, as shown in Figures 1-13b, c, and d. It was programmed to acquire vertical wind profiles with a 10-m (33-ft) vertical resolution from 40 to 500 m (131 to 1,640 ft).

The NOAA HRDL installed south of the sodar operated for 2 weeks in early September 2003. Figure 1-14a pictures the location of the lidar with respect to the 120-m tower. Figure 1-14b

shows the HRDL being used to observe the evolution of an LLJ. Figure 1-14c presents a processed example of such an observed LLJ evolution.

The tower-based measurements were collected using two recording systems. A dedicated data logger collected a subset of the measurements at a rate of 1/s (not including the sonic anemometers) and saved it as statistics (means and standard deviations for wind-related parameters) calculated over a 5-minute period. A second computer-based system was employed to collect the high-resolution sonic information in addition to the other tower data. Data were collected at 20 samples per second on all data channels continuously each day from 1600 to 0800 LST to observe conditions primarily in the nocturnal boundary layer. The data were processed using a five-pass process and placed into archives of derived parameters that included up to fourth order statistics. For the analyses discussed in this report, we used more than 28,000 10-minute high-speed turbulence records collected from April 1, 2002, to March 31, 2003, and again from August 30, 2003, through September 16, 2003.

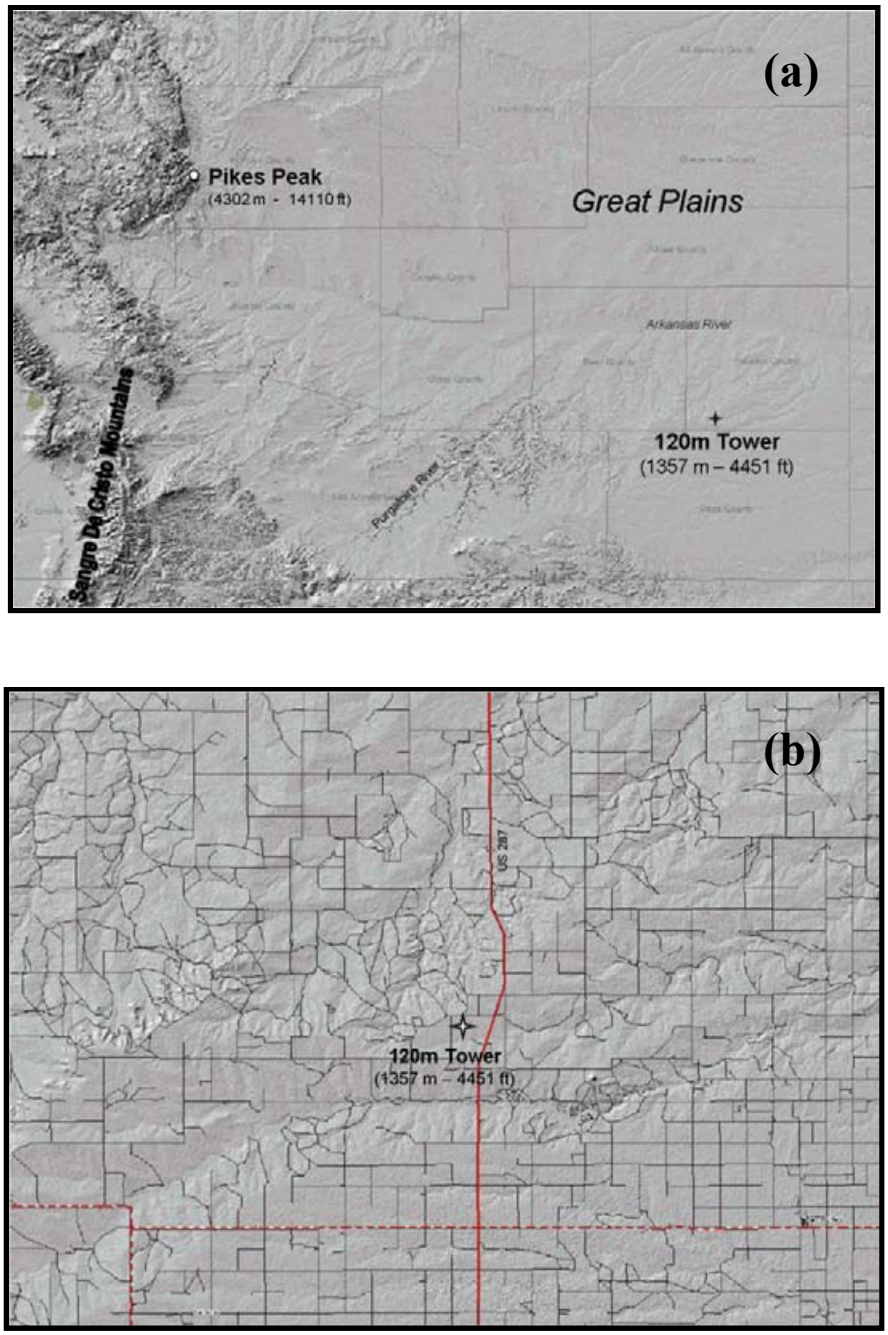

Source: U.S. Geological Survey

Figure 1-10. Location of LLLJP experiment site and 120-m tower in high plains of southeastern Colorado: (a) regional topography and (b) local topography

Source: N. Kelley, NREL

Figure 1-11. Enron (GE) Wind 120-m met tower, southeastern Colorado (LLLJP site)

Source: N. Kelley, NREL

Figure 1-12. Close-up of NREL turbulence-measuring instrumentation installed on Enron (GE) 120-m LLLJP tower

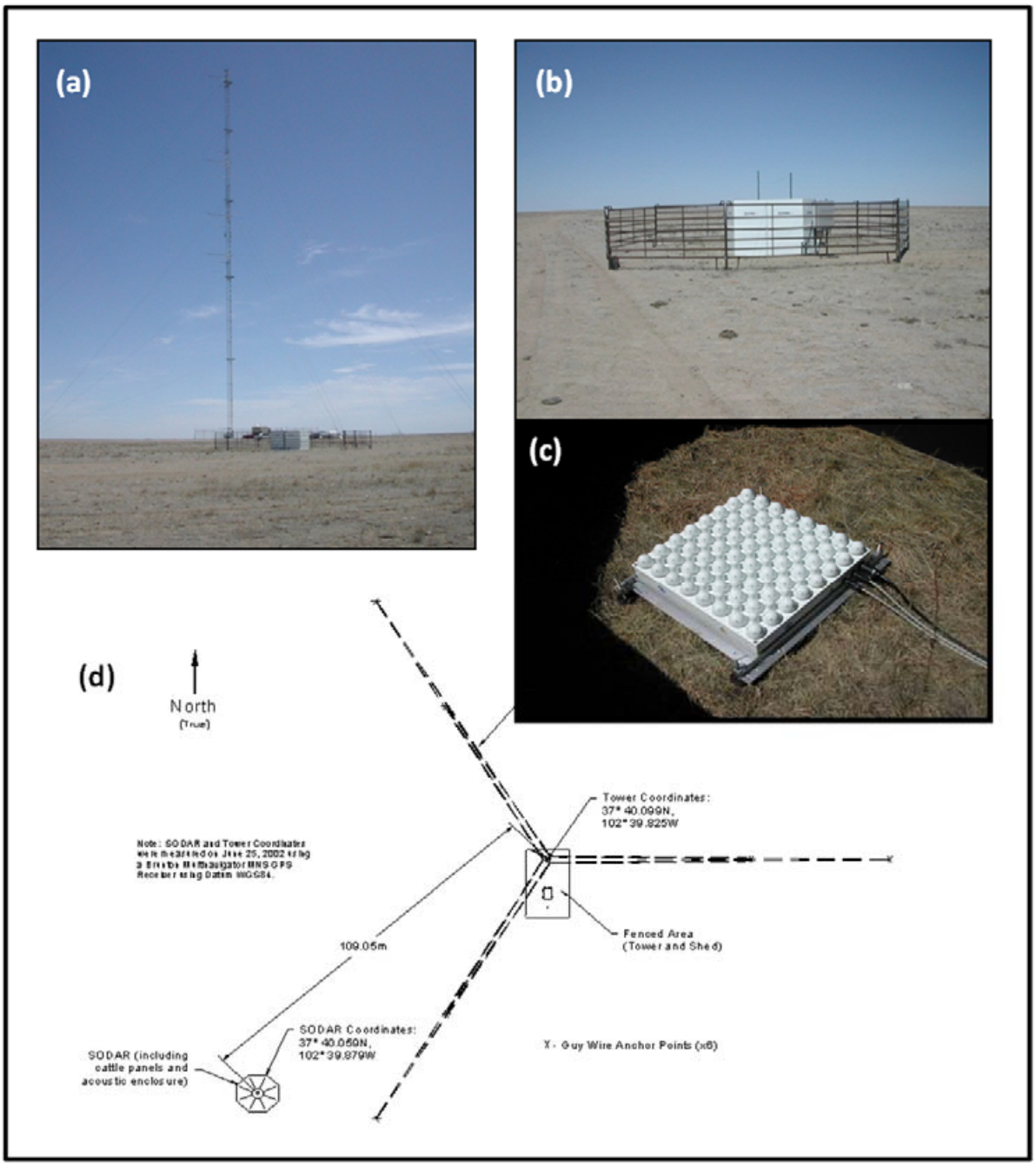

Photos Source: N. Kelley, NREL; Diagram: D. Jager, NREL

Figure 1-13. Instrumentation layout at LLLJP measurement site: (a) tower; (b) nearby sodar; (c) Scintec MFAS sodar antenna within enclosure; and (d) plan view of site layout

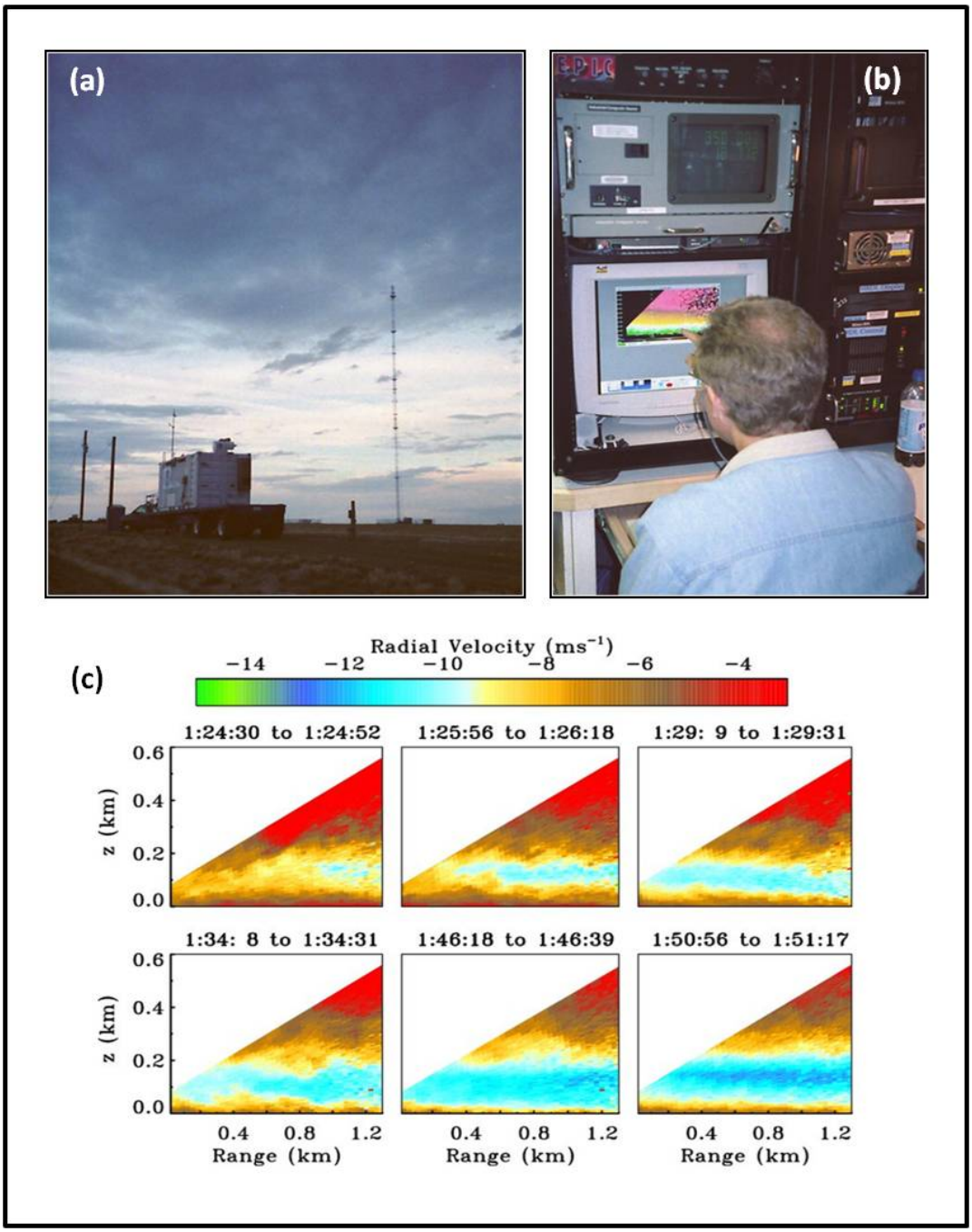

Photo Source: N. Kelley, NREL

Figure 1-14. NOAA/ESRL HRDL lidar in operation at LLLJP site: (a) position of lidar with respect to 120-m tower; (b) NOAA's Robert Banta making observations; (c) vertical scans through evolving LLJ. The strongest winds in the last frame on the lower right would be at the top of the GE 1.5-MW turbine rotors now installed at this site. Wind speed scale is at the top, with negative values indicating the wind was coming toward the lidar. Times are in UTC (18:24:30 to 18:51:17 MST).

2.0 Defining the Turbine Inflow Turbulence Characteristics

2.1 Wind Turbine Turbulence Operating Environment

Wind turbines operate in the lowest part of the atmosphere, which is called the planetary boundary layer (PBL). Until relatively recently, most turbines operated in the lowest portion of the PBL, the surface layer (SL). In this layer, the influence of the frictional drag induced by the ground is most significant. The SL is characterized by a strong diurnal variation in both the change of wind speed with height and turbulence characteristics. It is a consequence of heat being added to the atmosphere during the day and removed at night. The daytime or convective SL is generally deeper than its nocturnal counterpart because of the intense turbulent mixing by large buoyant eddies. This results in vertical transport (fluxes) of heat and momentum that are nearly constant with height. The nocturnal SL is usually much shallower. At some point the surface drag may become great enough to cause the winds above to decouple and accelerate relative to the slower moving air near the surface, which can create significant velocity shears and perhaps a low-level maximum (jet) in the wind profile. The vertical distribution of temperature and buoyancy determines the behavior of vertical air motions. The SL is considered statically unstable if the motions increase in intensity with height and stable if they are suppressed to some degree.

As wind turbine rotors have increased in size and height, their rotors have exceeded the maximum height of the SL and now reach into the mixed or residual layer (ML or RL). The depth of the ML can vary from a few hundred meters to as much as 2 km above ground level. Most important is that the turbulence characteristics of the ML can be quite different from those in the SL. In addition, the turbulence scaling relationships of the ML are not as well understood as those in the lower SL. The turbulence models currently used in the turbine design standards used for type certification are based on SL scaling and characteristics. As a result, they do not always adequately reflect the wind and turbulence characteristics that occur in the ML.

2.2 Turbulent Energy Production and Scaling

To understand how atmospheric turbulence—or perhaps the kinetic energy contained within atmospheric turbulence—induces dynamic responses in a wind turbine as its rotors ingest that turbulence or energy, it's helpful to see what controls the energy level within the turbine inflow. A useful device here is to define the components of the turbulent kinetic energy (TKE) budget.

2.2.1 The TKE Budget

If we assume that the turbulence is relatively homogeneous in the horizontal (at least over distances much greater than the turbine rotor disk diameter), neglect large-scale atmospheric sinking motions (subsidence), and ignore the effects of moisture, we can use a reduced form of the local TKE budget suggested by Panofsky and Dutton (1984) as

$$\frac{\partial \overline{E}_T}{\partial t} = \underbrace{-(\overline{u'w'})\left(\frac{\partial \overline{u}}{\partial z}\right)}_{\mathbf{I}} + \underbrace{\frac{g}{\overline{T}}(\overline{w'T'})}_{\mathbf{II}} \underbrace{-\frac{\partial}{\partial z}(\overline{w'E_T})}_{\mathbf{III}} - \varepsilon \,. \tag{2-1}$$

Here we define E_T as the total TKE present or contained with the volume of the air being measured, which we define as

$$E_T = E_{iso} + E_{coh} \quad , \tag{2-2}$$

where E_{iso} is the isotropic contribution to E_T and E_{coh} is the coherent portion, given by

$$E_{coh} = 1/2[(u'w')^2 + (u'v')^2 + (v'w')^2]^{1/2} . \tag{2-3}$$

By coherent we mean intermittent patches of turbulence, which have a definite spatial-temporal organization, in the flow. We have found that on average the ratio $\overline{E_{coh} / E_T}$ tends to be about 0.4, indicating that most of the time the observed turbulence was not purely isotropic (when E_{coh} would have been 0). The distinction between E_T and E_{coh} will become clearer later. The mean flow has been aligned with the mean wind direction, so *u, v,* and *w* represent the streamwise, lateral, and vertical velocity components in an orthogonal right-handed coordinate system. In this system, positive *u* points in the downwind direction, *v* is positive to the left, and positive *w* follows the direction of positive *z*. Height is indicated by *z* positive upward, *g* is the gravity acceleration, ε is the viscous dissipation rate of TKE, and θ is the potential temperature given by

$$\theta = T\left[\frac{p_o}{p}\right]^{0.286} , \tag{2-4}$$

where *T* is the air temperature in degrees Kelvin and the reference atmospheric pressure p_o is 1,000 if the atmospheric pressure *p* is in hectopascals (hPa; millibars [mb]). The primed quantities represent fluctuating values from which the mean has been removed.

Equation 2-1 expresses the contributions to the local rate of change in total TKE that a wind turbine blade passes through. Term **I,** a production term that is always positive, is the product of the mean vertical flux or transport of horizontal momentum $(\overline{u'w'})$ and the mean vertical shear. Term **II** can be either positive or negative, depending on the sign of mean vertical temperature flux $(\overline{w'\theta'})$. This is the buoyancy term that, if positive, adds energy to the TKE of the air. If negative, the buoyancy term removes energy from the TKE of the air by damping or slowing down the motions of the turbulent eddies. Buoyant turbulence production/damping is an anisotropic process because it acts only in the vertical (Stull 1988, p. 157). We will see this later in the report. The damping action, in particular, plays a significant role in the characteristics of the turbulence being generated and the resulting wind turbine rotor aeroelastic response. Term **III** represents the vertical transport of total TKE into and out of the local volume. Later we see that the vertical transport of the coherent content of the TKE ($w' E_{coh}$) can also be very important in the dynamic response of wind turbines to turbulence. The quantity ε represents the energy loss due to viscous dissipation.

The vertical transport or fluxes of heat, moisture, and momentum are relatively constant with height in the SL. The height of this layer can reach 100 m during the day, but it is much shallower at night. Monin and Obukhov (M-O; 1954; as referenced in Kaimal and Finnigan

[1994]) demonstrated that the turbulence in the SL can be scaled by only a few parameters measured at the surface (similarity theory). These include the velocity, temperature, and height scaling parameters, where the overbar indicates a temporal mean:

$$\text{friction velocity, } u_{*_o} = [-\left(\overline{u'w'}\right)_o]^{1/2} \tag{2-5}$$

$$T_* = \frac{-\left(\overline{w'\theta'}\right)_o}{u_*} \tag{2-6}$$

$$\text{M-O length, } L_{M-O} = \frac{-u_*^3 \overline{\theta}}{kg(\overline{w'\theta'})} \quad , \tag{2-7}$$

where $k \cong 0.4$. Equation 2-1 can now be rewritten as

$$\frac{\partial \overline{E}_T}{\partial t} = u_*^2 \left(\frac{\partial \overline{u}}{\partial z} \right) + \frac{g}{\overline{T}} (\overline{w'T'}) - \frac{\partial}{\partial z} (\overline{w'E_T}) - \varepsilon. \tag{2-8}$$

So the local mean rate of change of E_T within a turbine rotor disk is the sum of the turbulence being generated by the shearing stress, the turbulent buoyancy flux, the transport of externally generated E_T into the volume, and the energy being lost to viscous dissipation.

2.2.2 Atmospheric Stability

The vertical distribution of heat, momentum, and moisture has a strong influence on the characteristics of PBL turbulence, including the spectral distribution of E_T and therefore, by our definition, its constituents E_h *and* E_{coh}. A measure of stability that we have found very useful in correlating wind turbine aeroelastic responses is the gradient Richardson number, *Ri*, given by

$$Ri = \frac{\left(g / \overline{\theta}\right)(\partial \overline{\theta} / \partial z)}{\left(\partial \overline{u} / \partial z\right)^2}. \tag{2-9}$$

The *Ri* is the ratio of turbulence production/damping produced by buoyancy to that being produced by shear. A negative value of *Ri* (unstable conditions) indicates convective turbulence generation conditions. A positive value (stable conditions) indicates that turbulence generation is being suppressed. A value of zero is associated with neutral conditions in which turbulence is being created solely by shearing stress (vertical wind shear) and buoyancy plays no role. This condition is rare in the layers generally occupied by modern wind turbines, at least over a 10-minute period. For example, during an entire year of data collected at the Lamar Low-Level Jet Project (LLLJP) site on the high plains of southeastern Colorado, neutral stability conditions measured over heights ranging from 3 to 115 m above the surface were observed only 0.14% of the time.

In the SL under steady conditions, appropriate stability scaling is given by the ratio of the height to the M-O length $L_{M\text{-}O}$, or

$$z / L_{M-O} = -\frac{\left(g / \overline{\theta}\right)\left(\overline{w'\theta'}\right)_o}{u_*^3 / kz} \quad , \tag{2-10}$$

where the zero subscript indicates the buoyancy flux is measured at the surface (Kaimal and Finnigan 1994). A negative value of $z/L_{M\text{-}O}$ indicates unstable conditions; a positive one indicates stable conditions. Above the SL, M-O similarity scaling tends to break down, particularly in stably stratified nocturnal boundary layers. No universal consensus currently exists on how to scale ML turbulence. Today, because of their height, the rotor disks of most large wind turbines reside completely within the ML/RL, particularly at night. We believe that turbulence scaling that is sufficient for a turbine rotor operating within the SL is inadequate for one immersed in partially or entirely within the ML. It has been found that local scaling is often useful in the ML (Holtslag and Nieuwstadt 1986). Here locally measured values of the scaling parameters u_* and z/L are used to scale turbulence frequency spectra and other properties; therefore, they are functions of height.

As we will see when we discuss the turbulence scaling used in TurbSim stochastic inflow turbulence code (TurbSim), our approach is a hybrid arrangement that uses both surface-based and locally scaled parameters. The amplitude and frequency distributions of the spectral distributions of the turbulence wind components in the SL are functions of $[u_*]_o$ and $[z/L_{M\text{-}O}]_o$, as found by Kaimal and colleagues (1972). Our hybrid scaling approach uses the turbine layer gradient Richardson number (Ri_{TL}) as a primary scaling parameter for both the turbulent inflow and turbine aeroelastic responses. It is calculated over the height of the vertical layer from near the surface (2 to 3 m) to the maximum height of the turbine rotor disk. To properly scale the turbulence frequency spectra, then, we needed to find an equivalent value of local $z/L_{M\text{-}O}$ from Ri_{TL}. Businger and coauthors (1971) found the following relationships for the SL over flat, homogeneous terrain under steady (equilibrium) conditions:

$$Ri = \begin{cases} z / L_{M-O}, & -2 \le z / L \le 0 \\ (z / L_{M-O})(1+4.7)^{-1} & 0 \le z / L \le 1 \end{cases} . \tag{2-11}$$

Based on our measurements, we had to modify these relationships for two of the spectral models used in TurbSim. We give more detail on these modifications later in the report.

Finally, we define the flux Richardson number stability parameter (Ri_f) as

$$Ri_f = \frac{\left(g / \overline{T_v}\right)(\overline{w'\theta'})}{\overline{u'w'}\left(\partial\overline{u} / \partial z\right)} = \frac{(g / \overline{T}_v)(\overline{w'\theta'})}{u_*^2(\partial\overline{u} / \partial z)} \quad , \tag{2-12}$$

where T_v is the virtual temperature, defined as the temperature of a parcel of completely dry air that would need to have the same density if it contained moisture. The Ri_f is the ratio of the rate of turbulence production by buoyancy to the rate produced by shear (Kaimal and Finnigan 1994).

We will see later that Ri_f is useful in gaining insight into the physics of an atmospheric dynamic stability condition of importance to wind turbine operations.

2.2.3 Identification of Turbulence-Turbine Response Scaling Variables

The parameters in Equations 2-4 through 2-12 that are responsible for the production and transport (fluxes) of TKE or E_T and its constituents are a useful source of independent variables with which to correlate or scale the dynamic or aeroelastic response of wind turbine components to turbulent conditions. Turbulence variables are separated into mean and fluctuating (zero mean) parts such as $u = \bar{u} + u'$. In addition to height and time, we make particular use of the following turbulence (primed) variables or combinations and the vertical gradients of these variables (such as *Ri*) as predictors of turbine aeroelastic response:

- *u',v',w'* (or equivalently u_i') for the streamwise, lateral, and vertical turbulent (fluctuating) wind velocity components
- u_*, or equivalently $\overline{u'w'}$
- The Reynolds stress components *u'w'*, *u'v'*, and *v'w'*
- The potential θ' and absolute *T'* temperatures.

3.0 Analyzing Turbulence-Turbine Dynamic Response of Micon 65/13 Turbines

In this section we discuss the results of our correlation of the dynamic loads and fatigue damage observed on the Micon 65/13 turbines in the California wind farm. Our objective was to identify turbulence characterization parameters that showed strong correlations with the turbine structural and aeroelastic response and could be used to scale that response.

3.1 Identifying Turbine Response and Turbulence Scaling Parameters

A major objective of our study was to identify the inflow conditions responsible for significant accumulations of fatigue damage in turbine components. Accordingly, measurements of dynamic loads formed the basis of the turbine response variables. We used the measured loads data from the available 397 records and applied load cycle-counting using the Downing-Socie rainflow algorithm (Downing and Socie 1982). This gave us distributions of alternating bending moment loads or stress cycles ($M_{p\text{-}p}$). We found that these loading spectral distributions were of the mixed type and could be fitted as the sum of a Gaussian distribution for the frequent, low-amplitude stress cycles and (with the exception of the edgewise root bending stress) as a decaying exponential distribution for the less frequent higher amplitude stresses. This is schematically diagrammed in Figure 3-1. We then fitted individual exponential distributions of N_{cyc} for each of the available data records and found the corresponding slopes, β_1. This is schematically diagrammed in Figure 3-2 and given by

$$N_{cyc} = \beta_0 e^{-\beta_1 M_{p-p}} \quad . \tag{3-1}$$

As an example of a turbine of a different design, Figure 3-3 pictures an observed exponential alternating root bending load distribution measured by the National Renewable Energy Laboratory (NREL) on a two-bladed, downwind AWT-26 turbine installed in the Tehachapi Pass area of Southern California.

Figure 3-4 shows an example of the characteristic shape of a root edgewise cyclic load spectrum measured by NREL on a similar but modified Micon 65/13 (called a Micon 65/13M) turbine operated at a Great Plains site near Bushland, Texas. Again, the entire load spectrum can be expressed as a mixed distribution. The decaying high-cycle, low-amplitude peak at the left is

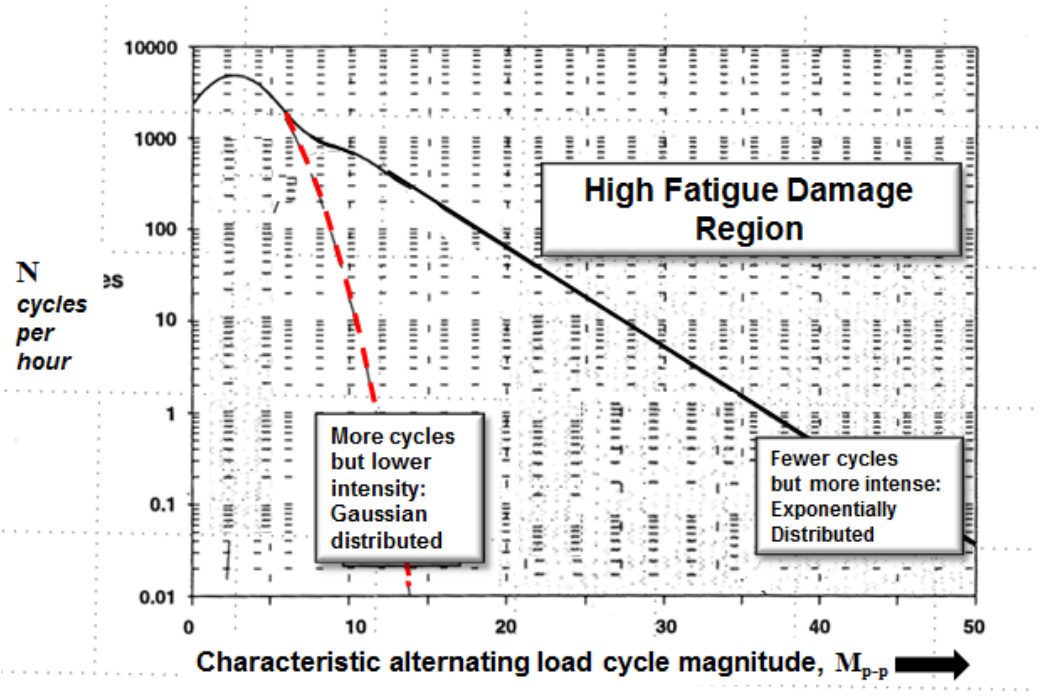

Figure 3-1. Schematic of relationship of high-frequency, low-amplitude Gaussian stress cycle distributions with lower frequency, high-amplitude exponentially distributed stress cycles

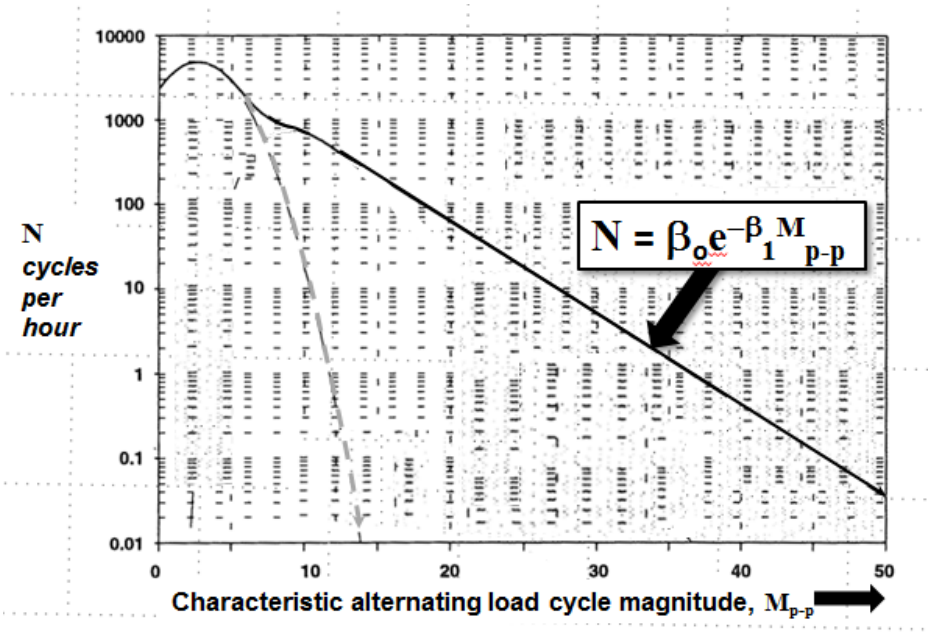

Figure 3-2. Schematic showing definition of exponential fit to high-amplitude, low-frequency tail of alternating stress cycle distribution

well approximated by a Gaussian distribution. We found that the more important (from a fatigue perspective) second peak could be accurately fit with a Type I extreme value distribution where this peak corresponds to the cyclic loading induced by gravity and is given by

$$N_{cyc} = \gamma_0 \exp\left[-\exp\left[-\left(\frac{M_{p-p}-\gamma_1}{\gamma_2}\right)\right]-\left(\frac{M_{p-p}-\gamma_1}{\gamma_2}\right)+1\right], \tag{3-2}$$

where γ_2 is the shape parameter that quantifies the high-loading slope portion of the rightmost peak distribution shown in Figure 3-4.

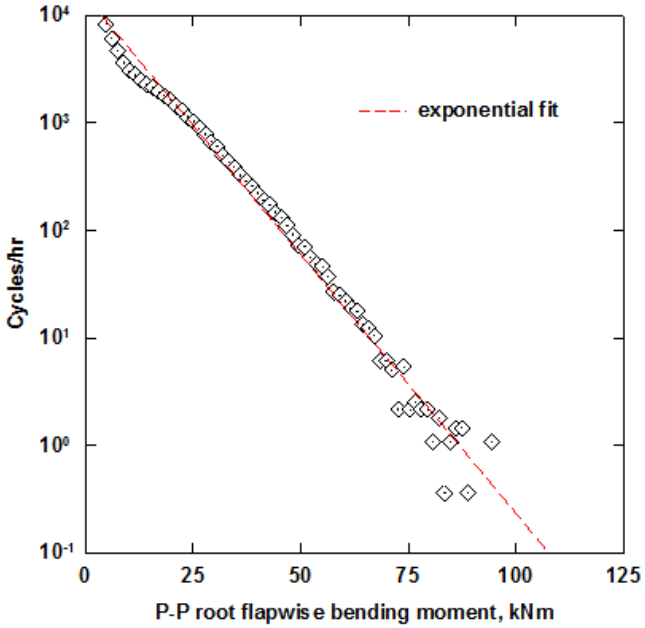

Figure 3-3. Example of root flapwise root bending spectrum from AWT-26 turbine installed in Tehachapi Pass, California

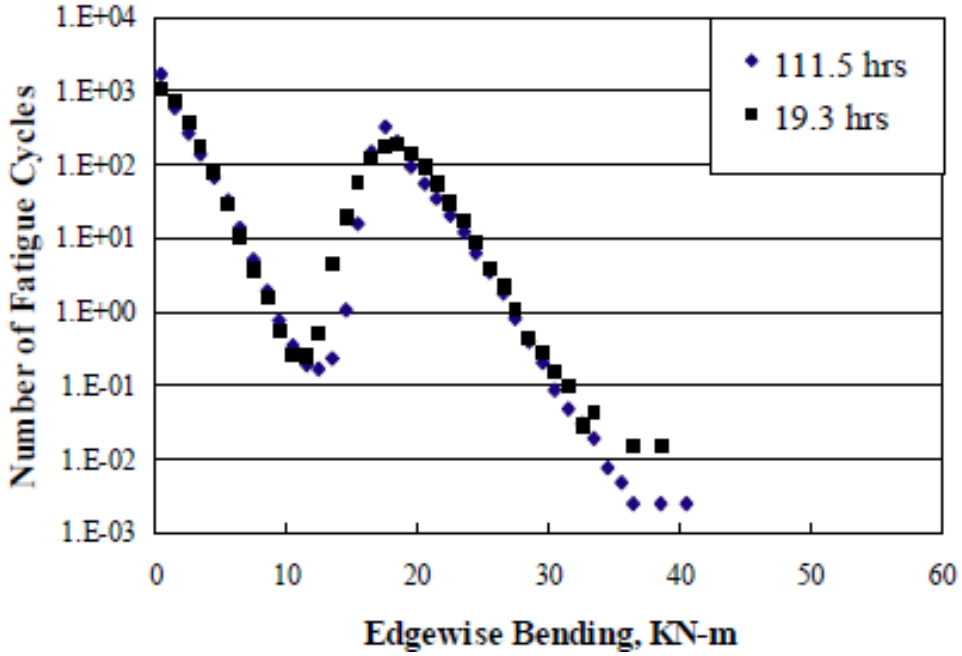

Source: Sutherland and Mandell (2004)

Figure 3-4. Examples of two aggregated record periods of 111.5 and 19.3 hours of root edgewise cyclic load spectra from modified Micon 65/13 "M" turbine installed in Bushland, Texas, for mean wind speeds in 11- to 13-m s^{-1} range. The peak near 20 kNm is the cyclic load induced by gravity.

The greatest fatigue damage occurs in the high-amplitude tail, particularly for the composite materials used in wind turbine blades (see Veers [1983] and Sutherland [1994, 1999]). We hypothesized that the slopes of the high-amplitude tails, as described by the exponential and extreme value distribution shape parameters β_1 and γ_2 in Figures 3-2 and 3-4, are proportional to the cumulative fatigue damage. A sharp downward slope indicates fewer large stress cycles and less fatigue damage, whereas a shallow slope is related to a greater number of higher amplitude loading cycles and greater fatigue damage.

Our preliminary analysis of the behavior of these slopes indicated that the rates of change were strongly related to the character of the inflow turbulence. To establish such a connection, we applied stepwise multiple-linear regression analysis techniques and analysis of variance (ANOVA). Next we identified the turbulence scaling parameters that were the most efficient in predicting the slopes of the high-amplitude loading cycles of the available turbine dynamic parameters. To accomplish this, we stratified the population of 10-minute records from the two Micon 65/13 turbines into three stability (Ri_{TL}) and six hub mean wind speed categories. Unfortunately meteorological scaling variables are often inherently cross-correlated to varying degrees. This results in significant colinearity in the multiple-regression modeling results and can mask the true relationships. The purpose of turbulence similarity scaling discussed earlier was to identify a set of independent scaling parameters for the surface layer (SL). Monin and Obukhov (1954) found that the u_*, the T_*, the M-O length $L_{M\text{-}O}$, and the height above the ground z

satisfied the independence requirement for turbulent flows that are in equilibrium (both mechanically and thermally) with the underlying surface.

We cross-correlated the following inflow turbulence characteristic parameters with values of the β_1 and γ_2 load spectral shape parameters:

- The mean hub-height horizontal wind speed, $\overline{U}_H$
- Standard deviation, σ_H
- Turbulence intensity, $\sigma_H / \overline{U}_H$
- Wind direction standard deviation, σ_{WD}
- The local (hub-height) and turbine layer friction velocities u_{*hub} and u_{*o} respectively
- The three mean turbulence Reynolds stresses, $\overline{u'w'}$, $\overline{u'v'}$, and $\overline{v'w'}$
- The turbine layer vertical stabilities *Ri* and $z/L_{M\text{-}O}$.

We used a stepwise regression process to correlate groups of turbulence parameter predictors with the response variables β_1 and β_2. The process was continued until the remaining predictors converged to a maximum value of the coefficient of multiple regression R^2 at the 95% confidence level.

The results from both turbines were combined here. In general, the values were higher (better correlations) for the turbine with the NREL rotor because it was more dynamically active and was better matched to the range of wind speeds available. More details are given in Kelley (1993), but Table 3-1 summarizes the results. It is clear from these results that the temporal correlation of the turbulent velocity component covariances (mean Reynolds stress components) can exert a significant influence on the high-amplitude loading events via the β_1 and γ_2 scaling parameters. Figure 3-5 plots the variation of both the flapwise and edgewise load shape parameters with the hub-height value of u_* and the turbine layer value of Ri_{TL}. These plots indicate that the large loading peak occurs not during neutral stability (adiabatic or $Ri_{\mathrm{TL}} = 0$) conditions but when the stability of the flow resides within a narrow and weakly stable range; i.e., $+0.01 < Ri_{\mathrm{TL}} < +0.05$. This means that diabatic flow conditions must be considered when simulating the turbulent inflows needed to drive the dynamic design codes. Considering these conditions allows us to reproduce the loading conditions seen over the important narrow and weakly stable Ri_{TL} range indicated in Figure 3-5.

Table 3-1. Correlation of Loading Distribution Model Shape Parameters with Turbulence Parameter Predictors

Turbine Dynamic	Statistical Model	Scaling Parameter β_1	
		Dominant Inflow Predictor(s)	***Coefficient of Multiple Regression R^2***
Root flapwise bending moment	Exponential	$u_{*_{hub}} = \left[-\left(\overline{u'w'}\right)\right]^{1/2}$	0.71
Low-speed shaft torque	Exponential	$u_{*_{hub}} = \left[-\left(\overline{u'w'}\right)\right]^{1/2}, Ri$	0.61
Low-speed shaft bending	Exponential	$u_{*_{hub}} = \left[-\left(\overline{u'w'}\right)\right]^{1/2}$	0.88
Yaw-drive torque	Exponential	$\left(\overline{u'w'}\right)^{1/2}, \left(\overline{u'v'}\right)^{1/2}, Ri$	0.76
Tower-top torque	Exponential	$\overline{U}_H, \left(\overline{u'w'}\right)^{1/2}$	0.77
Tower axial bending	Exponential	σ_H	0.61
Tower in-plane bending	Exponential	$\overline{U}_H, \left(\overline{u'v'}\right)^{1/2}$	0.67
Nacelle axial thrust	Exponential	$\left(\overline{u'w'}\right)^{1/2}, \left(\overline{u'v'}\right)^{1/2}$	0.26
Nacelle in-plane thrust	Exponential	$\overline{U}_H, \left(\overline{u'v'}\right)^{1/2}$	0.59
Tower axial thrust	Exponential	$\left(\overline{u'w'}\right)^{1/2}, Ri$	0.38
Tower in-plane thrust	Exponential	$\left(\overline{u'w'}\right)^{1/2}, \left(\overline{u'v'}\right)^{1/2}, \left(\overline{v'w'}\right)^{1/2}$	0.48
		Scaling Parameter γ_2	
Root edgewise bending moment	Extreme Value	$\left(\overline{u'w'}\right)^{1/2}, \left(\overline{v'w'}\right)^{1/2}$	0.74

Source: Kelley (1993)

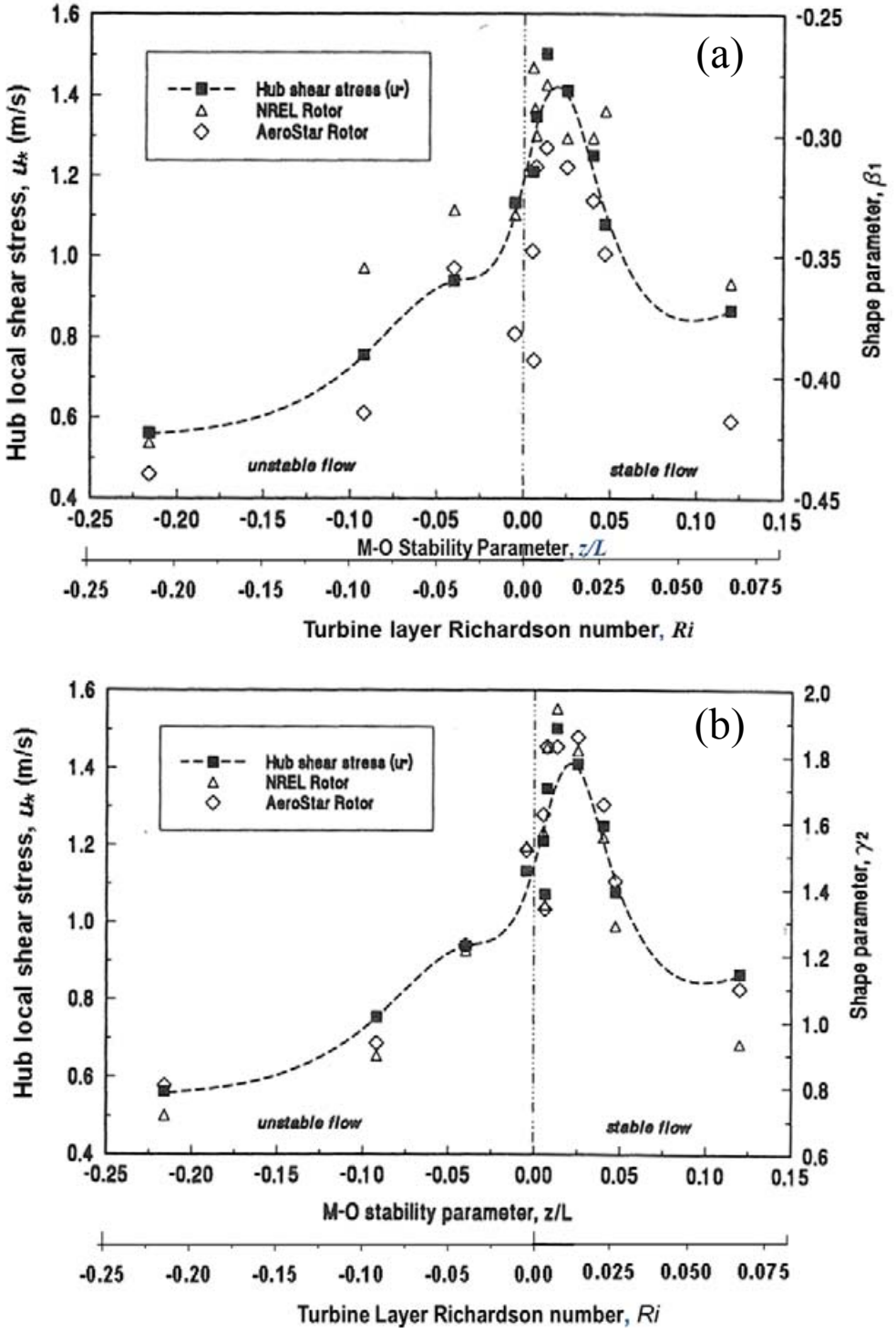

Figure 3-5. Variation of blade root load (a) flapwise (β_1) and (b) edgewise (γ_2) shape parameters with hub-height u_* and Ri_{TL}

3.2 Measuring Fatigue Damage

Sutherland and Kelley (1995) analyzed the flapwise root loads data collected from the two Micon 65/13 turbines. They computed the fatigue damage using Miner's rule for a GP 0/45 laminate material and based on the measured cyclic root flapwise load spectra from each of the blades. The results confirmed our hypothesis that the bulk of the damage occurs from the relatively infrequent, high-amplitude load cycles (100 cycles/h or less, that is, the exponentially decaying tail in the lower right of Figures 3-1, 3-2, and 3-3). The greater numbers of large load cycles in these tails also translate to a smaller or shallower slope β_1 in the exponential distribution. This is the condition that occurs in the narrow stability range shown in Figure 3-5, which would suggest that high fatigue damage occurs under such conditions. Sutherland and Kelley also found that most of the fatigue damage occurs in the 11- to 13-m s^{-1} hub-height mean wind speed range. This range includes the rated wind speed for the turbine equipped with the NREL rotor. The resulting fatigue damage for the available observations was almost identical for both turbines.

3.3 Using Stochastic Turbulence Inflow Simulation

In 1992 Kelley expanded the original stochastic inflow turbulence simulator SNLWIND developed by Veers (1988; see also Kelley [1992]). He used the measurements collected in 1989 from the two 50-m met towers upwind and downwind of the California wind farm. Using these data and Veers' single wind component adiabatic simulation as the computational kernel, he developed a diabatic simulation of the vector wind (three wind components: streamwise, *u*; cross-wind or lateral, *v*; and vertical, *w*). Kelley developed site-specific spectral distributions and spatial/temporal coherence models over the observed range of atmospheric stabilities, producing a simulation model called SNLWIND-3D. Along with much of the original SNLWIND, Kelley's work forms the basis of TurbSim. What has been called the "Sandia Method" of the original SNLWIND code continues to provide the computational kernel of TurbSim. In 1996, Kelley, in support of the collaboration with Sandia National Laboratories (SNL), added a spectral model simulation to the SNLWIND-3D code to simulate conditions at Row 37. He used the 1990 data taken from the met tower upwind of the two Micon 65/13 turbines to provide local scaling. The spectral models available in the SNLWIND-3D code were identified as Upwind or Row 1, Row 37 (7 D row-to-row turbine spacing), and Downwind (14 D spacing to nearest upwind operating turbines). Spectral models specified by the International Energy Commission (IEC) Kaimal and von Kârmân Normal Turbulence Models (NTMs; IEC 2005; IEC 1999) were also later incorporated.

Kelley and Sutherland (1996) compared the fatigue calculated from long-term simulations using SNLWIND-3D. The simulations included a full diurnal cycle with varying boundary conditions at Rows 1 and 41 of the California wind farm and an 8-hour simulation of with constant boundary conditions at Row 37. The inflow simulations were used to drive an aeroelastic model of the Micon 65/13 using the generalized, multibody dynamics code ADAMS® (now MSC.ADAMS®). The simulated results were compared with 2.3 hours of measured data from the Micon 65/13 with the NREL rotor. The fatigue damage calculated from the simulations was considerably less than that calculated from the measurements using Miner's Rule. Examining the predicted and observed load spectra revealed that the simulations lacked the few but very large-amplitude cycles that were present in the observed data. The lack of those large-amplitude cycles

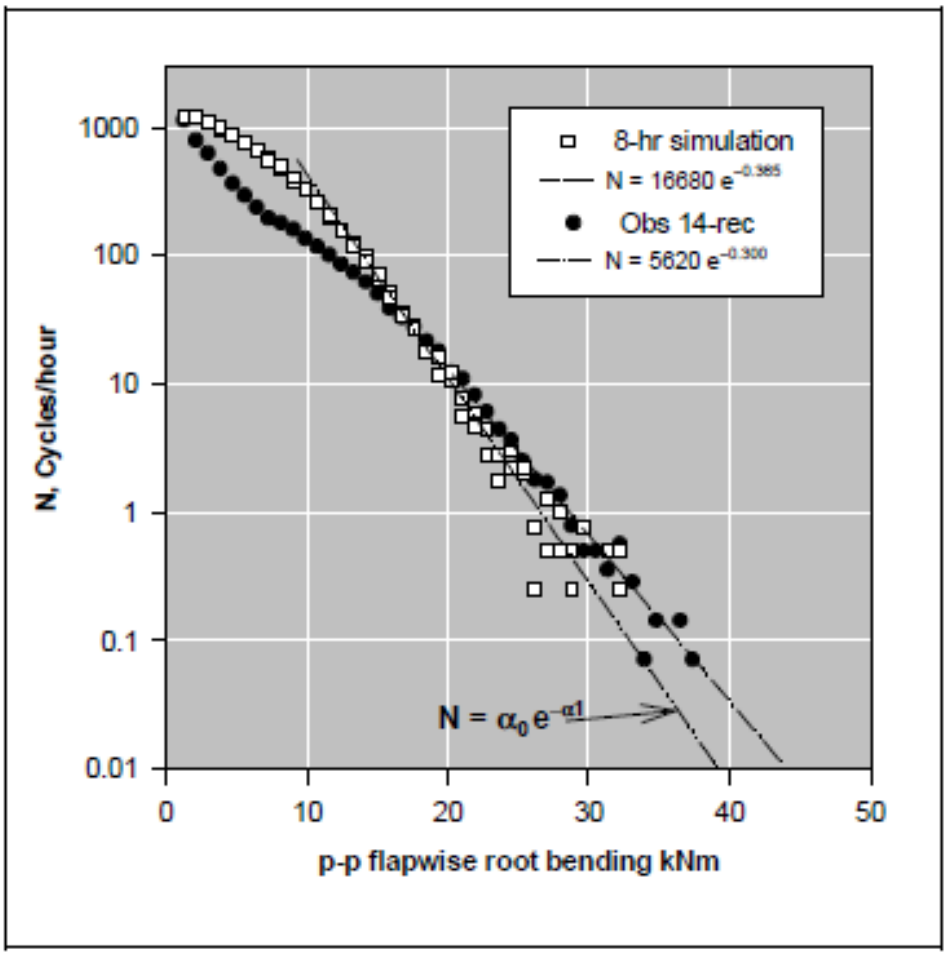

Figure 3-6. Comparison of measured and simulated Micon 65/13 turbine with NREL rotor root flapwise load distributions at Row 37 in California wind farm

had resulted in a slope β_1 that was steeper (less damaging) than that observed for the 8-hour simulation shown in Figure 3-6. We concluded that something was missing from the SNLWIND-3D inflow simulations and that missing element was responsible for the discrepancy. Other comparisons with measured data from other turbines pointed to the same situation.

3.4 Further Quantifying Micon 65/13 Turbine Dynamic Response to Turbulence Scaling Parameters

The TurbSim simulations must reproduce the turbulence characteristics that have a significant influence on turbine dynamic response. Correlations using the slope of the high-loading tail of the load spectra with a range of turbulence scaling parameters showed that only a few turbulence scaling parameters were efficient predictors for the responses of the turbine components listed in Table 3-1. Results from MSC.ADAMS simulations of the Micon 65/13 turbine with the NREL rotor using the Row 37 (7 D) spectral model in SNLWIND-3D showed good agreement with observations in the body of the load distributions. These results failed, however, to predict the few large load cycles that were responsible for the majority of the measured fatigue damage. To gain a more detailed understanding of what conditions are likely to produce these large loads, we

repeated the multiple-linear correlation analysis using the same turbulence predictor variables, but this time we used fatigue damage equivalent loads (*DEL*s) as the response variable. The *DEL* has become the wind industry standard for assessing fatigue damage. The fatigue *DEL* is given by

$$DEL = \left[\frac{\sum_i (L_i)^m N_i}{N_o} \right]^{1/m} , \qquad (3\text{-}3)$$

where N_i is the number of loads of magnitude L_i, N_o is 2,000, and m is the Wöehler exponent. An m value of 10 for is typically used for composite materials, and a value of 3 is used for steel. *DEL* is the value of the cyclic load amplitude that would create the equivalent amount of fatigue damage as the spectrum of loads L_i that was measured or simulated.

Sutherland (2002) and Nelson and coauthors (2003) statistically analyzed the response of the previously mentioned modified Micon 65/13M in Figure 3-4 that was operated with a natural upwind fetch at the Great Plains site near Bushland, Texas. This Micon turbine had been modified to operate at 55 rpm and incorporated a commercial version of the NREL 7.9-m blade used on the California wind farm turbine. With the higher rpm, the turbine rated power was increased from 65 to 115 kW. These investigators used many of the turbulent flow parameters that we used in correlating the slope of load spectra from the two turbines in the California wind farm, except they used the blade root flap bending moment (FBM) *DEL* as the response variable. In his analysis, Sutherland found a dependency on *Ri* that decreased with increasing mean wind speed, but observed that the *DEL* was also sensitive to the standard deviations of the lateral (v) and particularly the vertical (w) turbulence components. Similar to what we found from the San Gorgonio data, Sutherland showed that at higher wind speeds the sensitivity to the local friction velocity u_* became predominant and that *Ri* plays an important role overall.

Nelson and colleagues (2003) applied sophisticated numerical techniques to the same data set to isolate the turbulence parameters from their interdependencies as much as possible, to establish specific levels of sensitivity to the turbine response. They identified mean wind speed and the wind speed standard deviation as the primary inflow variables contributing to the turbine dynamic response. They also applied their numerical technique to the residuals after accounting for the two primary variables by using many of the same turbulence scaling or predictor variables as Kelley (1993) and Sutherland (2002). They concluded that none of these secondary turbulence predictors contributed significantly to the response beyond the primary variables of mean wind speed and wind speed standard deviation.

The turbulent inflow to the modified Bushland Micon 65/13M turbine was significantly different from that entering the rotors of the California wind farm turbines on Row 37, where 36 rows of turbines were operating upwind with the closest row 7 *D* upstream. The large-scale atmospheric dynamics that influenced the turbulence characteristics at the inflow of each of these turbines were also much different. At the California wind farm, the two 50-m towers yielded data suggesting that a high-speed flow stream (jet) forms above the wind farm at night in response to

the increased drag and warmer temperatures in the layer the wind turbines occupy near the ground (similar to nocturnal flows over forest canopies).

We found evidence that during the night this jet-like structure periodically becomes dynamically unstable and creates a strong downward flux of organized turbulence into the turbines below. The natural fetch upstream of the turbine at Bushland was flat and relatively homogeneous agricultural land whose surface roughness varies with the growing stage of the crops in the upwind fetch. This area is frequently under the influence of nocturnal LLJs during the warmer months. These streams of higher speed air create downward fluxes of organized turbulence two or three times per night when instabilities develop in the stratified layers beneath the jet maximum velocity.

How often LLJs occur at Bushland is unknown. Without directly comparing the turbulence statistics and corresponding turbine responses from the turbines on Row 37 of the California wind farm and the one on the Bushland site, it is impossible to quantify any differences arising from location, which is further complicated by the modified configuration of the Bushland Micon 65/13M test turbine.

Based on Sutherland's findings of the sensitivity of the blade root FBM *DEL*s to the Ri_{TL} and the hub-height u_*, we believe these parameters deserve more attention in establishing a broader perspective of the role of turbulence in the dynamic response of wind turbines. The California wind farm test turbines operated in the aggregated wake conditions created by 36 rows of upstream turbines, the closest of which was seven rotor diameters. It was much more energetic and organized than the natural inflow at the Bushland Micon 65/13M turbine. If anything, we believe that the observed sensitivities to the various turbulence parameters would be more pronounced in the response of the turbines at Row 37 in the wind farm because there is "more signal," meaning increased turbulence levels, to drive the turbine response dynamics.

3.5 Defining the Role of Coherent Turbulent Structures in Micon 65/13 Dynamic Response

Our comparisons of simulated loads with observed loads showed that we were missing the largest ones. To understand if the turbulence characteristics of the simulated inflow were somehow deficient, we examined a number of detailed records from the Micon turbines in which we synchronized the time series of load variables with turbulence parameters. Figure 3-7 illustrates a typical case in which there were several large load cycles observed with the corresponding Reynolds stress and associated local vorticity components. Figure 3-7b shows a coherent turbulent structure embedded in the flow between about 3.5 and 6.5 seconds, as indicated by the large cross correlations in the instantaneous *u'v'(t)* and *v'w'(t)* Reynolds stress components. We estimated the local vorticity components over a period of 1 second from the 16-per-second velocity components measured by the ultrasonic anemometer. The relative helicity indicated by *H* in the diagram is a measure of the intensity of the spin associated with this turbulent structure. In addition to the spin, this structure was coherent because it had a definite temporal as well as a likely spatial organization because both turbines responded to its presence, though not in the same way. The NREL rotor primarily responded in the root edgewise bending load, and all three of the blades of the AeroStar rotor responded in the flapwise bending direction.

3.5.1 An Application of Wavelet Analysis

To understand the role of coherent turbulent structures in inducing strong aeroelastic response in wind turbine rotors, we developed a capability to analyze this interaction with time-frequency analysis tools and specifically wavelets (see Kelley et al. [2000] for more details). Wavelet analysis allows one to examine both the frequency and temporal distribution of energy associated with transient events. Figure 3-8 presents a continuous wavelet transform decompositions (scalograms) of the three Reynolds stress components (shown in the top panel) of a measured turbulent inflow to the Micon 65/13 with the NREL rotor and the resulting root flapwise load response. Time is plotted on the abscissa and the cyclic frequency on each of the ordinate axes, with the nonlinear frequency scales inverted. The deep red represents the highest intensity of the variable and the darkest blue the lowest. Coherent patches, such as those at about 5 seconds in the record, show intense levels of kinetic energy in all three Reynolds stress components (covariances) that cover a wide frequency range. The flapwise bending load shows significant levels of high frequency energy between about 14 and 20 seconds, probably caused by the intense coherent structure identified by the Reynolds stress components.

We used the Row 37 spectral model in SNLWIND-3D to simulate higher wind speed flows that may produce the extreme loading events seen at the California wind farm. Figure 3-9 shows the time series of the hub-height wind speed, Reynolds stress components, and flapwise bending load with the mean removed. Although no discrete or sharp edge gusts in the wind speed are present, two coherent structures are indicated by the Reynolds stress components. The one in the center of the record is the more intense and it has a significant flapwise loading response.

The continuous wavelet transform decomposition shows intense levels of strain energy reaching frequencies greater than 5 Hz in the peaks. The lowest panel displays seven frequency bands from the discrete wavelet transform of the time series of the flapwise loading. The amplitude of the time series shown in the frequency bands indicates the intensity of the load within the band. The frequency ranges of the bands are 0.125–0.25, 0.25–0.5, 0.5–1.0, 1.0–2.0, 2–4, 4–8, and 8–16 Hz for the B7, B6, B5, B4, B3, B2, and B1 bands, respectively. Figure 3-10 shows the details of continuous wavelet decomposition of the three Reynolds stress components and their relationship to the transient flapwise bending load response. These diagrams demonstrate that the turbine responds with an organized or coherent loading response when an organized or coherent turbulent structure is ingested by the rotor and is likely a major contributor to the large, infrequent loading cycles seen in the tails of the stress distributions. Such a process can simultaneously drive several lightly damped vibrational modes in turbine structural components, which in turn can contribute by constructive interference (in-phase summation or addition) to produce the large load excursions clearly demonstrated in Figures 3-8, 3-9, and 3-10.

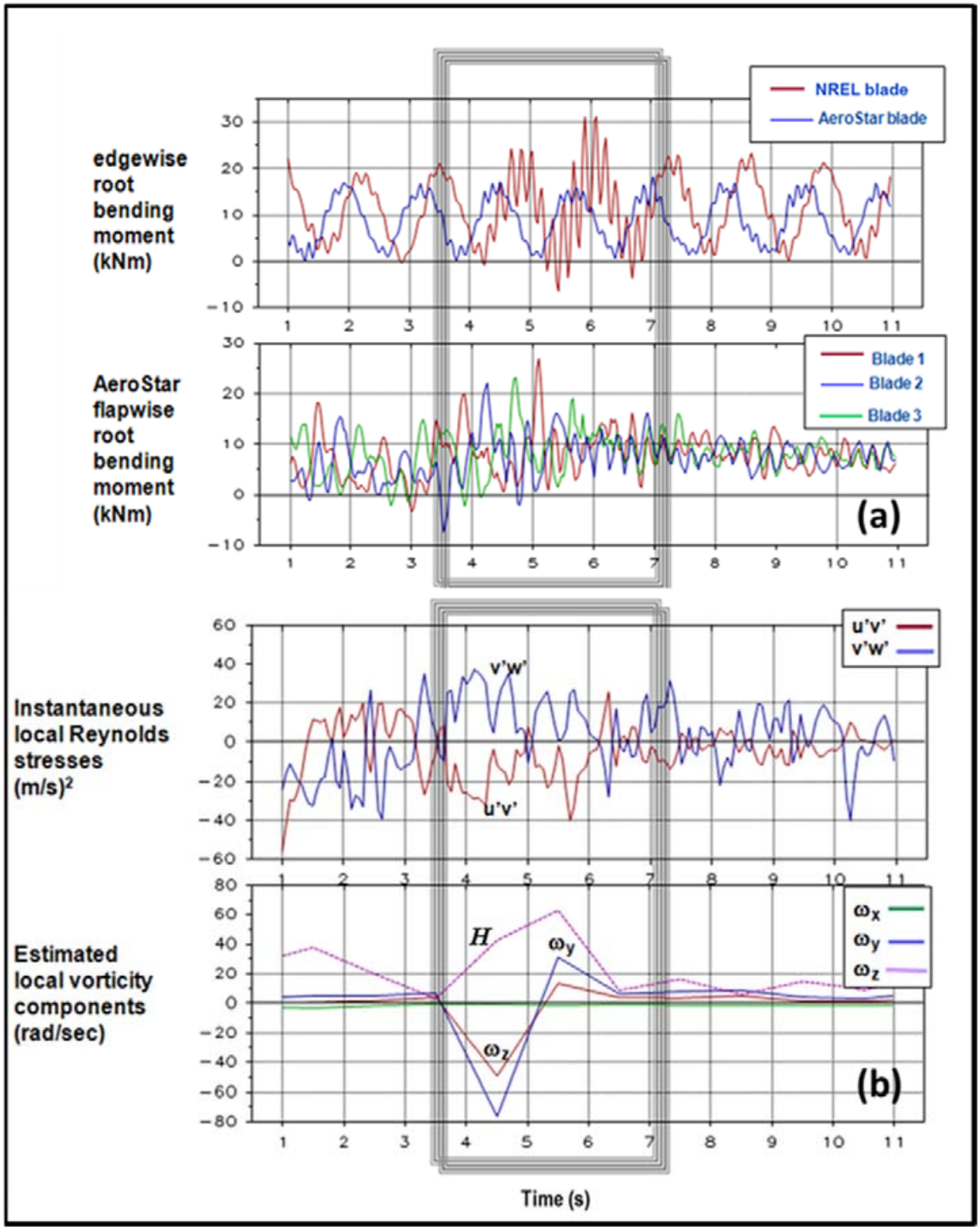

Figure 3-7. Significant loads seen on Micon 65/13 NREL and AeroStar rotors: (a) load excursions in flapwise and edgewise root loads; (b) corresponding instantaneous *u'v'* and *v'w'* Reynolds stresses and estimated local vorticity components ω_y and ω_z. *H* is the local relative helicity, a measure of the intensity of the spin in the structure. A coherent turbulent structure exists in the flow between about 3 and 6.5 seconds to which the turbine rotors responded.

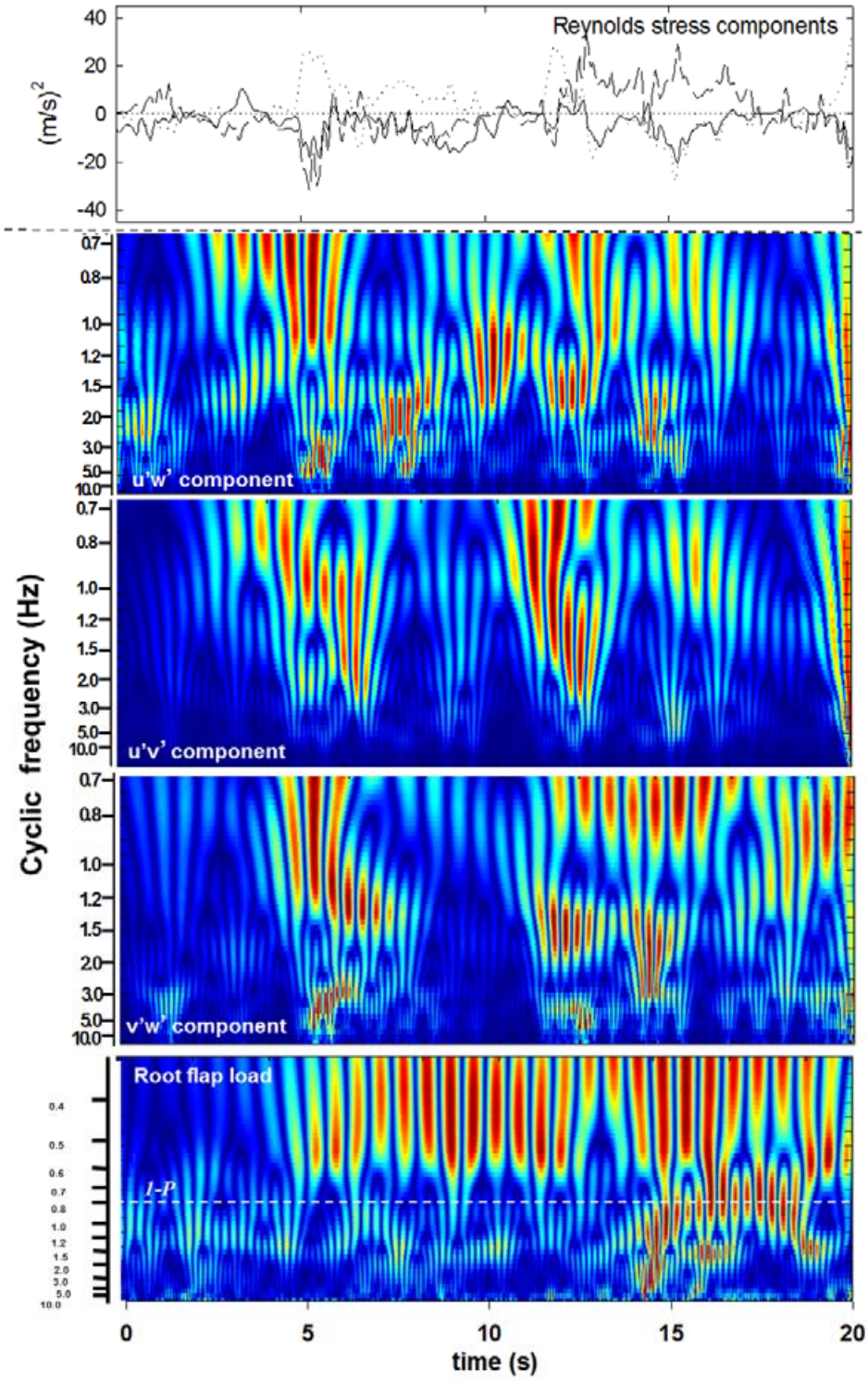

Figure 3-8. Continuous wavelet decomposition of inflow turbulence Reynolds stress components and root flapwise bending load of NREL-rotor-equipped Micon 65/13 turbine

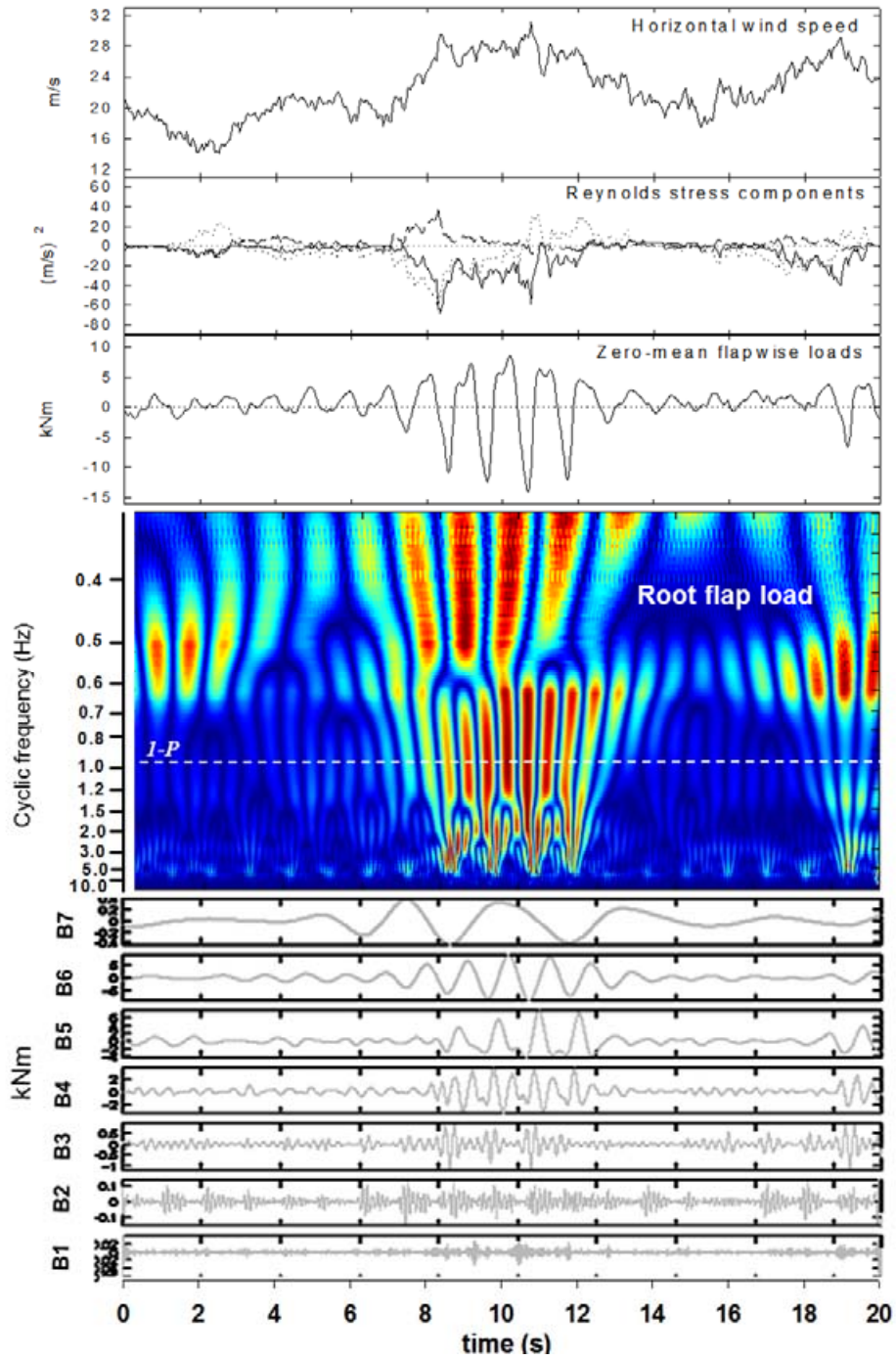

Figure 3-9. Continuous and discrete wavelet decomposition of Micon 65/13 turbine blade root flapwise bending response to SNLWIND-3D simulated inflow containing embedded coherent structure. The uppermost panel is the time series of the hub-height wind speed, the second panel contains the time series of the three Reynolds stress components, the third panel is the flapwise bending load with the mean removed, the fourth panel is the continuous wavelet transform decomposition of the flapwise bending load, and the bottom panel is the discrete transform decomposition into seven frequency bands, with B7 the lowest frequency (0.125–0.25 Hz) and B1 the highest (8–16 Hz).

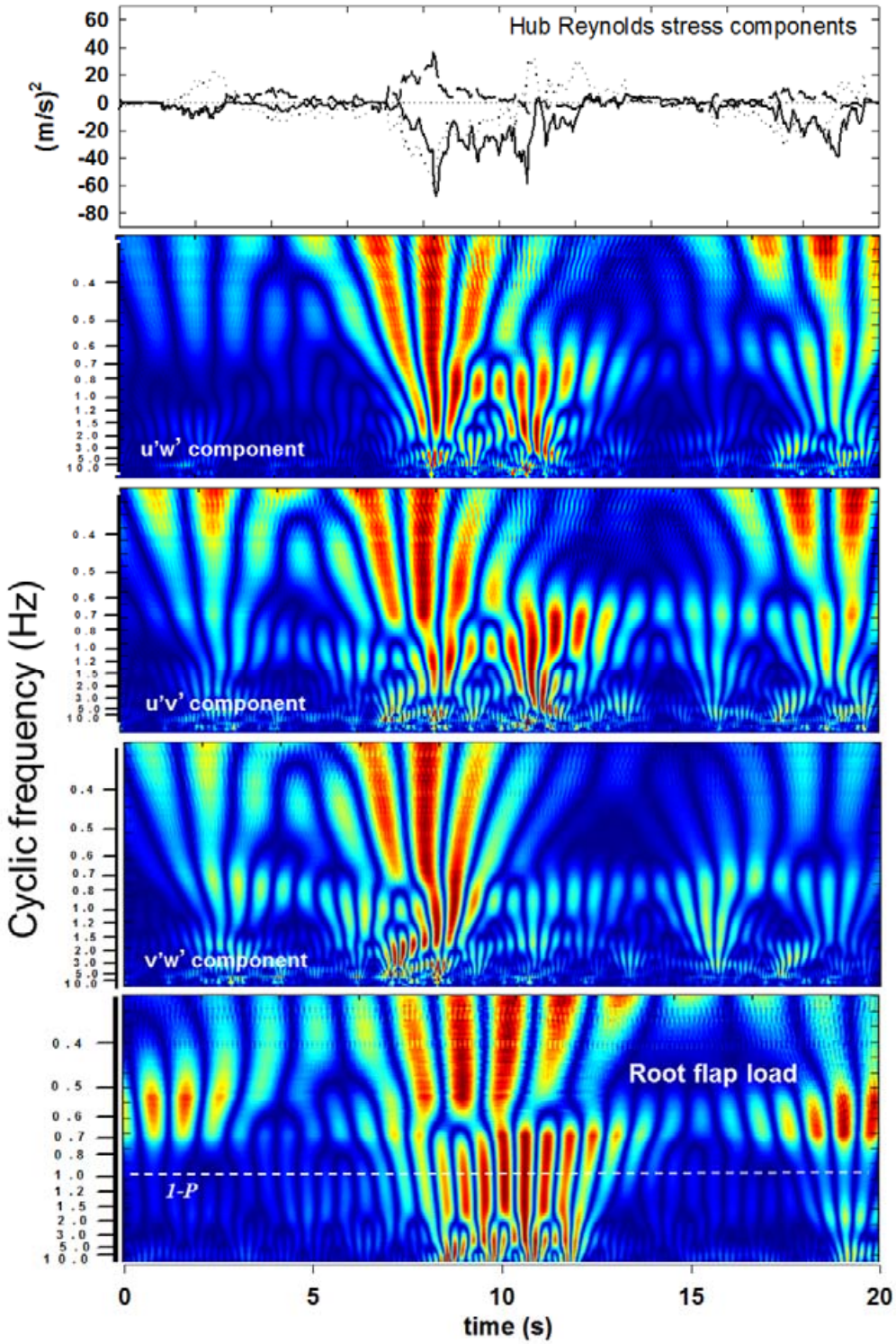

Figure 3-10. Continuous wavelet decompositions (scalograms) of simulated individual Reynolds stress components of coherent turbulent structure and corresponding response of Micon 65/13 turbine root flapwise bending load

3.5.2 Defining a Variable That Represents the Level of Coherent Turbulent Energy in the Flow

The *DEL* parameter gives us with a single number that represents the level of fatigue damage that has occurred in a data record. Other useful response variables would be the second statistical moments or extreme values. Using wavelet analysis, we demonstrated that the intensity of the Reynolds stresses in the flow have a significant influence on the level of dynamic response in turbine components such as the blades in addition to stability expressed as

$$E_{coh} = 1/2[(u'w')^2 + (u'v')^2 + (v'w')^2]^{1/2}. \quad (3\text{-}4)$$

This definition of E_{coh} allows us to include the influence of coherent turbulence with other predictor variables on the level of turbine component dynamic response expressed by a single quantity such as the *DEL*, standard deviation, or extreme value. For example, Figure 3-11a plots the population variation of the three-blade average *DEL* of the root FBM for the NREL rotor equipped Micon 65/13 against the hub-height maximum or peak value of E_{coh} More information is gained, however, from the smoothed contour plot of Figure 3-11b, where the FBM *DEL* values are plotted against both the peak value of E_{coh} and Ri_{TL}.

3.5.3 Statistical and Contour Analysis

Our approach to establishing the turbulence characteristic parameters that have the most influence on the scaling of the turbine dynamic response variables has been to use both multiple linear and stepwise regression and graphic presentations. The graphics are presented as bivariate scatterplots with and without smoothing and smoothed 3-D contour plots similar to those in Figure 3-11b. For the contour plotting we employed locally weighted linear regression, or LOESS (see Cleveland and Devlin [1988] for more information), for generating the smoothed contours. The LOESS algorithm is very useful for smoothing complex 3-D scatterplots that may contain complex underlying deterministic structures. No fitting function is required a priori, only a smoothing parameter that ranges from 0 to 1. For a highly populated raw scatterplot, we used 0.5 for most contour smoothing. For those that had fewer points, it was sometimes necessary to increase the value from 0.7 to 0.9. It was also necessary to detect and remove any outliers before applying the LOESS algorithm because of the local nature of the process, and the presence of outliers could introduce artifacts into the smoothed subsets of points.

3.5.4 Expansion of Candidate Turbulence Parameter Predictors

With the knowledge that coherent turbulence plays a role in the dynamic response of wind turbines, we expanded the list of candidate turbulence parameter predictors beyond those originally used to correlate with the slope of the load distributions or spectrums and whose results are listed in Table 3-1. We calculated the correlation matrix from the entire San Gorgonio data from Row 37 for these parameters as predictor or independent variables and four response variables. The response variables were the three-bladed average *DEL*s and the peak of the *DEL*s from the individual blades for the root FBM of each turbine. In Table 3-2 we summarize the turbulence parameters and their correlation coefficients that exceeded 0.3. Coefficients that exceed 0.7 are shown in red and those exceeding 0.5 are italicized in bold black. Two independent variables have not been previously defined, the buoyancy frequency, N_{buoy} and the standard deviation of the vertical flux or transport of coherent turbulent kinetic energy, $\sigma_{w'E_{coh}}$. The former is also referred to as the Brunt-Väisälä or buoyancy frequency given by

$$N_{buoy} = \sqrt{\frac{g}{\overline{\theta}} \frac{d\overline{\theta}}{dz}} \tag{3-5}$$

where θ is the potential temperature. N_{buoy} is the frequency at which a vertically displaced parcel of air will oscillate in a statically stable atmosphere. It is related to *Ri* as

$$Ri = \left(g / \overline{\theta}\right)\left(\partial\overline{\theta} / \partial z\right) / \left(\partial\overline{U} / \partial z\right)^2 = N_{buoy}^2 / (\partial\overline{U} / \partial z)^2 . \tag{3-6}$$

We find that the mean wind speed (either the horizontal or streamwise component) and their standard deviations are highly correlated, as did Nelson and coauthors (2003). Sutherland (2002) found that the Bushland data correlated well with Ri and u_{*hub} as well as parameters involving the vertical wind component *w*. We find the same in Row 37 in San Gorgonio along with several additional parameters tabulated in Table 3-2. Clearly parameters in this table that involve the second statistical moments of all three of the velocity components (kinetic energy) are highly correlated with the blade fatigue loads. We shall shortly see why the variation of the vertical transport of $w'E_{coh}$ " "makes the list." It is interesting to note the relatively low correlation with stability (Ri_{TL}) and the standard deviation of the vertical wind component *w* in this bivariate analysis. We shall see shortly that these low correlations are somewhat misleading in this format.

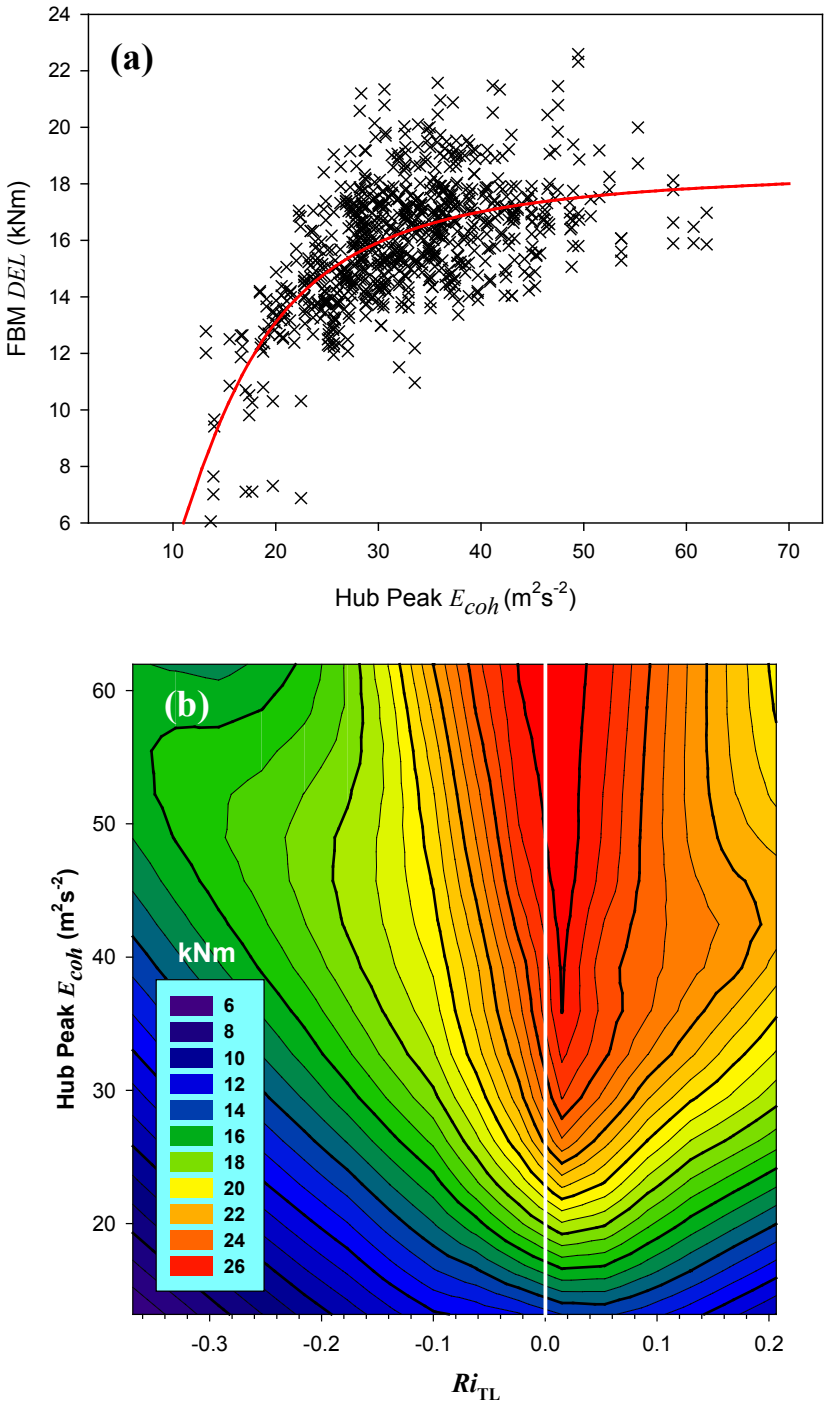

Figure 3-11. Variation of NREL-rotor-equipped Micon 65/13 three-blade peak root FBM *DEL* with (a) hub peak E_{coh} only and (b) Ri_{TL} and hub peak E_{coh}. Negative values of Ri_{TL} indicate dynamically unstable, zero neutral, and positive stable flow conditions.

Table 3-2. Cross-Correlation Coefficients for Inflow Turbulence Parameters with FBM *DEL*s for Values > 0.3

	NREL Rotor 3-Blade Average *DEL*	AeroStar Rotor 3-Blade Average *DEL*	NREL Rotor 3-Blade Peak *DEL*	AeroStar Rotor 3-Blade Peak *DEL*
$\overline{U}_{H_{hub}}$	**0.871**	**0.845**	**0.808**	**0.823**
σ_{U_H}	**0.742**	**0.720**	***0.684***	***0.697***
Ri_{TL}	0.371	0.359	0.328	0.338
u_{*_o}	***0.602***	***0.596***	***0.551***	***0.581***
u_{*hub}	***0.698***	***0.674***	***0.650***	***0.672***
N_{buoy}	0.349	0.341	0.311	0.311
Hub peak E_{coh}	***0.539***	***0.523***	0.495	0.480
$\sigma_{w'E_{coh}}$	***0.639***	***0.631***	***0.606***	***0.613***
$\overline{U}$	**0.868**	**0.842**	**0.804**	**0.820**
σ_u	**0.749**	**0.725**	***0.692***	**0.704**
σ_v	***0.518***	0.487	***0.508***	0.483
σ_w	0.365	0.375	0.349	0.361
E_T	**0.751**	**0.728**	**0.711**	**0.710**
$\sigma_{u'w'}$	**0.725**	**0.719**	***0.673***	***0.693***
$\sigma_{u'v'}$	**0.704**	***0.669***	***0.670***	***0.664***
$\sigma_{v'w'}$	***0.566***	***0.549***	***0.550***	***0.542***

3.6 Identifying Micon 65/13 Turbulence Scaling Sensitivities

It is apparent from Table 3-2 that the fatigue damage at the blade roots of the two Micon turbines is influenced by more than the mean wind speed and its standard deviation. Figure 3-12 shows a plot of the variation of the root FBM *DEL* with mean wind speed. Although the strong correlation with mean wind speed is obvious, several large loads deviate from the power law trend, particularly at greater than rated wind speed (12.5 m s^{-1}) on the Micon turbine with the NREL rotor. In Figure 3-5a we show that the slope of the large loading tail varied with the stability expressed as Ri_{TL} and the hub-height local shearing stress or friction velocity u_*. In Figure 3-13a, we plot the variation of the three-blade averaged FBM *DEL*s for the NREL and AeroStar rotors that has been minimally smoothed by LOESS local regression with a very small overlap (smoothing parameter). This allows smaller peak variations to be identified, albeit with somewhat less certainty. Figure 3-5a is repeated as Figure 3-13b for ease of comparison. We see that large levels of *DEL*s occur, and a greater number of large loading cycles (shallow or smaller value of β_1) occur over the same weakly stable and narrow Ri_{TL} range of about +0.01 to +0.025 and with higher values of the local value of u_*. For comparison, Figure 3-14 presents a LOESS-smoothed contour plot of the variation of the FBM *DEL*s from the NREL-rotor equipped Micon turbine with Ri_{TL} and u_*; this is similar information as in Figures 3-5a and 3-13b but with fatigue damage as the response variable. Even though the sensitivity of fatigue loading does not register as being that significant in Table 3-2, it is clear from Figures 3-13 and 3-14 that the stability as expressed by Ri_{TL} does play a central role in turbine dynamic response.

3.6.1 Turbine Dynamic Response Sensitivity to Turbulent Velocity Characteristics

The relationships between the various turbulence scaling parameters in Table 3-2 are best understood with a series of 3-D contour plots using the Richardson number as the independent variable. Using the entire available data set, Figures 3-15a and b show the relationships between the FBM *DEL*s and the largest load value in a 10-minute record as functions of Ri_{TL}, hub u_*, and the hub peak value of E_{coh} . The heaver solid and dashed vertical lines correspond to the Ri_{TL} range (0 to +0.05) in Figure 3-13a, where the most fatigue damage takes place from the definitions of β_1 and γ_2, which were confirmed by Sutherland and Kelley (1995). The vertical dash-dot-dotted line (0.025) is the value of Ri_{TL} when the loads are the most sensitive to the peak E_{coh} and to a somewhat lesser extent to the hub value of u_*. Figures 3-15c and d compare the sensitivities of the largest FBM loads with these same three parameters. Here the greater response associated with the larger and lighter NREL rotor and is particularly sensitive to the hub-height peak E_{coh} within the 0 to +0.05 Ri_{TL} range.

Figure 3-16 plots the sensitivity of the three-blade average FBM *DEL*s with stability and the standard deviations of the three hub-height turbulence components, σ_u, σ_v, and σ_w. Here the response characteristics are similar for both rotors, but the NREL rotor is a bit more sensitive. The sudden increase in fatigue loads to the turbulence energy in all three of the components as the flow becomes stable is dramatic. Both rotors are very sensitive to σ_w beginning at Ri_{TL} = +0.01 and extending to about +0.05. The dashed lines indicate a σ_v/σ_u ratio of 0.8, which is the value specified to scale the crosswind or *v*-component turbulence in the IEC Kaimal NTM (IEC 2005, Table B-1). The σ_w/σ_u ratio used to scale the vertical turbulence component is 0.5, which is less than the minimum value shown on the plots in Figure 3-17. These plots indicate that high

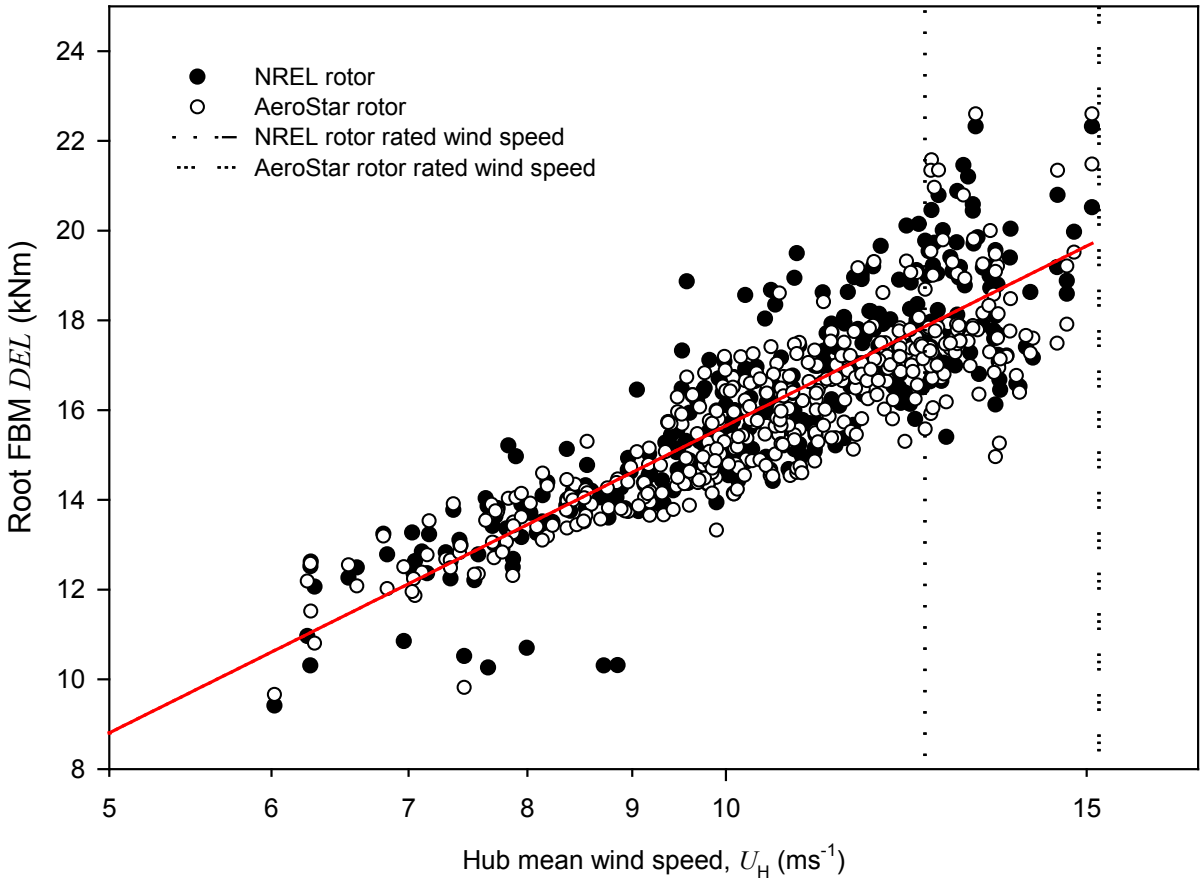

Figure 3-12. Variation of blade root FBM *DEL*s for NREL and AeroStar rotors with hub-height mean wind speed for all available records

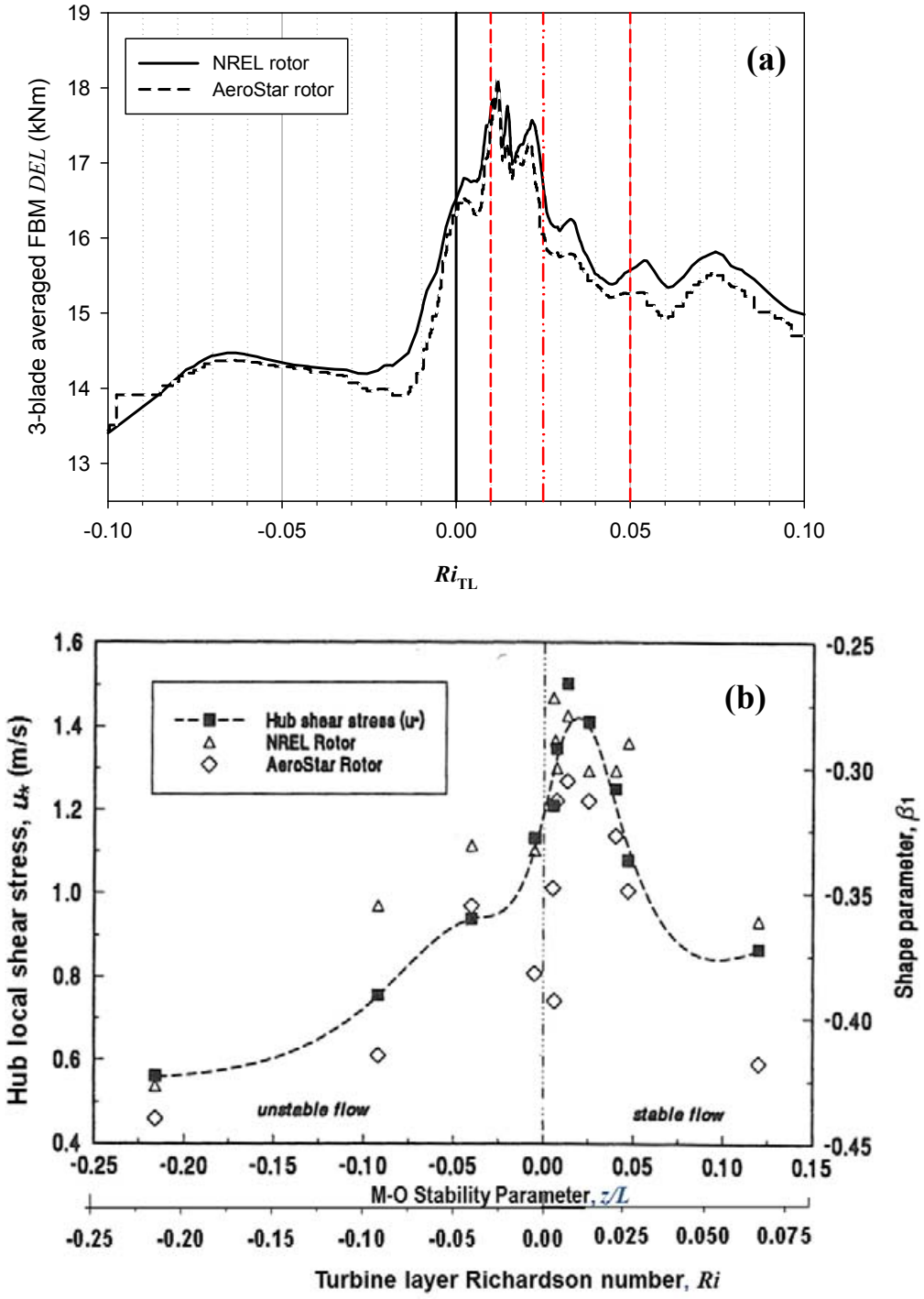

Figure 3-13. Comparison of variation of (a) three-blade averaged FBM *DEL* and (b) slope (β_1) of high-loading tail with Ri_{TL}. The dashed lines in (a) delineate a critical or sensitive stability range for loads with the dot-dot-dashed line representing the most sensitive *Ri* value.

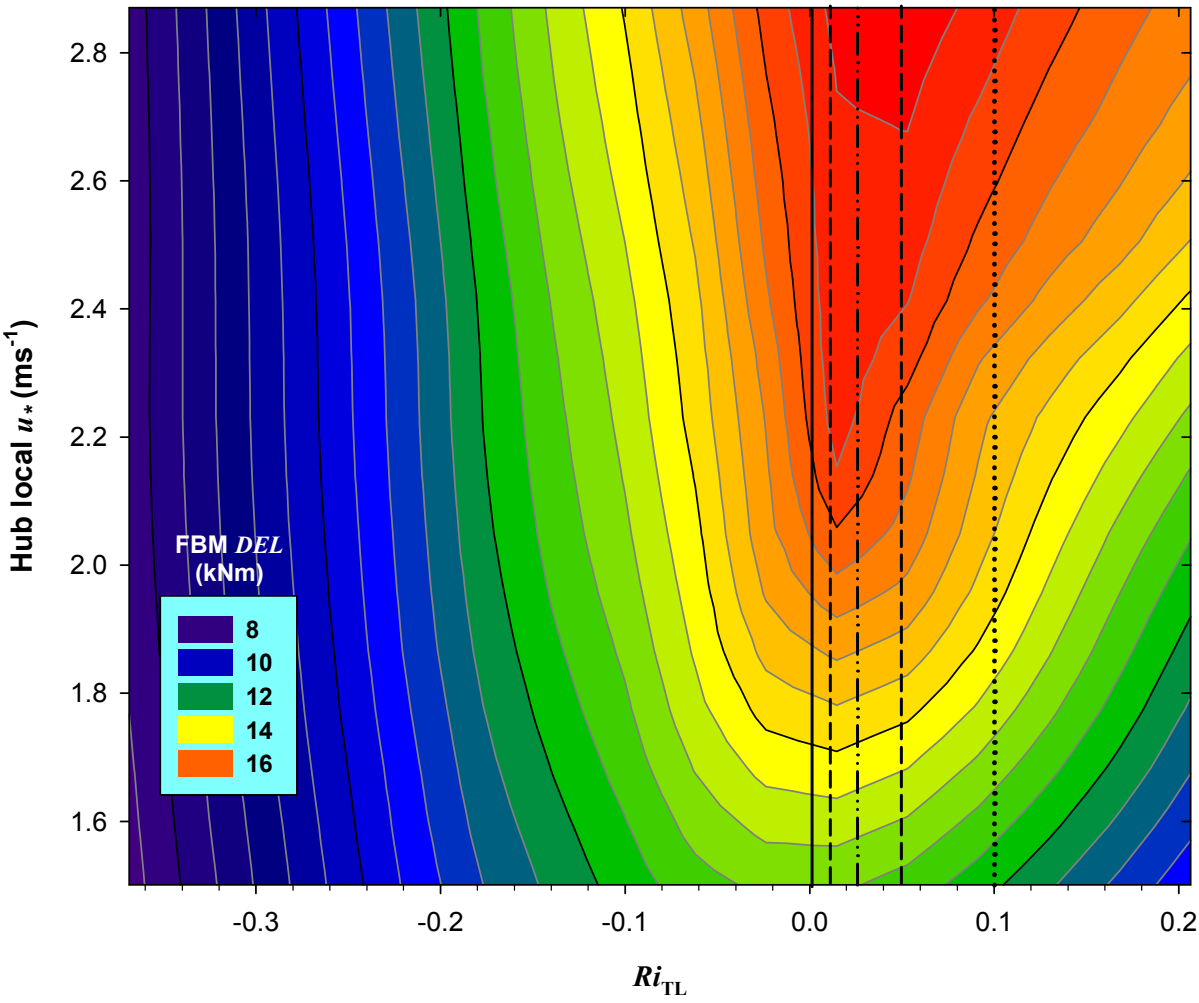

Figure 3-14. LOESS-smoothed contours of variation of FBM *DEL*s from NREL-rotor-equipped Micon 65/13 turbine with Ri_{TL} and hub-height local u_* value. Dashed and dot-dot-dashed lines correspond to those of Figure 3-13a delineating a critical stability range for loads.

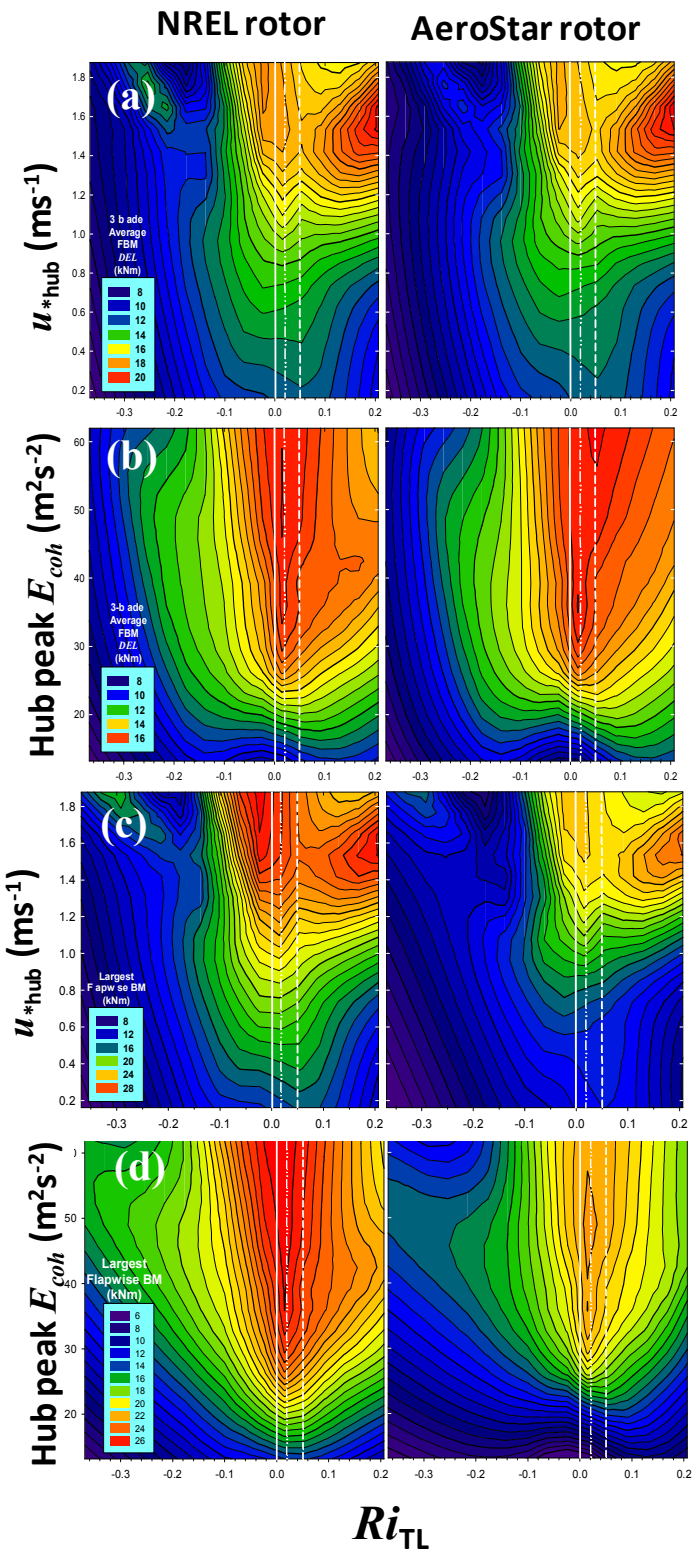

Figure 3-15. Variation of FBM loads: (a) three-blade average *DEL*s vs. Ri_{TL} and hub u_*; (b) three-blade average *DEL*s vs. Ri_{TL} and hub peak E_{coh}; (c) largest FBM value vs. Ri_{TL} and hub u_*; (d) largest FBM value vs. Ri_{TL} and hub peak E_{coh}

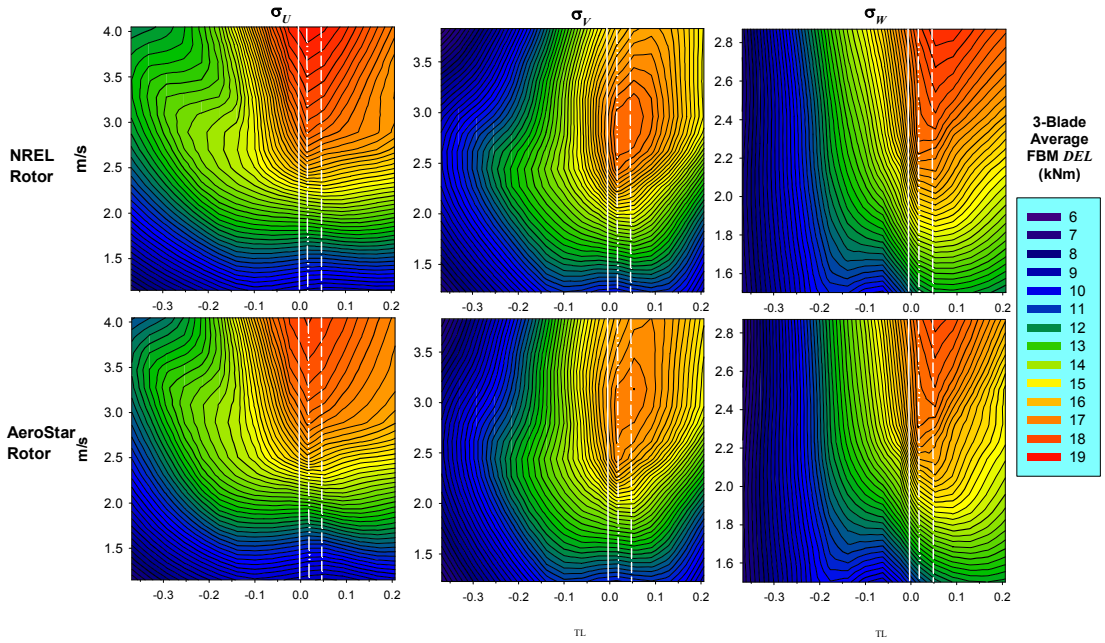

Figure 3-16. Variation of three-blade averaged FBM *DEL*s with Ri_{TL} and standard deviations of hub-height turbulence components σ_u, σ_v, and σ_w

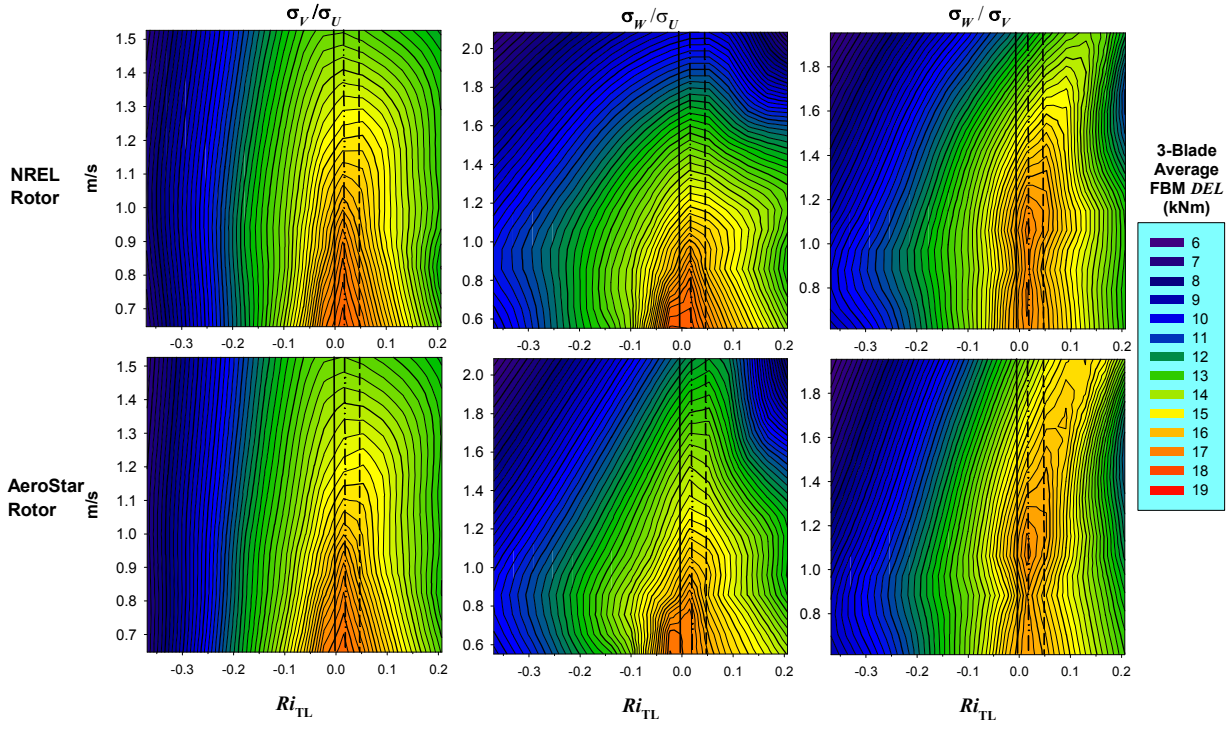

Figure 3-17. Variation of three-blade averaged FBM *DEL*s with Ri_{TL} and ratios of σ_v/σ_u, σ_w/σ_u, and σ_w/σ_v. The dashed line of 0.8 on the σ_v/σ_u plots indicates the scaling used in the IEC Kaimal NTM.

fatigue loads in this critical stability region are clearly related to the greater turbulent energies in the crosswind and vertical directions as compared with the streamwise direction. This characteristic is not simulated in the neutral IEC Kaimal NTM.

Figure 3-18 further underscores the sensitivity of this critical stability range. Here we show the variation of the peak FBM loads with stability and the three mean Reynolds stress components. We previously was that the turbine loading is a strong function of the vertical momentum flux $\overline{u'w'}$ when it is expressed as the local u_* value, but the highest peak loads are also associated over a wide range of magnitudes of the $\overline{u'v'}$ and $\overline{v'w'}$ components as well in this weakly stable regime. The highest load peaks occur with large values of these cross correlations, which can be interpreted as lateral fluxes of turbulent energy that are most likely are associated with the strong coherent turbulent motions and turbulent mixing occurring in this narrow stability range. It is within this range that the highest wind speeds are available, as is shown in Figure 3-19.

A primary scaling parameter for the IEC Kaimal NTM is the hub-height turbulence intensity, I_{hub}. Turbine loads are expected to increase with I_{hub}. For the two Micon turbines at Row 37 in the California wind farm, we found the opposite for the FBM peak loads, as plotted in Figure 3-20. In the left column of this figure the greatest peak loads on both rotors, although taking place within with the narrow stability range discussed previously, occur at the lowest turbulence intensities. For comparison, the variation in the peak FBM loads with hub-height peak E_{coh} is plotted in the right column, showing a strong positive correlation with the peak response, again within this narrow stability range.

3.6.2 Turbine Dynamic Response Sensitivity to Atmospheric Thermodynamics

The turbulence dynamics associated with this weakly stable stability range have a strong thermal component, as seen in Figure 3-21. Here we have plotted the variation of three-blade average FBM *DEL*s for the Micon equipped with the NREL rotor with the standard deviation of the hub-height temperature σ_T in Figure 3-21a and the temperature (buoyancy) flux $\overline{w'T'}$ in Figure 3-21b. The highest *DEL*s are associated with large variations in temperature and buoyancy flux in more stable conditions ($Ri_{\text{TL}} > 0.05$), but significant fatigue damage does occur in the narrow +0 to +0.05 range with lower values of σ_T and $\overline{w'T'}$. Similarly, the peak FBM loads on each turbine are strong correlated with the calculated mean buoyancy flux in the proper units, as shown in Figure 3-22, particularly in the critical *Ri* range. None of this occurs in a neutral atmosphere because the buoyancy forces do not exist.

Other turbine components are also affected by conditions within this critical stability range. For example, Figure 3-23 plots the variation of the peak low-speed shaft bending loads with stability and the $\overline{v'w'}$ covariance. Figure 3-24 shows the sensitivity of the peak low-speed bending loads with the hub local u_* and peak E_{coh} for both rotors. The loading associated with this critical stability range filters down through the entire turbine structure, as demonstrated in Figure 3-25. Here the variation of the peak axial thrust developed by the NREL rotor is correlated with the hub-height local u_* and the peak E_{coh}. The largest thrust forces in the downwind direction (+X) are generated within the critical stability range and are quite sensitive to high values of u_* and E_{coh}. By contrast, the largest upwind (–X) thrust forces occur during unstable flow conditions.

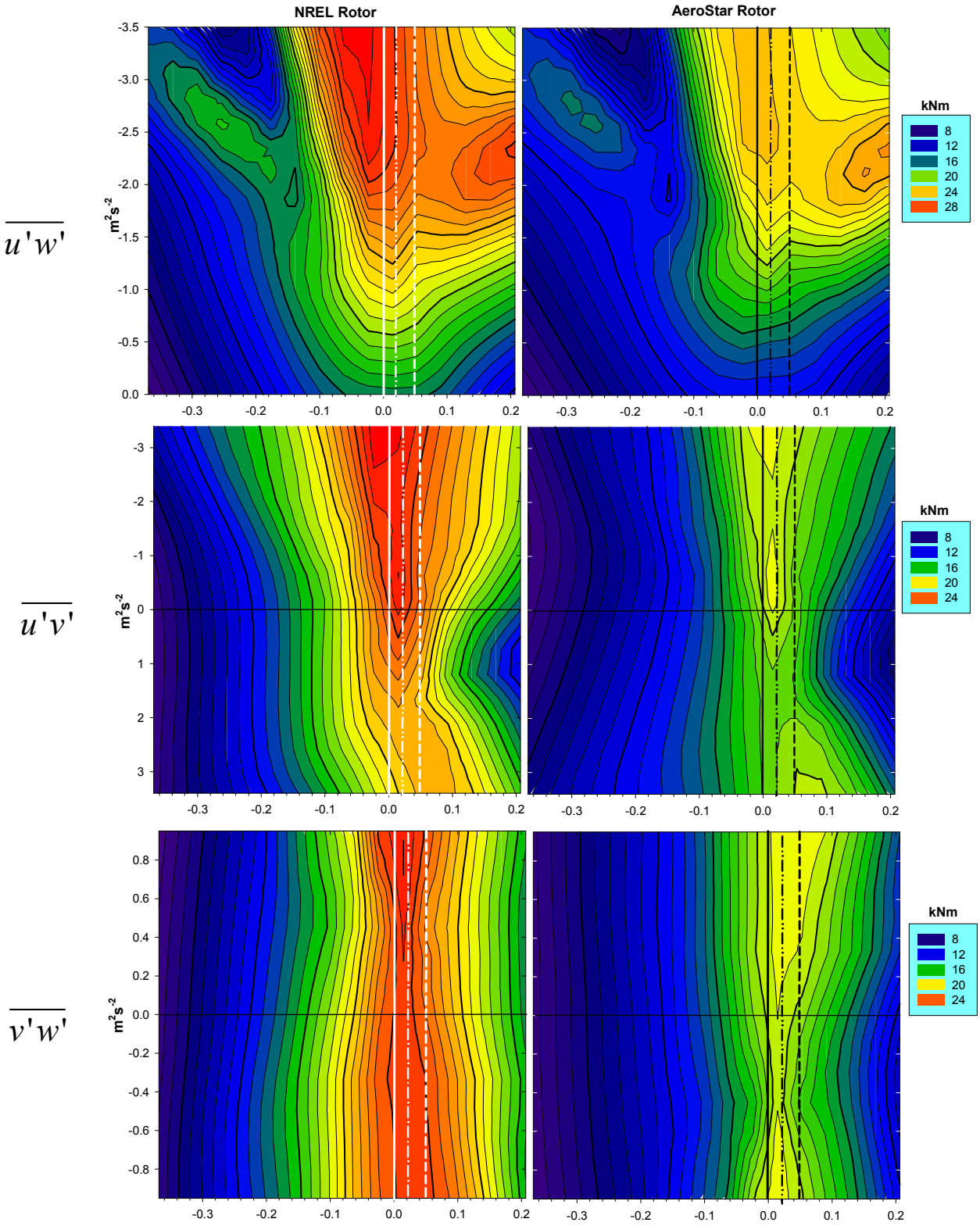

Figure 3-18. Variation of peak FBM loads with Ri_{TL} and hub-height mean Reynolds stresses

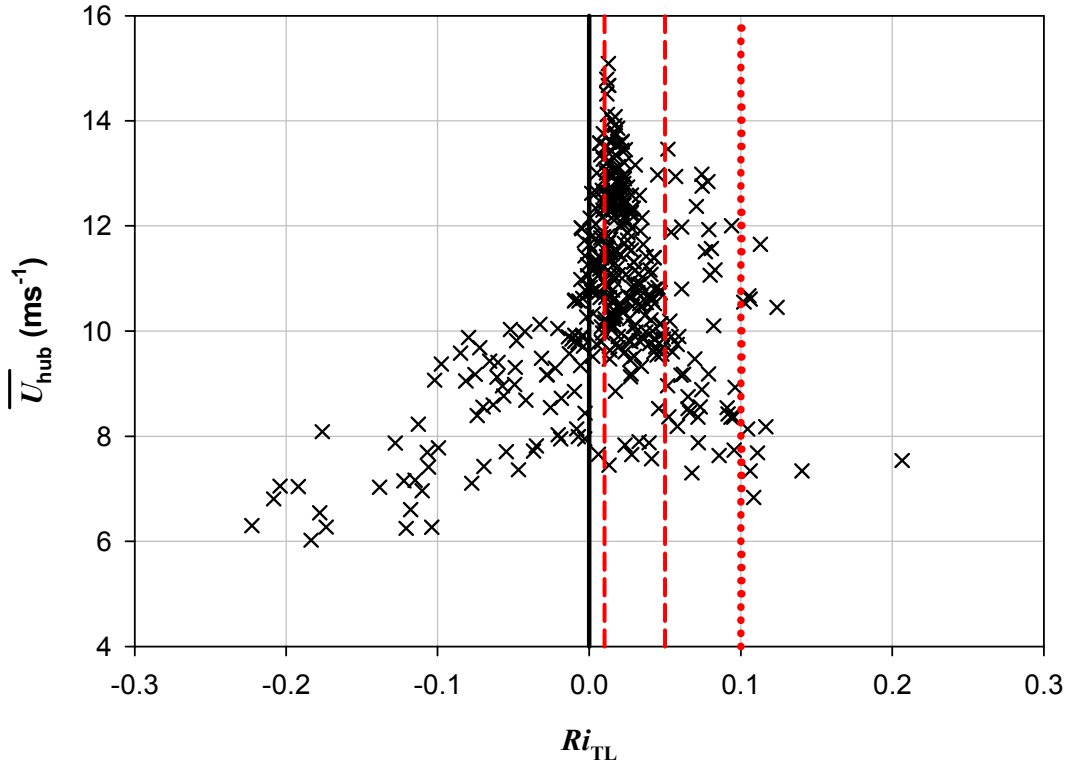

Figure 3-19. Variation of hub-height mean horizontal wind speed with Ri_{TL}. The critical Ri_{TL} range is shown between +0.01 and +0.05 (dashed lines).

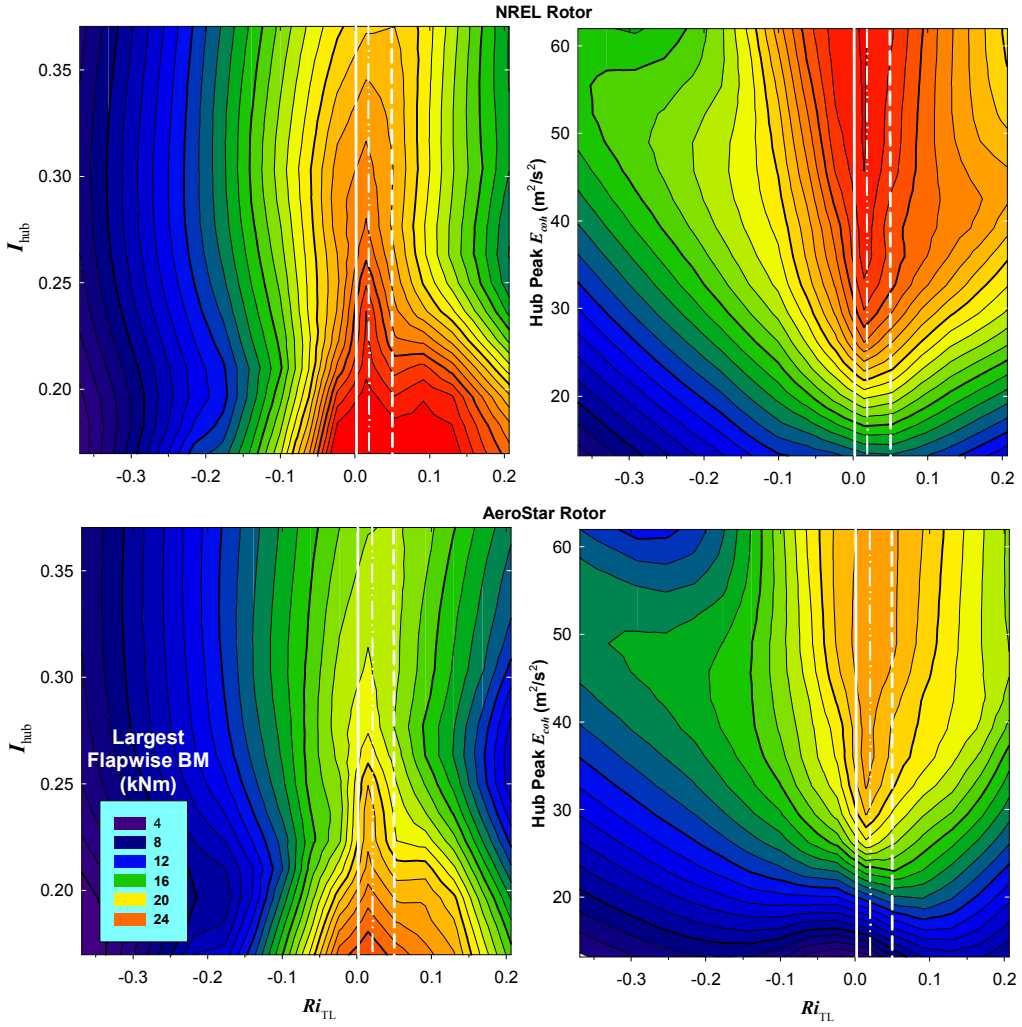

Figure 3-20. Variation of peak FBM loads with Ri_{TL}, hub-height turbulence intensity, I_{hub}, and peak E_{coh}

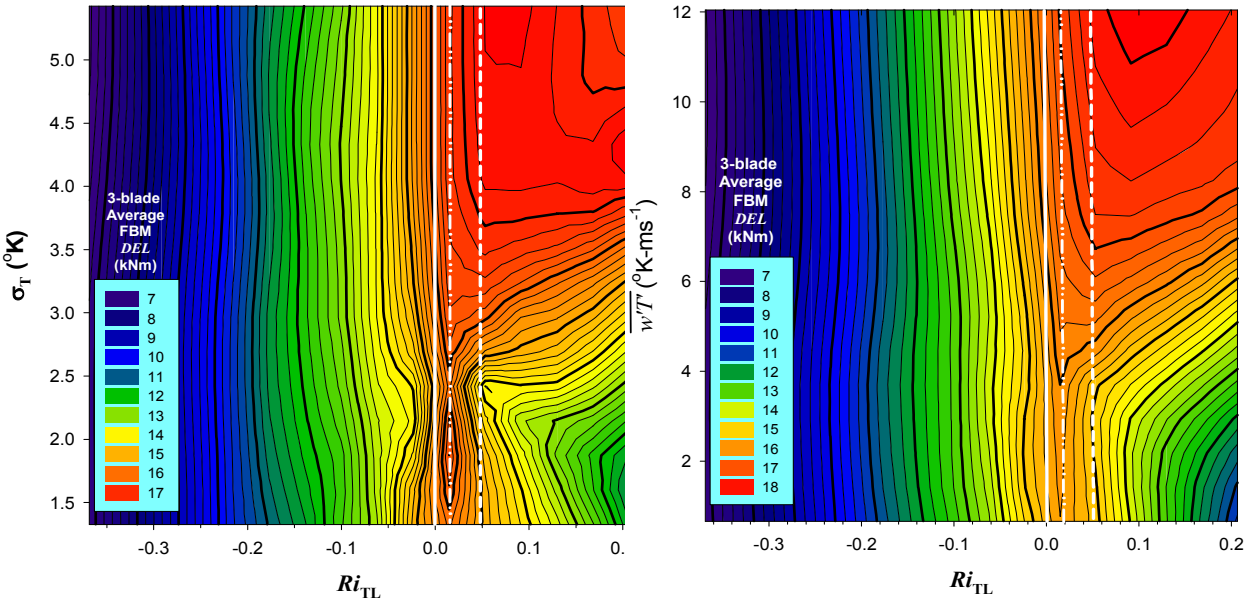

Figure 3-21. Variation of Micon 65/13 turbine with NREL rotor three-blade average FBM *DEL* with hub-height (a) σ_T and (b) buoyancy flux, $\overline{w'T'}$

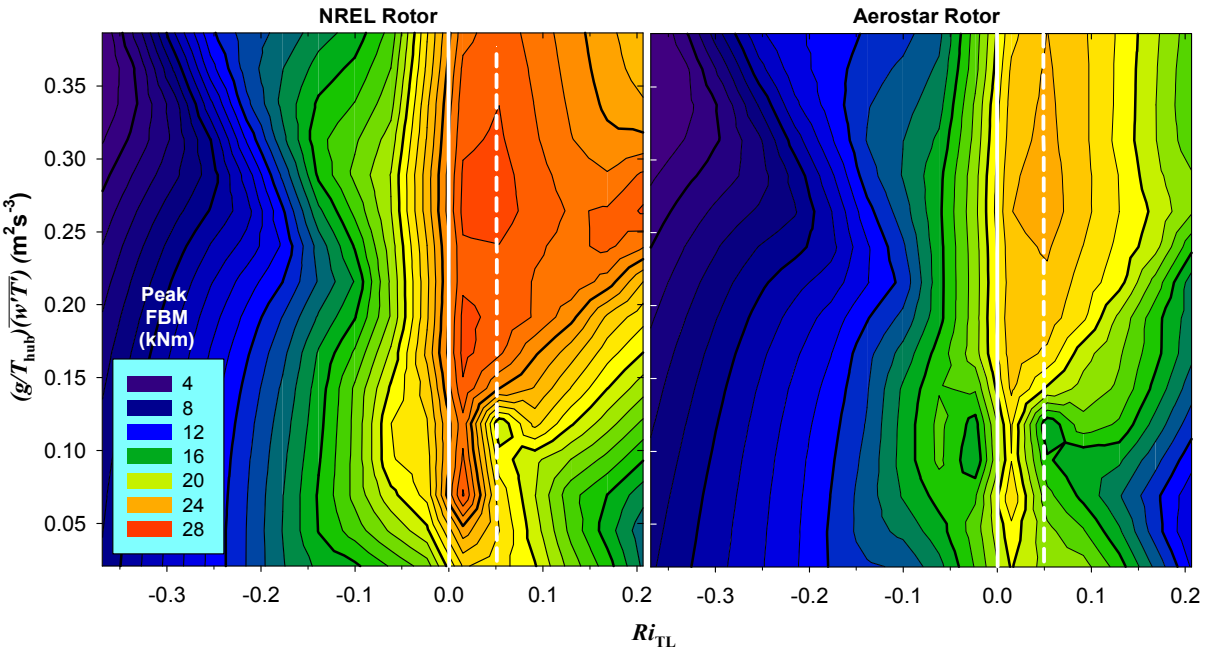

Figure 3-22. Variation of peak FBM loads with stability and mean buoyancy flux

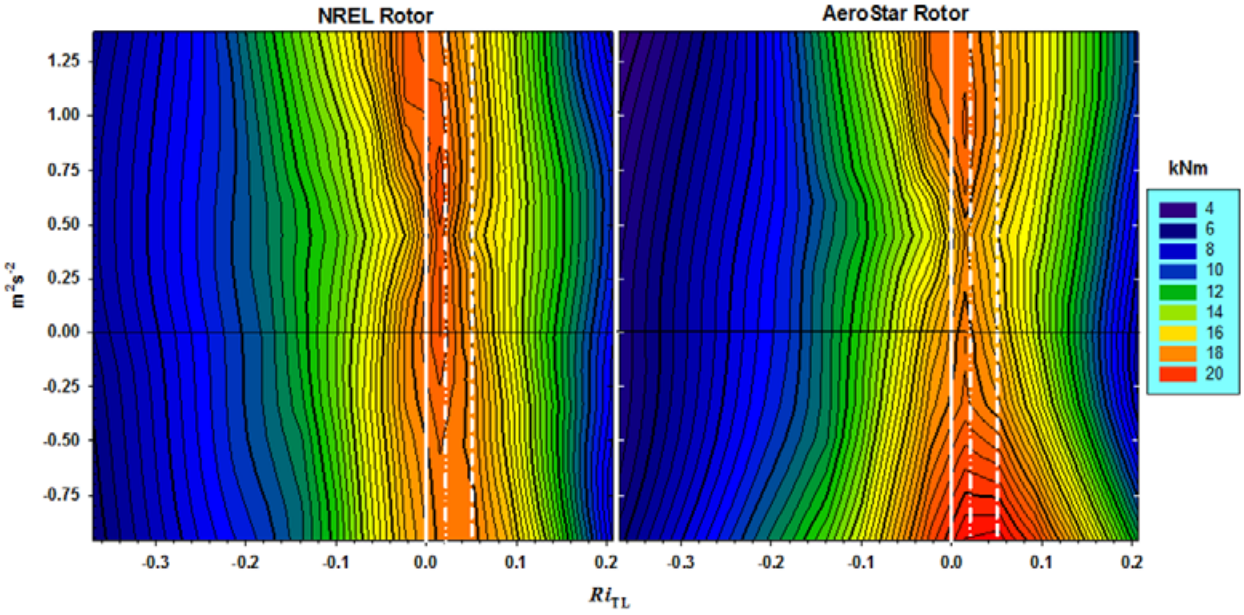

Figure 3-23. Variation of peak low-speed shaft bending loads with Ri_{TL} and the hub-height $\overline{v'w'}$ Reynolds stress component

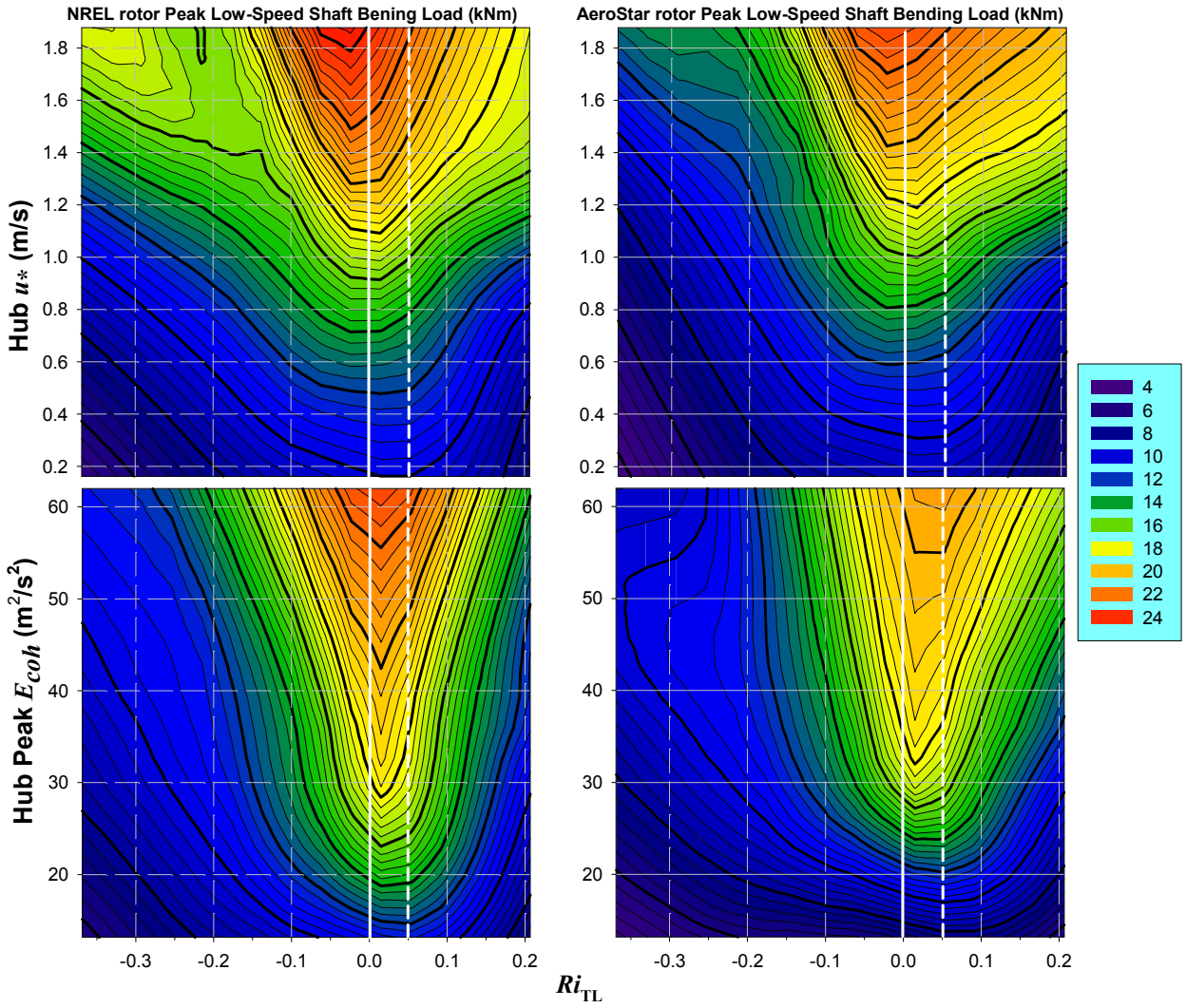

Figure 3-24. Variation of peak low-speed shaft bending loads with stability and hub u_* and E_{coh}

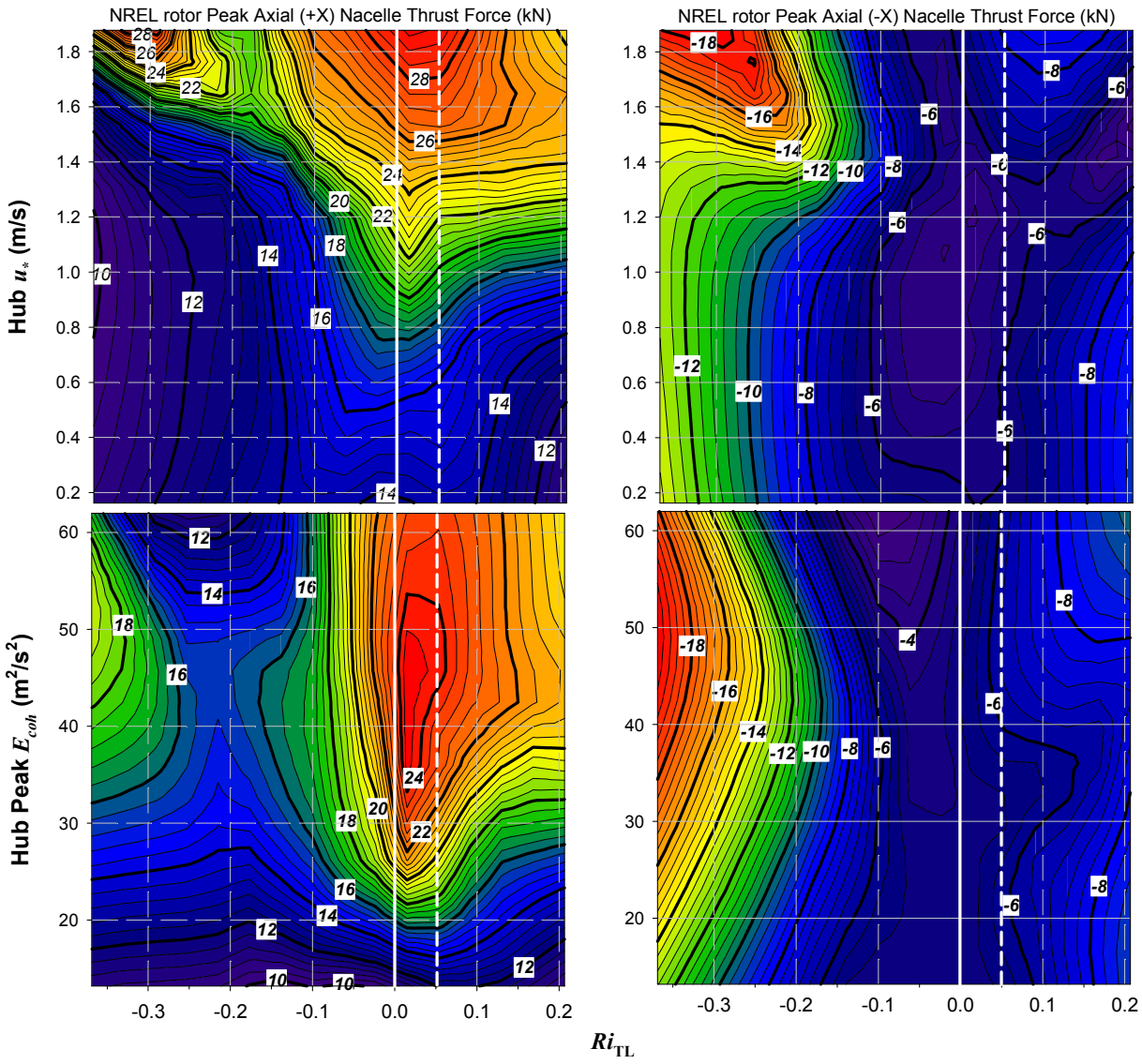

Figure 3-25. Variation of nacelle axial thrust force (kN) on Micon 65/13 turbine equipped with NREL rotor with hub-height u_* and peak E_{coh}

3.7 Flow Details of Critical Stability Range

Our previous results showed that the greatest turbine dynamic response and fatigue damage measured on the two Micon turbine rotors do not occur in neutrally stable boundary layer conditions. They do, however, take place within the narrow and weakly stable Ri_{TL} stability parameter range of +0.01 to +0.05, with maximum turbine dynamic responses at a value near +0.02. We believe it is useful to look at the details of the flow conditions associated with this stability range to understand why it is responsible for the fatigue damage seen in these two particular turbine rotors and operating environment and whether or not it is unique.

3.7.1 Role of Vertical Turbulence Transport

In Figure 3-26 we plot some of important flow details associated with this critical stability range. Figure 3-26a plots the hub-height mean momentum ($\overline{u'w'}$) and buoyancy fluxes ($\overline{w'T'}$) for the entire available data set. The locally measured downward momentum flux increases dramatically just as the flow becomes stable ($Ri_{TL} > 0$) and reaches a peak value at an Ri_{TL} of +0.02 (indicated by the dot-dot-dashed vertical line). The buoyancy flux increases under the same change in stability, except when Ri_{TL} reaches +0.02 it rapidly decreases. Above this value of Ri_{TL}, both fluxes decrease with increasing stability with rate of decrease in $\overline{u'w'}$ larger than in the buoyancy. We believe we are seeing the effects of negative buoyancy damping becoming dominant when the layer Ri_{TL} reaches +0.02. Between 0 and +0.02 are large, intense organized structures in the flow whose motions are not being significantly constrained by the limited damping in this stability range. As the stability and negative damping increase, an expanding number of oscillatory modes that form in the slightly stable flow are attenuated, this in turn reduces the turbulent energy in the corresponding turbulent eddy scales.

In addition to the locally evolving flow characteristics, Figure 3-26b shows the strong positive (upward) and negative (downward) transports (fluxes) of coherent TKE (E_{coh}) taking place within this critical stability range. The high surface temperatures are responsible for the positive fluxes of E_{coh} that are scaled on the left-hand ordinate. The downward flux into the rotor disk layer of E_{coh} (scaled on the right-hand ordinate) is, however, much greater. We know from the measurements taken from the taller 50-m towers the year before that under stable conditions a flow of higher speed air (jet) forms over the wind park. Turbulent momentum is then transferred downward toward the ground and into the wind farm from this higher speed air, which includes coherent turbulence structures, as indicated by Figures 3-26a and b. These conditions produce a very unsteady flow that is manifested by the high degree of variation in level of E_{coh} indicated by the plot of $\sigma_{E_{coh}}$ shown in Figure 3-26c. This variance reaches a peak in the Ri_{TL} range of 0 to +0.02 and decreases with increasing stability.

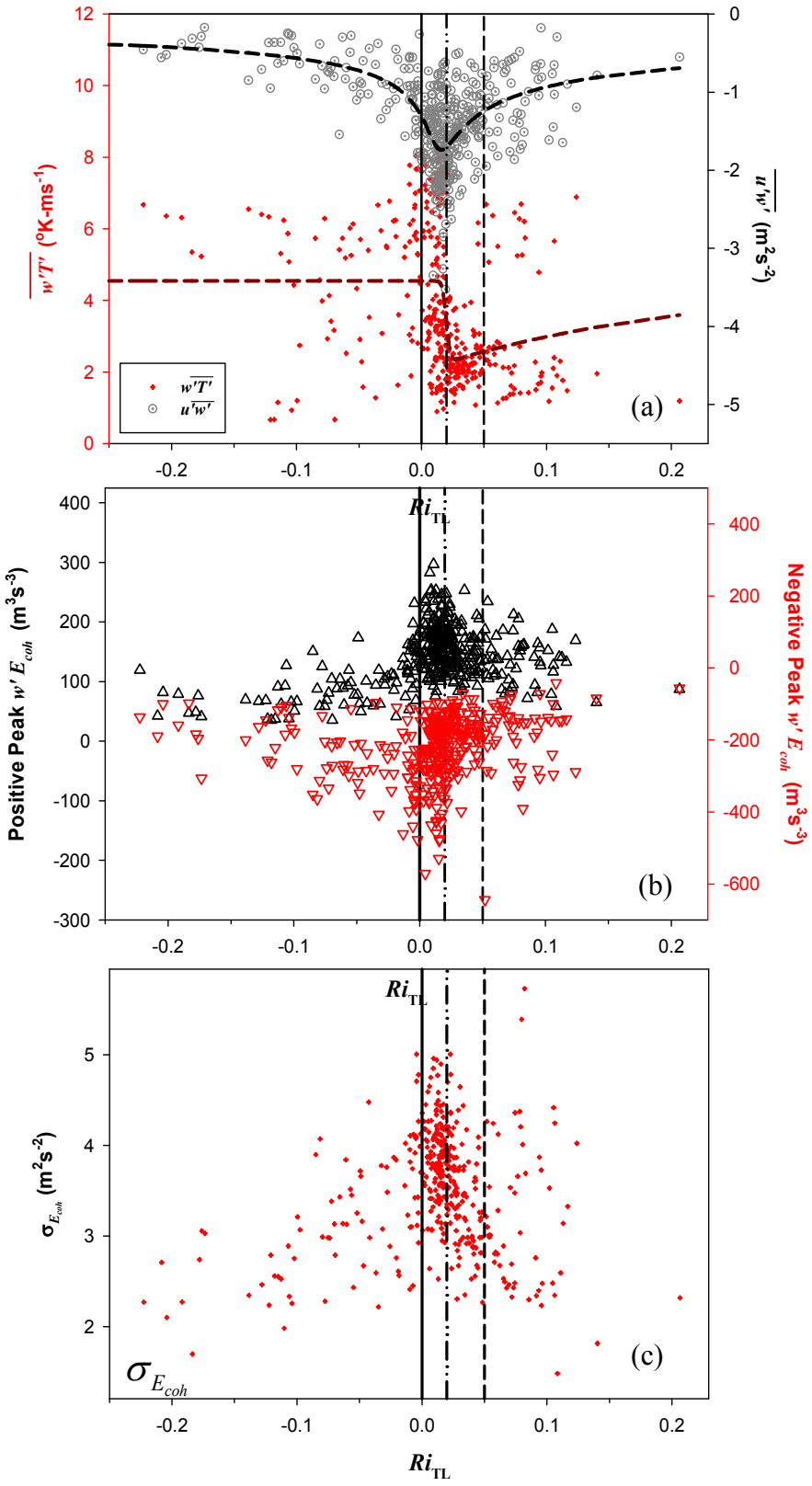

Figure 3-26. Details of variation of fluxes in critical stability range: (a) $\overline{w'T'}$ and $\overline{u'w'}$; (b) positive and negative $w'E_{coh}$ values; and (c) $\sigma_{E_{coh}}$

3.7.2 The Role of the Diurnal Variation and the Dynamics of the Critical Stability Range

Figure 3-27 plots the diurnal variation of some of the key parameters that influence the FBM *DEL*s on the two Micon 65/13 turbines. One of the characteristics of the California wind farm is the low wind speeds (frequently below turbine cut-in) between about 1000 to 1500 LST because of the larger scale atmospheric dynamics. The highest wind speeds typically occur about 3–4 hours after local sunset, or between 2100 and 2400 LST, which also happens to be when a significant number of the turbine outages occurred. As the figure shows, the Ri_{TL} is very close to +0.02 a significant amount of the time between about 1900 to 2300 LST, which is also when the largest fatigue loads tend to occur. The figure shows that the greatest FBM *DEL* values occurred on both turbines at 2000 hours. Concurrent with these elevated loads, the Ri_{TL} was near +0.02, the hub u_* and peak E_{coh} values were very high, and there were intense downward fluxes of coherent TKE ($w'E_{coh}$) of more than –500 $m^3 s^{-3}$. The period between midnight and about 0300 hours experienced some significant loads, and some records showed the stability within this narrow critical range and downward E_{coh} fluxes reaching as large as –400 $m^3 s^{-3}$.

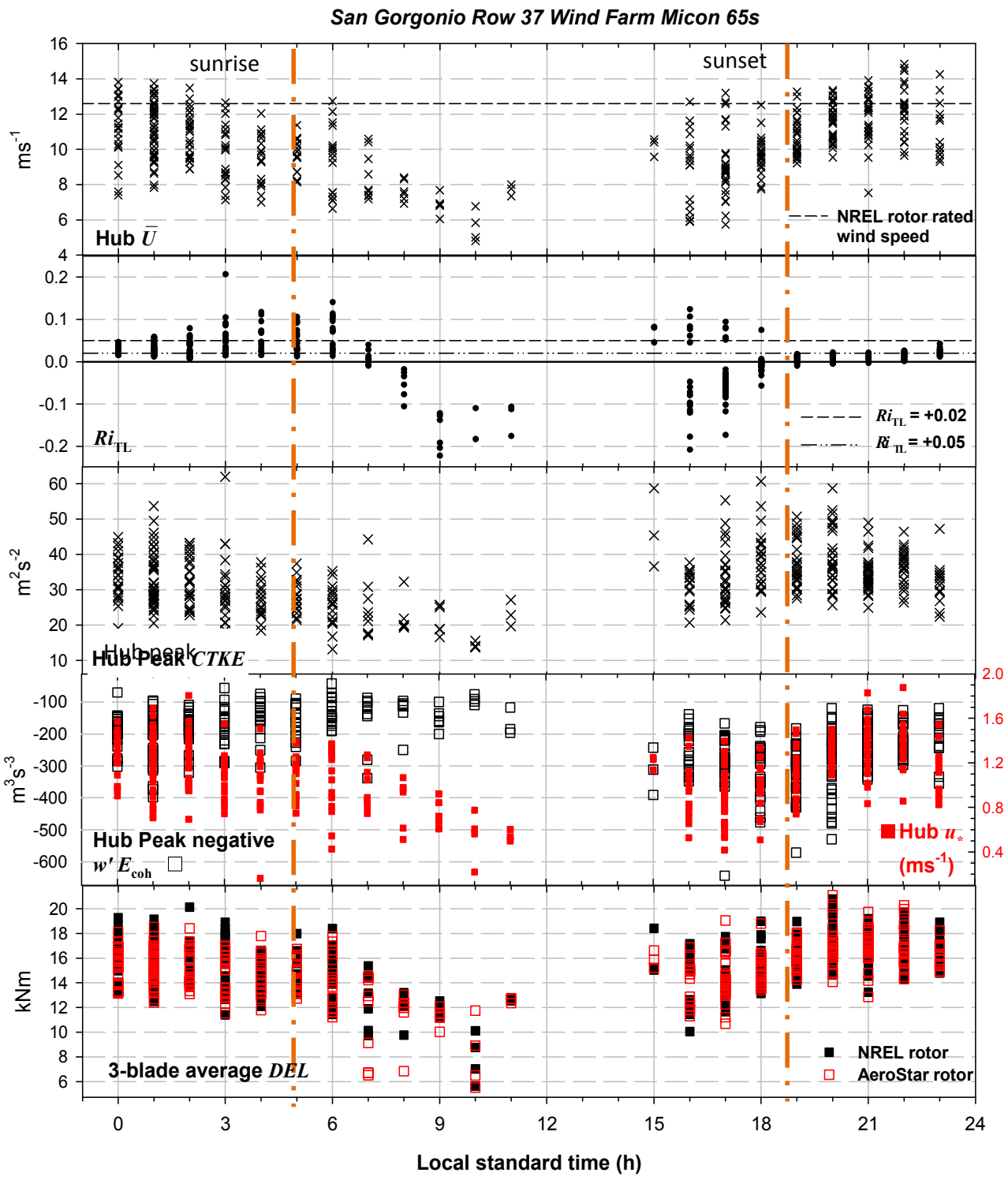

Figure 3-27. Observed diurnal variations of U_{hub}, Ri_{TL}, hub u_* and peak E_{coh}, negative peak $w'E_{coh}$, and three-blade average FBM *DEL*s for Micon 65/13 NREL and AeroStar rotors. Each data point represents the values from an individual 10-minute record.

4.0 Analyzing Turbulence-Turbine Dynamic Response of the NWTC ART

In 1999–2000, we were able to expand our research into examining the role of atmospheric turbulence in the dynamic response wind turbines through a measurement program using a larger, 600-kW turbine installed in the rigorous wind flow of the National Wind Technology Center (NWTC). This experiment was an integral part of the Long-Term Inflow and Structural Testing (LIST) Program jointly conducted by the National Renewable Energy Laboratory (NREL) and the Sandia National Laboratories (SNL).

The results from the Micon 65/13 turbine testing deep within the California wind farm showed that the greatest fatigue damage typically occurred within a weakly stable diabatic flow within the atmospheric layer occupied by the turbines. The level of damage was also sensitive to the local turbulent shearing stress or friction velocity u_*, the variation in the vertical velocity expressed as its standard deviation, and the turbulent vertical flux or transport of coherent turbulent energy. In 2002, SNL found similar sensitivities using a modified version of the Micon 65/13 turbine and an upwind planar array at a Great Plains site near Bushland, Texas.

The California wind farm experiment demonstrated the role of organized or coherent turbulent structures in creating significant dynamic loads in the turbine structural components. The NWTC LIST experiment allowed us to measure the turbine dynamic response to an energetic but natural turbulent inflow and then compare that with what was found in deep within the California wind farm. Further, the upwind planar array provided us with measurements of variation of the inflow turbulence characteristics both vertically and laterally across the dimensions of the turbine rotor disk.

In this section we present an overview the results of the measurements on the Advanced Research Turbine (ART) turbine similar to those from the Micon 65/13 turbines, i.e., the sensitivities to the turbulence characteristics found important in the California wind farm. We also use the much larger (1,569 LIST records versus 397 for the Micons) measurement database to more fully explain and validate some of the processes identified earlier and their relationships to turbine response and the atmospheric conditions that produce it. Finally, we present direct comparisons between the turbulence-induced dynamic responses observed on the San Gorgonio Micon turbines and the NWTC ART to demonstrate the underlying similarities for two significantly different inflow environments.

4.1 ART Dynamic Response to NWTC Inflow Turbulence Characteristics

The variations of the out-of-plane (flapwise) root bending damage equivalent load (*DEL*) with the hub peak E_{coh} and mean wind speed are shown in Figures 4-1a and b, respectively. Figure 4-1a shows that the *DEL* varies as a power law with Ecoh. Figures 4-2 and 4-3 present expanded versions of these plots, including, in addition to the flap bending moment (FBM) *DEL*s, the maximum alternating load cycle, the peak FBM, and the peak with the mean load removed for the entire available population and the observed with the mean below-rated wind speed . Two attributes stand out. First, Figure 4-3 shows greater scatter about the trend line in plots of the response variables to the mean wind speed as compared with the variation with E_{coh} in Figure 4-2. Second, Figure 4-2 clearly shows a significant number high load responses (a positively

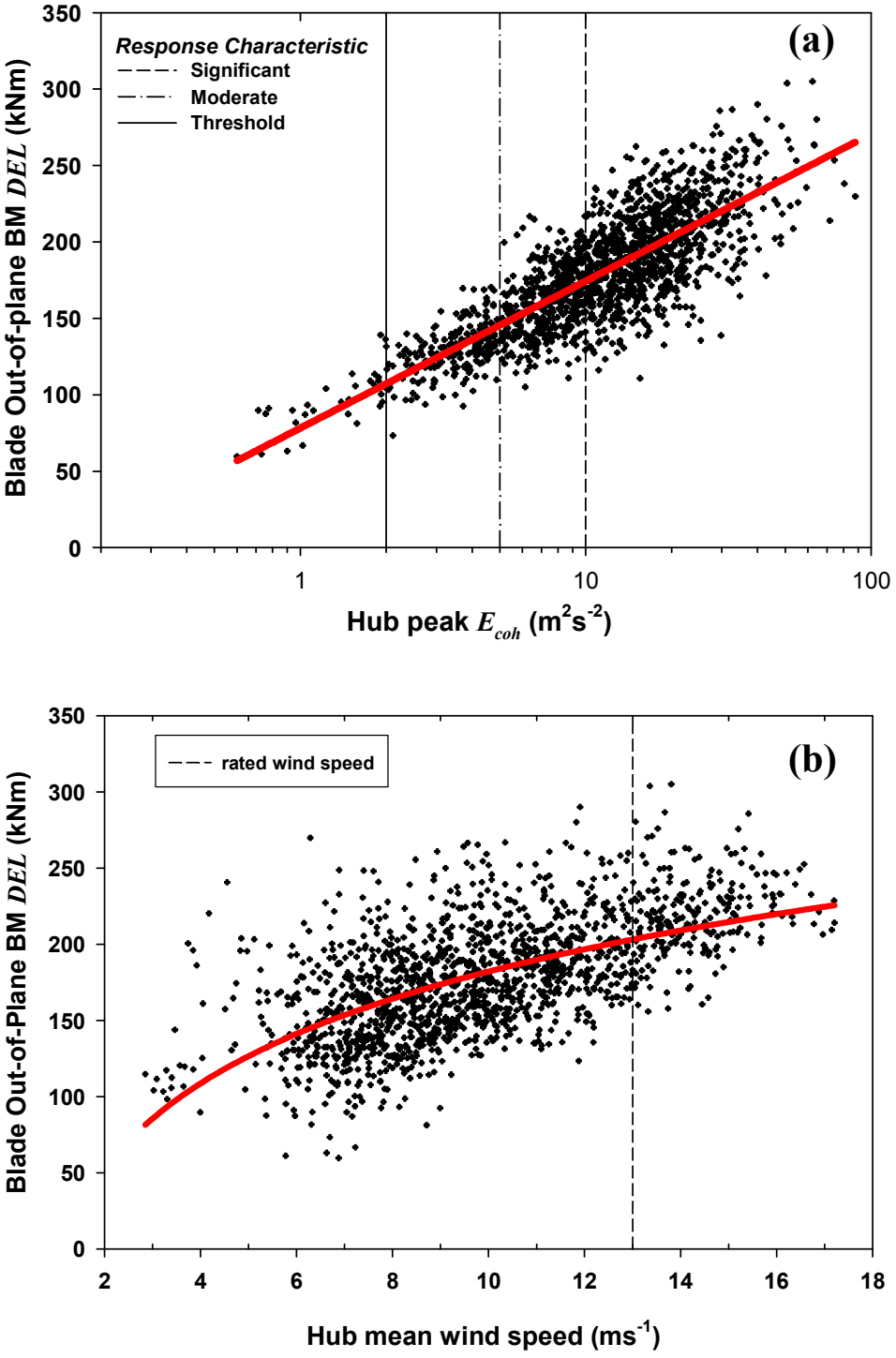

Figure 4-1. Variations of NWTC ART root bending moment *DEL* with hub-height (a) peak E_{coh} and (b) mean wind speed

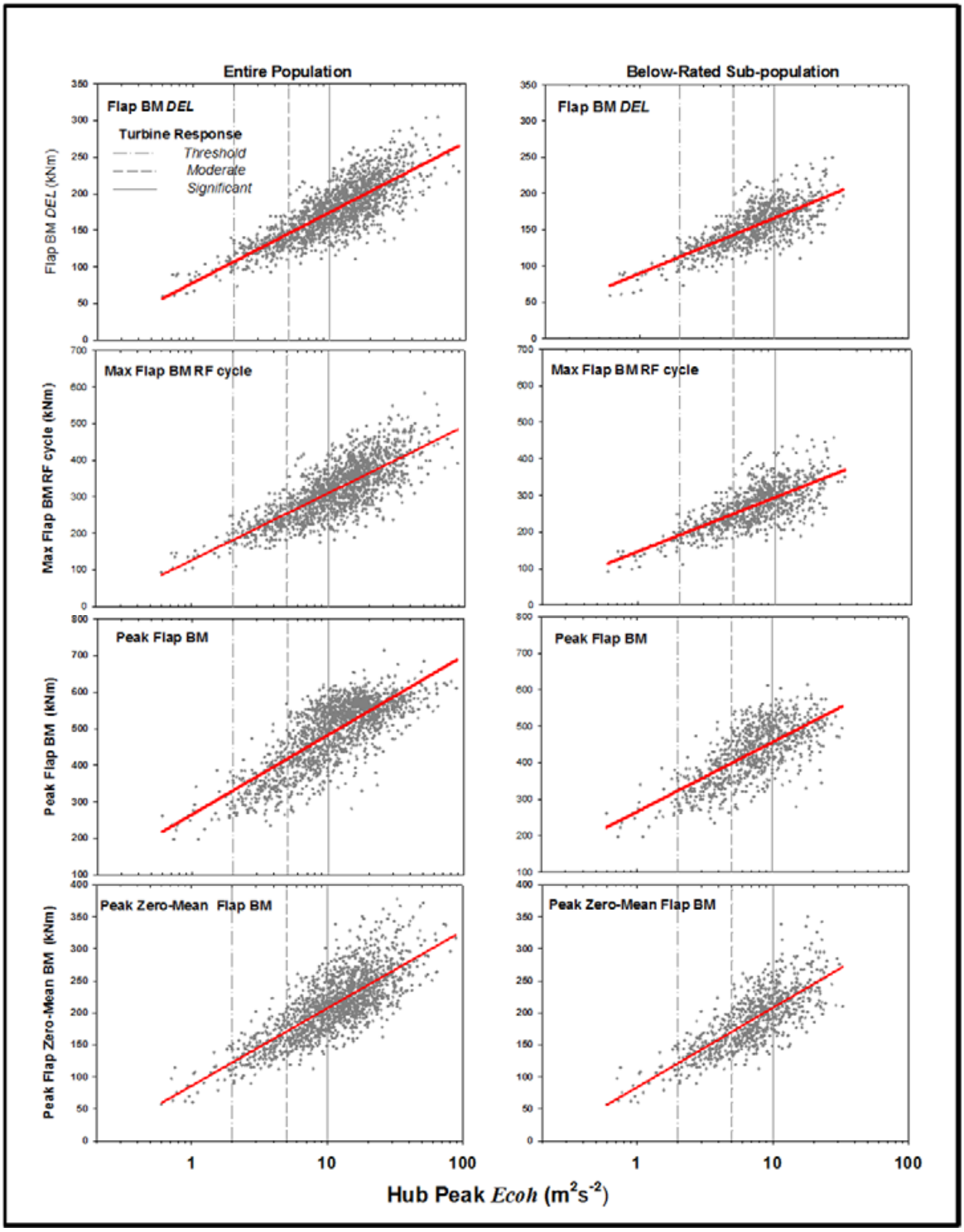

Figure 4-2. Variations of FBM with hub-height peak E_{coh}: (1) *DEL*s, (2) maximum alternating (rainflow) cycle, (3) peak value, and (4) peak value with mean removed for entire available population (left column) and below-rated wind speed (right column)

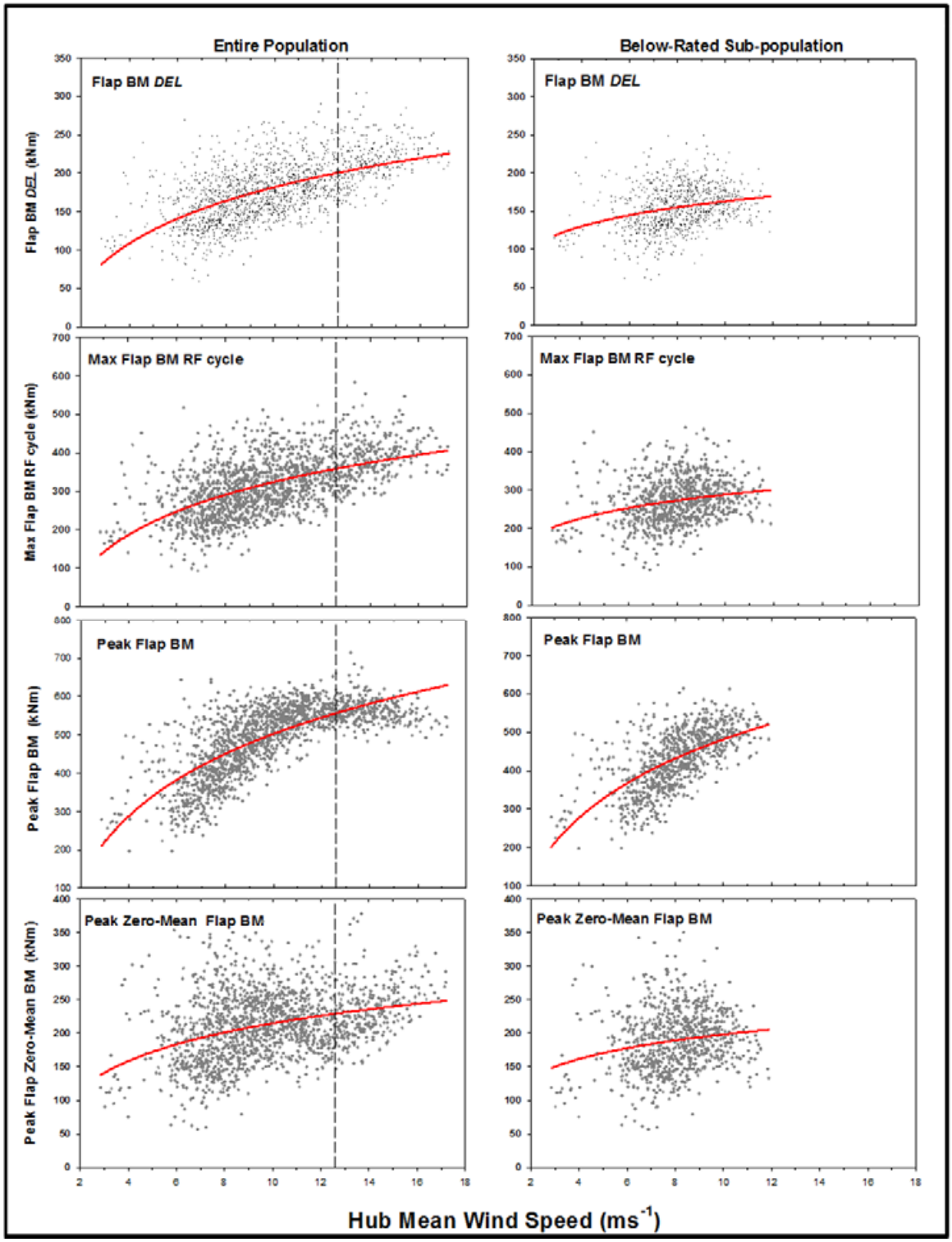

Figure 4-3. Same as Figure 4-2, except with variation with hub-height mean wind speed

skewed distribution) across almost the entire wind speed range, particularly in below-rated wind speed conditions in the right column.

Our analysis of the level of the FBM dynamic response with hub peak values of E_{coh} indicated a threshold of about 2 m^2 s^{-2}, a moderate response at 5 m^2 s^{-2}, and a significant response at 10 m^2 s^{-2} or more. These threshold criteria have been annotated on Figure 4-4a, which is further substantiated by the box plot distributions in Figure 4-4b. This significant response threshold is further supported by the *DEL* probabilities shown in Figures 4-1a and Figure 4-2, which show definite increases in the *DEL* values for peak values of E_{coh} of 10 m^2 s^{-2} or more.

One characteristic of the turbulent inflow to the NWTC ART is the low value of vertical shear, even in stable flow conditions. Figure 4-5a plots the expected values of the power law shear exponent α as function of the hub-height mean wind speed for unstable and stable flow conditions. Higher than about 11 m s^{-1} α is expected to remain below the commonly used value of 1/7 and the IEC Normal Wind Profile (NWP) value of 0.2 (IEC 2005; Section 6.3.1.2). Figure 4-5b shows the variation of the FBM *DEL*s, and demonstrates that they are poorly correlated except that the lowest fatigue loads occur at high values of α. Figures 4-6a and b plot the relationships among α, the mean hub-height wind speed, and Ri_{TL}. They also show the critical stability range found in the California wind farm (Ri_{TL} = +0.01 to +0.05). The figures show that the α value generally remains less than the IEC NWP value of 0.2 within the critical stability range but are accompanied by high mean wind speeds.

Figure 4-7b shows the observed variations of the FBM *DEL*s with Ri_{TL}. Figures 4-7a and 4-7c plot the corresponding variations in the hub peak E_{coh} and σ_w, respectively. The California wind farm critical *Ri* range has also been added to each plot showing the sensitivity of these parameters to this weakly stable flow condition. The FBM fatigue response and the corresponding turbulence parameters peak E_{coh} and σ_w decrease significantly for Ri_{TL} values greater than 0.1, as is indicated by the dotted line and indicating an approximate upper stability limit for larger loads. In the analysis of the California wind farm turbine fatigue and load excursion responses, the hub-height friction velocity u_* and Ri_{TL} were found to be sensitivity parameters, particularly for the former higher wind speeds. In Figure 4-8a we plot the observed variation of hub u_* with Ri_{TL} and indicate the critical stability range. Figure 4-8b plots the variation of hub u_* with the mean hub-height wind speed. Figure 4-8c shows the approximately monotonic variation of the FBM *DEL*s with hub u_*.

4.2 Vertical Inflow Inhomogeneity and Gradients within the ART Rotor Disk

The ART rotor disk is approximately twice the diameter of the California wind farm Micon 65/13 turbines and projects another 35 m (115 ft) deeper into the planetary boundary layer. We used the 23-m (75-ft) hub or 2 m (6 ft) below it (the location of the sonic anemometer) as the reference height on the Micons because it was considered reasonably representative of this smaller rotor. The ART rotor spanned twice the vertical distance of the Micons, however, and we cannot arbitrarily make the same assumption of flow homogeneity across such a large rotor. In Figures 4-9a and b, we compare the variations of the FBM *DEL*s with the standard deviations of the vertical wind component (σ_w) and the vertical flux (transport) of coherent turbulent kinetic energy ($w'E_{coh}$) with height. Figure 4-9a shows that the observed fatigue damage is very highly

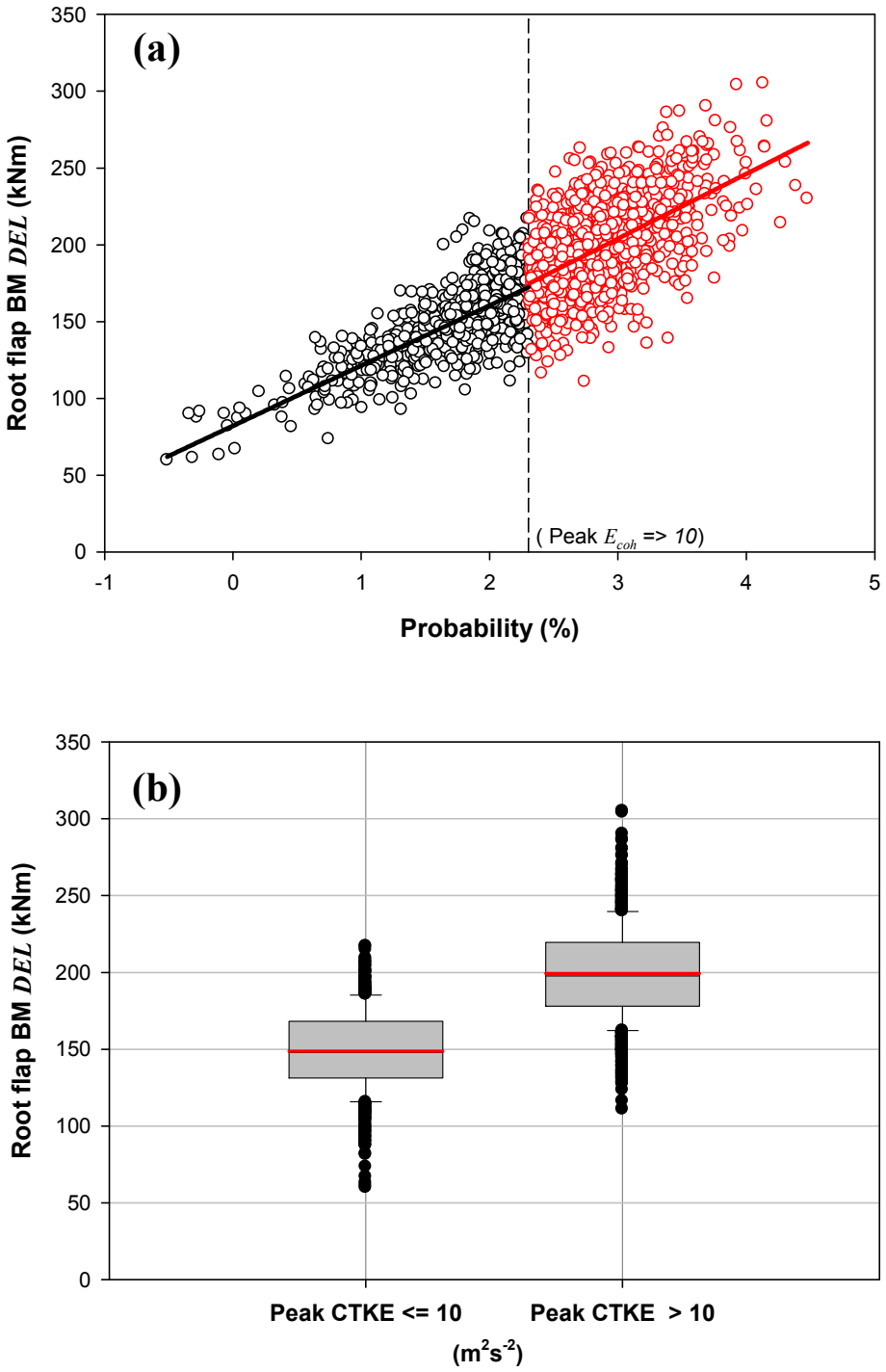

Figure 4-4. Confirmation that hub peak E_{coh} (CTKE) values greater than 10 m^2 s^{-2} are indicative of significant response and resulting *DEL*: (a) probability distribution of FBM *DEL* with 10 m^2 s^{-1} threshold shown; (b) box plots of FBM *DEL* distributions for values of peak E_{coh} ≤10 and > 10 m^2 s^{-2}

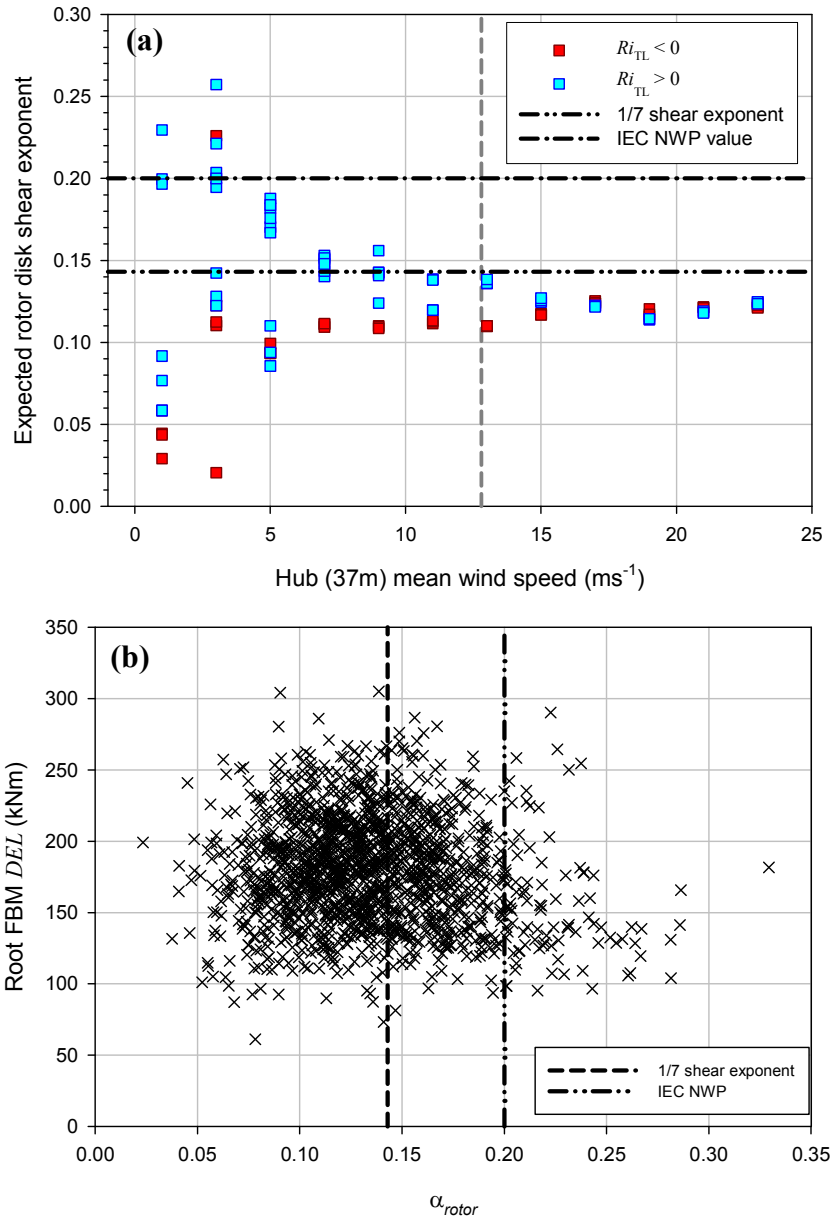

Figure 4-5 (a) Available population of expected variation of ART rotor disk shear exponent α with hub (37-m) mean wind speed for unstable (Ri_{TL} < 0) and stable (Ri_{TL} > 0) flows; (b) variation of FBM *DEL* with rotor disk α. In general, the FBM *DEL*s are not well correlated with α, although the lowest values tend to occur at its highest values.

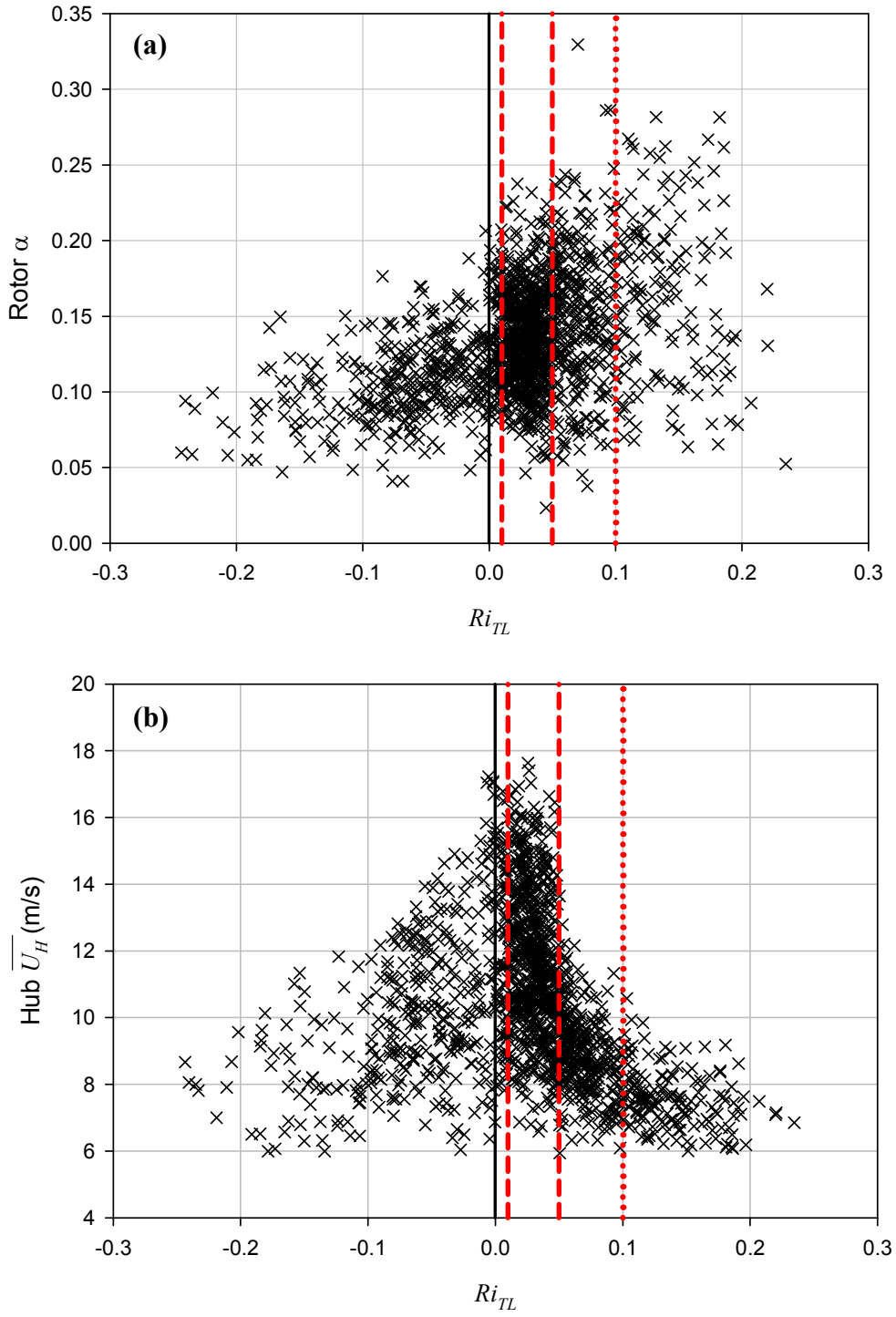

Figure 4-6. Variation of (a) rotor disk shear exponent α and (b) hub-height mean wind speed with Ri_{TL}. The critical Ri_{TL} value range of +0.01 to +0.05 found in the California wind farm is also shown. The mean wind speeds drop significantly above an Ri_{TL} value of +0.1.

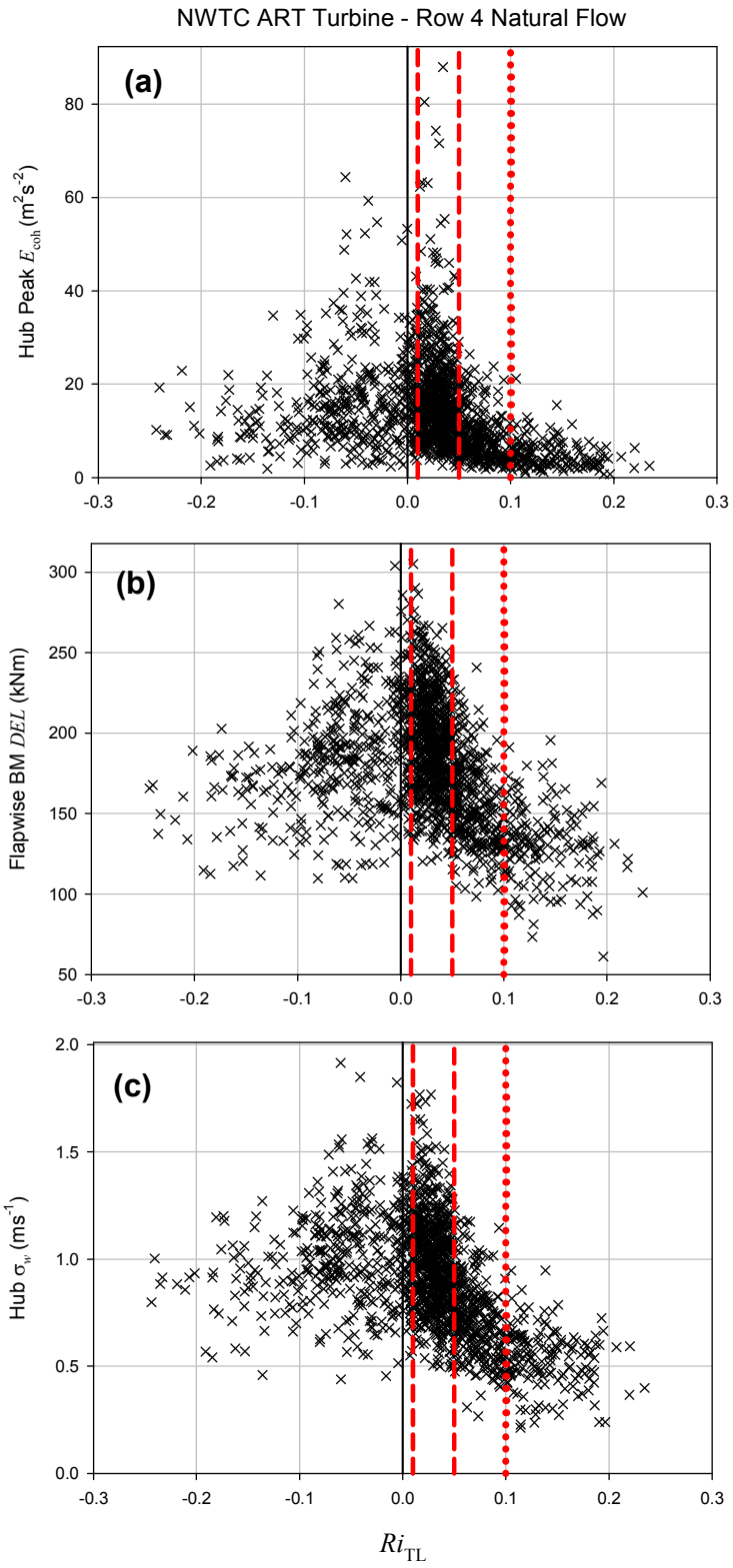

Figure 4-7. Variation of (a) hub-height peak E_{coh}, (b) FBM *DEL*s, and (c) hub-height σ_w with Ri_{TL}. The critical Ri_{TL} stability range found in the California wind farm (+0.01 to +0.05) is shown as dashed lines.

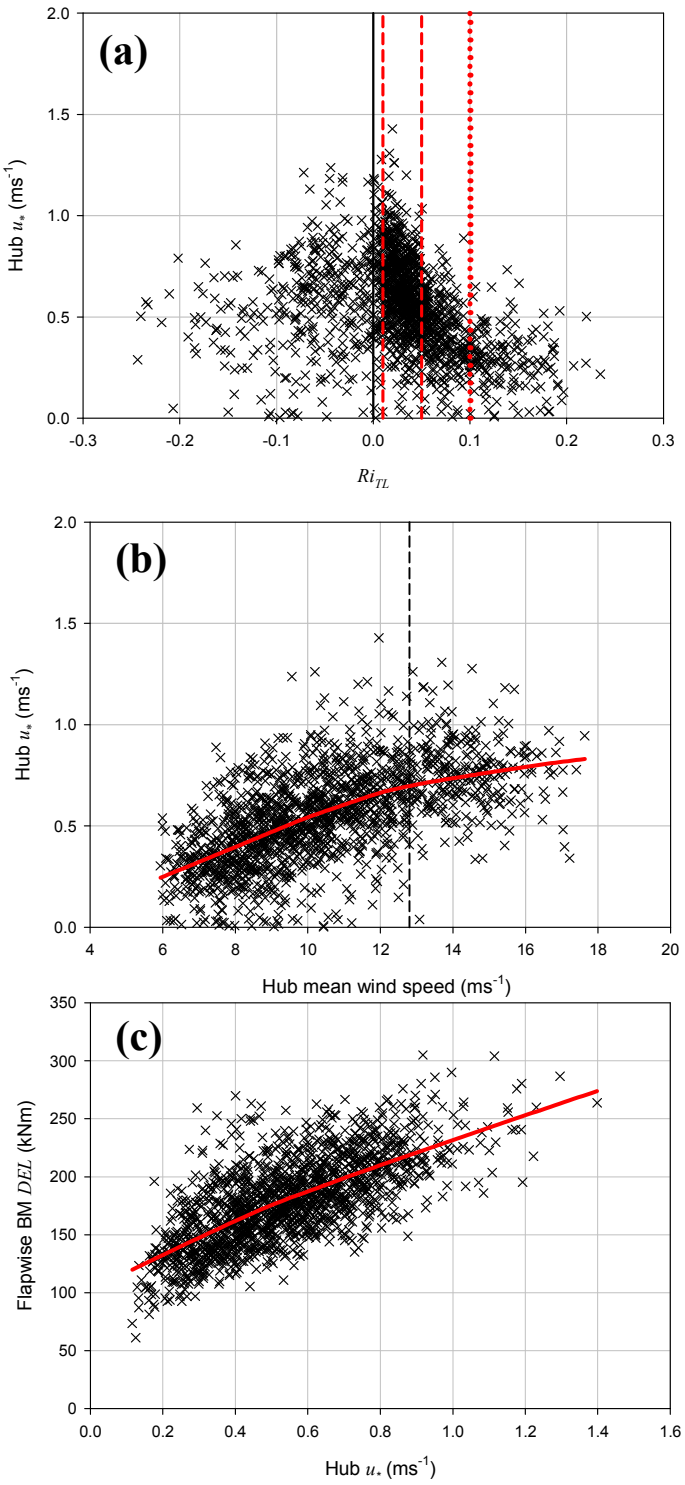

Figure 4-8. Observed variation of hub friction velocity u_* with (a) Ri_{TL} and (b) hub mean wind speed. Critical Ri_{TL} stability range is shown as red dashed lines in (a) and the ART rated wind speed is a black dashed line in (b). The variations of the FBM *DEL*s with hub-height u_* are plotted in (c).

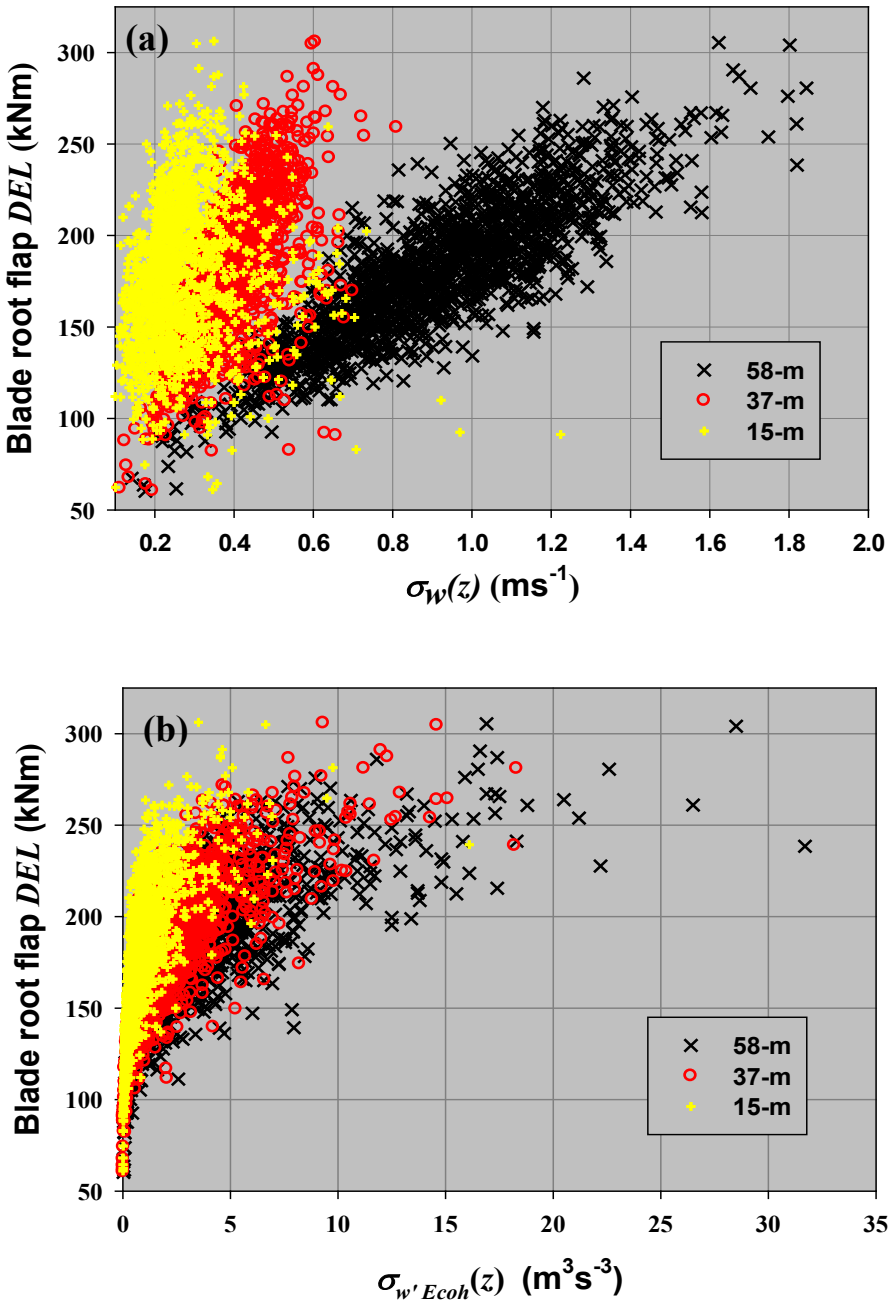

Figure 4-9. Correlation of blade FBM *DEL*s with height variation of standard deviations of (a) vertical wind component σ_w and (b) vertical flux of coherent turbulent kinetic energy, $w'E_{coh}$

correlated with variations in vertical velocity at the top of the turbine rotor (58 m or 190 ft) and less so at the hub height (37 m or 121 ft) and even less at the bottom (15 m or 49 ft). These large variations in the vertical wind also translate into significant fluctuations in the vertical transport of E_{coh} which can induce high levels of fatigue in the blade roots, as is shown in Figure 4-9b. The correlations with the FBM *DEL*s show that they are sensitive to E_{coh} vertical transport fluctuations in the upper portion of the rotor disk (37- and 58-m heights). The vertical inhomogenity is further underscored by Figure 4-10a. Here the FBM *DEL*s are shown to be more strongly correlated with peak positive (upward) values of the vertical flux of E_{coh} ($w'E_{coh}$) at hub height (37 m) but more correlated with negative (downward) $w'E_{coh}$ fluxes at the top of rotor (58 m). Figure 4-10b shows the largest variations in peak $w'E_{coh}$ take place within the critical stability range.

Figure 4-11 examines the heterogeneous flow conditions entering the ART rotor and their relationship to the fatigue loading further. Here the variations in the FBM *DEL*s and peak E_{coh} values correlate with the mean momentum flux $\overline{u'w'}$ at the 15-, 37-, and 58-m heights. The observed FBM *DEL*s correlate only over a narrow range of $\overline{u'w'}$ at the 15-m height that is mostly negative (downward flux), but small positive fluxes are also observed. The peak values of E_{coh} at this height are more correlated with the downward mean fluxes. At the 37-m height, we see the largest mean fluxes and the fatigue loads are correlated with both positive and negative values, with the former being more prevalent. Similarly, the peak E_{coh} values at this height tend to occur with positive momentum fluxes. The largest fatigue loads are associated with the greatest mean momentum fluxes, both negative and positive. Finally, using the 58 m as a reference, the fatigue loads are highly correlated with primarily downward momentum fluxes, as are the peak values of E_{coh} at this height. These graphs emphasize the significant spatial heterogeneity of the turbulent flows entering the 42-m layer occupied by the ART rotor disk. They indicate the following:

- A significant downward turbulent flux containing coherent elements is entering the rotor disk layer from above.
- Strong vertical mixing is taking place within the disk near hub height, which is contributing to the observed high levels of fatigue damage.
- The vertical momentum flux is being damped out as it approaches the ground, as seen at the lowest elevation of the rotor disk, and probably does not contribute as much to the observed fatigue loads as is taking place higher in the rotor disk layer.

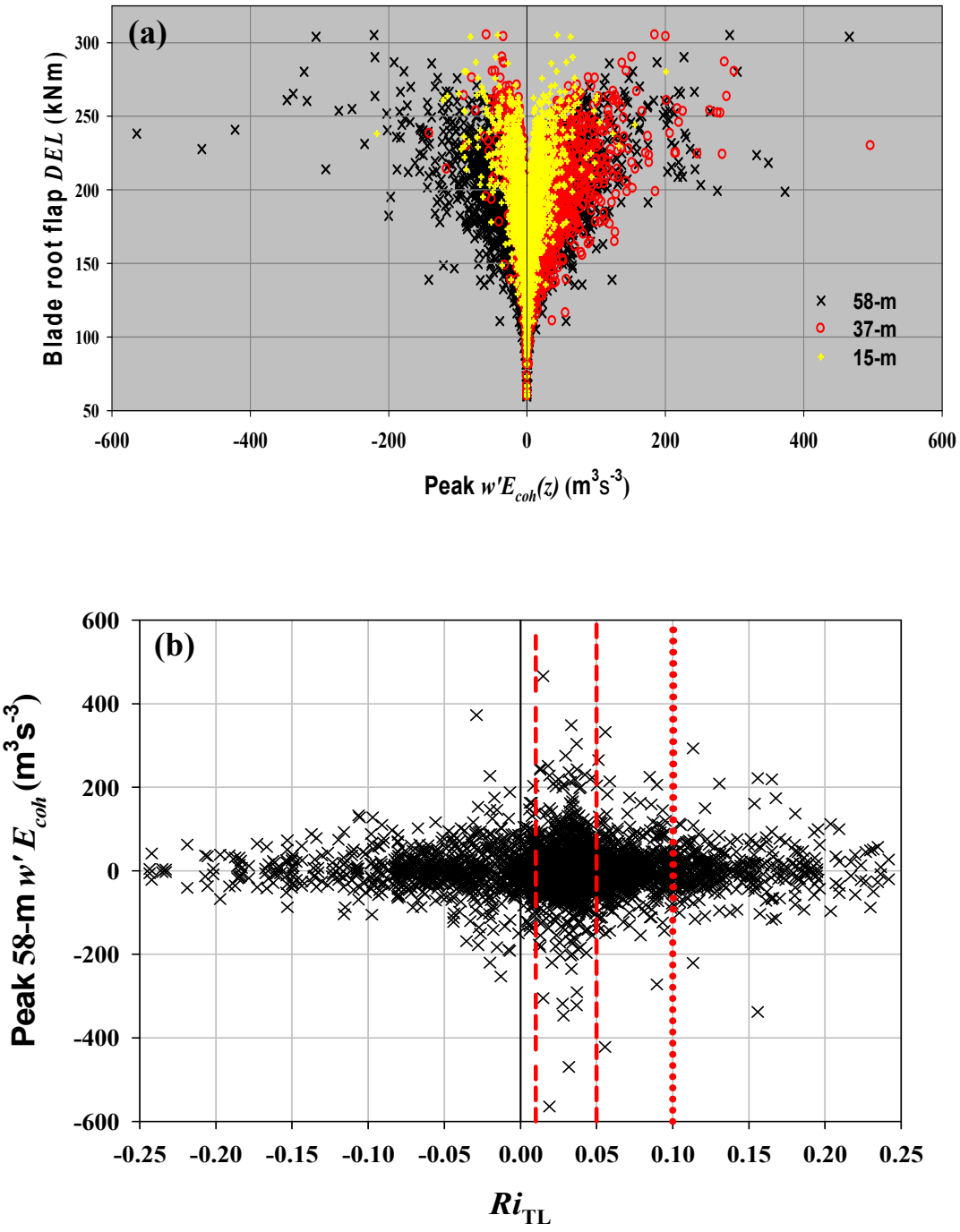

Figure 4-10. (a) Correlation of blade FBM *DEL*s with height variation of peak values of vertical flux of coherent turbulent kinetic energy, $w'E_{coh}$; (b) variation of peak value of $w'E_{coh}$ at the top of the ART rotor (58 m) with Ri_{TL}. The California wind farm critical stability range is shown between the vertical dashed lines.

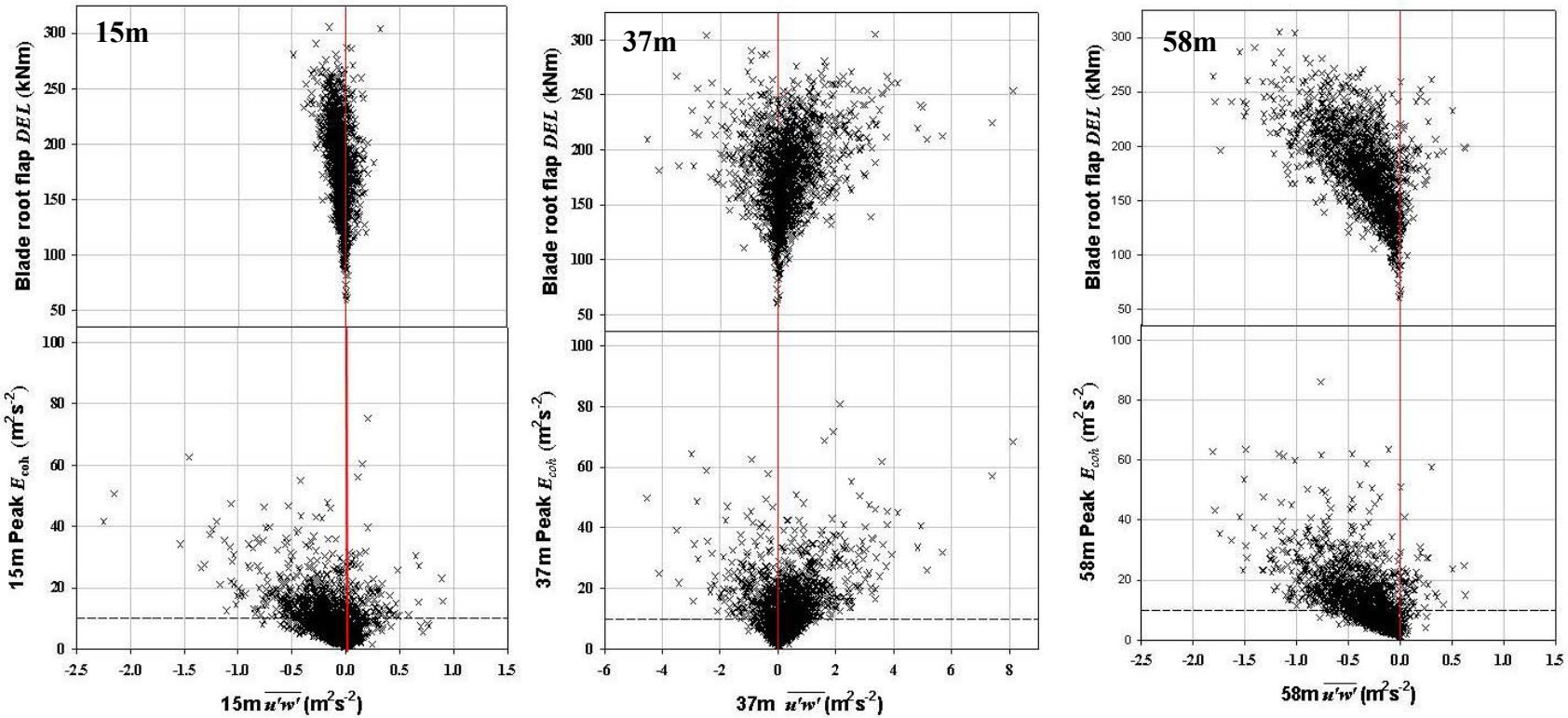

Figure 4-11. Relationship of blade root flapwise *DEL*s with height variations in peak E_{coh} and mean vertical momentum flux, $\overline{u'w'}$

4.3 NWTC ART Turbulence Scaling Sensitivities

We found when analyzing the California wind farm Micon 65/13 turbines that LOESS-smoothed 3-D contour plots are an excellent tool to visualize the relationships between the key turbulence scaling parameters and the turbine aeroelastic and fatigue damage as well as between the parameters themselves.

4.3.1 Turbine Aeroelastic Response to the NWTC Natural Inflow

We now examine both the mean and the dynamic response of key turbine structural elements to turbulence characteristics to which the Micon 65/13 turbines were most sensitive.

4.3.1.1 Mean Blade Root Flapwise and Edgewise Bending Loads

Figure 4-12 plots the smoothed variations of NWTC ART mean root flapwise and edgewise bending loads operating in a natural inflow environment as a function of Ri_{TL} in. In Figure 4-12a the variation of these mean loads is plotted as contours with Ri_{TL} and the hub-height average *U*-component wind speed with the flapwise load on the left and the edgewise on the right. The rated wind speed is indicated by a horizontal dashed line. The upper limit ($Ri_{\mathrm{TL}} = +0.05$) of the critical stability range identified with the Micon 65/13 turbines is shown as a vertical white dashed line. In general, the highest mean flapwise loads occur in the vicinity of the rated wind speed and do not become sensitive to the stability until it is reached. Afterward a strong correlation with the critical stability range extends up to a Ri_{TL} value of about +0.10. A similar correlation is seen for the mean edgewise bending loads, with the exception that the peak response occurs just below the rated wind speed and in slightly unstable (convective instability) flows ($-0.05 < Ri_{\mathrm{TL}} < 0$). Figures 4-12b and c show the influence of the critical stability range on the flapwise mean loads when coupled with the disk-averaged shear stress (u_*) and hub peak values of E_{coh}. The edgewise loads in contrast are more sensitive to unstable or convective flows. One exception is the sensitivity to relative high values of E_{coh} for Ri_{TL} values greater than about +0.15. We return to this later for further discussion.

4.3.1.2 Turbine Nacelle and Low-Speed Shaft Dynamic Response

Figure 4-13 summarizes the turbine nacelle response as indicated by the accelerometer triad in the inertial measurement unit (IMU) mounted on the forward low-speed shaft support bearing (pillow block) correlated with the turbine layer stability and the disk-averaged mean Reynolds stresses $\overline{u'w'}$, $\overline{u'v'}$, and $\overline{v'w'}$. Nacelle accelerations exhibit a strong sensitivity in the critical stability range, particularly when high degrees of cross-correlations exist in the fore-aft (*X*) and side-to-side (*Y*) directions; there is, however, much less sensitivity in the vertical (*Z*) direction. This significant sensitivity to the critical stability range is further underscored by the smoothed cross-correlation contours in Figures 4-14 and 4-15. The uppermost row of Figure 4-14 shows the variation of the nacelle accelerations with the disk-averaged mean buoyancy flux $\overline{w'T'}$. These plots show that nacelle accelerations along all three axes within the critical stability range are correlated with positive (upward) buoyancy fluxes and large values can also occur with strong negative buoyancy fluxes in unstable flows. The significant sensitivity of the 3-D nacelle motions to disk-averaged peak E_{coh} and its vertical flux or transport $\overline{w'E_{coh}}$ pictured in the center and lowest rows of Figure 4-14 within the critical stability range is unambiguous. This critical range sensitivity is further emphasized in the correlations of the nacelle accelerations with the disk-averaged variations in the *u*, *v*, and *w* turbulent wind components expressed by their standard deviations σ_u, σ_v, and σ_w in Figure 4-15. Figure 4-16 presents contour plots of the 50%

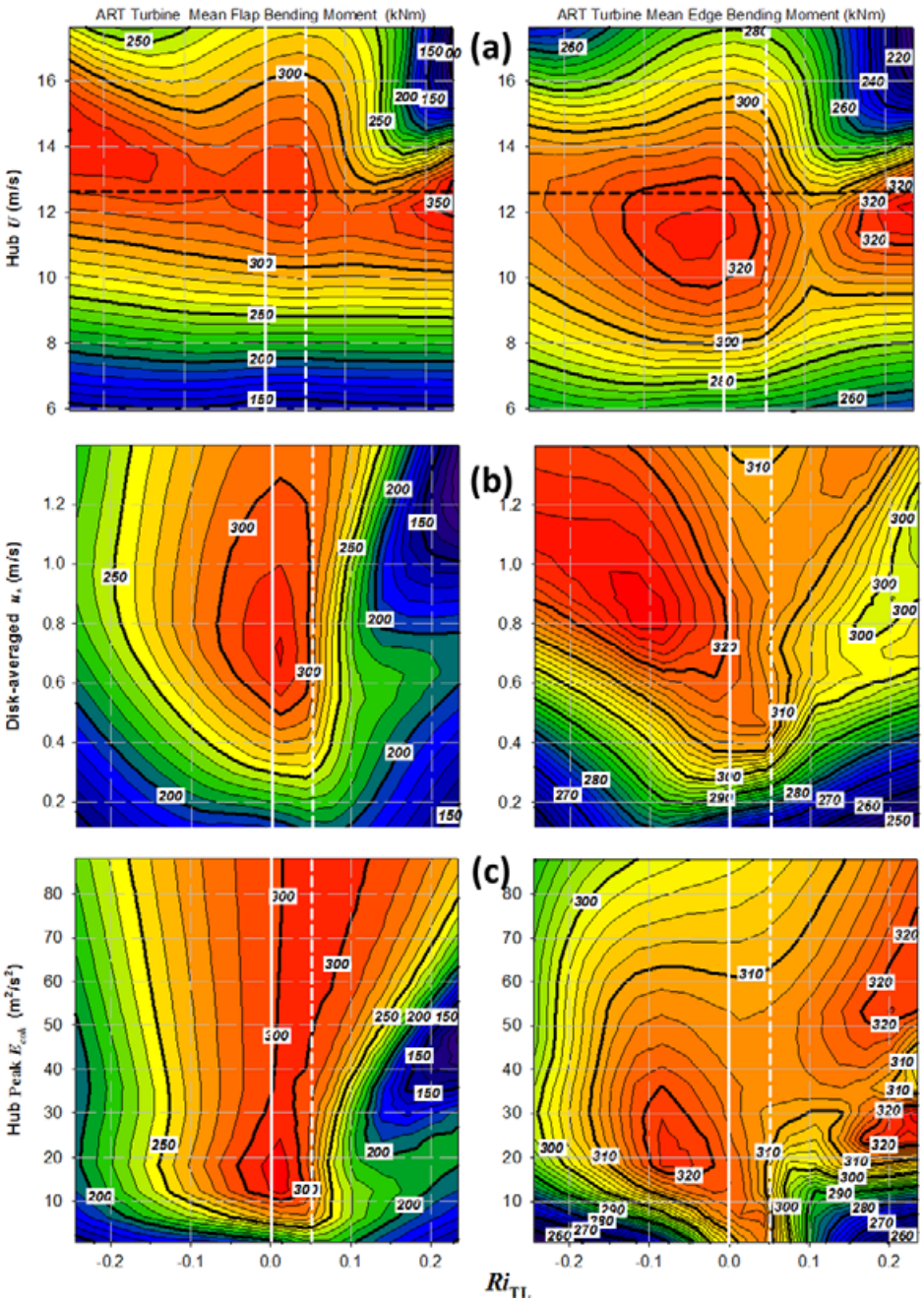

Figure 4-12. Smoothed variations of NWTC ART mean root flapwise (left) and edgewise (right) bending moments with Ri_{TL} and (a) hub-height $\overline{U}$; (b) disk averaged u_* ; and (c) hub-height peak E_{coh} . The dashed line in (a) represents the rated wind speed, 12.8 m s^{-1}. The vertical white dashed line indicates the upper limit of the critical stability range.

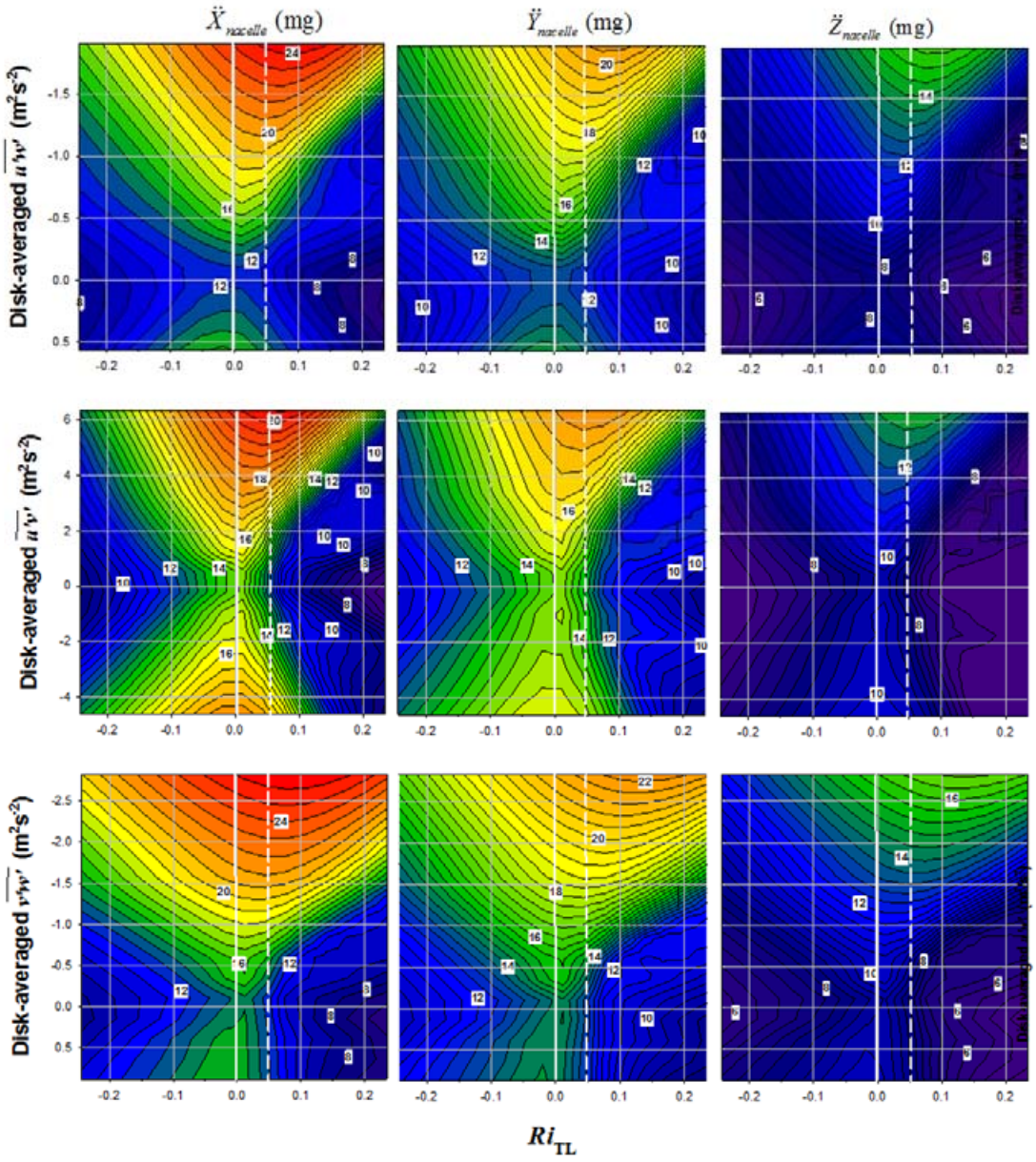

Figure 4-13. Smoothed variations of NWTC ART IMU forward nacelle accelerations with Ri_{TL} and mean disk-averaged turbulent Reynolds stress components $\overline{u'w'}$, $\overline{u'v'}$, and $\overline{v'w'}$. The variation of the fore-aft acceleration ($\ddot{X}$) is shown in the left column, the side-to-side or lateral acceleration ($\ddot{Y}$) in the center column, and the vertical acceleration ($\ddot{Z}$) in the right column.

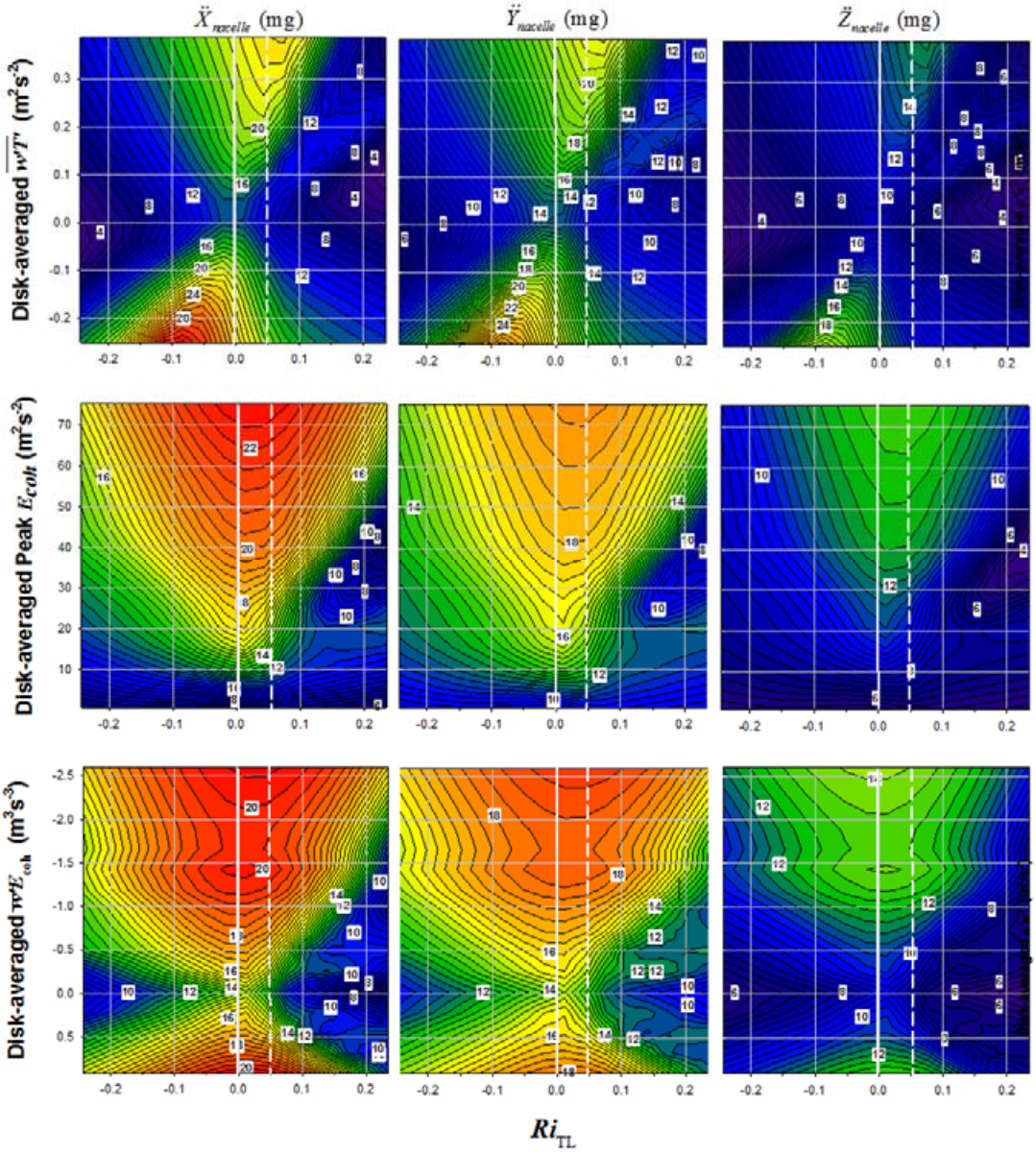

Figure 4-14. Smoothed variations of NWTC ART IMU forward nacelle *X*, *Y*, and *Z* acceleration responses (mg or g/1000) with Ri_{TL} and disk-averaged buoyancy flux $\overline{w'T'}$ in the top row, peak E_{coh} in the center row, and E_{coh} vertical flux, $w'E_{coh}$ in the bottom row

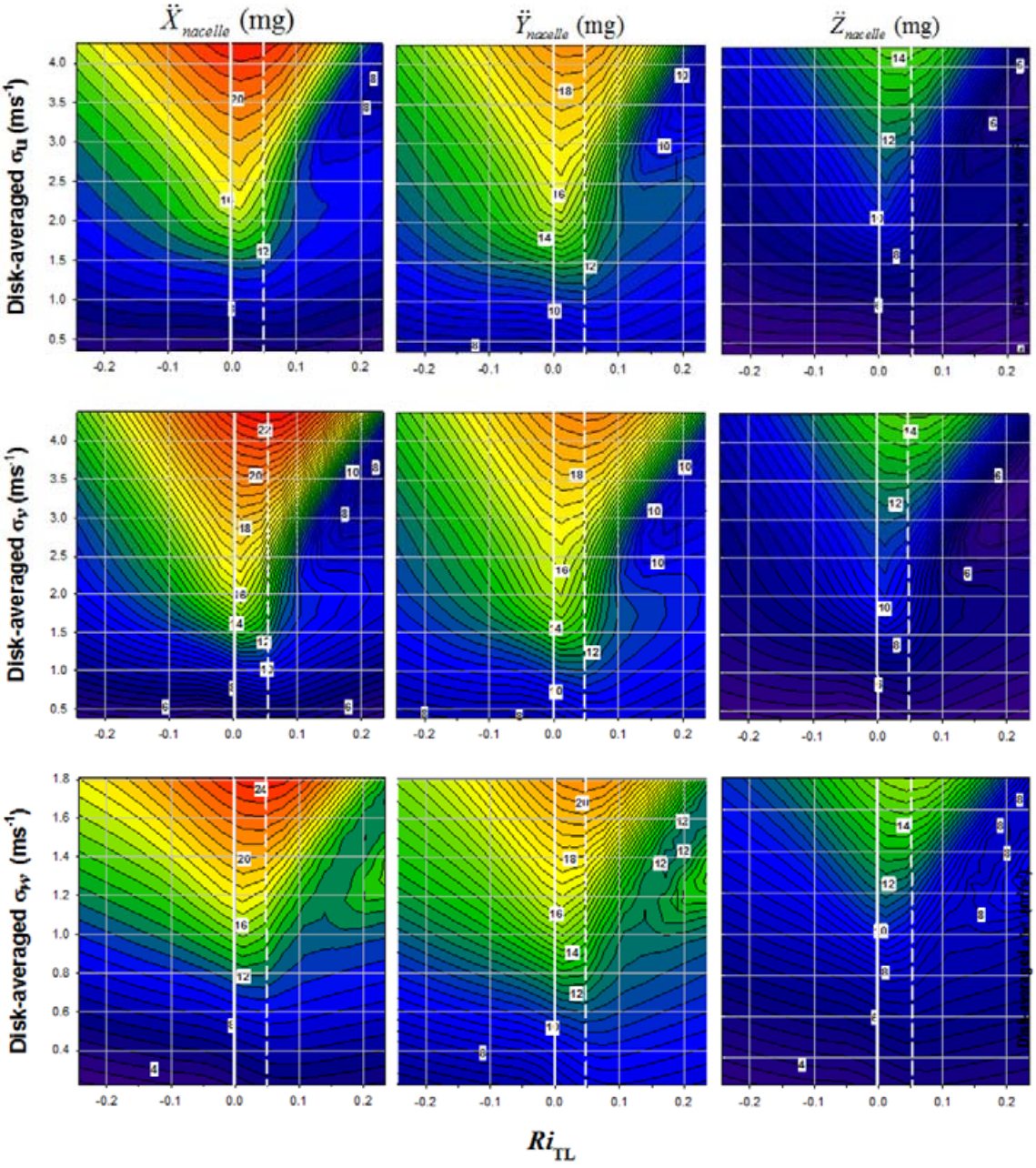

Figure 4-15. Smoothed variations of NWTC ART IMU forward nacelle *X*, *Y*, and *Z* mean acceleration responses (mg) with Ri_{TL} and disk-averaged standard deviations of *u*-component (σ_u) in top row, *v*-component (σ_v) in center row, and *w*-component (σ_w) in bottom row

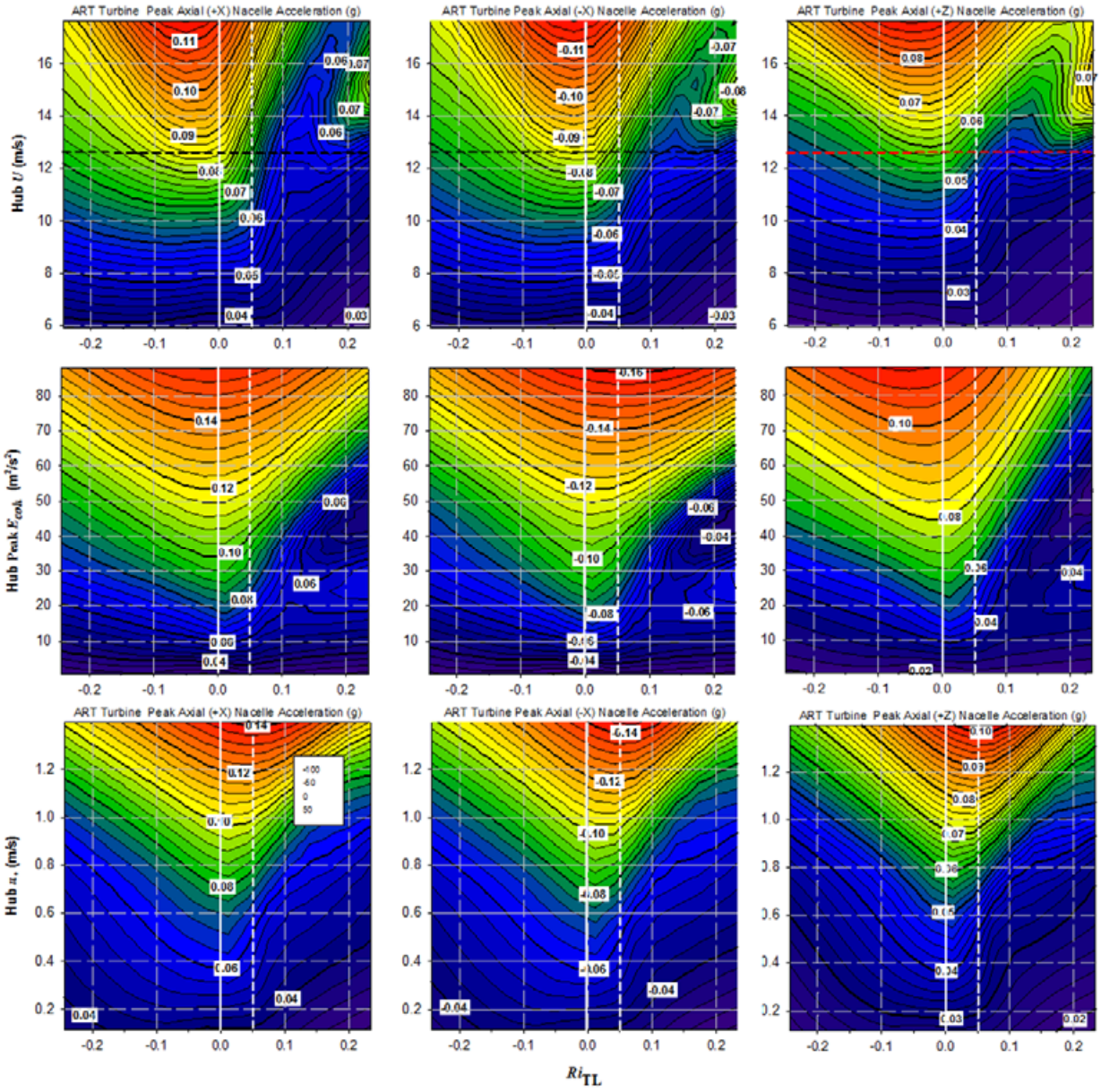

Figure 4-16. Smoothed variations of NWTC ART nacelle IMU peak longitudinal (±*X*) [columns (a) and (b)] and positive vertical (+*Z*) [column (c)] peak acceleration responses (g) with Ri_{TL} and hub height: $\overline{U}$ (top row); peak E_{coh} (center row); and local shear stress or friction velocity u_* (bottom row)

LOESS-smoothed variations of the peak positive (downwind) and negative (upwind) longitudinal (±*X*) and positive (upward) (+*Z*) accelerations with Ri_{TL} and the hub-height $\overline{U}$ in the top row, peak E_{coh} in the center row, and the mean shearing stress or friction velocity u_* in the bottom row. It is clear that the largest nacelle accelerations along all three axes are most sensitive to weakly convective or unstable flow conditions ($Ri_{TL} \cong -0.05$). They are also, however, the most sensitive to peaks in the hub-height values of E_{coh} and u_* within the critical stability range ($+0.01 \le Ri_{TL} < +0.05$), which indicates the presence of coherent turbulent motions of the right dimensions in the flow. Similar sensitivities are found in the nacelle peak pitch, roll, and yaw angular responses with the hub-height mean wind speed $\overline{U}$ in Figure 4-17. The significant sensitivity of the angular responses to peak values of E_{coh} in flows whose stability is within the critical stability range is shown in Figure 4-18, again indicating a response to the presence of turbulent coherent structures. Finally, Figure 4-19 shows the smoothed response of the low-speed shaft torque (τ) variations (σ_τ) to variations in stability and the disk averages of the Reynolds stress components and turbulent wind component standard deviations. Although there is some identifiable sensitivity with stability and the critical range in particular, the correlations in variations of low-speed torque are dominated by both the cross-axis turbulent wind correlations and variations in the 3-D wind vector.

4.3.1.3 Turbine Blade Root Flapwise Fatigue Response

We previously found in the California wind farm Micon 65/13 turbines that low-cycle, high amplitude loads and consequently the *DEL*s scaled with the hub-height mean shearing stress or friction velocity u_* and Ri_{TL}. We also found that the *DEL*s were highly correlated with the hub-height peak values of E_{coh}. In Figure 4-20 we plot the observed variation of the ART blade root FBM *DEL*s with Ri_{TL} and disk-averaged u_* and peak values of E_{coh}. Again we show the upper limit of Ri_{TL} of +0.05 as a white vertical dashed line. In Figure 4-21 we plot the smoothed variation of the FBM *DEL*s with Ri_{TL} and the hub-height turbulence intensity ($\sigma_U / \overline{U}$). Finally, in Figure 4-22, we display the variation of the largest observed FBM within an individual 10-minute record with the corresponding values of Ri_{TL} and the disk-average u_*. Clearly the critical stability range and these two choices of the other turbulence scaling parameters significantly influence the level of fatigue damage and peak loads observed for the ART in the NWTC operating environment.

In Figure 4-23 we plot the smoothed variation of the FBM *DEL*s with Ri_{TL} and the disk-averaged mean Reynolds stress components $\overline{u'w'}$, $\overline{u'v'}$, and $\overline{v'w'}$, and the buoyancy flux $\overline{w'T'}$. Again, the Ri_{TL} range is a significant feature of the response with these variables averaged over the entire rotor disk. Because the ART rotor is twice the dimensions of the Micon turbines and because it extended deeper into the planetary boundary layer (PBL), we analyzed the variations in Figure 4-24 at the three measurement heights of 15, 37, and 58 m available in the upwind planar array. The 37-m variables are the means of the three measurements at this height. Figure 4-24 shows these results for the same scaling variables as Figure 4-23 in columns [**a**], [**b**], [**c**], and [**d**], respectively. Although the general patterns agree with those derived from disk averages in Figure 4-23, a closer examination reveals distinct differences in the contours of the *DEL*s with some of the scaling parameters with height. For example, the *DEL*s with $\overline{u'w'}$ in column [**a**] vary with height with the largest *DEL* values

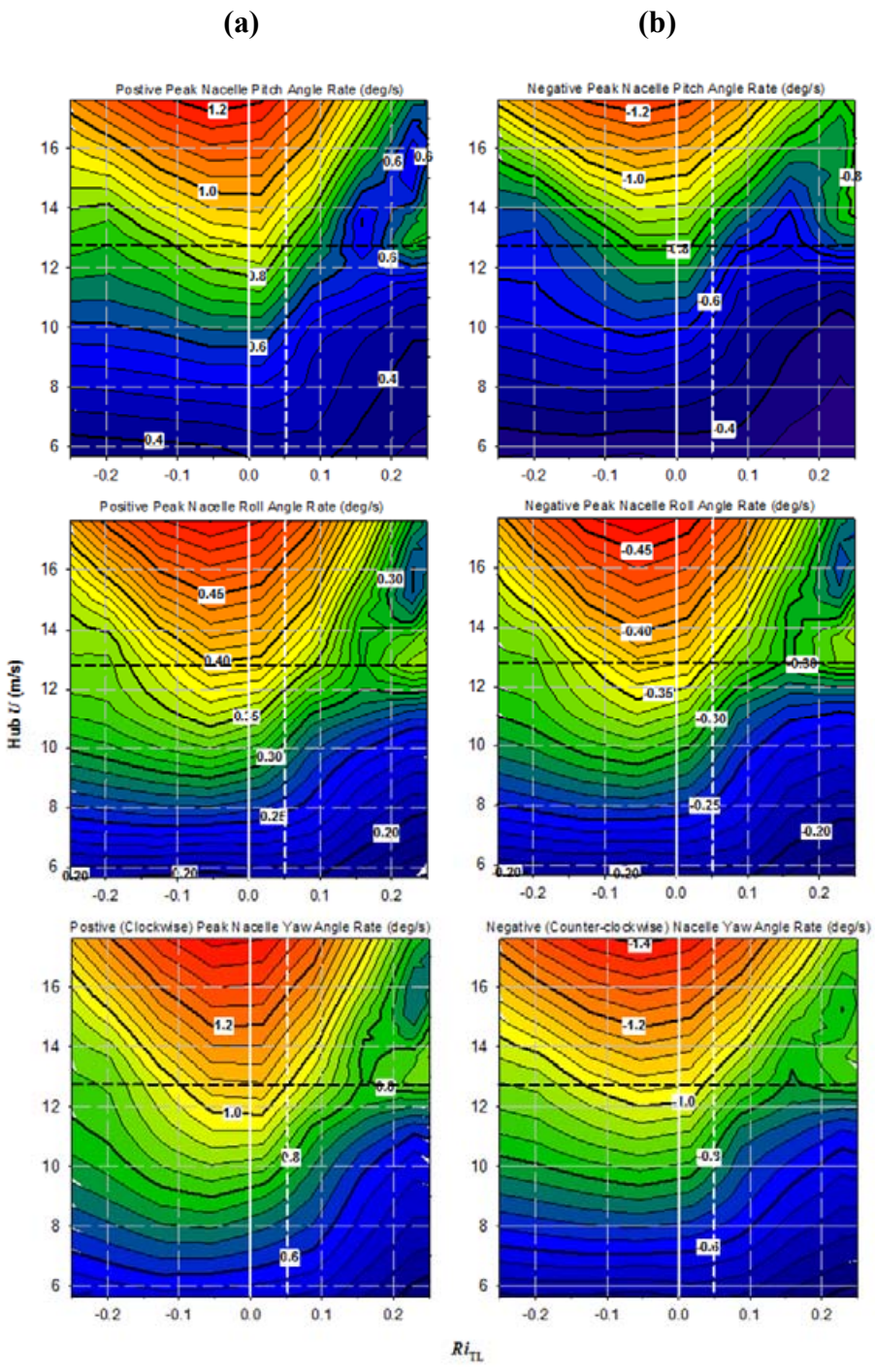

Figure 4-17. Smoothed variations of NWTC ART nacelle IMU peak angular response rates (positive in column [a] and negative in column b) with Ri_{TL} and hub-height mean wind speed $\overline{U}$ with pitch angle response (top row), roll angle response (center row), and yaw angle response (bottom row). Horizontal dashed line indicates rated wind speed.

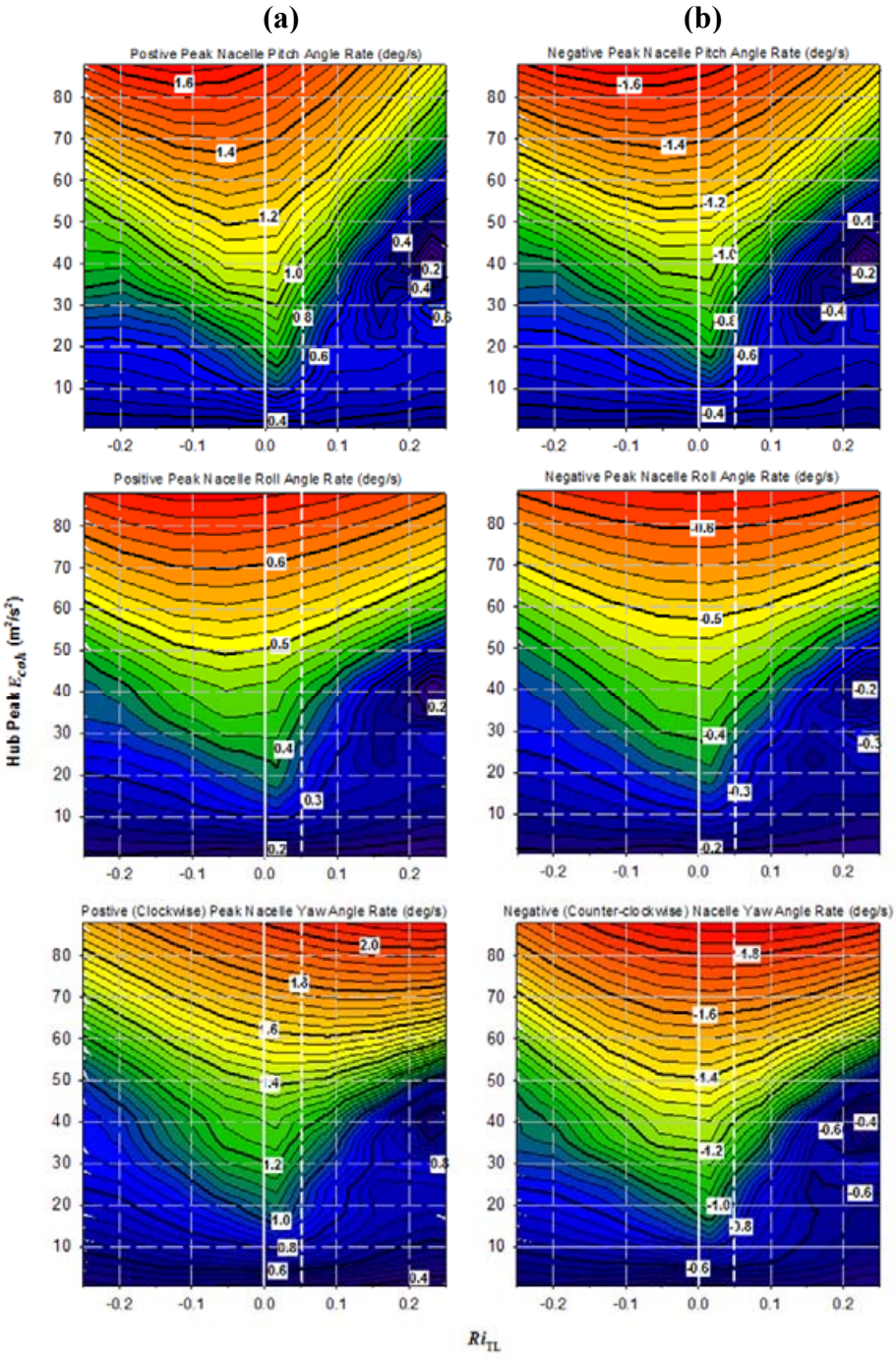

Figure 4-18. Smoothed variations of NWTC ART nacelle IMU peak angular response rates (positive in column [a] and negative in column [b]) with Ri_{TL} and hub-height peak E_{coh} with pitch angle response (top row), roll angle response (center row), and yaw angle response (bottom row)

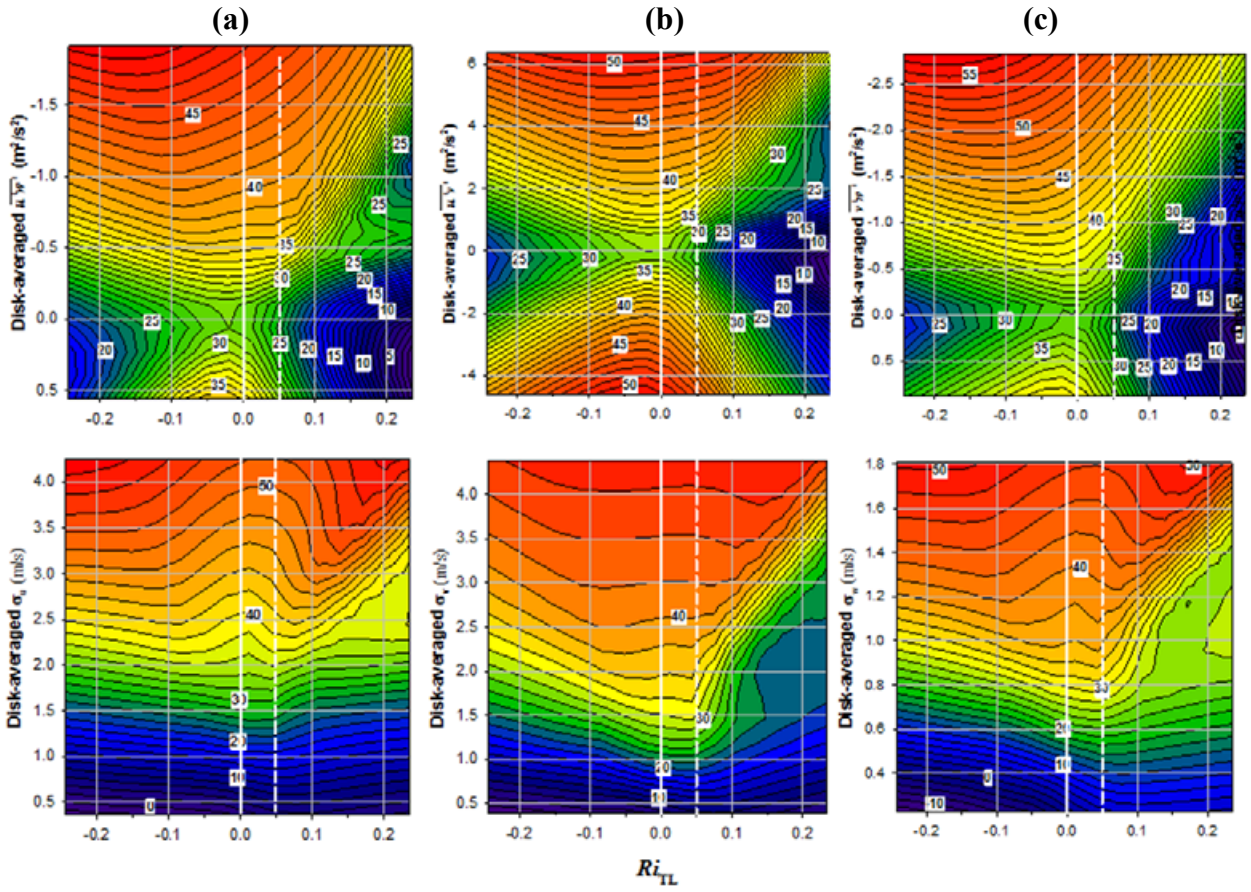

Figure 4-19. Smoothed variations of NWTC ART low-speed shaft torque standard deviation σ_τ (kNm) with Ri_{TL} and disk-averaged mean Reynolds stresses $\overline{u'w'}$, $\overline{u'v'}$, and $\overline{v'w'}$ in upper row and standard deviations of streamwise (u), lateral (v), and vertical (w) turbulent wind components in lower row

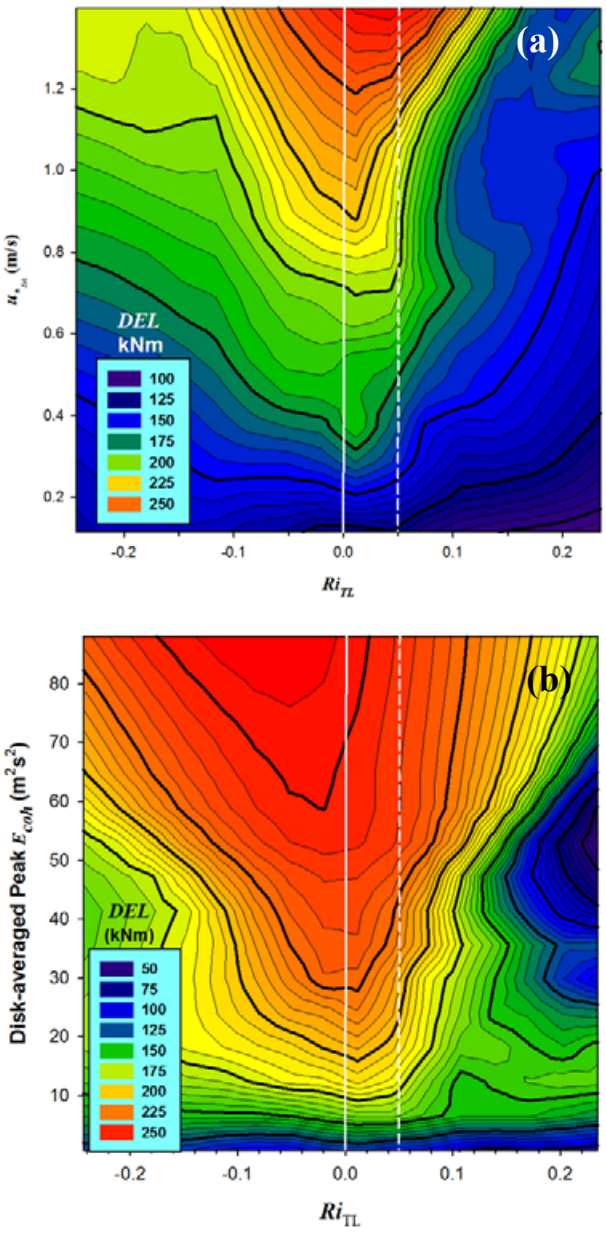

Figure 4-20. Smoothed NWTC ART variation of root FBM *DEL* with Ri_{TL} and disk-averaged (a) local friction velocity u_* and (b) peak E_{coh}. Upper limit of critical stability range is shown with vertical dashed line.

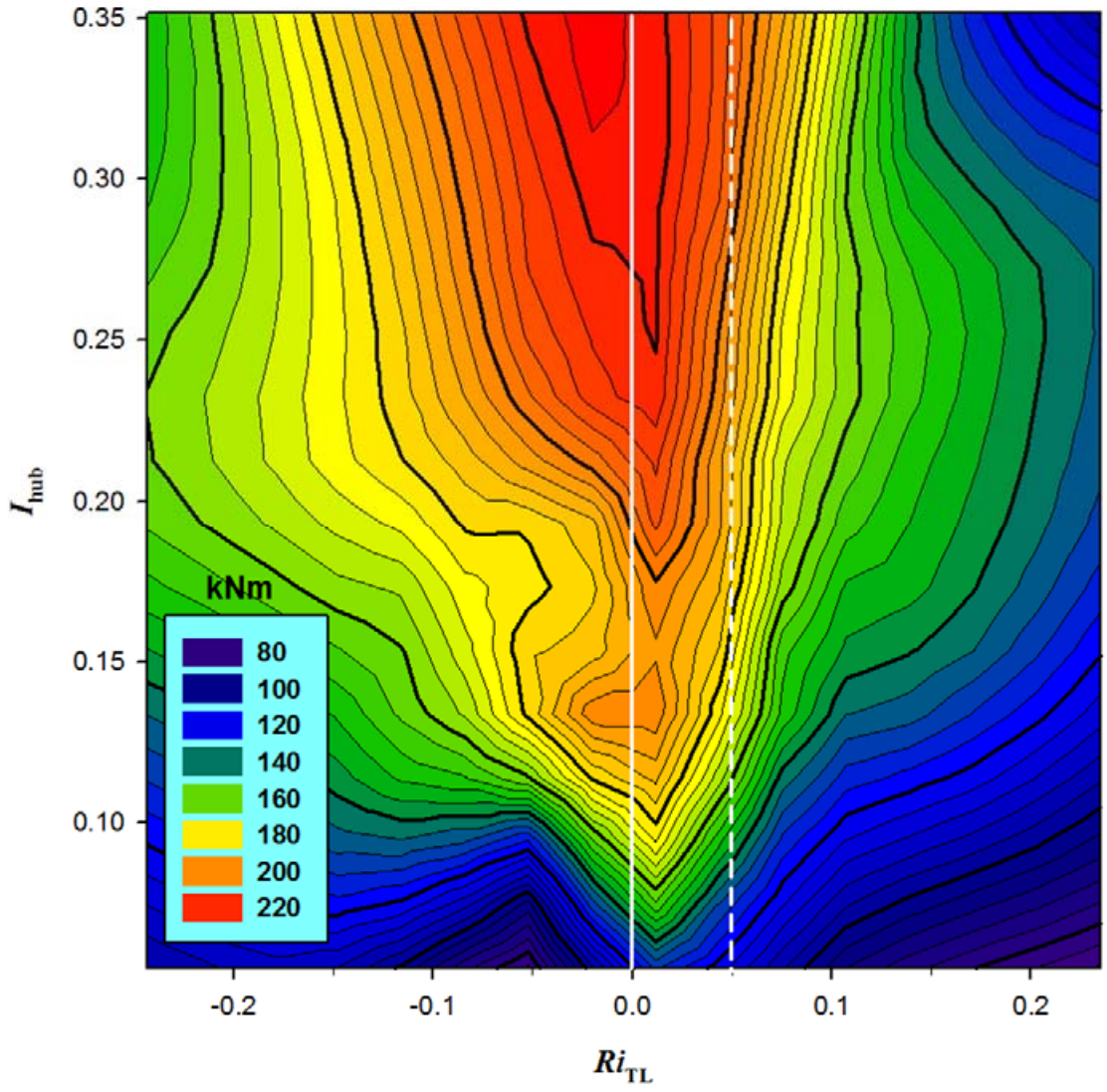

Figure 4-21. Smoothed NWTC ART variation of root FBM *DEL* with Ri_{TL} and hub-height turbulence intensity (I_{hub})

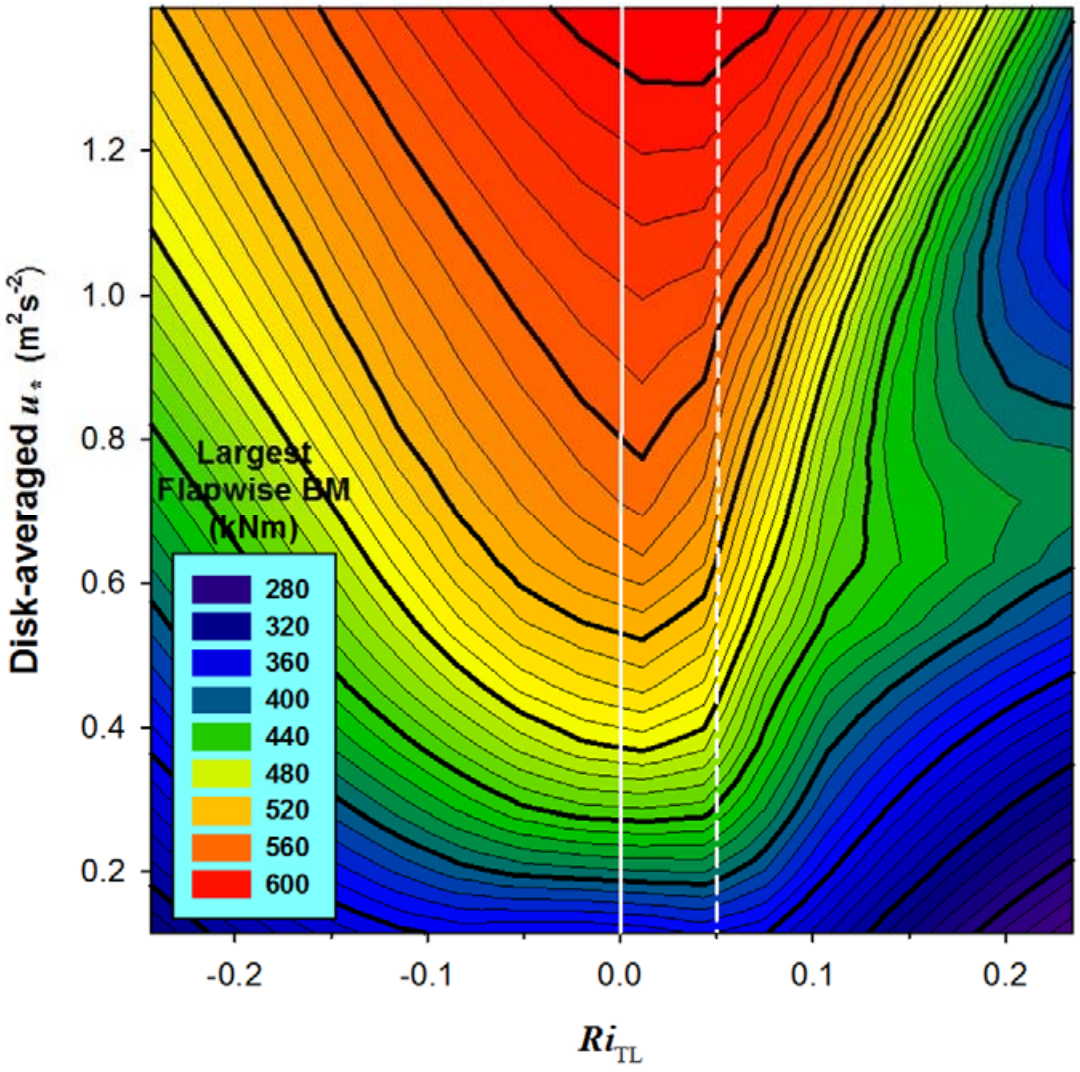

Figure 4-22. Smoothed variation of NWTC ART largest flapwise bending load with Ri_{TL} and disk-averaged local shearing stress or friction velocity u_*

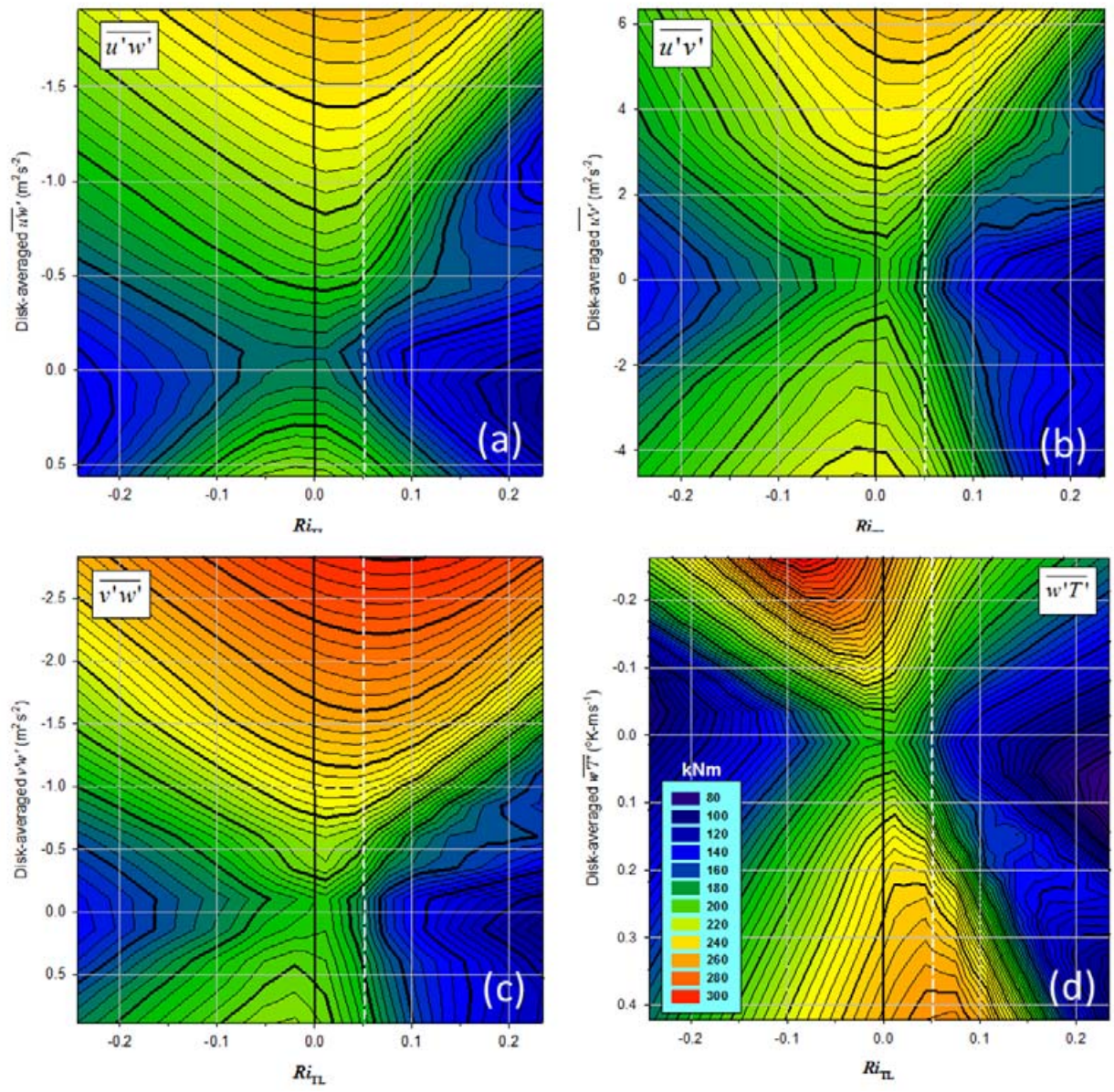

Figure 4-23. Smoothed variations of NWTC ART FBM *DEL*s with disk-averaged (a) $\overline{u'w'}$, (b) $\overline{u'v'}$, (c) $\overline{v'w'}$, and (d) $\overline{w'T'}$

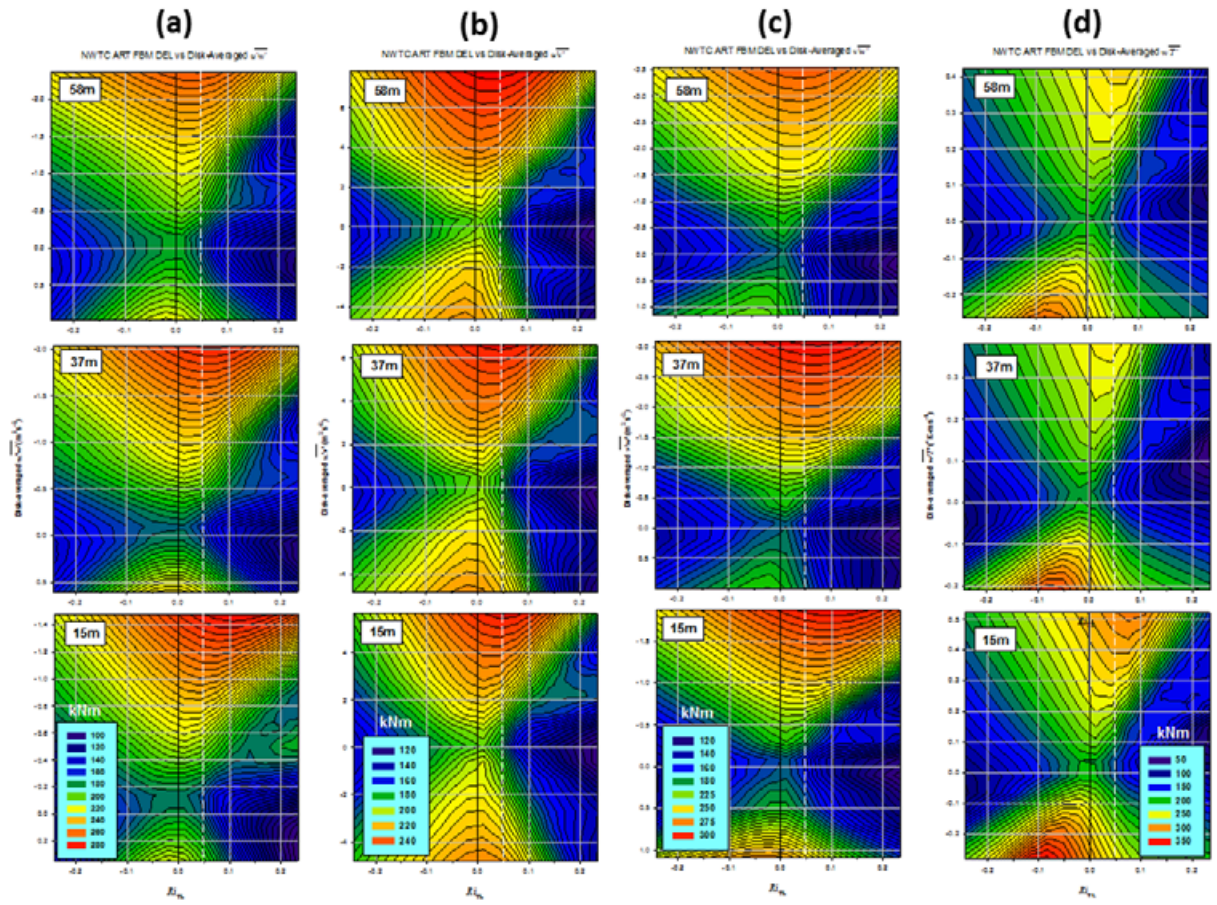

Figure 4-24. Smoothed variations with height of NWTC ART FBM *DEL*s with Ri_{TL} and (a) $\overline{u'w'}$, (b) $\overline{u'v'}$, (c) $\overline{v'w'}$, and (d) $\overline{w'T'}$

occurring in the critical stability range at the 58-m height. Also, these large *DEL* values take place in slightly more stable conditions as the height becomes closer to ground. The variations of the *DEL* with the buoyancy in column [**d**] follow a similar pattern. All of this points to the presence of significant heterogeneity in not only the 3-D velocity field but the thermal one as well in the naturally occurring flow into the ART rotor disk, which will need to be included to achieve a faithful and representative simulation of such conditions.

4.4 ART Dynamic Response and Inflow Statistical Characteristics

Between October 30, 1999 and May 15, 2000 there are 1,568 records in which we have turbine response data that are time synchronized with inflow turbulence data from the upwind planar array. We stratified these data into five categories based on Ri_{TL}. In analyzing the California wind farm data and the response of the Micon 65/13 turbines, we found there were at least four and possibly five ranges of Ri_{TL} where the turbine response differed. Initially we defined five stability ranges or classes (STC or STability Class) defined as STC01 ($-1 \le Ri_{TL}$), STC02 ($-1 < Ri_{TL} \le 0$), STC03 ($0 < Ri_{TL} < +0.10$), STC04 ($+0.10 \le Ri_{TL} < +0.25$), and STC05 ($+0.25 \le Ri_{TL} < +1.0$). As discussed previously, we found that class STC03 could be further subdivided into what we called the critical Richardson number range or CRR as defined by $+0.01 < Ri_{TL} < +0.05$, with the maximum turbine response taking place near $Ri_{TL} = +0.02$. Here we define the remaining interval $+0.05 \le Ri_{TL} < +0.10$ as CRR High or CRRH. Class STC01 contains very unstable (auto convective) conditions, STC02 ranges from moderate instability to neutral, STC03 and its subdivisions of CRR and CRRH are weakly stable with CRR being the weakest, STC04 is moderately stable, and STC05 is very stable. Our total available inflow data set for the LIST Program contains 7,041 10-minute records or a total of 1,174 hours, of which 261 h (1,568 records) have corresponding time-synchronized turbine response data. We often collected meteorological data when the turbine was not available or conditions would not allow it to run. It is the analysis of this much larger data set, which we discuss later, that forms the basis for the development of the NWTC Spectral Model in the TurbSim Code using the full ranges of classes STC02, STC03, STC04, and STC05.

The LIST data set had no records collected within the most unstable classification STC01 and only 16 in the most stable class STC05. Of the available population having the turbine and inflow synchronized information available, 98% of it occurred with Ri_{TL} values between –0.25 and +0.25. For the analysis that follows, we ignored the STC05 category because it contained such few records. We examined the effect of using the slightly smaller combined range of the CRR and CRRH classes with STC03 and found it to be insignificant. The STC02, CRR, CRRH, and STC04 classes contained 1,470 10-minute records or 95% those available. The pie chart of Figure 4-25 diagrammatically describes the relative sizes of the amount of data available in each of the stability classes. Therefore the CRR classification contains about twice as many records as the records contained in flows that are neutral to moderately unstable (STC02) and those that are slightly more stable (CRRH).

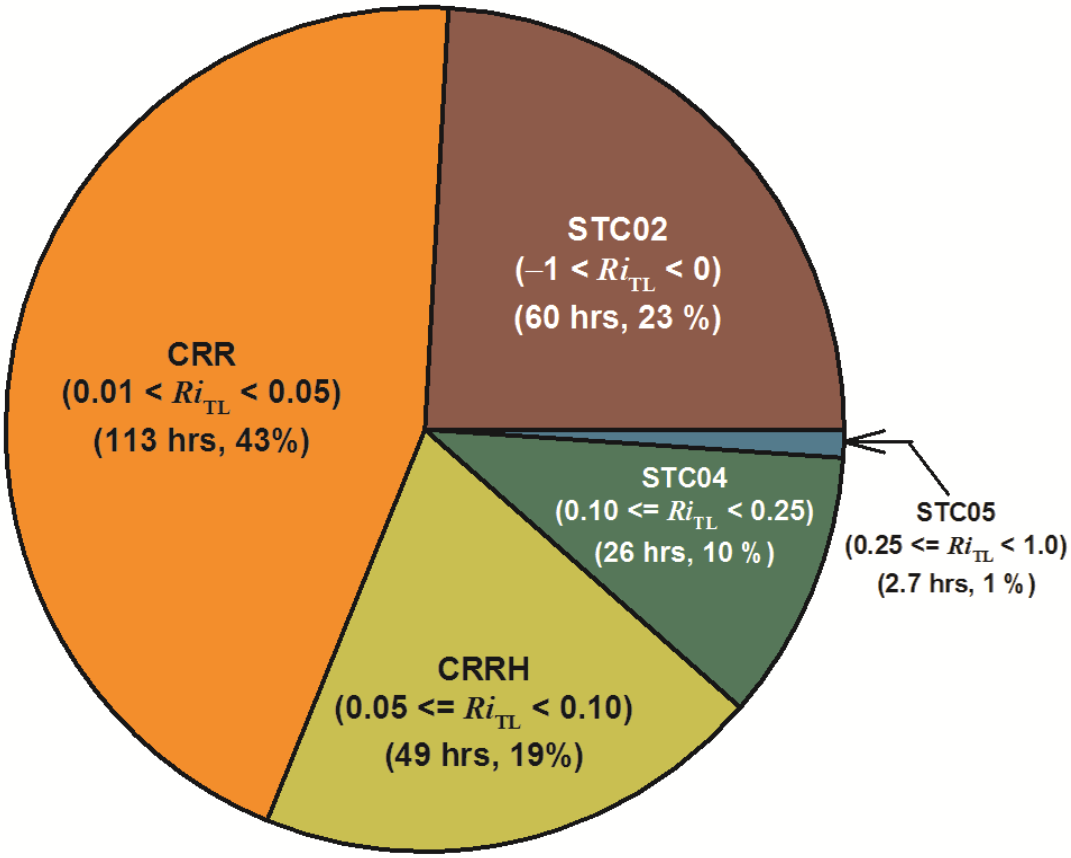

Figure 4-25. Available NWTC ART response and inflow turbulence data by stability class

4.4.1 Relationship of ART Load and Turbulence Parameter Probability Distributions by Stability Classification

In the leftmost vertical panel of Figure 4-26 we display the observed probability distributions in boxplot format of three turbine response variables related to the flapwise blade root bending moments (FBM) for the STC02, CRR, CRRH, and STC04. In this boxplot format, the outliers (less than P10 and greater than P90) are shown as black dots and the means and medians are indicated by red and black horizontal lines, respectively, within the quartile shaded box. In the center and right panels we plot the corresponding probability distributions for a range of inflow turbulence parameters and turbulence scaling parameters that we have found or have been shown to influence turbine loading response.

Examining the blade root responses in the leftmost panel of Figure 4-26, we see that the largest loads are associated with the CRR stability class followed by STC02, CRRH, and STC04 in descending order. We also see that the hub-height mean *U*-component wind speed, the disk-averaged local u_* or shear stress, and rotor disk peak E_{coh} values follow this same pattern as shown in Figures 4-26d, e, and g and are consistent with Figures 4-20 and 4-22. The higher response of the FBM variables in the CRR stability class is associated with small positive values of the flux Richardson number Ri_f and significant levels of the disk-averaged values of the vertical flux of E_{coh} ($w'E_{coh}$) shown in Figures 4-26f and h. Very small positive values of Ri_f are indicative of intense vertical turbulent mixing. This is an important clue to understanding the atmospheric dynamics associated with this stability class and is discussed in more detail in a later section. Finally, Figure 4-26i shows the influence of mean vertical wind shear on each of the stability regimes.

Figure 4-27 plots the corresponding distributions of the peak Reynolds stress components as measured at the top of the ART rotor (58 m). We chose the 58-m level as a height because it is located within the lower half of the larger wind turbine rotors now installed at the NWTC site and in wind farms around the world. Again we point out that the greatest peaks in the CRR and STC02 classes in the $u'v'$ component in Figure 4-27b reach levels almost twice those of the other two stress components, indicating the presence of very heterogeneous, non-Gaussian conditions in the lateral directions of the inflow. Lastly, the influence of the greater stability of the CRRH and STC04 classes is readily apparent on both the body of the distributions and peak excursions.

In Figure 4-28, we examine the statistical characteristics of the buoyancy fluxes within each of the four stability classes. Following the format of Figure 4-27, we present the distributions of the peak buoyancy fluxes at the top of the ART rotor. Here the largest positive fluxes are associated with the unstable class STC02 because of the convection occurring under such conditions. Still, however, positive (upward) peaks almost as large are seen in the CRR class distribution. Of particular importance is the larger downward peak fluxes seen in the body of the CRR class distribution, with similar but smaller distributions in the more stable CRRH and STC04 distributions. The reason for this is apparent in the distributions shown in Figure 4-28b. Here we plot the mean buoyancy flux distributions measured at the top and bottom of the ART rotor (58 and 15 m, respectively) for each stability class. Although some small differences exist with height, such as the slightly larger ranges of variation at the 58-m level, the influence of the stable flow conditions relative to the unstable STC02 class is the most obvious and a major player in influencing the turbulence characteristics and subsequent impact on the turbine response.

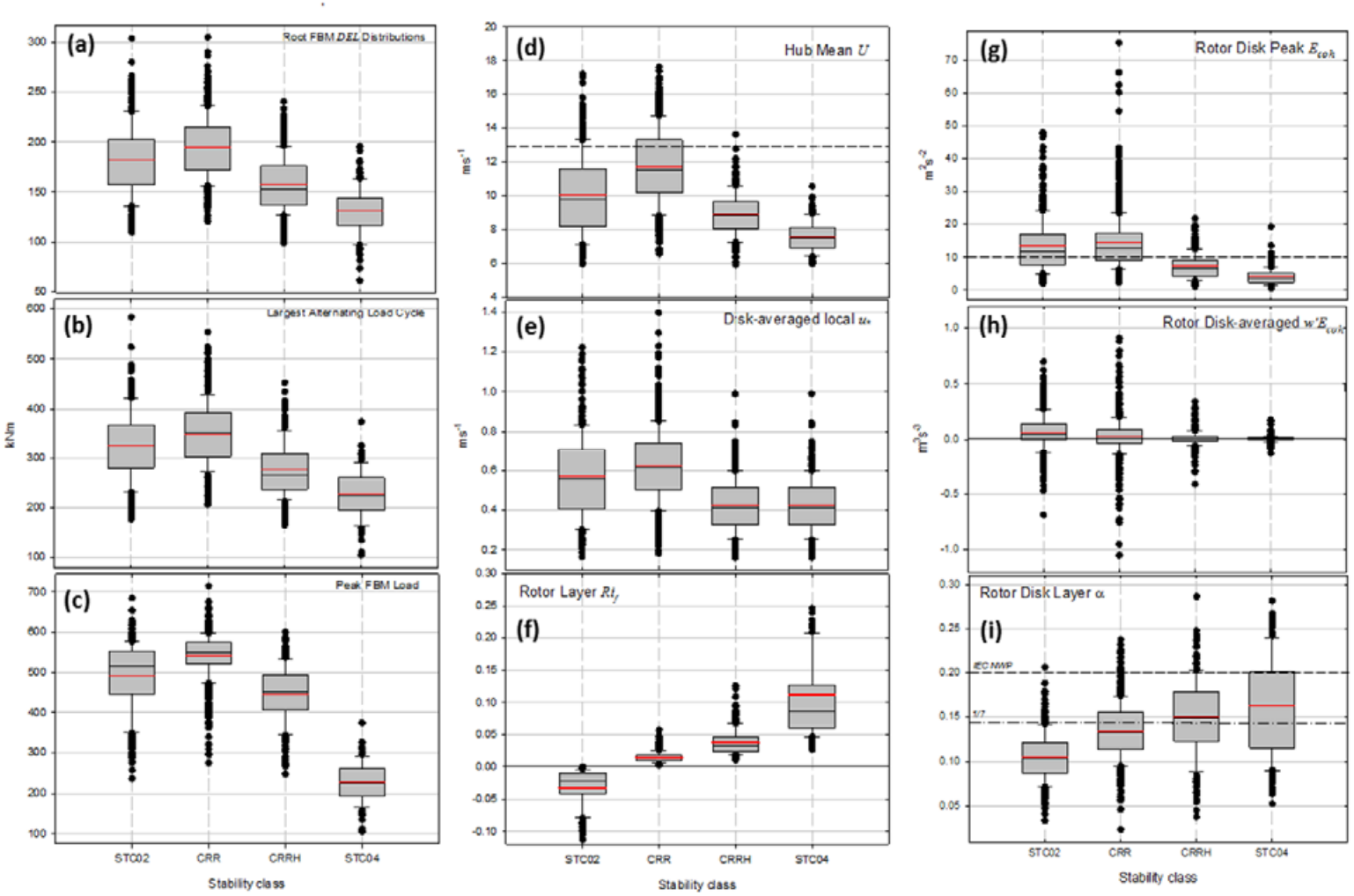

Figure 4-26. Probability distributions of both ART dynamic response and range of inflow turbulence parameters by stability class. Turbine response variables: (a) root FBM *DEL*s, (b) largest FBM load cycle, and (c) peak FBM load. Inflow parameters: (d) hub mean *U*, (e) disk-average local u_*, (f) rotor layer Ri_f, (g) rotor disk peak E_{coh}, (h) rotor disk-average $\overline{w'E_{coh}}$, and (i) rotor disk layer shear exponent α.

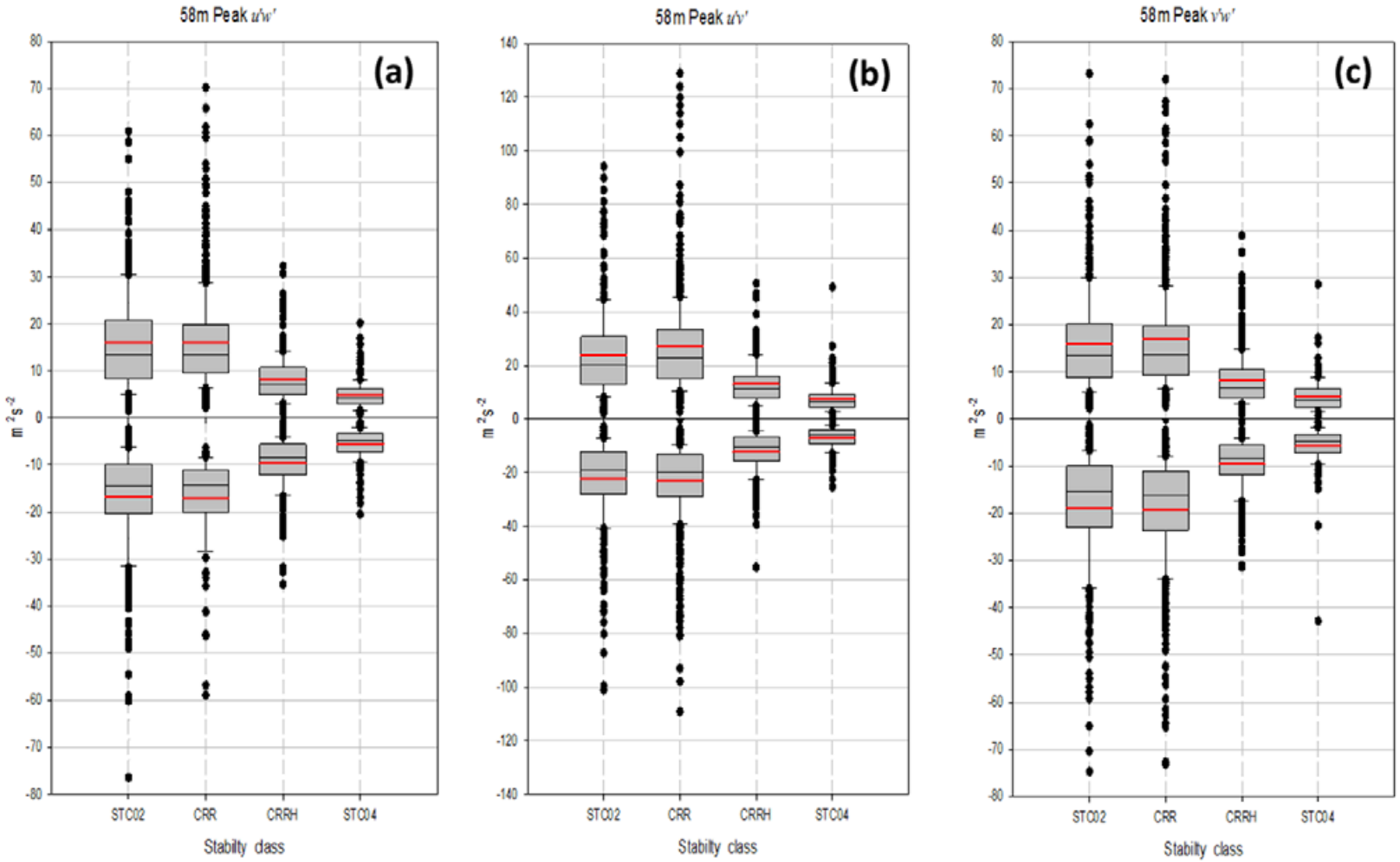

Figure 4-27. Probability distributions of 58-m height peak Reynolds stress components (a) $u'w'$, (b) $u'v'$, and (c) $v'w'$. Note the much greater values associated with the $u'v'$ component, particularly for the CRR stability class, and significant decreases for the more stable CRRH and much more stable STC04 classes. Also note the separations in the mean and medians for the STC02 and CRR stability classes that indicate the presence of strong, heterogeneous (non-Gaussian) conditions.

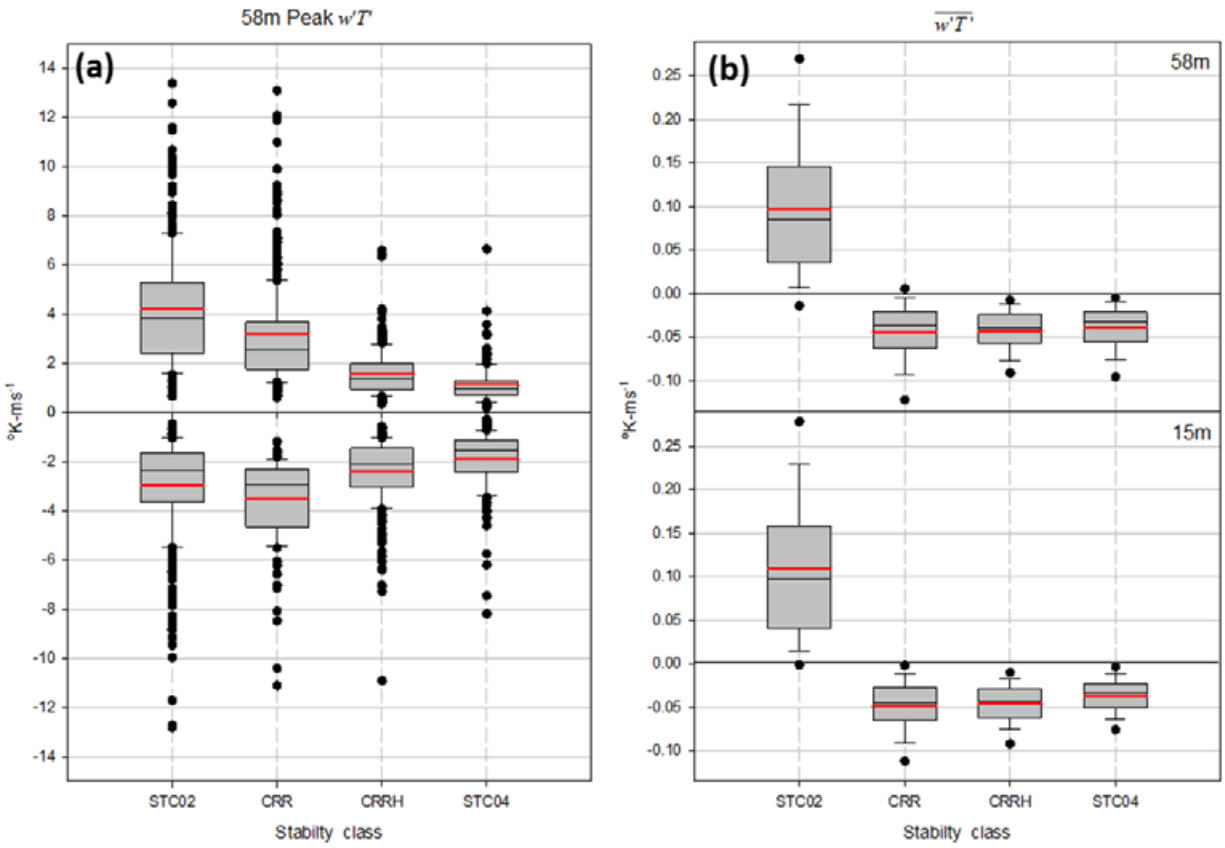

Figure 4-28. Probability distributions by stability class of (a) peak buoyancy flux ($w'T'$) at top of ART rotor (58 m) and (b) mean buoyancy fluxes at top and bottom of turbine rotor (15 m) where dots represent P05 and P95 quantiles

4.4.2 Diurnal Variations in NWTC Natural Inflow Characteristics and Observed ART Load Extremes

We found that the diurnal variation of the wind resource within the California wind farm had a significant influence on the loads seen on the Micon 65/13 turbines. Typically the hub wind speeds there were below or just near cut-in between about 1000 and 1500 LST during the period of the observations at the peak of the local wind season. Figure 4-29 plots the probability distributions of the diurnal variation in the 50-m mean wind speed from the NWTC M-2 met tower for the observational period of the LIST experiment from October 1999 through mid-May 2000. The cut-in wind speed for the NWTC ART is about 6 m s^{-1} and rated is 12.8 m s^{-1}. The significantly positively skewed distributions show that turbine operations were possible about 25%–30% of the time. The most frequent higher wind speeds, like those at the California wind farm, occur after sunset and before local midnight. This was also the period when conditions were often too severe for the turbine to operate.

The corresponding diurnal distribution of Ri_{TL} is shown in Figure 4-30. Here the upper limit of the CRR stability range (Ri_{TL} = +0.05) and the nominal upper limit for significant turbine response (Ri_{TL} = +0.10) are shown as dot-dashed and dot-dot-dashed lines. Also, a value of Ri_{TL} = +0.25 is indicated with a dashed line and identified as Ri_c. This is the theoretical upper limit for turbulence to exist and is often referred to the critical Richardson number. These distributions indicate that the flows resided within an Ri_{TL} range of 0 to +0.10, a significant amount between the time of local sunset and sunrise (~ 1700 to 0700 local time) and between 1700 and 0300 hours in particular, which also often corresponds to the periods with the strongest winds.

In Figure 4-31 we plot the observed diurnal variations in the tails of the blade root FBM load distributions and the corresponding number of data hours associated with each of the hourly periods. As shown in Figure 4-31b, on average each hourly bin had about 10–12 hours of data except just after sunrise (~ 0700 hours) and from 2100 to 2300 hours, when severe wind conditions precluded the turbine from operating numerous times. Using the P95 quantile of *DEL*s of 240 kNm or more as a high damage/load criterion, we see three main periods of an hour or more when this level is exceeded. They include between 0100 and 0300 hours, 0700 and 0900 hours (at sunrise and for 2 hours after), and 2000 and 2100 hours, which in all likelihood would also include the 2200 and 2300 hour bins if the turbine had been able to operate more. In Figure 4-32 we repeat Figure 4-31a as Figure 4-32b to allow an ease of direct comparison with the matching diurnal P10, P25, P50, P75, and P90 quantile distributions of $Ri_{TL.}$ We annotated this figure with a horizontal white dot-dashed line corresponding to Ri_{TL} = +0.02 that represents the maximum dynamic response seen on the Micon 65/13 turbines in California. We also used dashed lines to identify the Ri_{TL} values of +0.05 and +0.10 that indicate the upper limits of the CRR and CRRH stability ranges. The highest values of the P95 FBM *DEL*s, with one exception, occur during the hours in which the value of Ri_{TL} falls within the CRR stability class at least half the time. The exception is the largest P95 value, which occurs in the 0900 hour bin. This is when the boundary layer is in transition from nocturnal stable to daytime convective and when we have observed significant transient turbine loading events.

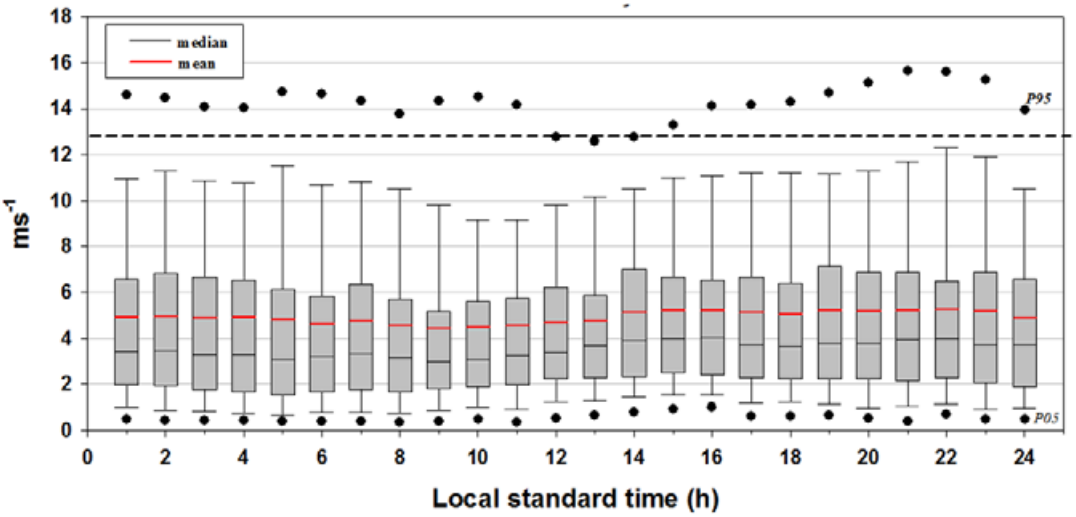

Figure 4-29. Boxplot presentation of probability in diurnal variation in NWTC 50-m mean wind speed observed during LIST observational period from October 1999 to May 2000. The horizontal dashed line represents rated wind speed for the ART. The cut-in wind speed was about 6 m s^{-1}.

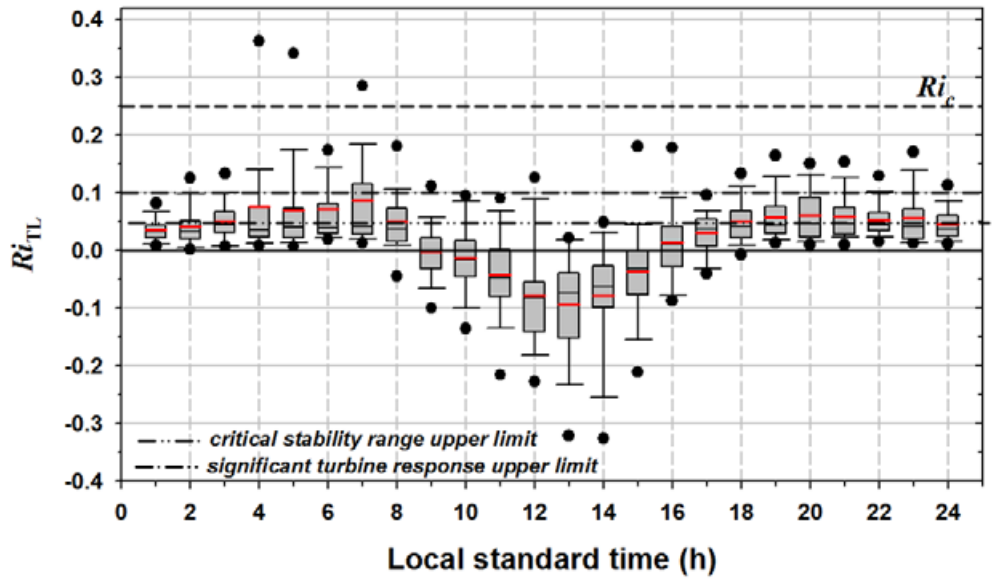

Figure 4-30. Boxplot presentation of probability distributions of diurnal variation of Ri_{TL} when ART was operating during LIST experiment

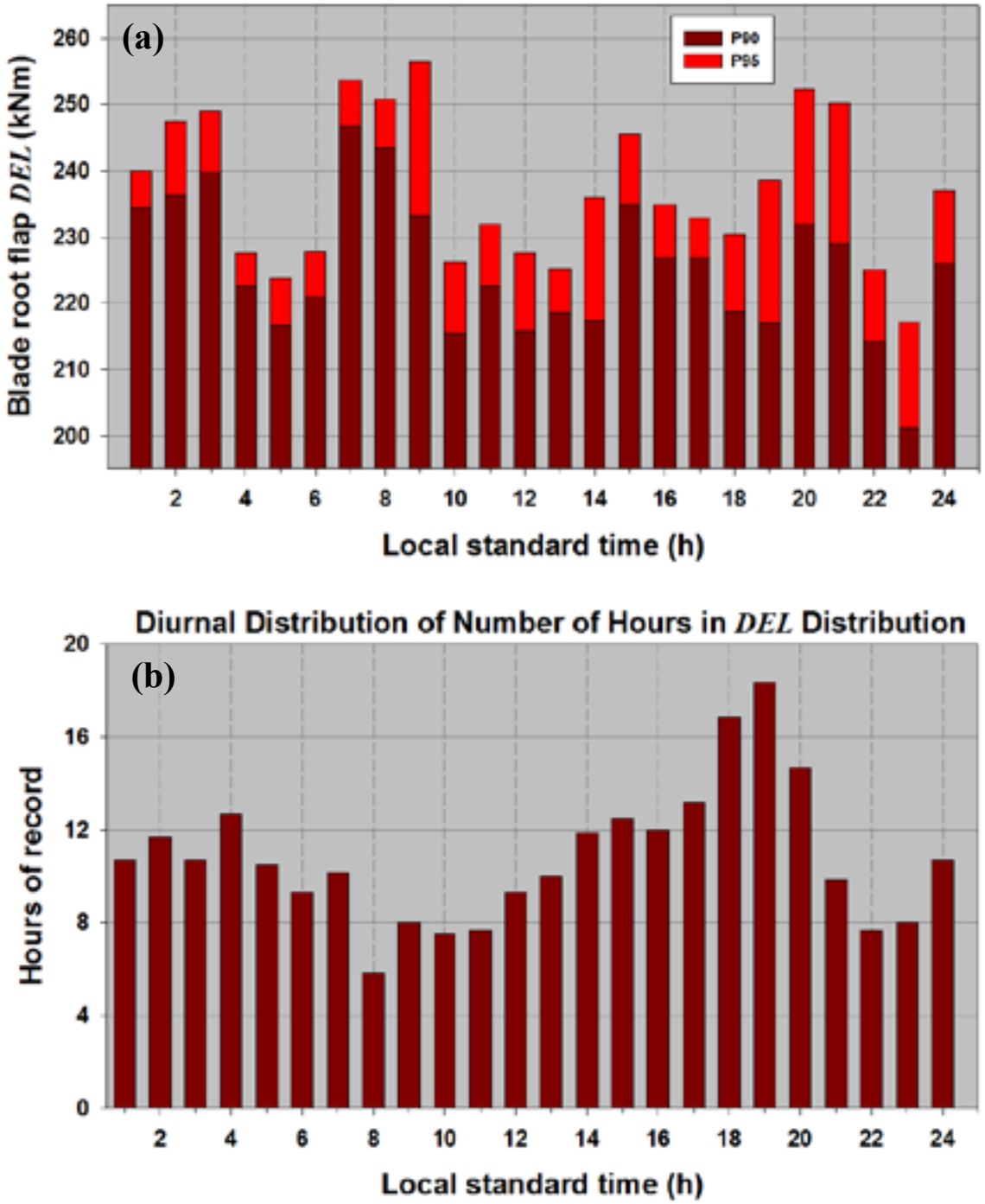

Figure 4-31. Diurnal variations in (a) P90 and P95 quantiles of ART root FBM *DEL* distributions and (b) corresponding total number of hours of available observations for each time hour period. The few observations from 2100 to 2400 hours are the consequence of wind conditions that were often too severe for turbine operation.

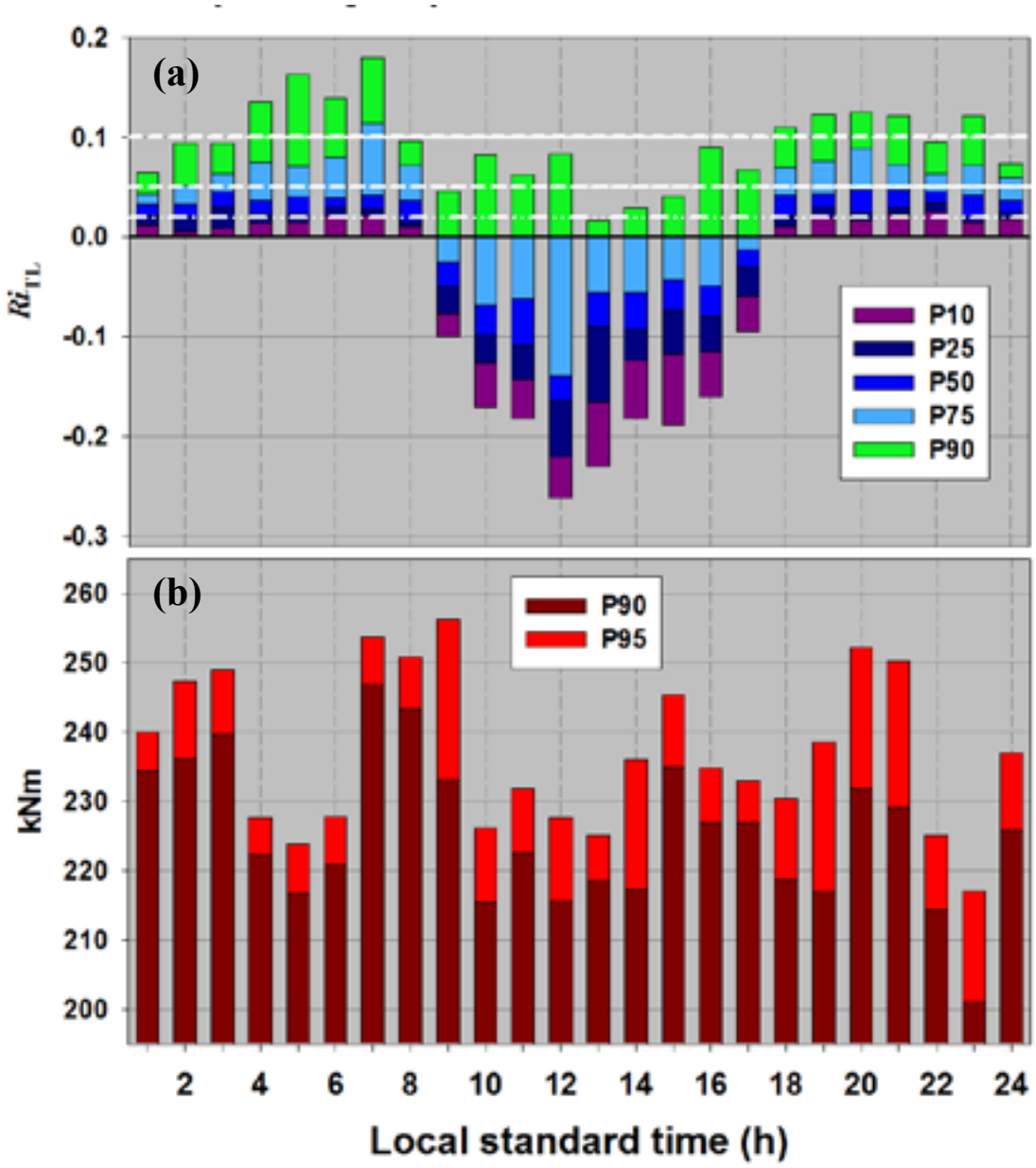

Figure 4-32. Diurnal variation in quantiles of (a) Ri_{TL} during ART operation and (b) corresponding P90 and P95 quantiles of probability distributions of observed root FBM *DEL*s. The low values in (b) between 2200 and 2400 LST are a consequence of the turbine frequently not operating because of severe wind conditions.

5.0 Comparing Micon 65/13 Turbines and ART Dynamic Responses in Their Turbulence Operating Environments

Our individual analyses of the dynamic responses of the Micon 65/13 turbines in the California wind farm and the National Wind Technology Center (NWTC) Advanced Research Turbine (ART) found that blade root and low-speed shaft bending loads and nacelle response dynamics, in addition to the mean wind speed, are highly correlated with the stability of the atmospheric layer in which the turbines reside. We also showed that these responses are also sensitive to the local turbulent shear stresses or friction velocities u_* within the rotor disks, the variation of vertical wind speed σ_w, and most important, the peak values of the turbulent coherent kinetic energy E_{coh}. For both turbine designs and operating environments, we also identified a narrow range of the turbine layer gradient Richardson number (Ri_{TL}) stability parameter in which the turbine dynamic responses were the greatest and which we refer to as the critical Richardson number range, or CRR. We now present direct comparisons of dynamic response sensitivities of the two turbine designs in their specific operating environments to ascertain just how common or universal they may be.

5.1 Comparing Full-Range Stability Classes

In Figure 5-1 we compare the sensitivities of the blade flap bending moment (FBM) equivalent fatigue damage equivalent loads (*DEL*s) as a function of Ri_{TL} for the two Micon 65/13 turbines operating in Row 37 of the California wind farm (Figure 5-1a) and the ART on Row 4 of the NWTC (Figure 5-1b). We annotated each plot with vertical dashed lines depicting the CRR stability range (+0.01 to +0.05). We also marked the value of Ri_{TL} = +0.02, where the peak response is seen on the Micon 65/13 turbines.

Previously we defined the Ri_{TL} range from +0.05 to +0.10 as the critical range high, or CRRH. We classified the Ri_{TL} range of +0.10 to +0.25 as the STC04 or moderately stable range. These more stable ranges are better defined in the NWTC ART data set because (1) almost four times as much data are available overall and (2) many more observations exist in the CRRH and STC04 ranges. The fact that the Micon 65/13 turbine dynamic responses were influenced by an aggregate wake flow from 36 rows of upstream turbines may have a distinct influence when compared with the response of the NWTC ART operating in a natural inflow. These differences may be manifested by the distinct and rapid increase in response seen on the two Micon turbines compared with the ART as the stability of the inflow transitions from unstable/neutral to stable, seen in Figures 5-1a and b (i.e., from stability class STC02 to CRR).

5.1.1 Turbine Dynamic Response Comparisons to Variations in E_{coh} and σ_w

In Figure 5-2 we further examine the response of the two turbine designs and operating environment by plotting the corresponding variations in the hub peak values of E_{coh} and σ_w in addition to the FBM *DEL*s. The change in peak E_{coh} as the inflow becomes stable ($Ri_{\mathrm{TL}} > 0$) and is quite noticeable especially after an Ri_{TL} value of +0.01 to +0.02 is reached, particularly in the variations of the FBM *DEL*s and hub σ_w measured on the Micon 65/13 turbines. These transitions are not as abrupt for the ART, as shown in Figures 5-1b and 5-2b. The ART has a significant number of FBM *DEL* relatively higher loads (greater than 200 kNm) in the Ri_{TL} range

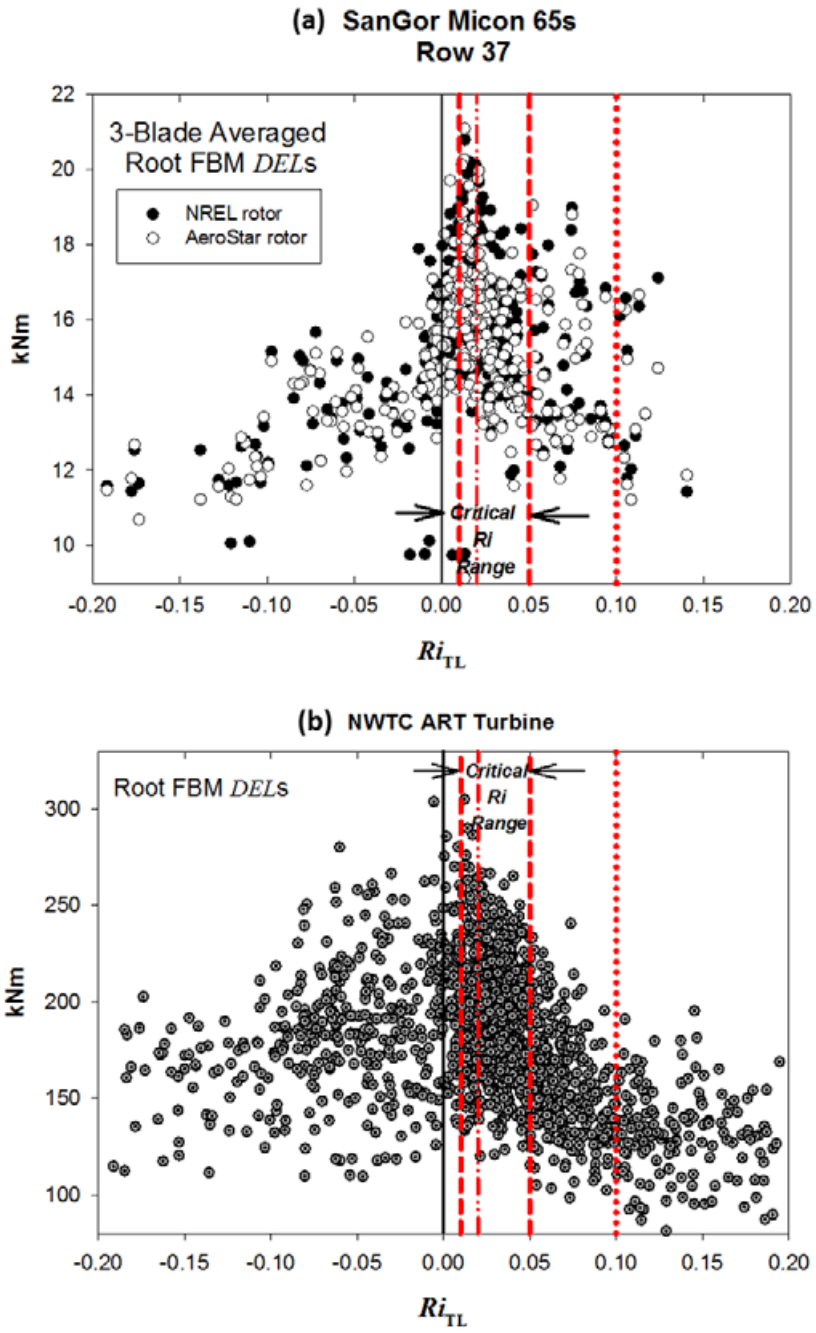

Figure 5-1. Observed variations of root FBM DELs with Ri_{TL} for (a) Micon 65/13 turbines in Row 37 of California wind farm and (b) NWTC ART operating in natural inflow at Row 4. The CRR stability range is identified by the vertical dashed lines and the value of peak Micon turbine response (+0.02) is shown as a vertical dot-dot-dashed line.

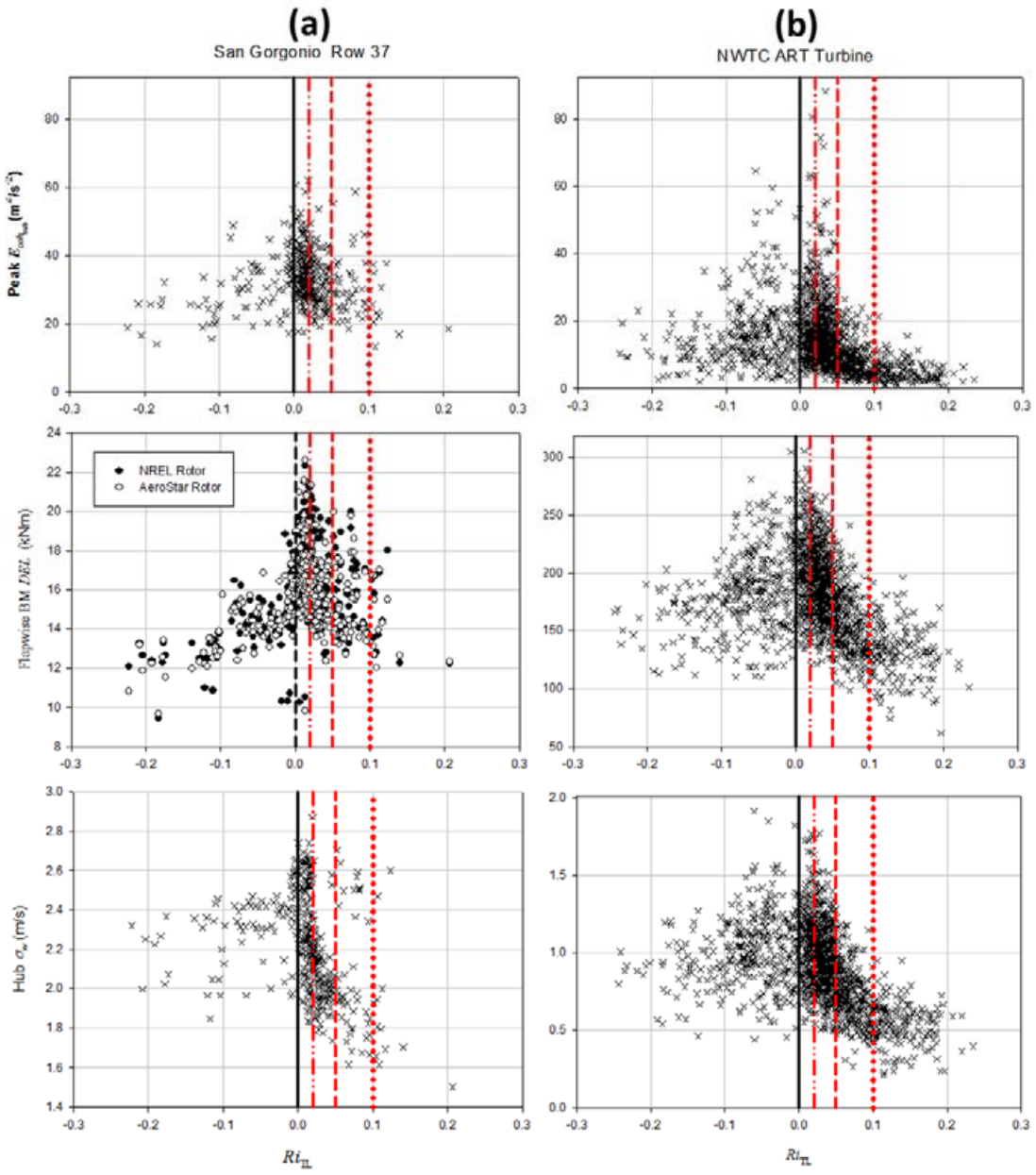

Figure 5-2. Comparisons of variations of hub-height peak E_{coh}, root FBM *DEL*s, and hub σ_w with Ri_{TL} observed at (a) Micon 65/13 turbines at Row 37 of California wind farm and (b) ART on Row 4 of NWTC. The Ri_{TL} associated with maximum Micon turbine response (+0.02), the upper limit of the CRR range (+0.05), and the nominal upper limit of observed significant Micon dynamic responses (+0.10) are shown as dot-dot-dashed, dashed, and dotted vertical lines, respectively.

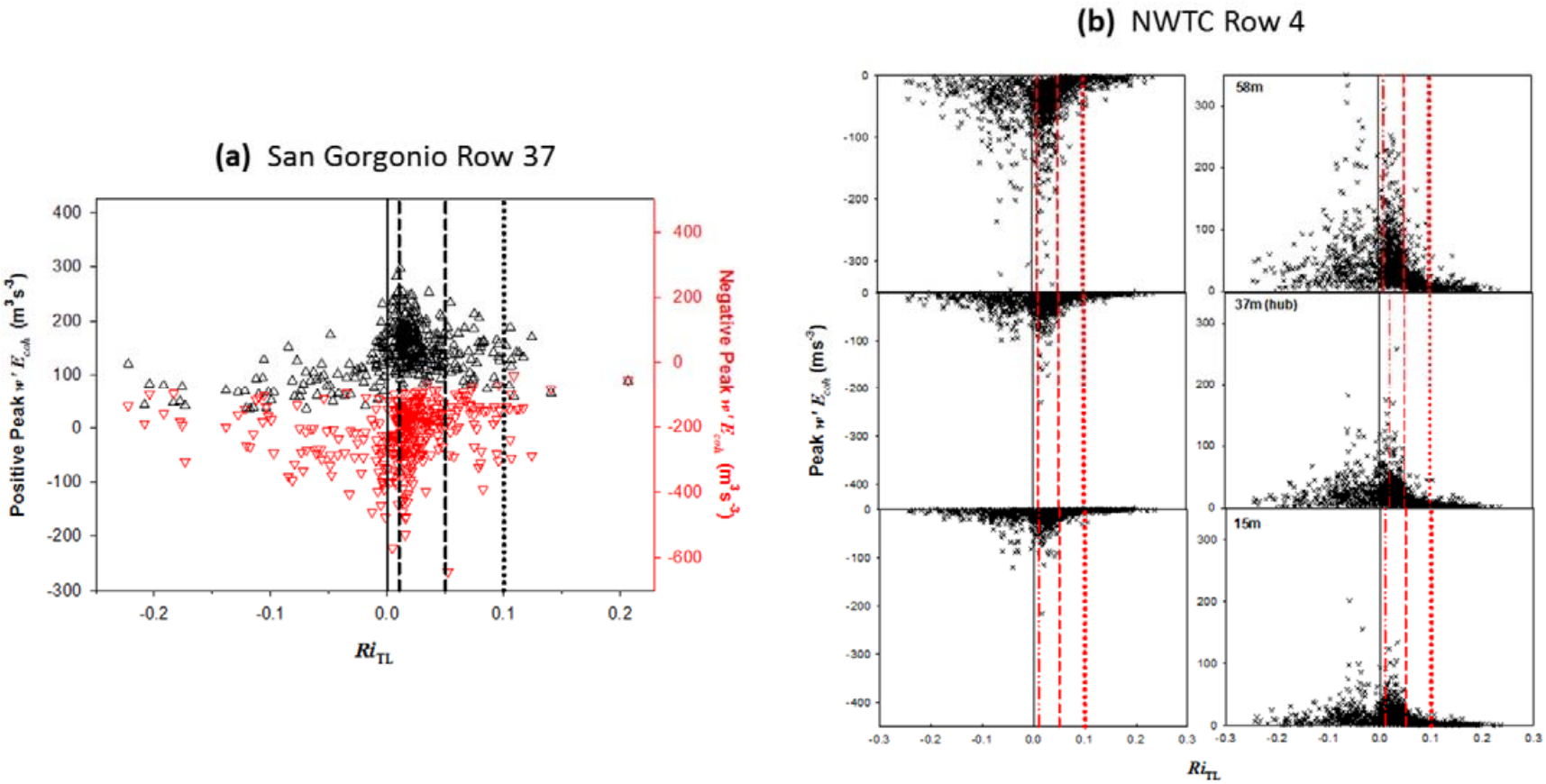

Figure 5-3. Comparison of vertical fluxes of peak coherent turbulent kinetic energy ($w'E_{coh}$) inflows to (a) hub height of Micon 65/13 turbine rotors at Row 37 in California wind farm; and (b) at the bottom (15 m), hub (37 m), and top (58 m) of NWTC ART rotor on Row 4 . The downward fluxes are shown in the left column and the upward in the right column. The CRR stability range is shown between the dashed vertical lines.

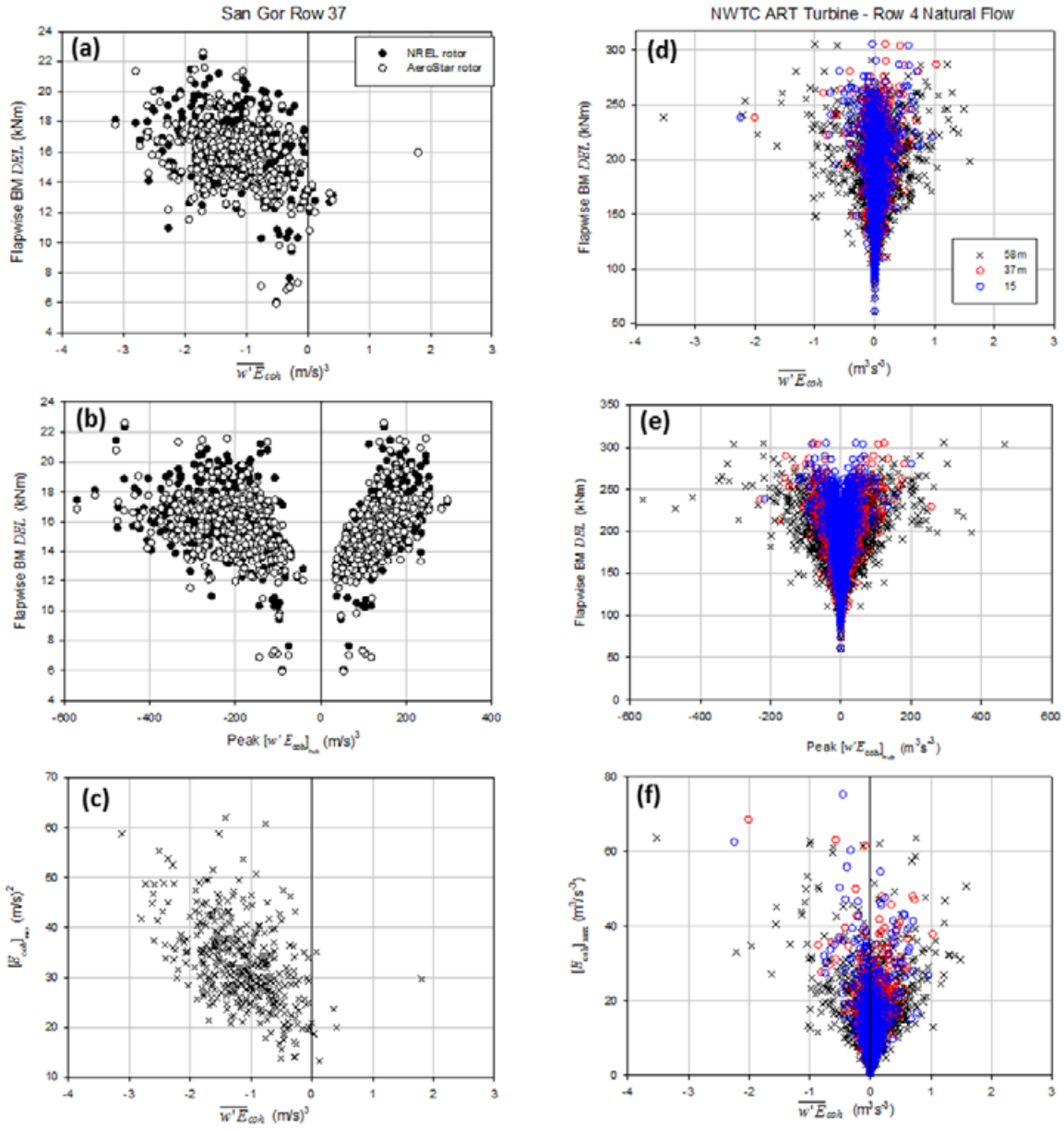

Figure 5-4. Observed variations of root FBM *DEL*s with mean and peak values of vertical flux of E_{coh} ($w'E_{coh}$) for (a,b) hubs of the California wind farm Micon 65/13 turbines and (d,e) 15-, 37- (hub), and 58-m heights of the NWTC ART rotor disk. Variations of the maximum values of $w'E_{coh}$ with the mean value for the wind farm turbines are shown in (c) and for the ART in (f).

of −0.1 to 0 compared with the two Micon turbines. The explanation for this phenomenon can be seen in the strength of the vertical fluxes of E_{coh} for the two locations as a function of stability as presented in Figure 5-3. Row 37 in the wind farm, shown in Figure 5-3a, has intense vertical fluxes of E_{coh}, but they primarily occur within the very weakly stable range of $+0.01 < Ri_{TL} < +0.02$. Even though the most significant vertical E_{coh} fluxes take place within the CRR stability class range at the NWTC, significant vertical fluxes occur in the unstable Ri_{TL} range of −0.10 to 0 and are the most intense at the height of the of the top of the ART rotor. Figure 5-4 compares further the differences in the vertical E_{coh} fluxes. Here the FBM *DEL* loads are plotted against the hub-height mean flux $\overline{w'E_{coh}}$ in Figures 5-4a and d, and the peak values of $w'E_{coh}$ in Figures 5-4b and e. In Figures 5-4c and f we plot the variations of the peak values of $w'E_{coh}$ with $\overline{w'E_{coh}}$. In Figure 5-4a we see that at Row 37 in the California wind farm the FBM *DEL* loads on the Micon 65/13 turbines are affected by a persistent contribution of a downward flux of E_{coh}.. In Figure 5-4d we see that at the NWTC the loads on the ART are influenced by both upward and downward mean fluxes that increase in intensity with height across its rotor disk. Figure 5-4b shows that the larger loads on the Micon turbines tended to be associated with larger peak downward fluxes of E_{coh} ($w'E_{coh} \geq 200$ m^3 s^{-3}) compared with the smaller upward ones. In contrast, the largest loads seen on the ART were related to both upward and downward peak E_{coh} transports seen at highest rotor elevation in Figure 5-4e. Figure 5-4c further demonstrates the existence of a persistent downward mean E_{coh} flux and its influence on the largest FBM *DEL* values at Row 37 in the wind farm. Figure 5-4f underscores the bi-directionality of the mean flux and its nearly balanced influence on the peak largest FBM *DEL* values seen on the ART. It is this bidirectional vertical transport of E_{coh} in the NWTC environment that accounts for the high values of E_{coh}, σ_w, and FBM *DEL* loads in the weakly unstable region and is most likely a consequence of the dynamics of flows emanating from the major mountain range to the west.

5.1.2 Turbine Dynamic Response to Variations in Turbulence Scaling Characteristics

5.1.2.1 Hub-Height Turbulence Intensity and Friction Velocity

Figures 5-5a and b plot the variations of the FBM *DEL* loads with the hub-height turbulence intensity (I_{hub}) and local turbulent shearing stress or u_* for the Micon 65/13 turbines and the ART. As one would expect, the loads increase (albeit with broadening scatter) increase with I_{hub} in the natural inflow to the ART. By contrast, as mentioned earlier, an opposite trend is seen for the Micon 65/13 turbines deep within the California wind farm. We believe this to be a consequence of the turbulent flow within the wind farm in which σ_{U_H} is larger and increases more rapidly with mean wind speed than is characteristic of the natural flow seen at the NWTC. A nominal monotonic increase in the FBM *DEL* loads with hub-height (local) u_* is seen in both the two Micon 65/13 turbines and the ART, again with a bit more scatter in the natural flow of the latter.

5.1.2.2 Rotor Disk Shear Exponent and Hub-Height Mean Wind Speed

Figures 5-6a and b present the variations of the FBM *DEL* loads with the rotor disk shear exponent α and hub-height mean wind speed $\overline{U_H}$ for the Micon 65/13 turbines and the ART, respectively. The intense turbulent mixing between the rows of the California wind farm limits

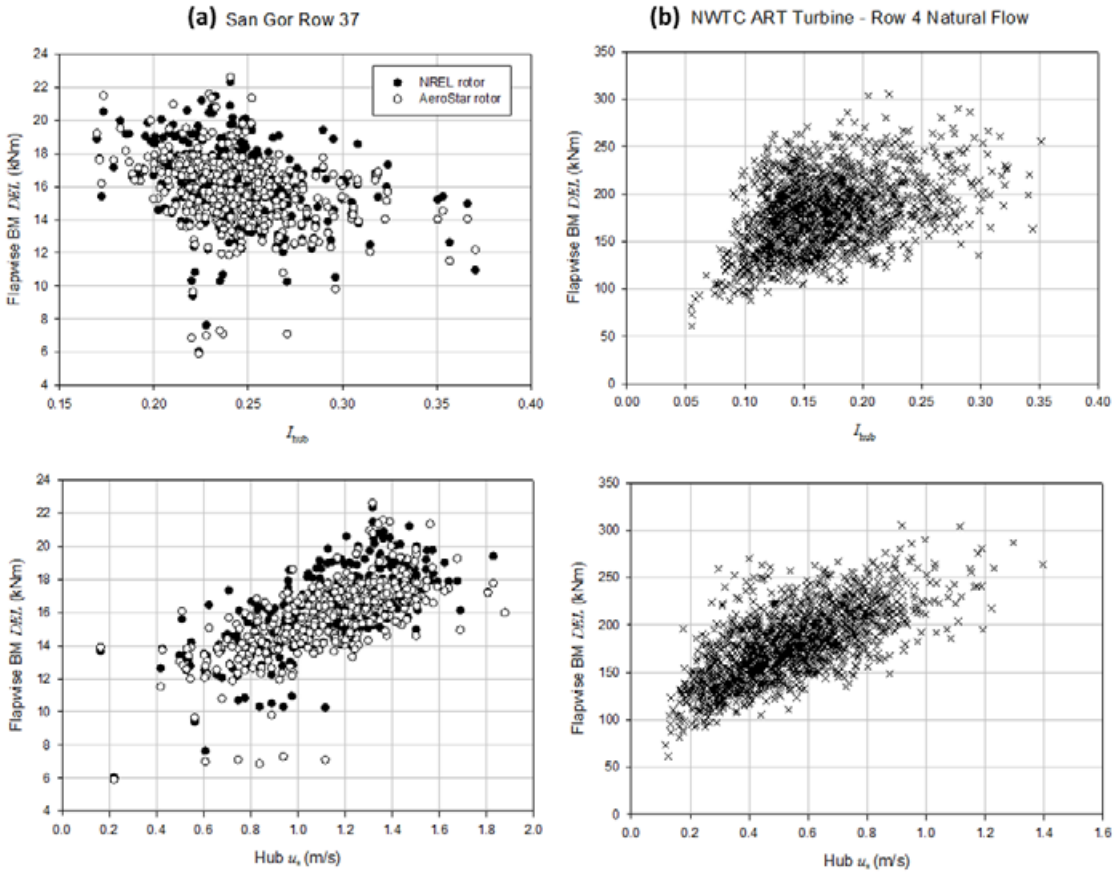

Figure 5-5. Observed variations of root FBM *DEL*s with hub-height turbulence intensity (I_{hub}) and local friction velocity u_* for the (a) Micon 65/13 turbines and (b) ART

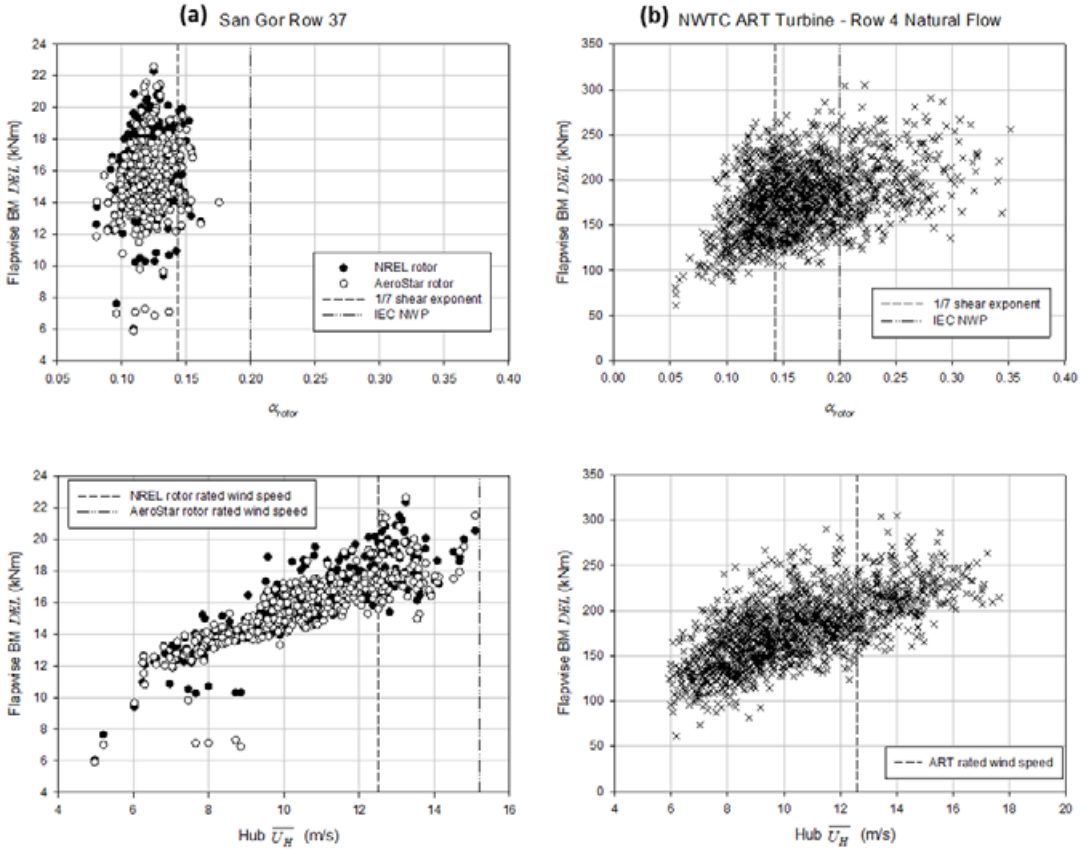

Figure 5-6. Observed variations of rotor disk shear exponents (α) and hub-height mean horizontal wind speed $\overline{U_H}$ of (a) Micon 65/13s and (b) ART root FBM *DEL*s

the observed shear to a narrow range. At the NWTC the natural flow is more stably stratified in the colder months when we conducted the field campaign. This limits the strength of the vertical mixing and the turbine dynamic loads increase with both shear and mean wind speed. This difference in shear is further compared for the two sites as a function of stability in Figure 5-7. Figure 5-7a demonstrates the effect of the intense mixing in the flow at Row 37 of the wind farm with no change in the shear exponent as the stability reaches the critical range and higher. In the natural inflow at the NWTC, however, there is effectively a significant step increase in the shear exponent when the stability reaches the CRR stability range and then continues to increase with rising stability, as shown in Figure 5-7b. The Ri_{TL} value of +0.02 where the greatest dynamic response of the Micon 65/13 turbines was observed is annotated on Figures 5-7a and b.

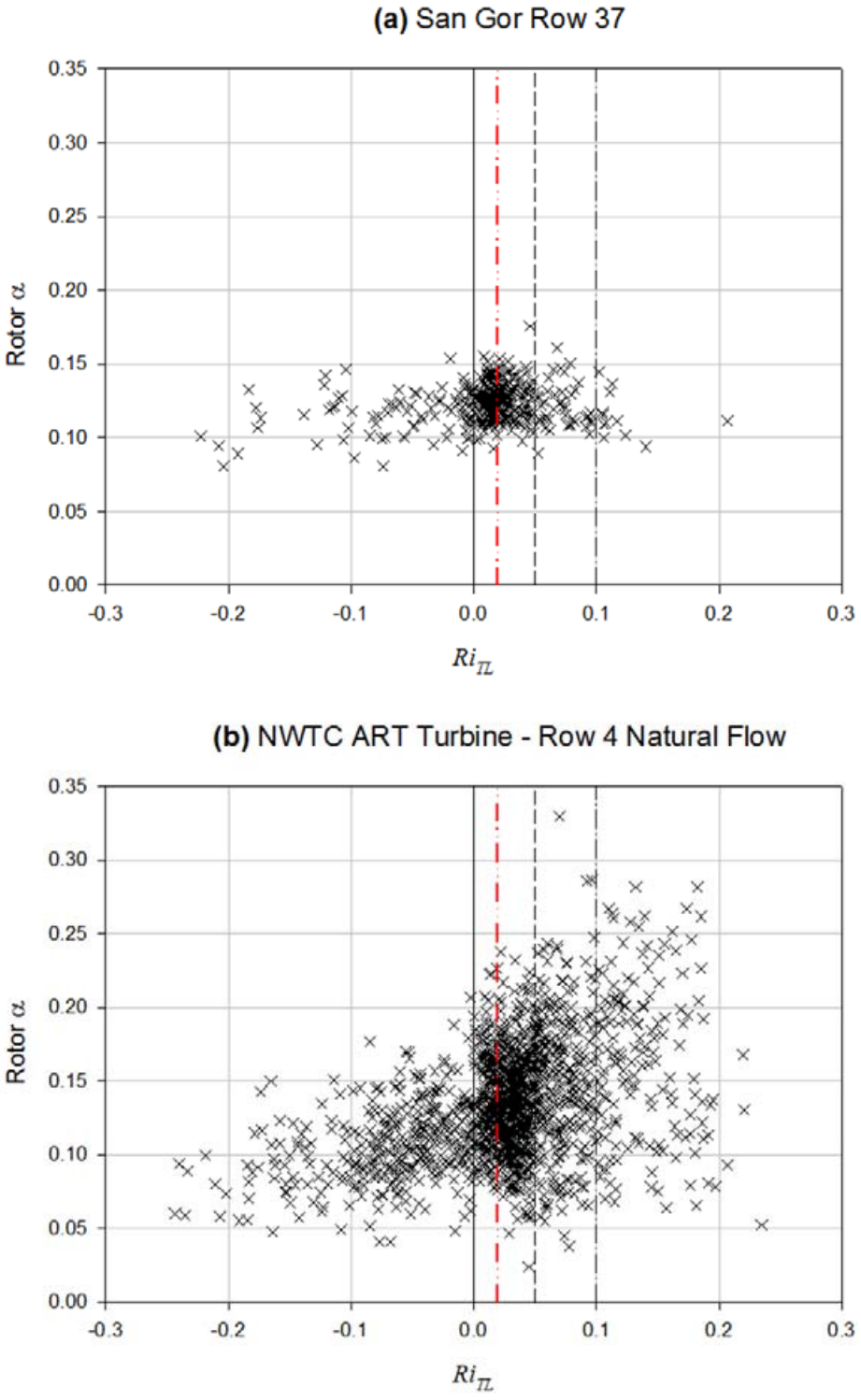

Figure 5-7. Comparison of variation of rotor disk shear exponents with Ri_{TL} for (a) Micon turbines and (b) ART

5.1.2.3 Variation of Hub-Height Friction Velocity u_* with Mean Wind Speed

The hub-height or local mean shearing stress or friction velocity u_* is an important scaling parameter for the dynamic responses of both the Micon 65/13 turbines and the ART. Here we compare its variation with the hub-height mean wind speed for both locations. Figure 5-8 depicts the variation of the hub-height shearing stress or local u_* with stability and the hub-height mean horizontal wind speed for Row 37 of the wind farm and the natural inflow at Row 4 of the NWTC. Figure 5-8a demonstrates the influence again of the cumulative wake dynamics of the 36 rows of upwind of the Micon 65/13 turbines in the wind farm, principally as a more rapid increase in u_* with wind speed compared with that observed in the natural flow of the NWTC in Figure 5-8b.

The highest values of u_* in the wind farm flow occur within the CRR stability regime and coincide with the maximum observed turbine dynamic response at a value of Ri_{TL} of +0.02, indicated by the red dot-dot-dashed line in the upper leftmost graph of Figure 5-8a. Although the upper range of positive stability is limited in the wind farm data, the rapid decrease in u_* with increasing stability compares favorably with that observed at the NWTC in the upper rightmost panel of Figure 5-8b. Although not as clear as that in the wind farm, the peak u_* value in the NWTC natural inflow also seems to occur at the same Ri_{TL} value, indicating that similar turbulence dynamics are occurring.

5.2 Comparing Hourly Diurnal Variations of Root FBM *DEL* Responses

Figures 5-9e and f compare the hourly diurnal variations in the FBM *DEL* [■] seen in the two Micon 65/13 turbines and the ART. In addition, Figures 5-9a and b plot in the topmost row the corresponding diurnal variations of the Micon 65/13 hub-height and ART disk-averaged values of the mean vertical momentum flux $\overline{u'w'}$, the hub-height values of vertical wind speed standard deviation σ_w. Figures 5-9c and d present in the center row the values of Ri_{TL} and Micon hub-height and ART disk-averaged values of the mean buoyancy flux $\overline{w'T'}$. The nominal times of the local sunrise and sunset are indicated by vertical blue lines.

We now examine the periods with the highest loads (>20 kNm for the two Micon turbines and >250 kNm for the ART) and the associated turbulence parameters for each site. Starting with $\overline{u'w'}$ [■] and σ_w [□] in the top row, the high loads are associated with large values of both variables with the wind farm wake flow having the greater absolute levels. In the second row, the Ri_{TL} values [■] occur often within the CRR range and the buoyancy flux $\overline{w'T'}$ [□] is negative in the wind farm wake and both positive and negative, with the latter more frequent at the NWTC. The peak values of E_{coh} [□] shown in the bottom row (Figures 5-9e and f) for the wind farm are all greater than the significant response threshold of 10 m^2 s^{-2} for the entire diurnal period. For the ART, however, the high load records are associated with E_{coh} values well exceeding this threshold, but the periods of lower response are dominated with values that are below the significant level. So similarities exist, but so too do some fundamental differences in the atmospheric dynamics associated with the high response loads at each location.

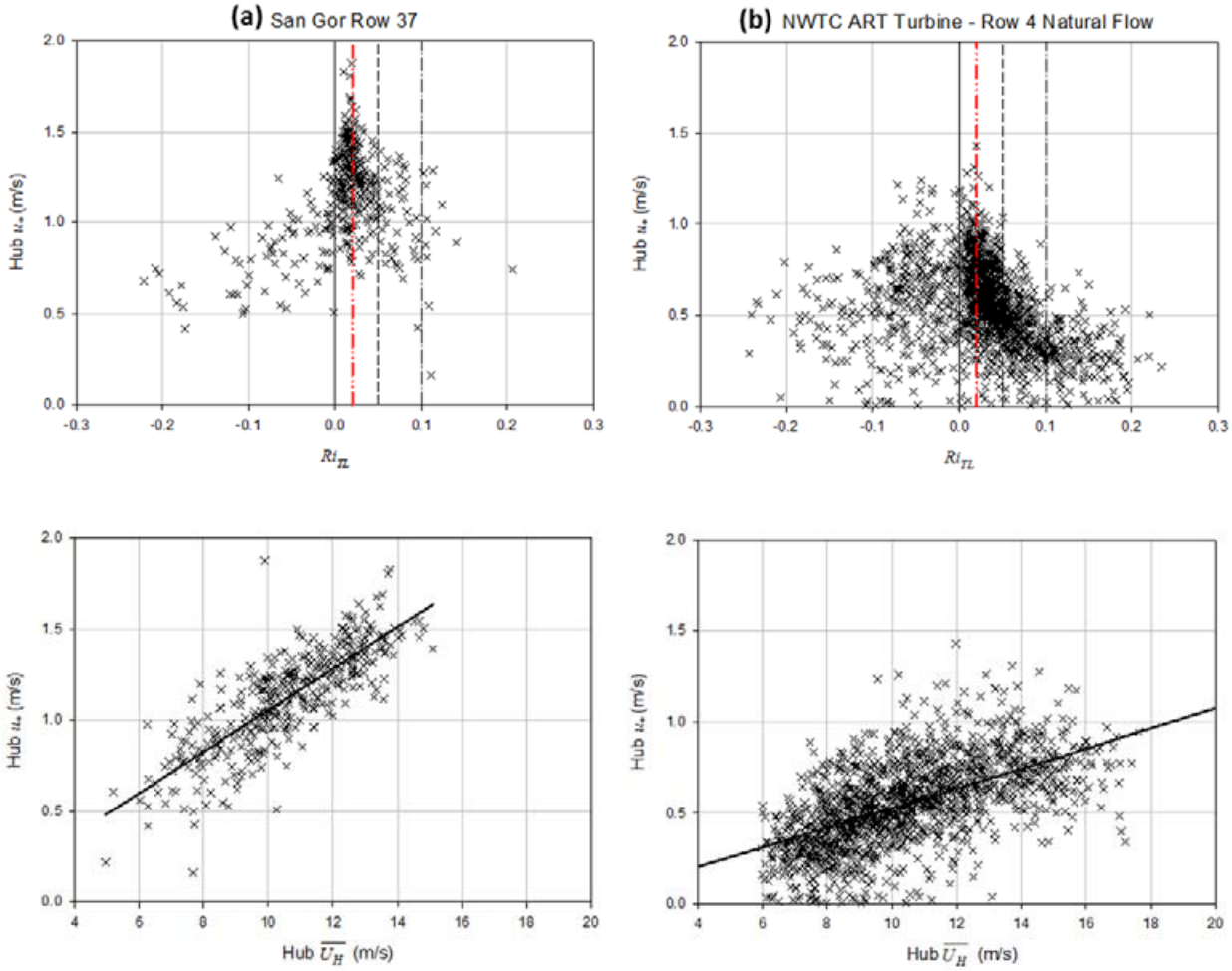

Figure 5-8. Observed variations of hub u_* values with Ri_{TL} and hub mean horizontal wind speed ($\overline{U_H}$) for (a) Row 37 of wind farm and (b) upwind of ART. The vertical red dashed lines shown in the upper row of graphs correspond to the value of Ri_{TL} (+0.02) in which the maximum dynamic response of the Micon turbines was observed.

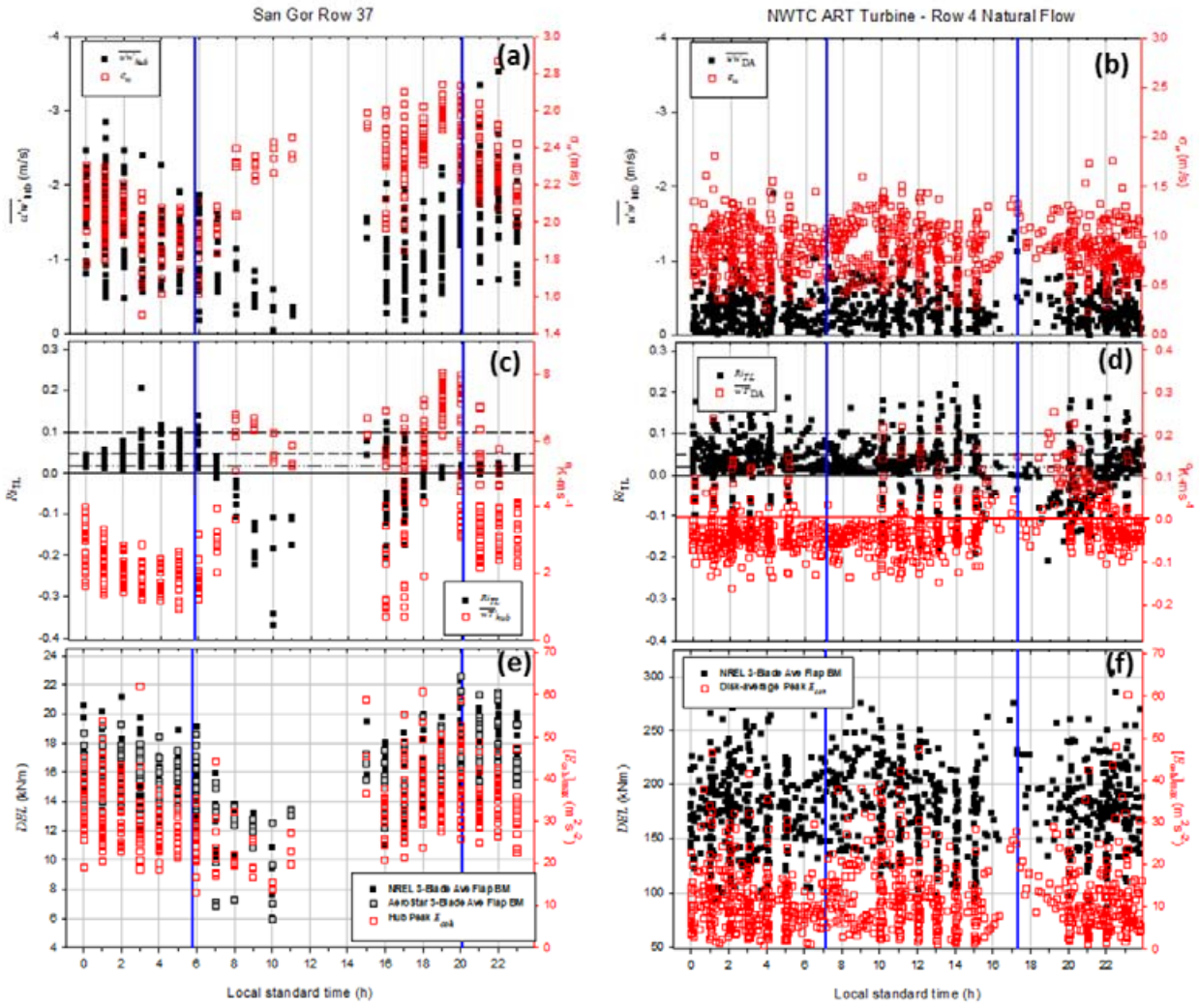

Figure 5-9. Comparison diurnal variations of root FBM *DEL* responses for (e) Micon 65/13 turbines and (f) ART with (a,b) $\overline{u'w'}$ and σ_w, (c,d) Ri_{TL} and buoyancy flux ($\overline{w'T'}$). Nominal sunrise and sunsets are indicated by solid blue vertical lines. The critical stability values ranges (Ri_{TL} = +0.02, +0.05, and +0.10) are shown as horizontal lines in (c,d). Disk-averaged values of σ_w, $\overline{u'w'}$, and $\overline{w'T'}$ are used for the ART variables.

5.3 Defining Common Turbulence Characteristics

Comparing the inflow turbulence characteristics associated with the blade root FBM equivalent fatigue damage measured on the Micon 65/13 turbines immersed in an internal wind farm wake flow and the ART operating in a high turbulent but natural flow, we note the following:

- The turbines respond in a very similar manner when operating in the STC02, CRR, CRRH, and STC04 stability classes, indicating that similar atmospheric dynamics are present.
- The observed FBM fatigue damage levels in the turbines at both sites are strongly correlated with the peak values of E_{coh}, with greater values seen in the natural flow at the NWTC.
- The intense vertical mixing present within the wind farm flow limits the vertical shear; at the NWTC the shear is highly correlated with the stability classification.
- The vertical transport or flux of E_{coh} is an important parameter in the level of turbine response at both sites, but the wind farm is characterized by a persistent mean downward E_{coh} flux and at the NWTC both upward and downward fluxes are involved.
- The variations of the vertical wind speed (σ_w) and buoyancy flux ($\overline{w'T'}$) within the turbine rotor disks are significant contributors to the turbine dynamic response.

5.4 Comparing CRR Turbine Response Scaling Parameters

We have seen that the most significant turbine responses in terms of peak loads and fatigue damage occur in both the California wind farm Micon 65/13 turbines and the NWTC ART within the CRR defined by the Ri_{TL} range of +0.01 to +0.05. It is useful to focus on the distributions of the turbulence parameters shown to scale the turbine dynamic response within the CRR range at both sites.

Figure 5-10 shows the diurnal variation of the probability of CRR conditions at the site of the Micon 65/13 turbines and in the inflow of the ART. With the exception of the high probability at 0100 hours at the California wind farm, the distributions are quite similar. CRR stability conditions are most likely to occur from late in the afternoon to around local sunrise, a period that coincides with a stable atmospheric boundary layer. Figure 5-11 plots the probability distributions of the hub-height $\overline{U}$ component for the available data populations in the CRR. In both cases the most frequent mean speeds occur at just below rated speeds and with equal probability at rated speeds. This is a sensitive wind speed range on most wind turbine rotors, where transient loading from unsteady aerodynamic processes can be significant.

Figure 5-12 plots the rotor thrust coefficient C_T for the NREL 7.9-m thin airfoil blades used on the Micon 65/13 turbine. For wind speeds between about 10 and 13 m s^{-1}, there is a maximum rate of change (the steep slope of line on the diagram) in the thrust loads with speed on the turbine rotor. The speed also has a high probability of occurrence in the CRR stability range, as shown by Figure 5-11, and is most likely a contributor to the high level of turbine dynamic

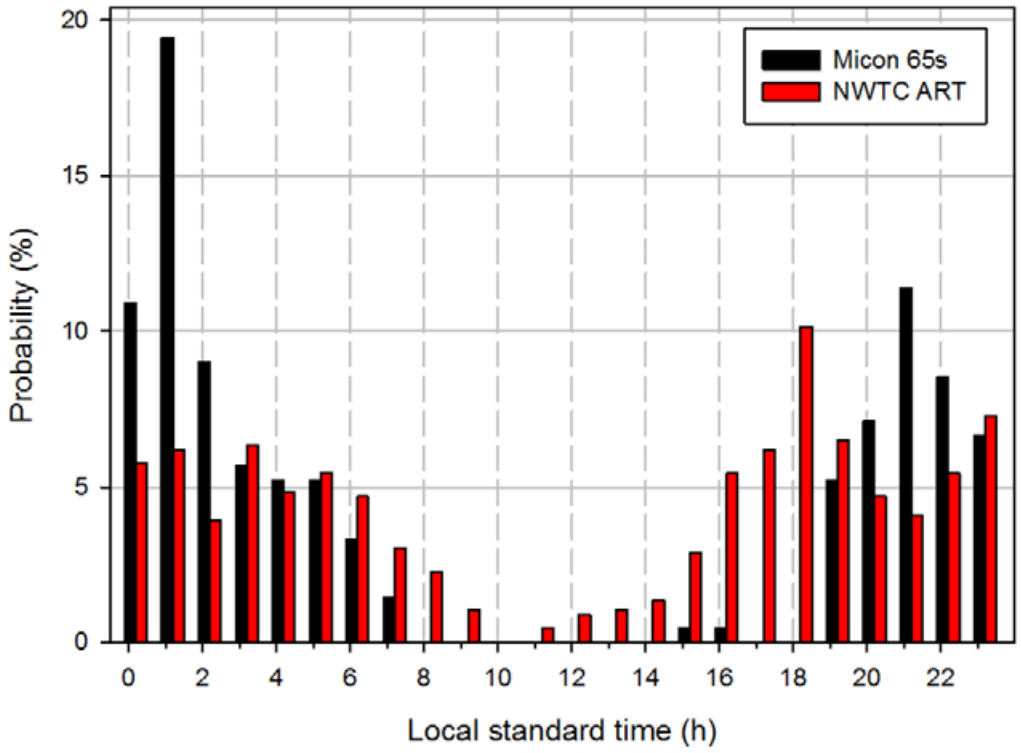

Figure 5-10. Diurnal hourly probability of occurrence of CRR stability class conditions as seen for Micon 65/13 turbines on Row 37 of California wind farm and for ART on Row 4 at NWTC

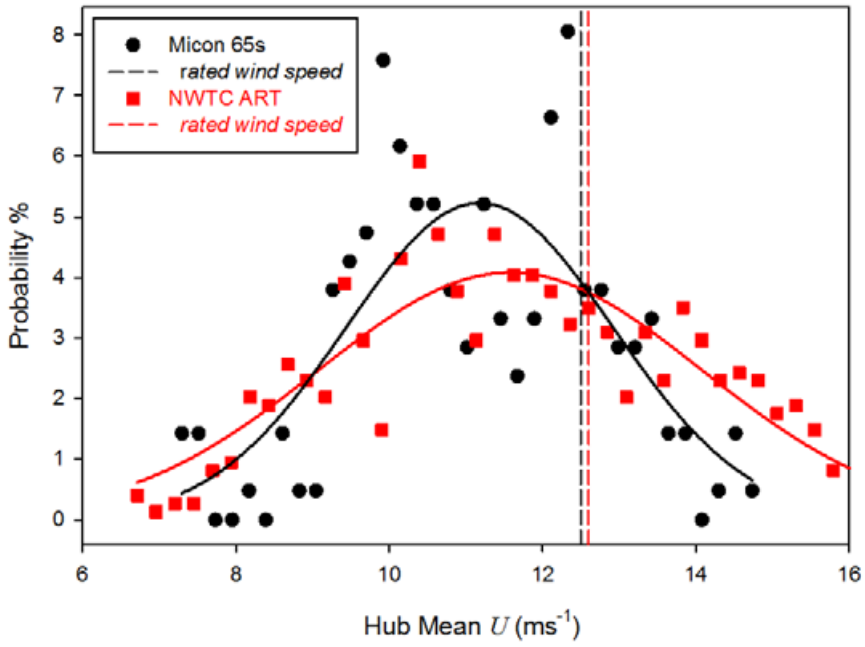

Figure 5-11. Observed hub-height mean *U*-component wind speeds probability distributions in the CRR stability range for the Micon 65/13 turbines and for ART. Each has been fitted with a Gaussian distribution, shown as solid lines. The rated wind speeds for the Micon 65/13 turbine equipped with the NREL rotor and the ART are shown as vertical dashed lines.

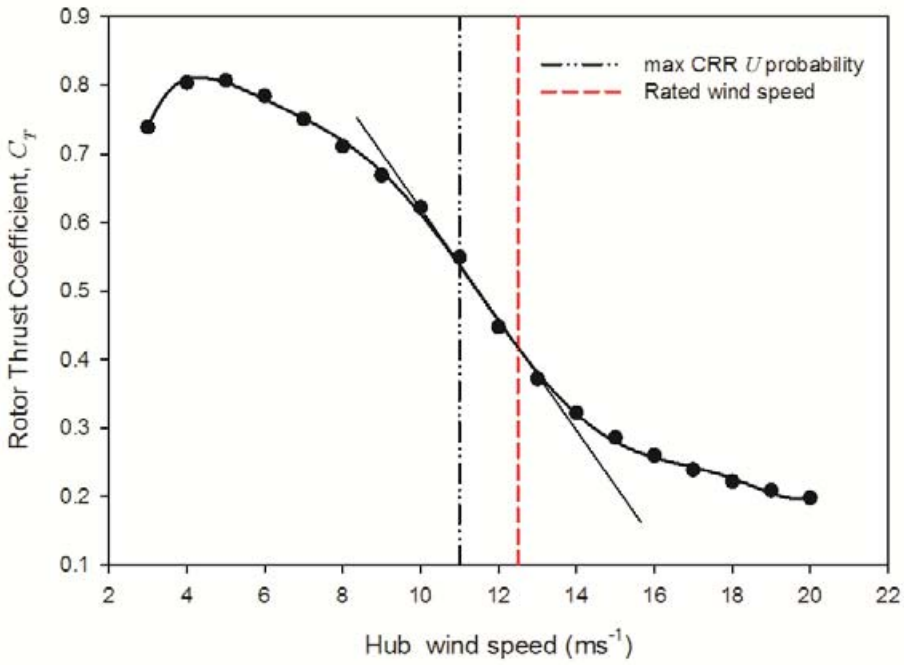

Figure 5-12. Variation of thrust coefficient C_T with mean wind speed for Micon 65/13 turbine with NREL rotor. Highest probable mean *U* wind speed in data set shown as vertical dot-dot-dashed line. (C_T data source: J. Tangler, NREL)

response observed. We do not have a C_T curve for the AeroStar and ART rotors, but they are likely to be somewhat similar depending on the blade shape and airfoil sections included. The ART blades were collective pitch controlled, but fluctuations at the most frequent peak wind speed are centered below rated at about 11.5 m s^{-1}. The most frequent speeds in the CRR range extend over a slightly broader range of about 9.5 to 14 m s^{-1} compared with the NREL Micon 65/13 rotor. During the testing of this turbine, significant audible noise level emissions were being radiated from the blades just as the controller began to pitch them to control peak power. Such emissions are indicative of the occurrence of significant unsteady blade loads.

Figure 5-13 shows the frequency/probability distributions of u_* within the CRR stability range for the wake inflow to the Micon 65/13 turbines and the natural inflow to the ART. Unmistakably, the turbulent shearing stresses are much higher within the wake flow entering the Micon turbines than are usually present in the natural flow upstream of the ART. Neither the wind farm nor NWTC hub local u_* distributions are Gaussian in the strictest sense, but the wind farm could be considered at least "quasi-Gaussian." The u_* distribution in the inflow to the ART, however, is significantly skewed to higher values and therefore is certainly not Gaussian within the CRR stability range.

Figure 5-14 presents the frequency/probability distribution of the hub peak values of E_{coh} within the CRR stability range for the two sites. Although the upstream turbine wake flow into the two Micon turbines contained higher levels of E_{coh} on average than the natural flow into the ART, the latter turbine was subjected very high transient values occurring much less frequently. These peaks are strongly correlated with the vertical fluxes of E_{coh} shown in Figure 5-15. Figure 5-15a shows that the frequent value of peak E_{coh} in the Micon inflows is associated with high occurrence of downward $\overline{w'E_{coh}}$, whereas both vertical and downward mean fluxes are contributing to the peak E_{coh} values in the inflow to the ART. Figure 5-15b shows that although these E_{coh} peaks observed in the Micon wake inflow are the result of both positive and negative maximum fluxes of E_{coh}, downward ones occur more frequently. In the case of the ART natural inflow, however, these more infrequent E_{coh} peaks are the consequence of more or less equally likely vertical and downward maximum values of $\overline{w'E_{coh}}$. Thus the presence of multiple rows of turbines ahead of a downstream turbine can significantly modify the vertical transport characteristics of coherent turbulent kinetic energy into the rotor.

5.5 Comparing Probability Distributions of Micon 65/13 Turbines and ART Root FBM Responses by Stability Class

Figure 5-16 shows the observed cumulative probability distributions of the root FBM *DEL*s in the left column and peak loads in the right column for the two Micon turbines and the ART. The distributions for the available populations for each turbine are plotted in light gray. The distributions associated with the stability classes STC02 (green open triangles), CRR (red open circles), CRRH (blue open diamonds), and STC04 (black open squares) are plotted atop the available populations. The STC04 stability class is not given for the two Micon turbines because of too few observations. The diagonal line across each diagram designates the expected cumulative probability of a true Gaussian process and is a reference to ascertain the degree to which the observed processes are normally distributed.

None of the distributions displayed in Figure 5-16 are representative of a true Gaussian or normal process. The loads measured on Micon 65/13 turbines in the wind farm wake flow, particularly the *DEL*s, generally are the closest, especially in the high loading tails. In contrast, the distributions in Figures 5-16e and f measured on the ART in a natural flow exhibit significant non-Gaussian behaviors characterized by the negative skew. We see more small loads and fewer large ones than would be expected from a normal process. The Micon loads in the stable CRR and CRRH classes are similarly distributed in the high loading tails. The effect of stability stratification on the ART is more pronounced as the amplitudes decrease with increasing stability but not so much in the distribution shapes themselves. As in the Micons, the ART high loading tails in the STC02 and CRR converge.

It is not clear if the differences highlighted by these results are a consequence of (1) operations in a wind farm wake environment as opposed to a rigorous but naturally occurring inflow; (2) three-bladed stall controlled rotors with a rigid hub design versus a two-bladed pitch controlled rotor with a teetered hub; or (3) some combination of both. For example, one could conclude that the skewed distribution seen in the ART response could be related to the teetering hub removing the large once-per-revolution loads but having no ability to minimize turbulence scales smaller than the rotor diameter. Similarly, one could hypothesize that the near-Gaussian response seen in the Micon turbines is linked to a combination of stall control and a rigid hub. Some of these questions could be answered if accurate design models of these two turbine designs were modeled with a suitable multibody dynamic code excited by a realistic turbulent inflow simulation of both operating environments.

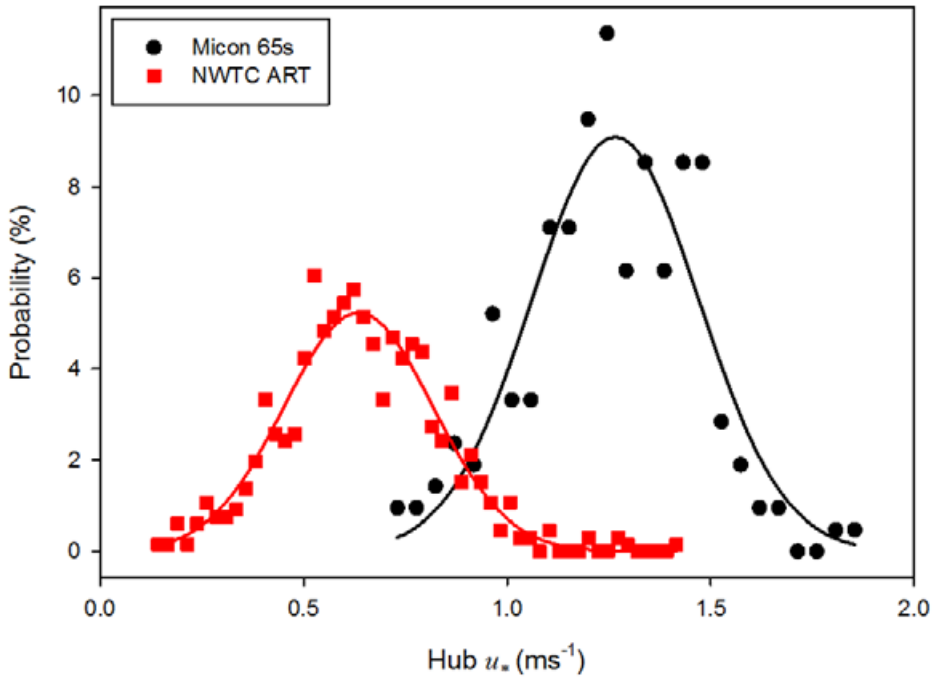

Figure 5-13. Observed hub-height shearing stress or u_* probability distributions in CRR stability range for the Micon 65/13 turbines and ART. Each has been fitted with a Gaussian distribution shown as solid lines.

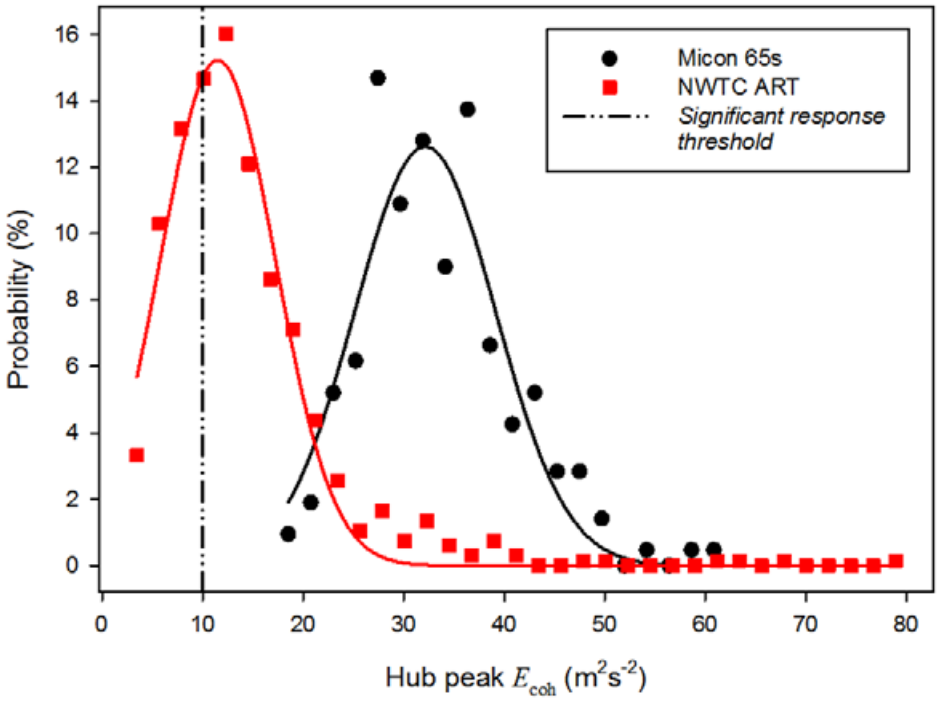

Figure 5-14. Observed hub-height shearing peak E_{coh} probability distributions in CRR stability range for Micon 65/13 turbines and ART. Each has been fitted with a Gaussian distribution, shown as solid lines.

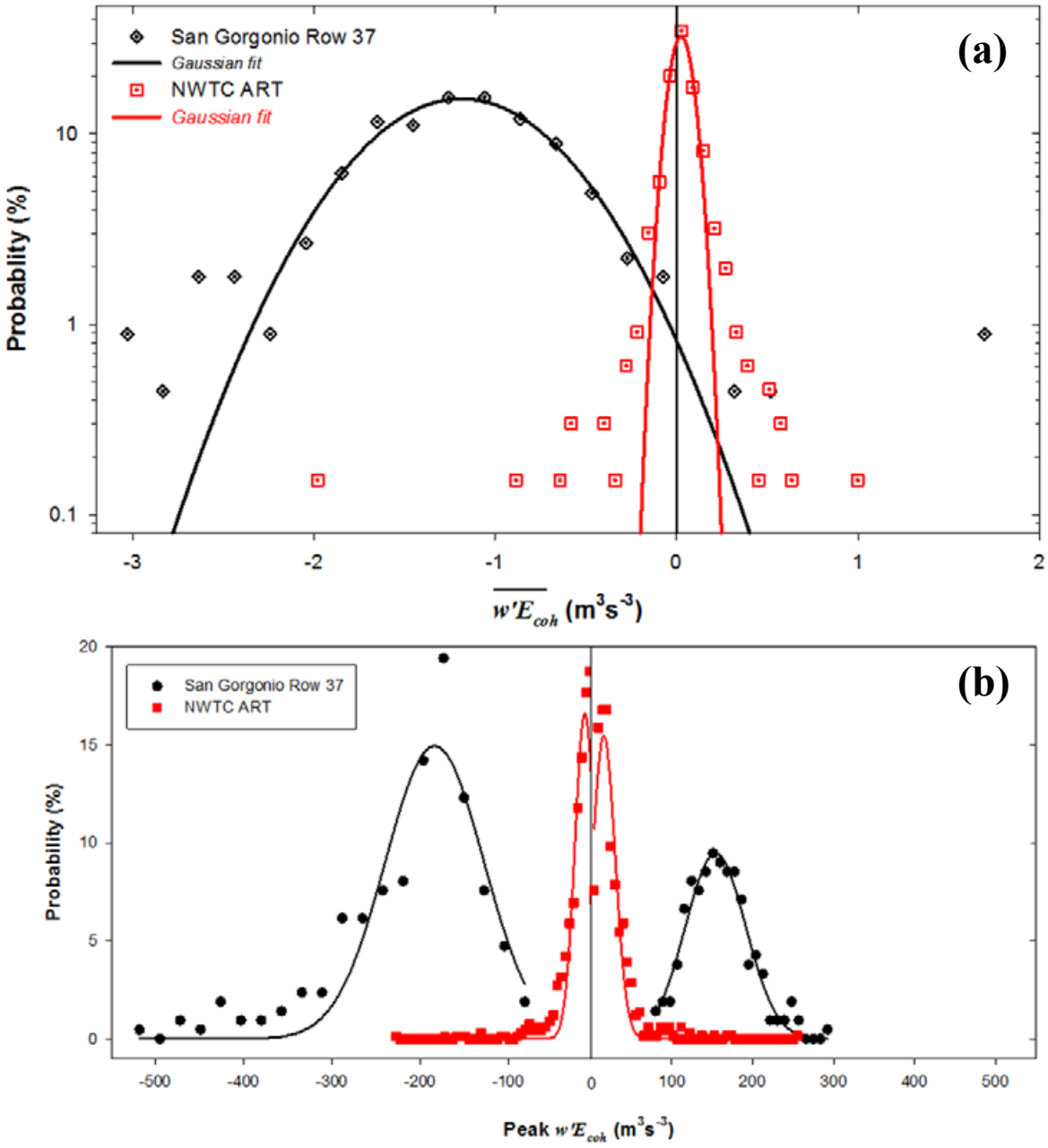

Figure 5-15. Observed hub-height fluxes of $w'E_{coh}$ for CRR stability range at Row 37 of the wind farm and Row 4 of the NWTC: (a) means and (b) peak values. Each has been fitted with a Gaussian distribution, shown as solid lines.

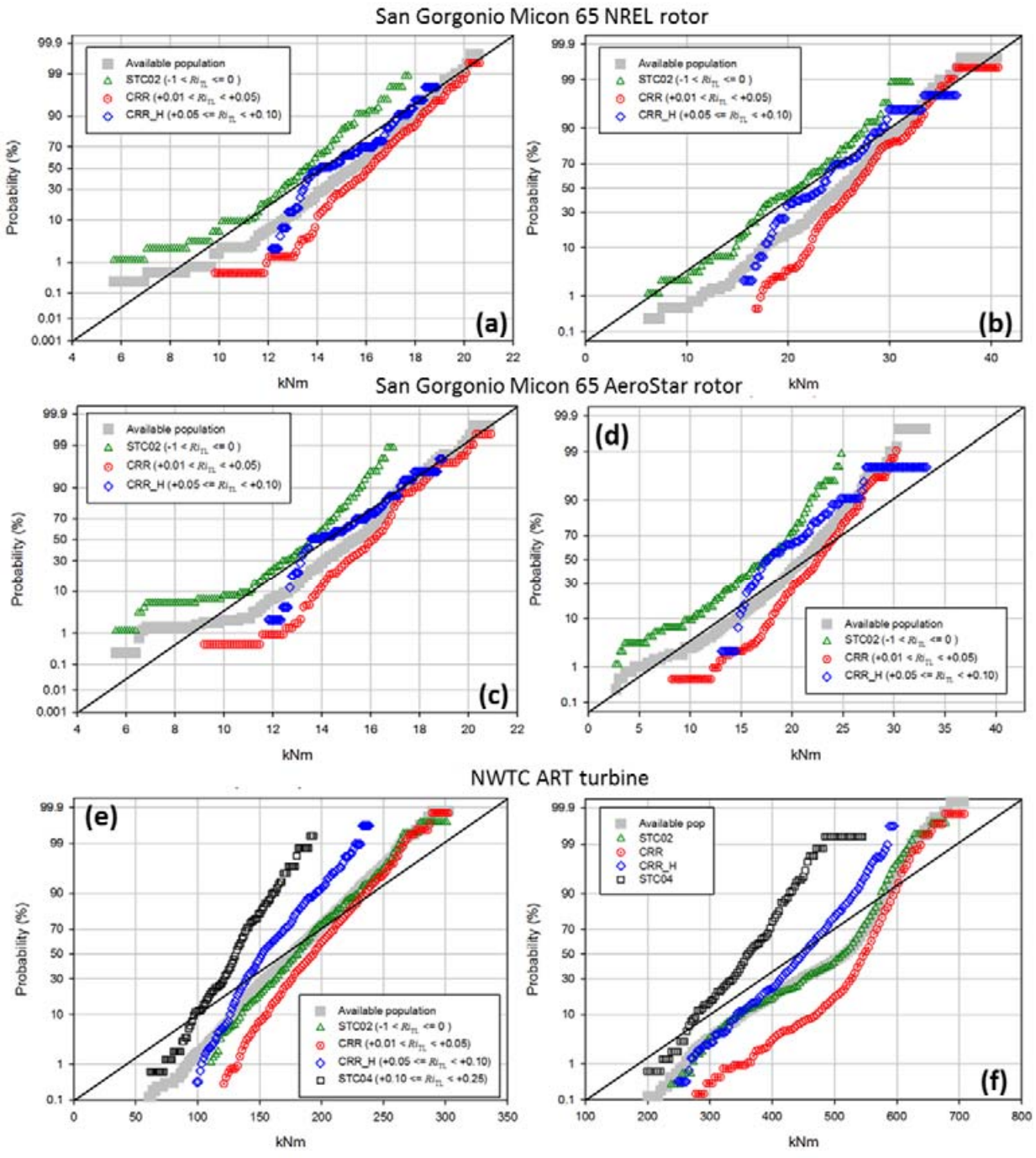

Figure 5-16. Comparison of Micon 65/13 turbine and ART cumulative probability distributions of root FBM *DEL*s and peak loads for available populations [■] and stability classes STC02 [Δ], CRR [○], CRRH [◇], and STC04 [□] . Micon 65/13 with NREL rotor FBM: (a) three-blade averaged *DEL*s; (b) three-blade peak. Micon 65/13 with AeroStar rotor FBM: (c) three-blade averaged *DEL*s; (d) three-blade peak. NWTC ART FBM: (e) *DEL*s; (f) peaks.

6.0 Atmospheric Dynamics Associated with Turbine Response

6.1 Comparing Turbine Responses by Stability Class

In Section 5 we found that the dynamic responses expressed in fatigue damage and peak loads of the California wind farm Micon 65/13 turbines and the National Wind Technology Center (NWTC) Advanced Research Turbine (ART) were similar when correlated against several turbulence parameters and atmospheric scaling parameters. Most important, we found that a key parameter influencing the severity of the response was the dynamic stability of the vertical atmospheric layer above the local ground level of the turbines. We expressed this parameter as the turbine layer gradient Richardson number, Ri_{TL}. Our analysis showed that the turbine responses could be further subdivided into at least five stability classification ranges that applied to both the Micon 65/13 turbines and the ART. Table 6-1 lists these ranges.

Table 6-1. Turbine Layer Stability Classifications for Turbine Response Correlations

Stability Class Designation	Range
Moderate to Weak Unstable Class, STC02	$-1 < Ri_{\mathrm{TL}} \leq 0.00$
Weakly Stable Critical Range, CRR	$+0.01 \leq Ri_{\mathrm{TL}} < +0.05$
Weakly Stable High Range Critical, CRRH	$+0.05 \leq Ri_{\mathrm{TL}} < +0.10$
Moderately Stable Range, STC04	$+0.10 \leq Ri_{\mathrm{TL}} < +0.25$
Very Stable Range, STC05	$+0.25 \leq Ri_{\mathrm{TL}} < +1.0$

Only 12 observations were available in the moderately stable STC04 classification in the Micon 65/13 data set and none in the very stable STC05. Similarly, the ART data set had only 17 observations available in the very stable STC05 classification. We used the few STC02 observations for the Micon 65/13 correlations for an estimate of completeness, but we advise caution in the level of acceptance. For the ART correlations, we decided to not use the few very stable STC05 observations because the other four classes encompassed 95% of the available data set, and the mean wind speeds for STC05 were very low. We also found that the maximum turbine dynamic responses for the Micon turbines and the ART occurred near $Ri_{\mathrm{TL}} = +0.02$.

Figure 6-1 shows boxplot probability distributions of the root flap bending moment (FBM) damage equivalent loads (*DEL*s) and peak load responses for the National Renewable Energy Laboratory (NREL)-rotor equipped Micon turbine and the ART for each stability class. Figure 6-2 shows the corresponding distributions for the hub-height mean *U*-component wind speeds, rotor disk shear exponent, and hub mean buoyancy fluxes ($\overline{w'T'}$), and Figure 6-3 plots the hub peak negative and positive vertical E_{coh} fluxes ($\overline{w'E_{coh}}$). As shown in Figures 6-1 and 6-2, the highest loads occur in the weakly stable CRR range, which also has the highest mean wind speeds. Significantly, in both cases, a greater percentage of these higher load distributions occur

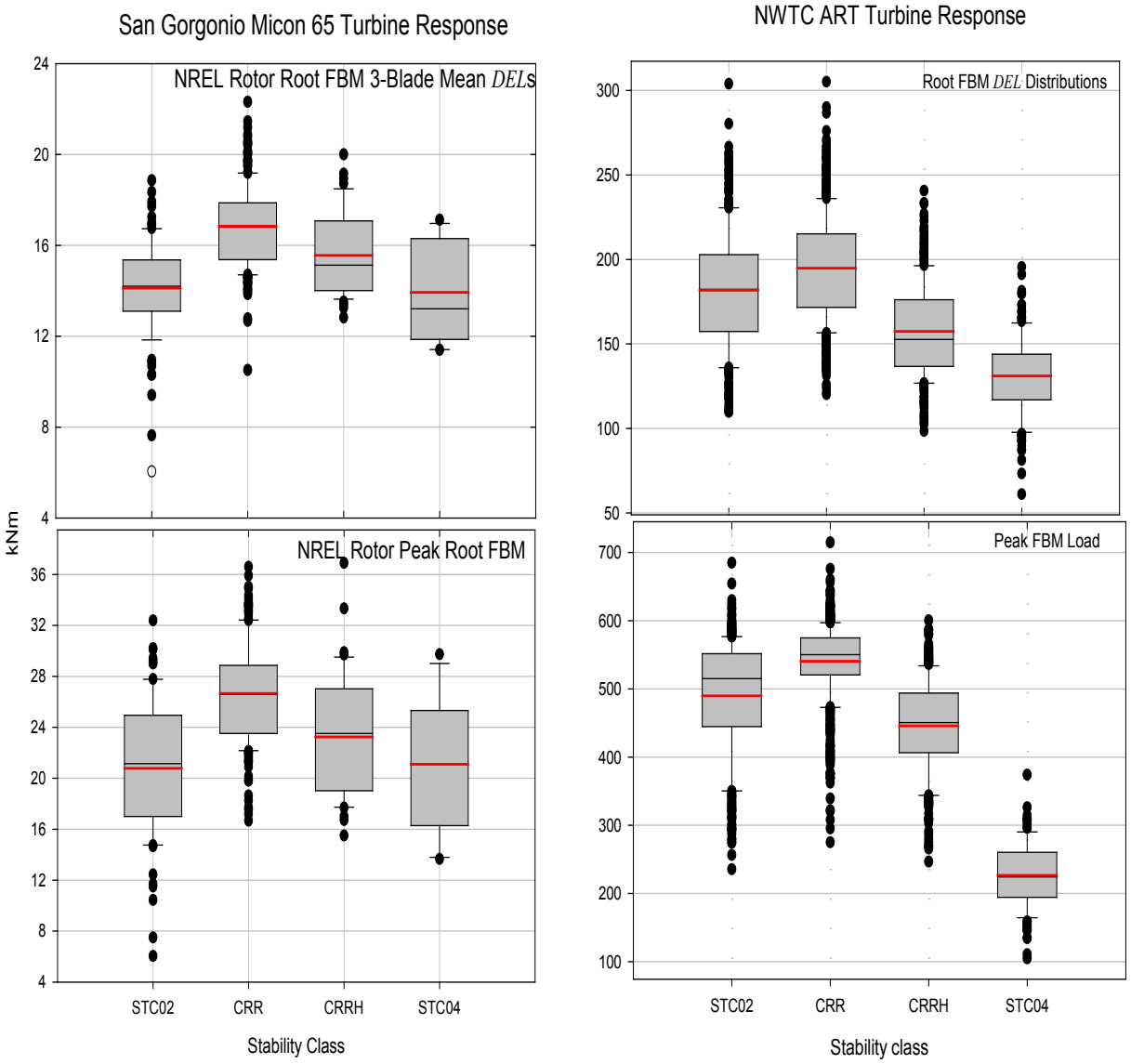

Figure 6-1. Boxplot probability distributions of observed root FBM *DEL*s and peak load responses by stability class for California wind farm Micon 65/13 (NREL rotor) turbine and NWTC ART. The dots represent values outside the P10–P90 range indicated by the whiskers.

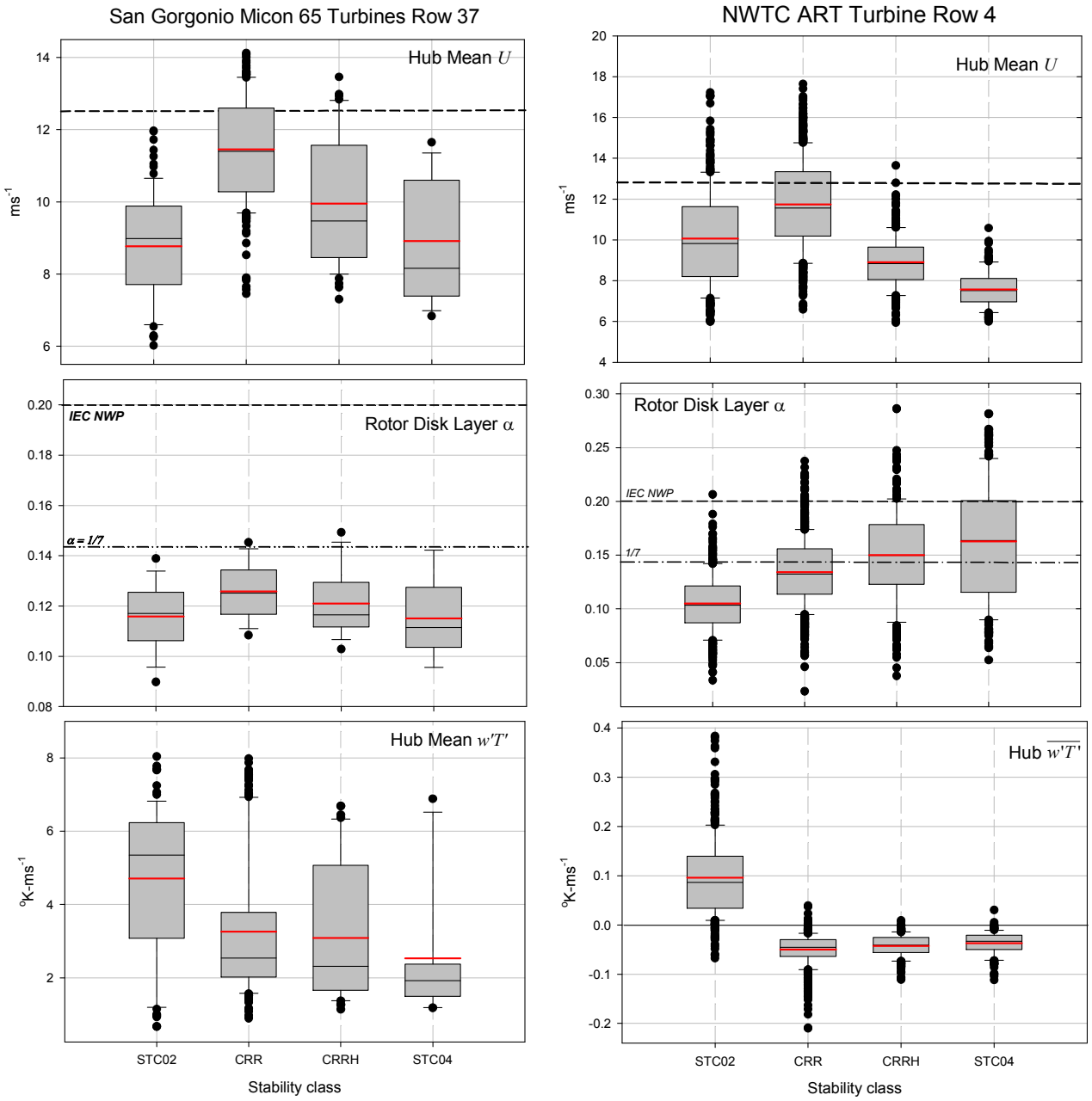

Figure 6-2. Probability distributions of observed inflow hub-height mean *U*-component, rotor disk shear exponent and hub mean vertical buoyancy flux by stability class for Micon 65/13 (NREL rotor) turbine and the ART. The dashed lines indicate the rated wind speeds. The boxplot nomenclature is the same as for Figure 6-1.

during at or below rated wind speed inflow conditions. In the wind farm, the intense vertical mixing caused by the high air and surface temperatures is responsible for the strong positive mean buoyancy. These buoyant motions combined with the upstream turbine wakes limit the vertical shear exponent α to the narrow range shown in Figure 6-2. The character of the buoyancy and to a lesser extent the shear in the critical Richardson number range or CRR is, however, quite different (we cannot make a judgment about the STC04 class because of the lack of observations). We note that the shear is the largest of the stability classes, and the mean buoyancy flux $\overline{w'T'}$ distribution is much more negatively skewed relative to the STC02 and CRR High, or CRRH, stability classes but has very long tails (high kurtosis). The latter is indicative of large buoyancy fluxes of short duration. In contrast, the shear in the natural inflow into the ART increases near monotonically with increasing stability that is much more Gaussian or normally distributed. Only the unstable class STC02 has a significant frequency of positive mean buoyancy occurrences at hub height. Here the mean buoyancy distribution in the CRR stability class has long negative tails, indicating periods of high buoyancy damping.

In Figure 6-3 we present box plots of the observed probability distributions of hub-height peak values of $w'E_{coh}$ measured in the inflow of the Micon turbines and the natural inflow of the ART stratified by stability class similar to those plotted in Figure 5-3. Here we see that the peak E_{coh} vertical fluxes at hub height in the wind farm are strongly skewed downward, with the largest range in the CRR stability range. By comparison, these peak fluxes in the natural inflow to the ART are nearly normally distributed, particularly for the most stable CRRH and STC04 classes. The CRR stability range where the largest turbine response is seen in Figure 6-1 has the largest tails, which are approximately symmetrically distributed. In the wind farm and natural inflows, the impact of increased stability and its associated damping effects are well demonstrated in the CRRH and STC04 classes. Figure 5-15 presents observed probability distributions of the vertical fluxes of the mean and peak values of hub-height E_{coh} ($\overline{w'E_{coh}}$ and $w'E_{coh}$ respectively) for the CRR stability range.

We found earlier that the dynamic responses of both the Micon turbines and the ART were very sensitive to peak values of E_{coh}. We compare probability distributions of the root FBM *DEL*s with the corresponding distributions of hub-height peak E_{coh} for each of the stability classes in Figure 6-4. Here we see that both the root fatigue loads and peak E_{coh} distributions have the largest positive tails (high kurtosis) in the CRR stability range, which has the smallest negative buoyancy turbulence damping (small positive values of Ri_{TL}) associated with it. This indicates these turbines when operating in the CRR stability range are subject to intermittent intense levels of coherent turbulence that result in high loading events more often than in the other stability classes. The damping impact of greater stability is most noticeable in the natural inflow to the ART in classes CRRH and STC04 where the body of the probability distributions remains below the significant peak E_{coh} response threshold (dashed line). A similar but much less distinct trend is evident in the upstream wake inflow to the Micon turbine. Here the entire distributions of the observed peak E_{coh} values remain higher than this threshold, with a much smaller variation between the CRR and CRRH stability classes. This suggests that this low variation seen between the stability classes is the consequence of another source of coherent turbulence in addition to that being locally created or being carried in the upstream wake flow within the turbine rotor

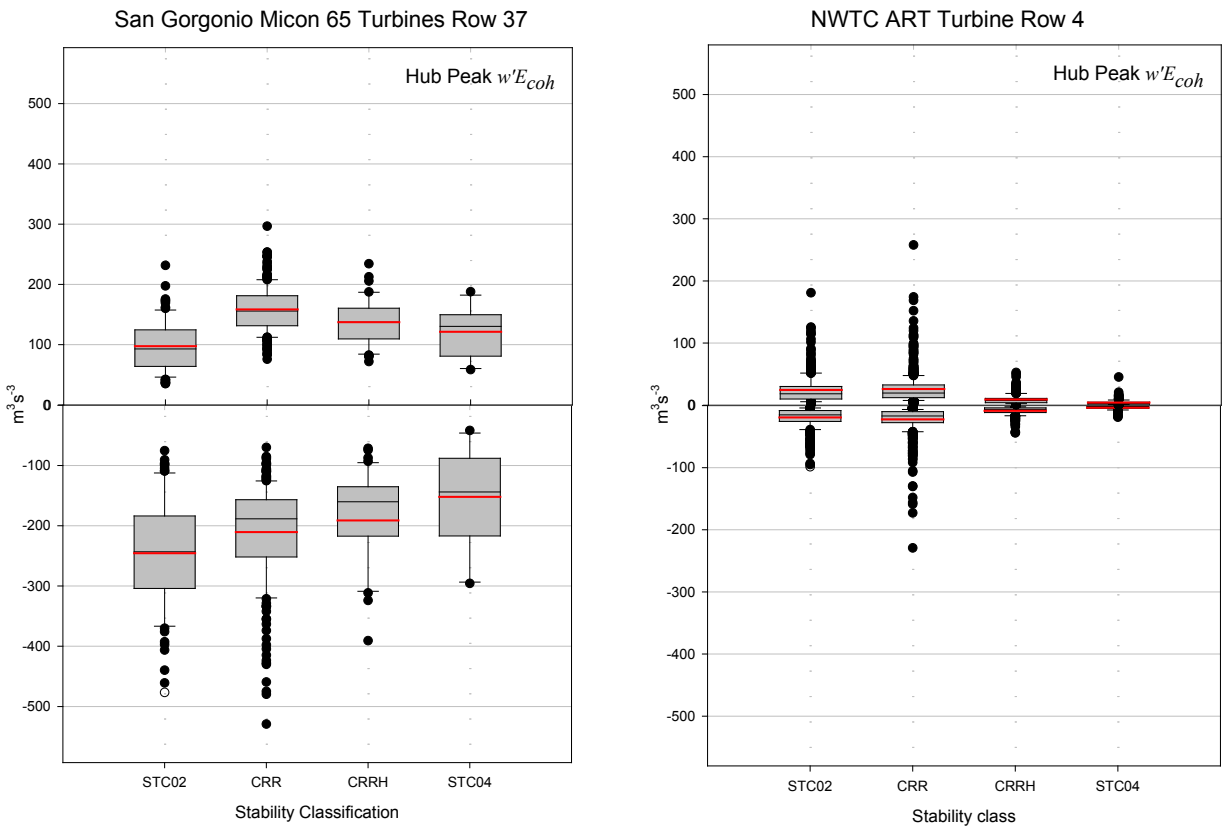

Figure 6-3. Probability distributions of inflow hub-height peak E_{coh} vertical fluxes ($w'E_{coh}$) for Micon 65/13 (NREL rotor) turbine and ART. The boxplot nomenclature is the same as for Figure 6-1.

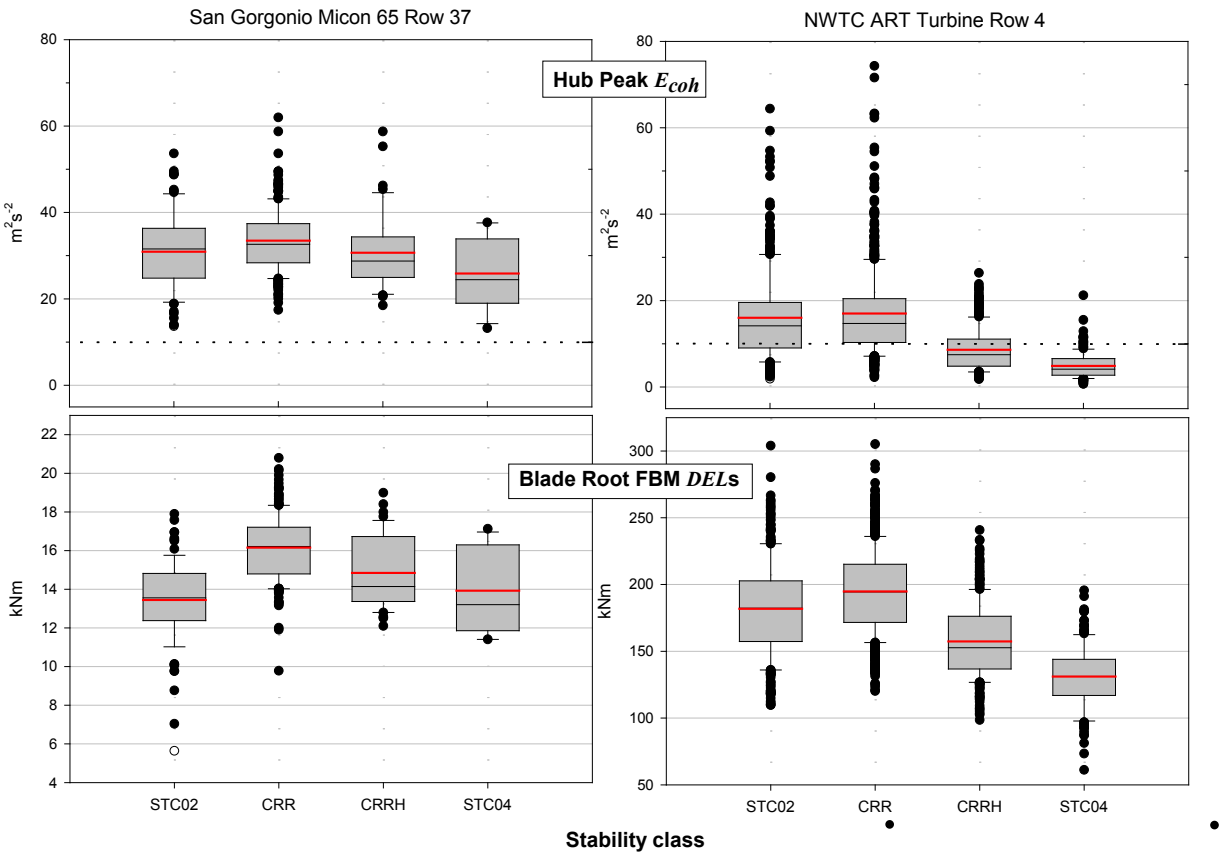

Figure 6-4. Comparison of probability distributions of Micon 65/13 (NREL rotor) turbine and ART hub peak E_{coh} (upper panels) and blade root FBM *DEL*s (lower panels) by stability class. Dashed line in upper panels (peak E_{coh}) represents the significant turbine dynamic response threshold. The boxplot nomenclature is the same as for Figure 6-1.

layer, i.e., a significant downward flux or transport of peak E_{coh} from the boundary layer above the turbine rotors which is unambiguously demonstrated in Figure 6-3. For the ART, vertical transport of peak E_{coh} is also operative, but high values are likely to be transported upward as well as downward within the turbine rotor layer. This further suggests that local creation of the coherent turbulence within the rotor disk layer is more important in the natural inflow to the ART.

6.2 Defining Role of Turbulent Buoyancy in Turbine Dynamic Response

The characteristics of the dynamic responses of turbine components are significantly influenced by the dynamic stability of the depth of the atmospheric boundary layer in which the turbines reside, i.e., expressed by Ri_{TL}. The relationship of Ri_{TL} to the turbulence kinetic energy budget within the turbine layer is discussed in sections 6.2.1 and 6.2.2.

6.2.1 Relationship between Shear and Buoyancy Turbulence Generation

Ri_{TL} is the ratio of turbulence generation/destruction to that being generated by shear over the atmospheric layer occupied by a turbine. Large, convective turbulent eddies grow when it is negative because of a positive (upward) flux of buoyancy. Conversely, when it is positive, the size and velocities of the largest eddies are damped (growth restricted or suppressed) and velocities are reduced first, which extend to smaller ones as Ri_{TL} increases (becomes more positive) because of the downward flux of buoyancy. Figure 6-5 shows this relationship by the contours of $\overline{w'T'}$ for the measured natural inflow to the ART on Row 4 of the NWTC at the bottom, hub, and top of the rotor. The warmer colors (yellows and reds) represent positive (upward) values and the cooler ones (light blue to purple) indicate negative buoyancy (downward) fluxes with white being extremely weak or zero. The CRR stability range is indicated by a pair of vertical dashed red lines. The value of $Ri_{\mathrm{TL}} = +0.02$ where the maximum turbine response often occurs is marked with a dash-dot-dotted line. Finally, the value of $Ri_{\mathrm{TL}} = +0.10$, above which the turbine response is generally minimal, is identified with a dotted line.

The contours of Figure 6-5 clearly demarcate the buoyancy fluxes in the unstable (left) and stable (right) regimes and the corresponding vertical momentum fluxes or shear stresses. Neutral conditions ($Ri_{\mathrm{TL}} \cong 0$) are clearly identifiable where turbulence generation is solely caused by shear. The weakly stable CRR range is obvious, as is the increasing negative flux gradient in the CRRH range from $Ri_{\mathrm{TL}} = +0.05$ to +0.10. Finally, at Ri_{TL} values greater than +0.10 the buoyancy flux reaches its negative maximum in conjunction with a high shearing stress. Figure 6-5 also shows that significant vertical buoyancy flux and shear stress gradients exist across the rotor under the most unstable ($Ri_{\mathrm{TL}} < -0.2$) and stable ($Ri_{\mathrm{TL}} > +0.2$) regimes, and these gradients' intensity decreases with height.

6.2.2 Buoyancy Damping and Length Scale

To obtain a measure of the spatial scale of vertically buoyant velocity motions in stable flow, we employ the buoyancy length scale L_b defined as in Stull (1988):

$$L_b = \frac{\sigma_w}{N_{buoy}}. \tag{6-1}$$

This scale is measure of the thickness of layers (the maximum vertical displacement of air parcels) of stratified turbulent layers and is the wavelength of the dominant instability mode (Rosenthal and Lindzen 1983; Smith et al. 2001). If we calculate L_b over the turbine layer depth

and normalize it with the rotor diameter D, we can relate the dominant vertical buoyancy spatial mode to the dimensions of the turbine rotor expressed as L_b/D. In Figure 6-6 we display the probability distributions of the observed L_b/D ratios for the Micon 65/13 turbine equipped with the NREL rotor and the ART for CRR, CRRH, and STC04. Noticeably this ratio falls within the P25–P75 percentile range (Q3–Q1 interquartile range) or 50% of the time in the CRR stability range. This says that the dominant vertical scale of the damped turbulent eddies (vertical motions) at the hub height on the Micon turbine and within the rotor disk of the ART is equivalent to the rotor diameter about half the time in the CRR stability range. As the turbine layer becomes more stable and the damping increases, the expected or characteristic vertical scale decreases to 0.6 D and about 0.35 D in the CRRH and STC04 ranges, respectively. The observed ranges of L_b/D in the wake inflow to the Micon turbine are smaller than in the natural flow into the ART where the scale of the vertical motions can exceed 2 D in the CRR range.

In the upper panels of Figure 6-7 we plot the variation of the observed L_b/D parameter for the Micon turbines and the ART with respect to stable range Ri_{TL}. In the lower panels we plot the corresponding root FBM *DEL*s with LOESS smoothed lines with a 0.3 overlap added to all. We annotated the figures with vertical dashed lines outlining the CRR stability range, a vertical dash-dot-dotted line marking $Ri_{TL} = +0.02$ where the peak response seen on the Micon turbines occurs, and a vertical dotted line indicating $Ri_{TL} = +0.10$ the upper limit of the CRRH range and above which the turbine response generally becomes minimal. In examining the relationships for the Micon turbines on the left of the figure, we see that the peak turbine response occurs when $L_b \cong D$ and the Ri_{TL} is between about +0.01 and +0.02. In the range $+0.02 < Ri_{TL} +0.05$, the damping increases rapidly as L_b decreases to 0.5 D. This decrease is accompanied by a reduction in the turbine response, as seen in the lower left panel. At Ri_{TL} values greater than +0.10, the buoyancy scale asymptotically approaches 0.35 D and the turbine response trends downward but with significant scatter. We believe this is a consequence of intense downward bursts of coherent turbulent energy entering the rotor disks from above (see Figure 5-3 and the left panel of Figure 6-3).

Comparing the data in the right-hand panels in Figure 6-7 from the ART operating in a natural, nonwake inflow, we see the variation of L_b/D with Ri_{TL} is very similar to that seen in the wind farm. In the lower right-hand panel we see that many more data points have a much greater scatter than those in the wind farm. Though much broader, the peak of the smooth curve resides in the same narrow Ri_{TL} range as in the Micon turbines, between +0.01 and +0.02. The peak turbine response takes place within a buoyant structure with a spatial dimension of about 1.5 D compared with 1.0 D for the Micon turbines. This is most likely a consequence of the larger ART rotor diameter operating in a more vertically heterogeneous layer. The consequences of the increased buoyancy damping shown in Figure 6-5 for Ri_{TL} values greater than +0.05 are quite marked, particularly above +0.10, and similar to that shown in Figure 6-6. Although there is greater scatter associated with measurements taken with a nonwake, natural inflow on the ART, the underlying variations with vertical stability are quite similar and suggest consistent physics even though the inflow environments of the Micon turbines were in many ways quite different, i.e., deep within the wake flow of a wind farm with 36 rows of upstream turbines and downstream of a major mountain range but with homogenous terrain immediately upwind.

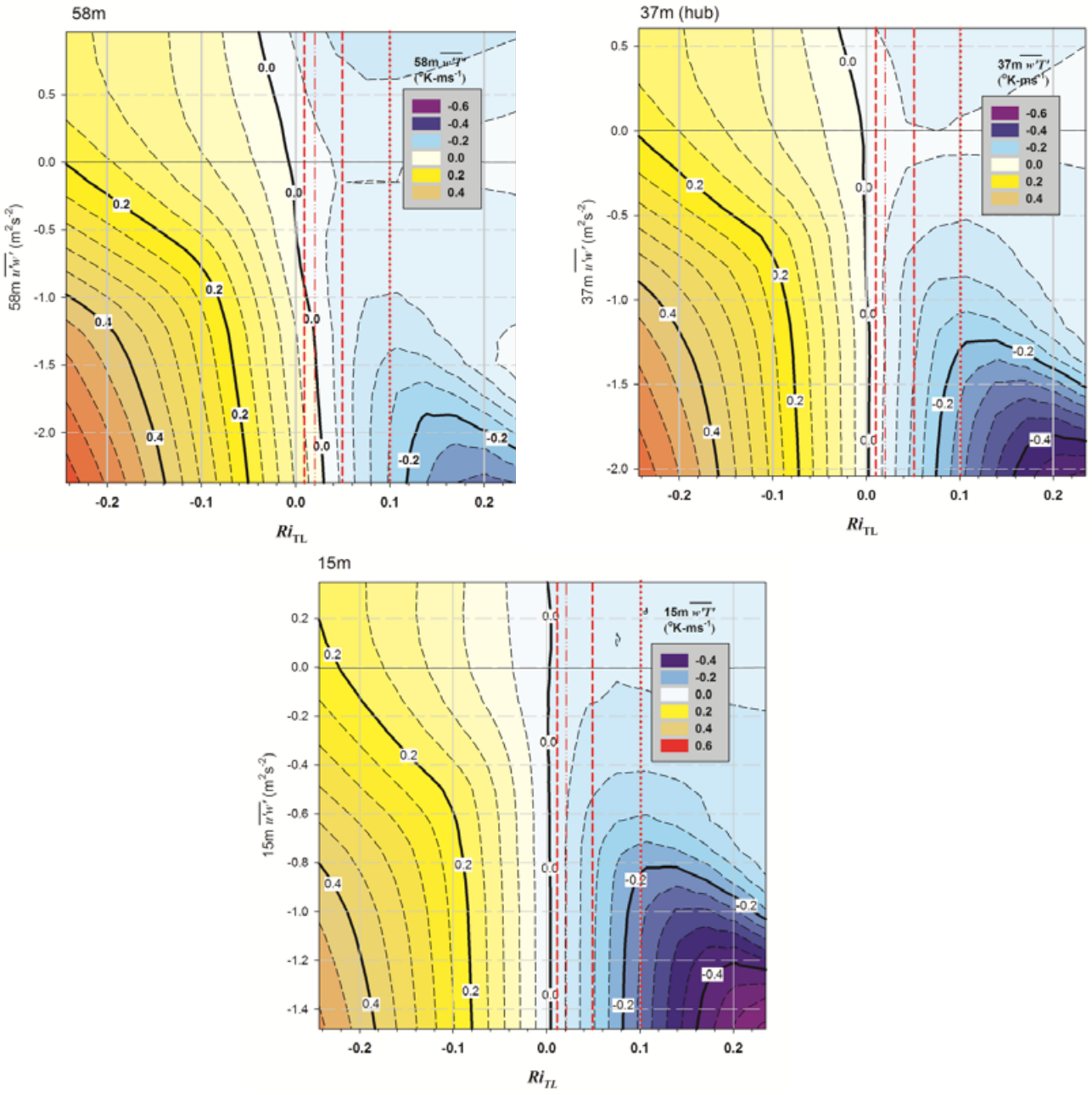

Figure 6-5. Variation of measured mean buoyancy flux ($\overline{w'T'}$) with Ri_{TL} and mean vertical momentum flux ($\overline{u'w'}$ or u_*^2) with height for natural inflow into ART. The red vertical dashed lines outline the CRR stability range, the dot-dot-dash line identifies the California turbines maximum response, and the dotted line indicates the upper limit of the CRRH stability range.

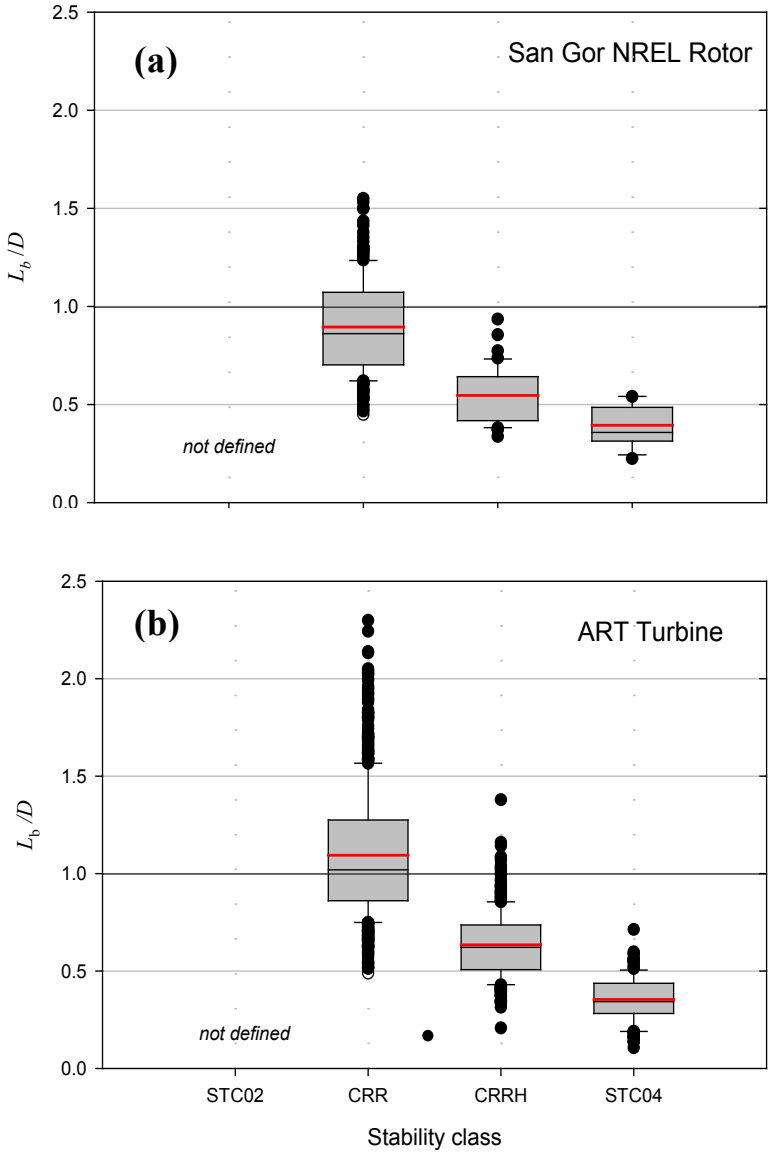

Figure 6.6. Probability distributions of L_b/D ratio by stability class for (a) Micon 65/13 turbine (NREL rotor) and (b) ART. The L_b for the Micon 65/13 turbine is based on the hub-height σ_w and the disk-averaged σ_w for the ART.

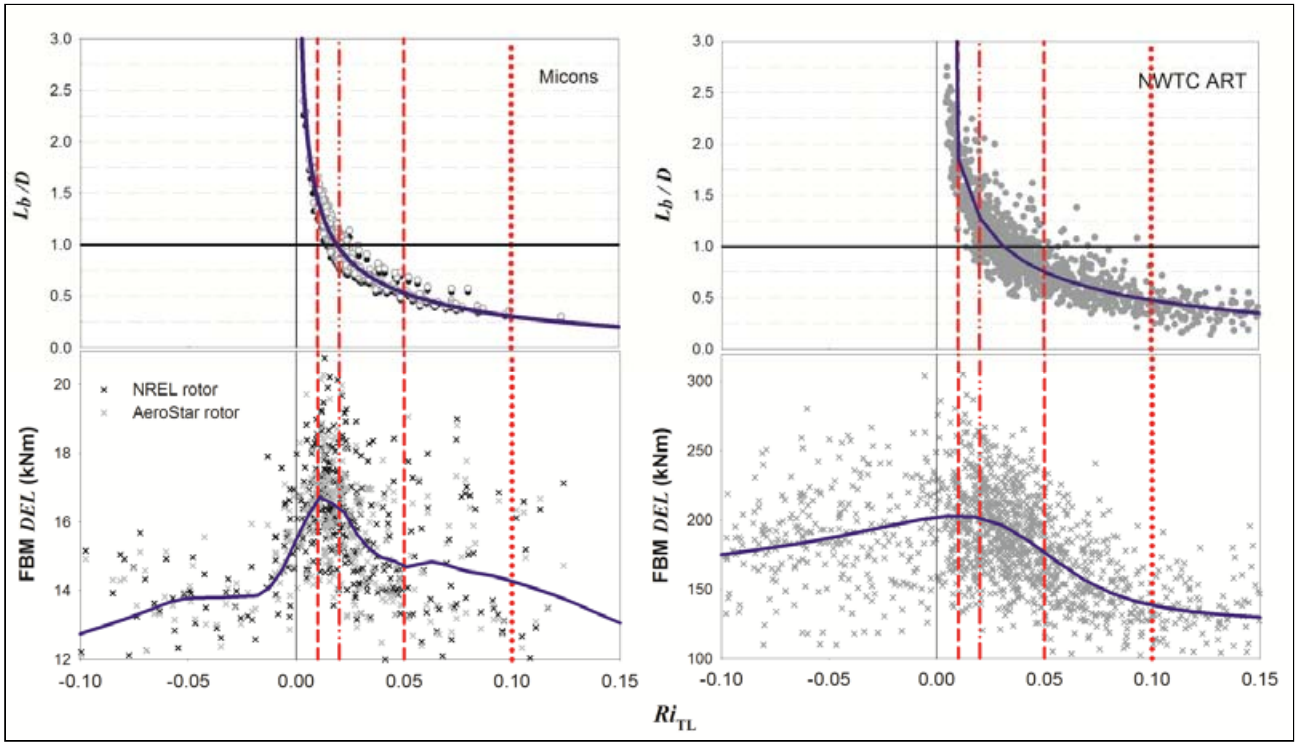

Figure 6-7. Correlation of L_b/D ratios and FBM *DEL*s with Ri_{TL} for Micon 65/13 turbines and ART. A trend line has been fitted to each of the distributions.

6.2.3 Effects of Turbulent Buoyancy Damping on Characteristics of Turbine Dynamic Response

In stable flows the buoyancy length scale L_b decreases with increasing turbine layer stability, but when it has roughly the spatial dimensions of the turbine rotor ($L_b = D$) the largest turbine dynamic responses occur. In Figure 6-8 we present an example using the NREL-rotor equipped Micon 65/13 turbine of the effects caused when the Ri_{TL} is less than the lower threshold of the CRR range (+0.01) and when it is greater than the maximum response value range of +0.01 to +0.02. Here we use a polar diagram to plot the instantaneous root FBM loads measured on each of the three blades as a function of the rotor azimuth. The azimuth blade order was Blade 1, Blade 3, and Blade 2 rotating clockwise and looking downwind in the field experiment nomenclature and coordinate system. The rotor loads shown on the left occurred within a record with a very weak stability of Ri_{TL} = +0.007 and less than the lower threshold of the CRR range. Here, over about half the rotor disk, the peak loads are occurring in the 15–18 kNm range. But for one revolution, when the blades were descending in order (Blade 1, Blade 3, and Blade 2), they encountered a more intense turbulence structure of sufficient dimension that all three blades were able to pass through it. On the right of Figure 6-8 we see another sequence in which the Ri_{TL} = +0.034 and is within the CRR range but is slightly more stable than the maximum response criticality of Ri_{TL} between +0.01 and +0.02, where damping has more influence. Here smaller load excursions are being induced throughout the entire rotor azimuth range, but for one rotation as the blades descended Blade 3 responded with a load peak of 30 kNm as it encountered an intense turbulent structure. This response occurred between the smaller load excursions seen earlier by Blade 1 and later by Blade 2. We interpreted this as Blade 3 encountering a small but very intense turbulent structure in which Blades 1 and 2 caught only a piece of it because of either its residence time within the rotor disk or its physical size. The turbulence associated with the response seen on the left of Figure 6-8 is the result of very weak buoyancy damping, but that on the right is being influenced to a greater extent, with the largest buoyant eddies being affected the most but also allowing for the occasional intense eddy to be advected through the flow into the turbine rotor.

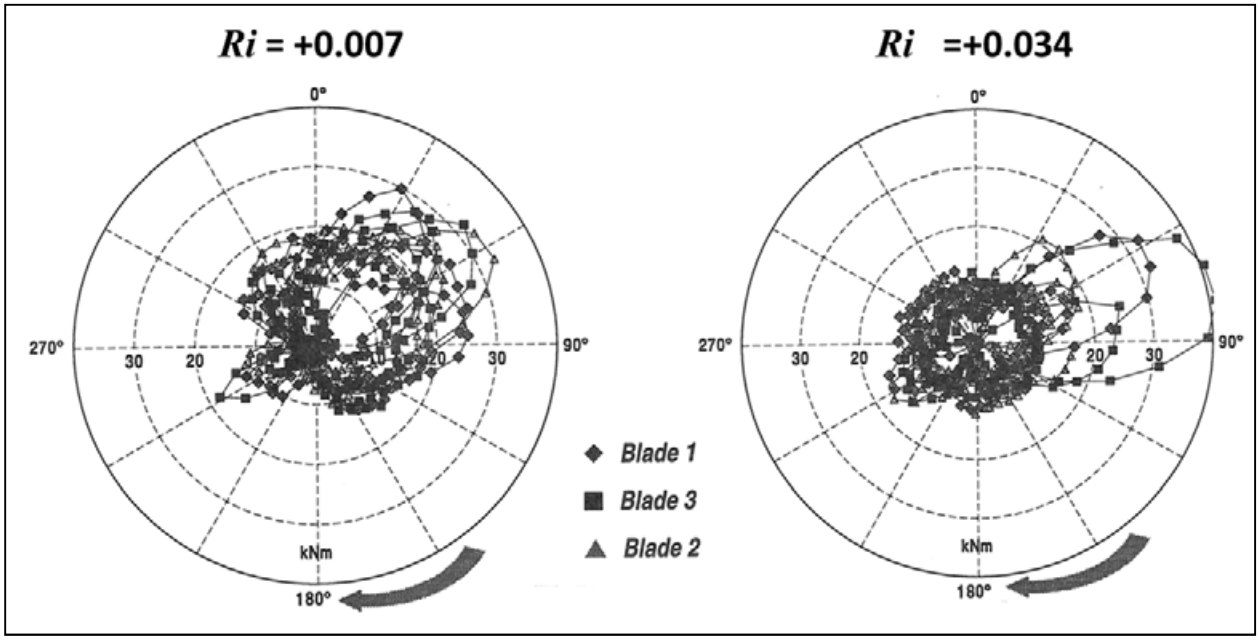

Figure 6-8. Example of effects of weakly stable flow buoyancy damping on loads seen on Micon 65/13 turbine with NREL rotor. Polar plots looking downwind of the rotor azimuth of FBM loads instantaneously measured on each blade.

In Figure 6-9 we summarize factors influencing the intensity of the root stress cycles induced in a turbine blade operating in a stable environment using the data from the ART. On the left of the diagram we plot the variation of these stress cycles (Figure 6-9a) in conjunction with the corresponding Ri_{TL} (Figure 6-9b), and the hub-height peak E_{coh} (or CTKE) values (Figure 6-9c) as a function of the buoyancy length scale normalized by the disk diameter L_b /D. We previously found that the maximum dynamic response takes place when L_b is 1 or slightly greater. Following the L_b /D value vertically through Figure 6-9, we see the following:

- This value intersects with the significant peak E_{coh} response threshold of 10 m^2 s^{-2} with larger loads above it and smaller ones below.
- It passes through the upper end of the CRR Ri_{TL} stability range.
- There is a distinct increase in the FBM cyclic stress levels at and above it.

Figure 6-9d on the right shows that buoyancy damping increases (L_b /D < 1) in the CRRH stability range (+0.05 ≤ Ri_{TL} < +0.10) and more rapidly for Ri_{TL} > + 0.25. Using the data from both the Micon 65/13 turbines and the ART, we schematically relate observed dynamic loading characteristics to the degree of buoyancy damping present as a function of the Ri_{TL} in stable inflows in Figure 6-10. Going from left to right:

- Left: many moderate intensity stress cycles interspersed with a few from long-lasting or dimensionally large turbulent structures
- Center: many intense stress cycles but with occasional very intense turbulent structures that can induce significant “rare” loading events
- Right: many relatively low-level stress cycles with an occasional intense loading cycle of short duration.

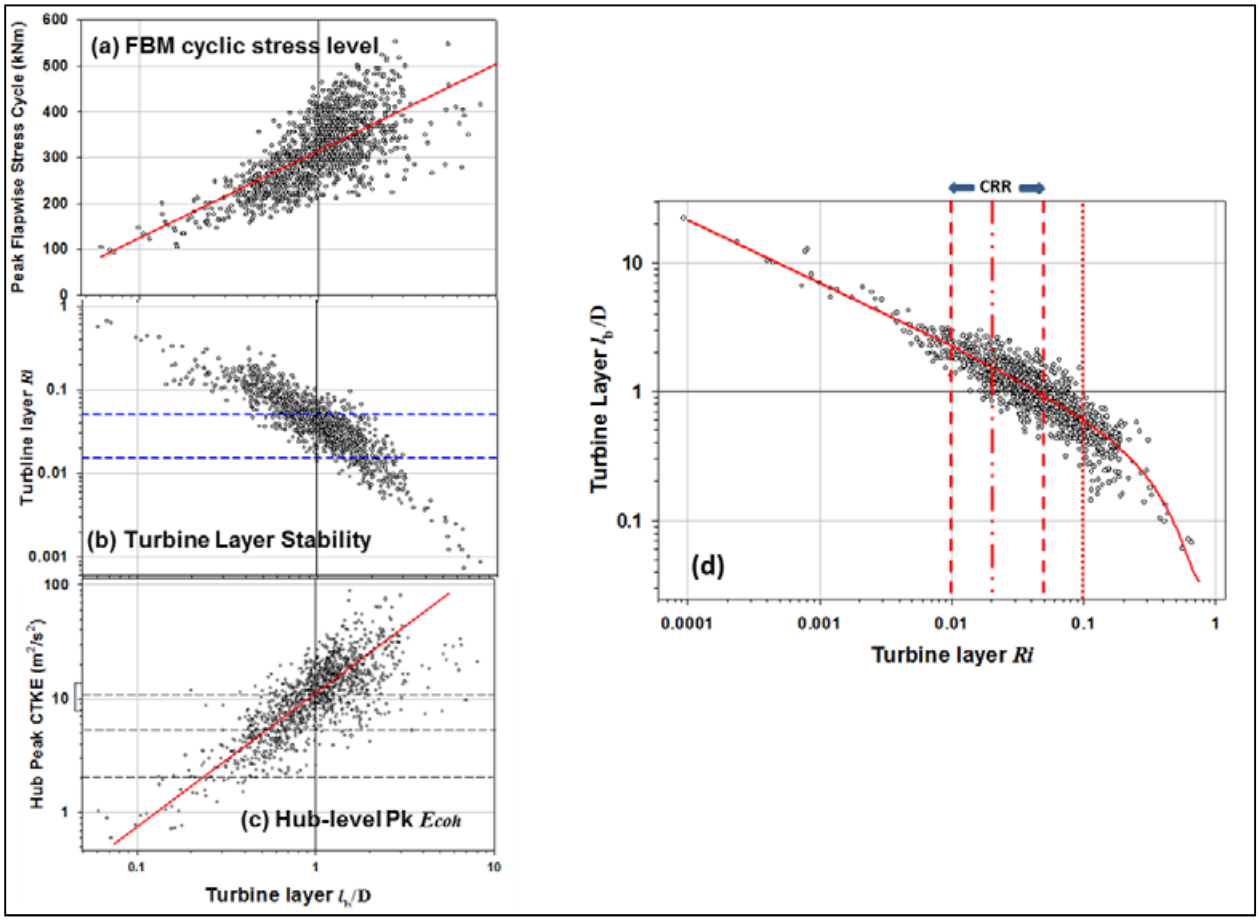

Figure 6-9. Summary of major inflow turbulence parameters influencing ART peak root FBM (a) peak cyclic stresses in stable flow; (b) Ri_{TL}; (c) intensity of coherent turbulent structures given by hub-level peak E_{coh} (CTKE); and (d) buoyancy length scale L_b/D with stability ranges shown

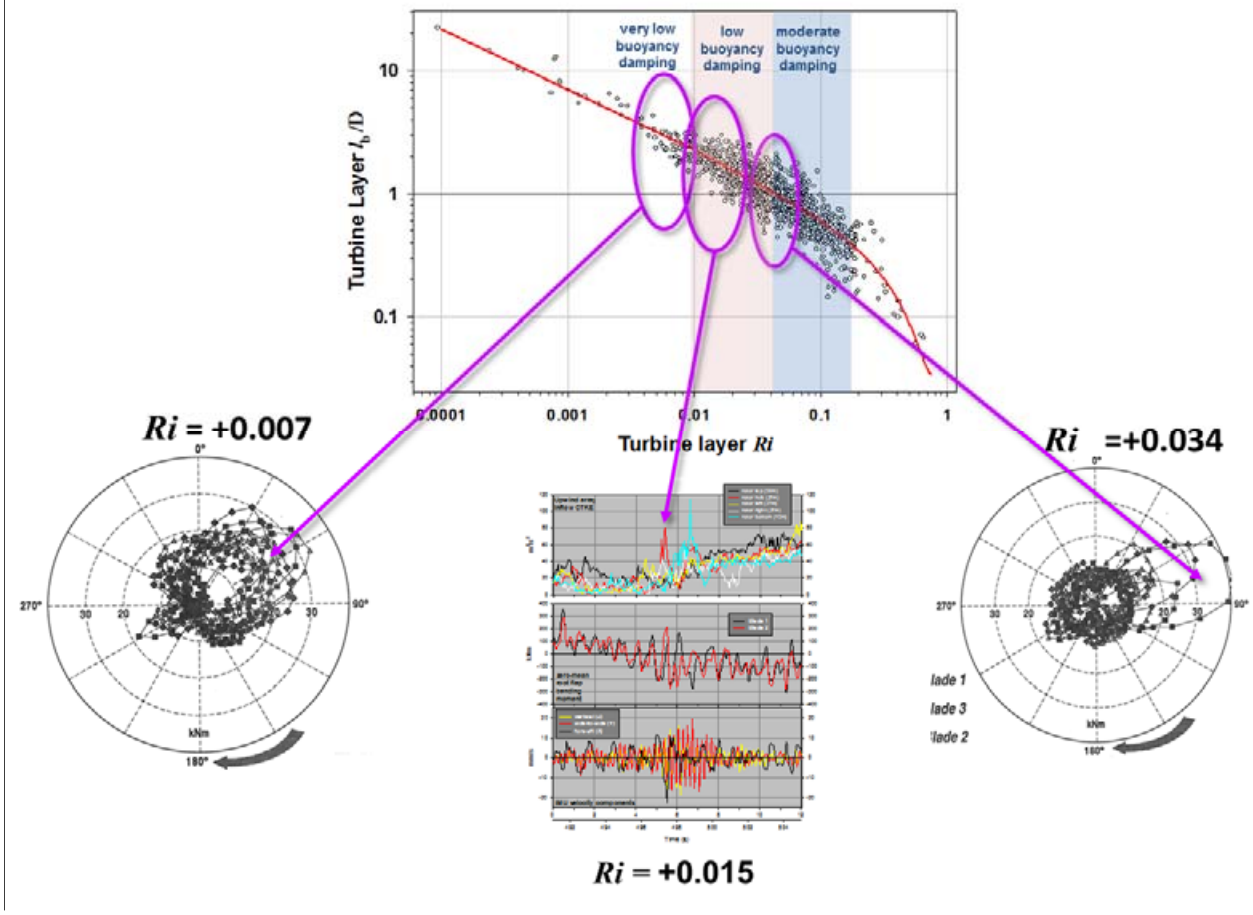

Figure 6-10. Schematic example of consequences on turbine FBM loads from stable turbine layer buoyancy damping using both Micon 65/13 turbines and ART

6.3 Atmospheric Dynamics Associated with CRR Stability Range

We showed that the CRR stability range is truly critical in terms of the nature of the dynamic loading response of wind turbine components. The question then is what are the atmospheric turbulence dynamics that are responsible for creating the turbulent flow conditions within this important range? From our analysis of the San Gorgonio and NWTC inflow data, and based on Figures 6-2 and 6-3, we know the following:

- The turbine layer Richardson number stability parameter covers a narrow range of $+0.01 < Ri_{TL} < +0.05$.
- The majority of the hub-height mean wind speeds are at or below rated.
- Vertical shear exists.
- For the NWTC, there is a predominant downward buoyancy flux that applies a stabilization action (damps) the largest turbulent eddies.
- The highest mean wind speeds occur in this stability range.
- The highest values of CTKE or E_{coh} occur in this range, suggesting the frequent appearance of the coherent turbulent structures seen in Figures 3-7, 3-8, and 3-9.
- The buoyancy length scale, L_b, was the same as the rotor disk diameter about half the time (Figure 6-6).

After reviewing this information, we concluded that we were dealing with some form of shear instability within the flow entering the turbine rotors in stable conditions. Under stable conditions, the boundary layer flow tends to form into parallel, stratified layers in the absence of the vertical mixing associated with the unstable, convective boundary layer. With the right conditions, perturbations moving through the flow within these layers can initiate turbulent disturbances that grow in size and intensity with time. Two types of instabilities are common in the stable lower boundary layer in which wind turbines reside: the Kelvin-Helmholtz Instability (KHI) and the internal gravity wave instability (GWI) that form through the action of buoyancy in vertically sheared flows.

KHI occurs in shear layers in which intense, 3-D coherent turbulent structures are created. The majority of the turbulent kinetic energy is contained within this shear layer and decays rapidly away from it. The KHI coherent structures (billows) follow a life cycle that typically lasts 15–30 minutes, which is why they are often described as turbulent patches. This cycle includes the initial rollup formation, a rollover or breaking that becomes very turbulent (turbulent breakdown), and finally a decay. During this last phase the energetic turbulence is mixed out, returning the turbulent kinetic energy back into a form of potential energy. The life cycle of an individual Kelvin-Helmholtz (K-H) billow is typically much shorter than the total length of the instability as a whole, often in the tens of seconds.

Internal GWI also occurs in shear layers, but the turbulent structures are often much less energetic, more 2-D, and much thinner than K-H billows. Although the KHI process takes place rather quickly, the GWI turbulent structure grows much slower and can persist for many hours. In contrast to KHI, the kinetic energy associated with GWI propagates away from the formation layer. The question is which of these types of shear instability is the dominant turbulence

generation mechanism in the important CRR stability regime and how does it relate to the other more stable ones, CRRH and STC04?

6.3.1 Dynamics of KHI

Linear analysis has been successfully applied to the initial stage of instabilities forming in a stably stratified sheared flow (Miles 1961; Howard 1961). The schematic diagram of Figure 6-11 illustrates the mean vertical profiles of wind speed and temperature of such a flow into a turbine rotor disk of diameter *D*. These are the background or reference conditions that determine if intense shear alone or in combination with small turbulent perturbations will grow or be suppressed with time. These regions of instability occupy finite space and the K-H billows or coherent patches of turbulence grow within them. Smyth (2004) points out that it is the fastest growing instability mode that fills this region of KHI. Although the coherent patches themselves are fully 3-D turbulent structures, the KHI process itself is essentially 2-D (i.e., characterized by the streamwise and vertical turbulent wind components u' and w', with emphasis on the latter). The theory of billow growth is an eigenvalue problem that is represented as a spectral superposition of temporally growing normal modes (Smyth 2004). The normal mode solution is of the form

$$\exp[ik(x-ct)] \quad , \tag{6-2}$$

where k is the wavenumber, the complex phase speed is $c = c_r + c_i$, and t is time. Here c_r is the perturbation phase speed in the direction of the background flow and kc_i is its rate of growth; i.e., growing modes are characterized by $c_i > 0$. Howard (1961) showed that the maximum growth within a shear layer for a mode with wavenumber k is limited by (Kundu 1990, p. 387):

$$kc_i < (k/2)(U_{\max} - U_{\min}) \, . \tag{6-3}$$

A necessary but not sufficient condition for instability (growing perturbations) within a stably stratified shear layer is $Ri < 0.25$. Figure 6-12, adapted from Figure 11 of Rosenthal and Lindzen (1983), shows the maximum K-H mode growth rates as a function the shear layer *Ri.* The Miles and Howard (1964) curve is for an infinite stratified fluid that resides only within the shear layer and corresponds to the wavelength of the most unstable K-H mode. The Lindzen curve is based on observations that encompassed a broader region (Lindzen 1974). Figure 6-13, adapted from Figures 3, 6, and 8 of Rosenthal and Lindzen (1983), plots the range of K-H mode wavenumbers (reciprocal wavelengths) and their corresponding growth rates for shear layer *Ri* values of 0.05, 0.10, and 0.15. A shear layer stability of $Ri = +0.05$ has the broadest wavenumber (wavelength) range of unstable normal modes, with the fastest growth rates associated with the highest wavenumbers (shortest wavelengths). As the layer stability increases, the peak mode growth rate decreases and the corresponding range of unstable wavelengths becomes narrower.

We can put these relationships into perspective relative to stability classes for the ART in Figure 6-14. Here we adapted Figure 3 from Hogg and Ivey (2003) by rescaling the wavenumber of the

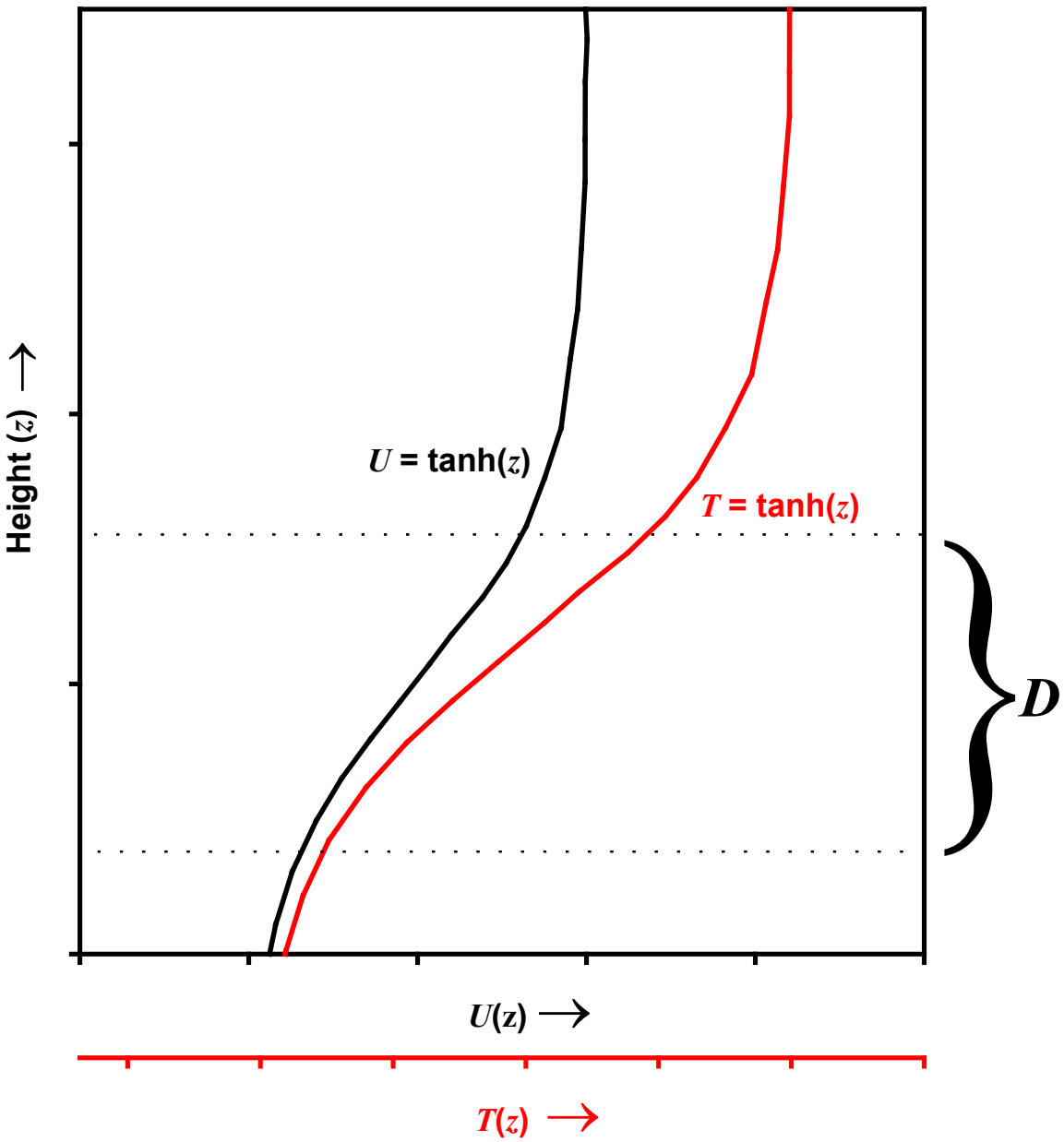

Figure 6-11. Schematic representation of vertical profiles of mean wind speed *U*(*z*) and temperature *T*(*z*) across turbine rotor disk layer *D* in stably stratified shear inflow. These profiles represent the background or reference flow conditions on which perturbations evolve linearly from this equilibrium state.

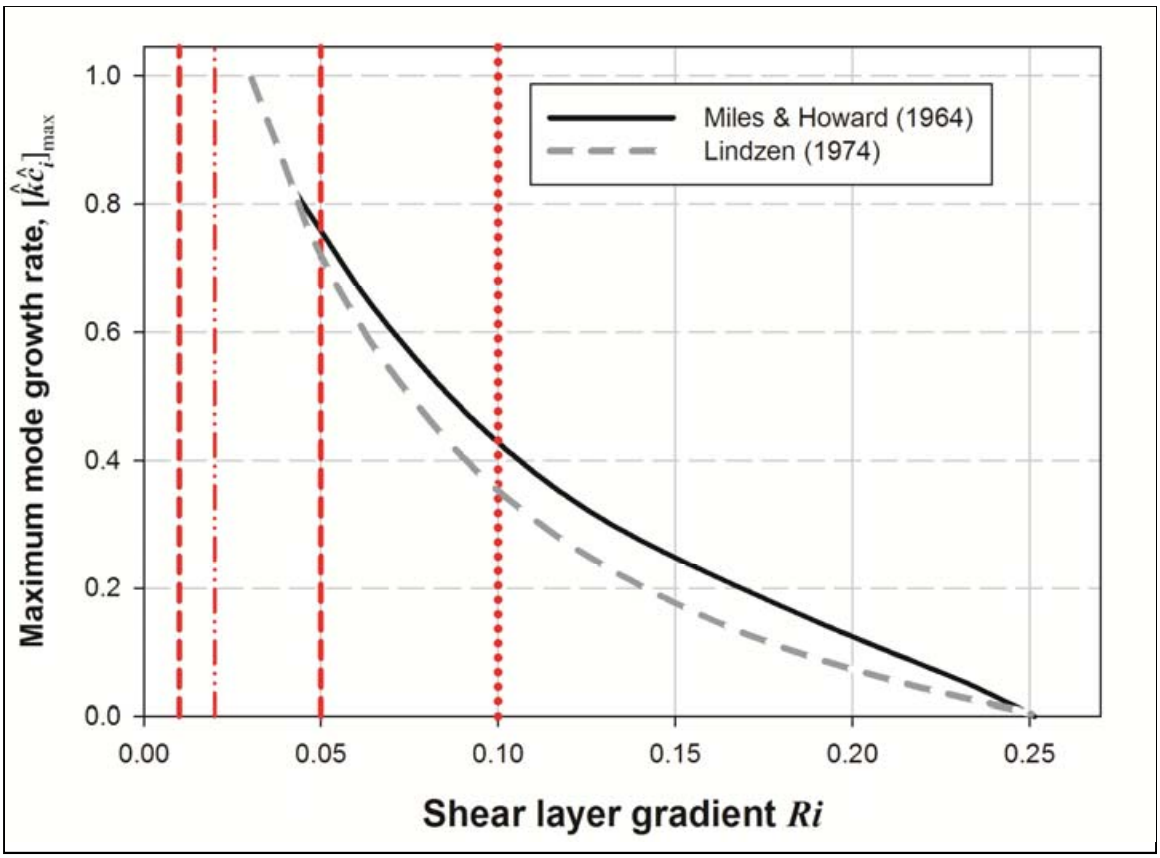

Source: Adapted from Rosenthal and Lindzen (1983), Figure 11

Figure 6-12. Growth rate of fastest growing K-H mode as function of shear layer *Ri*

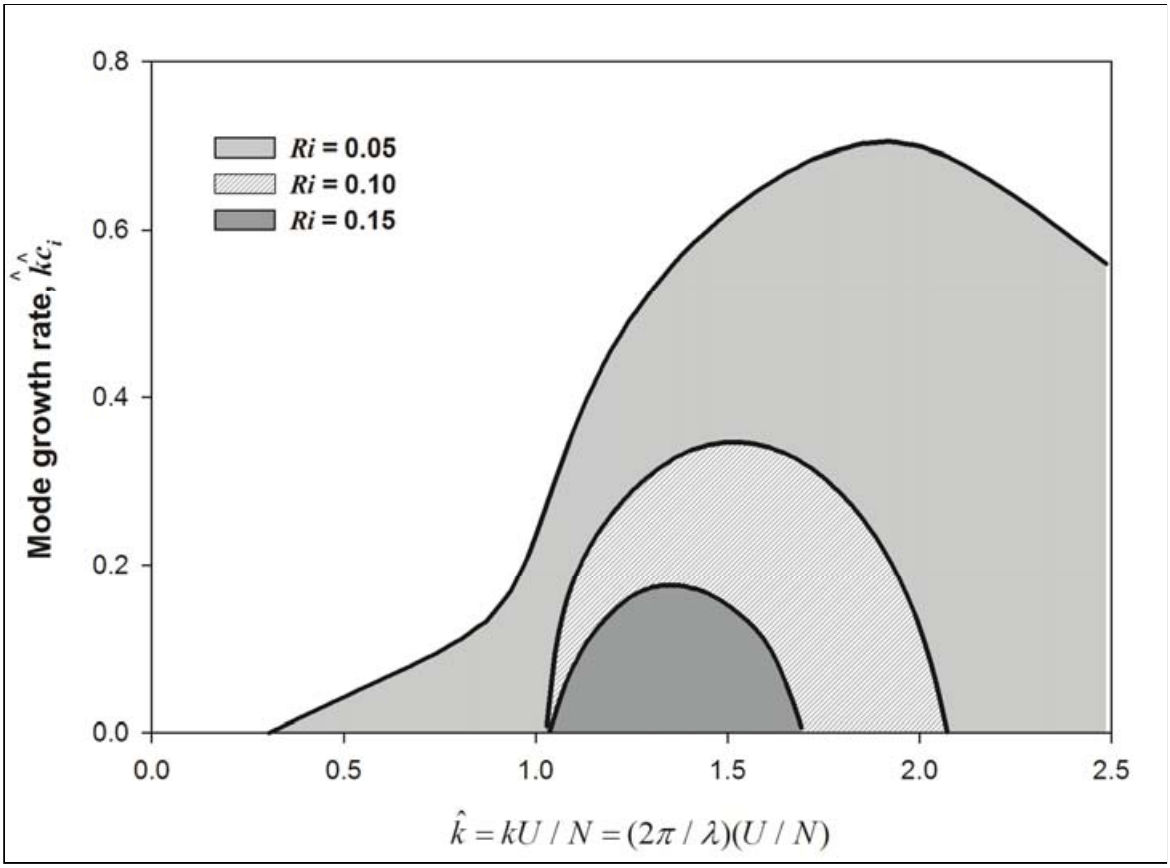

Source: Adapted from Rosenthal and Lindzen (1983), Figures 3, 6, and 8

Figure 6-13. K-H mode growth rates and wavenumber (wavelength) range for three values of shear layer *Ri*

K-H modes into rotor diameters. The original Hogg and Ivey figure is based on a somewhat shallower temperature inversion relative to velocity shear layer than is illustrated in Figure 6-11. We believe it is useful, however, in demonstrating the interrelationships between the range of the fastest growing K-H modes scaled in rotor dimensions and the stability classes. Figure 6-14 shows that the most rapid growing K-H modes occur at the low end of the CRR stability range and with wavelengths slightly greater than the rotor diameter at an *Ri* value of +0.02. This is the value where the maximum dynamic response has been observed on both the Micon turbines and the ART. The dashed line shows that maximum growth rates of the K-H modes increases with increasing rotor diameter. We repeat Figure 6-7 for ease of comparison. We previously noted that the buoyancy length scale L_b has been found to coincide closely with the fastest growing K-H mode and that maximum turbine dynamic response is when $L_b \cong D$ as shown in Figures 6-7 and 6-14. We see that this is in agreement with the fastest growing mode shape and range with a shear depth $\cong D$ and very low *Ri* values. The peak dynamic response seen on the Micon turbine and the ART at $Ri_{TL} = +0.02$ agrees well with the fastest growing K-H mode at that stability. Thus we must conclude that the L_b is a good predictor of significant turbine dynamic response in a stable atmosphere when it scales with the rotor diameter. As the stability increases the rate at which the mode peak grows declines and its wavelength no longer scales directly with the rotor diameter. This results in lower dynamic loads on the turbine. So the most energetic K-H modes, i.e., the fastest growing ones, have the greatest influence on the dynamic response of the turbines.

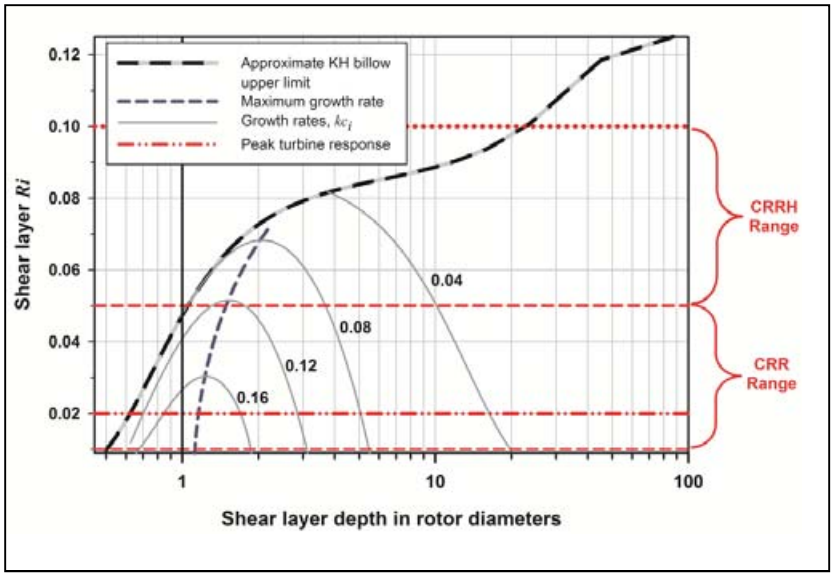

Source: Adapted from Hogg and Ivey (2003), Figure 3

Figure 6-14. Example of K-H mode growth rates as function of shear layer depth in ART rotor diameters and *Ri* over that layer. Observed Micon turbines and ART CRR stability class is indicated with dashed lines, upper limit of CRRH class as the dotted line , and maximum dynamic response with the dot-dot-dashed line.

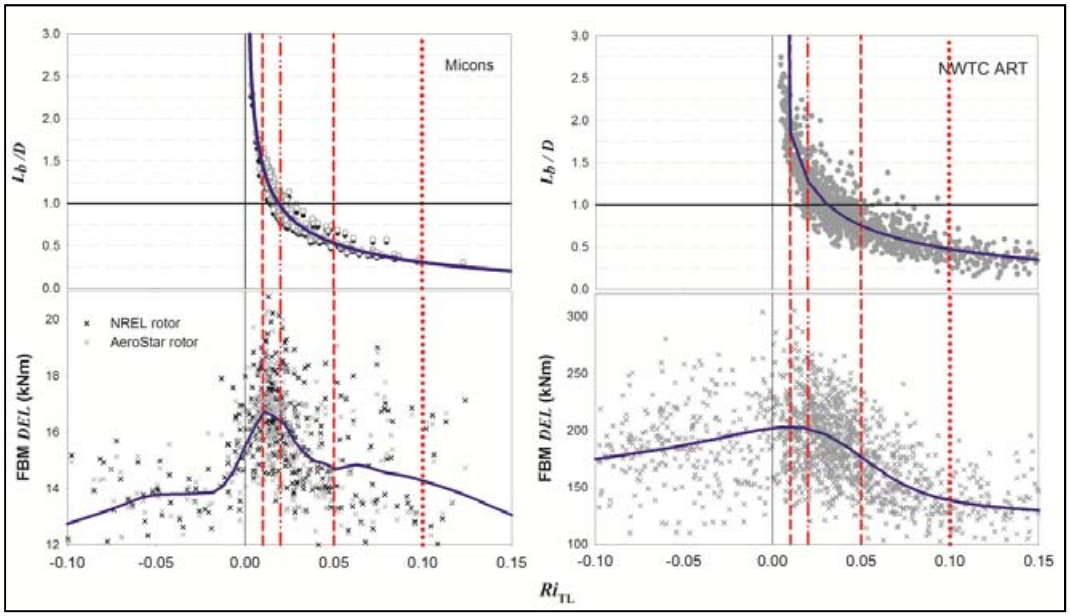

Figure 6-7. Same as Figure 6-7, repeated for ease of comparison. There is a strong correlation between the region of fastest growing K-H modes shown above in the CRR range and the L_b/D and root FBM fatigue damage on both the Micon turbines and the ART.

7.0 Coherent Turbulent Structures and Turbine Response

As a result of our field measurements in 1990 and 1999–2000, we established that the high levels of turbine dynamic response seen in the critical Richardson number range, or CRR, stability class are a consequence of Kelvin-Helmholtz Instability (KHI) taking place with the inflow to the turbine rotors. The characteristic billow flow structures that consist of organized or coherent vortical turbulence, such as those shown in Figure 3-7, are an attribute of KHI. In Section 3.5.1 we employed wavelet analysis to decompose such time domain coherent structures into the corresponding spectral energy distribution in the frequency domain. This was done to understand the relationship between the turbulent kinetic energy distribution of these transient events and the corresponding stress energy frequency distribution of the dynamic response measured in the turbine rotors (Kelley et al. 2000). Figure 3-9 shows such a spectral decomposition of the dynamic stresses measured in the blade root of one of the Micon 65/13 turbines to a coherent turbulent structure seen in the instantaneous Reynolds stress field of the turbine inflow. Using this information we defined the turbulence parameter coherent turbulent kinetic energy, or E_{coh}, as a measure of kinetic energy contained in such events. Subsequently we demonstrated that the turbine dynamic responses expressed as alternating load cycle spectra, equivalent fatigue damage equivalent loads (*DEL*s), or peak load excursions scale with peak values of E_{coh}.

We demonstrated that KHI is the dominant source of coherent turbulence in the atmospheric stability range in which the greatest turbine dynamic response is observed. We then expanded those details to develop a further understanding of the role of coherent turbulent structures in inducing damaging transient stress loads on turbine components so that the TurbSim stochastic simulator includes the turbulence characteristics that produce them. To do that we first needed to be able to numerically simulate the formation and evolution of a Kelvin-Helmholtz (K-H) billow and then use a National Renewable Energy Laboratory (NREL) turbine design code to document the dynamic response to the K-H billow using a realistic turbine design.

7.1 Kelvin-Helmholtz Billow Numerical Simulation

At Peter Sullivan's suggestion, he and Ned Patton of the National Center for Atmospheric Research (NCAR) created a large eddy simulation (LES) of the life cycle of a stationary K-H billow. This work was in part based on a much higher resolution (down to the dissipation scale) direct numerical simulation (DNS) of a nonstationary K-H billow evolution developed by Werne and Fritts (1999). In contrast, the minimum resolution of the NCAR LES simulation was about 1 m where a subgrid scale (SGS) was invoked. The simulation uses a Cartesian computational domain consisting of (180, 60, 180) nodes in the (*x, y, z*) directions representing nondimensional dimensions of (4π, $4/3\pi$, 25). Periodic boundary conditions are imposed on the horizontal directions *x* and *y*. The domain was initially stress free with fixed temperatures at the top and bottom. The continuously sheared streamwise background flow is defined as

$$u = U_o \tanh(z / h) \quad , \tag{7-1}$$

where U_o and h are constant velocity and length scales and z is the vertical direction. The background temperature vertical variation is linear with $T = \beta z$ where β is the mean vertical gradient. The gradient β is chosen to impose a gradient Richardson number (Ri) of +0.05 that corresponds to the fastest K-H mode growth, discussed in Section 6.3.1. A total of 6,000 time steps were used to describe the process.

Figures 7-1a, b, and c show the stationary evolution of a K-H billow created by the NCAR LES simulation. These graphs present the nondimensional temperature field in the x–z plane at $y = 30$ and time steps of approximately 8.4 seconds. The temperature contours are equivalent to streamlines and reveal the structure of the flow as it evolves. In Figure 7-1a, at $t = 0$, the flow in the shear layer is parallel and in equilibrium with warmer less dense air (red) at the top and colder more dense air (blue) at the bottom. A perturbation in the flow has initiated KHI by $t = 8.4$ seconds, with billow development growing at the maximum rate. About 22 seconds later, at $t =$ 30.1 seconds, the billow has reached its maximum 2-D structure. Secondary instabilities have formed by $t = 37$ seconds and the breakdown into 3-D turbulence has begun by $t = 50.9$ seconds. The flow is fully three-dimensionally turbulent by $t \approx 70$ seconds (Figure 7-1b) and reaches a fully mixed (saturated) state by $t \approx 170$ seconds (Figure 7-1c), with internal waves forming at the upper and lower boundaries. Figure 7-2 shows a good portion of an actual propagating K-H cloud billow evolution. This photo shows something that is missing in the individual, stationary billow simulation: the 2-D vortex strands or braids that connect the individual billows. These are thought to be an additional source of coherent turbulence. The time series of the velocity and turbulence parameters at $y = 30$ and $z = 85$ m for the simulated evolving, stationary K-H billow is plotted in Figure 7-3. The primary phases are indicated: the maximum 2-D structure, full 3-D turbulence, and the fully mixed or saturated state. Of particular interest are the bursts of E_{coh} that are associated with the U velocity maxima or gusts during the billow breakdown.

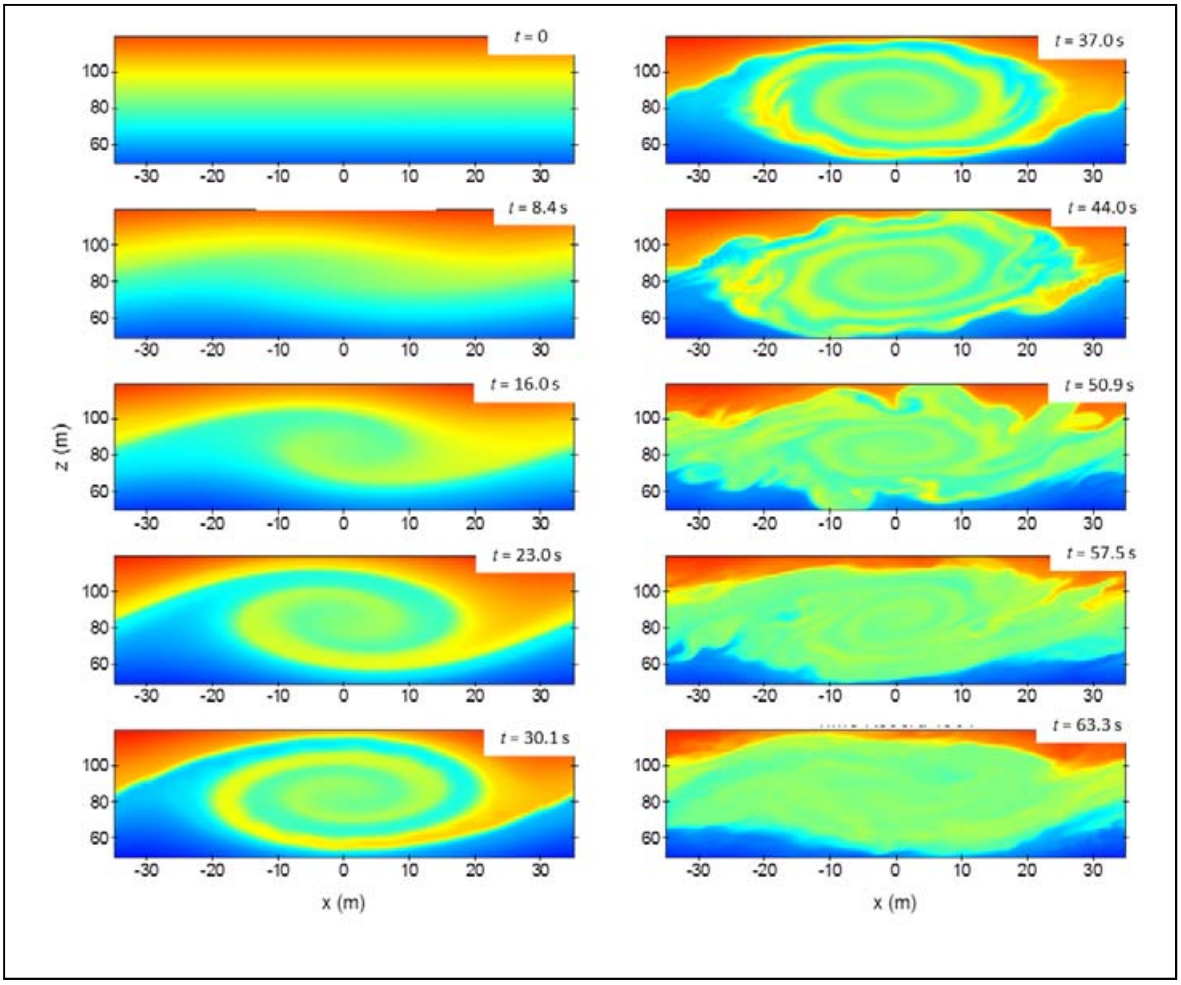

Figure 7-1(a). Maximum K-H billow 2-D structure at about *t* = 30 seconds, with secondary instabilities by *t* = 44 seconds and strong turbulence formation afterward

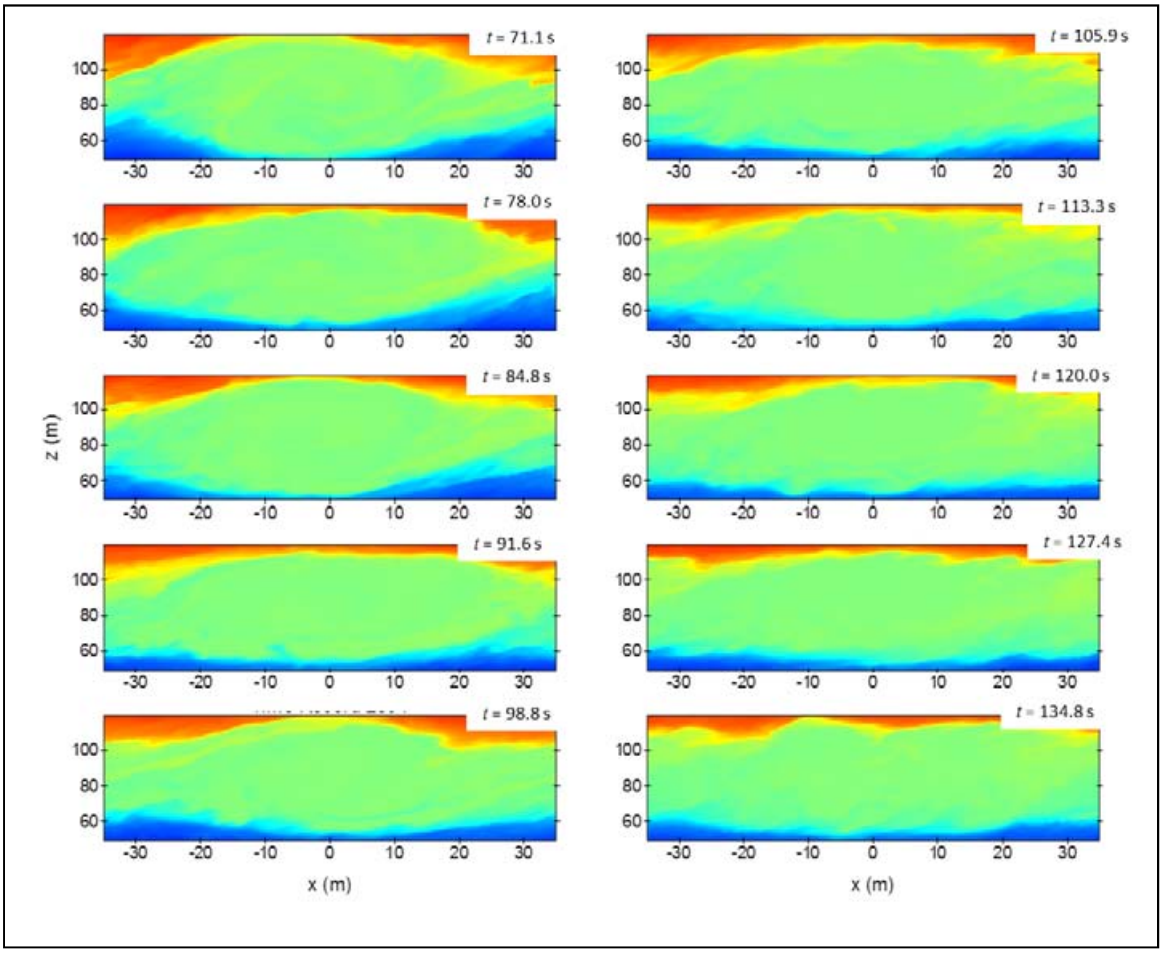

Figure 7-1(b). Fully 3-D turbulent flow by *t* = 70 seconds

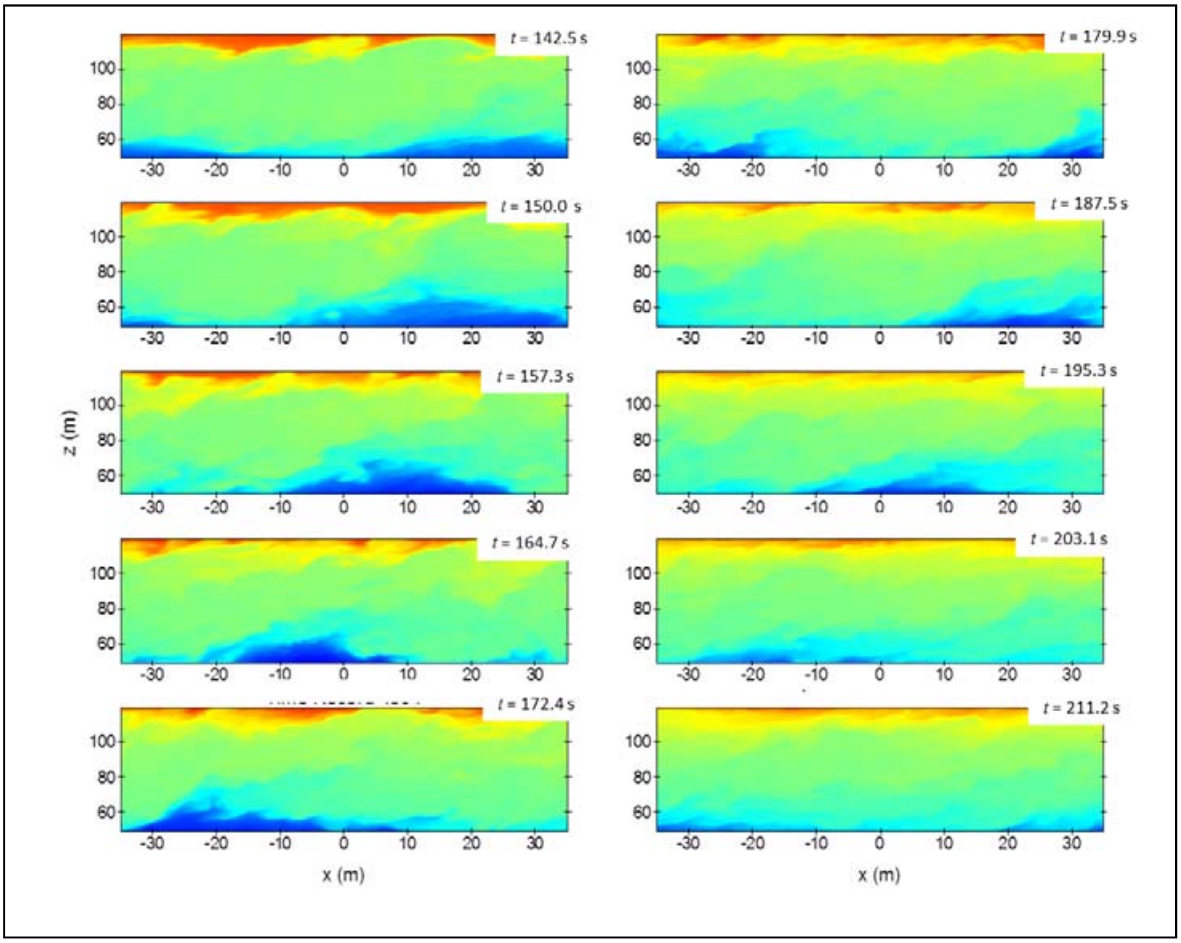

Figure 7-1(c). Fully mixed flow (saturated) by $t \approx 170$ seconds, with internal waves forming at upper and lower boundaries

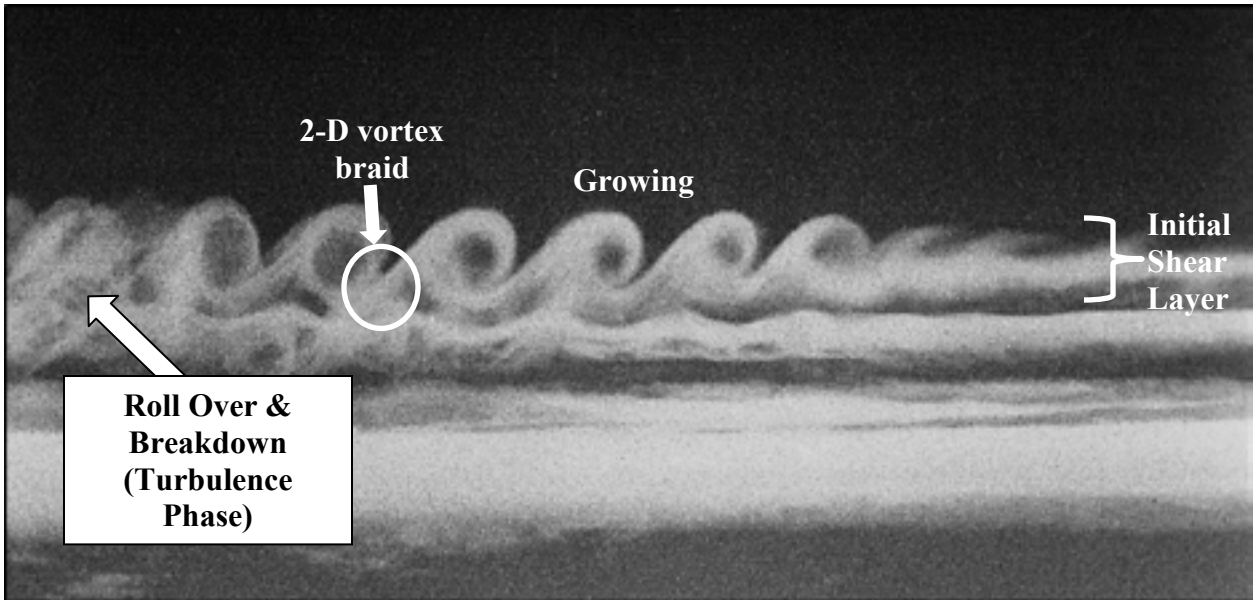

Source: Adapted from "Kelvin-Helmholtz Clouds" (DI00152) by Terry Robinson, copyright University Corporation for Atmospheric Research

Figure 7-2. Cloud formation of evolving K-H billows. Flow and evolution are from right to left.

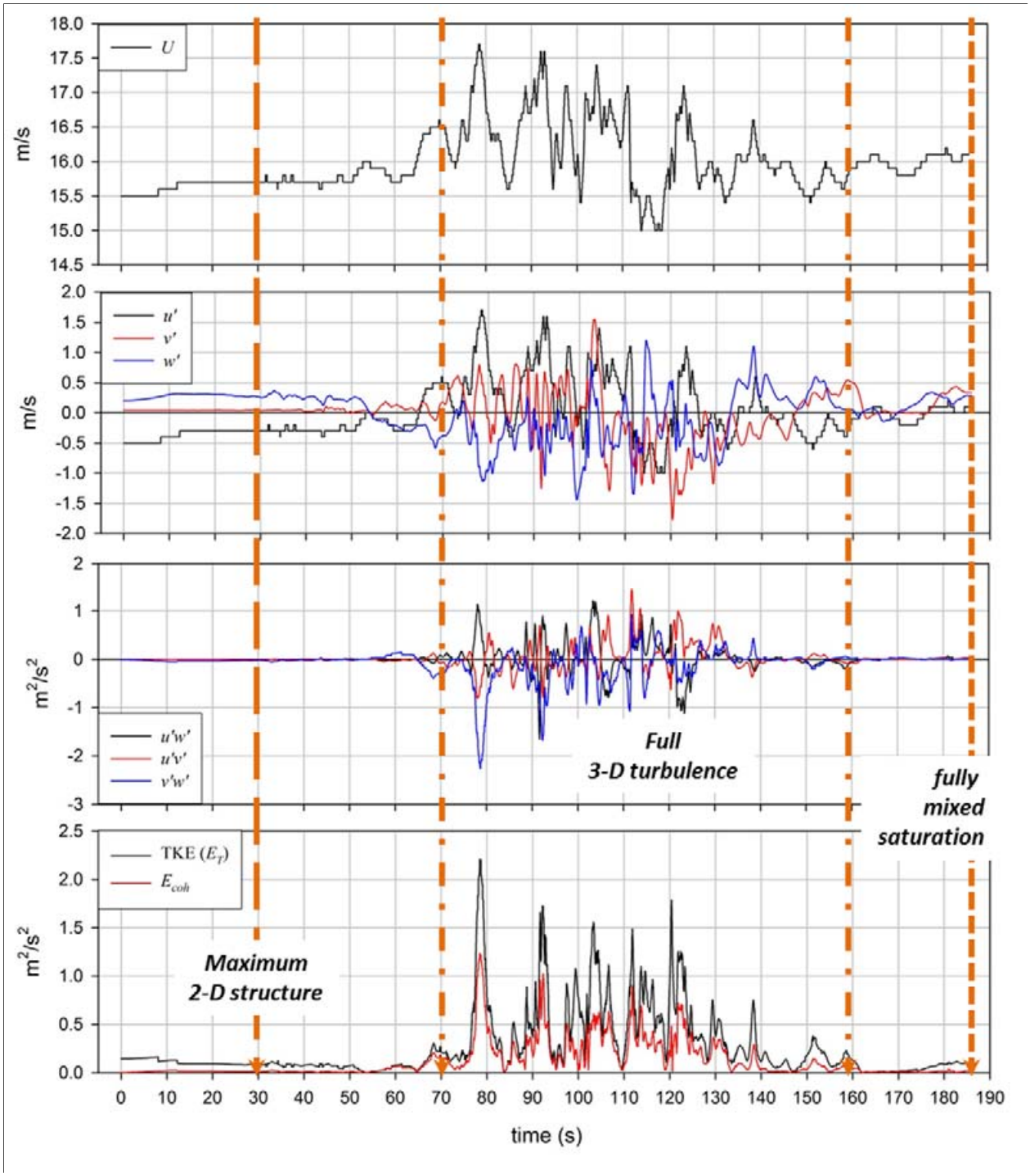

Figure 7-3. Time series of evolving stationary K-H billow at *y* = 30 and *z* = 85 m. The phases of the evolution—formation, turbulent breakdown, and fully mixed saturation—are indicated.

7.2 Turbine Dynamic Response to a Simulated K-H Billow

To understand the consequences of a turbine rotor ingesting a K-H billow, we interfaced the NCAR LES simulation into the NREL AeroDyn aerodynamics module and used the MSC.ADAMS® multibody dynamics code to derive the resulting turbine dynamic response. We simulated the 1.5-MW baseline virtual turbine developed for the rotor study of the Wind Partnership for Advanced Component Technologies (WindPACT) Project by D.J. Malcolm and A.C. Hansen (2002). For more details see Section 8 of Kelley and colleagues (2004).

The simulated K-H billow was scaled to encompass the entire 70-m rotor diameter of the WindPACT baseline turbine. The background hub-height mean wind speed was chosen to be 17 m s^{-1}, higher than the rated wind speed of 12 m s^{-1} so that peak power was modulated by the control system. The shear exponent across the rotor was 0.578. The actual period of wave excitation of the turbine model was 271.7 seconds in scaled time. Figure 7-4 maps inflow to the turbine in terms of the x–z temperature field (equivalent to velocity streamlines) in which scaled time was adjusted so that $t = 0$ seconds corresponds to when the billow has achieved its maximum 2-D structure but with little turbulence. At $t = 91.5$ seconds turbulent breakdown has been initiated, at $t = 166.2$ seconds the flow is fully three-dimensionally turbulent, at $t = 217.7$ seconds stabilization is beginning to take place, and finally at $t = 271.7$ seconds turbulent saturation has occurred and internal waves have formed at the upper and lower boundaries. Figure 7-5 plots the corresponding time series of the turbulence parameters. At the beginning of the turbulent breakdown, at about $t = 97$ seconds, at hub height there is a significant downward flux of horizontal momentum and turbulent kinetic energy, about half of which is coherent, as is shown in Figure 7-6a. This downward transport of momentum causes the hub-height wind speed to peak at about 17.8 m s^{-1}. Figure 7-6b shows the same parameters between about $t = 112$ and 146 seconds, when the turbulence has an energetic 3-D structure, which creates intense vertical mixing that decreases the shear, as shown in Figure 7-7. A short increase in the shear late in the record is related to the stabilization and the formation of internal gravity waves.

We began the K-H billow inflow to the WindPACT AeroDyn/MSC.ADAMS simulation at the point when the billow had reached its maximum 3-D structure (at $t = 0$ in Figure 7-4). Initially we started the simulation at the beginning (ignoring the first 30 seconds to allow numerical startup transients to decay), but found that because there was little or no turbulence during the billow rollup (see Figure 7-a and the first 50 seconds of Figure 7-3) we observed a very passive dynamic response in the turbine; i.e., the turbine was dynamically insensitive to the rollup phase of the billow. By initializing the inflow at the point of billow rollover and breakdown (~ 70 seconds into the simulation in Figure 7-3), we could examine the impact of the transition from the 2-D structure to the fully turbulent 3-D structure and then as it decayed to saturation as shown in Figure 7-5.

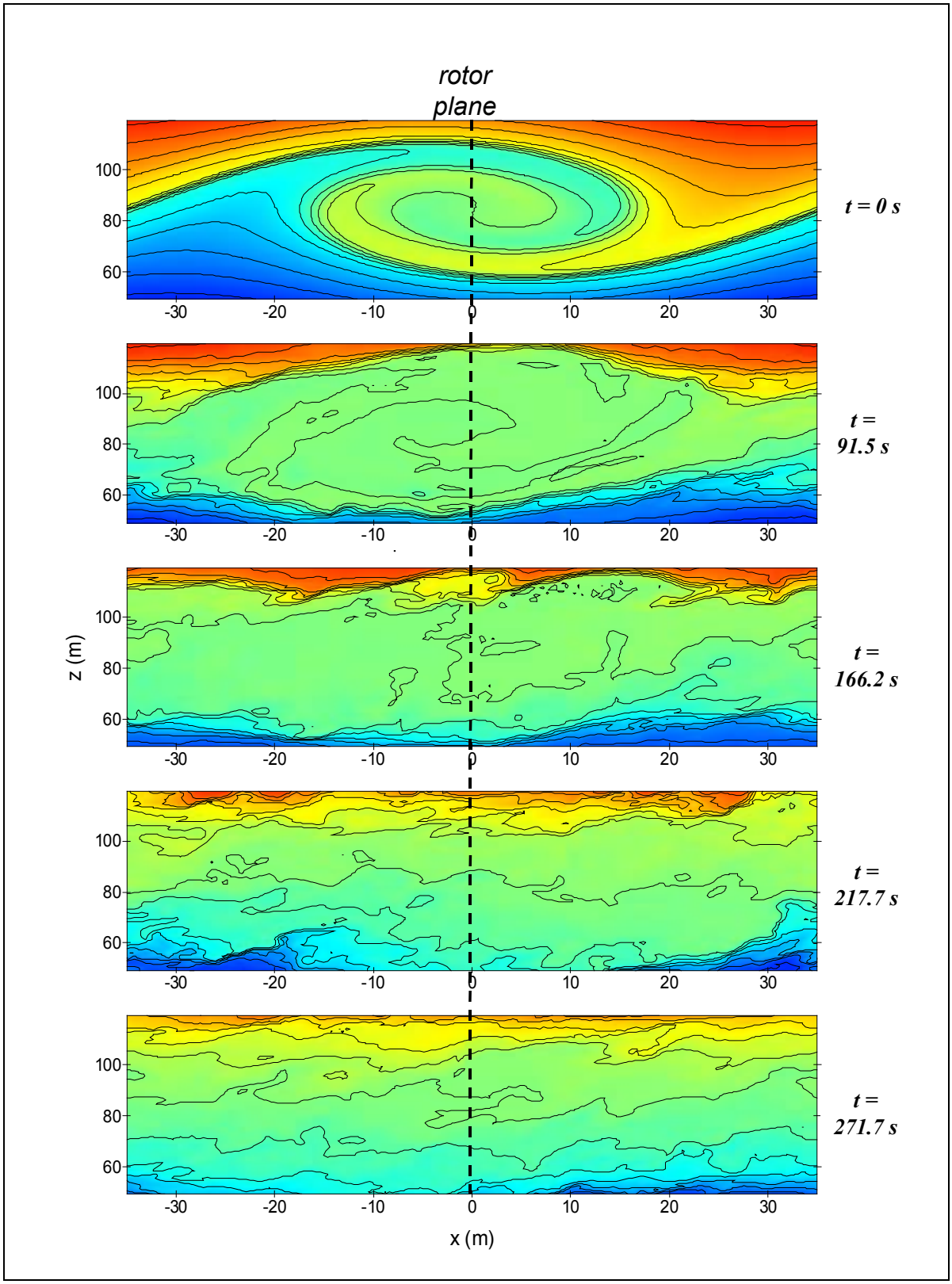

Figure 7-4. Evolution of K-H billow used as input to simulation of WindPACT 1.5-MW baseline turbine

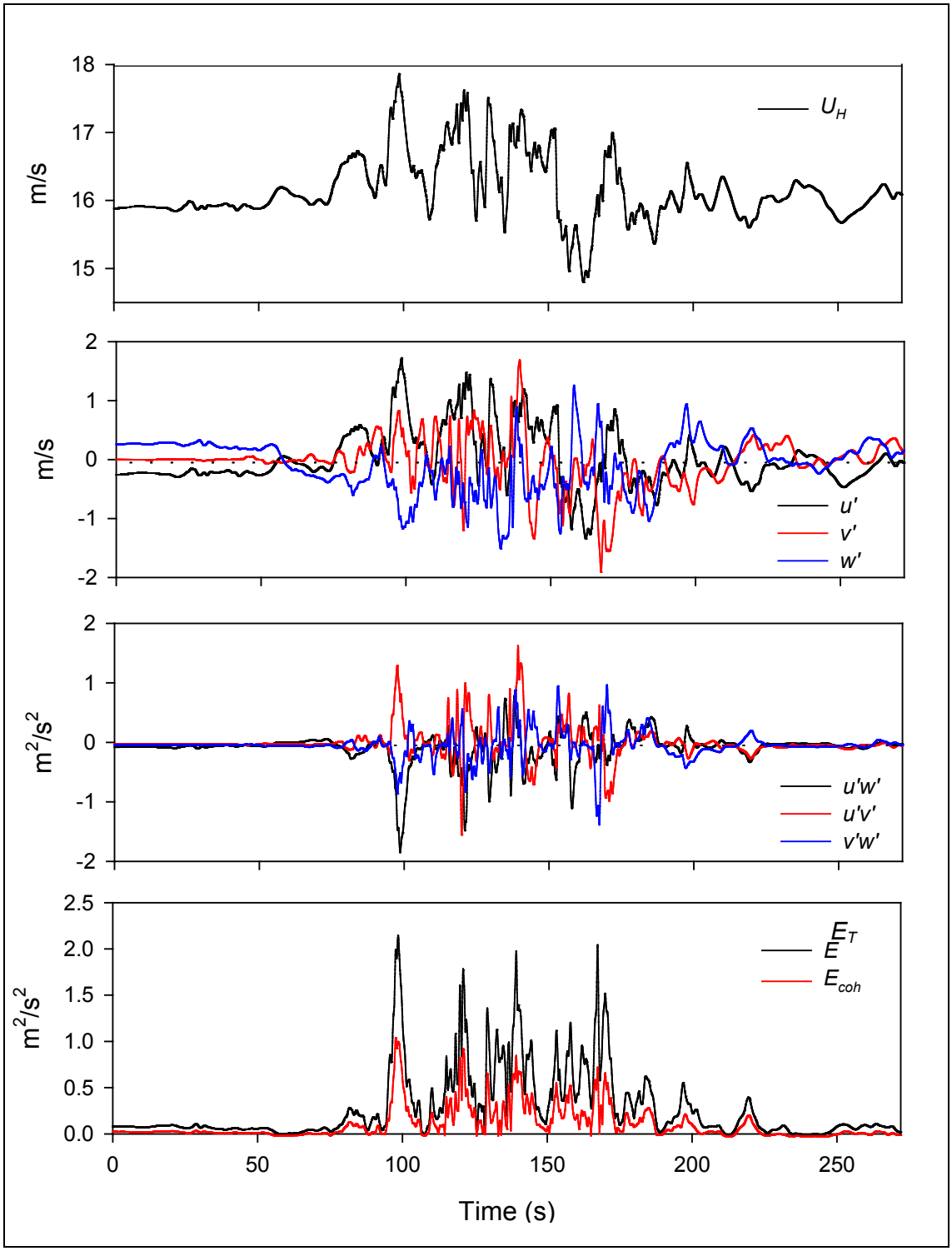

Figure 7-5. Time histories of hub-height U_H, u', v', and w', $u'w'$, $u'v'$, and $v'w'$ and E_T and E_{coh} input into WindPACT baseline turbine model

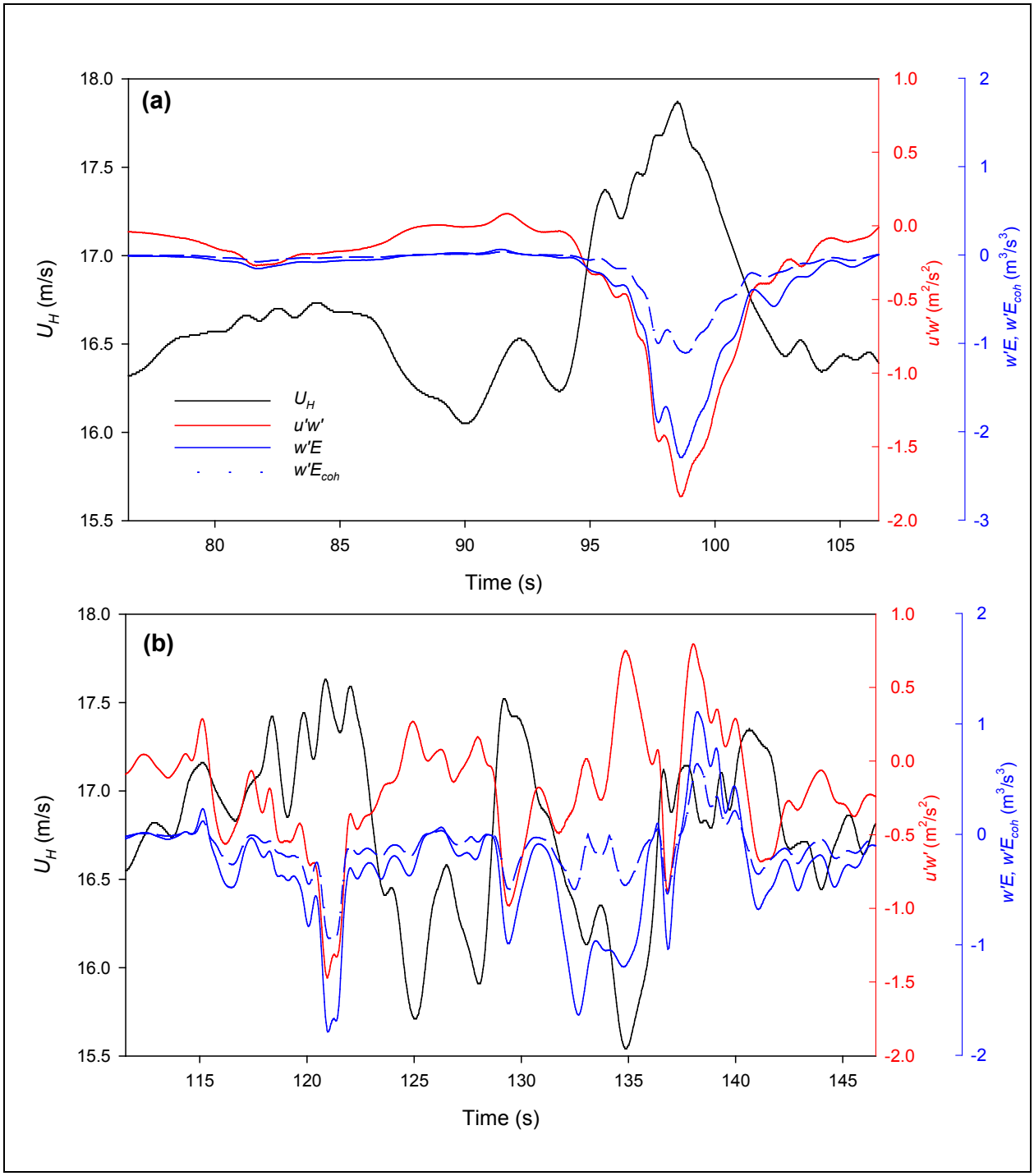

Figure 7-6. Time histories of hub-height U_H, and fluxes of momentum (shear stress) $u'w'$, E_T, and E_{coh} for two periods. Period (a) is characterized by the intense downward fluxes of momentum, total (E_T), and coherent (E_{coh}) turbulent kinetic energy as the K-H billow rolls over and breaks into fully 3-D motions. Period (b) is characterized by much smaller scale turbulent motions containing both positive and negative fluxes.

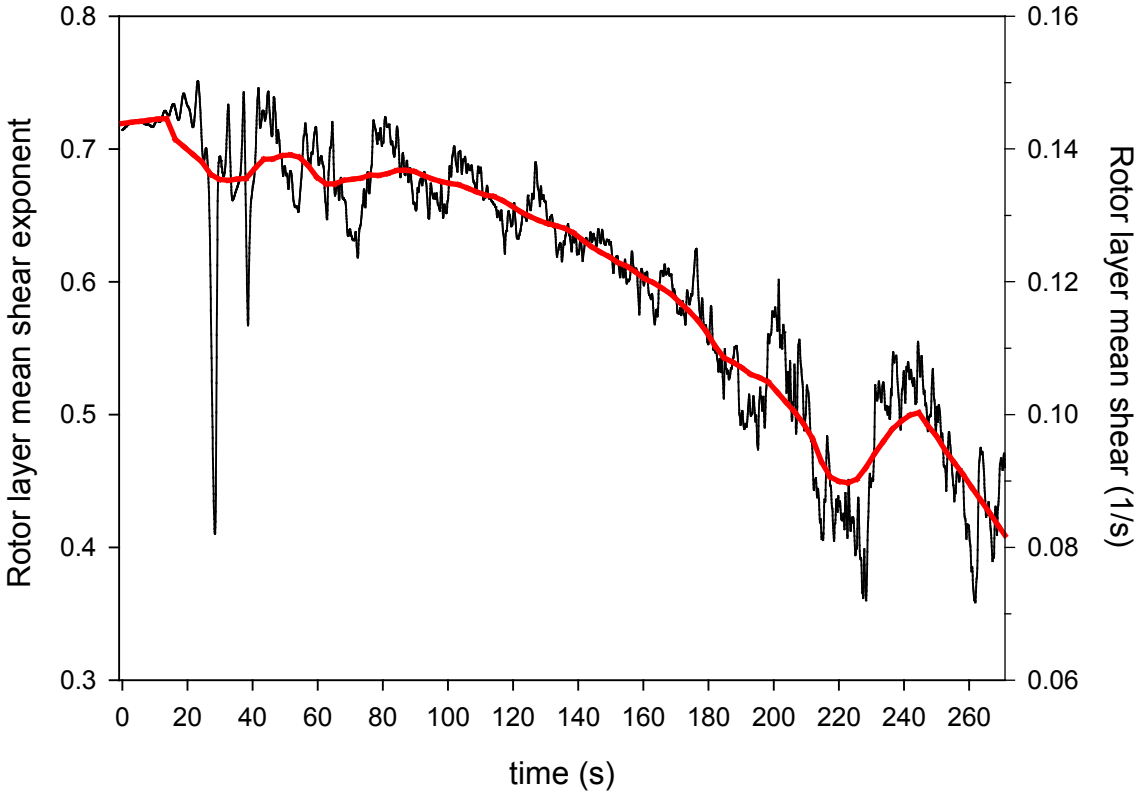

Figure 7-7. Decrease in rotor layer mean vertical shear during life cycle of simulated K-H billow

In Figure 7-8 we present time series graphs of the hub-height horizontal wind speed and Reynolds stress components and below that the turbine response in the form of the root out-of-plane or flapwise bending moment with the mean removed. In panel (a) we plot the continuous wavelet transform (CWT) scalogram of the root bend load. Frequency is inversely scaled nonlinearly on the ordinate and the intensity of the stress energy is indicated by the colors. Deep reds indicate the highest levels of stress and blue-black indicates minimal stress levels. This plot shows the distribution of stress energy levels as a function of frequency and time. The red oval indicates a period of high frequency response in the blade load. In panel (b) we plot time series of the load stress in kNm partitioned into six detail frequency bands, D4 through D9, by applying the discrete wavelet transform (DWT) to the loading signal. Table 7-1 lists the frequency ranges associated with these detail bands and their general modal characteristics.

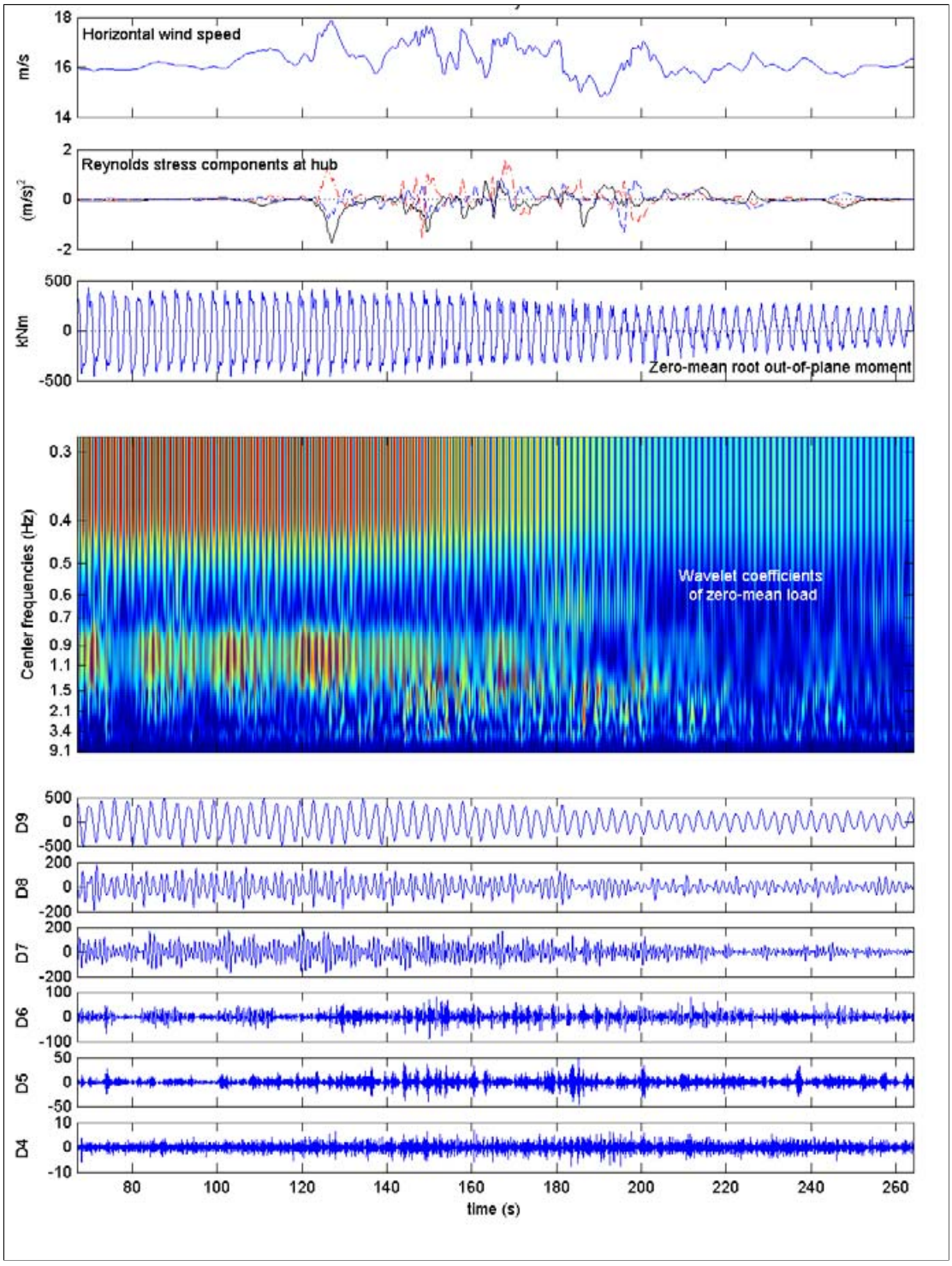

Figure 7-8. Wavelet analysis of dynamic response of WindPACT baseline turbine zero-mean root bending moment to simulated stationary K-H billow: (a) scalogram of decomposition by continuous wavelet transform—deep reds indicate high dynamic stress levels and dark blue low levels; (b) decomposition of root load time series with discrete wavelet transform. Bandwidths of the discrete wavelet transform frequency bands D4 through D9 are shown in Table 7-2. High frequency response in the root load time series is highlighted by the red oval.

Table 7-1. WindPACT Turbine Calculated Static System Frequencies

Wavelet Detail Band	Frequency Range (Hz)	Characteristic Modes	Total Number of Modes	Number of Blade/Tower Interacting Modes
D9	0.234–0.469	1-P, Tower bending	2	0
D8	0.469–0.938	2-P	0	0
D7	0.938–1.875	Blade 1st bending	3	0
D6	1.875–3.75	Blade 2nd bending	5	2
D5	3.75–7.5	Blade, blade/tower	3	1
D4	7.5–15	Blade, blade/tower	7	5
D3	15 – 30	Blade, blade/tower	7	3

Source: Adapted from Jonkman and Cotrell (2003)

Table 7-2. Calculated WindPACT Baseline Turbine System Nonrotating Modal Frequencies

Nominal Modal Frequency (Hz)	Mode Shape Descriptions		Indicated Rotor/Tower Coupling	Wavelet Detail Bands
	Primary Mode	Secondary Couplings		
0.407	Tower 1st lateral bending			D9
0.408	Tower 1st fore-aft bending			
1.153	Blade 1st asymmetric flap			D7
1.205	Blade 1st asymmetric flap			
1.258	Blade 1st symmetric flap			
1.608	Blade 1st symmetric edge			
1.842	Blade 1st asymmetric edge			
1.870	Blade 1st asymmetric edge			
2.912		Blade 1st flap, tower fore-aft bending	✓	D6
3.270		Blade flap, edge, & tower fore-aft bending	✓	
3.661	Blade 2nd asymmetric flap			
3.748	Blade 2nd symmetric flap			
5.568	Blade 2nd symmetric edge			D5
6.009		Blade flap, edge, & tower fore-aft bending	✓	
6.125	Blade 2nd symmetric edge			
8.143	Blade 2nd edge asymmetric	Tower 2nd lateral, blade tips in-plane bending	✓	D4
10.190	Blade 2nd flap asymmetric	Blade tips in-plane tip bending, tower 2nd fore-aft bending	✓	
12.614		Blade tips in-plane bending, tower 2nd lateral bending	✓	
13.541		Asymmetric flap, tower fore-aft bending	✓	
14.113		Blade symmetric flap, asymmetric edge		
14.122		Asymmetric flap, asymmetric edge, tower fore-aft	✓	
14.215		Asymmetric flap, asymmetric edge		
15.005		Asymmetric flap, asymmetric edge		D3
15.315		Symmetric flap, tower lateral, collective lag	✓	
16.022		Asymmetric flap, blade torsion, tower fore-aft	✓	
16.487		Blade torsion		
16.510		Blade torsion		
16.528		Blade torsion, slight tower fore-aft	✓	
20.407		Asymmetric flap		

Kelley and coauthors (2000) give a more complete discussion of wavelet analysis as we applied it to assessing wind turbine dynamics. Table 7-2 summarizes the nonrotating modal or natural frequencies for the WindPACT virtual turbine determined from a study of the model with the ADAMS /Linear eigenvalue analysis program.

The deep red areas in Figure 7-8a beginning at the left and continuing to about t = 100 seconds correspond to the tower bending and blade first flapwise bending modes listed in Table 7-2 that are being driven by the significant vertical wind shear shown in Figure 7-7. The time history variations in the tower bending and first blade symmetric and asymmetric bending loads can be seen in Figure 7-8b in the D8, D9, and D7 detail bands, respectively. The rapid decrease in level of these loads starting at about t = 180 seconds corresponds to the significant decrease in the vertical shear across the rotor shown in Figure 7-7 as a consequence of the intense mixing that accompanied the billow breakdown into intense 3-D turbulence.

The billow rollover and breakdown begin at about t = 135 seconds and continue until about t = 180 seconds. The highlighted area of Figure 7-8 of the panel containing the out-of-plane moment loading history shows the presence of much higher frequency components, particularly from about t = 140 to 180 seconds. During the period, as the turbulence become 3-D and contains coherent elements, loading bursts can be seen in the higher frequency D4, D5, and D6 detail bands. According to Table 7-2, this frequency range contains a significant amount of secondary or cross-coupling of modes (stress energy fluxes). From Figure 7-6b, the rotor inflow at this time is filled with energetic turbulent structures that have dimensions much less than the rotor diameter, and it is these smaller structures that are contributing to the excitation of these higher order modes. As the turbulence in the decaying billow begins to saturate at about t = 200 seconds, the modal excitation also decreases in both occurrence and intensity as a more stable temperature gradient (increasing Ri) begins to reestablish itself and the accompanying increase in buoyancy damping limits the growth rate and size of the turbulent eddies. This is demonstrated in Figure 6-14.

The role of coherent TKE, or E_{coh}, can be seen a bit more clearly in Figure 7-9. Here the format of Figure 7-8 has been modified to better describe the process. The three top panels contain rotor disk (y-z) contour plots for the indicated time period of (left) the vertical velocity field with darker shades of red and blue depicting higher values of rising and descending air, respectively; (center) regions of E_{coh} with the dark red signifying the more intense; and (right) the total wind speed (the vector sum of horizontal and vertical components) with deep red the greatest speed and dark blue the lowest speed. An idealized facsimile of the WindPACT turbine is superimposed on each of the panels with the blade root bending load measurements depicted in the time series and the CWT scalogram and DWT detail band time-frequency decompositions from it. The upper center panel shows that the coherent structures in this record are much smaller than the rotor disk in this highly turbulent flow as revealed by the left and right panels. The higher frequency content in the load time history is evident by the significant deviation from a sine wave shape that would be expected from the load variation from vertical wind shear alone. This deviation arises from the blade passing through this highly turbulent field (left and right panels) that contains coherent structural elements (center panel). The red vertical dot-dashed lines highlight the dynamic response transients across a wide frequency range to coherent structural elements encountered by the blade in the inflow. These represent coherent stress responses across the frequency range of 1.875 to at least 20.4 Hz, the highest modal frequency

listed in Table 7-2, which resides within the D3 (15 to 30 Hz) detail frequency band. This is in the modal frequency range where the contents of this table show that numerous cross-couplings exist between tower and blade modes and, though not determined, the drivetrain as well. These represent potential paths for the transfer or flux of stress energy to various parts of the turbine. This can be summed up by pointing out that a coherent excitation (from coherent turbulence) elicits a coherent dynamic response in the turbine.

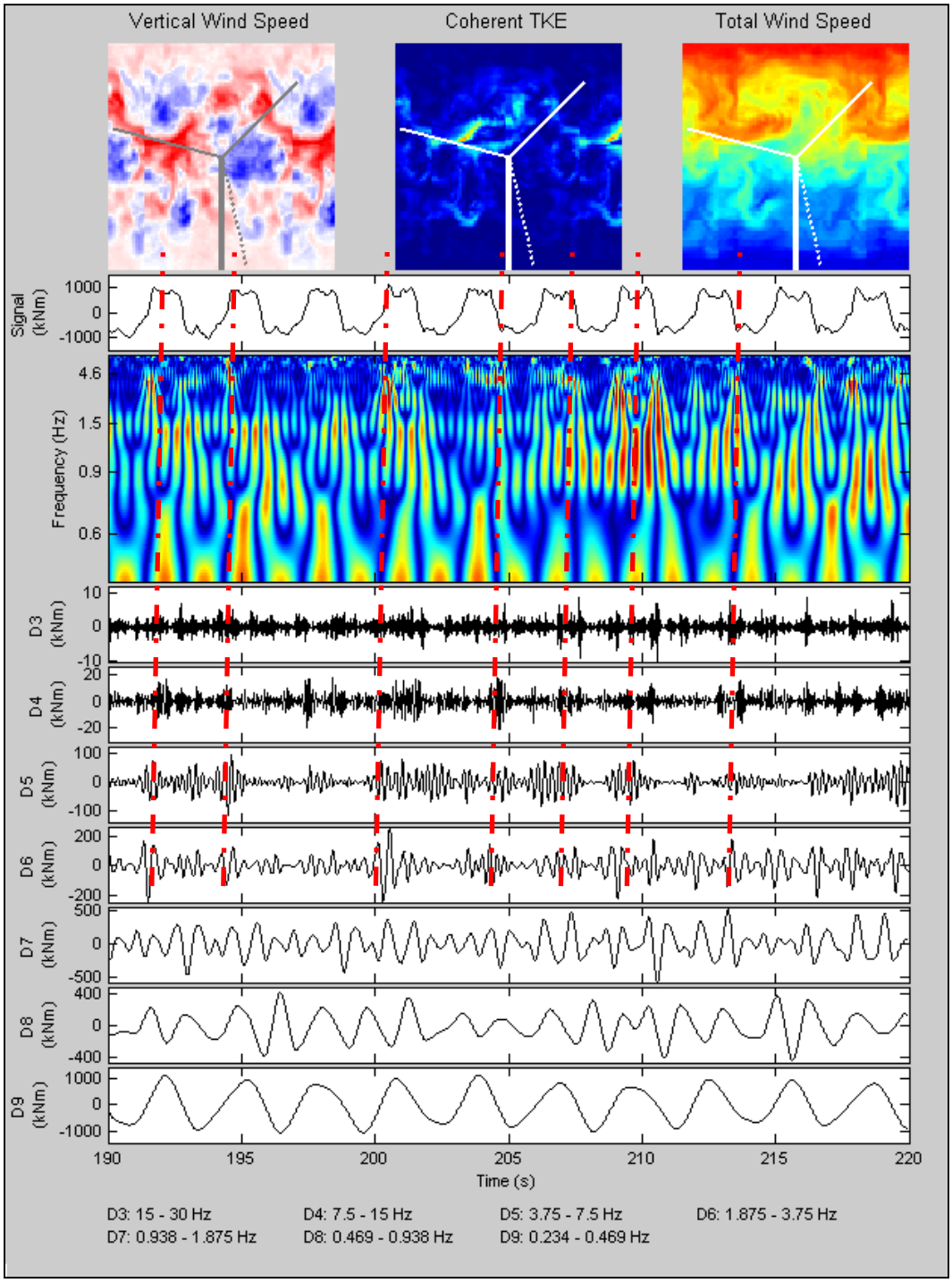

Figure 7-9. Continuous and discrete wavelet decompositions of root flapwise bending load induced in WindPACT turbine model from LES K-H billow simulation. The time history of the blade root flapwise bending load with the mean removed is plotted in the second panel from the top. The dot-dashed vertical lines mark coherent responses across a frequency range of 1.875 to 30 Hz as a result of the blade marked with the dashes encountering the coherent structures in the center top panel.

7.3 Flux of Coherent Turbulent Energy into Turbine Structures

Clearly the character of the waveforms in Figure 7-9 changes with the frequency ranges or, equivalently, the center frequencies of the detail bands rise. In Bands D6, D5, D4, and D3, the waveforms increasingly take on the characteristic of transient damped oscillations whose lengths become shorter as both the frequency bandwidth and center frequency of the bands increase. This indicates that the loads within these frequency bands are being applied more as an impulse as opposed to a load variation that is occurring over one blade revolution (1-P), i.e., in Band D9 and at the twice per revolution (2-P) rate in Band D8. As the peak amplitudes of the load time histories in Bands D6 through D7 decrease, the number of stress reversals increases as the rotor passes through coherent turbulent structures. Because of the nature of the load application and the existence of the small values of structural damping seen in most large turbines, it is likely that there is a significant transient storage of vibrational energy that must be dissipated. It also seems likely that, under these circumstances, the possibility of modal dynamic amplification may also exist, which could be a contributing factor in the lower than designed component service lifetimes being seen in operating wind farms.

The sources of these brief transient loads depicted in the higher frequency detail bands in Figure 7-9 are the coherent turbulent structures through which the rotor blades pass. In the work of Kelley and coauthors (2000), and previously in this report, we demonstrated using wavelet analysis tools that a blade encountering a coherent turbulent structure induces transient loads that couple energy into the rotor natural vibration (modal) frequencies. We demonstrate this process in which we examine the nonstationary time and frequency transport or flux of coherent turbulent energy E_{coh} from the velocity field to the rotor blade manifested as variations in the blade dynamic pressure or q_c at a given spanwise location. We use the wavelet technique of the coscalogram as applied by Gurley and Kareem (1999). The coscalogram, as used in this context, maps the time-frequency variation of the energy flux from the excitation (E_{coh}) to the response (q_c) variable. It is analogous in many respects to Fourier cross-spectral analysis but with the variation in spectral energy resolved not only in frequency but also in time.

We excited the WindPACT turbine model with the breaking portion of the LES K-H billow and obtained the individual time series E_{coh} of the blade dynamic pressure at the 78% span element and the velocity field in the inflow at that location. The coscalogram of these two variables represents the response of q_c to the E_{coh} excitation or the energy flux from the coherent velocity field to the blade as manifested by the time variation of q_c. The fluctuating dynamic pressure excites the blade modal frequencies, many of which are lightly damped. This results in the storing and propagation of vibrational energy within the remainder of the turbine structure.

In Figure 7-10 we demonstrate this flux transfer process. Here we plot the interaction between the local E_{coh} presented to the blade and the resulting q_c at the 78% blade span station for the modeled WindPACT rotor. The upper panel displays the time series of the E_{coh} in red and the q_c in blue. The time-frequency variations of the energy content of each of these variables are shown in the two panels immediately below, and variation of the energy transport or flux between E_{coh} and q_c is displayed in the lowermost panel. In this short record, the 78% blade span station encounters an intense region of E_{coh}, with a peak value approaching 40 $m^2\ s^{-2}$ at a time between 25 and 30 seconds into the record. Although the most intense flux of energy (dark red in lowermost panel) from the coherent turbulence to the blade is found in the lowest

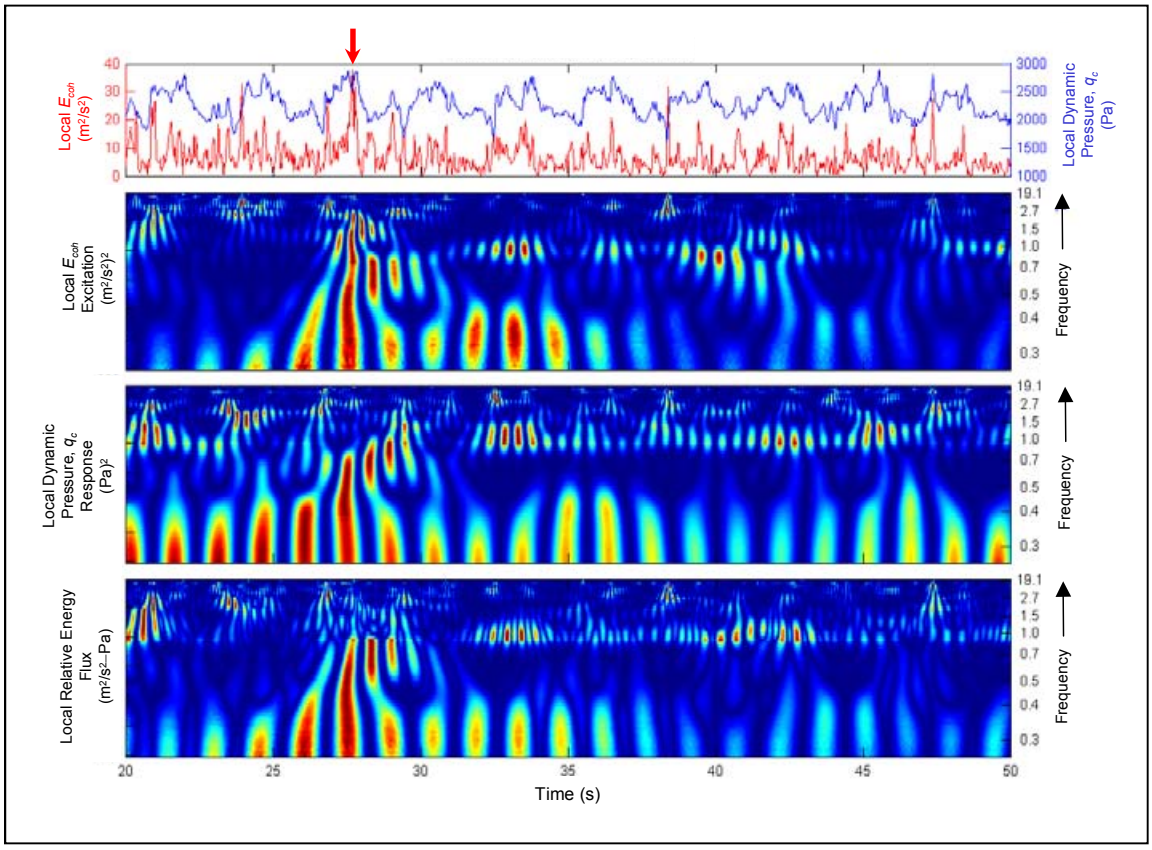

Figure 7-10. Spectral flux of coherent turbulent energy from NCAR LES simulated K-H billow into WindPACT rotor blade at 78% blade span station

frequencies, transfers also occur at the higher frequency vibrational modes in Table 7-2 (greater than ~ 3 Hz). These are somewhat difficult to see because of the nonlinearity of the frequency axis. This process can be described as a resonant coupling between the spatiotemporal structures in the coherent turbulent inflow field and vibrations created within the blade structure as a result of the lightly damped structural modes. We believe this explains the 1:1 correspondence observed in the spectral frequencies of the coherent turbulence field and the vibratory response of the turbine blades, discussed in Kelley and coworkers (2000) and illustrated in Figure 7-10.

The spatiotemporal characteristics of the turbine inflow turbulence field are very important in determining not only the aeroelastic response of the blades but also the rate and intensity at which turbulent energy is transferred from the turbulence to the rotor and subsequent structure. To demonstrate this we again use the virtual WindPACT turbine model by exciting it with TurbSim simulated inflow turbulence fields generated using a mean hub-height wind speed of 13 m s^{-1}: (1) in accordance with the specifications of the IEC Kaimal Normal Turbulence Model (NTM; TurbSim IECKAI spectral model) for "A"-level turbulence and the Normal Wind Profile (vertical shear exponent of 0.2; IEC 2005) ; (2) a stable flow above flat, homogenous terrain based on the models of Højstrup (1982) and Olesen and coauthors (1984) implemented in TurbSim as the smooth terrain (SMOOTH) spectral model with an intense vertical shear exponent of 1.49 but no added small-scale coherent turbulent structures; and (3) the breakdown of the NCAR LES simulated K-H billow with an initial shear exponent of 1.49 (the shear decreases during the breakdown because of the intense vertical mixing that takes place as shown in Figure 7-7).

In Figure 7-11 we compare the energy flux from coherent turbulence to the blade dynamic pressure at the 78% span station of the WindPACT turbine model for the three inflows defined previously. Here we present the information shown in the lowermost panel of Figure 7-10 but in a 3-D format with the magnitude of the energy flux logarithmically scaled by height on the vertical axis and not as shades of red and blue. Examining the three graphs reveals that at least an order of magnitude greater energy flux up to the highest frequencies with the breaking K-H billow in the inflow (Figure 7-11c) as compared with the IEC Kaimal NTM (Figure 7-11a) and highly sheared stable flow (TurbSim SMOOTH model) (Figure 7-11b). The IEC Kaimal NTM inflow transfers a smaller but significant energy flow into the turbine rotor up to about 3–4 Hz but then decreases rapidly at higher frequencies in comparison with the K-H billow breakdown and its intense, small-scale coherent structures. The stable, highly sheared flow (Figure 7-11b) creates similar levels of energy flux as the K-H billow at the lowest frequencies because of the strong wind shear. The flux then decreases rapidly with increasing frequency as a consequence of the lack of coherent turbulent structures. These three diagrams illustrate, at least in terms of the flux of energy from the turbulent inflow into the turbine rotor blades, that the character and structure of the inflow are very important in determining turbine structural response.

In Figure 7-12 we apply the wavelet coscalogram to examine the relative energy flux from the coherent turbulent kinetic energy E_{coh} to the local dynamic pressure q_c at the 78% blade span station for the WindPACT virtual turbine using the IEC Kaimal NTM spectral model for the inflow. We increased the hub-height mean wind speed to the above-rated value of 16 m s^{-1} but maintained the "A" turbulence level and the NWP shear exponent of 0.2. Immediately obvious is the significant tower bending response at ~ 0.4 Hz, as indicated by the modal mapping in Table 4-3. The tower appears to respond to one distinct coherent structure response at about 12 seconds

into the record. As in Figure 7-11a, above about 6–7 Hz the response falls rapidly, with no indication of reactions to coherent turbulent structures of any consequence.

In Figures 7-13 and 7-14 we also increased the hub-height mean wind speed to the same value for the smooth terrain (TurbSim SMOOTH spectral model) and the NCAR LES K-H billow inflow simulations. We added an inflow simulation shown in Figure 7-15 of a K-H billow derived from the Werne and Fritts (1999) Colorado Research Associates (CoRA) DNS model to obtain another coherent structure sequence. We increased the rotor disk shear exponent from 1.49 to 1.825 for all three simulations to increase the intensity of the coherent structures. Late in the record, between about 53 and 67 seconds of the SMOOTH spectral model inflow simulation in Figure 7-13, are significant responses in the lowest frequency mode shapes to coherent turbulence fluxes, but this response falls off rapidly with increasing frequency, indicating a lack of smaller scale coherent structures in the flow. Comparing the SMOOTH modeled inflow response to the NCAR LES and CoRA DNS K-H billows in Figures 7-14 and 7-15, we see slopes in the high frequency responses, but they are much shallower. This shallower slope coincides with a significant amount of modal cross-coupling in Table 7-3. At 10 Hz is almost an order of magnitude more coherent turbulent energy flux, which the time series of q_c reflect. In both K-H billow inflow simulations are two events with significant fluxes that affect the modal frequencies greater than 10 Hz, as indicated by the dashed lines. The presence of intense, coherent turbulent structures in the breakdown phase of a K-H billow clearly is an important source of kinetic energy influx into a turbine rotor blade, particularly for the higher frequency mode shapes where numerous cross-couplings exist.

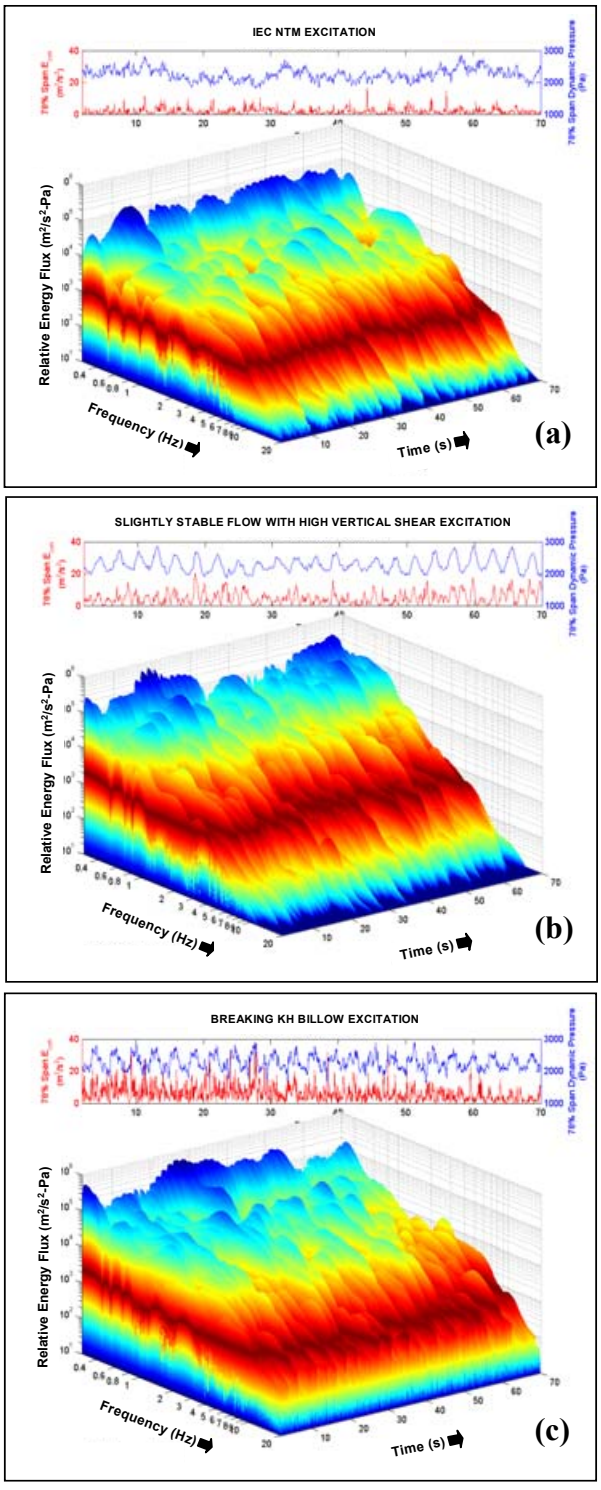

Figure 7-11. Relative spectral energy flux (coscalogram) of E_{coh} to blade dynamic pressure (q_c) at 78% span for simulated inflows of (a) IEC Kaimal NTM; (b) stable flow with high shear (SMOOTH spectral model); and (c) breaking NCAR LES K-H billow

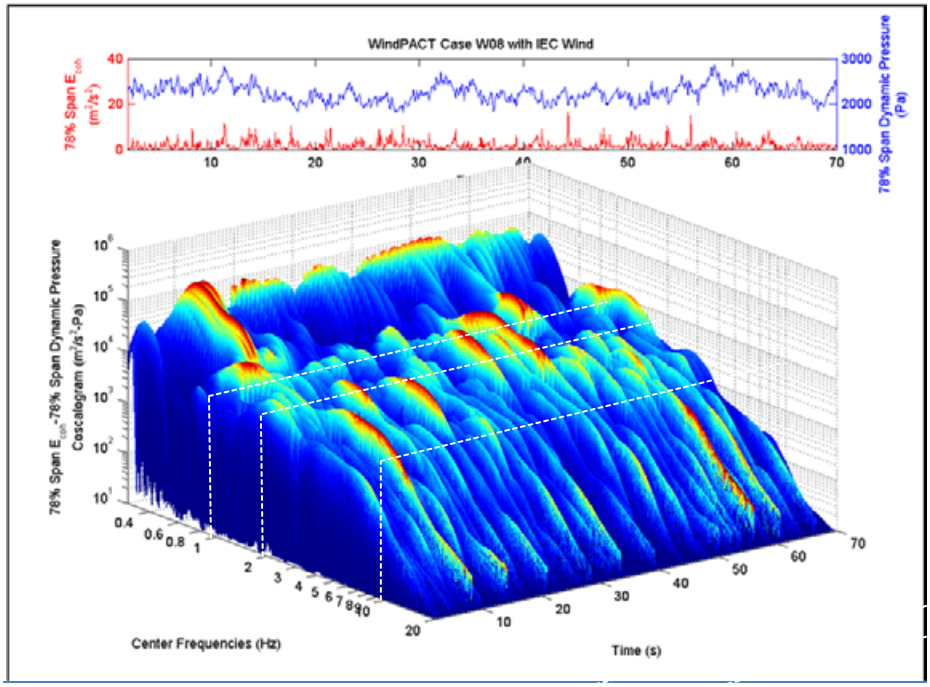

Figure 7-12. Relative energy flux coscalogram between E_{coh} and q_c at simulated WindPACT turbine 78% span station for inflow from IEC Kaimal NTM spectral model simulation

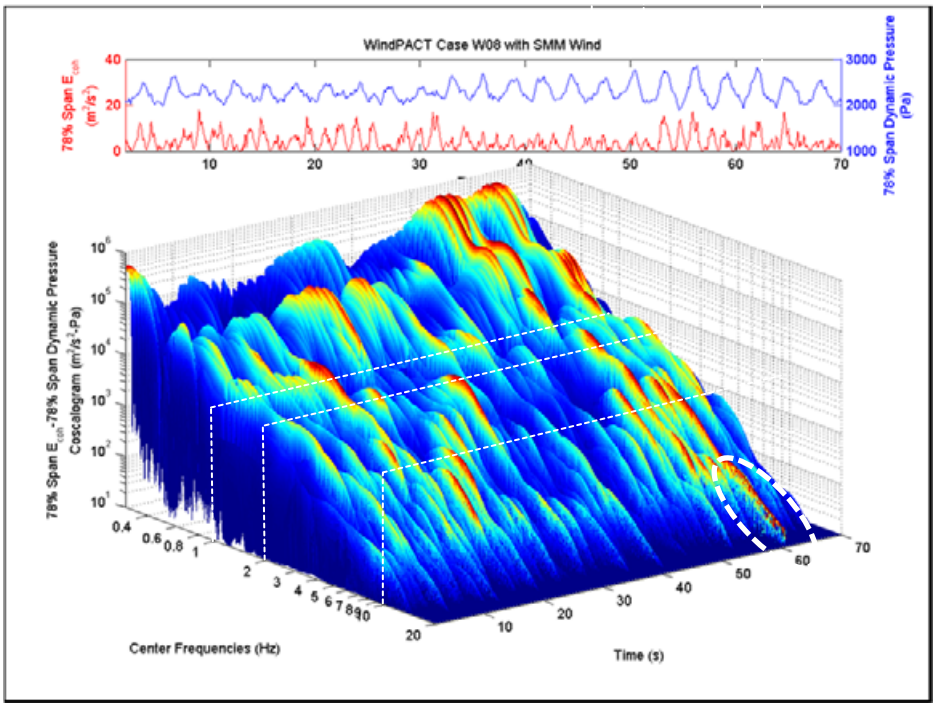

Figure 7-13. Relative energy flux coscalogram between E_{coh} and q_c at simulated WindPACT turbine 78% span station for inflow from high shear SMOOTH model simulation. Low-amplitude energy flux indicated with dashed lines is associated with frequencies greater than 10 Hz.

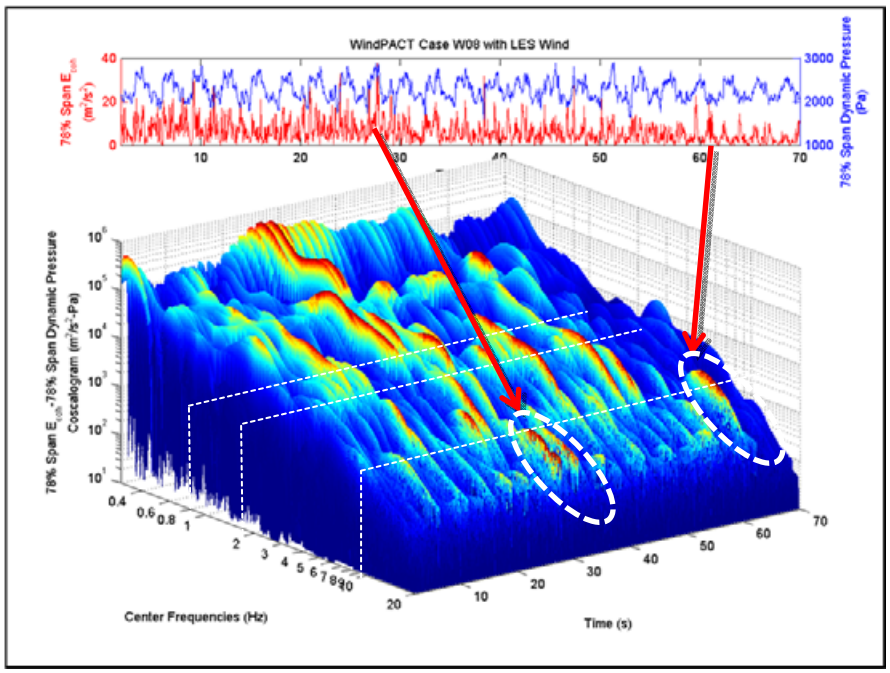

Figure 7-14. Relative energy flux coscalogram between E_{coh} and q_c at simulated WindPACT turbine 78% span station for inflow from NCAR LES K-H billow simulation. Significant energy flux indicated with dashed lines is associated with frequencies greater than 10 Hz.

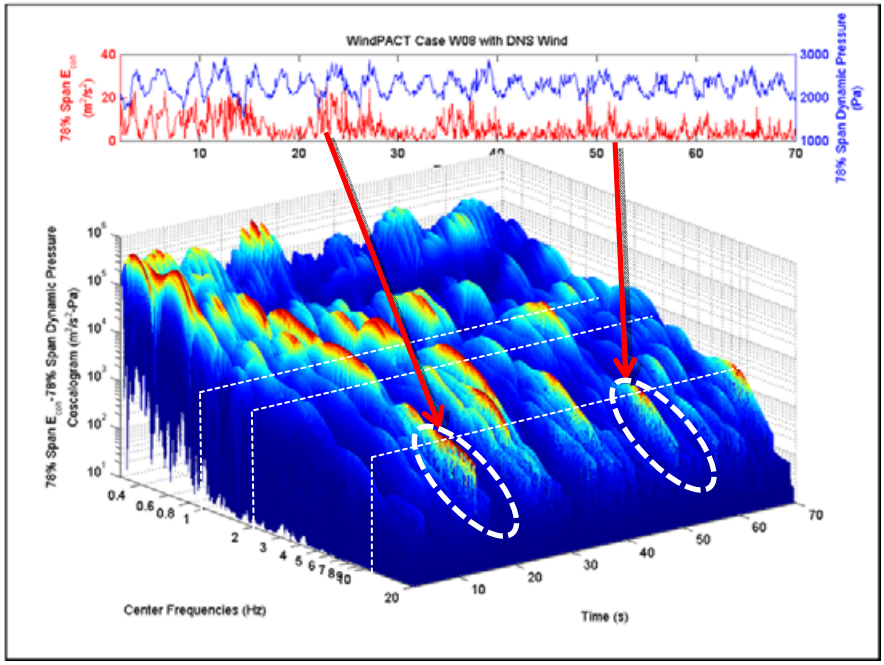

Figure 7-15. Relative energy flux coscalogram between E_{coh} and q_c at simulated WindPACT turbine 78% span station for inflow from CoRA DNS K-H billow simulation. Significant energy flux indicated with dashed lines is associated with frequencies greater than 10 Hz.

7.4 Propagation of Coherent Turbulent Energy into Turbine Structure

In analyzing the response of the WindPACT turbine to coherent turbulence, we are limited because it is a virtual machine and the details of the modeling were limited. For example, the drivetrain was not included in the linear modal analysis. As a result we were not able to perform more detailed analyses of the load path dynamics downstream of the rotor as it responds to coherent turbulence excitation. In the LIST Program using the NWTC ART, however, we can look deeper into such questions because of the extensive documentation and measurements available.

A full system modal test was included in developing the dynamics model of the controls test bed turbine (CART2), and it was performed on another original Westinghouse machine identical to the ART. Osgood and colleagues (2002) performed a full system modal survey that included a "snap back" transient load test (Osgood 2004) and estimates of modal damping. Wright (2004) developed the MSC.ADAMS model of CART2 (ART), which we used to perform an ADAMS/Linear modal analysis. We were then able to compare these results to those derived from Osgood's full system modal survey. Table 7-3 summarizes these results, and the modal frequencies where we found significant numbers of cross-couplings are shaded and bolded. Of particular importance is the inclusion of the drivetrain modes. A significant number of cross-coupled modes appear above about 3.8 Hz, some of which are very lightly damped. The upper frequency limit of the measured modal survey was slightly more than 6 Hz, so we have to depend on the eigenvalue analysis of Wright's MSC.ADAMS model for high frequencies.

Table 7-4 gives a detailed summary of the measured modal survey combined with the eigenvalue analysis. Modal frequencies with cross-coupling between the rotor and tower or drivetrain are highlighted. In general, there was reasonable agreement between the measured and the calculated modal frequencies where available, with the former showing more potential load paths. Of particular significance were the modal damping estimates within these cross-coupled frequency ranges, some of which were quite small and not available from the linear analysis. Of particular note are the number of cross-coupled modes among the rotor blades, the tower, and the drivetrain and the low modal damping associated with the majority of them. So with the ART, although smaller, we have a good picture of the modal dynamics that we lacked with the virtual WindPACT turbine.

We can now examine the details of the flux of coherent turbulent energy into the ART based on actual measurements. We use the loading transients created by the rotor blades encountering an intense coherent turbulent structure (CTKE) in the upper panel of Figure 7-16. The zero-mean root flapwise bending load response to this structure is plotted in the center panel. The fore-aft (X), side-to-side or lateral (Y), and vertical (Z) velocities measured by a triad of orthogonal accelerometers of an inertial measurement unit (IMU) attached to the top of the forward low-speed shaft bearing or pillow blocks are presented in the bottom panel. Before the intense transient event, the velocities (particularly those in the fore-aft direction) were reasonably high because of the high levels of coherent turbulence occurring in the inflow.

In Figure 7-17, we illustrate the observed time-frequency variation of the propagation or flux or vibrational energy between the ART root bending loads and the low-speed shaft during the rotor's encounter with the intense coherent turbulent structure indicated in the upper panel of Figure 7-16. In these presentations we plot the time series of the zero-mean root flapwise

bending load in red together with the fore-aft, side-to-side, and vertical nacelle velocities in blue and the low-speed shaft torque (blue) and flapwise bending (red) in the rightmost panel in Figure 7-17a. Figure 7-17b is the same, with the edgewise bending load replacing the flapwise load. In the second row of panels below the time series plots are the CWT scalograms of the excitation flap and edge bending loads. CWT scalograms of the nacelle X, Y, and Z velocities and the low-speed shaft torque are presented in the second row of panels. Finally, in the lowest row of panels are coscalograms indicating the energy fluxes of the excitation loads with the responses of the IMU velocity components and the low-speed shaft torque. In this presentation the coscalogram allows us to examine and quantify the time variation of the intensity and frequency content of the flow of vibrational energy as the blades pass through the coherent turbulent structure.

From Figure 7-16, we note that the impact of this encounter was applied over a period of about 2 seconds, but we cannot ascertain what the spectral content of the energy flow between the blade roots and the low-speed shaft is and what modal frequencies may be involved. The impulsive nature of this event is well demonstrated in Figure 7-17. With the exception of the side-to-side Y nacelle velocity, the coscalograms show that energy is flowing across a wide or broadband frequency range that is consistent with the application of a short-period, impulsive load. By comparison, the side-to-side or lateral energy flow resides within a narrowband range of frequencies near 6 Hz. According to Tables 7-3 and 7-4, this is a range dominated by numerous lightly damped and cross-coupled modes among the blades, the tower, and the drivetrain. Therefore vibrational energy that originates with the coherent turbulent structure is responsible for inducing unsteady aerodynamic loading of the blades. The resulting dynamic loads are transported throughout the blades and tower and into the low-speed shaft and nacelle in an impulsive manner. Even though this experiment did not directly measure tower loads, we would expect responses similar to those in Figure 7-17. The impulsive loading of turbine rotors by coherent turbulent structures is responsible for the transport of vibrational energy into turbine components through the action of lightly damped modes and, in particular, cross-coupled modes.

7.5 Extension to Larger Turbine Rotors

In comparing the detailed modal mapping of the ART in Table 7-4 with that of the larger WindPACT design derived from linear analysis alone in Table 7-2, we see that many of the cross-coupled modes nominally occur in the same frequency ranges, i.e., 3–9 Hz. Even though the detail available in the ART modal mapping does not exist for the virtual WindPACT turbine, it is clear from Table 7-2 that the frequency range of the cross-coupled modes seen in the blades and tower extends to about twice that of the ART. We have no estimate of the modal damping associated with these higher frequencies, but it is likely that at least some of them are equivalent to the low values seen in the ART. We would also expect, as in the ART, modal cross-coupling among the blades, tower, and drivetrain components. An increase from a 600-kW turbine with a 42-m-diameter rotor to a 1,500-kW turbine with a 70.5-m-diameter rotor leads to additional and higher frequency cross-coupling modes, most likely because of the unavoidable increase in flexibility with the larger turbine design.

To test this theory, we used the ADAMS/Linear program to analyze the linear mode shapes of the virtual NREL 5-MW Reference Turbine (Jonkman and Cotrell 2003). Using the animation graphic tool of ADAMS/Linear, we swept the model design over the excitation frequency range of 0.01 to 20 Hz in very small increments while paying close

Table 7-3. CART2 (ART) Measured and Calculated Static System Frequencies

Frequency Range (Hz)	**Characteristic Modes**	**Range of Measured % Critical Damping**	**Total Number of Modes[a]**	**Number of Blade/Tower/ Drivetrain Interacting Modes[a]**
0.716	1-P	~	~	~
0.867–0.886	Blade 1st bending, tower 1st fore-aft bending, drivetrain bending	0.68–2.66	7	3
1.390–1.580	Blade 1st bending, tower side-side bending, drivetrain lateral bending	0.74–1.52	3	2
2.060–2.081	Blade 1st & 2nd bending	0.70–0.93	3	0
3.886–4.451	**Blade 1st & 2nd bending, drivetrain lateral bending, tower torsion**	**0.70–0.72**	**6**	**7**
5.050–6.170	**Blade bending, drivetrain, tower lateral & torsion**	**0.24–0.95**	**8**	**10**
7.815[b]–8.411[b]	**Blade bending, tower fore-aft & lateral bending, drivetrain bending**	**n.a[c]**	**2**	**3**
9.305[b]–10.84[b]	Blade bending, drivetrain interaction	n.a.	2	1

[a]Measured plus modes from FAST model eigenanalysis
[b]Determined from FAST model eigenanalysis only
[c]Not available
Sources: Osgood, McFarland, and Johnson (2002); Osgood (2004); Wright (2004)

Table 7-4. CART2 (ART) System Nonrotating Modal Frequencies

Natural Frequency (Hz)			Measured % Critical Damping	Mode Shape Descriptions		Indicated Coupling	
Measured[#]		Eigenvalue Analysis[§]		Primary Mode	Secondary Couplings	Rotor/ Tower	Drivetrain
Blades Horiz	Blades Vert						
		0.0130[§]		Hub teetering	Blade 1st & 2nd symmetric flap		
0.867			2.660	Tower 1st lateral bending			
	0.858		0.661	Tower 1st fore-aft bending			
		0.878		**Tower 1st fore-aft bending**	**Blade 1st symm flap; 1st asym edge; tower 1st fore-aft bending; drivetrain**	✓	✓
0.870			0.683	Tower 1st fore-aft bending			
	0.877		1.800	Tower 1st lateral bending			
		0.866		**Tower 1st fore-aft bending**	**Blade 1st symm flap; 1st symm edge, 2nd symm flap; tower 1st lateral bending**	✓	
		1.390		Blade 1st symm[a] flap	Drivetrain; tower 1st lateral; blade 2nd symm flap		
1.45			**0.743**	**Blade 1st asym[b] edge; tower lateral bending & torsion**		✓	
	1.58		**1.520**	**Blade 1st asym flap**			✓
2.06			0.698	Blade 1st symm flap	Blade 1st asymmetric edge		
	2.06		0.927	Blade 1st symm flap			
		2.081		Blade 1st symm flap	Blade 1st symm edge; 2nd symmetric flap		
		3.886		Blade 1st asym flap	Blade 1st asym edge; 2nd asym flap; teeter		
3.90			**0.708**	**Blade 2nd asym flap**	**Blade 1st symm edge; drivetrain lateral bending; tower torsion**	✓	✓
	3.94		**0.717**	**Blade 1st symm edge**	**Blade 2nd asym flap; tower torsion**	✓	
4.02			**0.710**	**Blade 1st asym edge**	**Blade 2nd asym flap; drivetrain lateral bending; tower torsion**	✓	✓
	4.09		**0.695**	**Blade 2nd asym flap**	**Blade 1st symm edge; drivetrain yaw; tower lateral & torsion**	✓	✓
		4.451		Blade 1st asym edge	Blade 1st & 2nd asym flap		
	5.05		**0.951**		**Blade 1st symm edge; 2nd asym flap; drivetrain yaw; tower lateral & torsion**	✓	✓
	5.35		0.627		Blade 2nd symm flap; 1st asym edge		
5.39			0.584		Blade 2nd symm flap; 1st asym edge		
5.67			**0.569**		**Blade 1st symm edge; 2nd symm flap; drivetrain pitch & lateral; tower fore-aft, lateral, & torsion**	✓	✓
	5.77		**0.235**		**Blade 1st symm edge; 2nd asym flap; drivetrain pitch & lateral; tower fore-aft; lateral, & torsion**	✓	✓
6.01			**0.668**		**Blade 2nd asym flap; 1st symm edge; drivetrain; tower 2nd lateral bending; tower torsion**	✓	✓
		5.854		Blade 2nd symm flap	Blade 1st symm flap; 1st symm edge		
	6.17		**0.380**		**Blade 2nd asym flap; 1st symm edge; drivetrain pitch; tower fore-aft bending**	✓	✓
		7.815		**Blade 2nd asym flap**	**Blade 1st asym flap; 1st asym edge; tower 1st fore-aft bending**	✓	
		8.411		**Blade 1st symm edge**	**Blade 1st & 2nd symm flap; tower 1st & 2nd lateral; drivetrain**	✓	✓
		9.305			Blade 1st & 2nd asym flap		
		10.837			Blade 1st symm edge; 1st & 2nd symm flap; drivetrain		

[a]Symmetric
[b]Asymmetric
Sources: Osgood, McFarland, and Johnson (2002); Osgood (2004); Wright (2004)

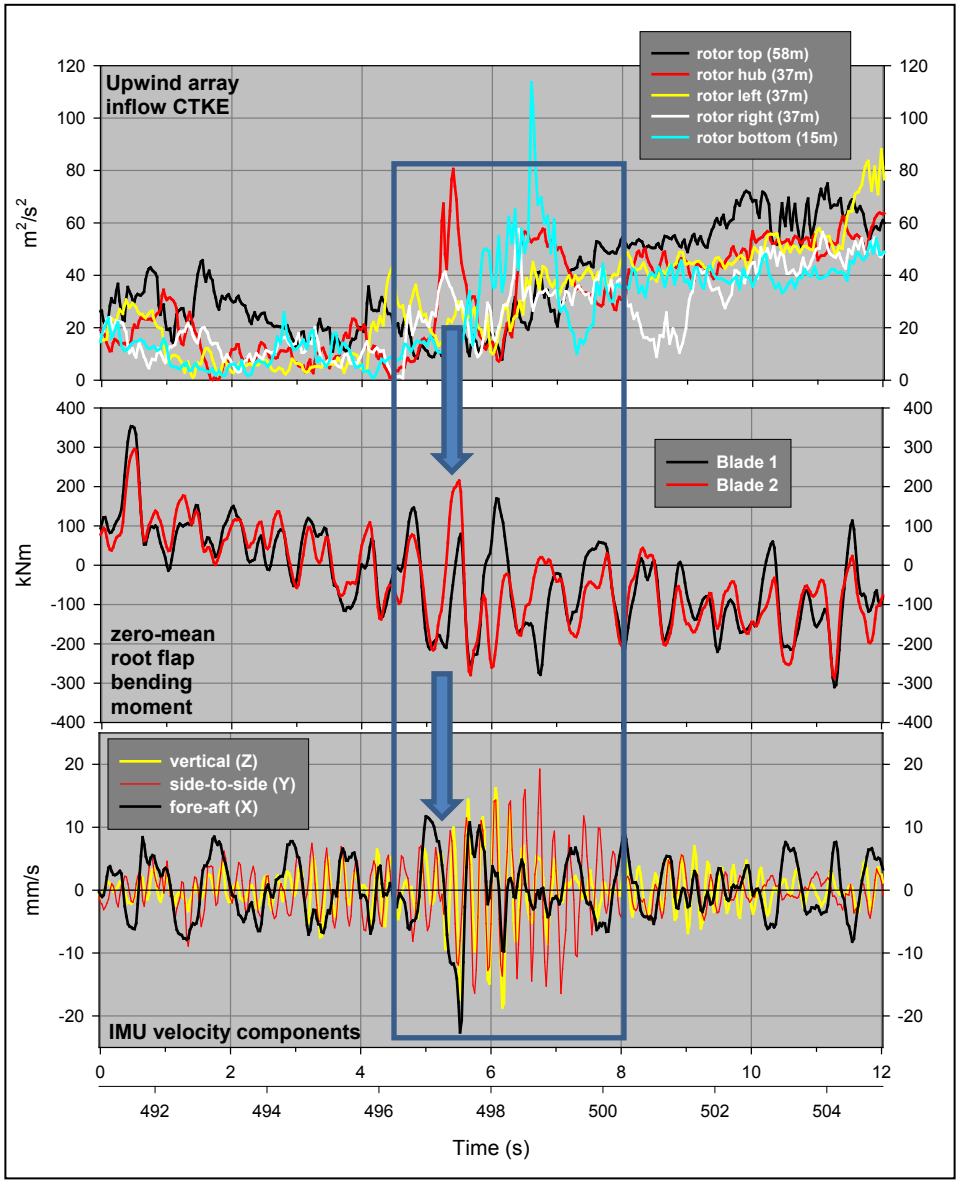

Figure 7-16. Coherent turbulence induced severe transient loading event measured on NWTC ART during LIST Project by blade zero-mean root loads and nacelle velocities measured on forward low-speed shaft support bearing

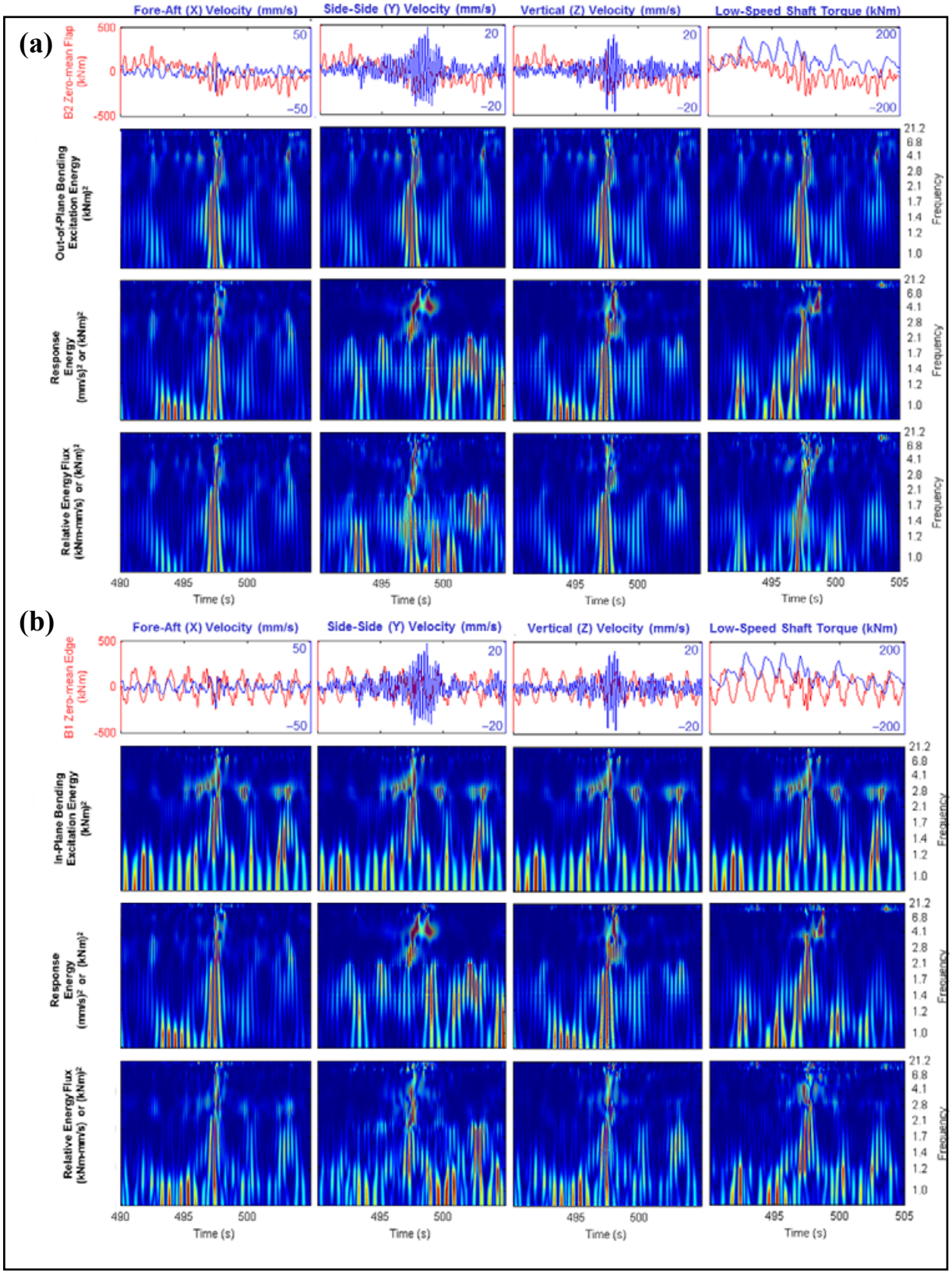

Figure 7-17. Observed energy propagation caused by coherent turbulent event excitation between low-speed shaft torque and (a) out-of-plane and (b) in-plane root bending loads and nacelle velocities measured on forward low-speed shaft support bearing immediately behind rotor

attention to locating and identifying cross-coupled modes. Table 7-5 summarizes the 52 mode shapes we found. We realize that not all of these listed will participate. From our experience with the measured modal survey of the CART2, however, it is also likely that mode shapes not on this list would exist on an actual, physical turbine. Also, some of them would undoubtedly be related to strongly nonlinear processes not resolved by ADAMS/Linear. We highlighted the cross-coupled modes for greater visibility and ease of comparison with the CART2 and the WindPACT turbines. Table 7-5 indicates that there is more potential cross-coupling below, within, and above the frequencies seen on the CART2 and the WindPACT turbines. At frequencies greater than about 10 Hz, the potential exists for complex, higher order modal coupling within the blades themselves and between the blades and the tower. What modal damping is associated with such interactions is unknown. Again, the drivetrain was not available in this model, so we do not know how the blades and the tower interact with it, but given the CART2 experience, it surely exists. These results suggest that as the turbine rotors and their towers increase in size, the increase in flexibility creates pathways for vibrational energy transfer throughout these components, which may be critical in terms of local fatigue damage when coherent turbulence is encountered during operations.

Table 7-5. NREL 5-MW Reference Turbine Nonrotating System Modal Frequencies

Nominal Modal Frequency (Hz)	Mode Shape Descriptions		Indicated Rotor/Tower Coupling
	Primary Mode	Secondary Couplings	
0.2017	Max rotor rotation rate (1-P)	n.a.	
0.3162	1st tower lateral (side-to-side) bending		
0.3193	1st tower fore-aft bending		
0.6110	1st drivetrain bending		
0.6384	1st blade asymmetric	Nacelle yaw	
0.6690	1st blade asymmetric	Nacelle pitch	
0.7023	1st blade collective symmetric flap		
1.0751	1st blade asymmetric with edgewise pitch		
1.0744	1st blade asymmetric with flapwise yaw		
1.0886	1st blade asymmetric with edgewise yaw		
1.8576	2nd blade asymmetric with flapwise pitch		
1.9618	2nd blade collective symmetric flap		
2.6549	**2nd blade collective edgewise**	**1st tower lateral**	✓
2.8452	**2nd tower fore-aft**	**2nd blade asymmetric**	✓
2.9427	**2nd tower lateral**	**2nd blade flap and edge**	✓
3.0216	1st flapwise asymmetric blades 2 & 3		
3.9586	1st edgewise asymmetric blades 2 & 3		
4.0278	2nd blade flapwise and edgewise asymmetric		
4.0412	**2nd blade flapwise and edgewise asymmetric**	**Tower 1st fore-aft**	✓
4.4685	**1st torsion blade tips**	**Tower 1st fore-aft**	✓
4.9650	Complex interaction blade tips & nacelle yaw		
6.6997	2nd blade edgewise asymmetric collective		
7.0510	**2nd blade flapwise & torsion**	**2nd tower fore-aft**	✓
7.2607	**2nd blade torsion**	**2nd tower lateral**	✓
7.7588	1st blade collective torsion		
7.7781	1st torsion blade 1, 1st edgewise blades 2 & 3		
7.8609	1st torsion blades 2 & 3		
7.9732	1st torsion blades 1 & 3		
8.1035	1st blade collective torsion		
8.1736	1st torsion and 1st flapwise blades 2 & 3		
8.2865	**2nd blade collective torsion**	**2nd tower fore-aft**	✓
9.2865	**2nd blade collective asymmetric edgewise**	**2nd tower fore-aft**	✓
9.3381	2nd blade collective asymmetric edgewise		
11.7076	**2nd flapwise asym blade 1, 2nd torsion blades 2 & 3**	**2nd tower fore-aft**	✓
11.7215	**3rd blade collective asymmetric flapwise**	**2nd tower fore-aft**	✓
11.8544	3rd blade collective symm flapwise & 2nd torsion		
11.8902	3rd flapwise & 2nd torsion blades 2 & 3		
11.9246	3rd blade collective flapwise and 2nd torsion		
12.3317	3rd flapwise and 2nd torsion blades 2 & 3		
12.9411	**3rd blade collective torsion**	**3rd tower lateral**	✓
12.9972	3rd torsion blades 1 & 3		
13.0147	**3rd blade collective torsion**	**3rd tower lateral**	✓
13.0758	**3rd blade collective torsion**	**3rd tower lateral**	✓
13.2910	**3rd blade collective torsion**	**3rd tower lateral**	✓
14.2462	**3rd blade collective asymmetric flapwise**	**3rd tower fore-aft**	✓
16.3927	3rd blade collective asymmetric edgewise		
16.5404	**3rd symmetric edgewise blades 2 & 3**	**3rd tower fore-aft**	✓
16.5876	3rd asymmetric edgewise blades 1 & 3		
17.3138	4th blade collective symmetric flapwise		
17.3383	**4th symmetric flapwise blade 1, 1st torsion blades 2 & 3**	**3rd tower fore-aft**	✓
19.8192	3rd blade collective torsion		
19.8306	**3rd blade collective torsion**	**3rd tower fore-aft**	✓
19.8372	3rd torsion blades 1 & 2		

Source: Jonkman et al. (2009)

7.6 Modeling Coherent Turbulent Structures

Ingesting a coherent turbulent structure generated within the background flow as the result of Kelvin-Helmholtz Instability (KHI) can induce significant dynamic response in wind turbine structures. Such a response includes increased fatigue damage on the blades themselves through the direct application of cyclic stress loads or as vibratory energy that is transported from the blades impulsively through the drivetrain and into the tower. We have seen that the latter can be transported through the mechanism of lightly damped, cross-modal coupling. The coherent nature of K-H billows generates a range of stress loads at discrete frequencies when the blade passes through them, which in turn create an impulsive, coherent structural response in the turbine components. We need to develop a suitable engineering model of these turbulent coherent structures that can be scaled in terms of atmospheric boundary layer turbulence parameters.

We analyzed the instantaneous time series of coherent kinetic energy (E_{coh}) derived from a sonic anemometer for each usable 10-minute record at hub height (23 m) from the experiment in the California wind farm upwind of Row 1, upwind of Row 37 (the location of the two Micon test turbines with 7D upwind spacing), and downwind of Row 41 (14D downwind of the next operating row of turbines). Similarly, we analyzed the 7,041 10-minute records available from each of the five sonic anemometers in the upwind planar array of the NWTC LIST Program. Finally, the same process was applied to more than 28,000 10-minute records from the four sonic anemometers installed on the 120-m meteorological tower used as part of the Lamar Low-Level Jet Project (LLLJP) in the high plains of southeastern Colorado.

Our initial analysis revealed that the number and intensity of coherent structures found within a 10-minute record were exponentially distributed. Our further analysis found that these distributions could be reasonably described by an inhomogeneous Poisson random process.

A Poisson process is a counting process in which $\boldsymbol{N} = \{N(t),\ t \geq 0\ \}$ refers to the number of events occurring in the interval (0, t]. The probability of n events occurring in (0, t] is

$$P\{N(t) = n\} = e^{-\lambda t}\frac{(\lambda t)^n}{n!} \quad n = 0, 1, 2, \ldots \quad , \tag{7-2}$$

where λ is the intensity or rate of occurrence. If $\lambda > 0$ and has a constant value, the process is referred to as homogeneous Poisson. If, however, λ is a function of time or other variables that are a function of time, the process is considered inhomogeneous Poisson. It is assumed that $N(0) = 0$; that it is stationary and events can be considered independent of one another; and that two events cannot occur simultaneously within a very small increment of time. If S_n is the time of the arrival of the nth event with $S_o = 0$, the time between events or interarrival time X_n is given by $S_n - S_{n-1}$ or

$$S_n = \sum_{k=1}^{n} X_k \quad n = 1, 2, 3, \ldots \quad . \tag{7-3}$$

A key characteristic of a Poisson process is that the event interarrival times (*IAT*s) are exponentially distributed over the interval (0, t] where $IAT = 1/\lambda$ and represents the mean time between events.

We analyzed the time variation of the instantaneous values of E_{coh} for each 10-minute record for which we assumed the process creating E_{coh} was at least quasi-stationary and is nominally homogeneous Poisson. This means we are assuming that the structures are occurring on a continuous basis at a constant rate for the boundary conditions prevalent during the 10-minute record. We further assume that two events cannot occur within one sample period (i.e., 0.02 seconds for Rows 1 and 41 and 0.06 seconds for Row 37 in the California wind farm; 0.025 seconds for the LIST Project; and 0.05 seconds for the LLLJP).

The original E_{coh} time series was initially smoothed over a 3-second period using a centered (non-causal) finite impulse response (FIR) digital filter whose odd numbers of weights were based on the specific sampling rate. A detection threshold was used to identify individual coherent structures. Because we were interested only in values of E_{coh} that could induce at least the threshold dynamic response in a turbine, we initially used 2 $m^2\ s^{-2}$. We found, however, that the turbulence was severe enough in the California wind farm and at Row 4 of the NWTC that we detected hundreds of very short coherent structures. We then revised this threshold upward to 5 $m^2\ s^{-2}$ for these two locations, but found it was adequate for the Lamar site because it was less energetic than the others.

As each individual coherent structure with a 10-minute record was detected, the length and intensity or peak values of the smoothed E_{coh} were logged. The total length and number of coherent structures and the overall peak value of E_{coh} found within the record were added to the log. These data were annotated with Ri_{TL} and the local values of the mean U-velocity component, the shearing stress or friction velocity u_*, and the vertical velocity standard deviation σ_w to facilitate later scaling in TurbSim. A second data file was created that contained X_n or IAT between each of the structures detected. A program was written to process this second data file, to first make sure that there were at least 60 seconds between each event and to obtain the mean IAT, i.e., the mean time between encountering coherent structures.

7.7 Measured Turbine Dynamic Response to Observed Coherent Structures

We used the California wind farm Micon 65/13 data set to examine the turbine response to the coherent turbulent structures measured by the previous procedure. We were able to obtain coherent structures from all but 2 of the 397 records in which we had both the turbulent inflow and the matched responses from the two turbines. The information contained within the coherent structure data format included inflow parameters that we have shown to scale turbine dynamic responses, including the hub $\overline{U}$, local u_*, Ri_{TL}, and σ_w. We correlated the turbine response variable FBM *DEL*s and peak values with the total length of coherent structures in the record, T_{coh}; the number of these structures, N_{coh}; and the maximum value of E_{coh} or intensity within the record.

Figure 7-18 presents the correlations of the FBM *DEL*s and peak values with Ri_{TL} from the matched records. We also annotated these graphs with the CRR stability range (pair of vertical dashed lines indicating the range of $+0.01 < Ri_{\mathrm{TL}} < +0.05$), the Ri_{TL} value of maximum response $Ri_{\mathrm{TL}} = +0.02$ as a vertical dot-dot-dashed line, and a dotted line ($Ri_{\mathrm{TL}} = +0.10$) indicating the

upper limit of the CRRH stability class. The moderately stable STC04 class extends from the dotted line to the right edge of the graph. As we have seen before, the greatest response occurs in the CRR range for the reasons discussed previously.

In Figures 7-19, 7-20, and 7-21 we plot the observed variations of the two Micon 65/13 turbine root FBM *DEL*s and peak values with T_{coh}, N_{coh}, and peak E_{coh} of the coherent structures found in a population of 10-minute matched records where the peak values of $E_{coh} > 5$ m^2 s^{-2}. We noticed that the slope of the LOESS-smoothed trend lines with each variation changed significantly at some point as the independent variable increased. This suggested perhaps a systematic change occurring in the loading process associated with the higher values of these coherent structure characteristics. We created a subset of the records in which the FBM *DEL*s from the NREL rotor exceeded the P90 (18.95 kNm) of the entire population. Table 7-6 summarizes the means, medians, and standard deviations of the turbine FBM *DEL*s, the inflow turbulence scaling parameters, and the coherent structure attributes for the matched records in this subpopulation. This table reveals that the turbine loads in the tail above P90 occur fully within the CRR stability class, whose means and medians agree with the value of $Ri_{\mathrm{TL}} = +0.02$ as stability where we previously found the maximum loads. Also, the distribution central values of the hub wind speeds are just slightly above rated (at least for the NREL rotor), and the one standard deviation variation about these speeds would coincide with significant unsteady aerodynamics of these stall-controlled rotors. Finally, the values of both local u_* and σ_w are high. The high value of the shearing stress u_* ensures a large reservoir of energy is available to be turned into coherent turbulent energy by the action of buoyancy-damped K-H billows, which is supported by the high value of σ_w and the magnitude of the central measures of the mean peak E_{coh}.

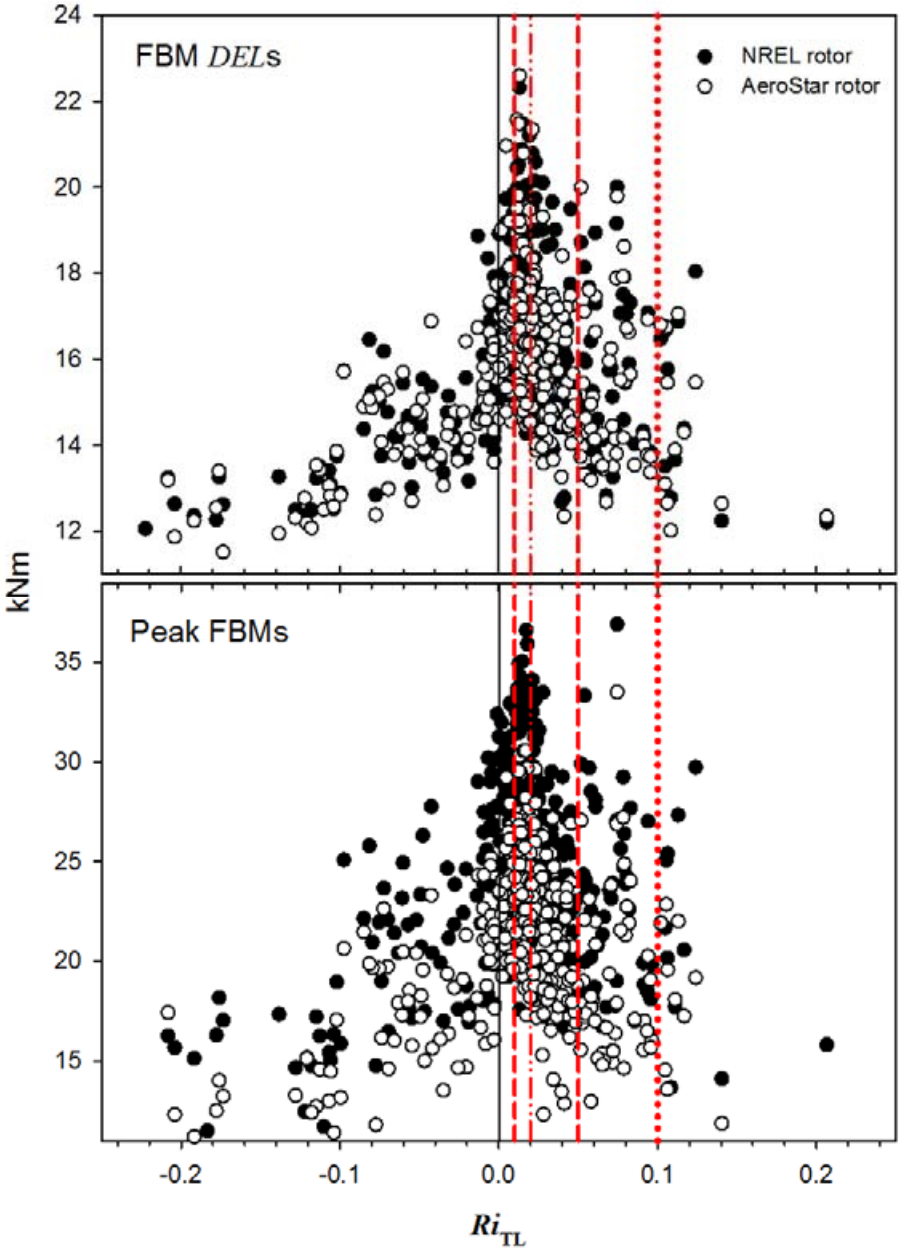

Figure 7-18. Correlation of Micon 65/13 FBM *DEL*s and peak values with Ri_{TL} from records in which peak E_{coh} exceeded 5 m^2 s^{-2}. The pair of vertical dashed lines represents the range of the CRR stability class, the dot-dot-dashed line the Ri_{TL} value (+0.02) of maximum response, and the dotted line the upper limit of the CRRH stability class (+0.05 ≤Ri_{TL} < +0.10). The moderately stable STC04 class extends from this dotted line to the limit of the diagram (Ri_{TL} = +0.25).

Table 7-6. Statistics of Matched Micon 65/13 Turbine Responses, Turbulence Scaling Parameters, and Corresponding Coherent Structure Attributes for Peak E_{coh} > 5 m^2 s^{-2} and NREL Rotor FBM *DEL* > P90 (18.95 kNm)

Statistic	NREL FBM *DEL* (kNm)	AeroStar FBM *DEL* (kNm)	Ri_{TL}	Hub U (m s^{-1})	Hub u_* (m s^{-1})	Hub σ_w (m s^{-1})	Coherent Structures		
							T_{coh} (s)	Peak E_{coh} (m^2 s^{-2})	N_{coh}
Mean	19.77	18.50	0.020	12.90	1.360	2.323	58.46	18.28	43
Median	19.60	17.88	0.016	12.93	1.356	2.257	55.43	16.80	42
Standard Deviation	0.784	1.501	0.015	0.813	0.151	0.203	13.11	4.46	9

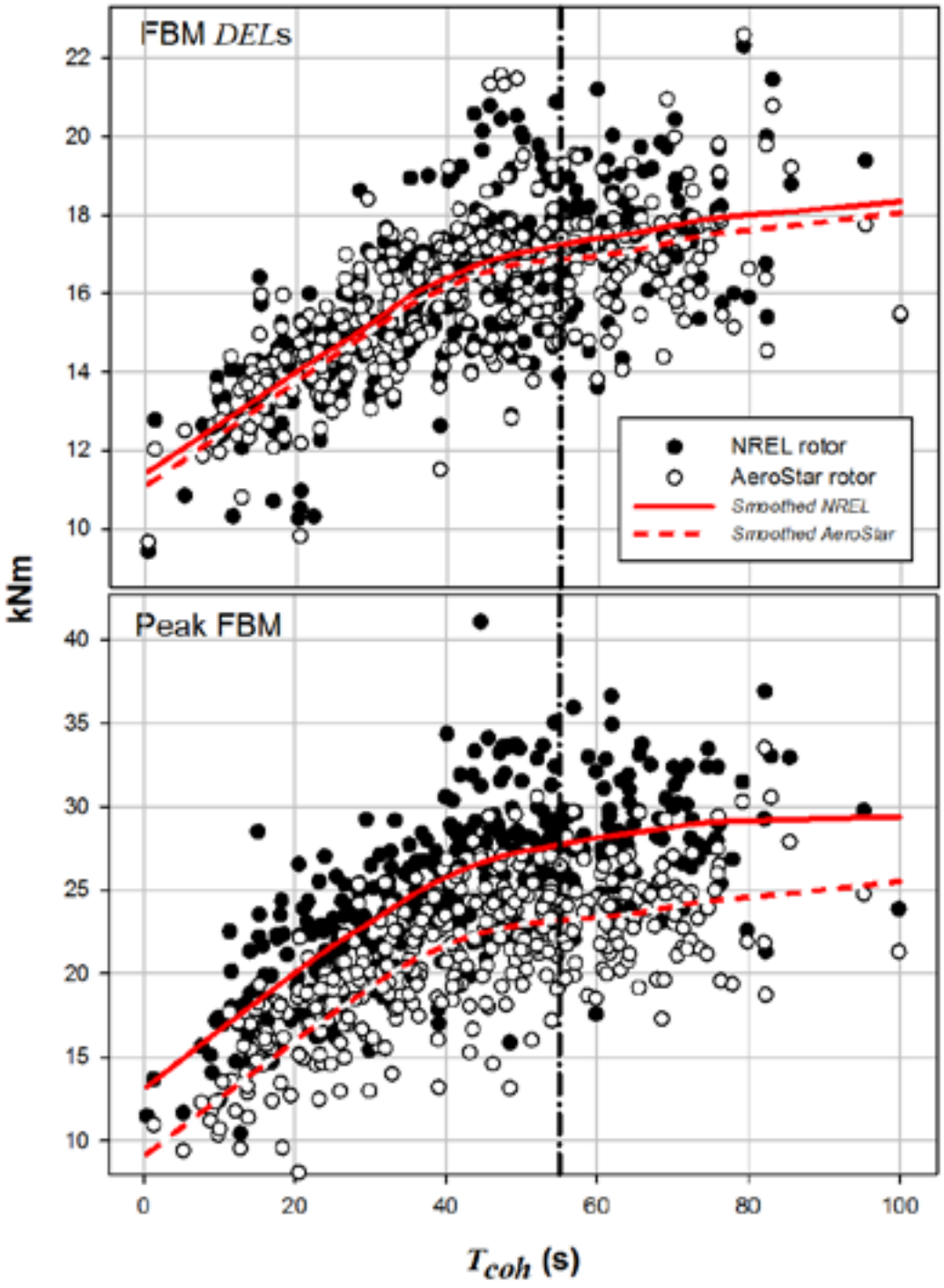

Figure 7-19. Observed variations of Micon 65/13 FBM *DEL*s and peak values with total length of coherent structures (T_{coh}) in a 10-minute record. The vertical dot-dashed line indicates the median T_{coh} value associated with records with the NREL rotor FBM *DEL* > P90. The red solid and dashed trend lines represent LOESS smoothing with a 0.5 overlap.

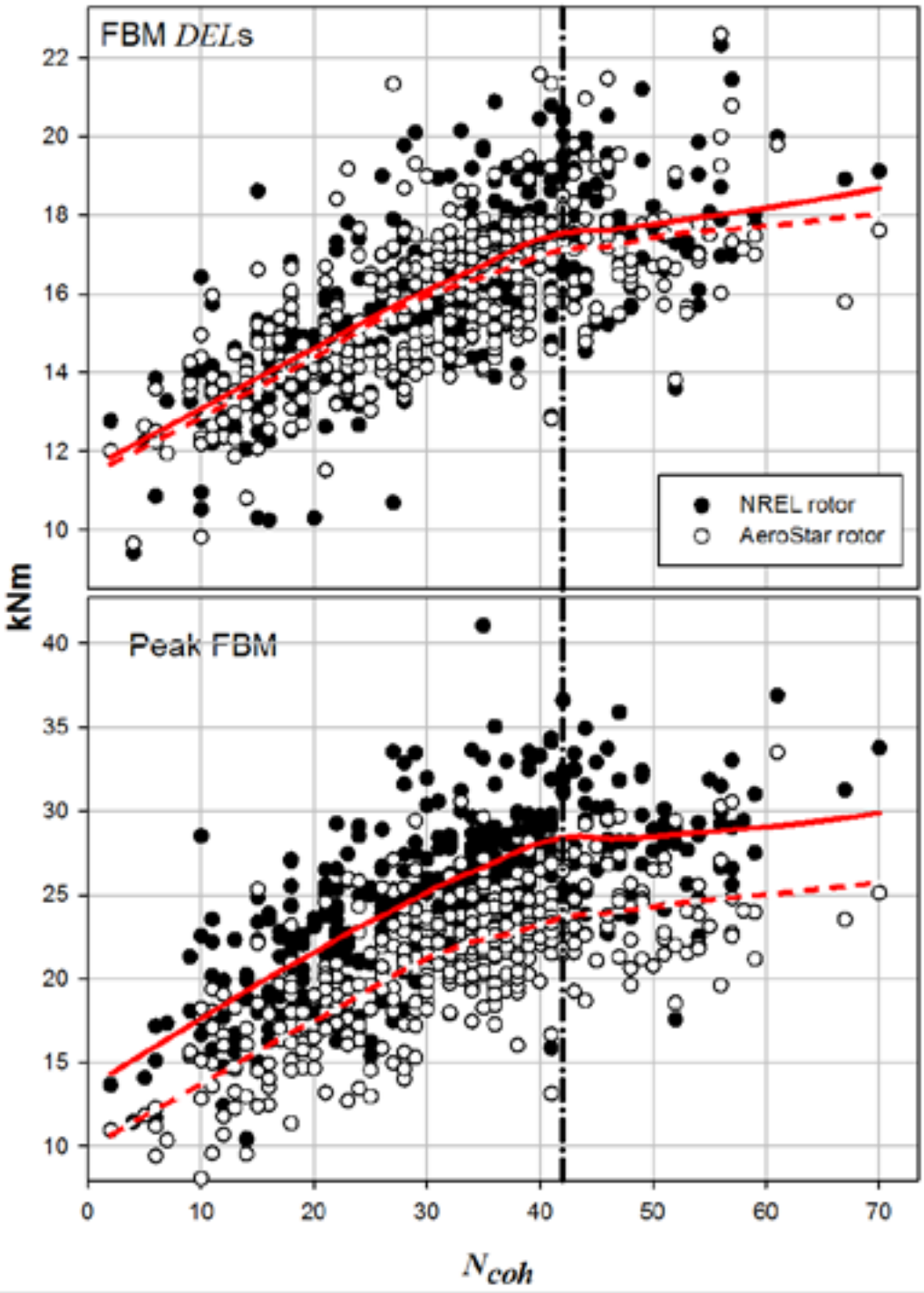

Figure 7-20. Observed variations of the Micon 65/13 FBM *DEL*s and peak values with number of coherent structures (N_{coh}) in a 10-minute record. The vertical dot-dashed line indicates the median N_{coh} value associated with records with the NREL rotor FBM *DEL* > P90.

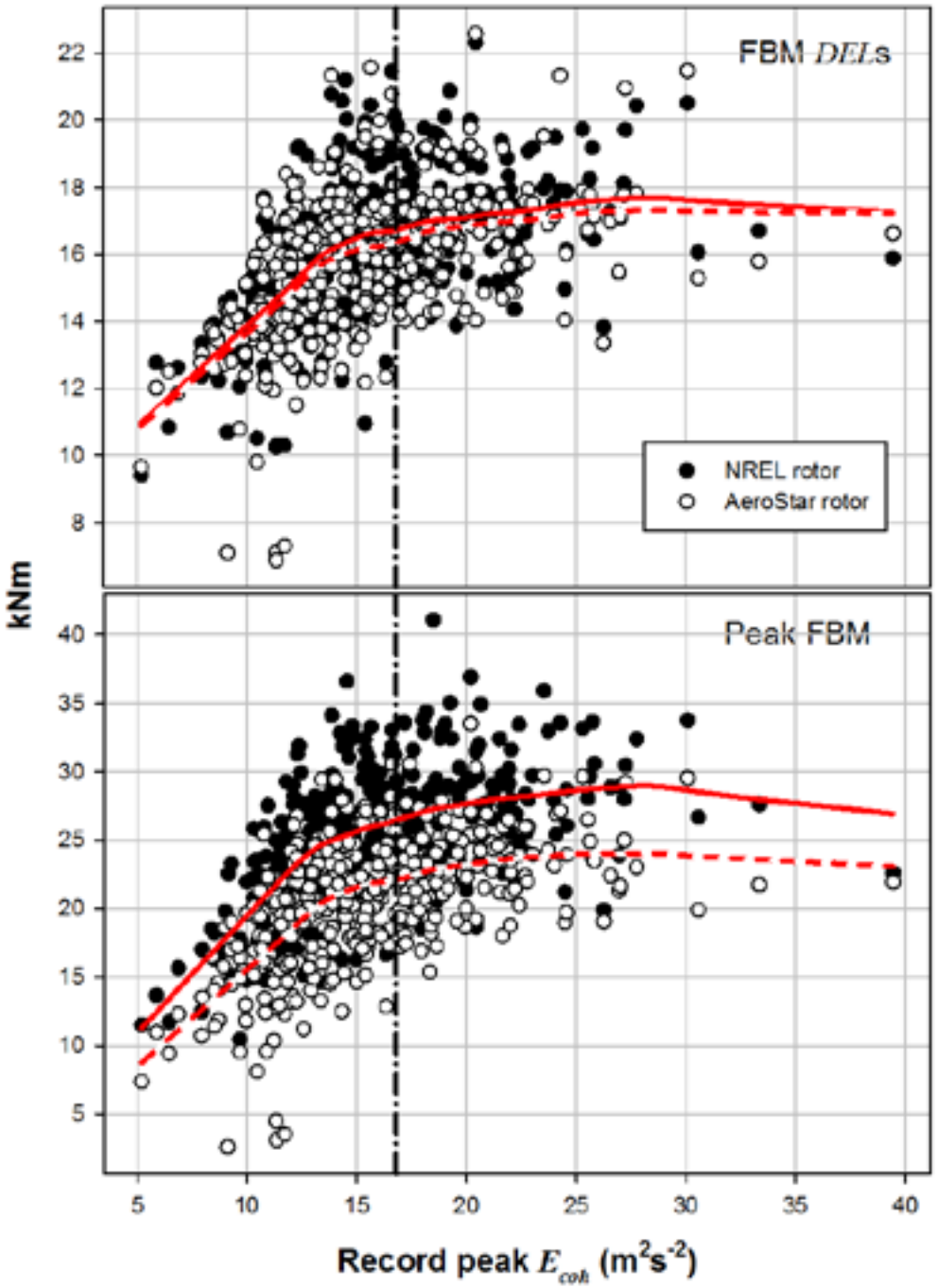

Figure 7-21. Observed variations of Micon 65/13 FBM *DEL*s and peak values with intensity (peak E_{coh}) found in coherent structures within a 10-minute record. The vertical dot-dashed line indicates the median peak E_{coh} associated with records with the NREL rotor FBM *DEL* > P90.

We annotated Figures 7-19, 7-20, and 7-21 with vertical dot-dashed lines corresponding to the medians of T_{coh}, N_{coh}, and peak E_{coh} listed in Table 7-6. In all cases the change in the observed trends in the slopes of these variables with the turbine responses occurs near the medians associated with the largest 10% turbine fatigue loads. This indicates that the turbine responses in the high loading tail become less sensitive to one or more of the dynamic characteristics of the coherent structures the turbine blades are encountering. To understand what such characteristics may be, we plotted the variation of the buoyancy length scale normalized by the NREL rotor diameter (L_b /D) as a function of Ri_{TL} in Figure 7-22, in which a decaying exponential curve has been fitted. We annotated this chart with the P25-P50-P75 of the measured Ri_{TL} values associated with the FBM high loading tail summarized in Table 7-6. The fitted curve and the median of the Ri_{TL} values in the high loading tail intersect at a value of L_b /D of one; i.e., the buoyancy length scale is equivalent to the rotor diameter. We know from our previous discussion in Section 6.2.2 that the buoyancy length scale is the spatial equivalent of the fastest-growing K-H instability mode and the source of the greatest dynamic response in the turbine, as depicted in Figure 6-7. Going further, in Figure 7-23 we plotted the variation of the measured coherent structure intensities (maximum value of E_{coh} in a 10-minute record) with L_b/D. We added a LOESS-smoothed trend line in red and the median value of the peak E_{coh} associated with the high loading tail in Table 7-6 as a horizontal dot-dot-dashed line. This line intersects with the smooth trend line within the indicated circle at an L_b /D value of 1, which also is the fastest growing K-H mode with dimensions of the rotor diameter. So the source of the inflection points in Figure 7-21 reflects the change from coherent structures associated with L_b /D from less than to greater than one, i.e., the fundamental or fastest-growing K-H modes with scales smaller than the rotor diameter to larger with the perfect coupling at L_b /D = 1.

Table 7-7 summarizes the turbulence and coherent structure parameters taken from the San Gorgonio/Micon data set for an L_b/D range of 0.95 to 1.05. This table shows for such conditions the mean wind speed into the turbine would be near rated for the NREL turbine and below rated for the AeroStar. Although there would be near-perfect to perfect coupling with K-H billows for the NREL rotor, it would not be optimum for the AeroStar rotor, which is in part why Table 7-6 shows the lower loads for it.

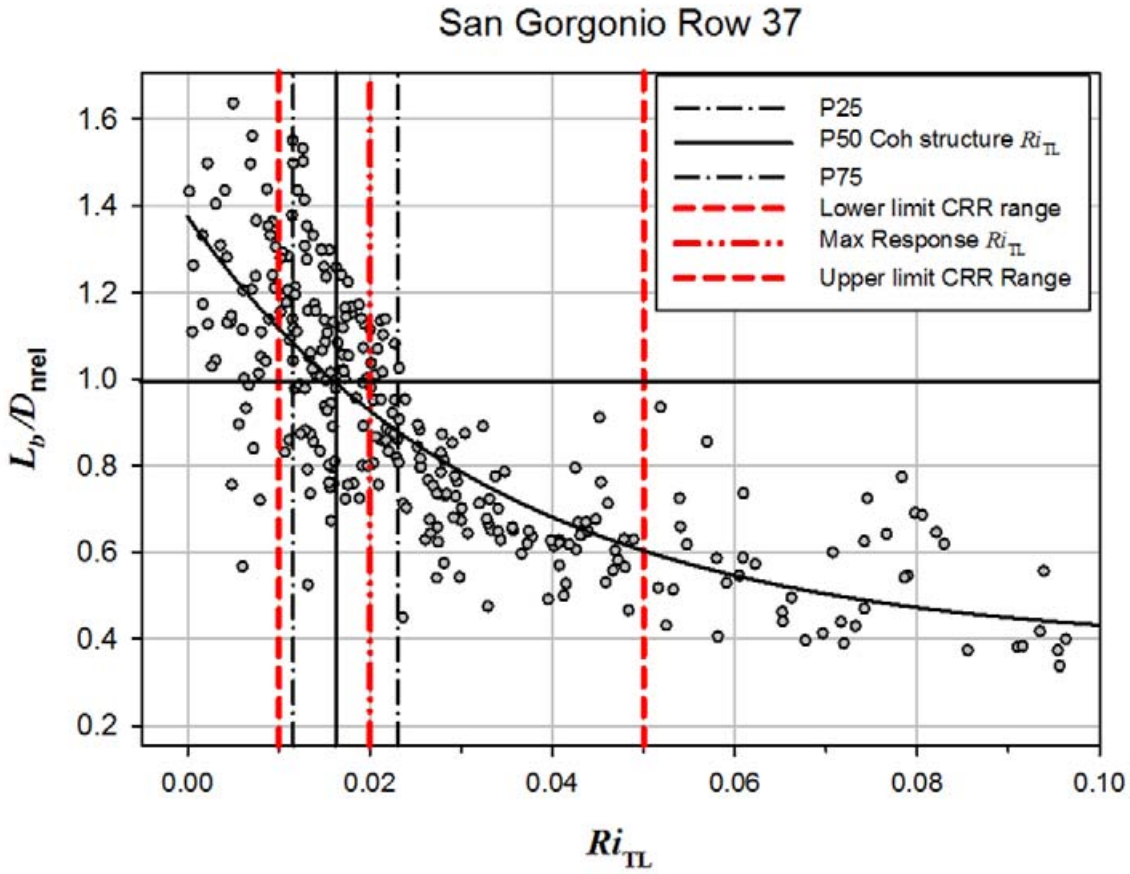

Figure 7-22. Variation of L_b/D ratio for Micon 65/13 (NREL rotor) with Ri_{TL}. The black vertical lines indicate the P25-P50-P75 range of the Ri_{TL} associated with the high loading tail (FBM *DEL* > P90). The stability classes and the max response Ri_{TL} = +0.02 are also as red vertical lines. Note that at the median Ri_{TL} value of +0.016 in Table 7-6, the L_b/D ratio for the NREL rotor is 1 or the buoyancy length scale is equivalent to the rotor diameter. This indicates that the fastest growing K-H mode is the same scale as the rotor diameter and a source of the high fatigue loads.

Table 7-7. Inflow Turbulence Parameters and Coherent Structure Characteristics from San Gorgonio Row 37 Data Set for $0.95 < L_b/D_{nrel} < 1.05$

Statistic	Ri_{TL}	Hub U ($m\ s^{-1}$)	Hub u_* ($m\ s^{-1}$)	Hub σ_w ($m\ s^{-1}$)	L_b/D_{nrel}	L_b/D_{aero}	T_{coh} (s)	Peak E_{coh} ($m^2\ s^{-2}$)	N_{coh}
Mean	0.018	11.91	1.272	2.270	1.000	1.063	51.78	17.02	37
P25	0.016	10.92	1.118	2.172	0.980	1.041	43.56	14.71	33
Median	0.016	12.16	1.302	2.220	1.002	1.065	49.24	16.05	39
P75	0.020	12.79	1.419	2.364	1.020	1.084	61.29	18.44	41
Standard Deviation	0.006	1.117	0.234	0.183	0.028	0.030	12.56	3.52	7

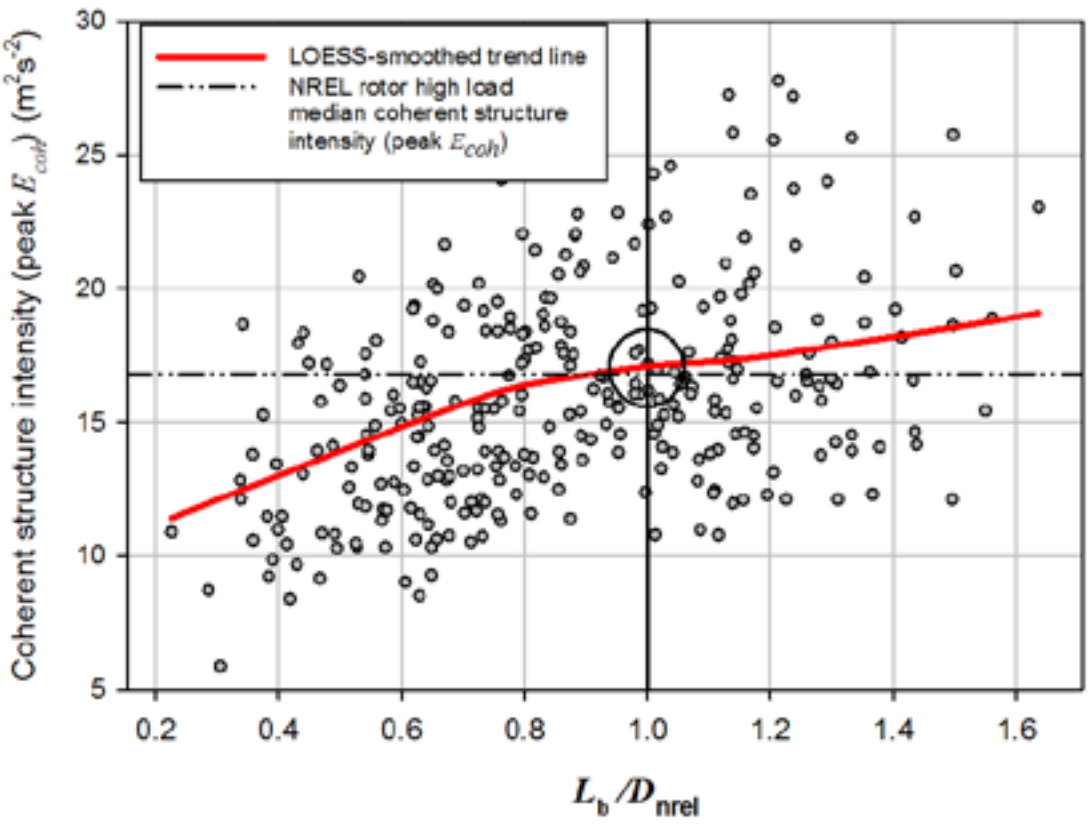

Figure 7-23. Observed variation of intensity of the coherent structures (peak E_{coh}) within a 10-minute record as a function of buoyancy length scale L_b normalized by Micon 65/13 NREL rotor diameter. The median of the peak E_{coh} (16.80 $m^2 s^{-2}$) in Table 7-6 for the high loading tail shown by the dot-dot-dashed horizontal line. This value intersects with the LOESS-smoothed trend line at a L_b/D ratio of 1 as highlighted by the circle.

7.8 Observed Coherent Structure Characteristics

Figure 7-24 plots the measured probability distributions of peak E_{coh}, T_{coh}, and N_{coh} for the three locations within the California wind farm (upwind of Row 1, upwind of Row 37, and downwind of Row 41), upwind of the NWTC ART, and on the LLLJP 120-m met tower. In Figure 7-25 we plotted the corresponding probability distributions of the local mean U-velocity component, the shear stress or u_*, and the standard deviation of the vertical velocity component σ_w. As would be expected, the characteristics of the coherent structures upwind and within the wind farm vary with the location, as do the three turbulence parameters, $\overline{U}$, u_*, and σ_w. The most energetic structures occur at the NWTC and the least energetic at the Lamar site. Figure 7-25 shows that the wind farm is distinguished by the significant spatial heterogeneity, which influences the characteristics of the coherent turbulent structures. Compared with the Lamar site, the vertical heterogeneity of the NWTC (seen particularly in the local friction velocities [u_*] and the vertical wind field [σ_w]) is responsible for the energetic characteristics of the coherent structures. Figure 7-26 shows that for the NWTC site, the greater the length of coherent structures within a 10-minute record, the greater the intensity.

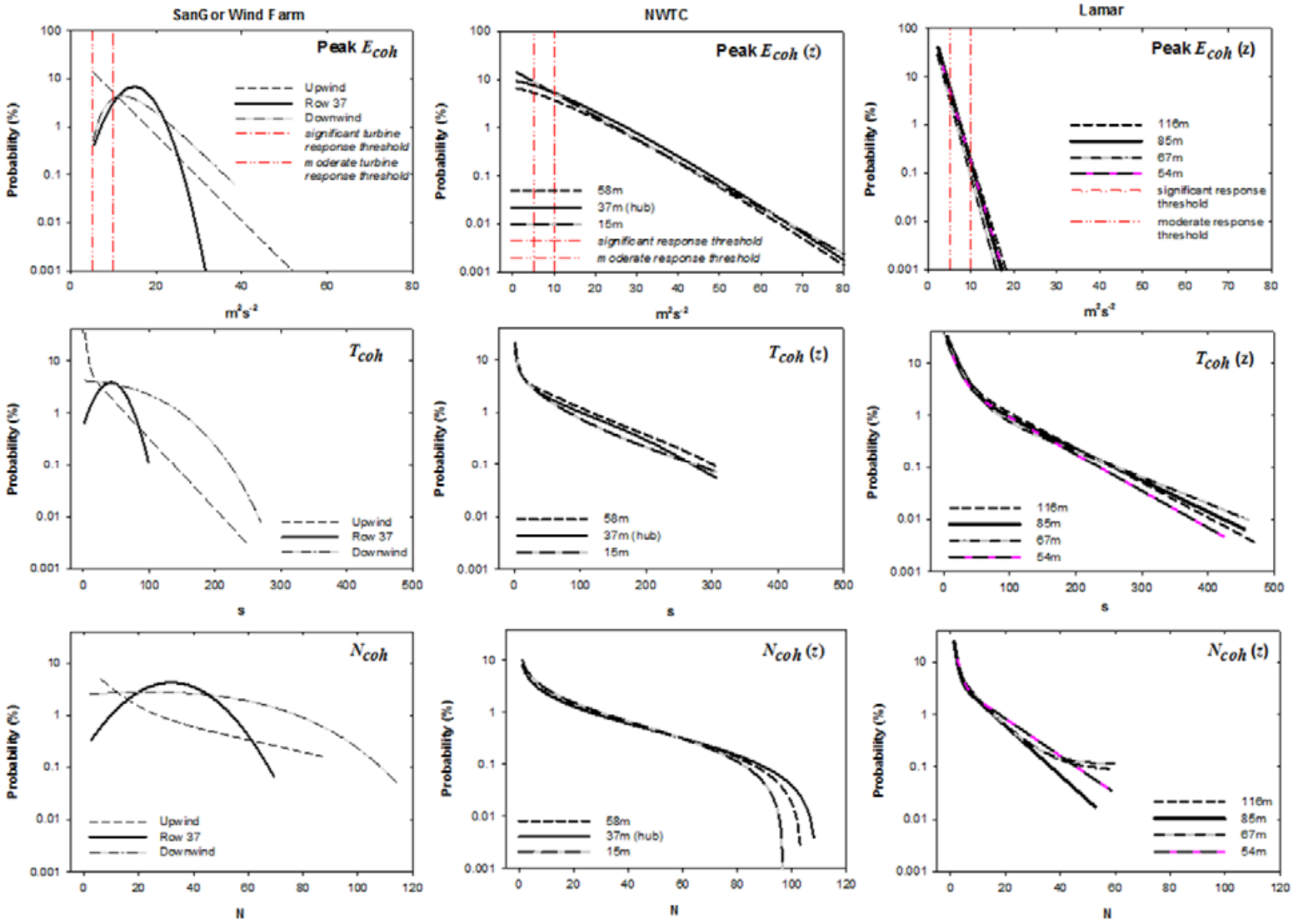

Figure 7-24. California wind farm, NWTC, and Lamar probability distributions of measured coherent structure characteristics with 10-minute records: intensity (peak E_{coh}), total length (T_{coh}), and number of structures (N_{coh})

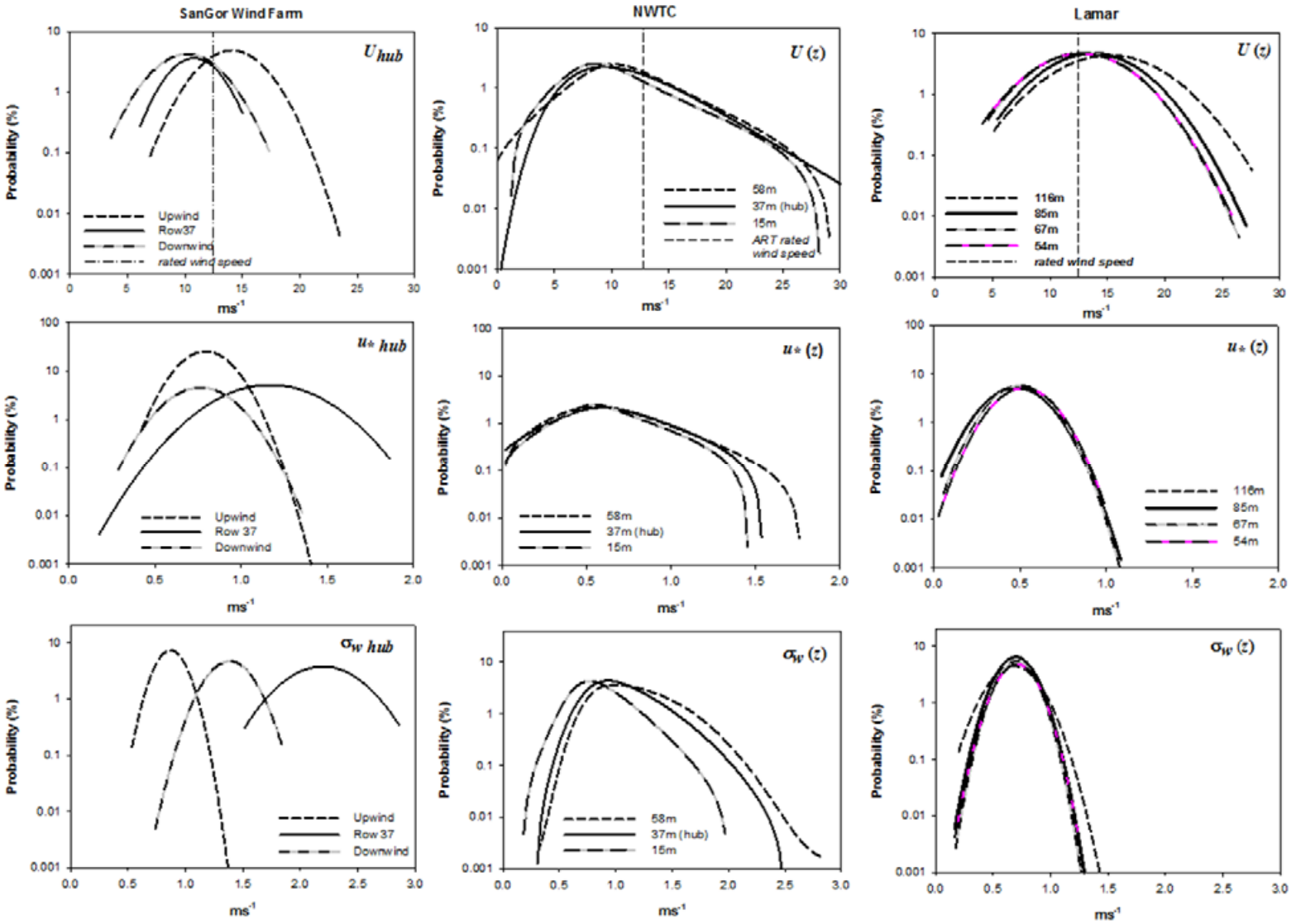

Figure 7-25. California wind farm, NWTC, and Lamar probability distributions of local U, friction velocity u_*, and vertical velocity standard deviation σ_w corresponding to measured coherent structure characteristics in Figure 7-18

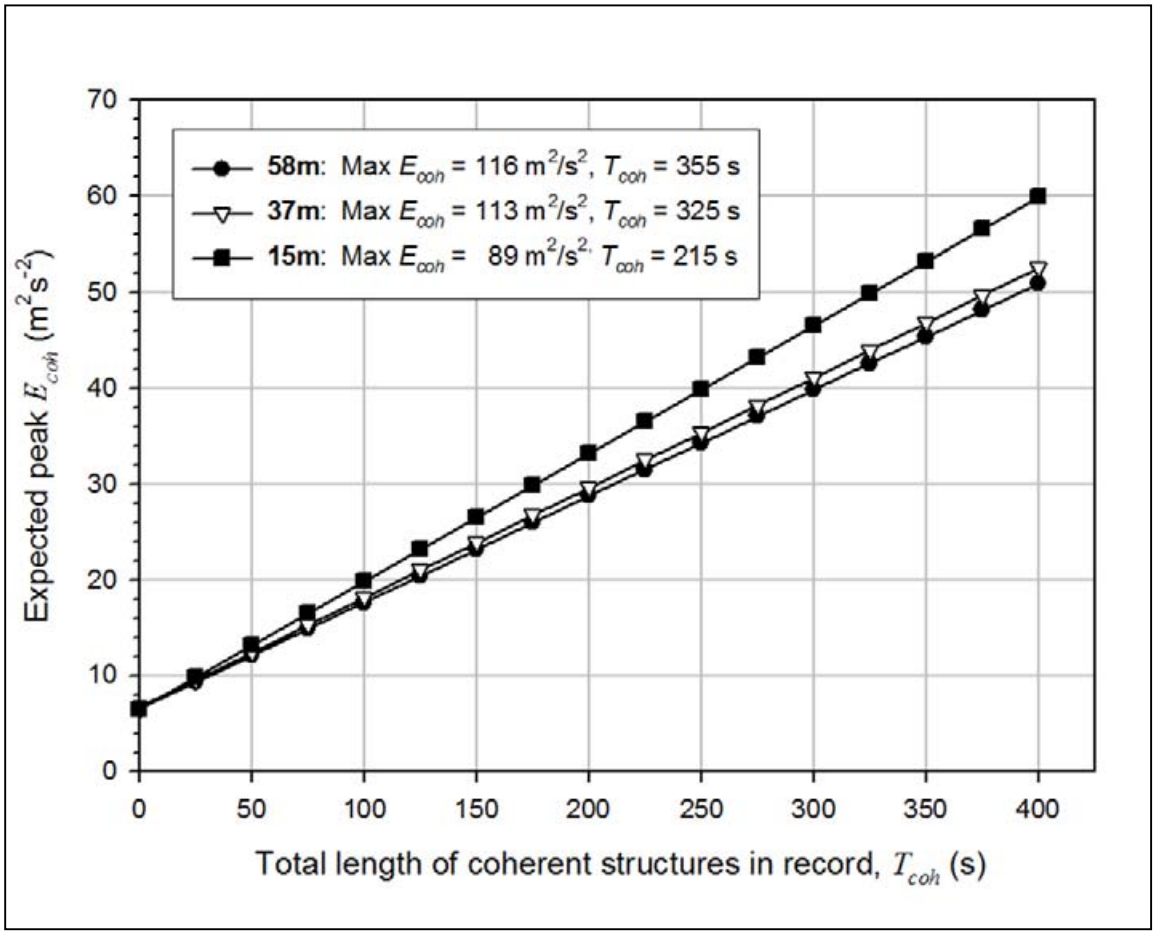

Figure 7-26. NWTC measured variation of peak E_{coh} with T_{coh} within a 10-minute record

To apply the distributions of coherent structures in TurbSim, we need to scale the rate parameter λ (or equivalently $IAT = 1/\lambda$) in Equation 7-2 to accommodate the inhomogeneous Poisson distribution model. Our analysis has shown that $\lambda = f[U(z), Ri_{TL}]$ are the dominant scaling parameters. In Figure 7-27 we summarize the variations of IAT as a function of the local mean U velocity and Ri_{TL} for the three locations in the wind farm, the NWTC, and the Lamar site. For the wind farm, both velocity and stability vary greatly. Comparing the San Gorgonio upwind location with the NWTC and Lamar sites, we see that the variations with both velocity and stability are similar because they were measured in naturally occurring flows. Although the NWTC has a large degree of variation , probably because of the high level of flow heterogeneity within the ART rotor disk, the distributions with stability are similar for all three sites, i.e., much shorter IAT in and near the CRR stability range compared with longer periods outside of it. The natural flows have distinct variations in IAT with velocity. At lower wind speeds the periods are

longer and there is more variation, but there is a point at all three sites where the *IAT* suddenly becomes much shorter and has less variation. The *IAT*s for the NWTC and Lamar site asymptotically approach the same value of 70 seconds for wind speeds greater than 20 m s^{-1} and more than four times shorter than the *IAT*s seen at 5 m s^{-1}.

As turbine rotors increase in diameter and their hub heights ascend deeper into the atmospheric boundary layer, it is important to determine the coherent structure scaling parameters with these increased elevations. To date, our measurements from these greater heights come from the LLLJP and its 120-m tower. We plotted contours of the *IAT* and N_{coh} as functions of the local velocity U and turbine layer stability Ri_{TL} for 54, 67, 85, and 116 m in Figure 7-28. To see how the maximum T_{coh} varies with height, we summarize the data from all three sites in Figure 7-29. Although lengths of coherent structures are relatively short at the wind farm, the variations with height in the natural flows from the NWTC and the Lamar site are very consistent.

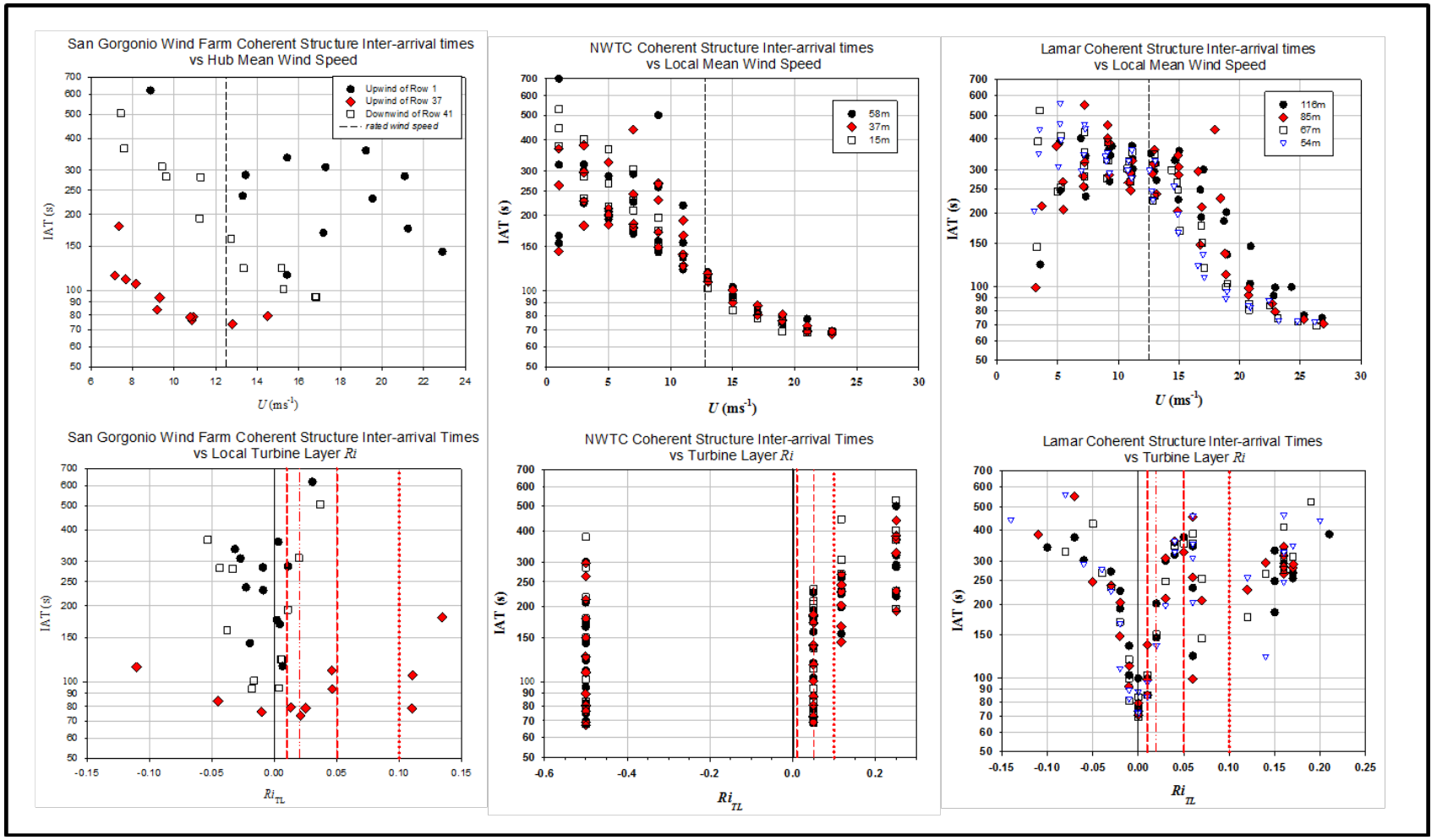

Figure 7-27. Variations of coherent structures *IAT* with local *U* velocity and Ri_{TL} for upwind of Rows 1 and 37 and downwind of Row 41 in California wind farm; at 15-, 37-, and 58-m heights at NWTC; and at 54-, 67-, 85-, and 116-m heights at LLLJP site. The vertical dashed lines in the upper row represent the nominal rated wind speeds and those in the lower row represent the stability classifications.

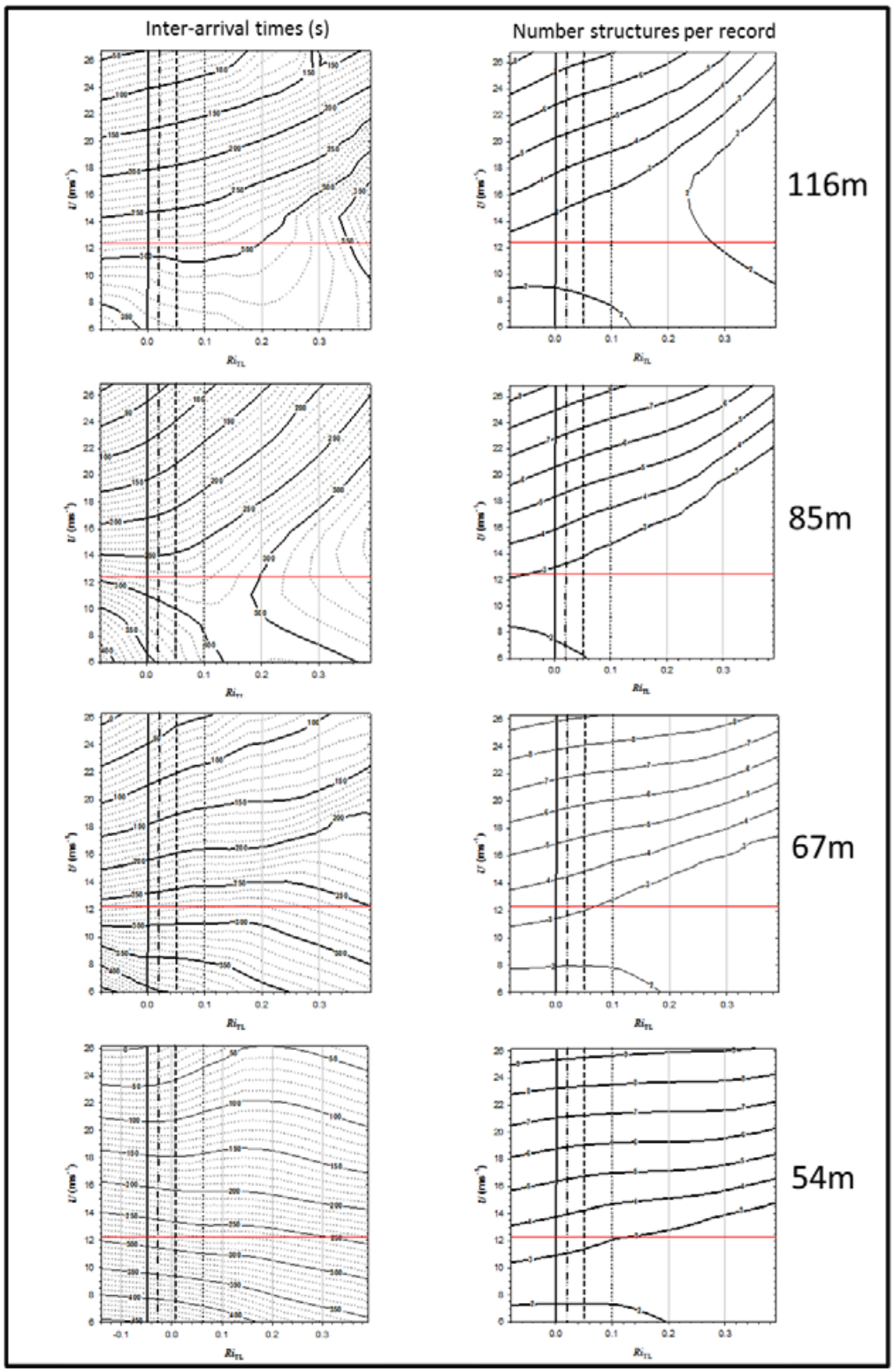

Figure 7-28. Variations of *IAT* and N_{coh} with height and local *U* velocity and Ri_{TL} at LLLJP site. The horizontal red line represents a nominal turbine rated wind speed of 12.5 m s^{-1} and the vertical black lines represent the stability classifications.

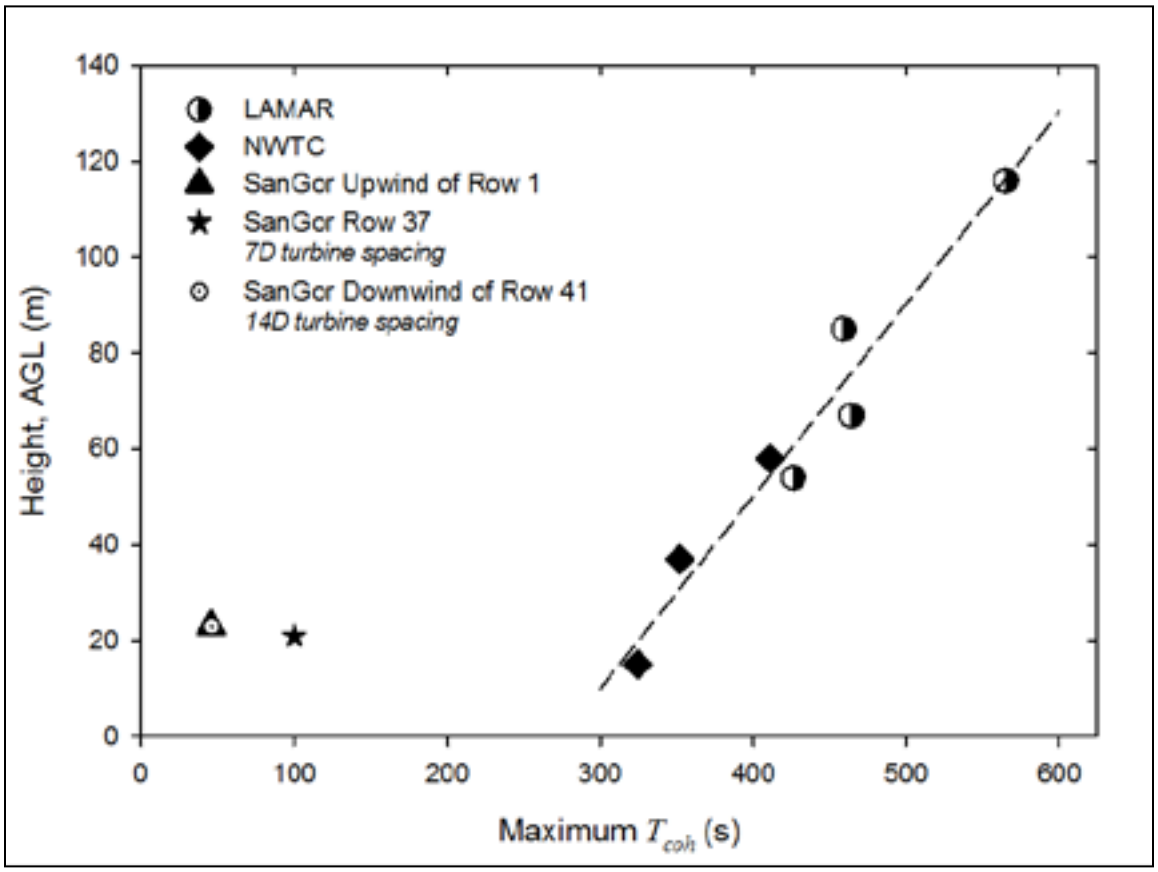

Figure 7-29. Observed variation of maximum T_{coh} as function of height for California wind farm, NWTC, and LLLJP sites

8.0 Supporting the Extension of Larger Turbine Rotors to Higher Elevations in the Great Plains Operating Environment

As we've noted, the trend has been toward larger turbine rotors with the higher hub heights to take advantage of better wind resources. This is particularly true over much of the Great Plains, which contains the greatest resource in the United States. The northern plains benefit from the winter storm tracks that bring strong winds to these regions. In the southern plains, however, the best wind resources occur in the warmer months from April through September, but generally at night. This nighttime low-level jet (LLJ) of air occurs from West Texas northeastward into northwest Iowa and southwest Minnesota. This excellent nocturnal wind resource arises from diurnal atmospheric boundary layer dynamics that create a low-level, higher speed region of wind flows between 70 and about 500 m above the ground.

Because of the fundamental thermodynamic diurnal cycle in the atmospheric boundary layer, such nocturnal wind systems are far more prevalent beyond the Great Plains, though they often are more localized, such as in and around terrain features with at least moderate changes in elevation. In addition, such nocturnal flows have lower frequencies of occurrence and strengths. They do all have in common, however, often intense vertical wind speed and sometimes directional shears within the height elevations or layer of multimegawatt wind turbine rotors. Increasingly warmer temperatures usually accompany this increase in wind speed with height , creating a statically stable environment below the height of the wind speed maximum. When these vertical temperature and wind speed gradients are combined, they define the degree of dynamic instability that exists, which can be quantified by the gradient Richardson number (*Ri*). As we have seen, the relative strengths of the negative buoyancy associated with a stable environment and the turbulent energy contained within the sheared wind flow determine if turbulence will be generated and, if so, its intensity and spatial characteristics. We showed that given the right vertical variations in temperature and wind speed, Kelvin-Helmholtz Instability (KHI) can develop and create organized or coherent turbulent patches that induce undesirable dynamic responses in wind turbine structures.

Although no concurrent turbine measurements were available during the Lamar LLJ Project (LLLJP), we now can interpret these results based on we learned from the field campaigns in the San Gorgonio wind farm and its Micon 65/13 turbines and the Advanced Research Turbine (ART) at the National Wind Technology Center (NWTC). These discussions will be useful to the wind turbine community because they represent the interpretation of atmospheric conditions seen by the current deployment of large, multimegawatt turbines at heights much higher than previously had been available. As we discuss later, we attempted to create a comprehensive simulation of this inflow conditions with the Great Plains Low Level Jet, or GP_LLJ, spectral model in the TurbSim stochastic simulator code.

8.1 Interpreting LLLJP Results

In our previous discussions we have shown that the dynamic response seen in wind turbine structures to the turbulent inflow results from the ingestion of organized or coherent patches of turbulence into the turbine rotors. We have shown that these patches of turbulence arrive in a rotor inflow after evolving directly upstream as well as being created at heights outside of the rotor layer and then carried into it by vertical motions.

8.1.1 Analyzing the Lamar Measurement Database

We analyzed the year record from the 120-m LLLJP met tower for 1600 to 0800 LST in terms of the key turbulence scaling parameters that we identified using the Micon turbine and ART inflow measurements and dynamic responses. These include the hub-height mean wind speed, the mean shear, and shearing stress (u_*) across the vertical dimensions of a GE 1.5-MW turbine rotor disk stratified by stability classification. After removing records that did not pass our stringent quality control criteria and where the flow was coming through the tower, we were initially left with 28,594 ten-minute records. This figure represents 82% of the records that would be expected if no data were lost and if quality control and flow distortion considerations were ignored. To make the statistical analyses more meaningful, we retained only records in this reduced data set in which a turbine would be operating, which is a hub-height (85-m) mean wind speed between an approximate cut-in of 3.5 m s^{-1} and cutout of 25 m s^{-1}. This further reduced the final data volume available for analysis to 27,544 records, or 79% of those expected. In Table 8-1 we summarize the distribution of this final data volume by stability class. One would expect the important CRR stability class to occur about 5% of the time at this site. We did not analyze the records when $Ri_{TL} \geq +1.0$ because the data became highly suspect owing to very unsteady flow conditions that created observational issues of one sort or another. We also chose to ignore the most unstable classification STC01 because so few records were available.

Table 8-1. Distributions of LLLJP Nocturnal Data Records by Stability Class after Applying Described Constraints

Stability Class	Stability Range	Records	Hours	Percent
STC01	$-1 \leq Ri_{TL}$	299	50	1.2
STC02	$-1 < Ri_{TL} \leq 0$	2040	340	8.4
CRR	$+0.01 \leq Ri_{TL} < +0.05$	**1225**	**204**	**5.0**
CRRH	$+0.05 \leq Ri_{TL} < +0.10$	2888	481	11.8
STC04	$+0.10 \leq Ri_{TL} < +0.25$	6359	1060	26.1
STC05	$+0.25 \leq Ri_{TL} < +1.0$	7504	1251	30.8
	$Ri_{TL} \geq +1.0$	3944	657	16.2

We saw in our analysis of the Micon 65/13 turbines and the ART that their dynamic response is strongly correlated with peak E_{coh} because of the coherent characteristics of KHI turbulence. Figure 8-1 plots the diurnal distribution of peak E_{coh} measured by the four sonic anemometers at 54, 67, 85, and 116 m on the LLLJP 120-m tower. Here the lower abscissa is calibrated in UTC time and the upper one is in equivalent local standard time (LST). The dynamic response thresholds found on the Micon turbines and the ART are indicated as a horizontal dot-dot-dashed line for the threshold response of 2 m^2 s^{-2}, a dashed line for the moderate response level 5 m^2 s^{-2}, and a solid line for significant response level of 10 m^2 s^{-2}. The highest levels of coherent TKE occur most frequently between local sunset and midnight (1700 to 0000 LST or 2300 to 0900 UTC), i.e., in the boundary layer day-night transition period. This is in agreement with the diurnal variations seen in the wind farm and at the NWTC. Although not as energetic as at the internal wind farm and NWTC sites, values of E_{coh} exceeding 20 m^2 s^{-2} do occur. Figure 8-2 displays the non-Gaussian cumulative probabilities of the peak E_{coh} at the four measurement heights. Coherent events with intensities greater than the significant response threshold level of 10 m^2 s^{-2} are more or less equally probable to occur 2% of the time. In contrast, moderate level responses or greater would occur 10% or more of the time.

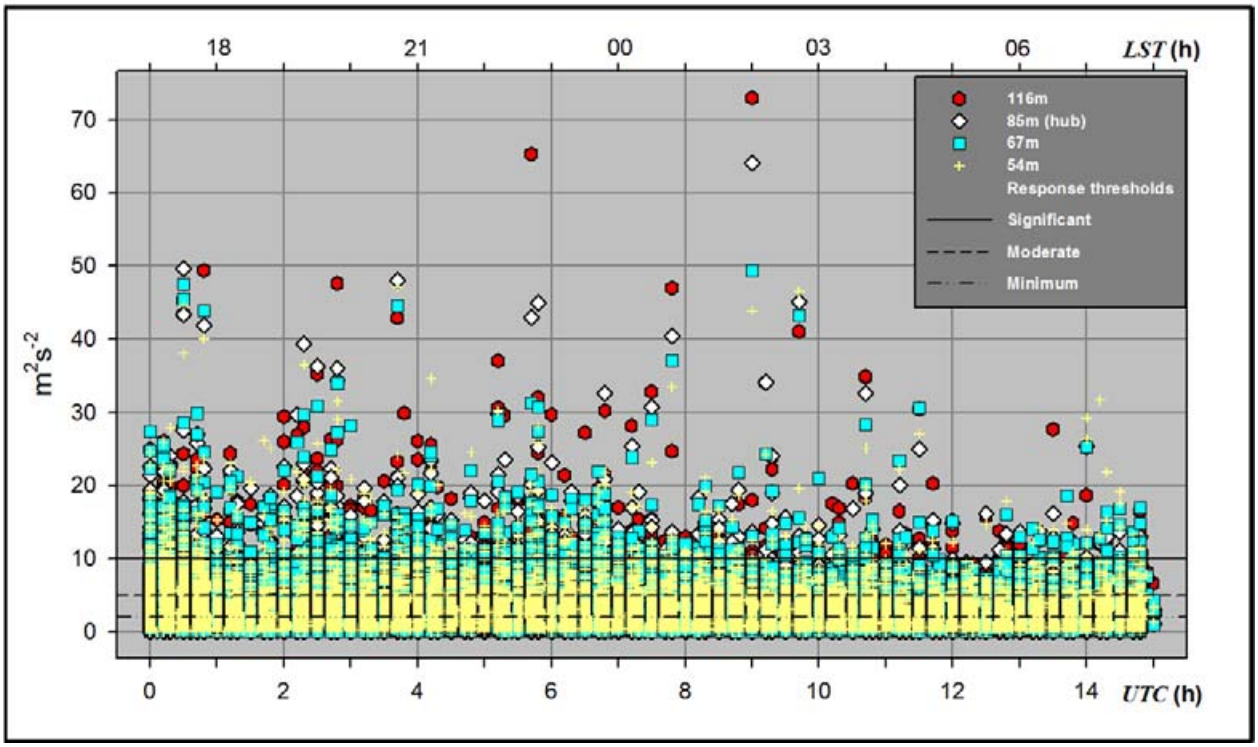

Figure 8-1. Diurnal distribution of observed 10-minute record peak E_{coh} values measured at 54-, 67, 85-, and 116-m heights on LLLJP 120-m turbine at 1700–0800 LST (0000–1500 UTC). The three turbine response thresholds measured on the Micon 65/13 turbines and the ART are shown as the dashed and solid horizontal lines.

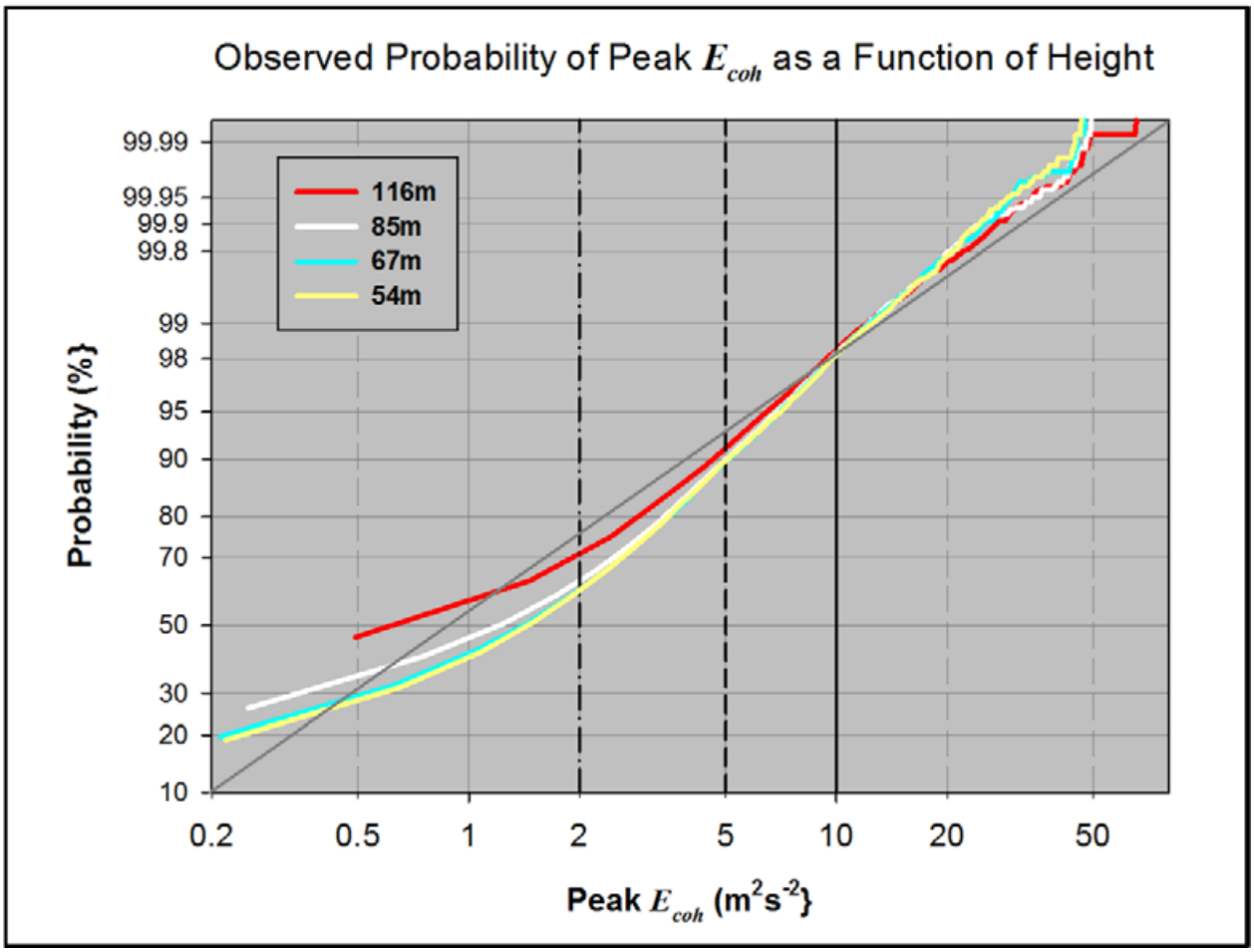

Figure 8-2. Observed LLLJP probability distributions of peak E_{coh} over 54- to 116-m layer. The dot-dashed, dashed, and solid vertical lines indicate the threshold (2 m^2 s^{-2}), moderate (5 m^2 s^{-2}), and significant (10 m^2 s^{-2}) dynamic response levels seen on the turbines.

Because the stability of the turbine layer is a major factor in the scaling of the turbulence and the subsequent turbine dynamic response, with the critical Richardson number range, or CRR, being the most important, we examine the cumulative probability distribution of Ri_{TL} in Figure 8-3. Here the CRR stability range is indicated by the pair of vertical dashed lines. The inset on the upper left indicates that CRR conditions existed during 285 hours or 7% of the aggregate filtered record length. The combined ranges of the CRR and CRR High, or CRRH, classes form the STC03 classification, which we used when we developed the TurbSim Code; it occurs 20% of the time. Within the CRR range we see in Figure 8-4 that the most prevalent intensity of coherent events is at the moderate turbine dynamic response level. Events with intensities greater than the significant response level occur more often, however, than would be expected if the distribution were normally distributed.

We now plot in Figures 8-5 and 8-6 for the stability classifications the cumulative percentile distributions of both the key scaling parameters and the associated turbulence characteristics that we previously showed are important in determining the level of turbine dynamic response. As we saw previously in the wind farm and at the NWTC, the highest hub-height mean wind speeds are associated with the CRR class, as shown in Figure 8-5a. This means, of course, with the stronger background flow more energy is available to create more intense levels of KHI turbulence and greater turbine dynamic responses. The strong vertical mixing associated with such turbulence reduces the vertical shear, as is shown by the rotor disk shear exponent distributions in Figure 8-5b. Only the unstable STC02 class has lower shears; the remaining classes all exhibit significant values. This transfer of energy from the background flow into turbulence by the KHI is documented by the rotor layer mean shear stress or u_* for the CRR range when compared with the other stability classes in Figure 8-5c. The frequent high levels of peak E_{coh} in Figure 8-5d demonstrate why larger turbine loads and fatigue exist in the CRR range. Figure 8-5d also reveals that the KHI mechanism can create larger variations in the vertical velocity in this stability range than the large convective eddies seen in the STC02 unstable class. We showed that the largest and most damaging loads occur in the CRR range when the buoyancy length scale normalized by the rotor diameter D is $L_b/D \approx 1$; this is demonstrated in Figure 8-5e. Here we highlight the P25–P75 (Q1–Q3) range over which the the L_b/D parameters varies from 0.5 to a bit more than 1. Even at L_b/D ratios of less than 1, some vibrational energy is likely to be transferred from the coherent turbulence into the turbine rotor, nacelle, and tower given the blade's second symmetric and asymmetric modes and numerous modal cross-couplings found in the eigenvalue analysis of the 1.5-MW WindPACT turbine listed in Table 7-2.

Turbulent fluxes or transports may not be uniform across the 1.5-MW turbine rotor disk and larger turbines, as is shown in Figures 8-6a and b. Here we see that L_b Q1–Q3 variation over the upper half of the turbine rotor is from 0.5 D to about 0.7 D with a median of 0.6 D. In the lower half it is from 1.0 D to about 1.15 D with a median of about 1.1 D. As we saw with the Micon turbines and the ART, the largest peaks in the mometum ($u'w'$) and buoyancy ($w'T'$) fluxes across the depth of the rotor are skewed downward, as indicated by the negative tail P01, P05, and P10 percentiles.

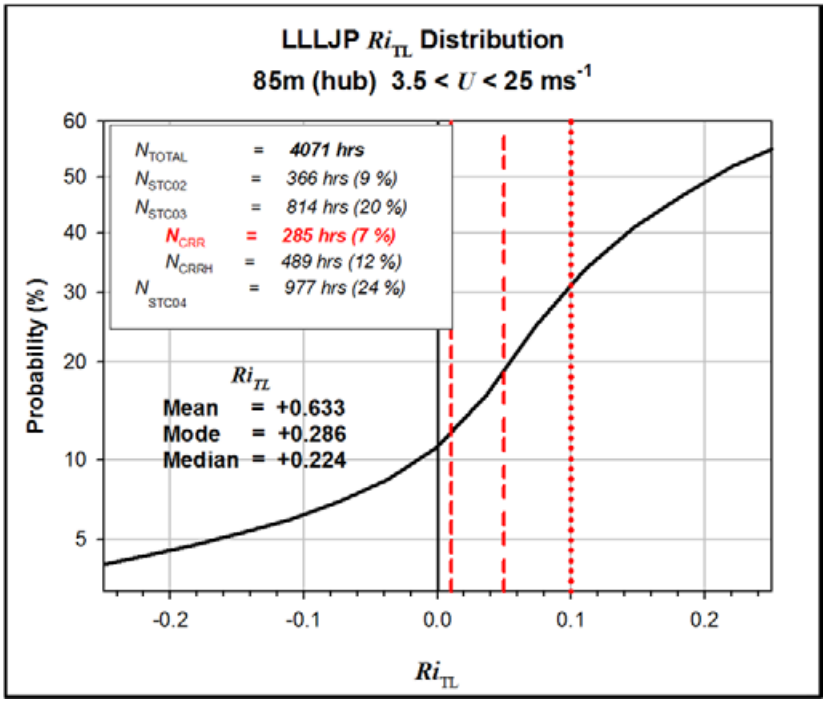

Figure 8-3. Observed LLLJP probability distribution of Ri_{TL} for filtered data set

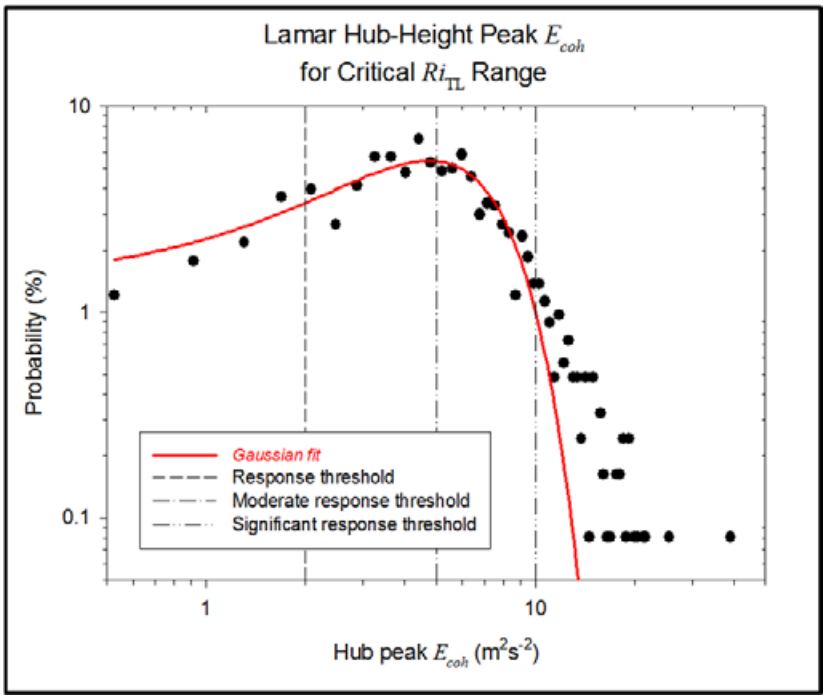

Figure 8-4. Observed LLLJP probability of hub-height peak E_{coh} within the CRR range. The dynamic response thresholds from the Micon turbines and the ART are shown as vertical dashed lines.

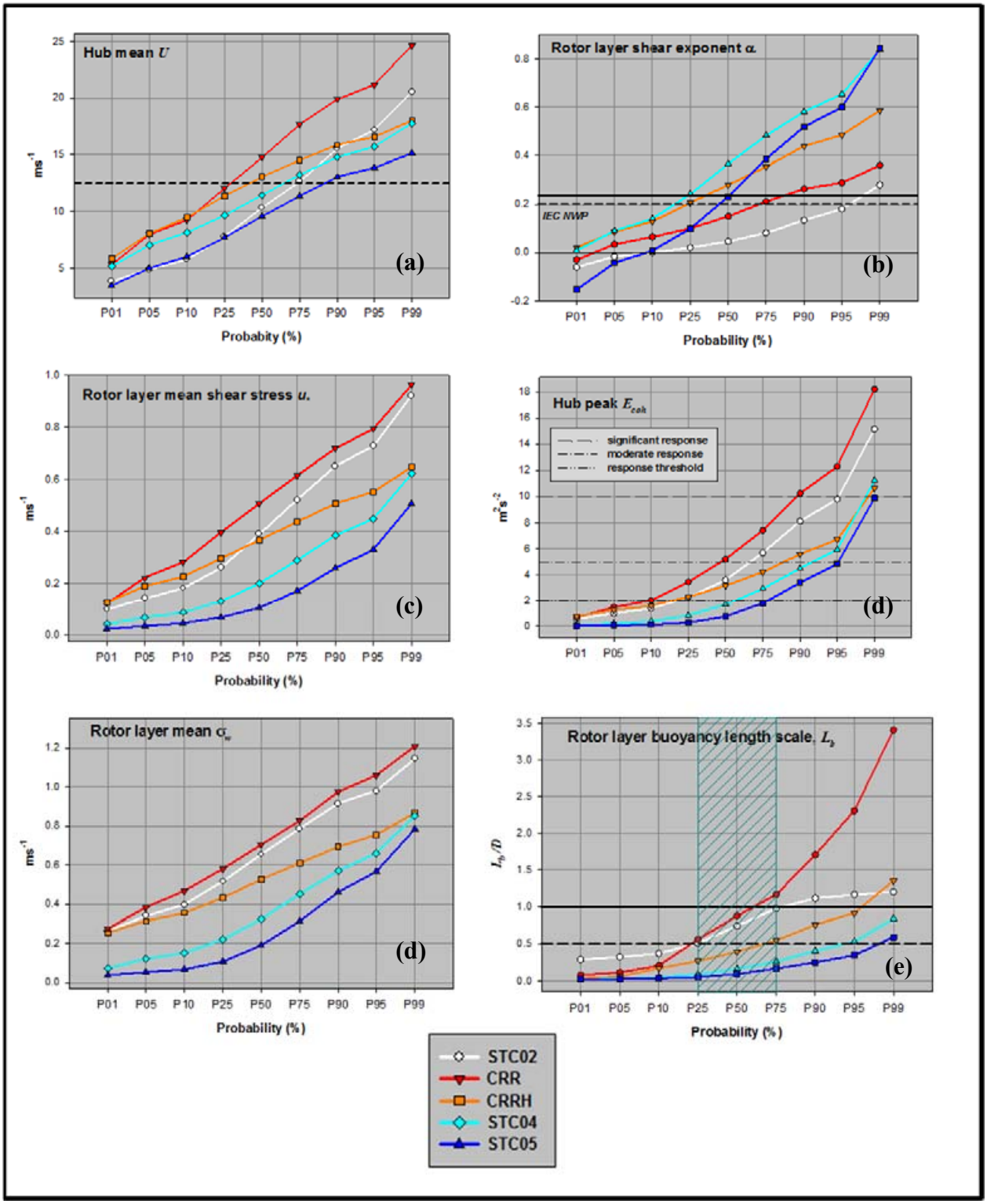

Figure 8-5. Observed LLLJP percentile probability distributions key scaling and turbulence parameters associated with turbine dynamic response for reduced analysis data set by stability class

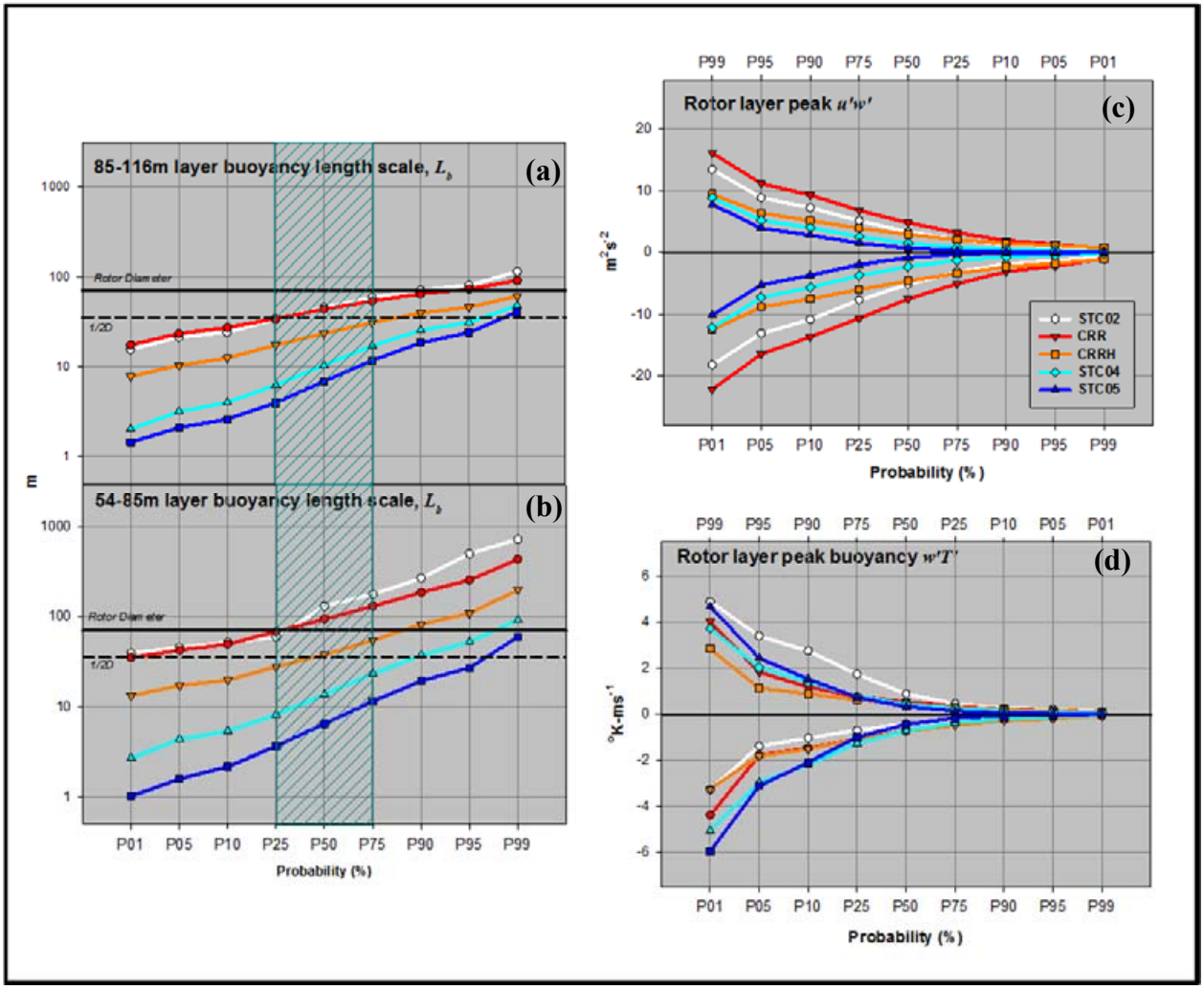

Figure 8-6. Observed LLLJP percentile probability distributions of variation by stability class of buoyancy length scale L_b in (a) upper half rotor disk (85–116 m) and (b) lower half (54–85 m). The cross-hatched areas indicate the P25–P75 (Q1–Q3) range. The distributions of the rotor layer peak momentum (*u'w'*) and buoyancy fluxes (*w'T'*) are shown in (c) and (d), respectively.

Intense vertical fluxes of E_{coh} are concentrated in the CRR range, as shown in Figure 8-7. Figure 8-8 displays an example of such fluxes beneath an LLJ. Here we present a portion of a fixed azimuth, vertical sector scan from the NOAA HRDL lidar taken between 18:11:12 and 18:11:34 MST (01:11:12 to 01:18:34 UTC) on September 15, 2003. Energetic turbulence is indicated within the layer that would be occupied by a GE 1.5-MW turbine rotor, with strong downward bursts of higher speed air indicated by the arrows. A series of K-H billows might exist between 50 and 70 m, with a horizontal wavelength of about 100 m.

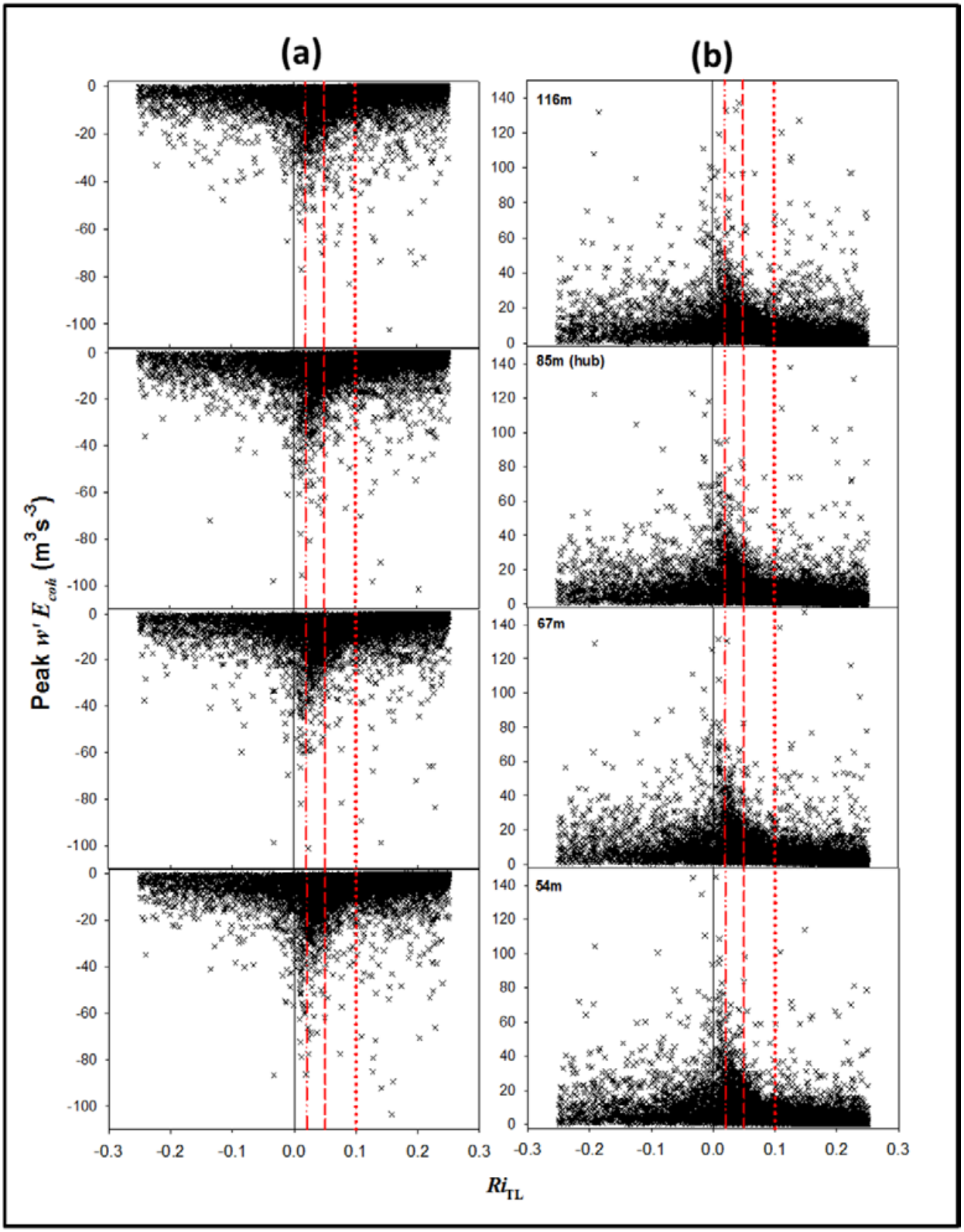

Figure 8-7. Observed peak instantaneous vertical fluxes of E_{coh} as function of height across WindPACT rotor disk: (a) downward and (b) upward

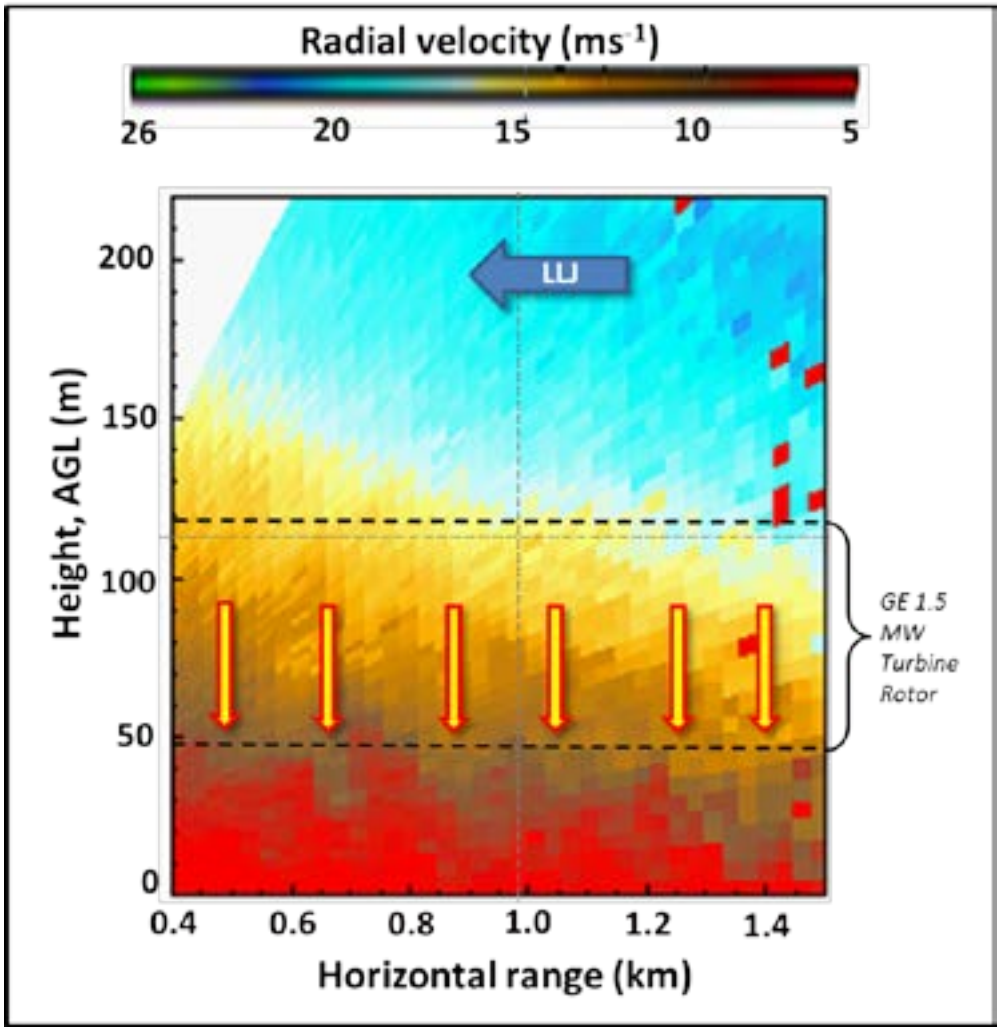

Figure 8-8. Portion of fixed azimuth, vertical sector scan measured by NOAA HRDL lidar on September 15, 2003, 18:11:12 to 18:11:34 MST. The vertical arrows indicate strong downward bursts of higher velocities into the shear layer below a 20-m s^{-1} LLJ at about 200 m, which would be occupied by a GE 1.5-MW turbine rotor. There is some indication that KHI also may exist.

8.2 Role of the Great Plains LLJ in Coherent Turbulence Generation and Transport within the Rotor Disk

We noted previously that the stable layer accompanied by intense shear beneath a low-level jet maximum velocity is a prime environment for the development of KHI and one of the major reasons for undertaking the LLLJP. The information that we gathered from this effort was used to develop the TurbSim GP_LLJ spectral model discussed in the next section.

In addition to collecting measurements from the LLLJP 120-m met tower, we needed to obtain vertical LLJ wind speed and direction profiles up to at least 500 m above ground level (AGL). As we will see, a jet maximum located well above the top of a wind turbine rotor can still have significant influence within the rotor disk and thus we need to examine this maximum height. The instrument used to obtain the velocity profiles was a midrange Scintec MFAS sodar programmed to measure the speed and direction over 20-m increments from 40 to 500 m. We also recorded the standard deviations of the horizontal and vertical wind components, though they are not always reliable, particularly the horizontal standard deviation. In Figure 8-9 we present an example of raw (circles) and smoothed (red lines) sodar-derived wind speed and direction profiles collected on September 9, 2002 at 0730 LST. The raw sodar profiles were smoothed with a Chebyshev polynomial recursively up to 10^{th} order. Met tower data were used to derive the profiles between the lowest sodar measurement and the lowest tower measurement (3 m). The chart on the right in Figure 8-9 indicates a measure of the sodar signal-to-noise ratio or confidence level for each measurement height. A value of 1 is the poorest and 4 is the best. We used only profiles that had values of 3 (high confidence) or 4 (very high confidence). The plot shows an LLJ speed maximum at 241 m AGL (a common LLJ height).

8.2.1 Case Studies for June 17, 2002

The role of the jet stream in influencing turbulent conditions within the turbine layer is well demonstrated by conditions seen in the early morning and again in the day-night transition period of June 17, 2002. Figure 8-10 displays the 10-minute mean wind speed profiles measured by sodar for these two periods. Figure 8-10a documents the jet evolution between 0010 and 0400 LST (0710 to 1100 UTC) in 10-minute increments. Though fluctuating, the jet height is nominally about 250 m AGL. In contrast, Figure 8-10b plots the vertical profiles from 1900 to 2350 LST (0200 to 0650 UTC). In this case the jet maximum is at 200 m AGL. There is a stark contrast in the behavior of the jets in these two time periods. The jet during the early morning hours is higher and weaker and becomes stable with a maximum velocity of 19 m s^{-1} and intense vertical shear after about 0230 LST. During the day-night transition the next evening, the jet begins to form around 1910 LST. It gradually gains both strength and height until reaching a maximum speed of 25 m s^{-1} at 250 m AGL at 2140 LST. At this point it becomes unstable and breaks down into strong turbulence, which mixes out the shear significantly.

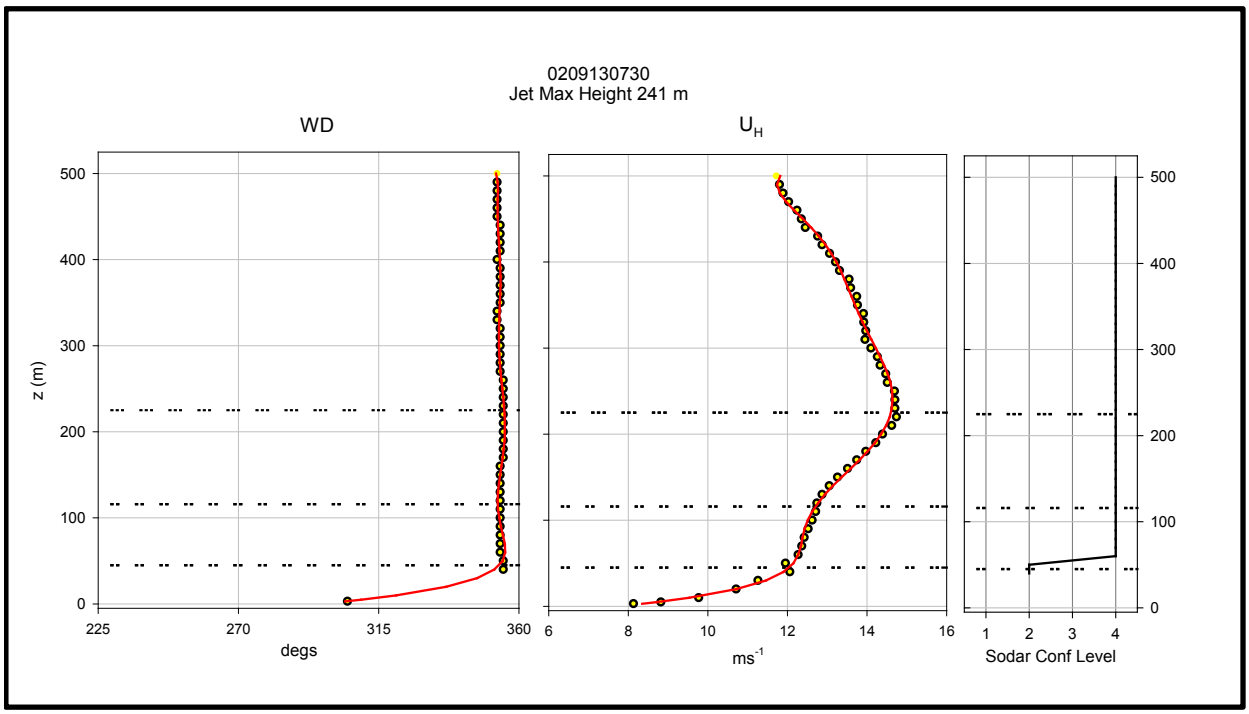
0209130730
Jet Max Height 241 m
WD
U_H
z (m)
500
400
300
200
100
0
225
270
315
360
degs
6
8
10
12
14
16
ms^{-1}
1
2
3
4
Sodar Conf Level

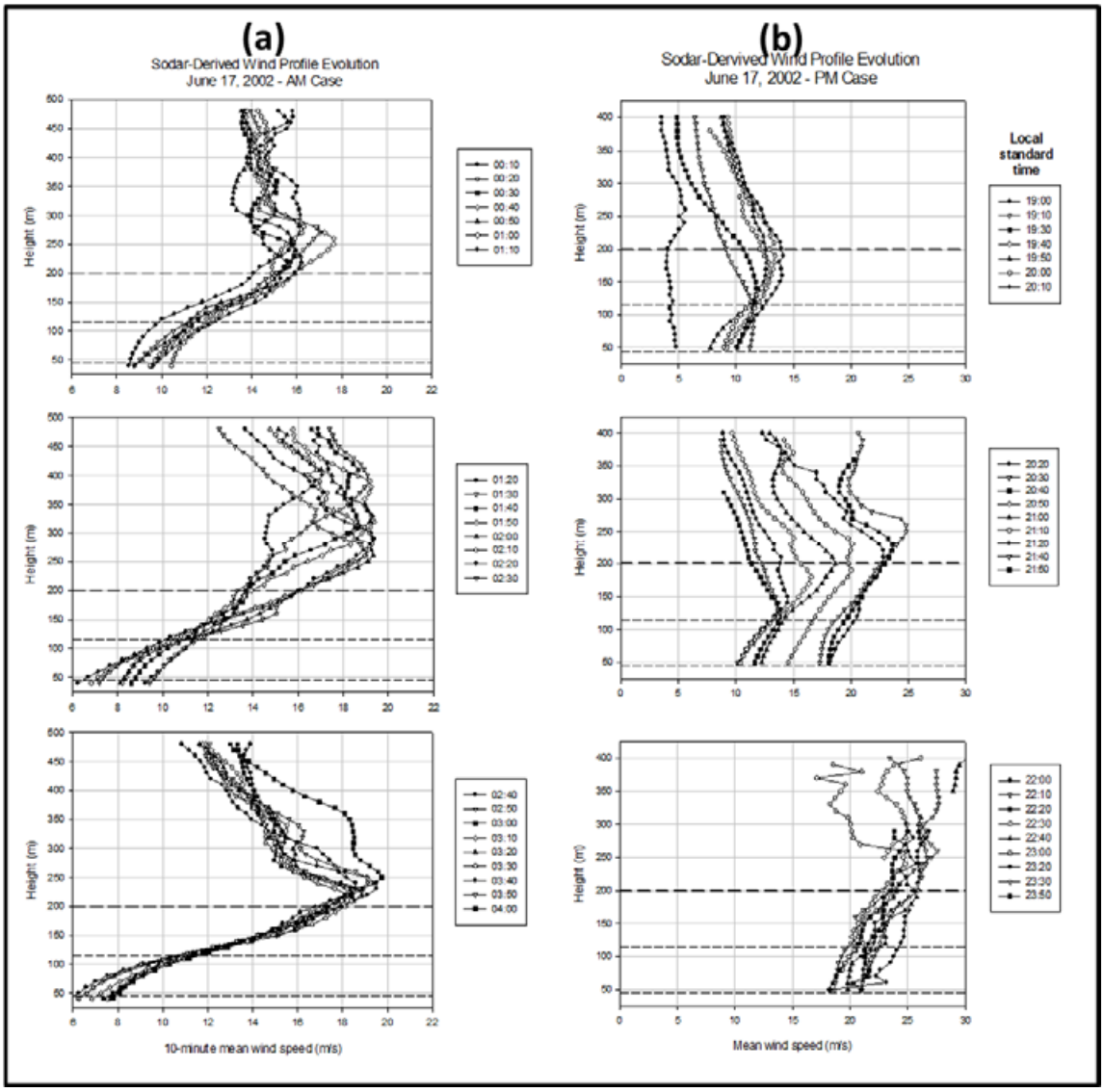

Figure 8-10. Profiles on June 17, 2002, 1900 to 2350 LST. Jet on left (a) remained stable and did not break down. Jet on right (b) broke down into turbulence after 2100 LST. The lower dashed lines outline the height range of a GE 1.5-W turbine and the upper longer dashed line represents a possible maximum height of a 10-MW turbine.

We now document the turbulent conditions seen in the layer measured by the 120-m met tower, which would have been experienced by a GE turbine. Figure 8-11 compares the time series of the time variation of both the background flow conditions and the turbulence parameters for the early morning period (Figure 8-11a) and the day-night transition (Figure 8-11b). The plots in the topmost row (Figures 8-11a and d) display the variations in the hub-height mean U speed and Ri_{TL}. A well-established LLJ exists at the beginning of the period, and the wind strength and stability support the generation of fairly intense coherent turbulence (Figure 8-11b) with a dominant buoyancy length scale L_b/D of 0.5 to 0.6 (Figure 8-11c). As time goes along, however, the turbine layer stability increases and the damping slows the winds and reduces the coherent turbulence level, which also significantly shortens the buoyancy length scale and the coupling to a turbine rotor.

The day-night transition characteristics in the right column of Figure 8-11 in some ways mirror those of the early morning event sequence. Initially the stability suppresses both the jet formation and turbulence in the turbine layer, but at about 2040 LST destabilization begins and the jet velocity increases. As the jet peak velocity continues to increase, a relatively rapid destabilization and turbulent breakdown occurs between 2050 and 2100 LST, creating strong vertical motions (Figure 8-11e) and coherent turbulence with buoyancy length scales closely equivalent to the rotor diameter (Figure 8-11f). Just before 2200 the turbine layer goes fully turbulent as Ri_{TL} approaches +0.02, the coherent turbulence level exceeds the significant response threshold of 10 $m^2 s^{-2}$, and the buoyancy length scale becomes greater than the rotor disk diameter. This intensification of the LLJ was responsible for creating significant coherent turbulence activity within the rotor disk and increased loads and fatigue on turbine components.

These two case studies are an excellent example of how the turbine layer dynamic stability plays a crucial role in the generation of coherent turbulence at the scales of turbine rotor. In Figure 8-12 we plot the disk-normalized buoyancy length scale L_b/D as a function of the Ri_{TL} with the CRR, CRRH, and STC04 stability class boundaries annotated for these two June 17 observational periods. It is clear why we have referred to the CRR range as “critical,” with the CRRH range as a transition to the highly damped turbulent environment of STC04.

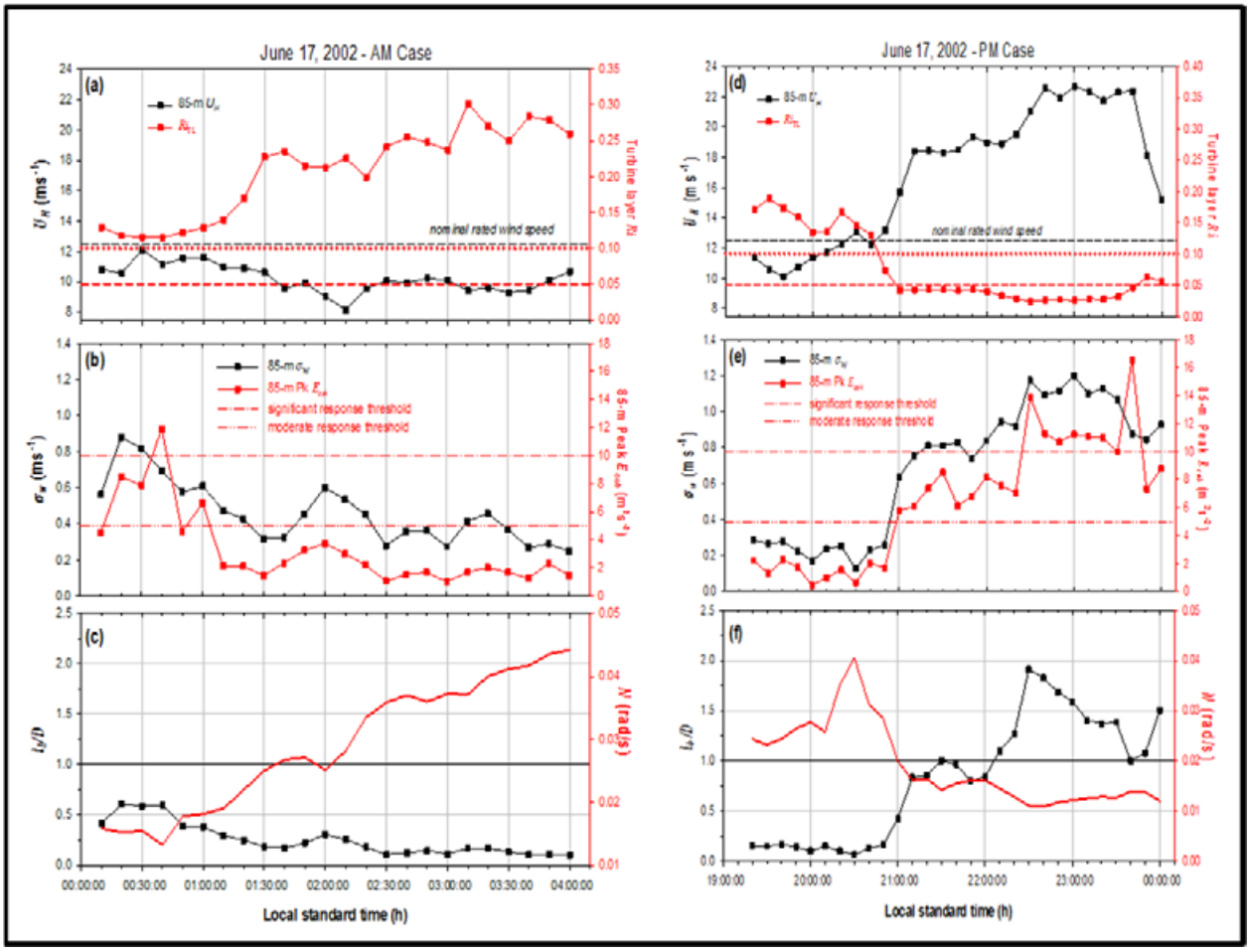

Figure 8-11. Turbulent and background flow characteristics for June 17, 2002, morning and evening case studies. The hub-height (85-m) mean wind speed *U* and Ri_{TL} are plotted in (a) and (d); the hub-height σ_w and peak E_{coh} are plotted in (b) and (e); and the disk-diameter normalized buoyancy length scale L_b/D and the turbine layer buoyancy frequency N_{buoy} in (c) and (f).

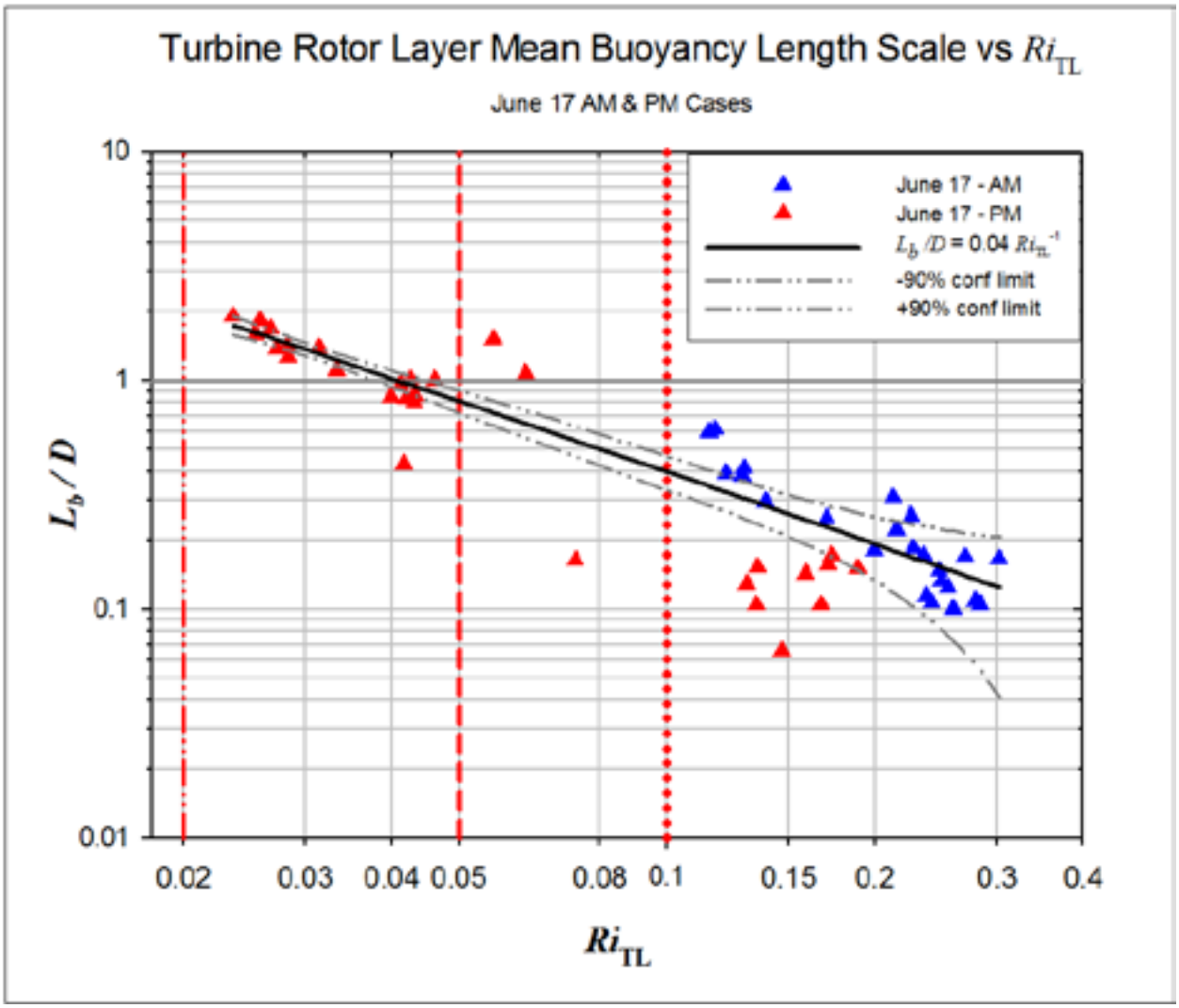

Figure 8-12. Observed variations of buoyancy length scale of mean rotor disk layer with Ri_{TL} for 0010 to 0400 LST and 1900 to 0000 LST on June 17, 2002

8.2.2 Lidar Measurements of LLJ-Induced Turbine Layer Coherent Turbulence

We were fortunate to have had the NOAA HRDL lidar to help us visualize and confirm the role of the LLJs in influencing the coherent turbulence seen within turbine rotor layers beneath the LLJs. In the early morning hours of September 9, 2003, we observed coherent waves present beneath an LLJ whose peak velocity was about at about 230 m AGL at the Lamar site. As part of our procedure, we aligned the HDRL laser beam into a fixed azimuth aligned with the mean wind direction (as determined by the sodar) and a 10 degree fixed elevation angle. This allows us to measure the wind velocity as it passes through each of the hundred 30-m wide velocity range gates with a vertical resolution of 5 m at a sampling rate of 4/s. Using various signal processing techniques when postprocessing these data, we were able to produce the contour plots of Figure 8-13. Banta and coauthors (1997) showed that in stable flows, TKE (or E_T) can be estimated from the HRDL velocity measurements.

In Figure 8-13a we plotted contours of the estimated TKE, whose intensity is color coded by the legend in the upper left of the diagram. The corresponding instantaneous TKE values directly measured by the sonic anemometers on the met tower are shown in the lower panel. In Figure 8-13b we added the lidar-derived mean vertical wind profile for the period of the observation, shown as a white dot-dot-dashed line annotated as $U_{\text{lidar}}(z)$. We superimposed the corresponding profiles of the horizontal wind speed [solid white line, $U_{\text{sodar}}(z)$] and the vertical velocity standard deviation (yellow line, σ_w) as measured by the sodar. These profiles indicate that the vertical turbulent fluxes or transports may not be uniform across the rotor disk. In the lower panel of Figure 8-13b we plotted the instantaneous values of E_{coh} measured by the sonic anemometers with the minimum and moderate dynamic response thresholds indicated by dashed lines. The lower extent, hub, and upper extent of a GE 1.5-MW turbine are shown as horizontal light dashed lines on both of the contour plots.

Figure 8-13b visibly demonstrates the relationship between the shear intensity and the development of patches of coherent turbulence. It also shows moderate vertical motions just above hub height. The tower measurements of E_{coh} in the lower panel confirm that many of the structures seen in the contour plot have coherent energy intensities greater than the minimum response threshold, with the most intense at about 450 seconds. In Figure 8-14 we plot the time series of the instantaneous Reynolds stress components ($u'w'$, $u'w'$, and $v'w'$) and their vector sum E_{coh} measured by the sonic anemometers. We highlighted several of the more intense structures (a–f) and the period (f) when the structures are vertically correlated. We plotted the instantaneous values of E_{coh} and the associated instantaneous buoyancy fluxes ($w'T'$) over the same time period and marked the same structures seen in Figures 8-15a–f and the vertically correlated region (g). A close examination of these structures reveals that the coherent turbulent bursts are always associated with negative buoyant fluxes, which add damping to the largest turbulent eddy structures.

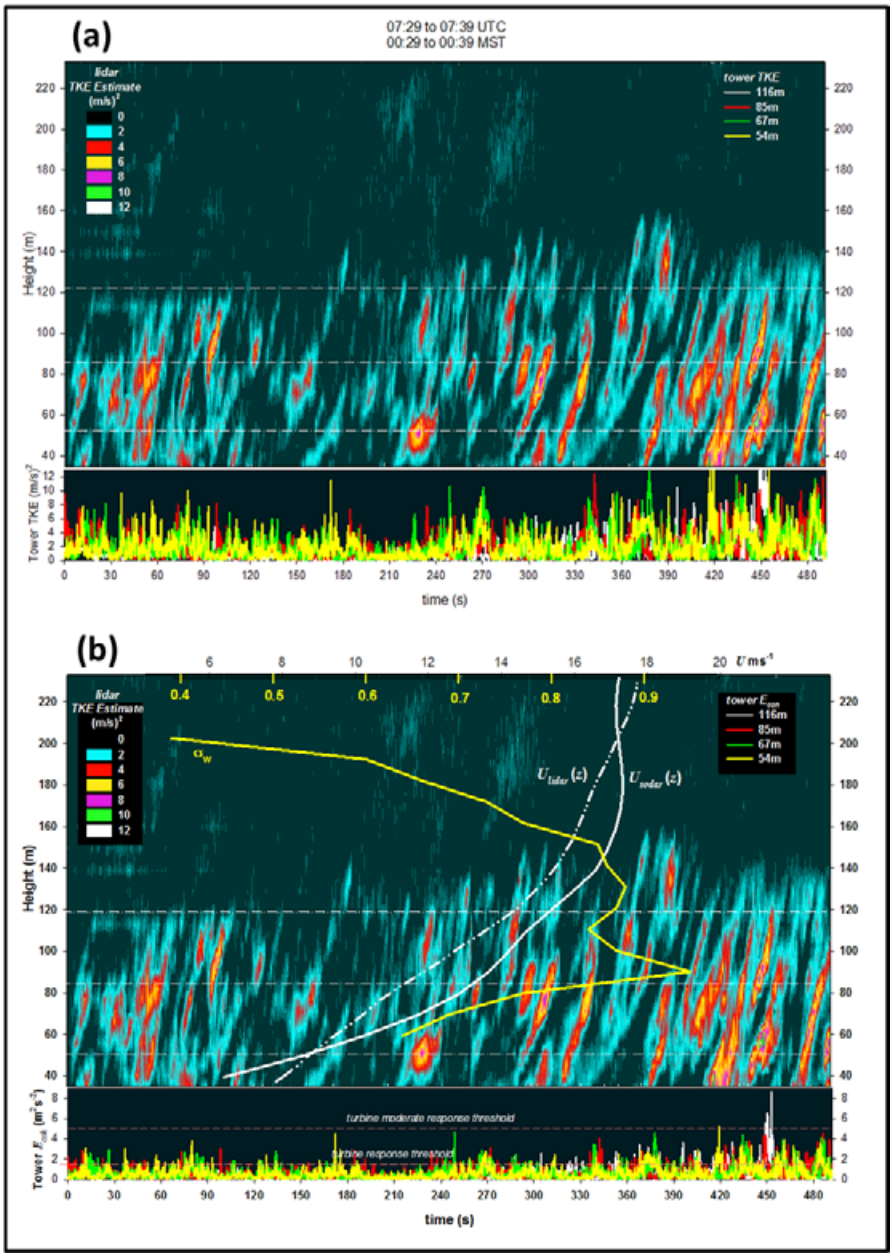

Figure 8-13. NOAA HRDL lidar observations of coherent turbulent patches: (a) lidar estimated TKE patches in upper panel with corresponding tower measurements below; (b) same as (a) but with mean wind speed *U*(*z*) profile (dot-dot-dashed line) with corresponding sodar-measured wind speed and σ_w profiles (yellow line). Time series of the instantaneous measurements of E_{coh} at the four heights on the met tower are shown in the lower graph. The light dashed lines outline the bottom, hub, and top of the WindPACT (GE) 1.5-MW turbine rotor. The minimum threshold and the moderate dynamic response levels are shown in the lower graph of (b) as horizontal dashed lines.

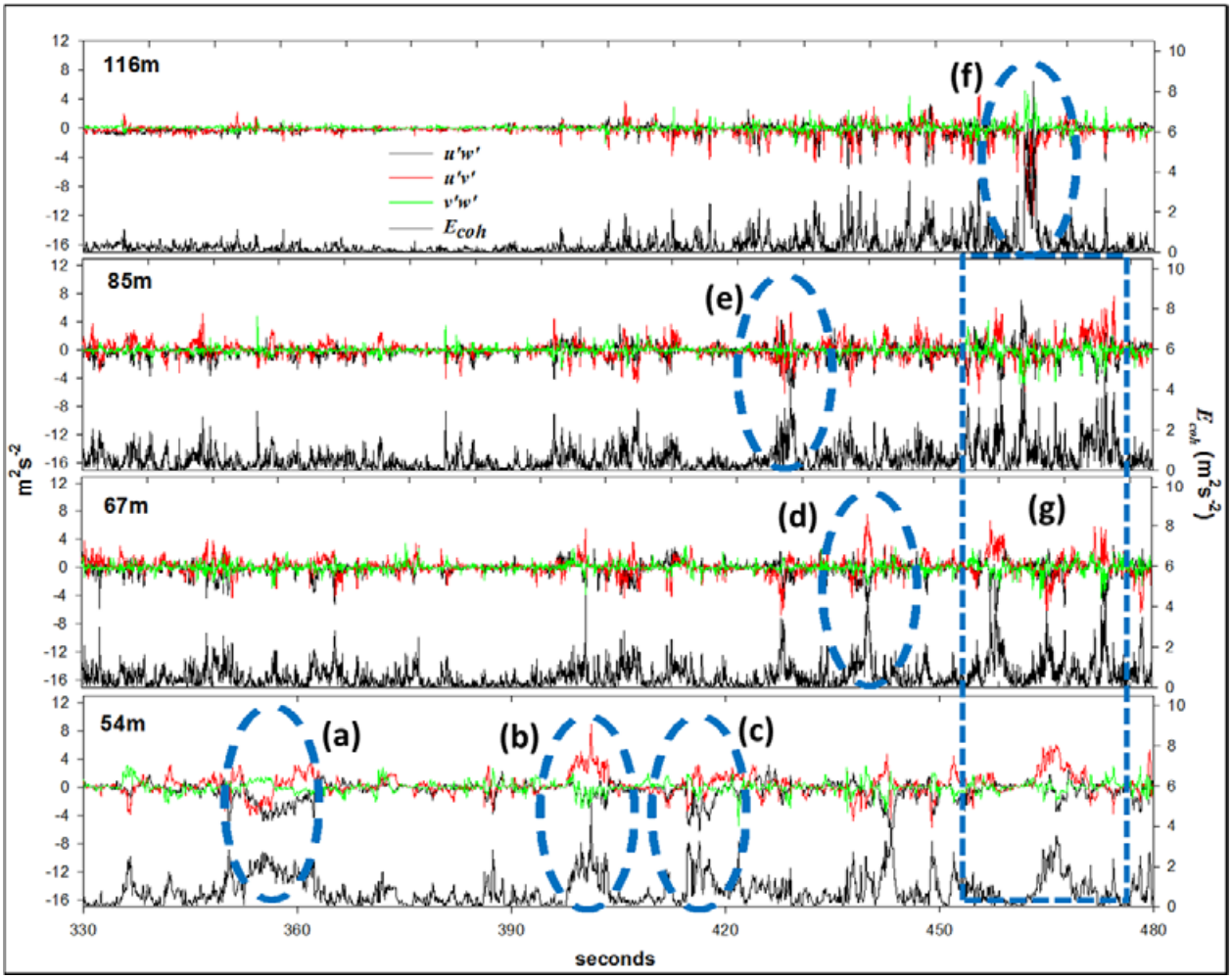

Figure 8-14. Time series of tower-measured instantaneous Reynolds stress components and E_{coh} values corresponding to HRDL profiles in Figure 8-13 between 330 and 480 seconds. Individual coherent structures are indicated by dashed lines marked (a–f) and vertically correlated structures are indicated by the rectangle identified as (g).

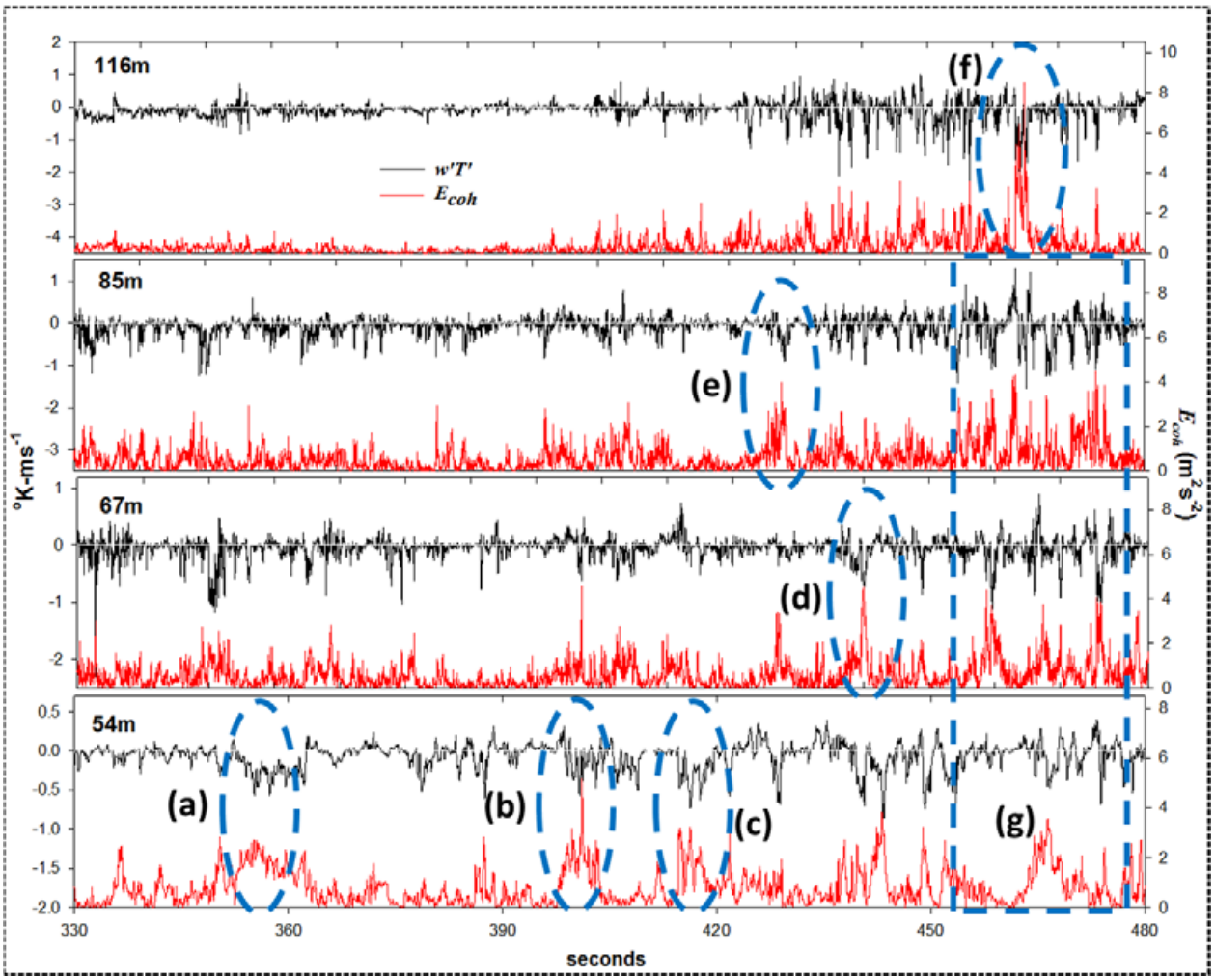

Figure 8-15. Time series plots of instantaneous local values of buoyancy flux $w'T'$ and E_{coh} for 330 and 480 seconds in Figures 8-13 and 8-14. The same coherent structures identified in Figure 8-14 are marked with the same letters. The effects of turbulent damping can be seen on each of the identified individual structures.

8.2.3 Low-Level Jet Statistical Characteristics

To simulate LLJs in the TurbSim Code, we needed to know more about their statistical properties which then could be introduced as part of the intended stochastic variation in the simulations. We derived the bulk of this information from the sodar observations at the Lamar site taken between May and November 2002. After applying postprocessing and quality control procedures, we had more than 9,000 ten-minute vertical profiles of mean wind speed and direction that contained at least one LLJ between 70 and 500 m AGL. LLJs not only have a distinct vertical wind speed profiles, i.e., one or more inflexion points, but also have characteristic wind direction profiles. With turbine rotor sizes increasing, we needed to include the direction profiles as well to estimate the effects of vertical directional shear in TurbSim Great Plains model simulations.

In Figure 8-16 we present histograms of the lowest jet maximum velocities and the corresponding wind directions derived from the 4,466 profiles whose usable maximum measurement height reached 500 m. We annotated the maximum velocity plot (Figure 8-16a) with the maximum rotor elevations of the GE 1.5SE, the National Renewable Energy Laboratory (NREL) 5-MW Reference Turbine, and a future land-based 10-MW turbine. Although not applicable directly to the sodar measurements, we annotated the direction histogram in Figure 8-16b to indicate the direction exclusion range for which the flow passes through the tower structure. This exclusion is important when the tower measurements are correlated with the sodar profiles. Corresponding to Figure 8-16, we plot the boxplot probability distributions of the lowest jet wind speeds with height in Figure 8-17. Figure 8-18 plots the vertical variation of the same information as contours varying with time for 1600 and 0800 LST (2300 to 1500 UTC). This plot shows that the strongest and highest jets occur between about midnight and 0300 LST but are strongest nearest the ground between 1900 and 2300 LST (0200-0600 UTC) during the late day-night boundary layer transition period. Figure 8-19 summarizes the variation of vertical wind direction shear beneath the measured jets. Here we plot probability (Figure 8-19a) and cumulative probability plots (Figure 8-19b) of the distributions of mean and maximum wind direction shear between 50 m AGL and the height of the lowest jet. Generally these tend to be small, but long tails do exist.

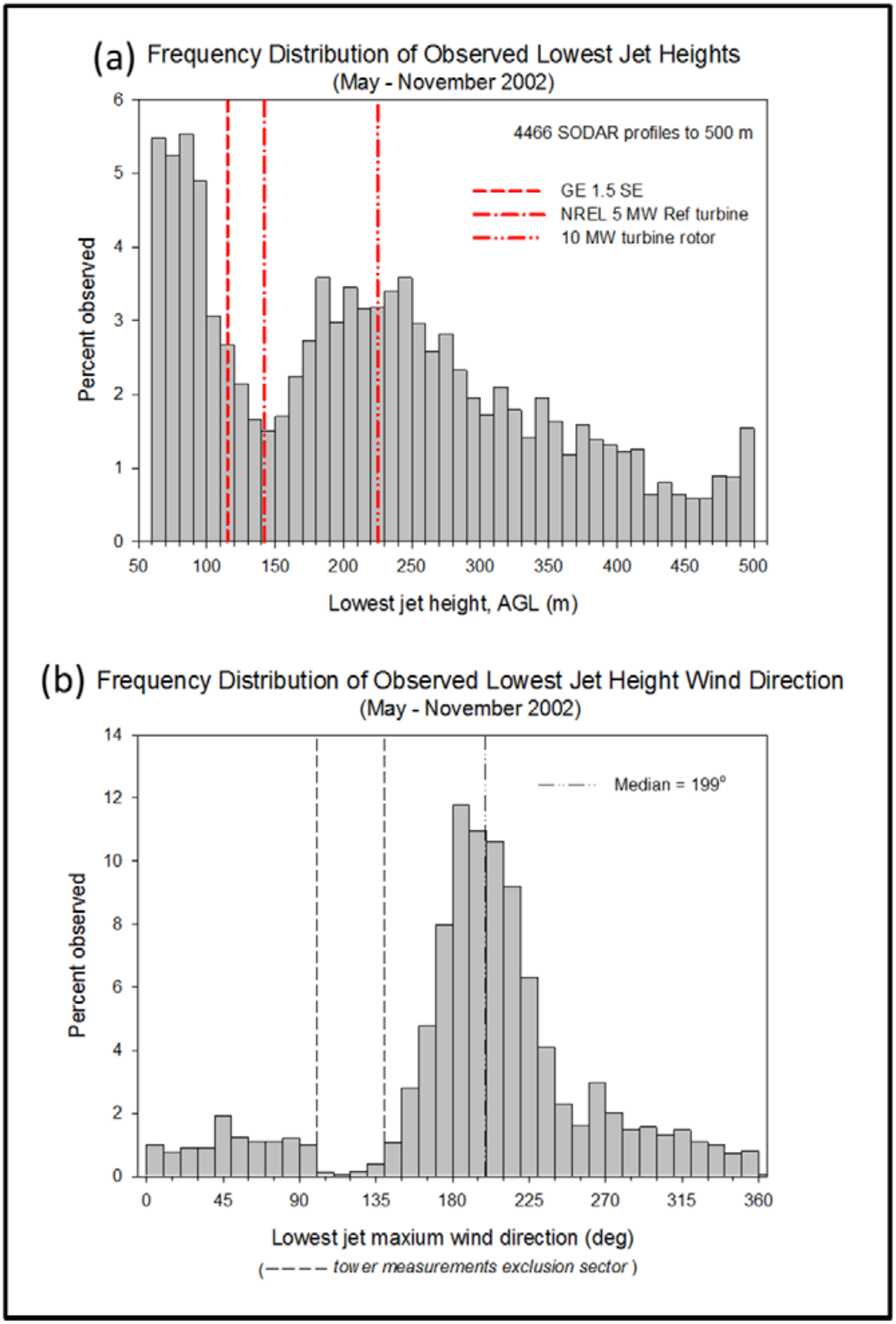

Figure 8-16. Observed frequency distributions of (a) lowest jet heights and (b) corresponding wind direction for May–November 2002 at Lamar site

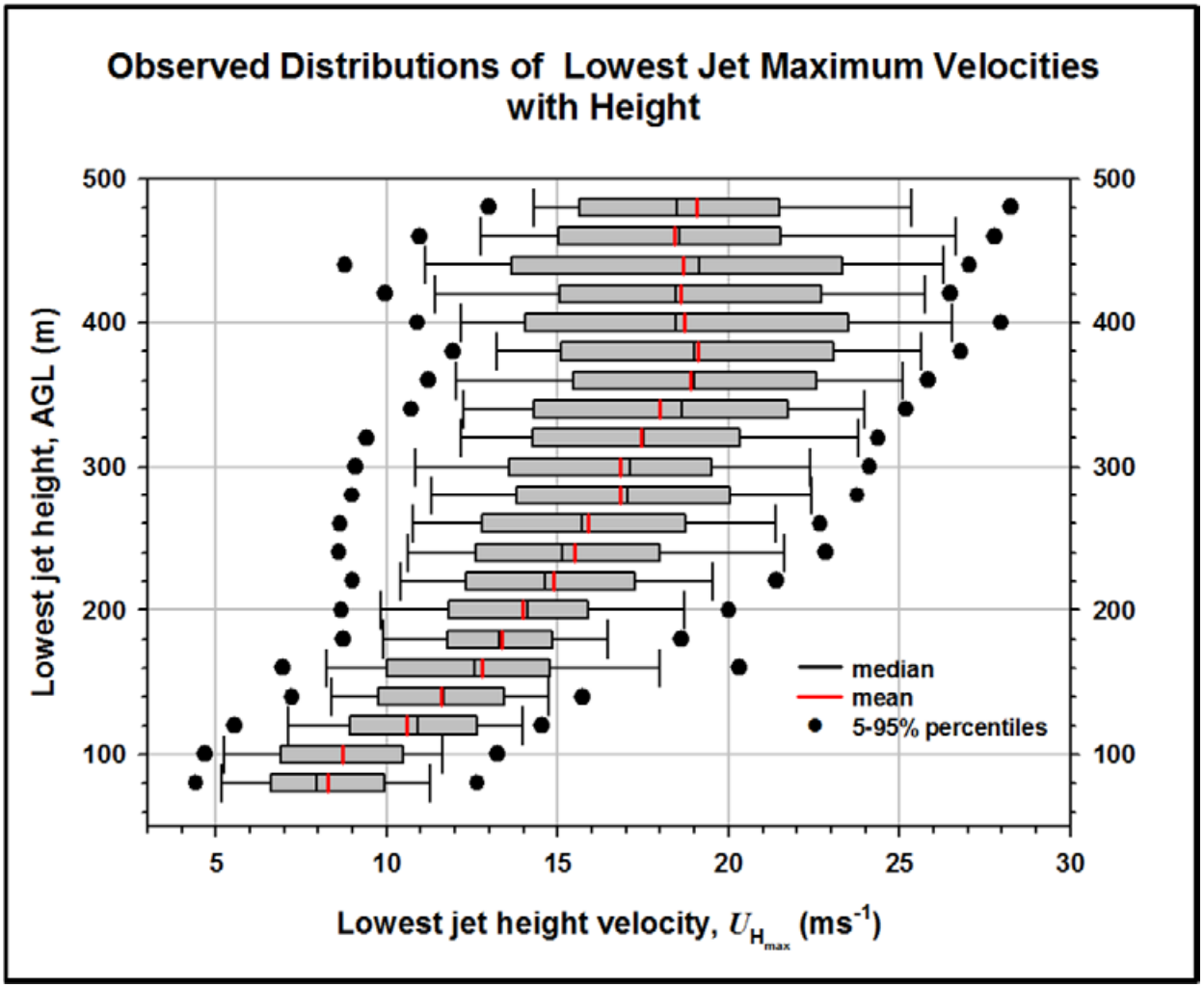

Figure 8-17. Probability variations of maximum velocities of lowest jets with height

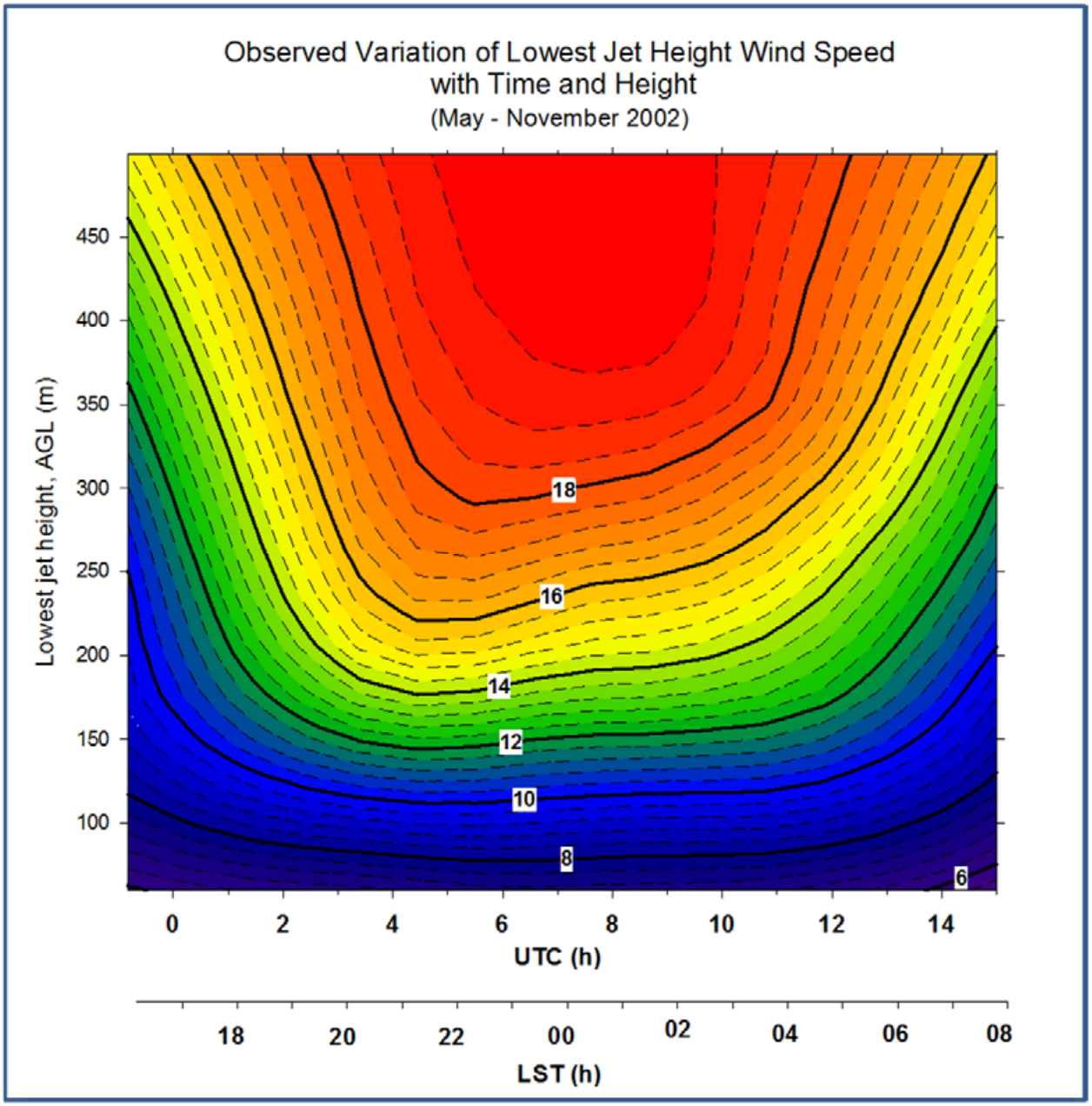

Figure 8-18. Observed variation of wind speed of lowest LLJ height for Lamar site for May–November 2002

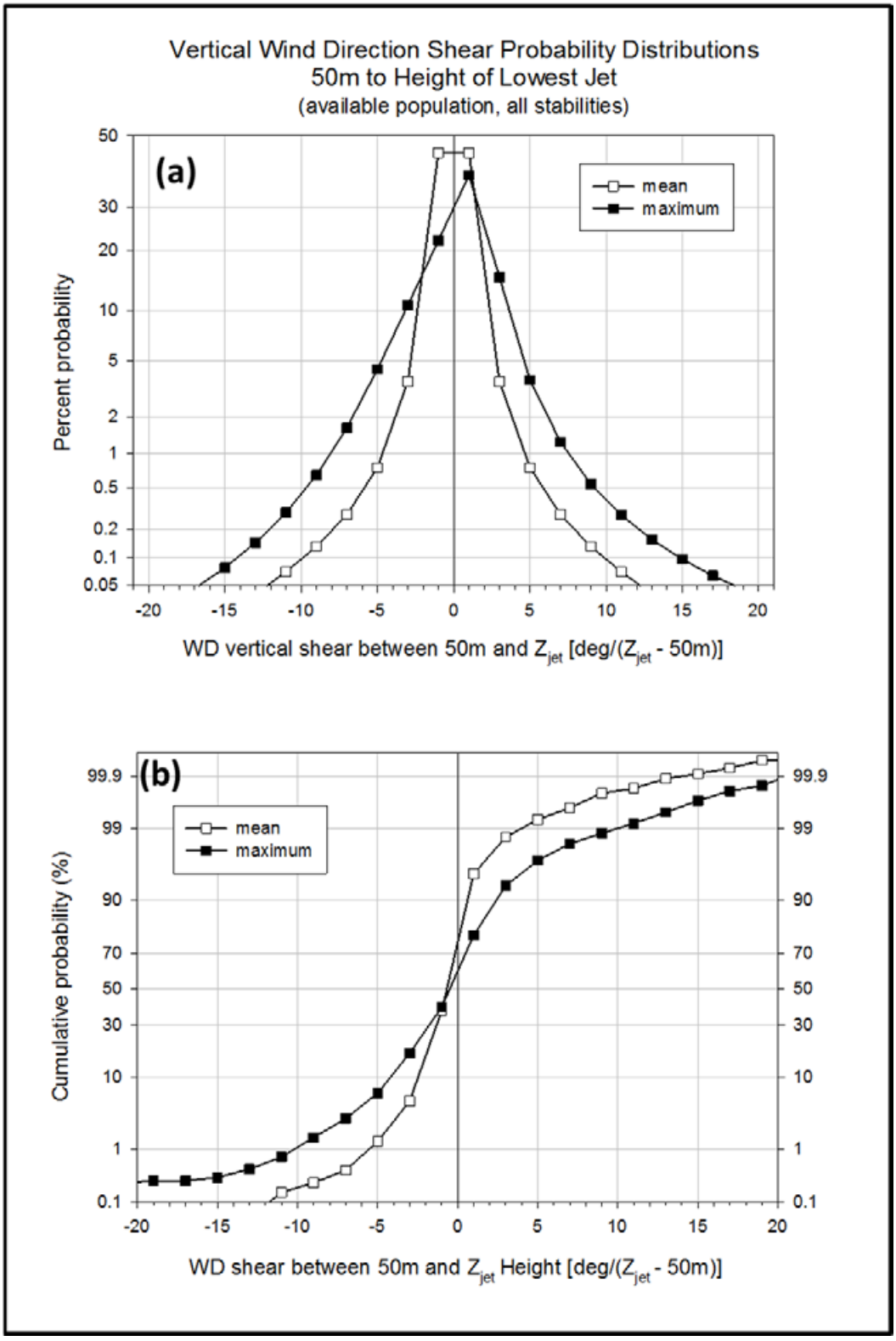

Figure 8-19. Probability distributions of variations of wind direction shear from 50 m to height of the lowest jet: (a) probability and (b) cumulative probability

8.2.4 LLJs and Turbulent Coherent Structures

Nocturnal LLJs in the Great Plains in particular are more frequent and intense during what has been described as the warm season—April through September (Panofsky and Dutton 1984; Mitchell, Arrit, and Labas 1995; Whiteman, Bian, and Zhong 1997). This was a consideration in choosing the first 2 weeks of September for the observation period with the NOAA HRDL lidar: we wanted to document the seasonal shift from "warm" to "cold" periods, which takes place during September. Several theories exist about why the preference for southerly winds occurs. Great Plains nocturnal LLJs are much more likely to form when boundary layer winds through the region have a strong southerly component, and this occurs more often in the warmer months (Panofsky and Dutton 1984; Whiteman, Bian, and Zhong 1997). We found this was certainly true from May through November 2002 at the Lamar site, where the median wind direction for the jets measured was 199 degrees as shown in the histogram of Figure 8-16b.

Given this warm season, we wanted to see its effect if any on producing conditions that increase dynamic loading of turbines, such as the presence of coherent turbulent structures. First we divided the available data record into two subsets, one of which had at least one coherent structure within the rotor disk layer and one in which there were none. In Figure 8-20a we present a histogram of the percent occurrence of the STC02, STC03, STC04, and STC05 stability classes in which coherent structures did or did not occur. Here we more finely divided the STC02 class into two sub-ranges one of which is narrow and weakly unstable while the other is wider and more unstable. We combined the CRR and CRRH classes into STC03 for use with the later scaling of TurbSim. We can see that coherent turbulent structures are most frequent in the weakly stable STC03 stability class, as might be expected based on our previous discussions. In Figure 8-20b, we again differentiate between the presence and lack of coherent structures within the rotor disk layer. With the exception of the most stable class, the mean hub wind speeds equal or exceed the corresponding rated values.

To understand the worst case situations for simulation purposes, we correlated stability and hub mean wind speed conditions when coherent turbulent structures were found simultaneously at all four tower measurement heights within the nocturnal turbine layer at the Lamar site. Figure 8-21 summarizes our results. We plotted two slightly different presentations of the interquartile range (IQR; P25–P75 or Q1–Q3) distributions of Ri_{TL}. In Figure 8-21a, the monthly IQR distributions as a function of Ri_{TL} with the warm season months are shown in red. In Figure 8-21b, the Ri_{TL} IQR is plotted for each month of the year. We annotated each figure with the stability classes CRR, CRRH, STC04, and STC05 and note that the class STC03 is composed of CRR and CRRH. We present the IQR distributions for the hub-height mean wind speed in the same formats in Figures 8-21c and d. We annotated this figure with the rated wind speeds for the WindPACT and NREL 5-MW Reference virtual turbines. We find that the highest observed nocturnal wind speeds are prevalent from April through June, with June having the best winds. Based on an earlier 2-year wind prospecting record from this site, we believe that the dip in the wind speeds in July is an anomaly for this particular year because of intense drought conditions (intense subsidence that created very high surface air temperatures) that summer, which peaked in July. The July distributions are probably closer to those seen in May in more normal years. From Figure 8-21b, when coherent structures are simultaneously occurring at all levels of the 120-m tower in April, May, and June, we see that CRR stability conditions are also taking place at least 50% of time and are accompanied by above-rated wind speeds. At this site then, these

three months, and possibly July as well in a more normal year, are productive from a power generation perspective, and it is very likely that the level of cumulative fatigue damage in turbine components is also high. August and September are less energetic, but they still may be contributing a significant amount of damage. It is very likely that LLJs are the dominant source of the conditions that are responsible for what we are seeing in Figure 8-21. So it is critical that TurbSim be capable of simulating the details of the flow conditions indicated.

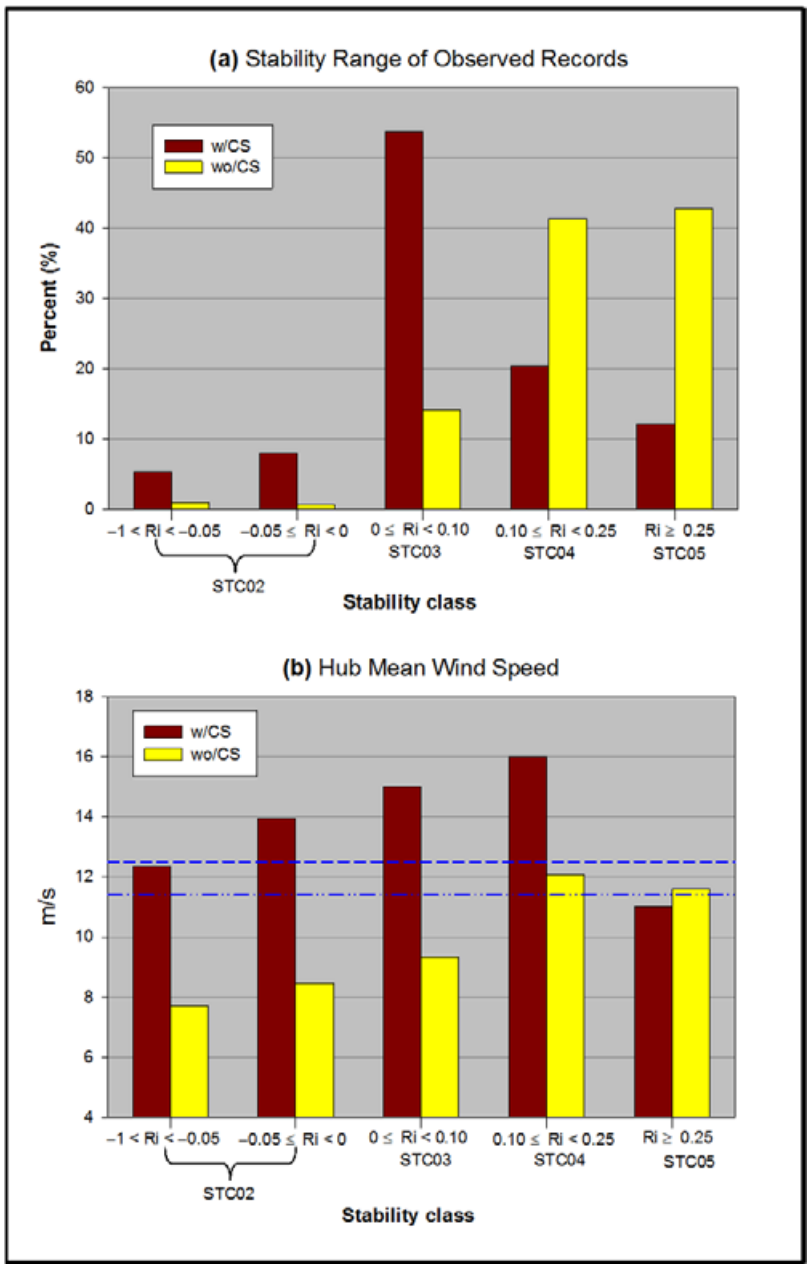

Figure 8-20. Available distributions of (a) stability classes; and (b) hub-height mean wind speeds by stability class with coherent structure (w/CS) and without (wo/CS) within the rotor layer. Rated wind speeds for the WindPACT and NREL 5-MW Reference turbines are indicated by blue dashed and dot-dot-dashed lines, respectively.

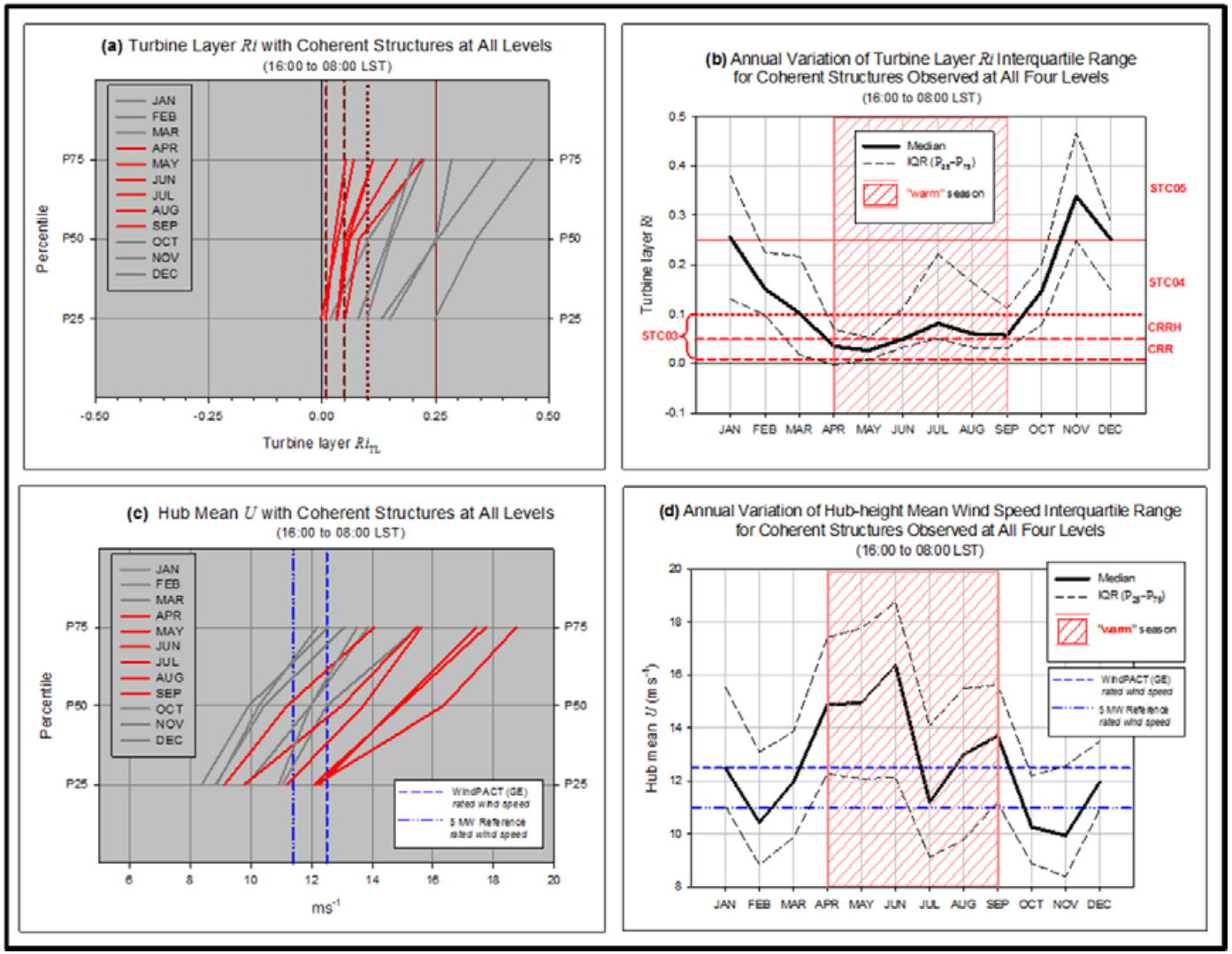

Figure 8-21. Monthly IQR distributions of (a) and (b) Ri_{TL}; and (c) and (d) hub-height mean wind speed *U*. The low-level jet warm season is highlighted in red. The stable stability classes are annotated in red in (b) and the rated wind speeds for the WindPACT and NREL 5-MW Reference turbines are shown as dashed lines in blue in (c) and (d).

9.0 TurbSim Scaling—A Brief Overview

9.1 Background

The TurbSim stochastic inflow turbulence code generates numerical simulations of full-field flows that mimic the statistical characteristics of atmospheric boundary turbulence present in both natural and internal wind farm environments over a wide range of operating conditions. These simulated wind fields are then used to create the wind and turbulence input to aeroelastic design codes used to model the dynamic response of actual wind turbine structures. TurbSim was specifically designed to interface with the National Renewable Energy Laboratory (NREL) AeroDyn aerodynamics routine (Moriarty and Hansen 2005) used with the NREL FAST design code (Jonkman and Buhl 2005) and the commercial MSC.ADAMS® multi-body dynamics simulation code.

TurbSim has its origins in the seminal work of Paul Veers in his SNLWIND stochastic inflow simulator (Veers 1988) and more recently Kelley's expansion of Veer's work into the diabatic (non-neutral) full-field, full vector flow simulator SNLWIND-3D (Kelley 1992). Most designers depend on inflow simulations that are based on one of the normal turbulence models (NTMs) recommended by International Electrotechnical Commission (IEC) in their 614001-1 standard (IEC 2005). The latest revision includes an implementation of the Mann uniform shear turbulence model (Mann 1998) and recommends its use, although a neutral version of the Kaimal et al. (1972) spectral model is still included and accepted. While the Mann model is very sophisticated (it applies turbulence rapid distortion theory to a sheared flow) and includes explicit physics, it still assumes neutral stability as does the much more empirical Kaimal model. The Mann model is less encumbered in this regard, but the Kaimal model is based on neutral surface layer (SL) turbulence statistics. The surface or constant stress layer occupies perhaps the first 100 m (328 ft) of the atmospheric boundary layer during the day in unstable and neutral conditions, but it becomes much shallower in stable nighttime flows. Neither model, then, can take into account the influence of buoyancy that we have found so pervasive in shaping the temporal and spatial characteristics of turbulence and the subsequent dynamic response of wind turbine components. Finally, the very large turbine rotors now becoming the norm reside either partially or fully above the height of the SL. This region, which extends to the top of the atmospheric boundary layer, is called the mixed layer (ML), and turbulent conditions and their scaling can vary significantly from those in the SL. In the ML (also referred as the residual layer in stable, nocturnal flows), buoyancy is a major player. We need inflow simulations that reflect the reality of turbine operating environments and not idealized ones—this is what TurbSim strives to do in an efficient manner.

Given that TurbSim is an outgrowth of Veers' original SNLWIND and Kelley's expansion SNLWIND-3D, much of the fundamental basis for the stochastic simulator was discussed in Veers (1988) and Kelley (1992), and we encourage the reader to look at those documents. Here we concentrate on what has gone into scaling the important features of the turbulence fields being simulated by the site-specific spectral models offered by TurbSim and to a limited extent how it has been implemented. For information on how to use the code, the reader is referred to Jonkman (2009).

9.2 Important Parameters and Conditions To Be Simulated

The basic process of simulating a realistic full-field flow for the National Wind Technology Center (NWTC) and Lamar sites functionally is the same as that followed in Kelley (1992) to develop what became SNLWIND-3D. As we pointed out previously, however, one significant omission in our initial simulation of the inflows to the two California wind farm Micon 65/13 turbines was the lack of small-scale coherent turbulent structures. We addressed this issue by including such structures in the wind farm models (upwind location [WF_UPW], the flow at Row 37 with the upwind 7D turbine spacing [WF_7D], and downwind of Row 41) with the nearest operating turbine row 14D upstream (WF_14D). We incorporated this feature in the development of the NWTC (NWTCUP) and the Great Plains Low-Level Jet (GP_LLJ) spectral models based on our field measurements from each site.

The California wind farm turbines operated very close to the ground, which allowed us to apply SL turbulence scaling exclusively. At the NWTC site, however, at the highest measurement in the planar array (58 m), we found that under stable flow conditions SL scaling was breaking down; i.e., the shearing stress or local friction velocity u_* was becoming a function of height. In Lamar the entire depth of the equivalent rotor was well within the ML except during strong convection and high surface wind speeds. Earlier we noted the levels of heterogeneity within the Advanced Research Turbine (ART) rotor disk at the NWTC and the equivalent heights of the virtual WindPACT rotor in Lamar, which violated the equilibrium conditions of SL scaling as well. Because there is no universal ML equivalent to SL scaling theory, we applied what can be described as an SL-ML hybrid (modified local scaling) approach based on our empirical measurements. Velocity and temperature fluctuations in the SL are based on the velocity, temperature, and height scaling parameters u_{*_o}, T_{*_o}, and $L_{M\text{-}O}$ defined by Equations 2-5, 2-6, and 2-7 and measured at the surface. The vertical variation of $U(z)$ in a non-neutral or diabatic atmosphere is given by the diabatic log wind profile

$$U(z) = (u_{*_o} / \kappa)\left[\ln\left(z/z_o\right) + \psi\left(z, z_o, L_{M-O}\right)\right] \tag{9-1}$$

where κ is the von Kârmân constant ≈ 0.4, ψ is the diabatic correction term, and z_o is a characteristic surface roughness length. In developing our empirical scaling equations for the various turbulence parameters, we initially used u_*, z, and the stability variable $z/L_{M\text{-}O}$ averaged over the disk layer.

We found, because of departures from SL theory, many parameters we were trying to scale were more highly correlated with Ri_{TL} than with $z/L_{M\text{-}O}$. The variable $z/L_{M\text{-}O}$ is, however, necessary to scale the target velocity frequency spectra to which the inverse Fourier transform process is applied to obtain the velocity time series. It therefore was necessary to obtain the variation of $z/L_{M\text{-}O}$ with Ri_{TL}. For the wind farm models, we used a relationship between Ri and z/L_{MO} suggested by Panofsky and Dutton (1984), which is based on the Businger-Dyer flux-profile relationships (Dutton et al. 1979). This was necessary because the available instrumentation did not allow us to directly determine z/L_{MO}. The relationships used for the wind farm models are

$$z/L_{MO} = \begin{cases} Ri \text{ for } Ri < 0 \\ Ri/(1\text{-}5*Ri) \text{ for } 0 \le Ri < 0.18 \\ 5.616 \text{ for } Ri \ge 0.18. \end{cases} \quad (9\text{-}2)$$

Businger and coauthors (1971) found that for an unstable ($Ri < 0$) surface layer over homogeneous terrain conditions, setting $z/L_{MO} = Ri$ was a reasonable approximation. For stable conditions they found

$$z/L_{MO} = (0.74 + 4.7Ri)/(1+4.7Ri) \; . \quad (9\text{-}3)$$

It was no surprise that neither of these relationships fit the observed NWTC data given the level of intense heterogeneity in part caused by the significant downward momentum and buoyancy fluxes common to this site. This was also true at the Lamar site, where the bulk of the measurements were taken well above the surface layer and during stable conditions by design. These fluxes are similar to those at the NWTC but have low-level jets in the nocturnal boundary layer.

For both sites we correlated the rotor disk layer mean values of the locally measured $z/L_{MO}(z)$ values (now referred to as z/L_D) with the corresponding Ri_{TL}. We found that the variation in z/L_D fell into three distinct ranges of Ri_{TL}, including two unstable classes and one stable class. The measured relationships for the NWTC are

$$z/L_D = \begin{cases} -0.254 + 1.047Ri_{TL} \text{ for } -1 < Ri_{TL} \le -0.10 \\ (10.379Ri_{TL})/(1 - 19.393Ri_{TL}) \text{ for } -0.10 < Ri_{TL} < 0 \\ (2.535Ri_{TL})/(1 - 6.252Ri_{TL}) \text{ for } 0 \le Ri_{TL} < 0.155 \\ 12.7\, Ri_{TL} \ge 0.155 \; . \end{cases} \quad (9\text{-}4)$$

For the Lamar site we found

$$z/L_D = \begin{cases} -0.047 + 1.054Ri_{TL} \text{ for } -1 < Ri_{TL} \le -0.10 \\ (2.213Ri_{TL})/(1 - 4.698Ri_{TL}) \text{ for } -0.10 < Ri_{TL} < 0 \\ (3.132Ri_{TL})/(1 - 6.762Ri_{TL}) \text{ for } 0 \le Ri_{TL} < 0.137 \\ 5.66\, Ri_{TL} \ge 0.137 \; . \end{cases} \quad (9\text{-}5)$$

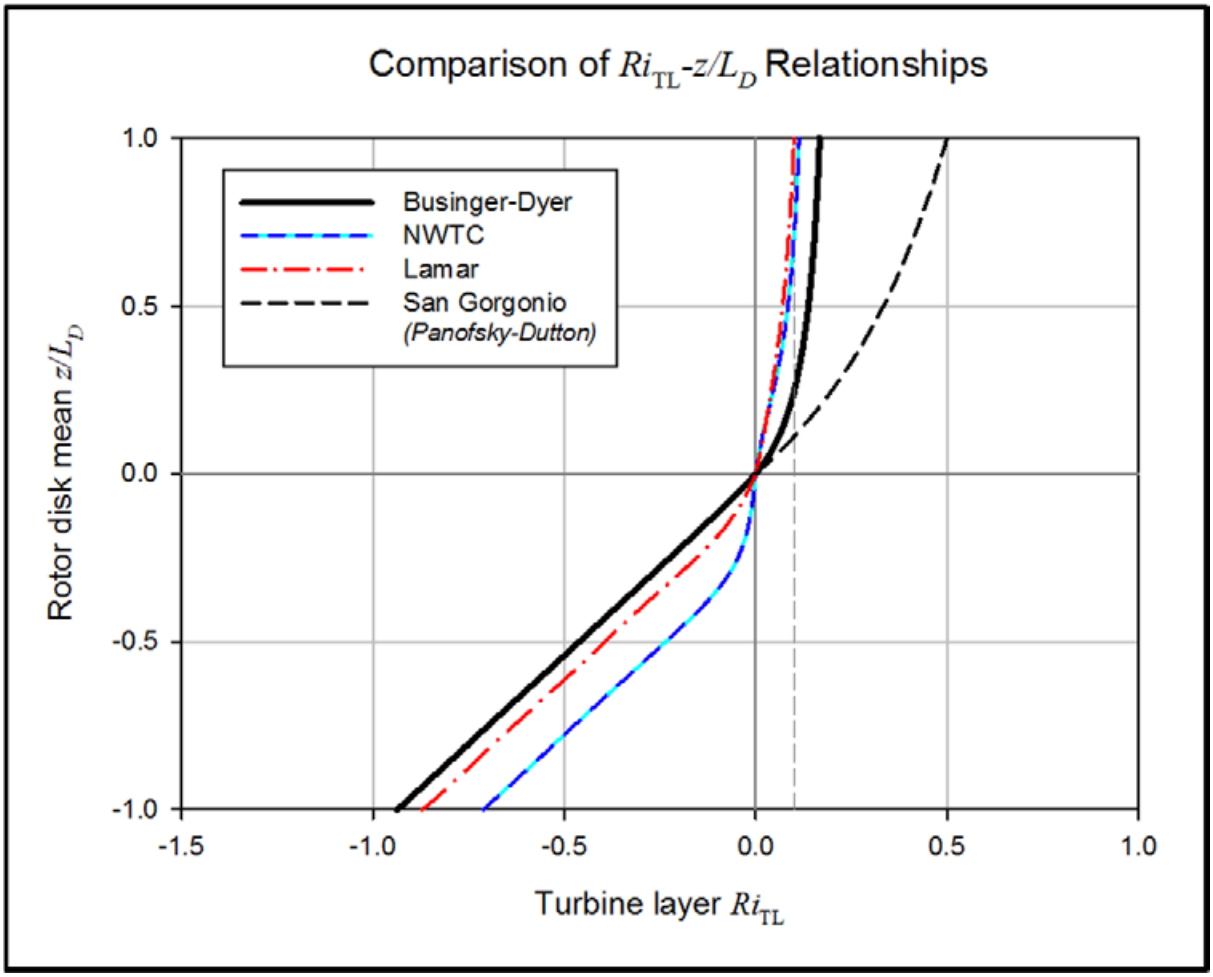

Figure 9-1. Estimated values of rotor disk layer average stability parameter z/L_{MO} as function of Ri_{TL}. The NWTC and Lamar relationships were empirically determined from direct measurements of local values of z/L_{MO} and Ri_{TL} at these two sites. The vertical dashed line at Ri_{TL} = +0.10 corresponds to the nominally upper limit of turbine dynamic response seen on the Micon turbines and the ART.

We found we could limit the scaled range of z/L_D to ± 1. Figure 9-1 compares the variations of the estimated values of z/L_D as a function of Ri_{TL}.

9.3 TurbSim Independent Scaling Variables

SNLWIND-3D and now TurbSim use only a very limited number of user defined boundary conditions or independent variables to scale the simulated full-field turbulence for each of the supported spectral models. These include characteristic measures of the following:

- Mean wind speed at a specified height within the rotor disk being modeled
- Velocity shear across the rotor disk
- Turbulence level or intensity
- Dynamic stability of the turbine layer
- Presence of coherent turbulent structures
- Height and intensity of a low-level jet stream.

The variables implemented in TurbSim to satisfy these criteria are the:

- Mean wind speed at a specified height within the rotor disk (U at z)
- Power law shear exponent across the rotor disk (α)
- Mean shearing stress or friction velocity over rotor disk layer (u_{*D})
  (a specific the turbulence intensity can be used to scale the IEC spectral models)
- Ri_{TL}
- Presence and location of coherent turbulent structures within the rotor disk
- Height and intensity of a low-level jet.

The turbulence spectral models that have been implemented in TurbSim include:

- The IEC Kaimal model (IECKAI)
- The IEC von Kârmân model (IECVKM)
- The Risø diabatic homogenous- or smooth-terrain model (SMOOTH).

The NREL site-specific models include:

- The NREL San Gorgonio wind farm models
  - Upwind of Row 1 (WF_UPW)
  - Upwind of Row 37 (WF_7D) (7D row-to-row spacing)
  - Downwind of Row 41 (WF_14D) (14D row-to-row spacing)

- The NREL NWTC model (NWTCUP)

    - KHTEST model (severe but observable implementation of NWTCUP)

- The NREL Great Plains Low-Level Jet Model (GP_LLJ)
    - No LLJ present (power law shear profile)
    - LLJ jet present (LLJ shear profile)
    - Coherent turbulent structures present/not present.

The choice of including coherent structures in the simulation is available only with the NREL site-specific spectral models, and only the GP_LJJ supports low-level jets. So, with the exception of the discrete choices, including coherent structures or low-level jets, the scaling of the simulated turbulence within the user-defined turbine rotor disk height geometry is accomplished by specifying only the U, α, u_{*D}, and LLJ characteristics (if used), and Ri_{TL}. The first four describe the velocity field and the last introduces the influence of the important vertical variation of temperature (buoyancy on the simulated background turbulent wind flow) within the simulated rotor disk. As we discuss later, the coherent structures are superimposed on this background, much in the same way KHI-induced billows occur in natural flows.

9.4 Developing Turbulence Scaling for NREL Site-Specific Spectral Models from Field Measurements

We developed the scaling of the predicted turbulence statistics as functions of height (z) across the rotor disk of the:

- Turbulent spectral energy distributions $S_{u_i}(n)$ where i= u, v, w turbulent velocity component and n is the cyclic frequency in hertz
- Vertical variation of the mean U (and V if the GP_LLJ with a LLJ is specified)
- Temporal coherence via the mean Reynolds stress components, $\overline{u'w'}$, $\overline{u'v'}$, and $\overline{v'w'}$
- Spatial coherence for u, v, and w turbulence components within and extending slightly beyond the specified rotor disk diameter to accommodate large yaw and teeter angle variations in the subsequent turbine simulations
- Coherent structure characteristics: locations, intensity (peak E_{coh}), total length (T_{coh}), and number (N_{coh})
- The LLJ jet characteristics of height and intensity of the jet maximum velocity when the GP_LLJ model is used and if not specifically defined by the user.

9.4.1 General Analysis and Modeling Procedure

Using the independent variables, we applied multiple-linear regression (MLR) coupled with LOESS smoothing to develop empirical scaling models of the target turbulent statistical parameter. In one or two instances, a nonlinear transformation of one of the predictor variables was included in the MLR model if it would improve the model performance. We examined the probability distributions of the residuals after identifying and retaining the most efficient predictors to achieve the maximum coefficient of multiple regression statistic R^2 as well as other measures of goodness-of-fit such as the F-statistic. An additional offset correction was made to

the final regression equation if it was found that a significant bias was present in the residuals. If the residual probability distribution differed significantly from Gaussian, we fitted it to an appropriate parametric model. A random sample from this residual model distribution was then added to the MLR model to provide the best estimate of the target scaling parameter with its inherent random variability.

Our two primary independent variables in developing the MLR and associated random models are the mean hub-height U wind speed and Ri_{TL}. The observed available range of wind speeds were first divided into 2-m s^{-1} categories. The Ri_{TL} values were stratified by the stability classes STC01, STC02, STC03, STC04, and STC05. The STC03 class included both the critical Richardson number range, or CRR, and the CRR High, or CRRH, ranges. In practice the most unstable STC01 class ($-1 \le Ri_{\mathrm{TL}}$) was not included in the MLR modeling because (1) there were so few observations within this range for all three sites and (2) the mean wind speeds were typically low and often below cut-in speed. Our first wind speed bin range began at 3 m s^{-1}, which was usually just below cut-in speed for most of the turbine designs, virtual or otherwise, discussed here. Typically the combination of available wind speed and stability classes produced up to 70 or more statistical degrees of freedom (DOF) in modeling the observed ranges of the target parameters for the wind farm, NWTC, and Lamar sites. We performed the stepwise MLR procedure for each stability class that contained a statistically significant number of observations within each wind speed category. This procedure initially included one or more of the candidate predictor variables u_{*D}, the surface $u_{*\mathrm{o}}$, α, z/L_D, and the local value of $z/L(z)$, and whether coherent structures were present or not. In developing the models with coherent structures present, we used only the cases in which these turbulent patches had been detected simultaneously at all measurement (sonic anemometer) locations. This ensured that we were scaling the potentially most influential situation on turbine dynamic response. We also included the jet height and intensity as additional predictor variables when modeling the Lamar site if an LLJ had been detected by the sodar below a height of 500 m above ground level (AGL).

The shearing stress or friction velocity u_* is the parameter that scales the turbulence level, as we see in our discussion of the spectral energy distributions. For the wind farm sites, we used the direct measurements at the equivalent turbine hub heights. At the NWTC, we found that we could use the disk-averaged value based on the mean surface stress or u_{*o} computed from Equation 9-1. The variation of u_{*D} with u_{*o} was found to be weakly correlated with Ri_{TL} and is plotted in Figure 9-2a. A random correction to Figure 9-2a is plotted in Figure 9-2b, and the final value of u_{*D} is estimated in TurbSim as

$$u_{*D} = u_{*o} + 0.205 - 0.0101 U_{\mathrm{hub}} + 0.00904 Ri_{\mathrm{TL}} + \text{RANDOM contribution} . \qquad (9\text{-}6)$$

The same approach is taken to estimate a disk-averaged value of z/L_D by Equation 9-1 and random adjustment from the probability distribution in Figure 9-3:

$$z/L_D = z/L_o - 0.247 + 0.0188 U_{\mathrm{hub}} - 0.251 Ri_{\mathrm{TL}} + \text{RANDOM contribution} . \qquad (9\text{-}7)$$

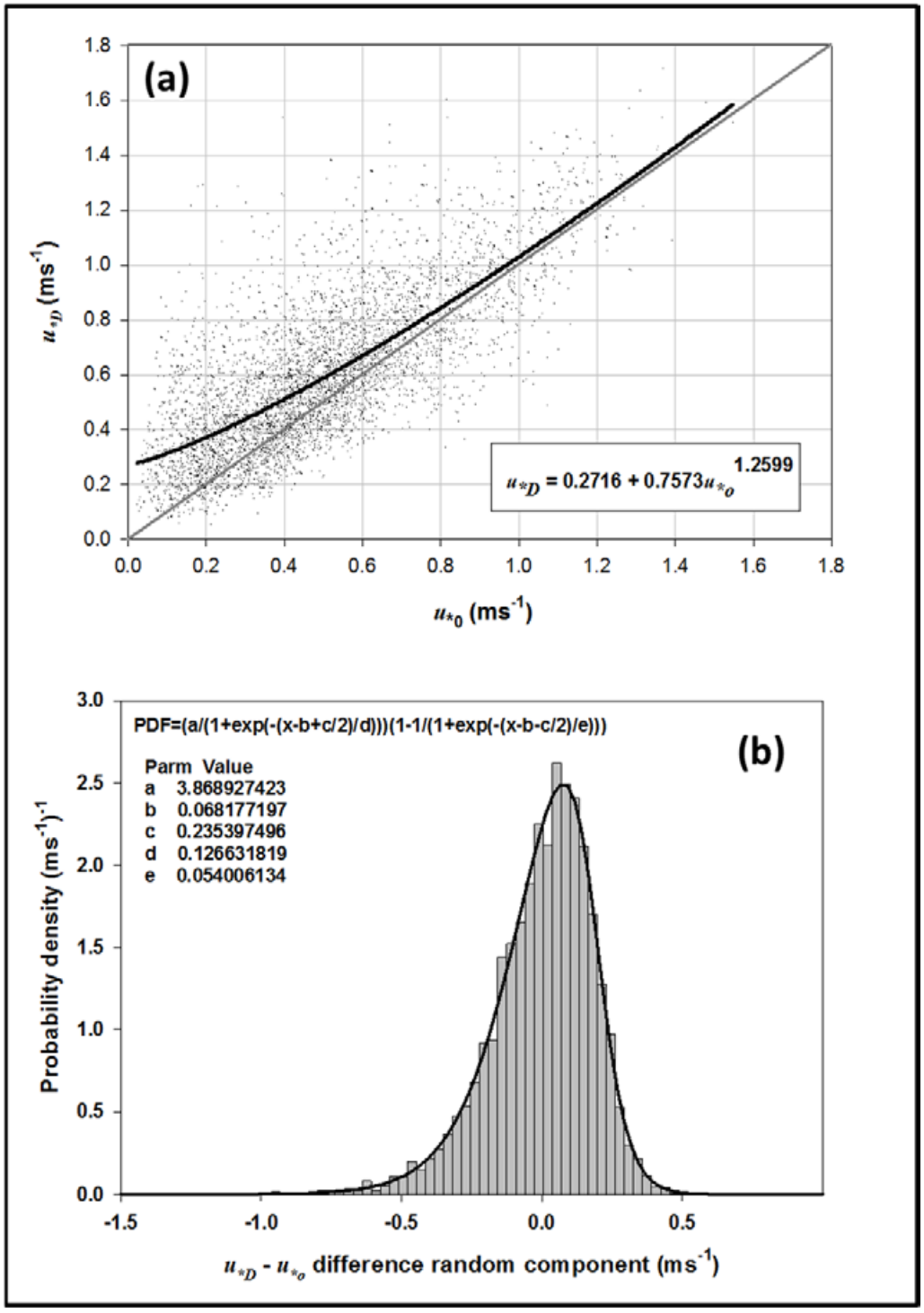

Figure 9-2. (a) Variation of NWTC ART rotor disk average value of local u_* (u_{*D}) with diabatic surface value, u_{*o}; (b) probability density distribution of $u_{*D} - u^*o$

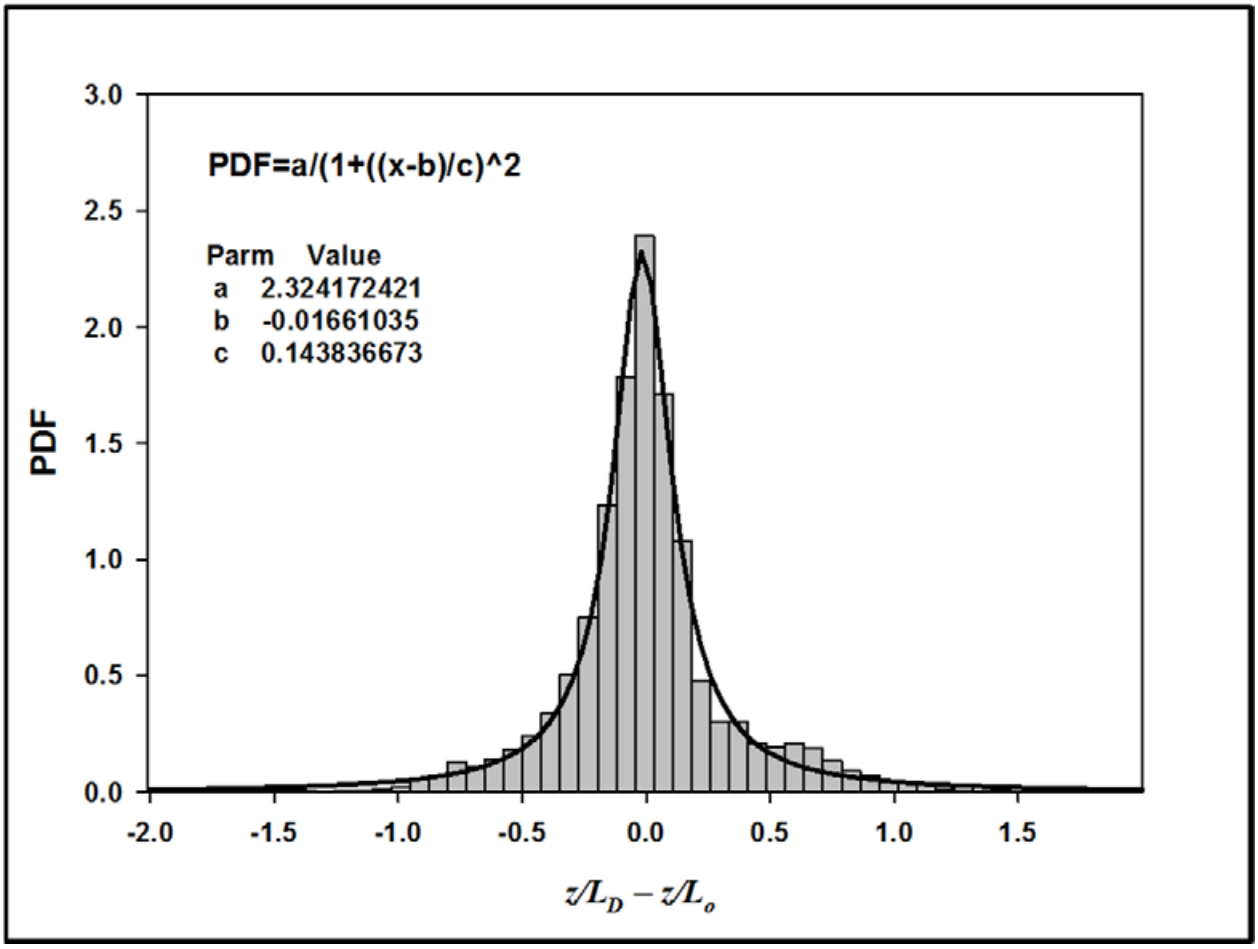

Figure 9-3. Probability density function *of* $z/L_D - z/L_o$ difference for NWTC ART rotor disk

For the Lamar site we found u_{*D} to be

$$u_{*D} = 0.0702 + 0.0249U_{85} - 0.0473Ri_{\mathrm{TL}} \quad , \tag{9-8}$$

where U is the mean speed at the 85-m (hub) height.

The variation of $u_{*\mathrm{D}}$ with $u_{*\mathrm{o}}$ for the Lamar site is plotted in Figure 9-4 for (1) all observations, (2) those with coherent structures at all heights, and (3) no coherent structures at any height. A best fit curve for all of the cases is also plotted. Figure 9-5 plots the observed variation of the local values of the stability parameter $z/L(\mathrm{z})$ at the four measurement heights on the tower with the surface value z/L_{o}. The largest difference occurs at the 116-m level, which is well into the ML. We also included the variation of the disk layer mean z/L_{D} shown as the blue-white dashed line. These curves show the level of decoupling near the surface and with the increasing penetration into the ML.

9.4.2 Modeling the Turbulent Spectral Energy Distributions

We applied the procedures discussed in Kelley (1992) to the NWTC and Lamar data that we used to derive the spectral scaling of the three turbulent velocity components $S_u(n)$, $S_v(n)$, and $S_w(n)$ at the three locations within the California wind farm. For stable SL scaling

$$nS_i(n)/u_*^2 = F(f, z/L_{M-O}) \quad , \tag{9-9}$$

and for unstable scaling

$$nS_i(n)/u_*^2 = F(f, z_i) \quad , \tag{9-10}$$

where $i = u, v,$ and w; n is the cyclic frequency; f is the reduced frequency given by nz/U; and z_i is the mixed layer depth. We estimate z_i using the relationships derived from Dutton, et al. (1979) and ESDU (1993)

$$z_i = \begin{cases} \dfrac{400U}{\log_{10}\left(\dfrac{z}{z_o}\right)} & \text{for } u_* < u_{*\mathrm{o}} \\ \\ \dfrac{u_*}{6f_c} & \text{for } u_* \geq u_{*_o}, \end{cases} \quad , \tag{9-11}$$

where U is the mean wind speed at height z, z_o the surface roughness length, u_{*o} is the surface value of u_*, , and f_c is the Coriolis parameter $2\omega \sin(\Omega)$, with ω being the Earth's rotation rate and Ω the latitude.

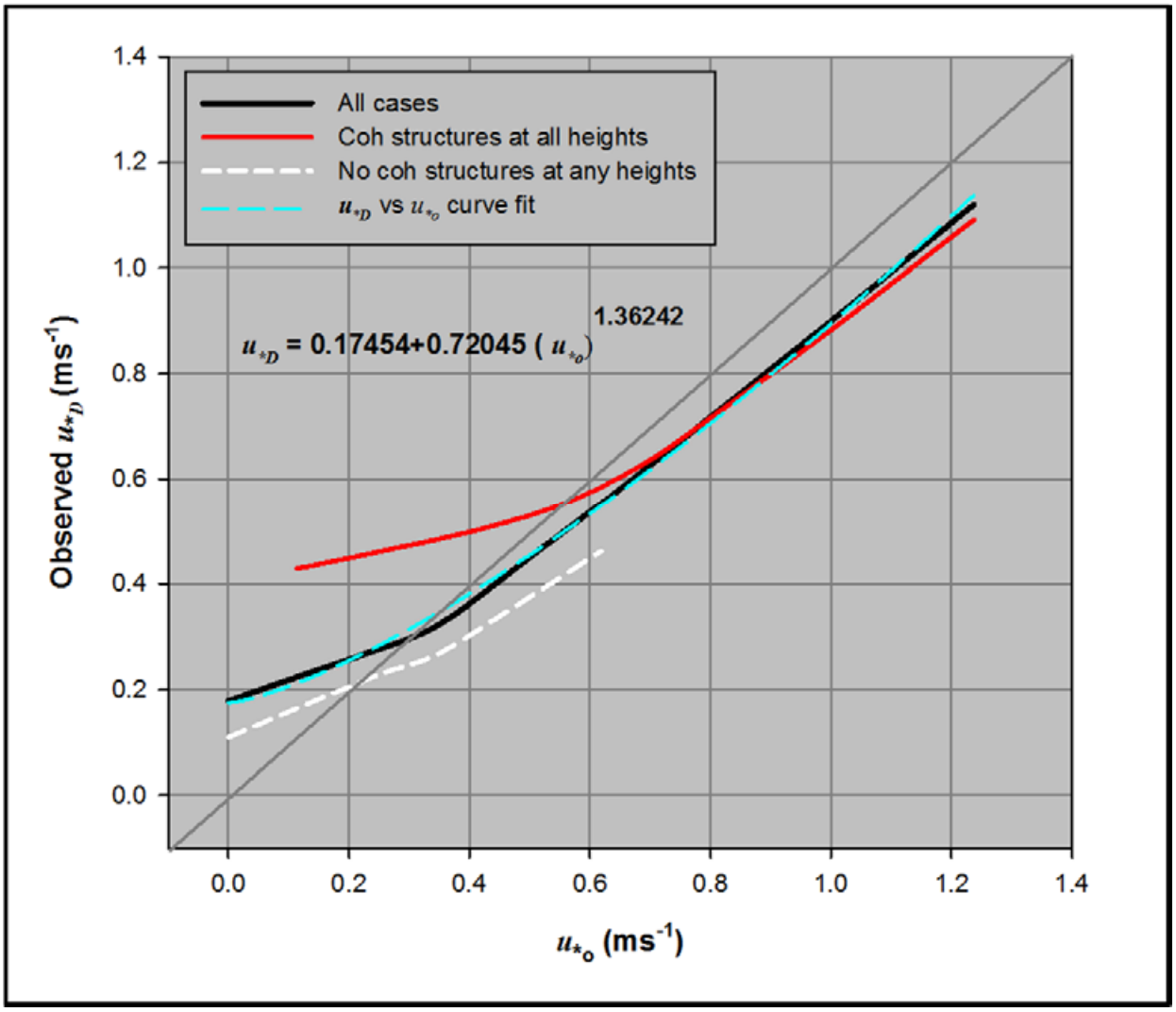

Figure 9-4. Variation of rotor disk layer mean value u_{*D} with surface value u_{*o} for all cases (black line), with coherent structures at all heights (red line), and with no coherent structures at any height within rotor disk layer (white dashed line). The dashed blue line is the best fit curve for all cases.

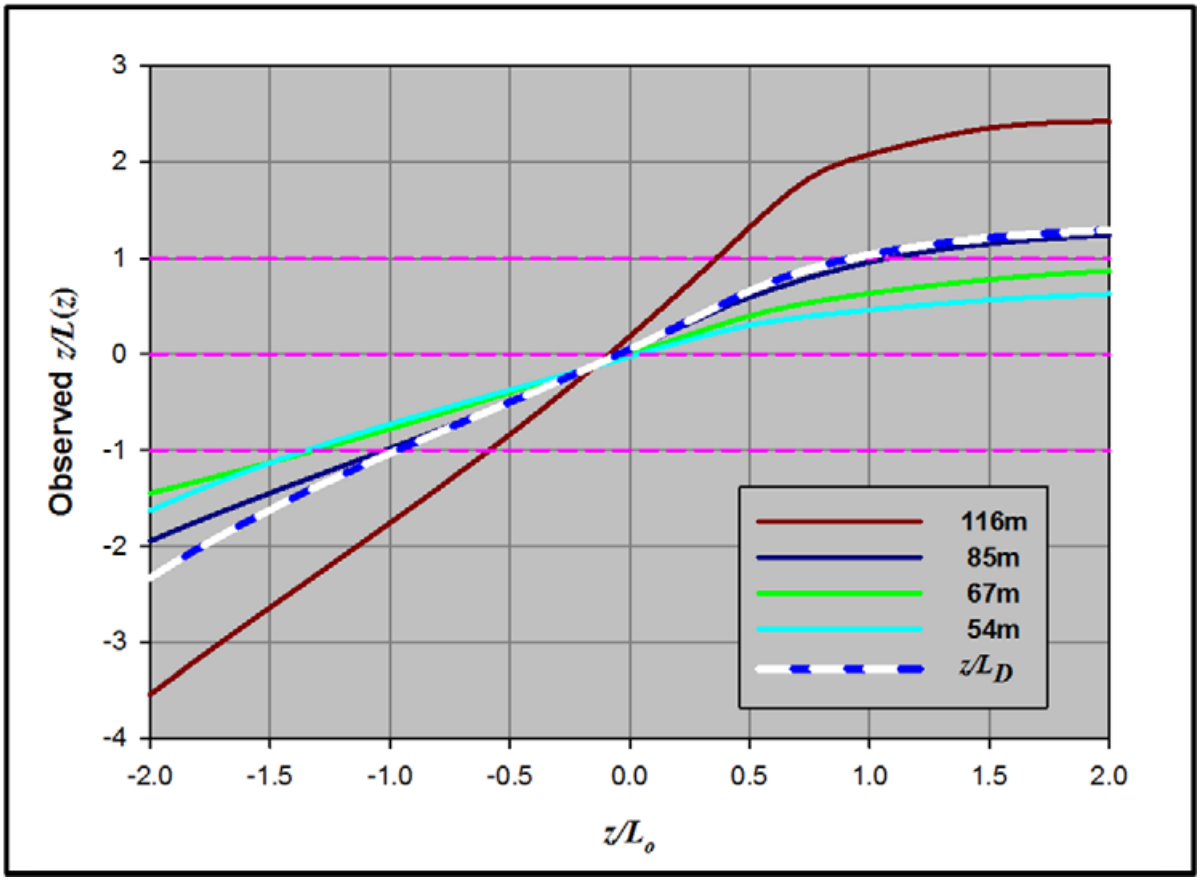

Figure 9-5. Lamar site variation of local stability parameter z/L and z/L_D with z/L_o by height. Horizontal and vertical dashed lines outline observed z/L value range of ±1.

We used the Risø SL spectral models (Højstrup 1982; Olesen, Larsen, and Højstrup 1984) for unstable and stable flows as the basis spectrum description and derived empirical scaling ratios Ψ, Φ to adjust the amplitudes and positions of the spectral peaks to agree with the site-specific measurements. For flat, homogeneous terrain, Kaimal and Finnigan (1984) and Kaimal et al. (1972) found that the *u* and *v* turbulent spectra in unstable flows could be modeled as the sum of two spectral peaks, as follows:

$$S(n) = S_L(n) + S_H(n) \quad , \tag{9-12}$$

where $S_L(n)$ and $S_H(n)$ are independent low- and high-frequency spectral contributions from turbulent kinetic energy created by buoyancy and shear, respectively. They found that the vertical velocity spectrum $S_w(n)$ had only a single peak. We found in analyzing the field data from the California wind farm, NWTC, and Lamar sites that multiple peaks existed in the *u* and *v* components for stable as well as unstable flows, probably from the influence of the mountainous terrain upstream, including Colorado. We also identified the existence of low- and high-frequency peaks in the vertical wind component in all except the Lamar site. Again this was probably related to the upstream mountainous terrain in San Gorgonio and at the NWTC.

To resolve these low frequency spectral peaks, we extended the length of the records to 30 minutes by concatenating contiguous triplets of 10-minute records that were at least quasi-stationary based on their second statistical moments. The amplitude and position of the spectral peaks were identified in each of these expanded records. We stratified the resulting spectral peaks by first stability class and then wind speed class. Empirical relationships with boundary turbulent scaling parameters and the spectral scaling ratios Ψ and Φ were then obtained for the low- and high-frequency peaks in each of the stability and wind speed classes. The same procedure was employed in analyzing the turbulence measurements from the NWTC and Lamar sites using the STC02, STC03, STC04, and STC05 stability classes and each of the 2-m s^{-1} mean wind speed categories appropriate for the particular site.

Figures 9-6 and 9-7 display the resolved low- and high-range spectral peaks found upwind of Row 1 and downwind of Row 41 in the wind farm as a function of Ri_{TL}. Figure 9-6 shows the cyclic frequencies associated with spectral peaks for each of the turbulent wind components. The 1/rev rotor rpm rates are indicated by the horizontal dashed lines. The same format is followed in Figure 9-7, but the peaks are presented as wavelengths scaled as equivalent rotor diameters for rated wind speed conditions. We were able to identify two spectral peaks for the vertical wind component in stable flows that were not found by Kaimal and Finnigan (1994), Kaimal and coauthors (1972), or Olesen and coauthors (1984) over flat, homogeneous terrain. The IEC Kaimal NTM equivalents are shown in both figures for neutral stability conditions. There is reasonable agreement with the observed *u*-component peaks, but significant deviations exist both upwind and downwind in the *v*- and *w*-components with the IEC Kaimal NTM. Figure 9-7 shows that spectral peaks in these components are much smaller than the rotor disks but at least one of the observed peaks is very close to coinciding.

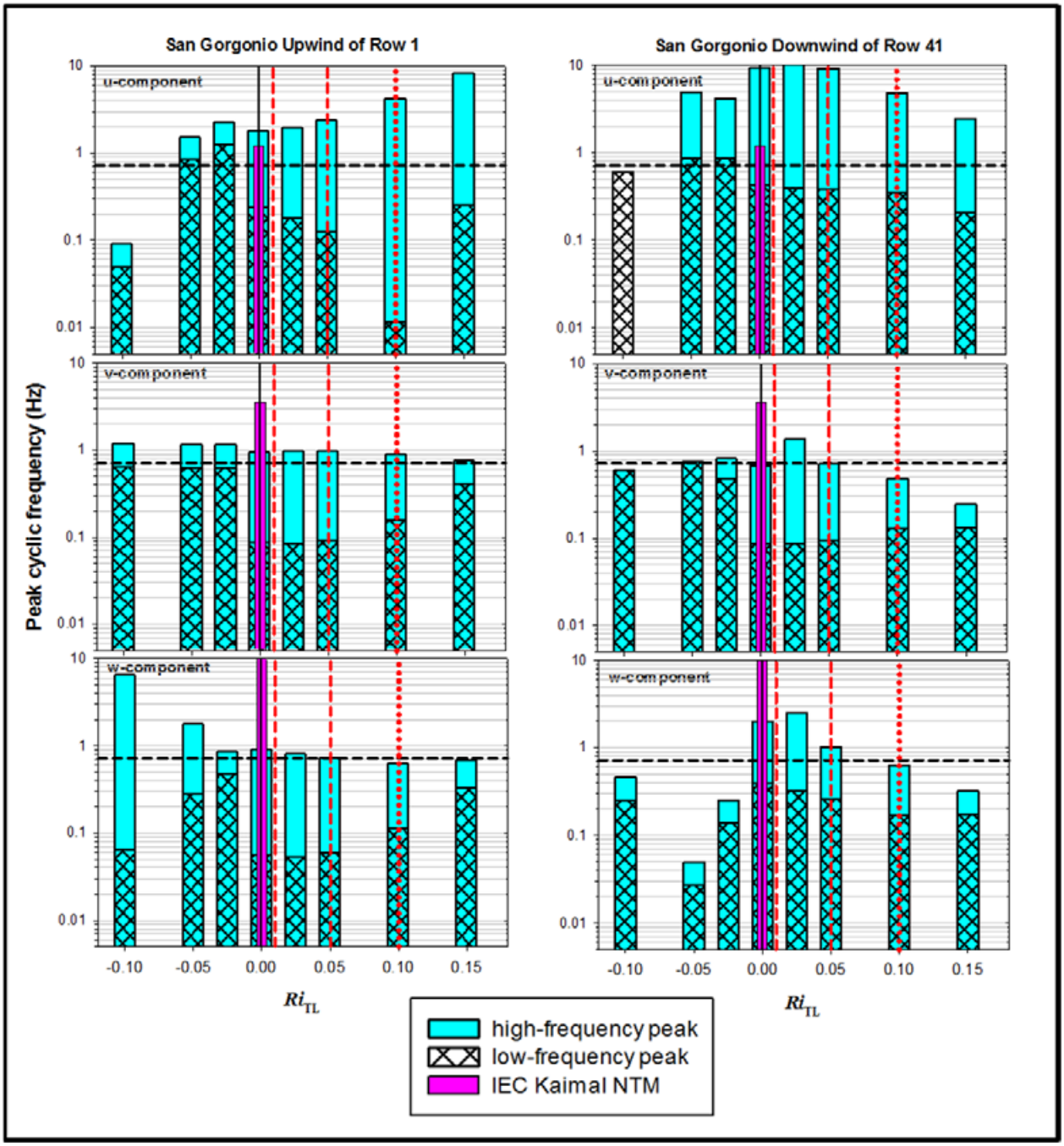

Figure 9-6. Variations of resolved turbulence high and low cyclic frequency spectral peaks upwind of Row 1 and downwind of Row 41 of California wind farm environment with Micon 65/13 Ri_{TL}. Horizontal dashed line represents 1/rev cyclic frequency. The CRR and CRRH stability class boundaries are shown as vertical dashed and dotted lines, respectively.

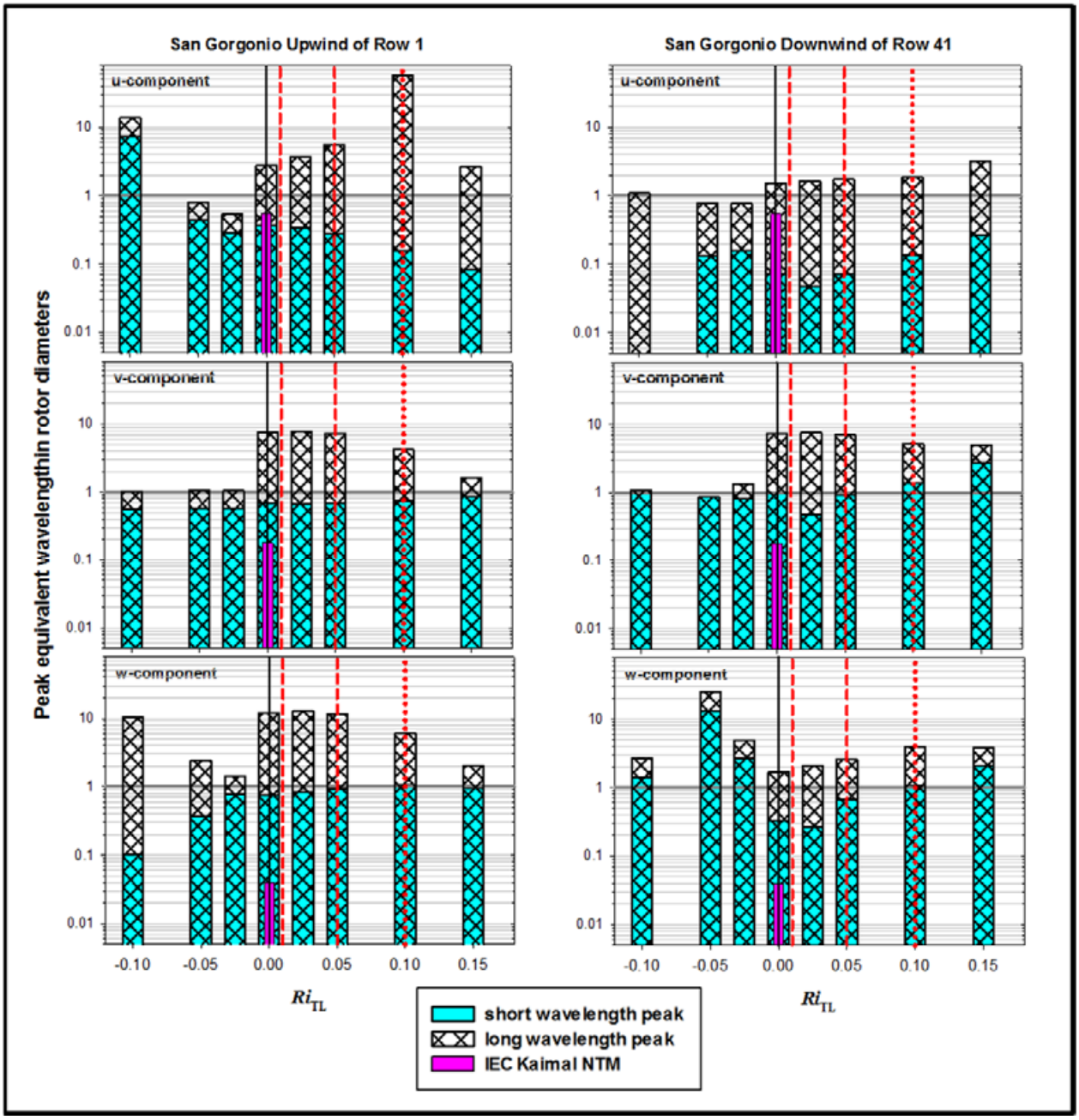

Figure 9-7. Same as Figure 9-6, but spectral peaks are scaled with equivalent Micon 65/13 rotor diameter for rated wind speed conditions

Figures 9-8 and 9-9 show the resolved low- and high-range spectral peaks found for the NWTC ART and the virtual WindPACT turbine operating in the Lamar site environment using the same format. In agreement with Kaimal et al. (1972) and Olesen et al. (1984), the Lamar site vertical turbulence component exhibits the single spectral peak characteristic of flat, homogeneous terrain. Flow at the NWTC, however, like the wind farm, contains both low- and high-frequency peaks. We believe this is a consequence of the mountainous terrain upwind of both sites. This signals a significant difference in the flow conditions that turbines are exposed to that is not replicated in the IEC Kaimal neutral NTM. Under neutral conditions, there is reasonable agreement in the *u*-component peak between the IEC Kaimal NTM and the observed peaks at the NWTC and Lamar sites. Much larger variances exist for the *v*- and *w*-components, however, which is consistent with our earlier observations of the greater levels of turbulent energy in these lateral components and again a likely consequence of the nearby complex terrain. Looking at the both the upwind and downwind San Gorgonio data in Figure 9-7 that falls within the CRR stability class ($+0.01 \leq Ri_{\mathrm{TL}} < +0.05$), we see that the short (high-frequency) and v- and *w*-component wavelength peaks occur very near the rotor diameter. The NWTC *w*-component short and long wavelength peaks in this same stability range closely bracket the equivalent rotor diameter. These peaks in the vertical component of turbulent energy in this critical stability range could easily be manifestations of Kelvin-Helmholtz Instability (KHI), and having scales closer to the rotor diameter could easily reflect a buoyancy length scale L_b near the same dimension since $L_b \propto \sigma_w$ by definition. We previously demonstrated that enhanced turbine dynamic response occurs when $L_b \approx D$.

The target frequency low- and high-frequency range spectra were arrived at by scaling the Risø SL models (Højstrup 1982; Olesen, Larsen, and Højstrup 1984) with the amplitude and positional scaling factors Ψ and Φ, respectively, which are empirical functions of u_* and $z/L_{M\text{-}O}$ derived for each of the wind speed and Ri_{TL} ranges. The source of the u_* and z/L scaling parameters varies with the site. For the wind farm models, the hub-height measured value of u_* was used and the z/L stability parameter was derived from Ri_{TL} using Equation 9-2. The neutral and stable NWTC model (NWTCUP) scaling factors Ψ and Φ use only the measured turbine layer mean z/L or z/L_D, but for the unstable spectra they depend on both the turbine layer mean values of u_{*D} and z/L_D. For the Lamar site, in the GP_LLJ we apply local scaling because the atmospheric layer of interest is well within the ML. Here Ψ and Φ are functions of height within a given wind speed and stability classification and we use empirical relationships based on the locally measured values of $u_*(z)$ and z/L (z) for both unstable and stable turbine layer conditions.

Figure 9-10 given examples of the wind farm spectra for the same hub wind speed and u_* value, but for Ri_{TL} values of –0.05, 0, and +0.05. The spectral distributions for the WF-07D and WF-14D spectral models inside the wind farm are the same and overlap. The *u*-component spectra show a larger contribution of low-frequency streamwise energy that increases with stability upwind of the wind farm. The lateral components *v* and *w* show a general increase in turbulent energy with increasing stability. Figures 9-11a and 9-11b plot similar information for the NWTCUP and GP_LLJ models, respectively. The NWTC site has a greater contribution of low frequency turbulent energy in the *u* and *v* components downwind of mountainous terrain compared with that seen in the flatter and more homogenous terrain associated with the Lamar site. The spectral distributions associated with the eight

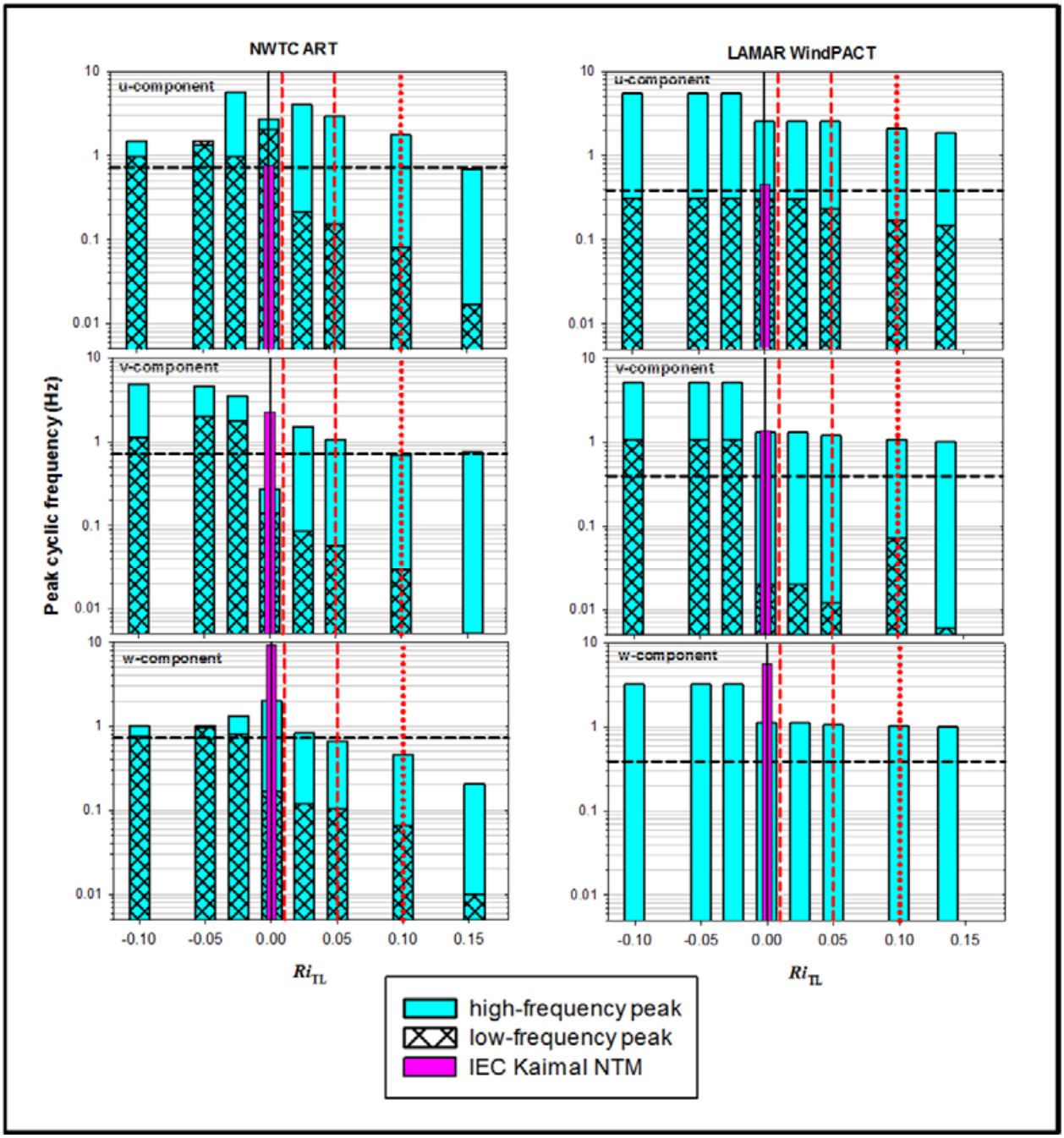

Figure 9-8. Same as Figure 9-6, but for NWTC ART and virtual WindPACT turbine in Lamar site environment

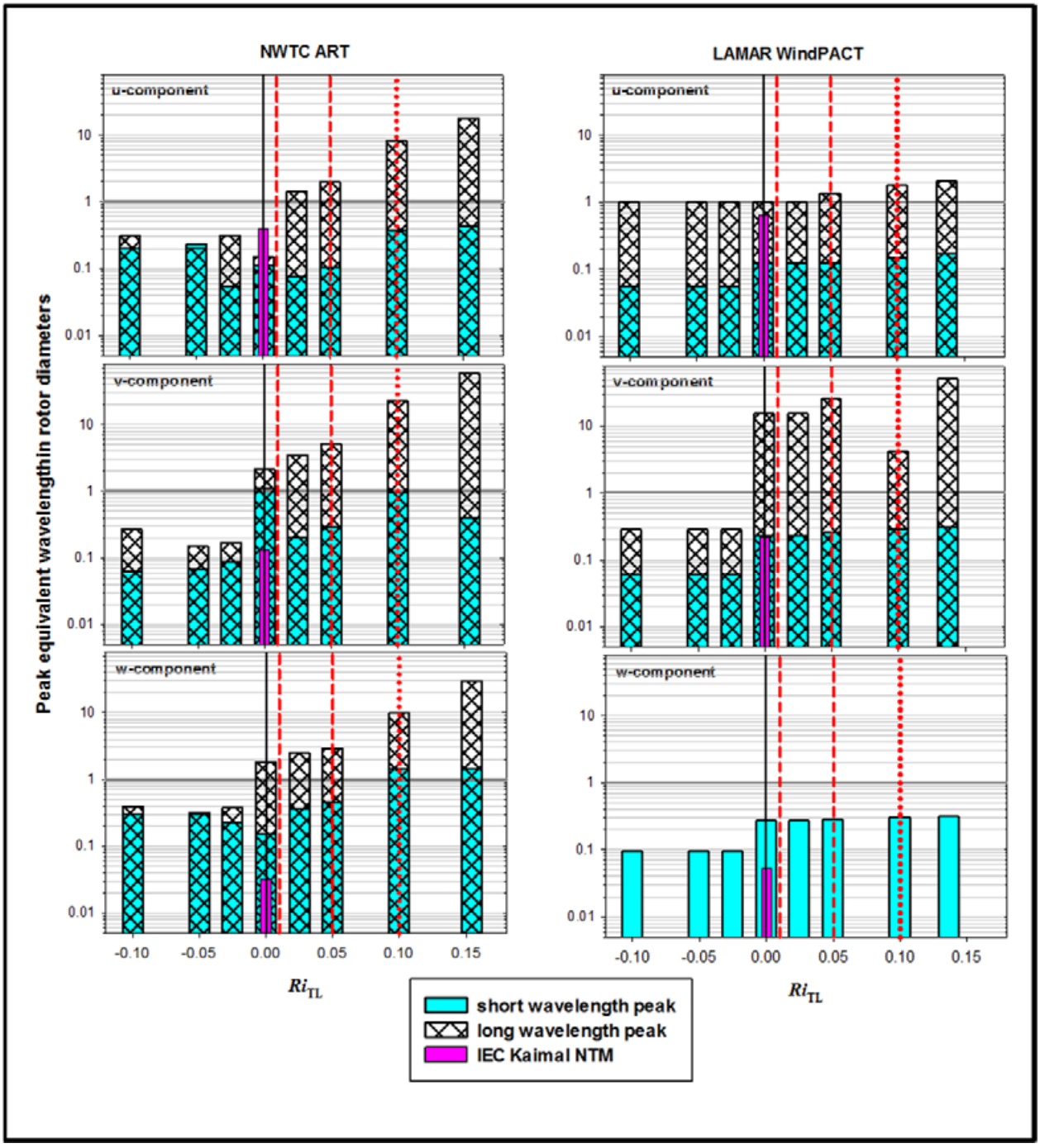

Figure 9-9. Same as Figure 9-8, but spectral peaks are scaled in equivalent rotor diameters for rated wind speed conditions

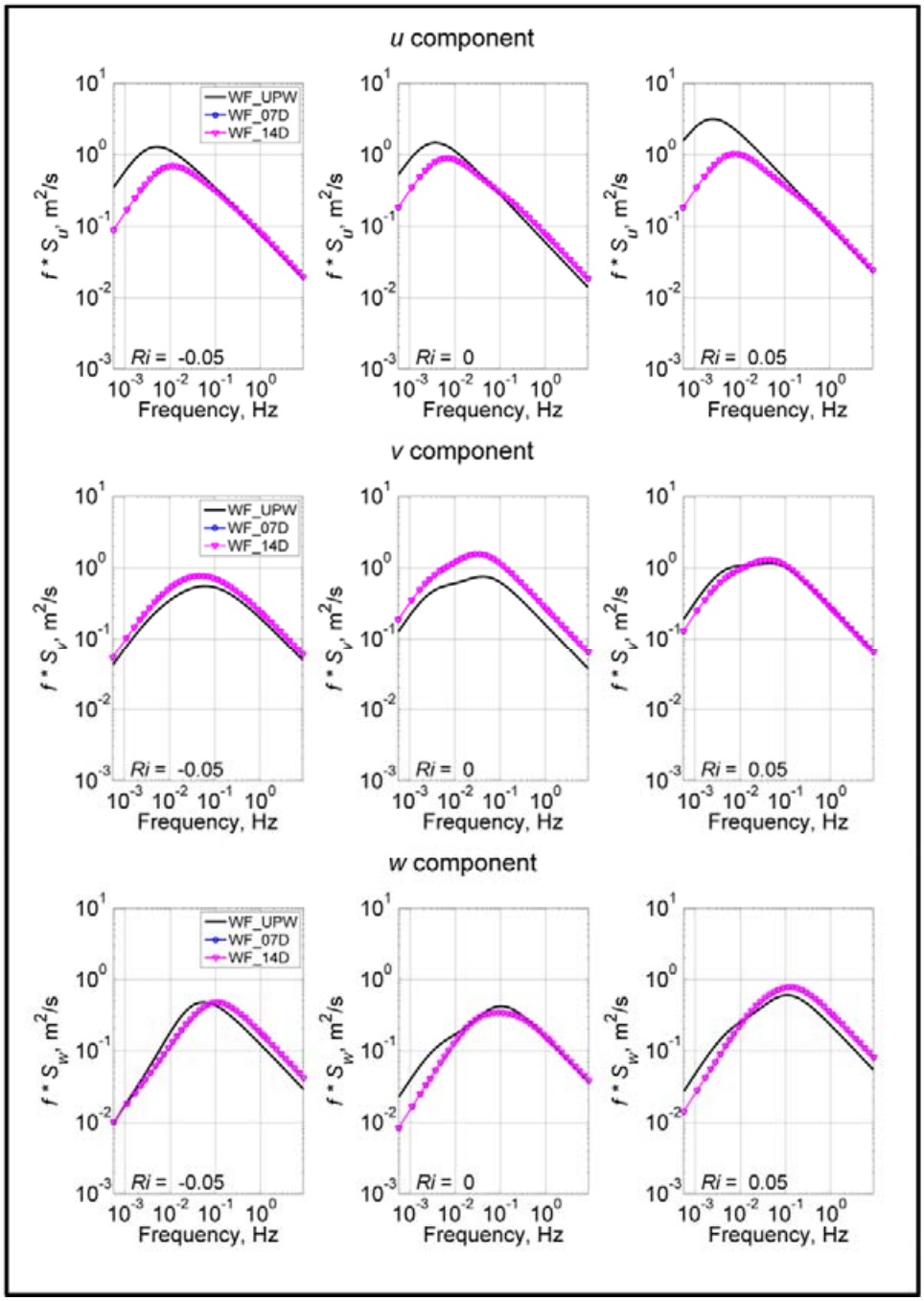

Figure 9-10. Example of turbulent component logarithmic spectral variations with stability for wind farm models (WF_UPW, WF_7D, and WF_14D). The WF_7D model uses the same spectral distribution as the WF_14D model, and therefore the plotted spectra for these two positions in the wind farm are identical because a common value of u_* was used to scale all three models.

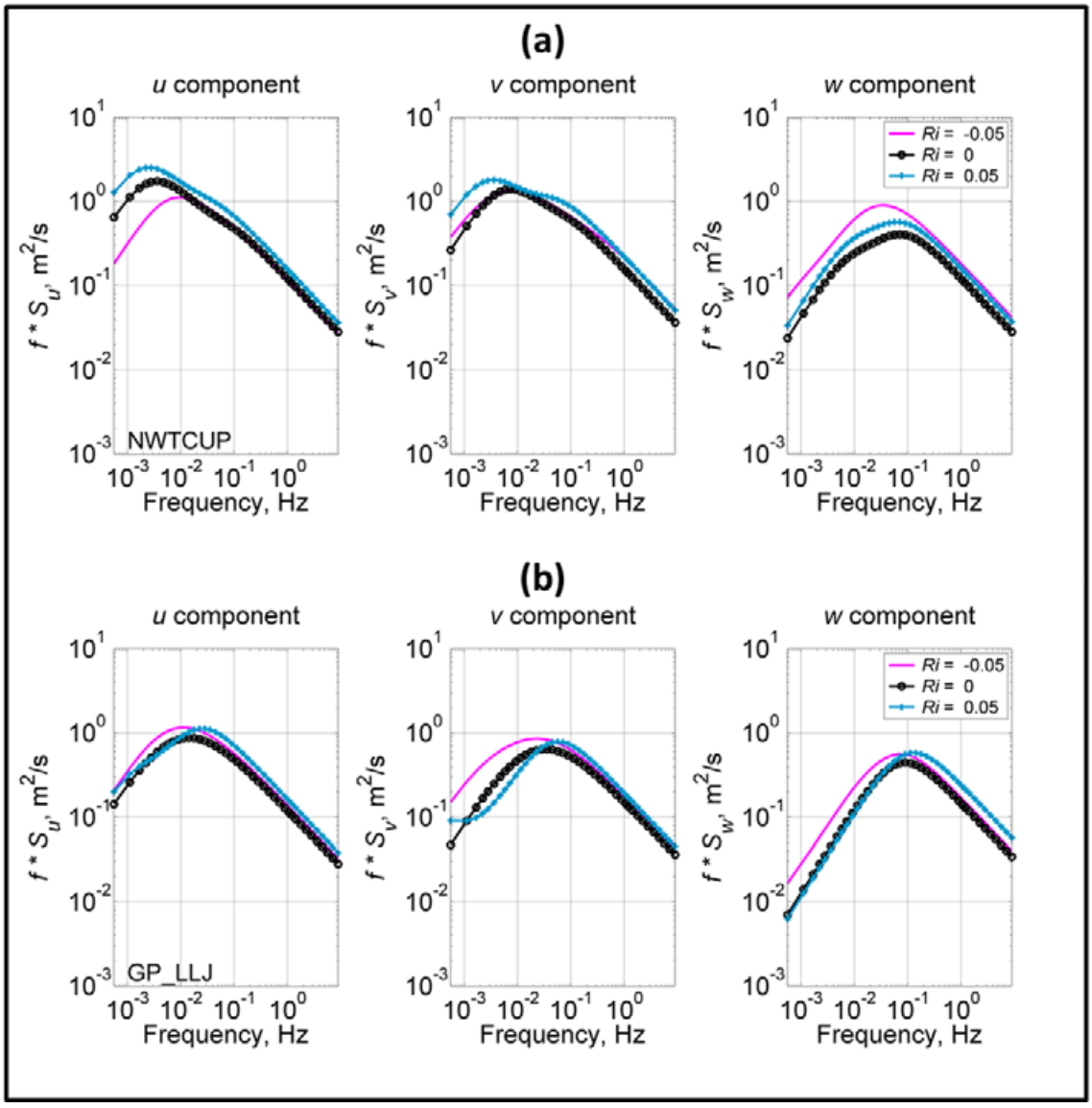

Figure 9-11. Comparison of variation of turbulent component logarithmic frequency spectra with stability for hub height of 80 m, U_{hub} = 15 m s^{-1}, and u_{*D} = 1.1 m s^{-1} for (a) NWTCUP and (b) GP_LLJ models

models available in TurbSim are summarized in Figure 9-12 for a hub height of 80 m, mean wind speed of 15 m s^{-1}, and a turbine layer mean u_{*D} value of 1.1 m s^{-1} by Ri_{TL} values of –0.05, 0, and +0.05 in columns (a), (b), and (c). The grey shaded areas outline the IEC Kaimal (IECKAI) NTM and the light blue line with the x-symbol the IEC von Kârmân (IECVKM) neutral spectral models. The largest obvious deviation from the IECKAI model is the energy in the *w*-component spectra, which generally increases with increasing stability.

In Figure 9-13 we plot the variation with stability of the equivalent wavelengths (space scales) of the high-frequency spectral peaks of the turbulence components found at the 23-m hub height downwind of the wind farm. The rotor diameters of the NREL and AeroStar rotors are shown as

horizontal solid and dashed lines, respectively. The CRR stability range is annotated with the vertical dot-dot-dashed line within its boundaries as the value of Ri_{TL} where we found the maximum dynamic response of the Micon 65/13 turbines. Clearly the wavelengths of these spectral peaks coincide with the rotor diameters within the CRR stability range, and the vertical component peak also coincides closely with the Ri_{TL} of the maximum turbine dynamic response. In Figure 9-14a we compare the ratios of the hub-height turbulence components *u*, *v*, and *w* with the local value of u_* and σ_v / σ_u and σ_w / σ_u upwind of the wind farm Row 1 for stable conditions, and Figure 9-14b contains the same information for downwind of Row 41.

We know from our previous discussion that the CRR range is dominated by the fastest-growing turbulent structures created by KHI, and their equivalent dimensions are similar to the turbine rotor disk diameters. The strong correlation between the Micon turbine dynamic loads and the σ_v / σ_u and σ_w / σ_u ratios is pictured in Figure 3-17. We are assured thus that the TurbSim WF-07D and WF-14D spectral models reproduce this aspect of wind farm internal background wake flows. We also know, however, that the most intense coherent structures are not included in this flow and must be introduced by other means. These results also underscore the fact that the nature of internal wake flows within a large wind farm is heavily influenced by KHI, which must be included in any microscale simulations of such phenomena. The need to include KHI is further supported by comparing Figure 9-14a (WF_UPW) and the modeled conditions by over flat, homogenous terrain (Risø SMOOTH model) and downwind of complex terrain at the NWTC (NWTCUP model) in Figure 9-15. In Figures 9-14 and 9-15 we see that the models simulating flows near mountainous complex terrain have similar characteristics, but conditions in smooth, homogenous terrain are significantly different. The IECKAI is approximately equivalent to a neutral scaling of the TurbSim implementation of the Risø SMOOTH spectral model. The turbulent conditions within the wind farm in Figure 9-14b are, however, even more disparate compared with the others. We are seeing the effects of an atmospheric resonance created by K-H instability that occurs with such frequency as to influence the background flow within the wind farm under weakly stable conditions (CRR and CRRH stability ranges). Such conditions occur outside of the wind farm but much less frequently, as hinted at by the σ_w / u_* ratio peaks occurring within the CRR stability range in the SMOOTH and NWTCUP models in Figure 9-15.

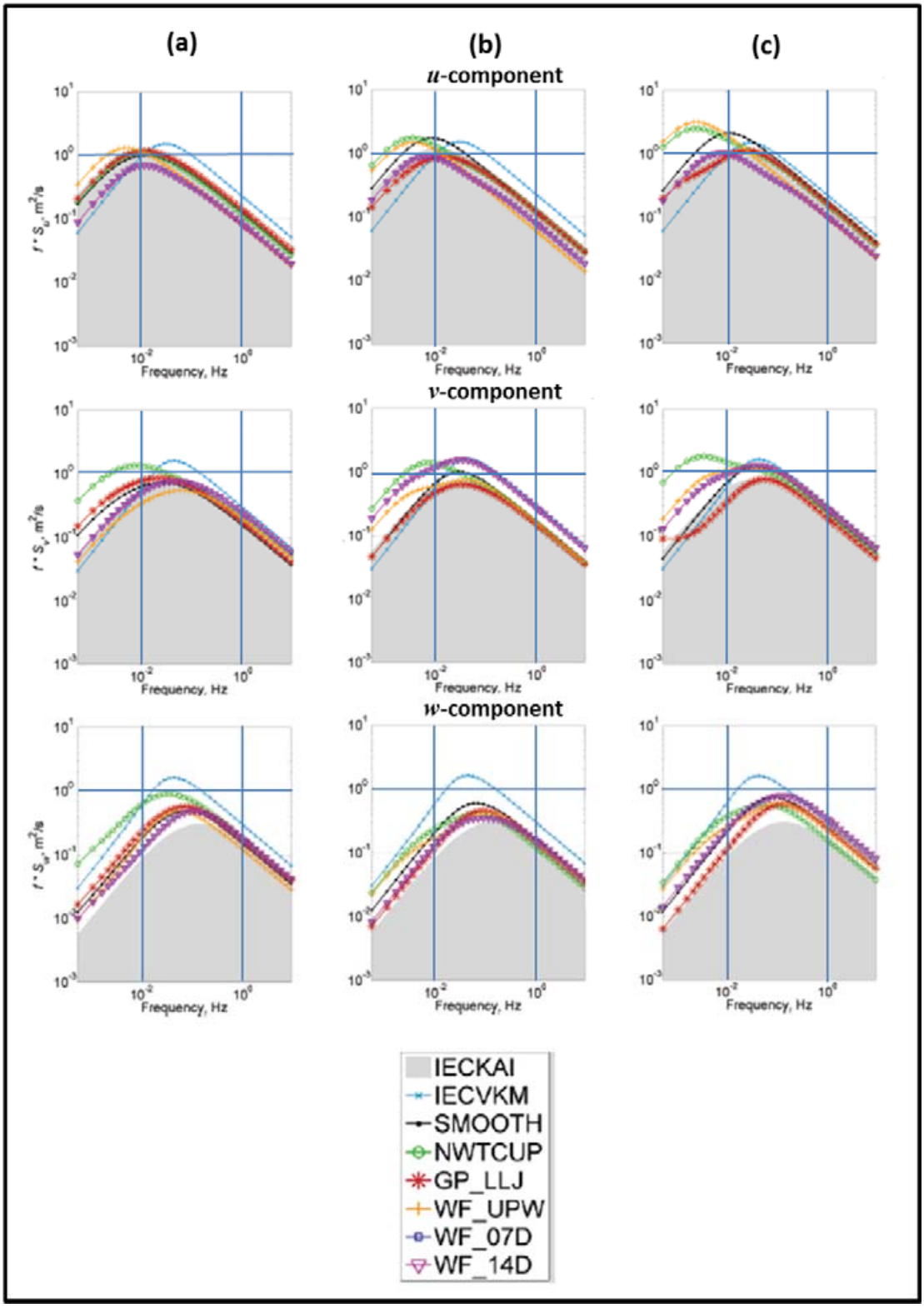

Figure 9-12. Comparisons of TurbSim model turbulent component spectra for hub height of 80 m, U_{hub} = 15 m s^{-1}, u^*_D = 1.1 m s^{-1}: (a) Ri_{TL} = –0.05; (b) Ri_{TL} = 0; (c) Ri_{TL} = +0.05

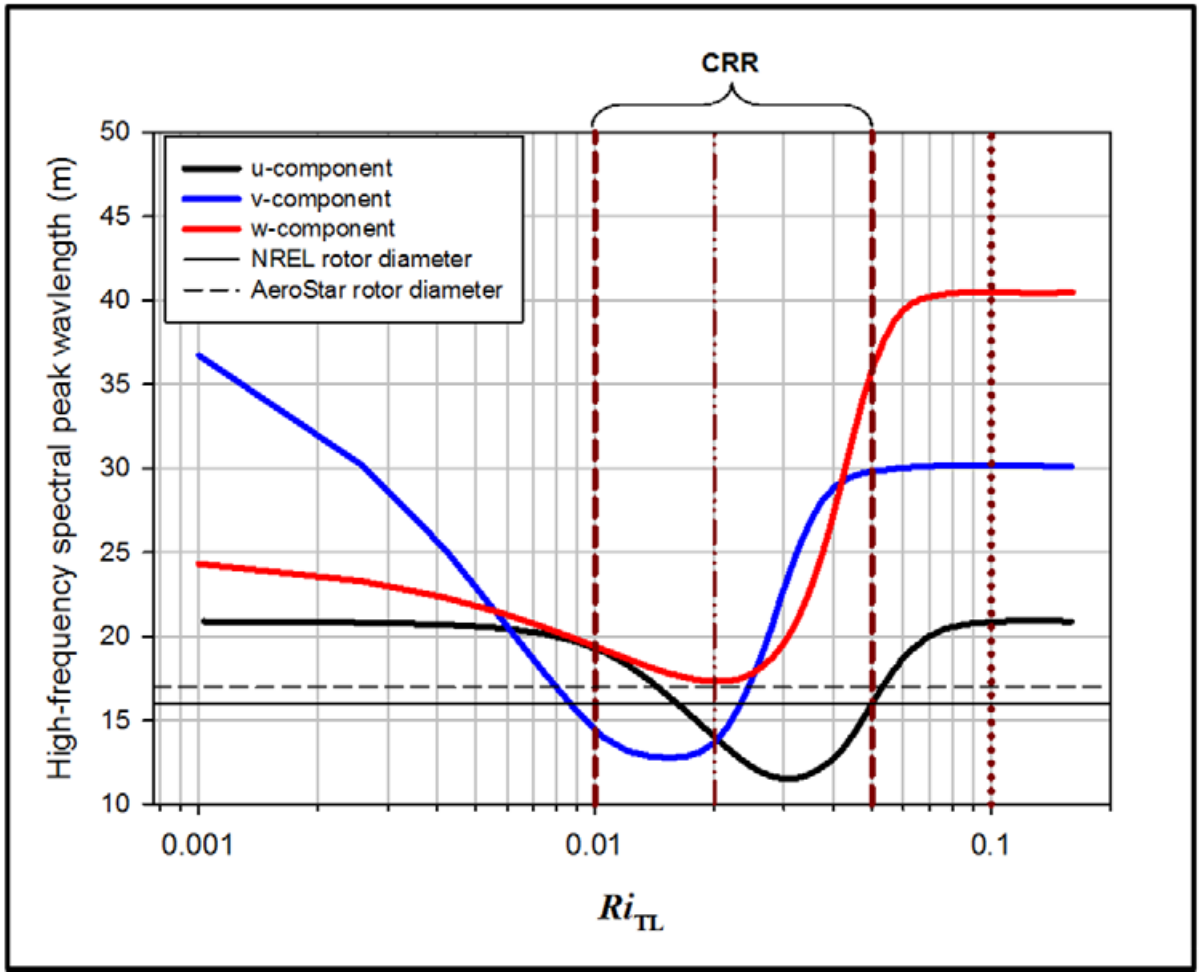

Figure 9-13. Variations of equivalent wavelengths of high-frequency turbulence component spectral peaks with Ri_{TL}. San Gorgonio WF_7D and WF_14D spectral models scaled with the hub height of 23 m, U_{hub} = 12 m s^{-1}, and u_* = 1 m s^{-1}.

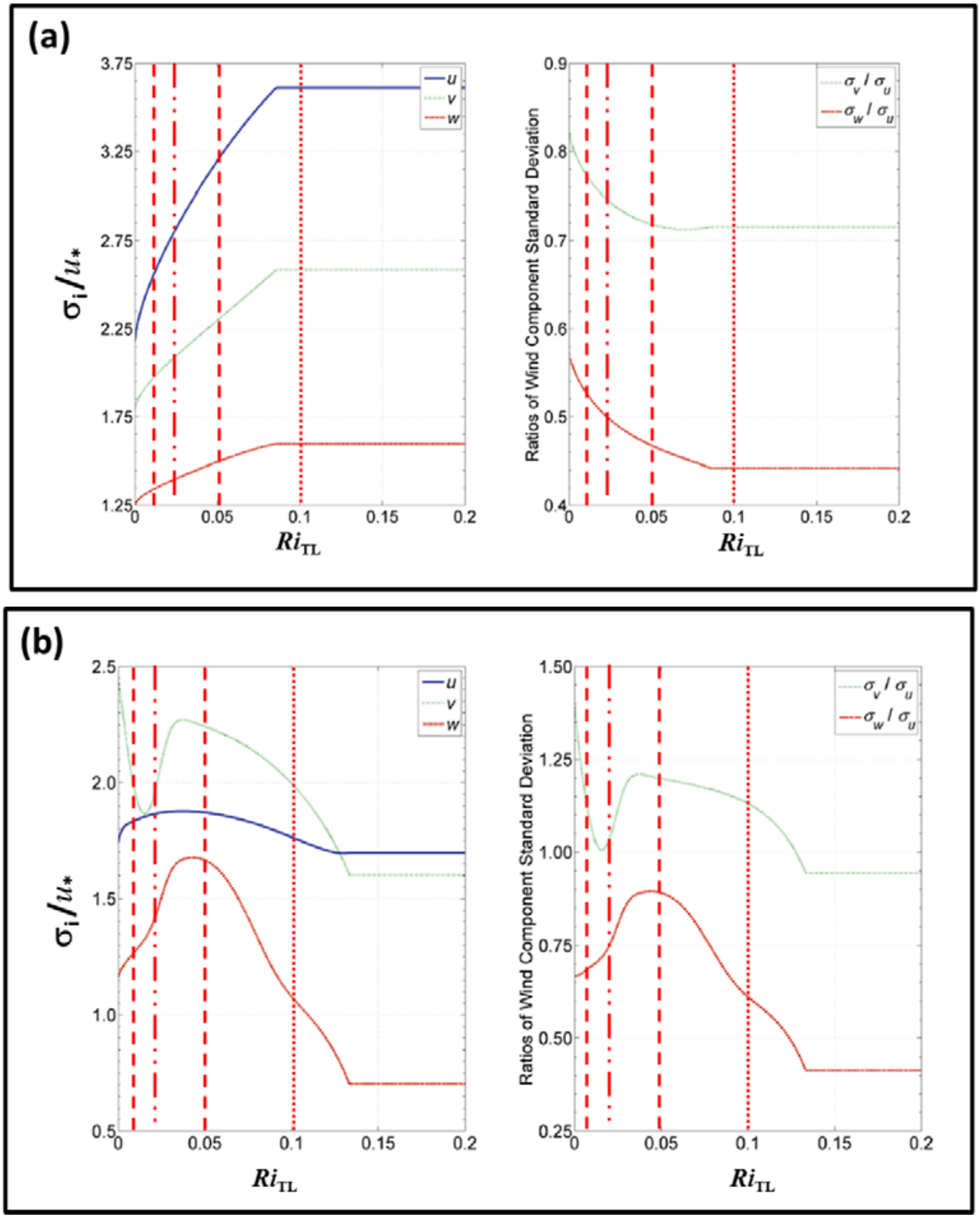

Figure 9-14. California wind farm variations of ratios of σ_u , σ_v , and σ_w with hub u_* and σ_v /σ_u , σ_w /σ_u with stable stability for (a) upwind of Row 1; and (b) upwind of Row 37 (7D) and downwind of Row 41 (14D)

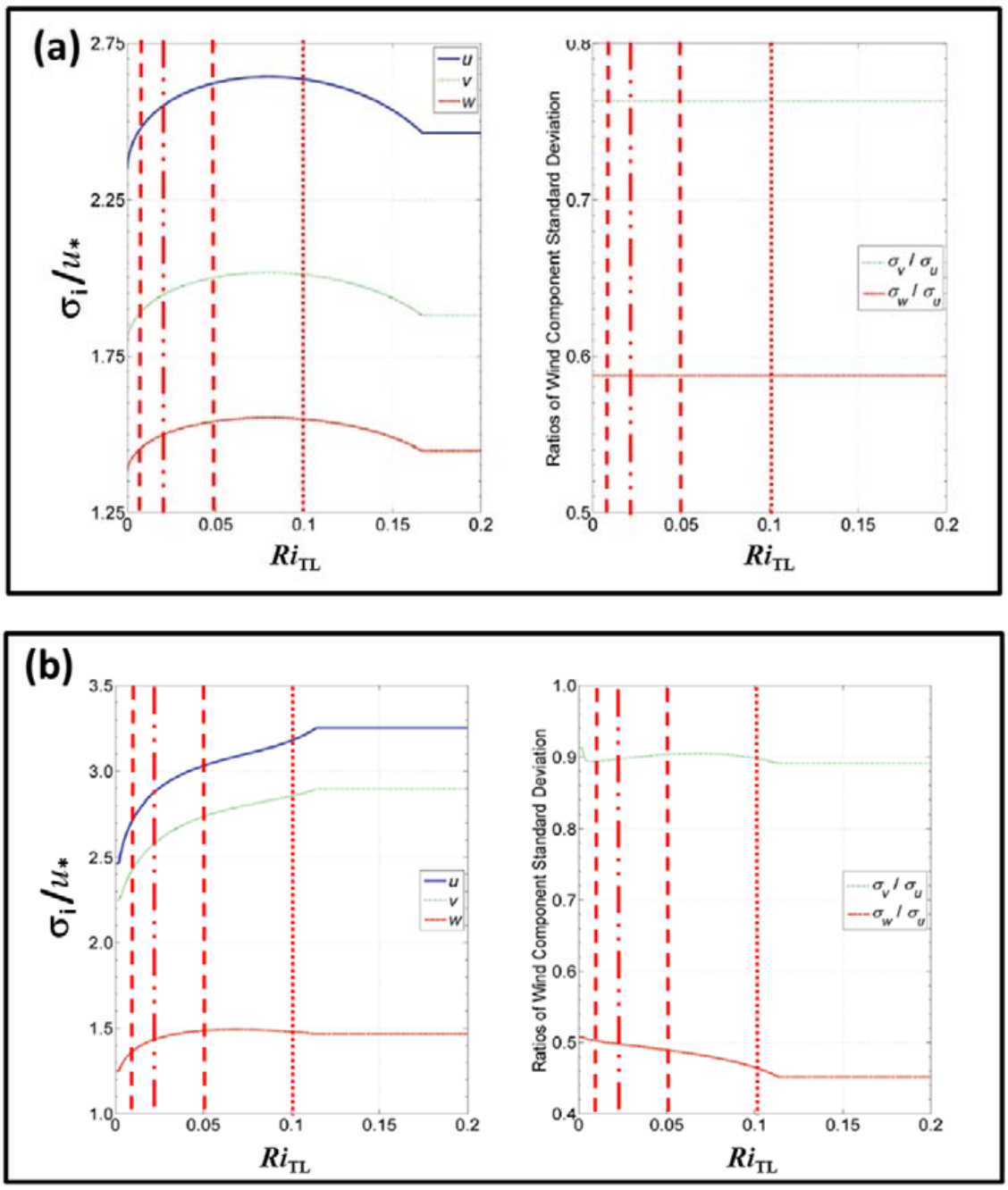

Figure 9-15. Variation of ratios of σ_u , σ_v , and σ_w with hub u_* and σ_v/σ_u , σ_w/σ_u with stable stability for (a) TurbSim SMOOTH and (b) NWTCUP spectral models

9.4.3 Cross-Component Correlation and Mean Reynolds Stress Component Scaling

We demonstrated the importance of coherent turbulence in the dynamic response of wind turbines. Turbine blade root damage equivalent and peak loads were shown to scale with coherent kinetic turbulent energy or E_{coh} (CTKE), which defined as the magnitude of the vector sum of the Reynolds stress components $u'w'$, $u'v'$, and $v'w'$. These components are measures of the degree of cross correlation between the orthogonal turbulence velocity components *u*, *v,* and *w* that exists in the background flow over a 10-minute record. Figure 9-16 summarizes the probability distributions of the cross-correlation coefficients r_{uw}, r_{uv}, and r_{vw} for the available unstratified populations from hub height at the three wind farm locations and the available measurement heights at the NWTC and Lamar sites. These plots reveal that the local background flow velocity components at all three sites and heights, with perhaps one exception, have a significant level of correlation and therefore nonzero Reynolds stress components. The flows upstream, within, and downstream of the multirow wind farm have narrower distributions than the purely natural flows seen at the NWTC and Lamar sites. So it is important that flows simulated by TurbSim reproduce these turbulence correlation characteristics at the three sites.

By design, the Fourier inversion process creates a velocity time series with random phase from the target frequency spectrum. Cross-component characteristics must be introduced into the simulated time series to reproduce the correlation or phase distributions seen in Figure 9-16. This is accomplished by specifying target mean Reynolds stress components at the hub height of the turbine being modeled. We developed MLR models of the variation of these mean stresses as the dependent variable and the available input scaling parameters as the independent variables. Table 9-1 lists the parameters with a statistically significant influence on the three hub-height mean Reynolds stress components for the three locations at the wind farm. It is interesting to note that stability was not one of the parameters. Tables 9-2 and 9-3 present the sensitivity matrices for the available measurement heights at the NWTC and Lamar sites. Height relationships were then developed to scale these independent variables to define vertical variation of the magnitudes of the mean Reynolds stress components across the height of the disk layer.

These models produce only estimates of the mean stress components and do not include their polarity. In Figure 9-17 we plot the residuals from the hub-height MLR fits, which provide the polarity distribution about the mean. These can be described as a bias plus a random component. As an example, the residuals from the $\overline{u'w'}$ MLR model for the internal San Gorgonio sites (Figure 9-17a) at Rows 37 and 41 have a substantial negative bias because of the strong downward momentum fluxes discussed earlier. The equivalent Gaussian distribution fits are shown with dashed lines. All three of the random distributions follow Gaussian distributions closely. The $\overline{u'v'}$ and $\overline{v'w'}$ components exhibit much smaller or near zero biases and also are Gaussian distributed, but the variability (breadth) varies considerably with the 7*D* upwind row-to-row spacing conditions at Row 37 creating the greatest variability in the $\overline{u'v'}$ mean stress. With the exception of the $\overline{u'v'}$ stress, the residual distributions from the natural inflows at hub height at the NWTC and Lamar sites (Figures 9-17b, c) have zero or very small biases but generally non-Gaussian distributions. The $\overline{u'v'}$ stress distributions have very long negative tails. The negative tail at the NWTC extends 10 times greater than that at the Lamar site. We implemented the target mean Reynolds stress components in TurbSim derived from the site-specific MLR model plus a random component whose probability distribution is particular to the

site and stress component. Figures 9-16 and 9-17 show the significant variation between the sites, particularly for the $\overline{u'v'}$ and $\overline{v'w'}$ stress (correlation) levels, none of which is included in the IEC Kaimal NTM or von Kârmân spectral models. The neutral IEC Mann constant stress model includes the full Reynolds stress tensor or components, but it is not clear if it would reproduce the contents of Figure 9-17. It seems doubtful since these distributions are empirical and site specific. We saw in Figures 3-17 and 3-18 for the Micon turbines and Figure 4-23 the ART that root bending fatigue damage and peak loads are very sensitive to the level of these two mean Reynolds stress components in the CRR stability range. The Micon low-speed shaft dynamic response is also very sensitive to the $\overline{v'w'}$ component within the same stability range, as is shown in Figure 3-23. Clearly, simulating these mean stress distributions is very important to fully induce the dynamic loading seen in actual turbine operations in these environments!

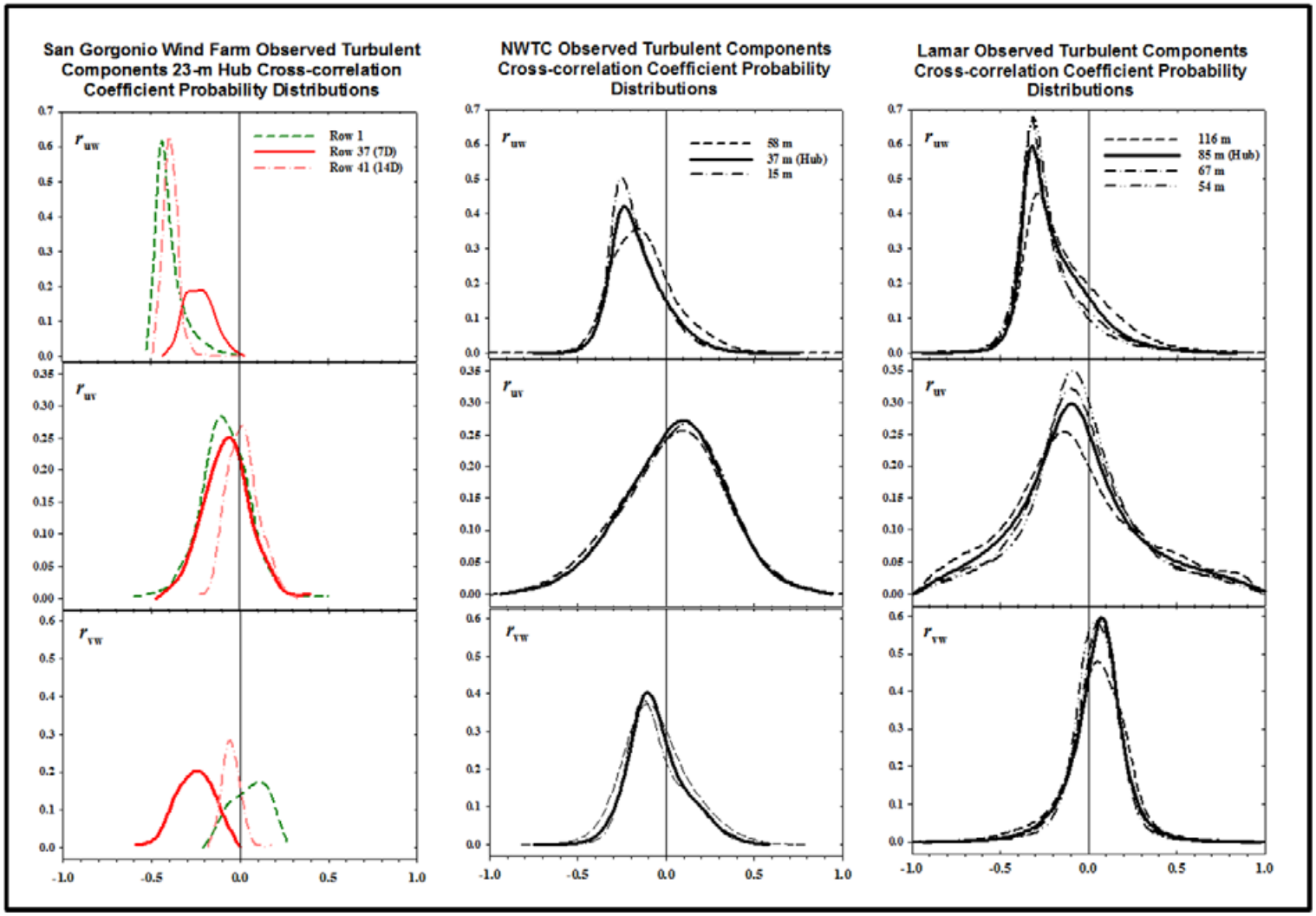

Figure 9-16. Observed turbulence component cross-correlation coefficient probability distributions (r_{uw}, r_{uv}, and r_{vw}) for 23-m hub height at three locations at California wind farm, three heights within ART rotor disk on Row 4 of NWTC, and at five heights within virtual WindPACT 1.5-MW turbine rotor disk layer at Lamar site

Table 9-1. Mean Reynolds Stress Scaling Magnitudes Sensitivities at California Wind Farm Locations with Turbine Layer Turbulence Parameters

$\left\|\overline{u'w'}\right\|$ component			
Location	U_{hub}	$\partial\overline{U}/\partial z_D$	$u_{*\,hub}^2$
Upwind (Row 1)	✓	✓	
7D (Row 37)	✓	✓	
14D (Row 41)	✓		
$\left\|\overline{u'v'}\right\|$ component			
Upwind (Row 1)		✓	✓
7D (Row 37)			✓
14D (Row 41)			✓
$\left\|\overline{v'w'}\right\|$ component			
Upwind (Row 1)		✓	✓
7D (Row 37)			✓
14D (Row 41)			✓

Table 9-2. Sensitivities of Mean Reynolds Stress Component Magnitudes to Turbine Layer Turbulence Scaling Parameters in NWTC Row 4

z	U_{hub}	Ri_{TL}	${u_*}^2{}_{\mathrm{D}}$	$(\partial\overline{U}/\partial z)_{\mathrm{D}}$	z/L_{D}
$\left\lvert\overline{u'w'}\right\rvert$ **component**					
58 m	✓	✓	✓	✓	
37 m	✓	✓	✓	✓	
15 m	✓		✓		
$\left\lvert\overline{u'v'}\right\rvert$ **component**					
58 m	✓	✓	✓	✓	
37 m	✓	✓	✓	✓	
15 m	✓		✓		
$\left\lvert\overline{v'w'}\right\rvert$ **component**					
58 m	✓	✓	✓	✓	✓
37 m	✓	✓	✓	✓	
15 m	✓		✓		

Table 9-3. Sensitivities of Mean Reynolds Stresses Magnitudes to Turbine Layer Turbulence Scaling Parameters at Lamar Site

z	U_{hub}	Ri_{TL}	z/L_D	$\partial\overline{U}/\partial z_D$	$u_*^2{}_D$
$\lvert\overline{u'w'}\rvert$ component					
116 m	✓	✓	✓	✓	✓
85 m	✓	✓		✓	✓
67 m	✓		✓	✓	✓
54 m	✓		✓		✓
$\lvert\overline{u'v'}\rvert$ component					
116 m	✓		✓		✓
85 m	✓		✓		✓
67 m	✓		✓		✓
54 m	✓	✓			✓
$\lvert\overline{v'w'}\rvert$ component					
116 m	✓	✓		✓	✓
85 m	✓	✓		✓	✓
67 m	✓	✓		✓	✓
54 m	✓	✓		✓	✓

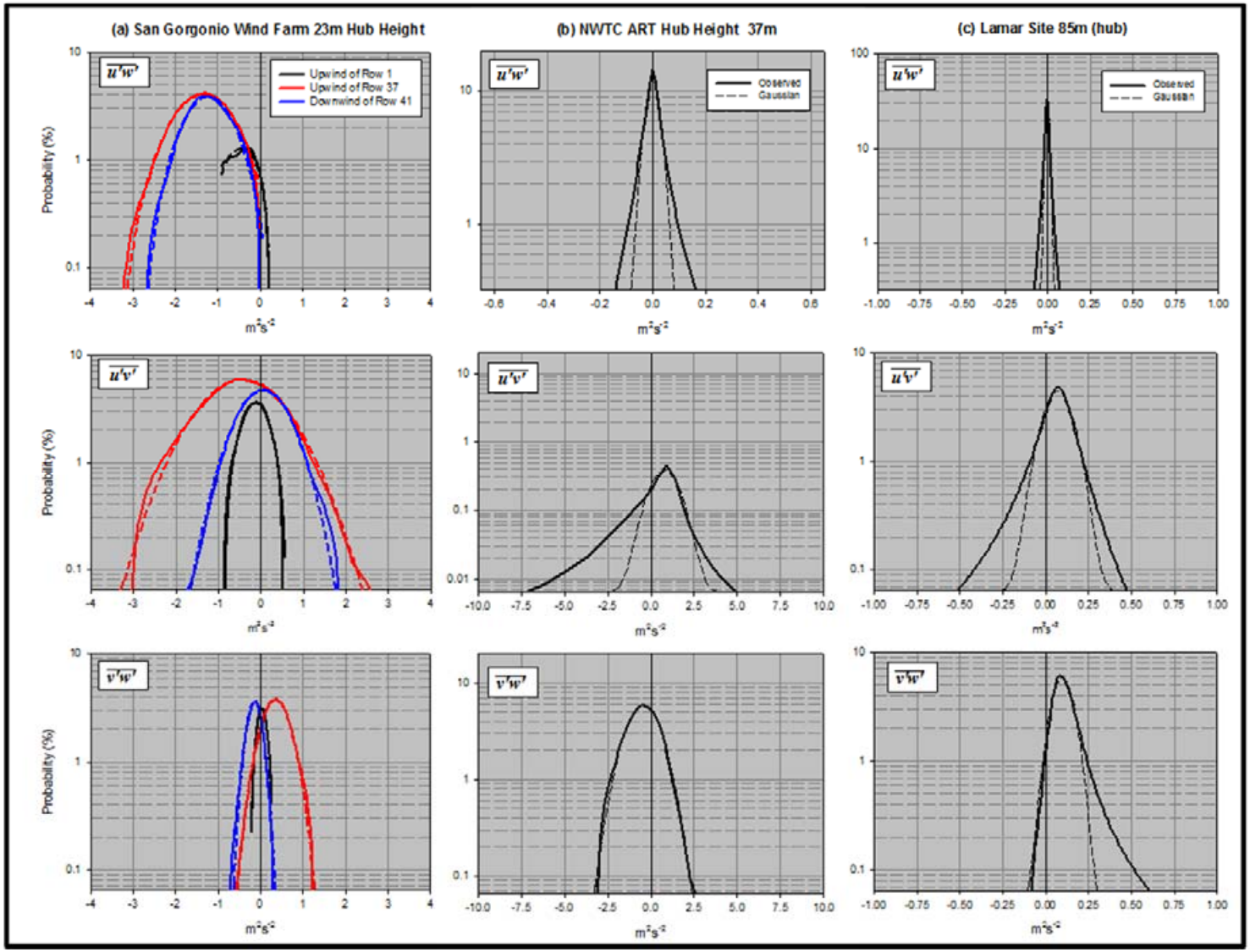

Figure 9-17. Available population Reynolds stress component residual distributions for hub heights at (a) wind farm; (b) ART; and (c) Lamar site (virtual WindPACT 1.5-MW turbine). Dashed lines represent the Gaussian distributions for the observed residual populations.

9.4.4 Spatial Coherence Scaling

The coherence function for the wind farm (WF_UPW, WF_07D, and WF_14D), the NWTC (NWTCUP), and the Great Plains (GP_LLJ) spectral models is given by

$$Coh_{i,j_\kappa} = \exp\left(-a_\kappa \sqrt{\left(\frac{f_r}{\overline{u}_m} \right)^2 + \left(b_\kappa r \right)^2} \right), \tag{9-12}$$

where κ is the turbulence component u, v, or w; f is the cyclic frequency; r is the distance between points i and j; z_m is the mean height of the two points; and $\overline{u_m}$ is the mean wind speed over the entire simulation. It is based on the form suggested by Thresher et al. (1981) where a and b are the coherence decrement and offset parameters. We analyzed the "a" decrement and offset "b" terms as functions of wind speed and stability for the wind farm, NWTC, and Lamar sites. In the wind farm we found them to vary only with mean wind speed. At the NWTC and Lamar sites, however, we found that although they were generally most sensitive to wind speed, the u and v components did also vary with the stability class (STC01, STC02, STC03, STC04, and STC05), with the vertical component w somewhat less so.

In Figure 9-18 we compare the NWTC and Lamar site variations of the decrements a_κ as a function of height and Ri_{TL} for hub-height mean wind speeds in the 12–14 m s^{-1} range. In general, for both sites the horizontal velocity decrements a_u and a_v increase with increasing stability, whereas the vertical decrement a_w reaches a minimum under neutral to slightly stable conditions and maximum when it becomes very unstable or very stable. The variations of the u, v, and w decrements (a_κ) and offsets (b_k) with mean wind speed for each of the available stability classes are plotted in Figures 9-19, 9-20, and 9-21, respectively, for the NWTC and Lamar sites. Figure 9-19 plots the IEC values for the u-component from IEC (1999; 2005). The v and w decrements and offsets are not specified by the standard. Figure 9-22 plots the variations in these parameters for the u and v components in the wind farm in a similar format. These values are based on cup anemometer data because sonic anemometers were available only at a single height and so there is no measurement of the w-component and its coherent scaling parameters. In applying these data we assumed that the coherence conditions are similar at Rows 37 and 41 and that $a_w \approx a_u$ and $b_w \approx b_u$.

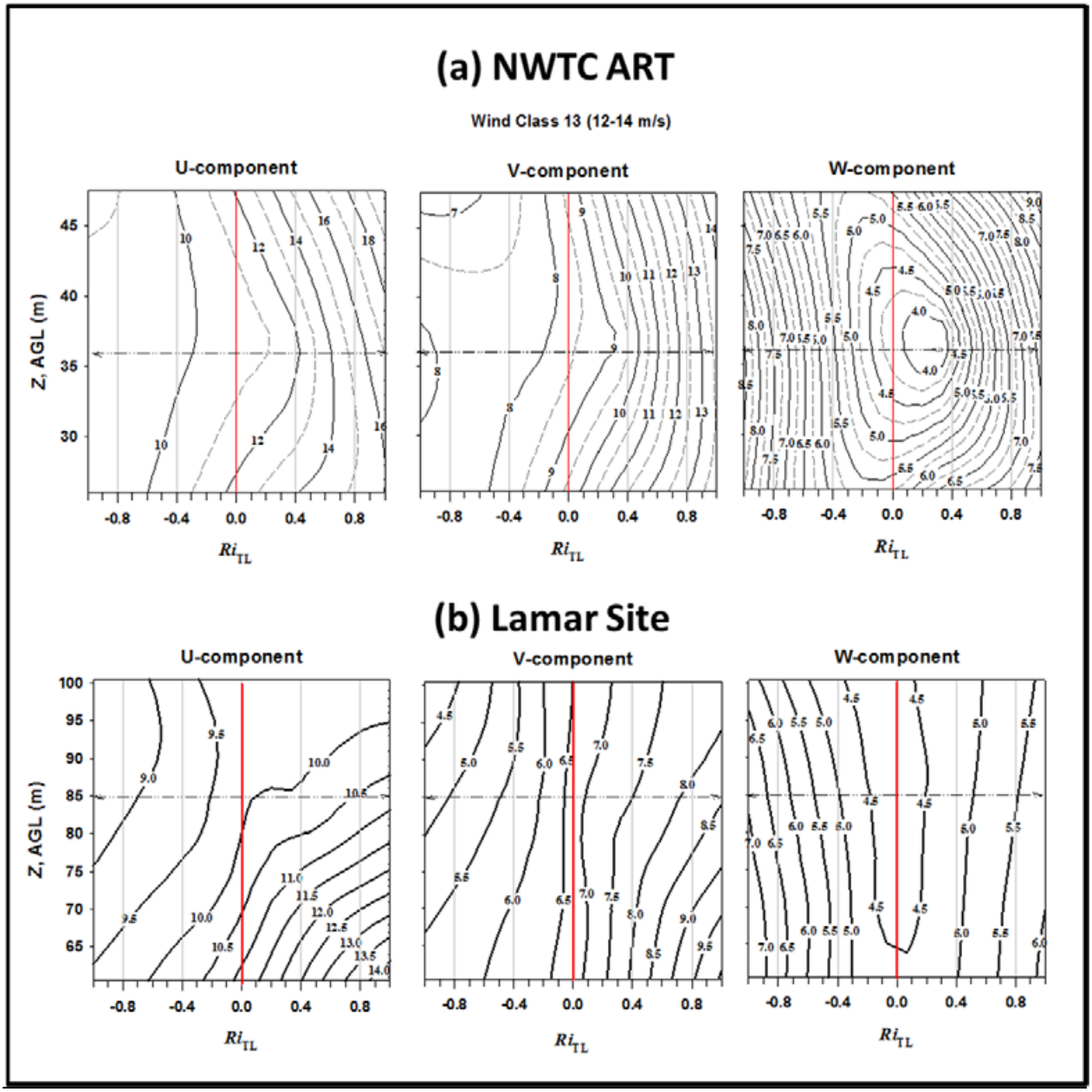

Figure 9-18. Variation of coherent decrement "a" with height and Ri_{TL} for mean wind speed range of 12–14 m s^{-1} for (a) NWTC ART and (b) Lamar site (WindPACT 1.5-MW turbine)

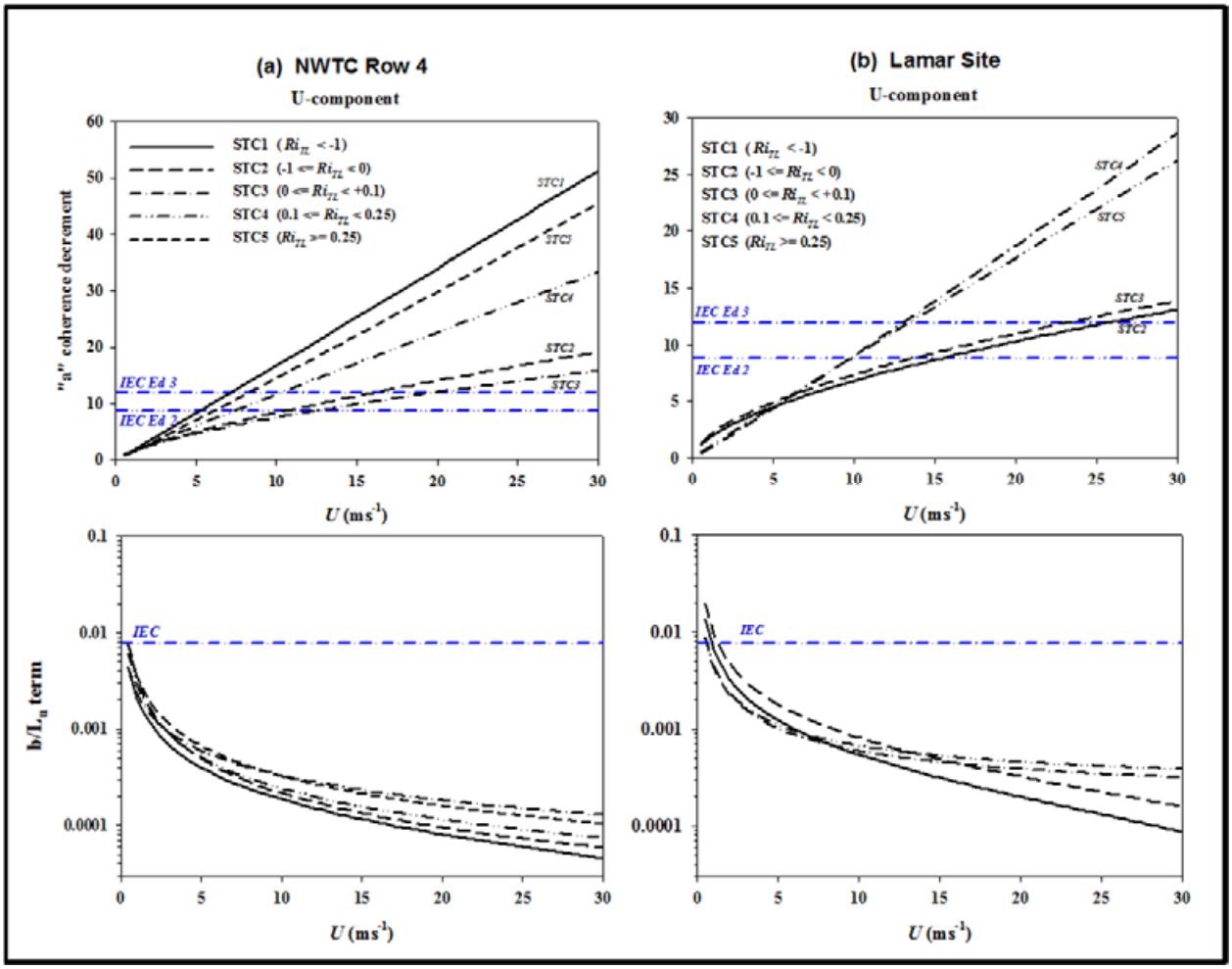

Figure 9-19. Variation of *U*-component coherence decrement "*a*" and offset term "*b*" normalized by L_u integral length scale by stability class and hub mean wind speed: (a) NWTC ART and (b) Lamar site (WindPACT 1.5-MW reference turbine)

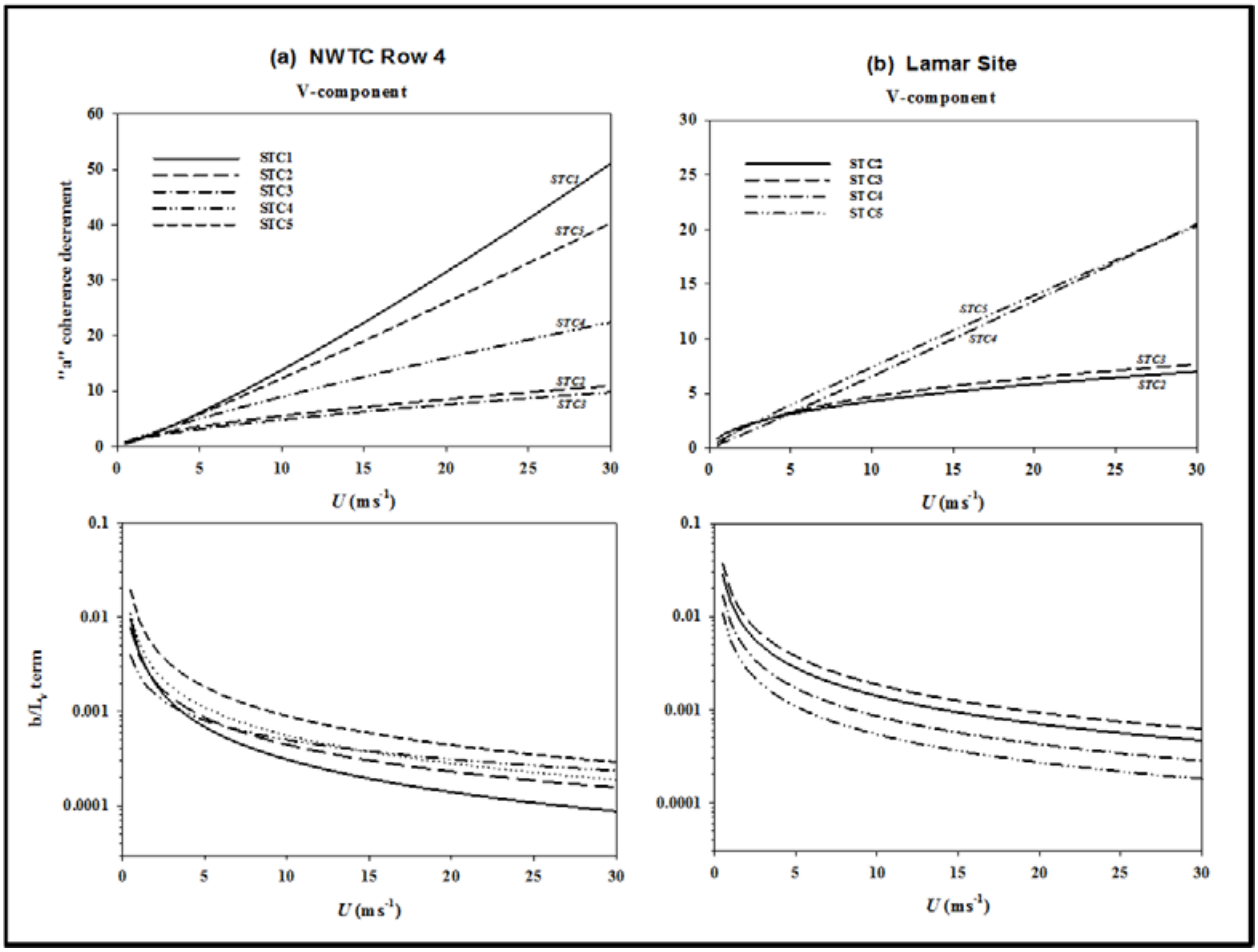

Figure 9-20. Same as Figure 9-19, but for *V*-component

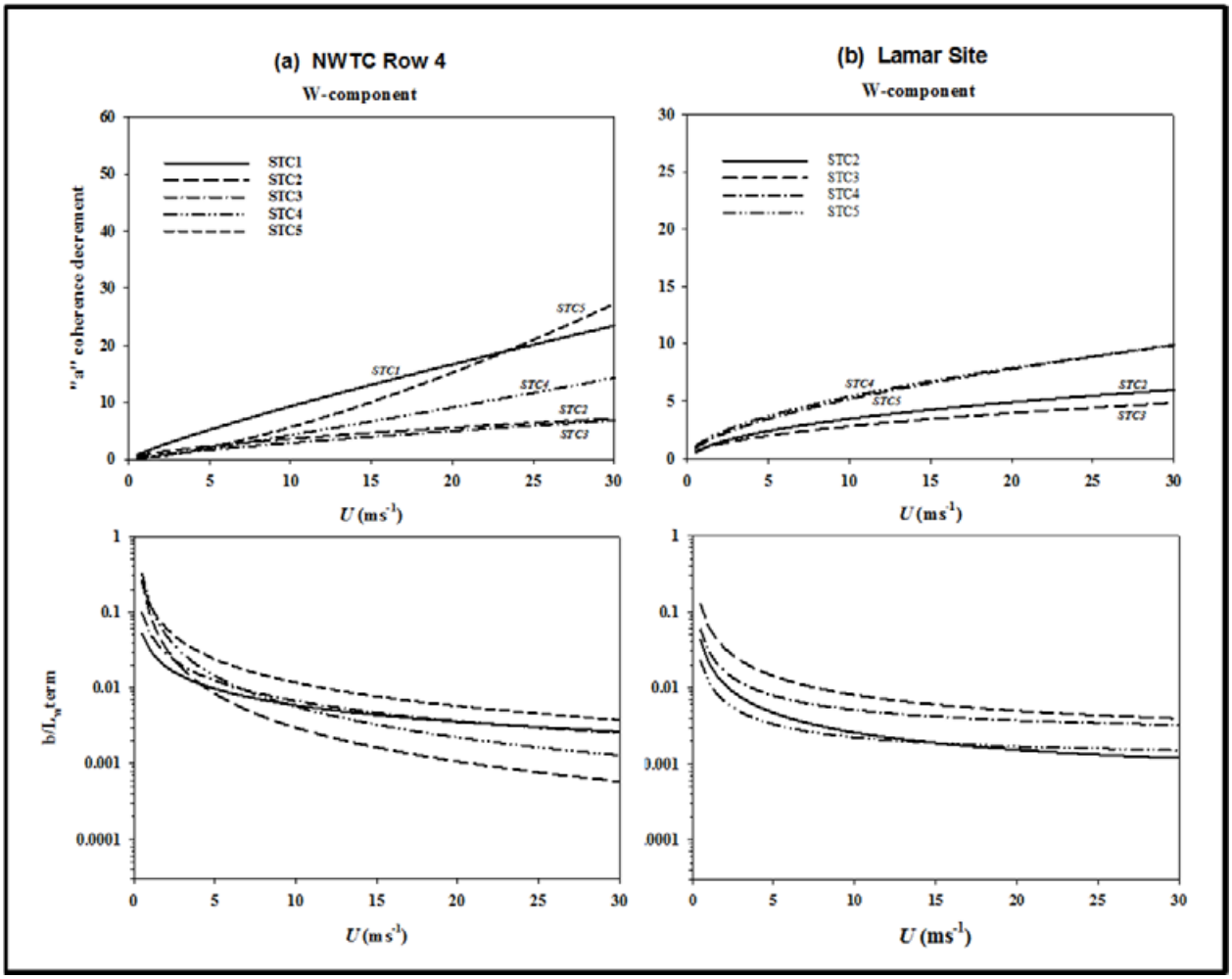

Figure 9-21. Same as Figure 9-19, but for *W*-component

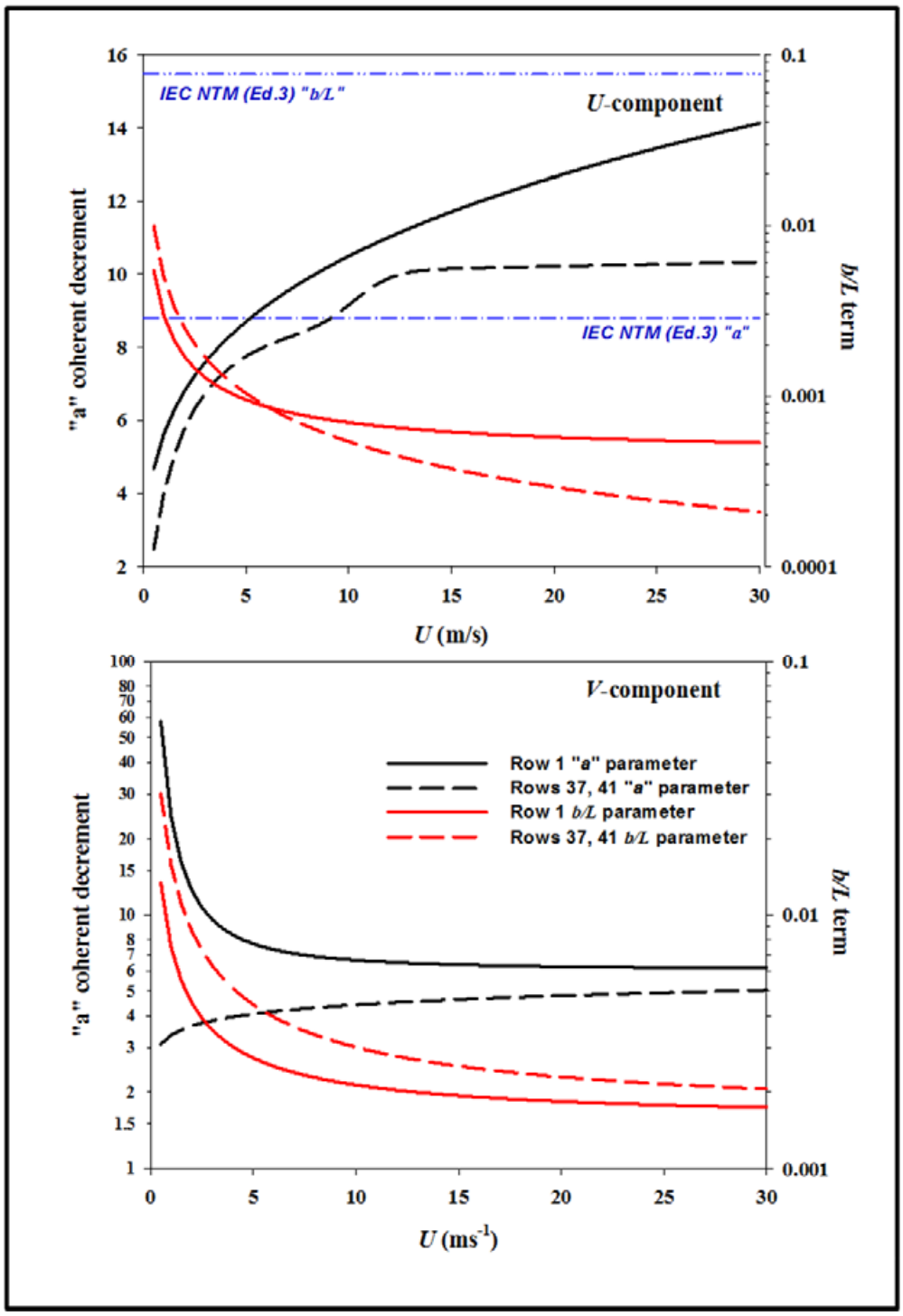

Figure 9-22. Variation of *U*- and *V*-component coherence decrement "*a*" and *b* offset term normalized by integral length scale *L* for California wind farm upwind of Row 1 and at Rows 37 and 41. Vertical component coherence scaling was unavailable because of a lack of vertical velocity measurements.

9.4.5 Coherent Structure Scaling and Implementation

In Section 6 we discussed the role of coherent turbulent structures in the dynamic response of wind turbines. We saw that these structures, because of the nature of the KHI that creates them, are superimposed on the background flow from which they derive their energy. We pointed out that KHI is a highly nonlinear process that cannot be fully reproduced by the linear inverse Fourier transformation used in TurbSim to produce the simulated velocity field from target frequency spectra. We found that the random occurrence of these structures is non-homogeneous Poisson distributed which can be used to describe the time between coherent events (interarrival times). These structures also exhibit random intensities defined by the peak values of E_{coh} within a 10-minute record as well as their number and total or aggregate length. Figure 9-23 shows the key elements of a stable, sheared flow containing superimposed coherent structures created by KHI. In Figure 9-23a we reproduce the specially processed NOAA HRDL lidar "stare" observation from Figure 8-13a, but also include the corresponding mean U velocities at the heights measured by the met tower that agree well with the lidar-derived mean wind profile. The details of some of the structures seen by the lidar for the subperiod of 330 to 480 seconds are plotted as the time series of the Reynolds stress components and their vector magnitude E_{coh} in Figure 9-23b. The salient points from these figures follow:

- Existence of the intense vertical mean shear in a stably stratified layer
- Presence of coherent structures principally within the lower, more intense shear layer
- Variation of intensity of the coherent structures as indicated by both the lidar and corresponding tower measurements
- Random temporal variation in the $u'w'$, $u'v'$, and $v'w'$ Reynolds stress components seen in each of the structures in the expanded record of Figure 9-23b
- Random occurrence and time between structures at a given height
- Existence of periods when coherent structures occur continuously across the depth of the shear layer (between 420 and 430 seconds).

The scaling of the occurrence and intensity of coherent structures superimposed on a mean, stably-stratified background shear flow such as seen in Figure 9-23a must thus include the random variation within the simulated Y-Z plane of the following:

1. Total length of coherent structures within a simulated record (typically 10 minutes) (T_{coh})
2. Energy intensity of the structures (peak E_{coh})
3. Period of time between the arrival of individual structures (IAT)
4. 3-D distribution of the internal velocity fields that are spatially and temporally correlated.

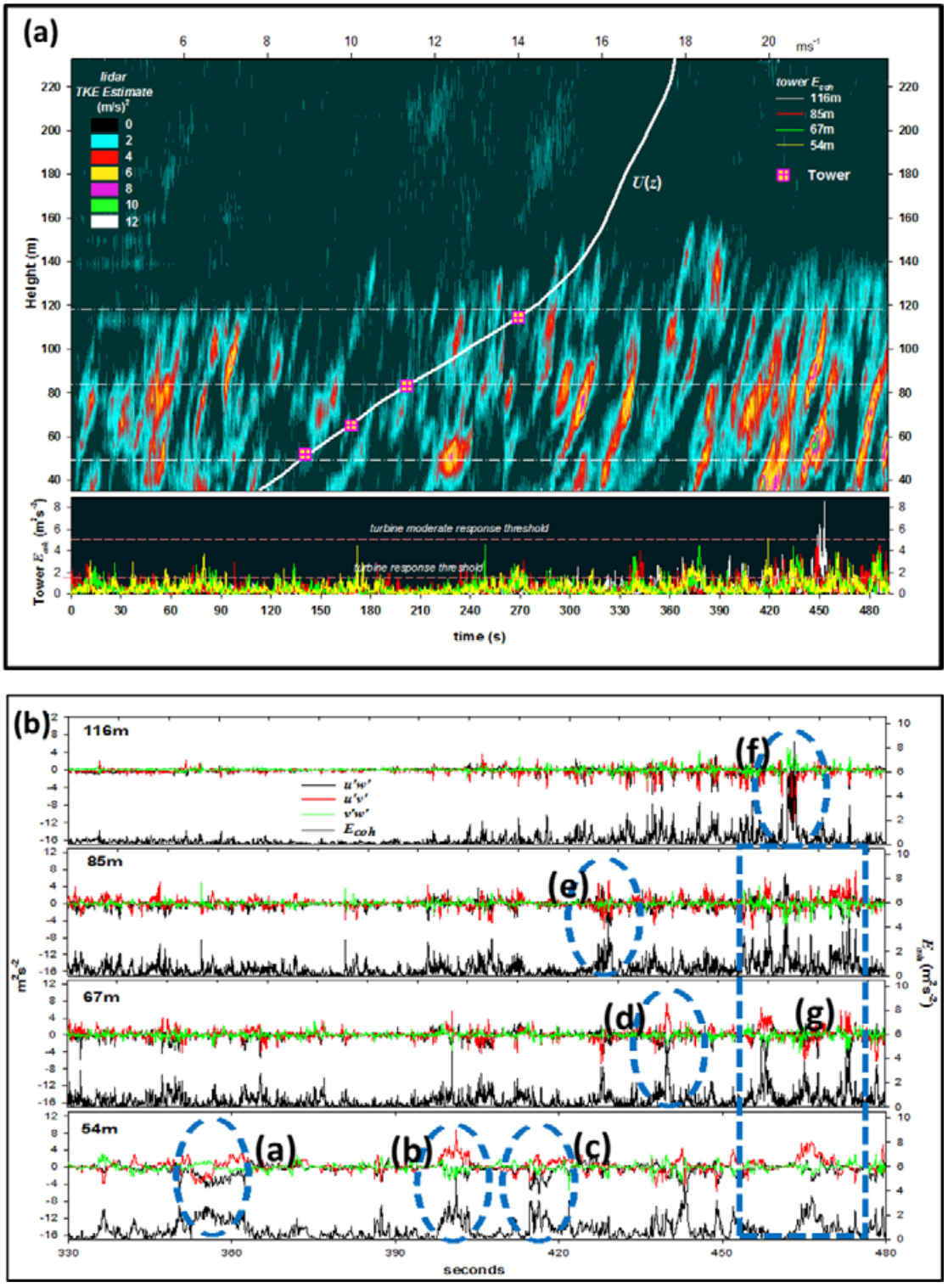

Figure 9-23. Same nomenclature as Figures 8-13a and 8-14 of (a) specially processed HRDL lidar "stare" observation with tower-measured E_{coh} in lower panel; and (b) corresponding tower-measured time series for subperiod of 330–480 seconds of Reynolds stress components and E_{coh}. Individual (a–f) and regions (g) of coherent structures are outlined by the dotted lines.

To accomplish items (1), (2), and (3) for the TurbSim simulation spectral models simulating turbulence conditions, we applied the coherent flow characterizations peak E_{coh}, T_{coh}, and IAT measured at the wind farm, NWTC, and Lamar sites discussed in Section 7-6. To improve our scaling correlations, we chose to restrict the scaling of the flow characterization parameters to only those observations in which coherent structures were occurring simultaneously at all available measurement locations. These included the sonic anemometers at the five locations within the NWTC ART upwind planar array and the four heights on the Lamar met tower. Only hub-height data are available at the three locations within the wind farm. The distributions of Ri_{TL} and the hub-height mean wind speeds for these subsets are plotted in Figure 9-24. The most prevalent value of Ri_{TL} for such conditions falls within the CRR stability range. The distributions of the rotor disk mean shearing stresses $u_{*\mathrm{D}}$ and vertical shear $\left[\partial\overline{U}/\partial z\right]_{\mathrm{D}}$ scaling parameters are plotted in Figures 9-25a and b and 9-25c and d. The median of the NWTC $u_{*\mathrm{D}}$ distribution is about 20% higher and has much larger high value tail than seen at the Lamar site. The situation would, however, be reversed for the mean shear across a WindPACT turbine rotor disk installed in Lamar that is most likely a consequence of the frequent occurrence of LLJs.

The total expected length of coherent structures within a 10-minute record (T_{coh}) was found not to scale directly with any of the turbulence parameters but could be modeled as a probability distribution specific to a given site, listed in Table 9-4. We found, for example, that a single model plotted in Figure 9-26 was appropriate for the hub height at all three locations within the wind farm. Individual probability models developed for the NWTC and Lamar sites are also functions of height within the simulated rotor disks.

The expected value of the maximum coherent structure energy intensity (peak E_{coh}) within a 10-minute record is scaled in terms of turbulence parameters but the Row 37 (WF_07D), NWTC, and Lamar sites also include a random component. Table 9-5 summarizes the scaling sensitivities of the turbulence parameters for the TurbSim spectral models. The parameters $\overline{u}_{bc}$, $\sigma_{w_{bc}}$, and $\Delta\overline{u}_{b}$ refer to the center mean u velocity, standard deviation of the vertical velocity, and u-velocity difference (shear), respectively, across the simulated coherent structure (K-H billow). The scaling parameters and random contribution are also functions of height for the Lamar site.

The time between coherent structures (interarrival time, or IAT) is the reciprocal of the Poisson rate parameter λ. Table 9-6 summarizes the IAT scaling parameter sensitivities. We found for the wind farm and NWTC sites it systematically varies with Ri_{TL} and $\overline{u}_{bc}$ at the center of the simulated coherent structure or K-H billow. For the Lamar site, we found it was not stability sensitive but was a function of height.

Coherent structures are added to the $u(t)$, $v(t)$, and $w(t)$ background flow turbulence components in the Y-Z grid. TurbSim randomly chooses between the available population of 16 contiguous nondimensional coherent structures isolated from the NCAR LES stationary K-H billow simulation (Kelley et al. 2004) or from the 11 structures extracted by Werne from the Colorado Research Associates (CoRA) DNS K-H billow simulation by Werne and Fritts (1999). It does

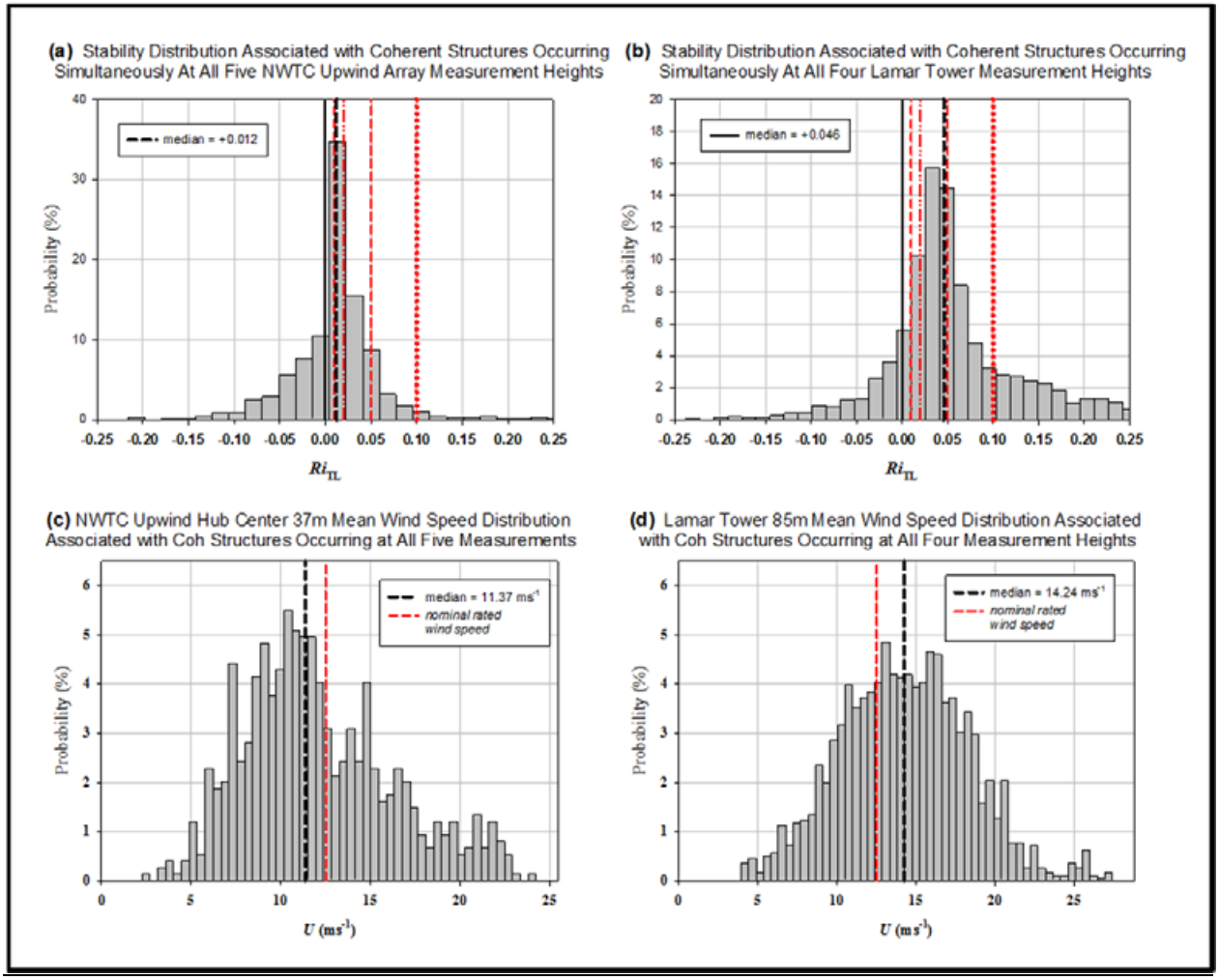

Figure 9-24. Observed probability distributions of turbulence scaling parameters associated with coherent turbulent structures occurring simultaneously at all available measurement locations for ART upwind planar array and Lamar site 120-m met tower. The distributions of Ri_{TL} are shown in (a) NWTC and (b) Lamar. The distributions of the equivalent hub-height mean U speed are plotted in (c) NWTC and (d) Lamar.

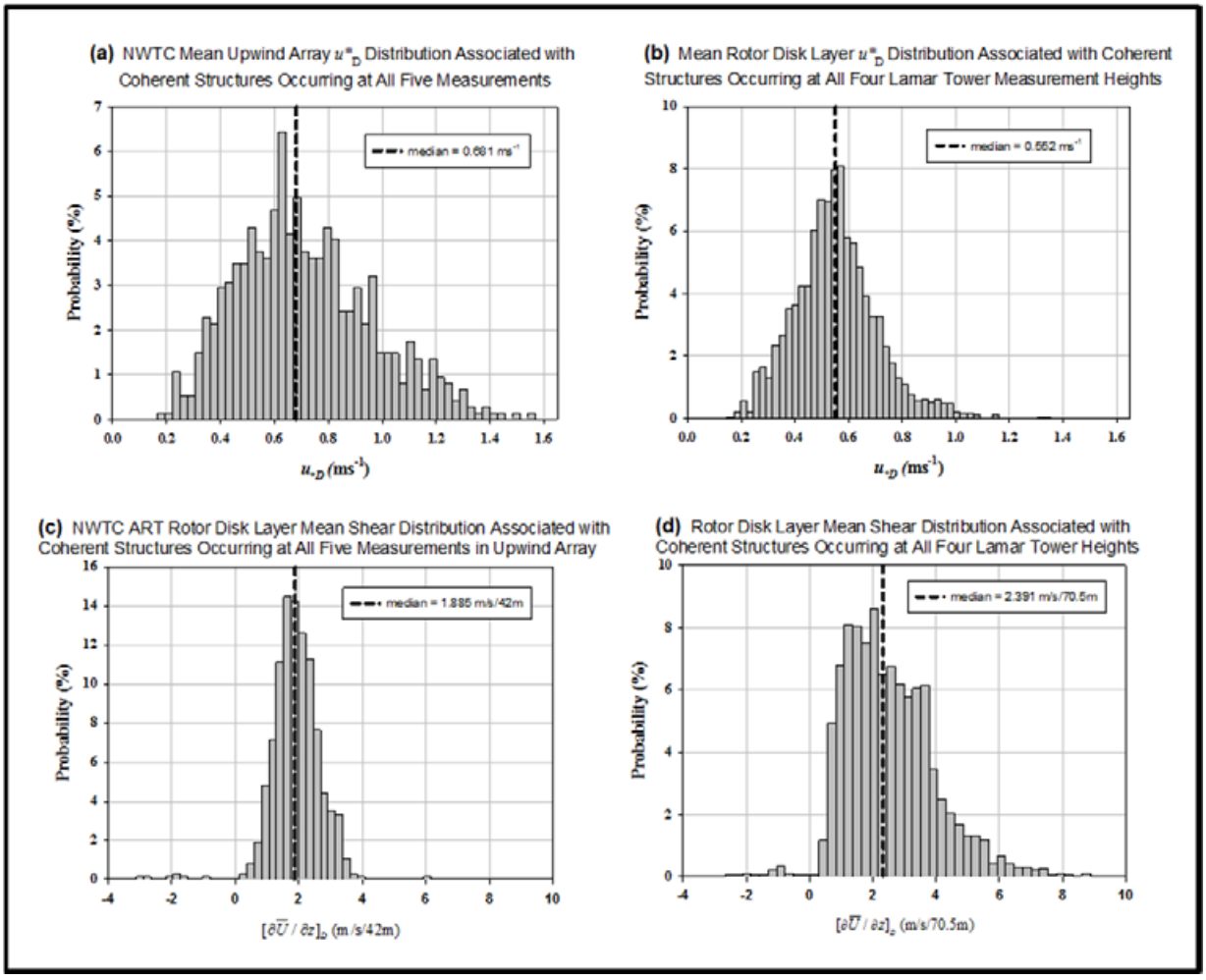

Figure 9-25. Same as for Figure 9-24, but for rotor disk mean shear stress u_{*D}: (a) NWTC and (b) Lamar; and rotor layer mean shear $\left[\partial \overline{U} / \partial z\right]_D$ across respective ART and WindPACT rotor diameters: (c) NWTC and (d) Lamar

Table 9-4. Scaling of Expected Length of Coherent Structures (T_{coh}) within a Simulated Record by Location

Location	Spectral Model	Scaling Source	Coherent Structure height (z)
California Wind Farm Upwind of Row 1	WF_UPW	WF Random Model	
California Wind Farm Upwind of Row 37	WF_07D	WF Random Model	
California Wind Farm Downwind of Row 41	WF_14D	WF Random Model	
NWTC Row 4	NWTCUP	NWTC Random Model	✓
Lamar Site (LLLJP)	GP_LLJ	GP_LLJ Random Model	✓

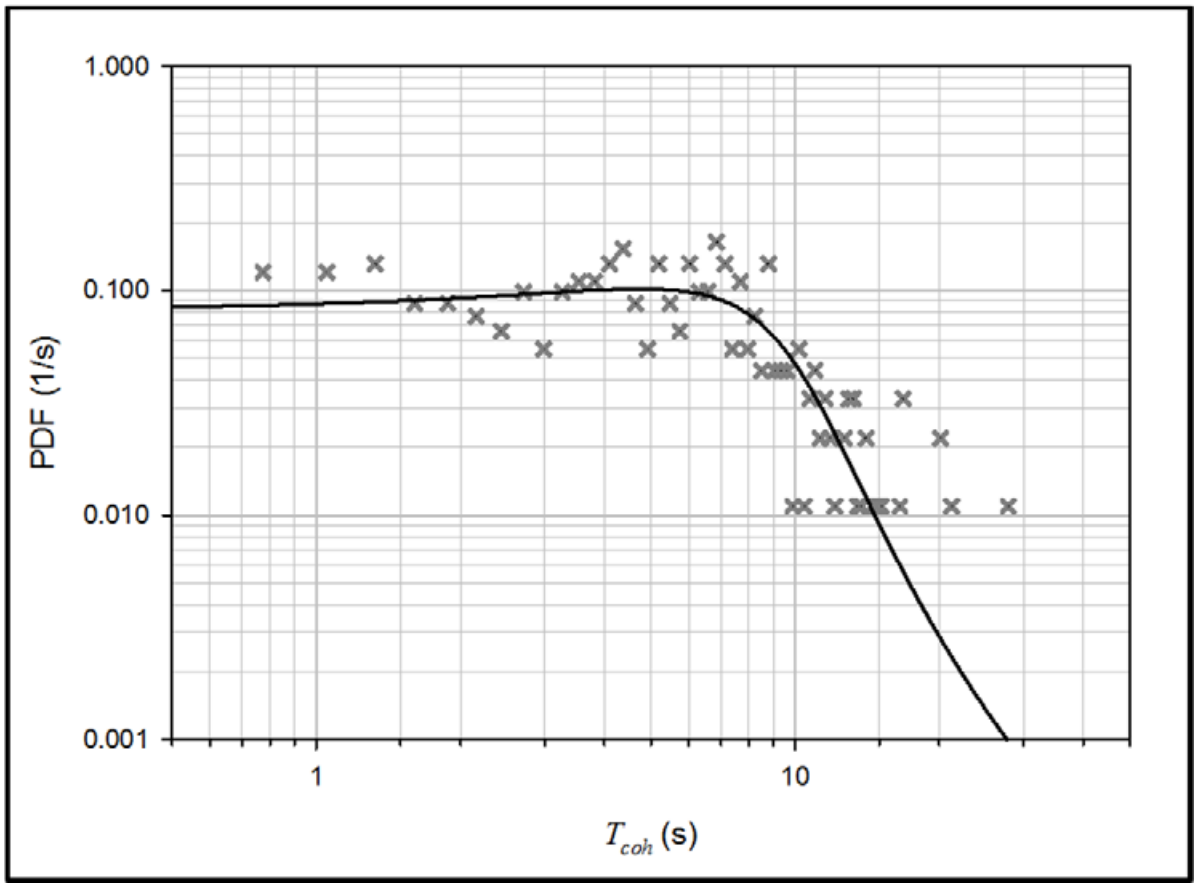

Figure 9-26. Probability density distribution of observed T_{coh} at hub height for the wind farm measurement locations within the California wind farm

Table 9-5. Coherent Structures Maximum Intensity (Peak E_{coh}) Scaling Parameter Sensitivities by Location

Location	Spectral Model	Ri_{TL}	$\bar{u}_{bc}$	u_{*D}	$\Delta\bar{u}_{b}$	$\sigma_{w_{bc}}$	Height (z)	Random Component?
California Wind Farm Upwind of Row 1	WF_UPW	✓	✓		✓	✓		No
California Wind Farm Upwind of Row 37	WF_07D	✓		✓		✓		Yes
California Wind Farm Downwind of Row 41	WF_14D	✓	✓			✓		No
NWTC Row 4	NWTCUP	✓	✓			✓		Yes
Lamar Site (LLLJP)	GP_LLJ	✓		✓	✓		✓	Yes

Table 9-6. Coherent Structures Interarrival Time ($1/\lambda$) Scaling Parameter Sensitivities by Location

Location	Spectral Model	Ri_{TL}	u_{bc}	Height (z)
California Wind Farm Upwind of Row 1	WF_UPW	✓	✓	
California Wind Farm Upwind of Row 37	WF_07D	✓	✓	
California Wind Farm Downwind of Row 41	WF_14D	✓	✓	
NWTC Row 4	NWTCUP	✓	✓	
Lamar Site (LLLJP)	GP_LLJ		✓	✓

not mix the sources of these structures. Dimensions are then applied to these structures based on the boundary conditions of the simulation to obtain fluctuating (zero mean) velocity components. This scaling includes the depth and location of the layer containing the billow within the simulated rotor disk, the velocity difference (shear) across it, and the billow center mean wind speed. The rotor disk layer is used as the default billow depth, though the user can redefine that. Realizations of the expected total length of coherent structures (T_{coh}) and the peak value of E_{coh} are derived from appropriate entries in Tables 9-4 and 9-5, respectively, for the spectral model being simulated. A sample realization of arrival times is derived from the Poisson distribution based on the rate parameter $\lambda = (1/IAT)$ that has been scaled with the appropriate parameters in Table 9-6. Samples from the available populations of dimensionalized coherent structures whose peak intensities have been randomly chosen based on Table 9-5 are summed until their aggregate length approximates T_{coh} or reaches maximum length of the requested record. These requested records are typically slightly more than 10 minutes to accommodate the requirements of the turbine dynamic simulation codes. Each coherent structure velocity component is added to the background components at each grid point in the time domain.

Figure 9-27 shows an example of the background and coherent structure superposition and summation process at a single grid point. The upper three time series plot the background streamwise (U), crosswind or lateral (V), and vertical (W) wind components in black and the fluctuating (zero mean) coherent structure velocity components (u', v', and w') are depicted in red. The bottom panel shows the corresponding E_{coh} values for the background and with the coherent structure velocity components included. Although some of the structures in the background exceed the significant threshold limit, the presence of the coherent structure is much more damaging, particularly at about 340 seconds into the record. Figure 9-28 gives a similar presentation. Here again the background flow contains at least two significant coherent events, but adding coherent structures increases it to at least three and possibly four that also more intense and damaging.

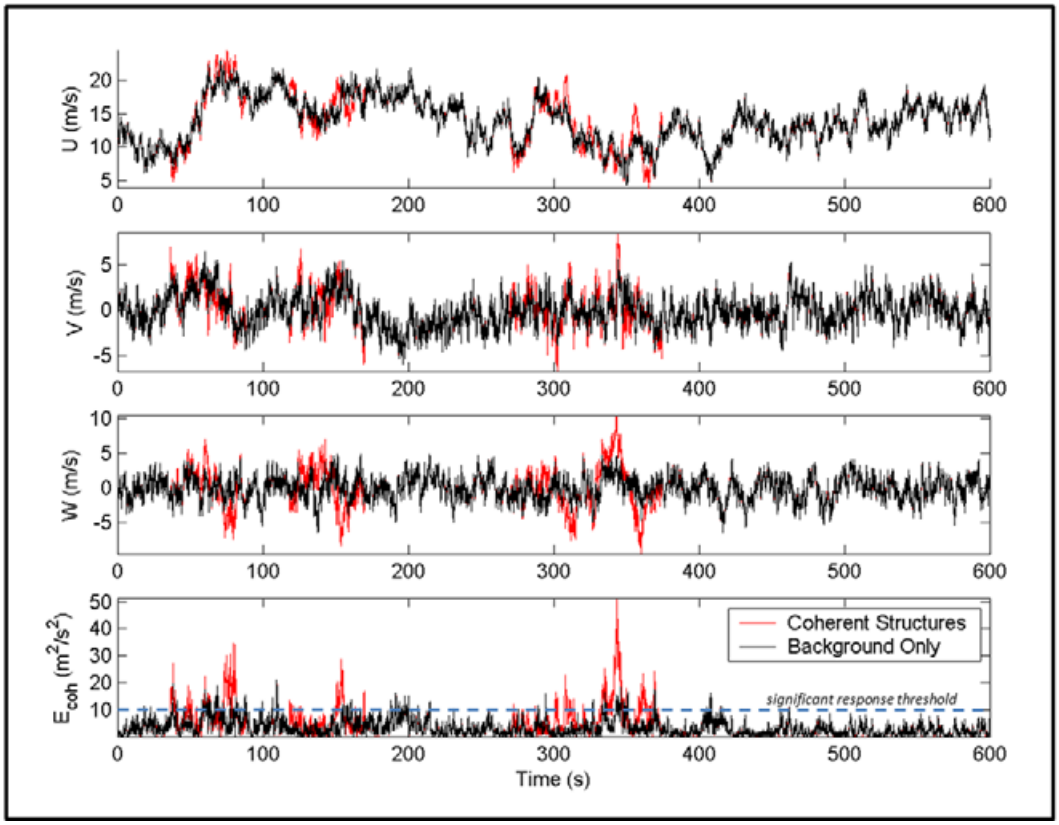

Figure 9-27. Example of background (U, V, W) plus added coherent structure wind components (*u'*, *v'*, and *w'*): streamwise (U + *u'*), crosswind (V + *v'*), and vertical (W + *w'*) at specific grid point location

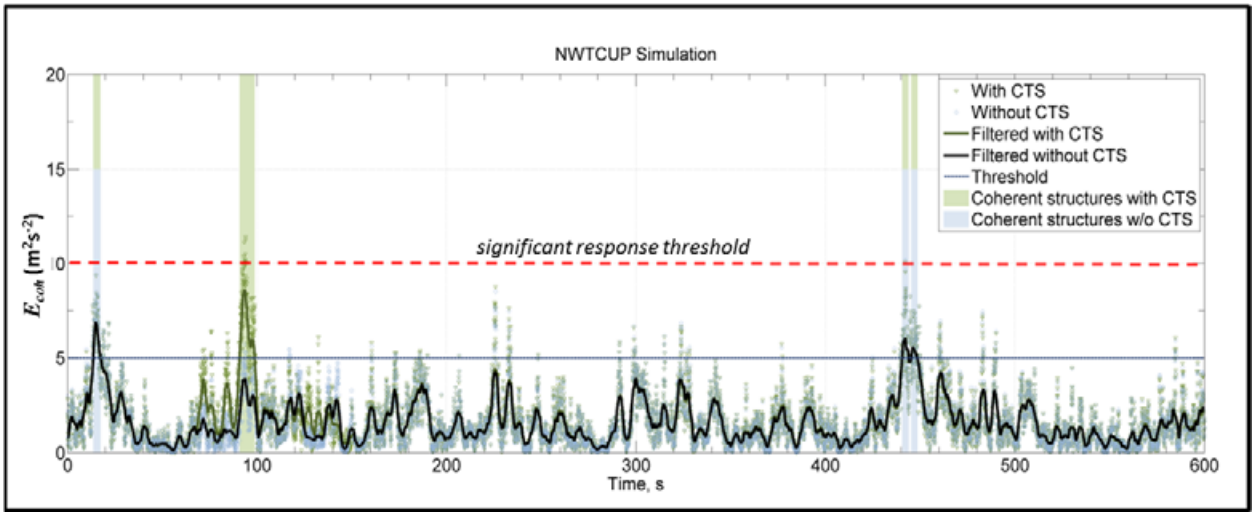

Figure 9-28. Example of a TurbSim NWTCUP spectral model simulation with and without coherent turbulent structures (CS) added. Light gray shows significant (~450 seconds) but fewer CS generated within the background flow compared with the CS added (~90 seconds).

9.4.6 Lamar Site LLJ Wind Speed and Direction Profile Scaling

Including vertical profiles of wind speed and direction in the TurbSim GP_LLJ spectral model is crucial in simulating turbulence conditions encountered in the Great Plains. As we previously discussed, a midrange sodar at the Lamar site measured the 10-minute mean vertical profiles from 40 to 500 m in 10-m increments from May to November 2002, as well as during the 2-week period in September 2003 when the NOAA HRDL lidar was deployed. A total of 31,774 ten-minute raw profiles were obtained during those periods, of which 29,244, or 92%, were usable for further analysis. Each profile was analyzed for the existence of LLJs. When identified, only the lowest altitude jets were retained. This process resulted in 4,466 profiles that contained jets, which is about 16 % of the available usable records.

The profiles were then processed in the following sequence:

1. Contiguous vertical profiles of speed and direction were formed from the raw data.
2. Each of the contiguous wind speed and direction profiles was fitted recursively with a Chebyshev polynomial up to 10th order and the resulting coefficients were retained.
3. The profile Chebyshev coefficient vectors were matched with the corresponding Ri_{TL} and the local values of $U(z)$, $z/L(z)$, $u_*(z)$, $\sigma_U(z)$, and $\sigma_w(z)$ from the met tower.
4. The wind speed profiles from the surface to the lowest sodar measurement height were estimated using the diabatic wind profile and available tower measurements and the Chebyshev-smoothed profiles from 40 to 60 m. The wind direction profile was estimated using a generalized least square procedure.
5. The resulting Chebyshev coefficient vectors of wind speed and direction and corresponding tower parameters were stratified by jet height in 20-m increments from 80 to 480 m.
6. MLR models were calculated for each of these height-stratified subpopulations using the tower measurements or derivatives as the independent variables and the Chebyshev coefficients as the dependent variables.

Figure 9-29 plots the probability distributions of the time of day and the wind direction and speed of the jets within each 20-m height bin by the stability classes STC02, STC03, STC04, and STC05. We previously established that the STC03 stability class is potentially the most damaging to wind turbines. Here we see in Figure 9-29a that LLJs below 120 m and within the turbine rotor disk occur in the early evening hours local time, but those above about 150 m generally appear near midnight. Figures 9-29b and c show that strongest jets appear at 200 m and above within a very narrow southerly wind direction range. Figure 9-30 presents the distributions of the corresponding tower measurements of the rotor disk layer mean values of the Monin-Obukhov stability parameter z/L_{D} in Figure 9-30a, the shearing stress $u_{*\mathrm{D}}$ in Figure 9-30b, and the vertical shear $\left[\partial\overline{U}/\partial z\right]_{\mathrm{D}}$ in Figure 9-30c. In the STC03 stability class we see that the jets within the turbine layer (below 120 m) occur in less stable environments with smaller shear stresses and vertical shears across the turbine rotors. Figure 9-31a, a characteristic jet profile plots the smoothed profiles of the variation of the median jet maximum velocities and accompanying wind directions. Figure 9-31b shows the corresponding variations in the Ri_{TL} and

9

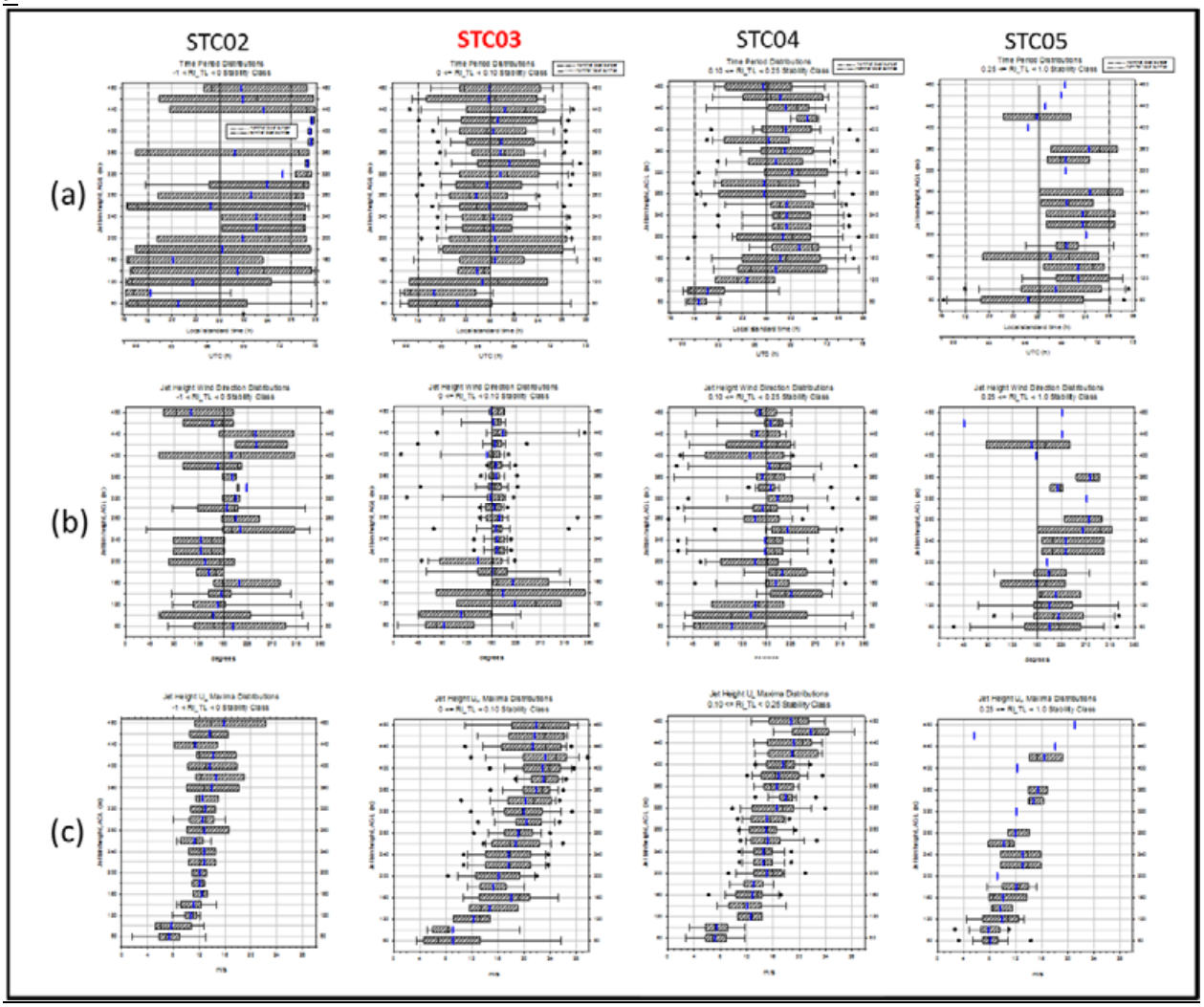

Figure 9-29. Probability distributions of Lamar site LLJ characteristics with height: (a) time period; (b) wind direction at LLJ maximum; and (c) wind speed of LLJ maximum for the STC02, STC03, STC04, and STC05 stability classes. The largest turbine dynamic responses occur in the STC03 class. The boxplot dots represent the P05 and P95 percentiles.

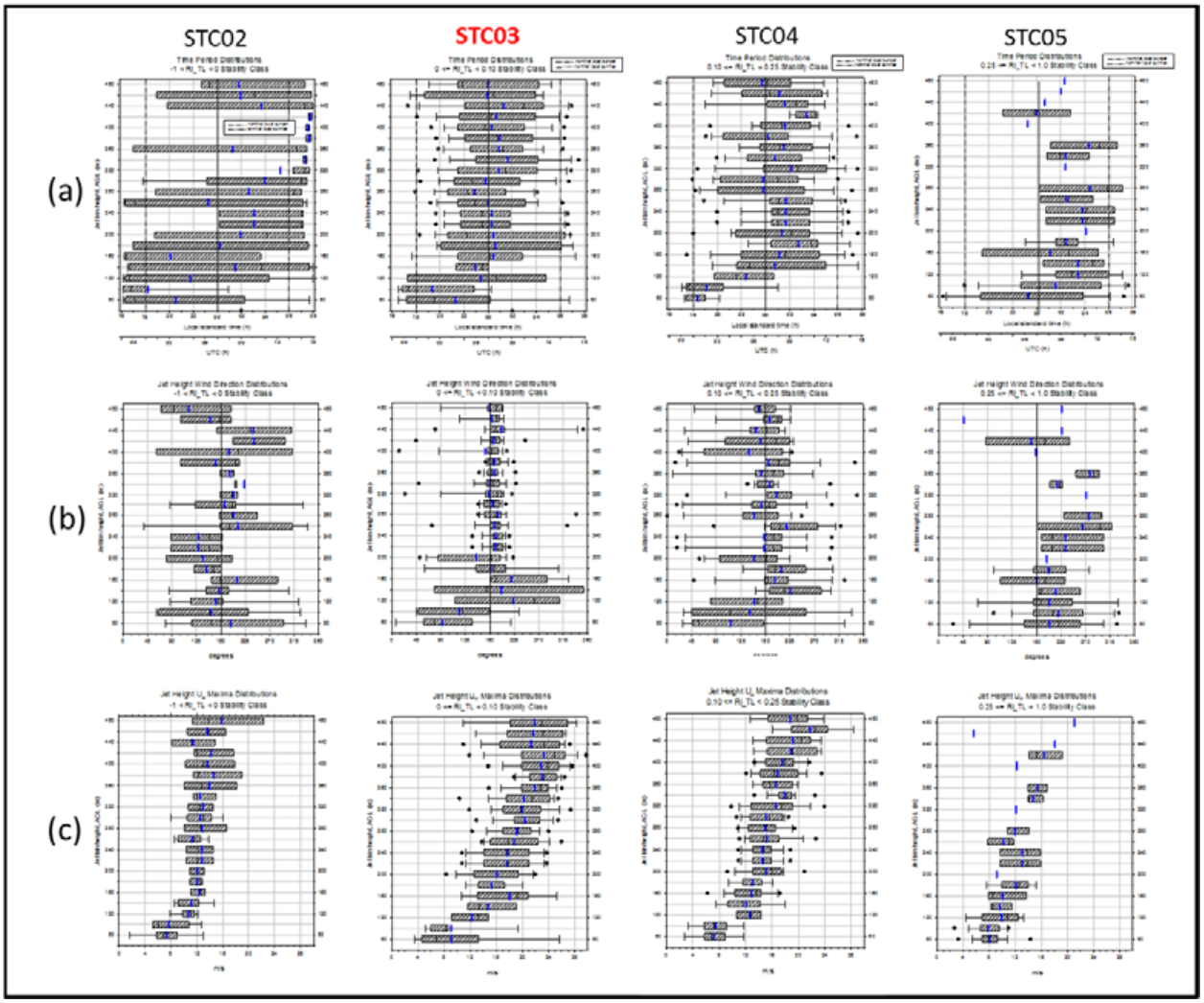

Figure 9-30. Probability distributions by stability class of WindPACT (GE) 1.5-MW rotor layer turbulence scaling parameters for corresponding LLJ heights: (a) z/L_D; (b) u_{*D}; and (c) $\left[\partial \overline{U} / \partial z\right]_D$.

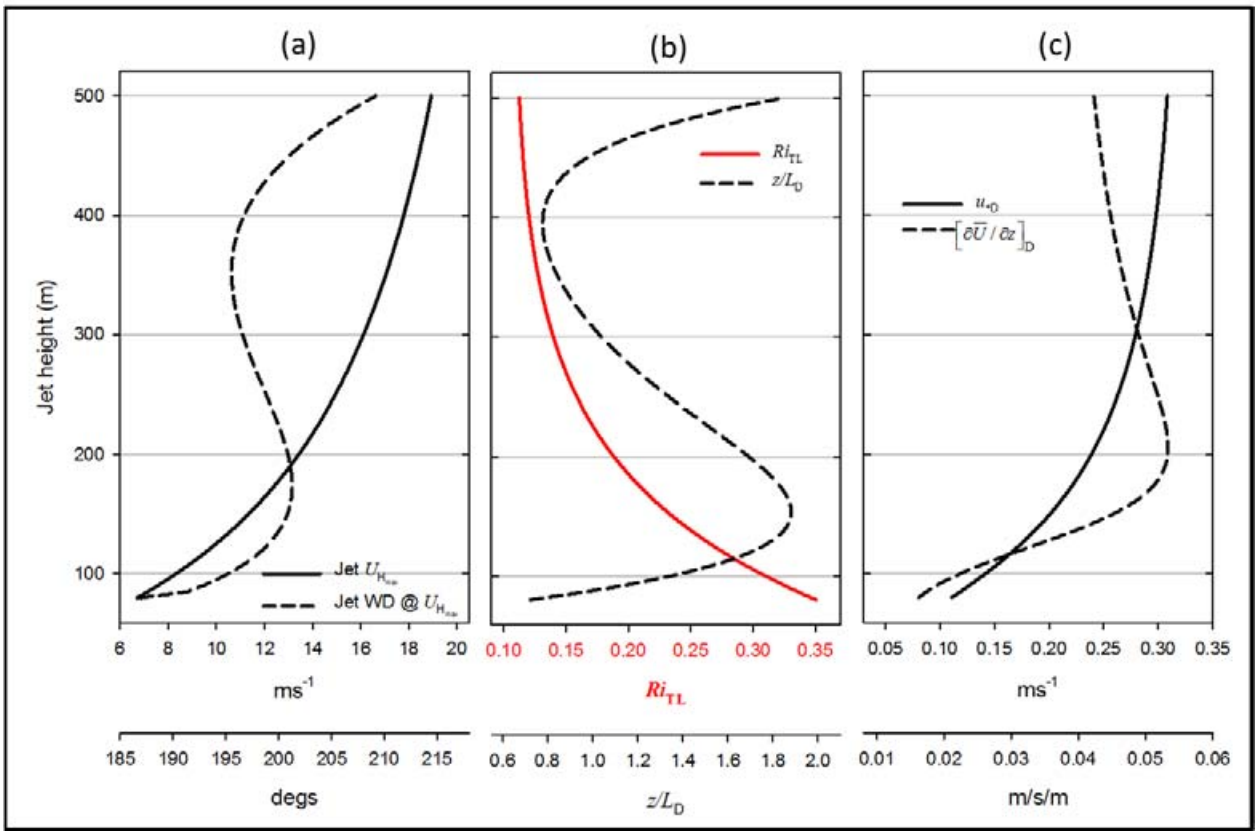

Figure 9-31. . Vertical profiles of the median: (a) LLJ peak U_H and corresponding wind direction WD; (b) Ri_{TL} and rotor disk layer mean z/L; (c) rotor disk layer mean u_* and $\left[\partial\overline{U}/\partial z\right]$ for subset of sodar vertical profiles that reached 500 m.

disk rotor layer mean M-O z/L_D stability parameters. These curves indicate that the stronger jets at higher altitudes contribute to destabilizing the rotor disk layer while increasing the shearing stress u_{*D} (downward momentum flux) and vertical shear across it, as shown in Figure 9-31c.

Our MLR analysis found that shape and magnitude of the jet profiles associated with a given jet maximum height scaled with the jet maximum velocity, Ri_{TL}, and u_{*D}. The modeled mean jet velocity profile is then expressed as

$$U(z) = \sum_{n=0}^{10} c_{n_U} T_n(z) \tag{9-13}$$

and the corresponding mean wind direction profile is

$$\Phi(z) = \sum_{n=0}^{10} c_{n_\Phi} T_n(z) \quad , \tag{9-14}$$

where c_{n_U} and c_{n_Φ} are the Chebyshev coefficients for the velocity and wind direction and T_n are the corresponding n^{th} order Chebyshev polynomials. The modeled jet speed and direction profiles given by Equations 9-13 and 9-14 are thus scaled by

$$c_{n_U} = c_{1,n_U} U_{jet_{\max}} + c_{2,n_U} Ri_{\text{TL}} + c_{3,n_U} u_{*D} + c_{4,n_U} \tag{9-15}$$

and

$$c_{n_\Phi} = c_{1,n_\Phi} U_{jet_{\max}} + c_{2,n_\Phi} Ri_{\text{TL}} + c_{3,n_\Phi} u_{*D} + c_{4,n_\Phi} . \tag{9-16}$$

The height of the jet Z_{jet} and its $U_{jet_{\max}}$ are specified by the user or random defaults can be used. Figure 9-32 plots the observed $U_{jet_{\max}}$ velocities with height.

Figures 9-33, 9-34, and 9-35 show the sensitivity of the shape of the vertical profiles of wind speed, wind direction, and wind speed standard deviation to variations in $U_{jet_{\max}}$, Ri_{TL}, and $u_{*\text{D}}$ and the influence on the wind speed, direction, and turbulence level (σ_U) profiles. In Figure 9-33 we vary $U_{jet_{\max}}$ over ranges characteristic of the 80-, 260-, and 460-m jet heights for Ri_{TL} of +0.50 and +0.05. The most noticeable variation is in the wind direction profile associated with an 80-m jet height. The results in the variations of Ri_{TL} in Figure 5-34 are most pronounced in both the wind speed and direction profiles for a 460-m jet height. Finally, the results of varying the mean turbine layer shearing stress in Figure 9-35 are most pronounced in the wind direction profiles for a 460-m jet height though some smaller effects are seen in both the wind speed and direction for jet heights of 80 and 260 m. Figure 9-36 illustrates examples of 80-, 260-, and 400-m low-level jet wind speed and direction profiles generated by the TurbSim GP_LLJ spectral model for an 80-m mean wind speed of 12 m s^{-1} and an Ri_{TL} of +0.05. The significant speed shears over deep vertical layers for the 260- and 400-m heights are quite evident and are potential source regions for KHI and downward fluxes of E_{coh}.

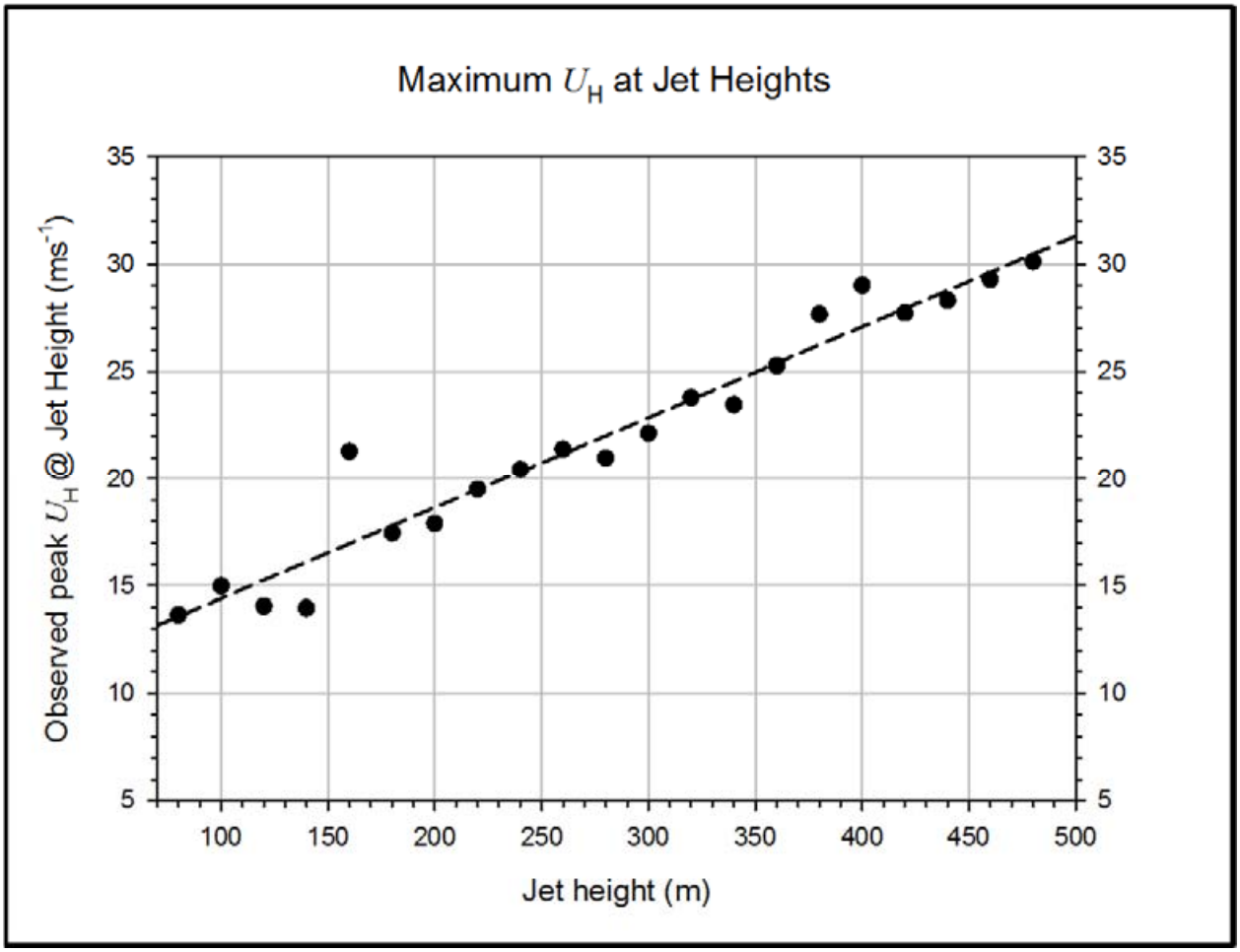

Figure 9-32. Observed Lamar site maximum LLJ velocities with height

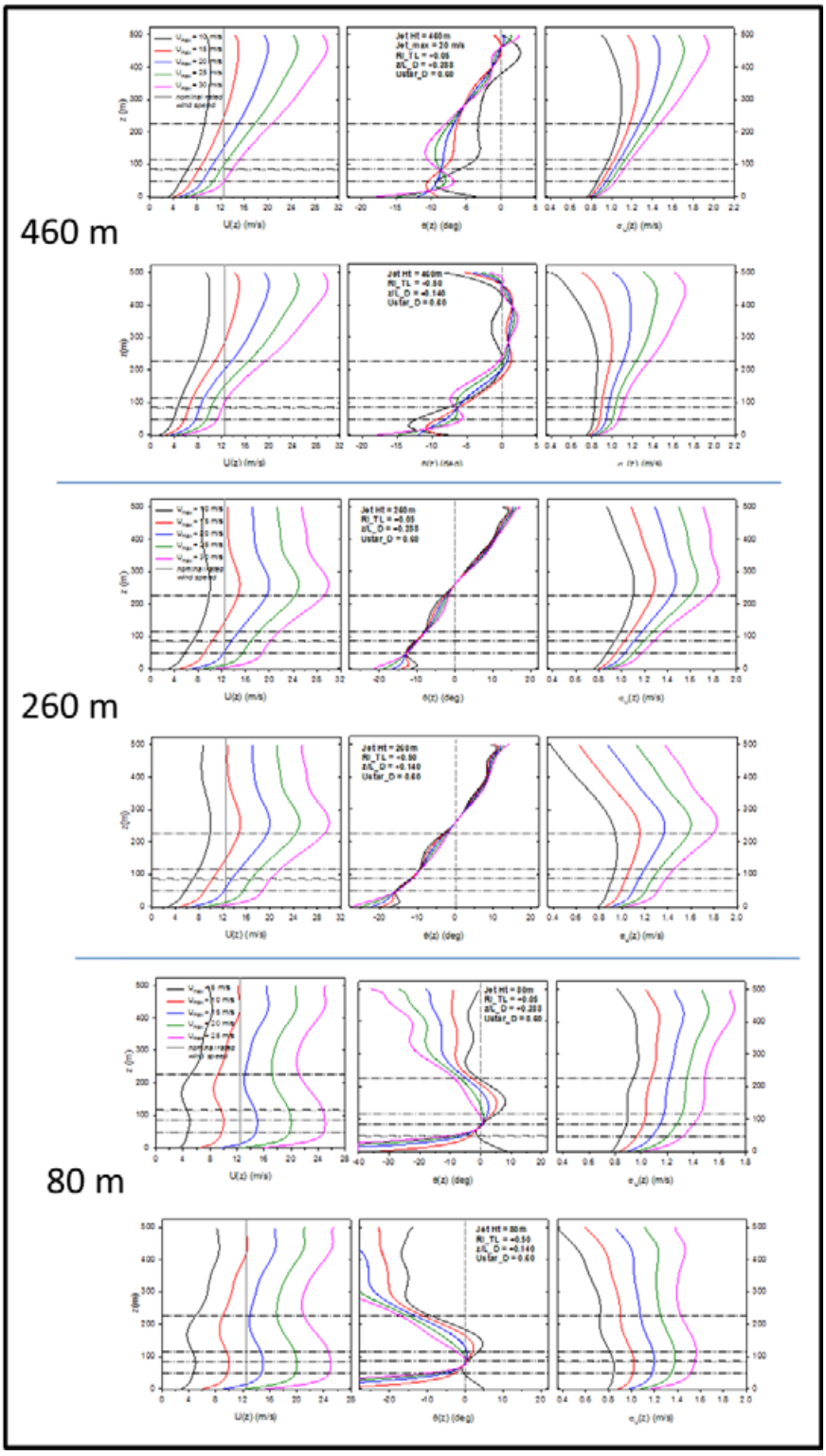

Figure 9-33. GP_LLJ model profile variations for 80-, 260-, and 460-m jet heights with variations in $U_{jet_{max}}$ and Ri_{TL} values of +0.50 and +0.05. The three lower dashed lines represent the rotor disk layer and hub height of the WindPACT 1.5-MW turbine and the upper is an approximate maximum elevation of a 10-MW turbine rotor.

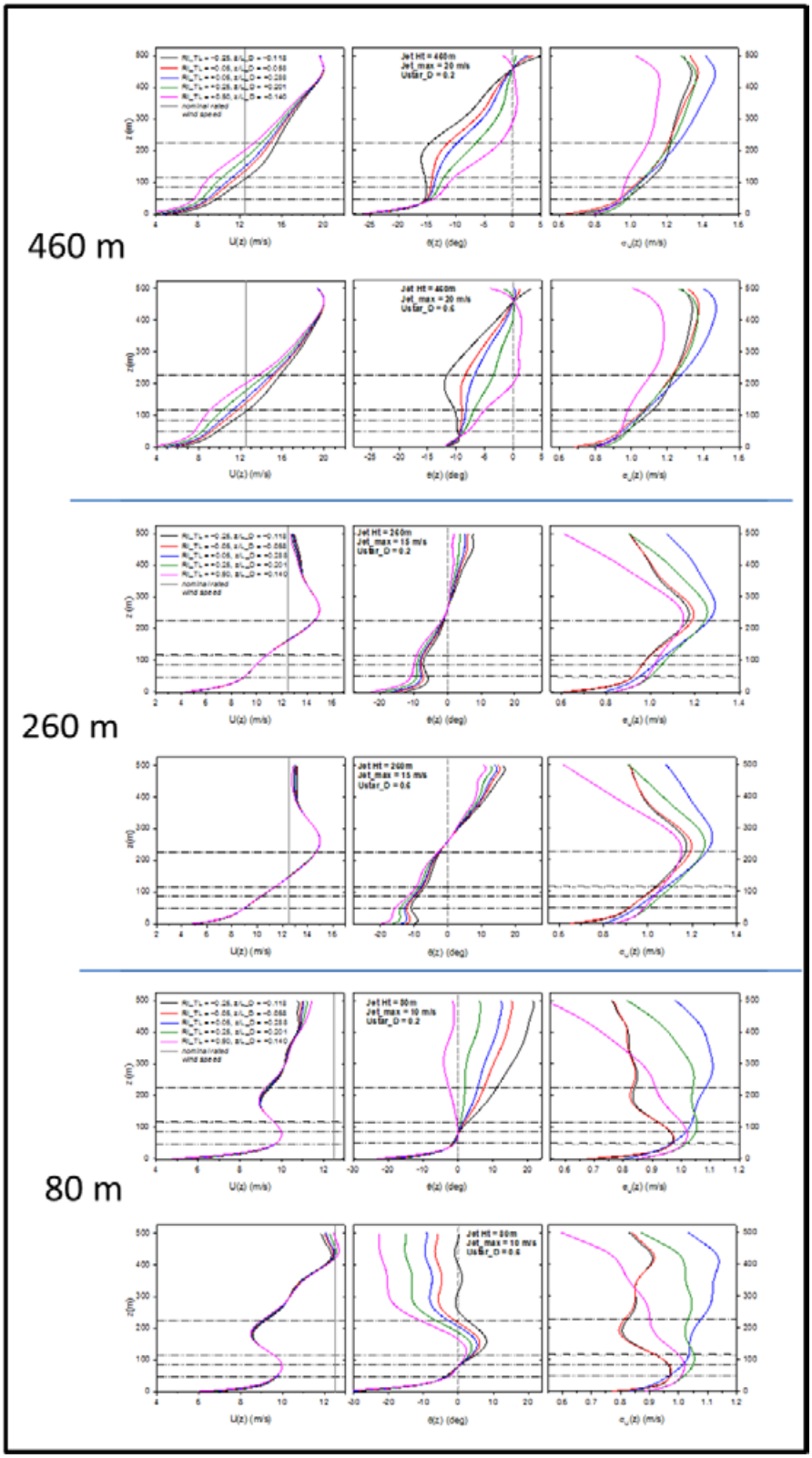

Figure 9-34. GP_LLJ model profile variations for 80-, 260-, and 460-m jet heights with variations in Ri_{TL} and u_{*D} values of +0.2 and +0.6 m s^{-1}

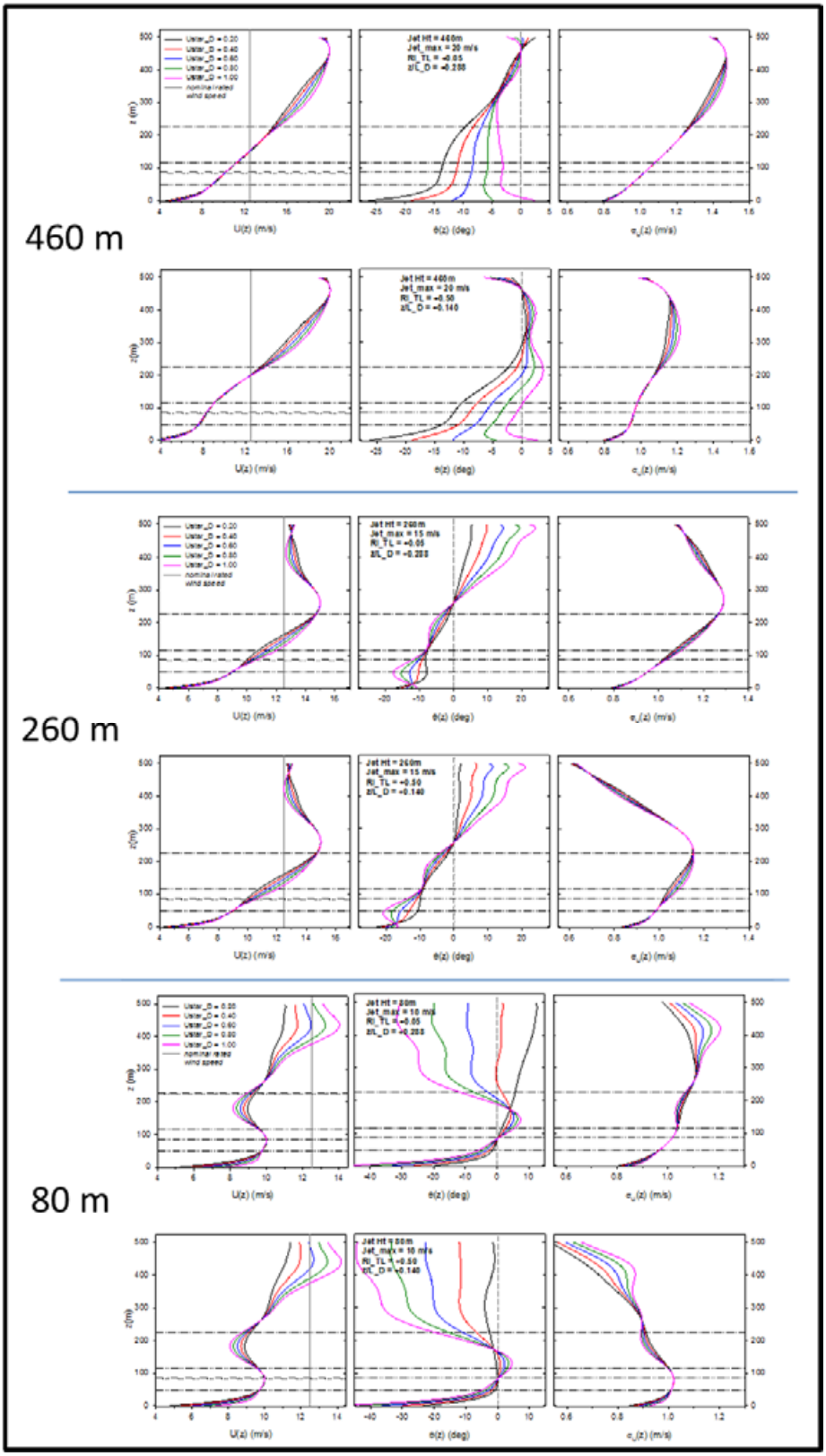

Figure 9-35. GP_LLJ model profile variations for 80-, 260-, and 460-m jet heights with variations in u_{*D} and Ri_{TL} values of +0.50 and +0.05

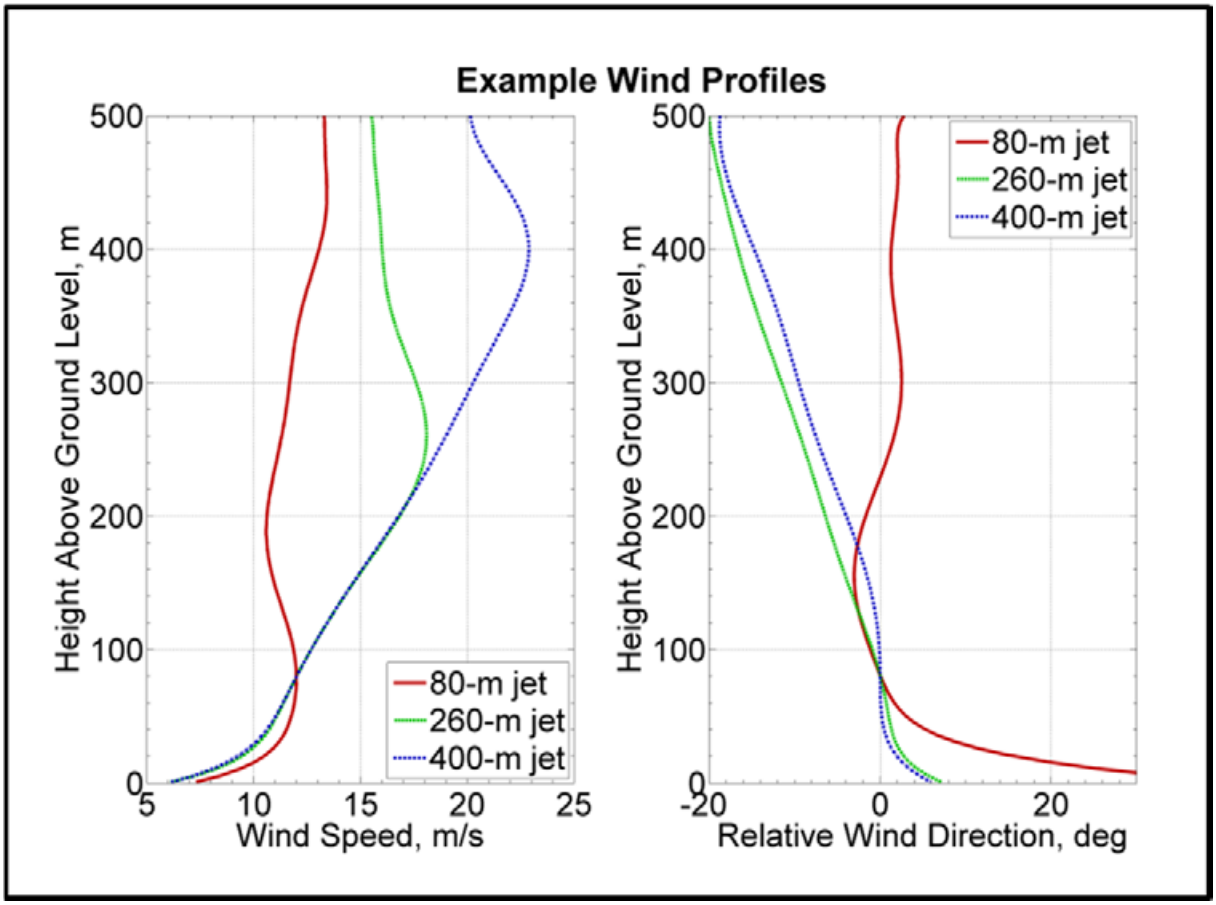

Figure 9-36. Examples of three TurbSim GP_LLJ spectral model LLJ wind speed and direction profiles for 80-m mean wind speed of 12 m s^{-1} and Ri_{TL} of +0.05. The wind direction is relative to the direction at 80 m.

9.4.7 TurbSim Spatial Simulations

An example of the spatial aspects of the TurbSim simulated turbulent inflow NWTCUP spectral model is scaled based on measurements from the ART upwind planar array at 0730 MST on December 15, 2001. The specified boundary conditions derived from the measurements and required for this simulation are shown above the dashed line in the following list and other non-scaling but supplementary measured results are below it:

- Hub-height mean wind speed of 12.78 m s^{-1}
- Ri_{TL} of +0.020
- Disk-averaged mean shearing stress u_{*D} of 0.711 m s^{-1}
- Disk layer power law exponent α of 0.103
- ----------
- Hub peak value of E_{coh} of 15.2 m^2 s^{-2}
- Disk-diameter normalized buoyancy length scale L_b/D of 1.27.

The parameters below the dashed line are not used as boundary conditions but are given for reference. Figure 9-37 plots isocontours of E_{coh} from a single simulation realization for 290 to 330 seconds of the 600-second simulated record. No coherent structures were added to the simulated background flow in Figure 9-37a but were added in Figure 9-37b. An examination of the latter reveals the presence of larger areas of 7.5 or greater values (red and black) of E_{coh} than in the former.

The most turbulent episode recorded by the LIST experiment occurred late in the 10-minute record on February 5, 2001, at 0505 MST. We simulated the near-rated wind speed turbulent inflow with the TurbSim NWTCUP spectral model using the following 10-minute mean values measured on the upwind planar array:

- Hub-height mean wind speed of 12.58 m s^{-1}
- Ri_{TL} of +0.017
- Disk-averaged mean shearing stress u_{*D} of 0.702 m s^{-1}
- Disk-layer power law exponent α of 0.108
- ----------
- Hub peak value E_{coh} of 80 m^2 s^{-2}
- Disk-diameter normalized buoyancy length scale L_b/D of 3.01.

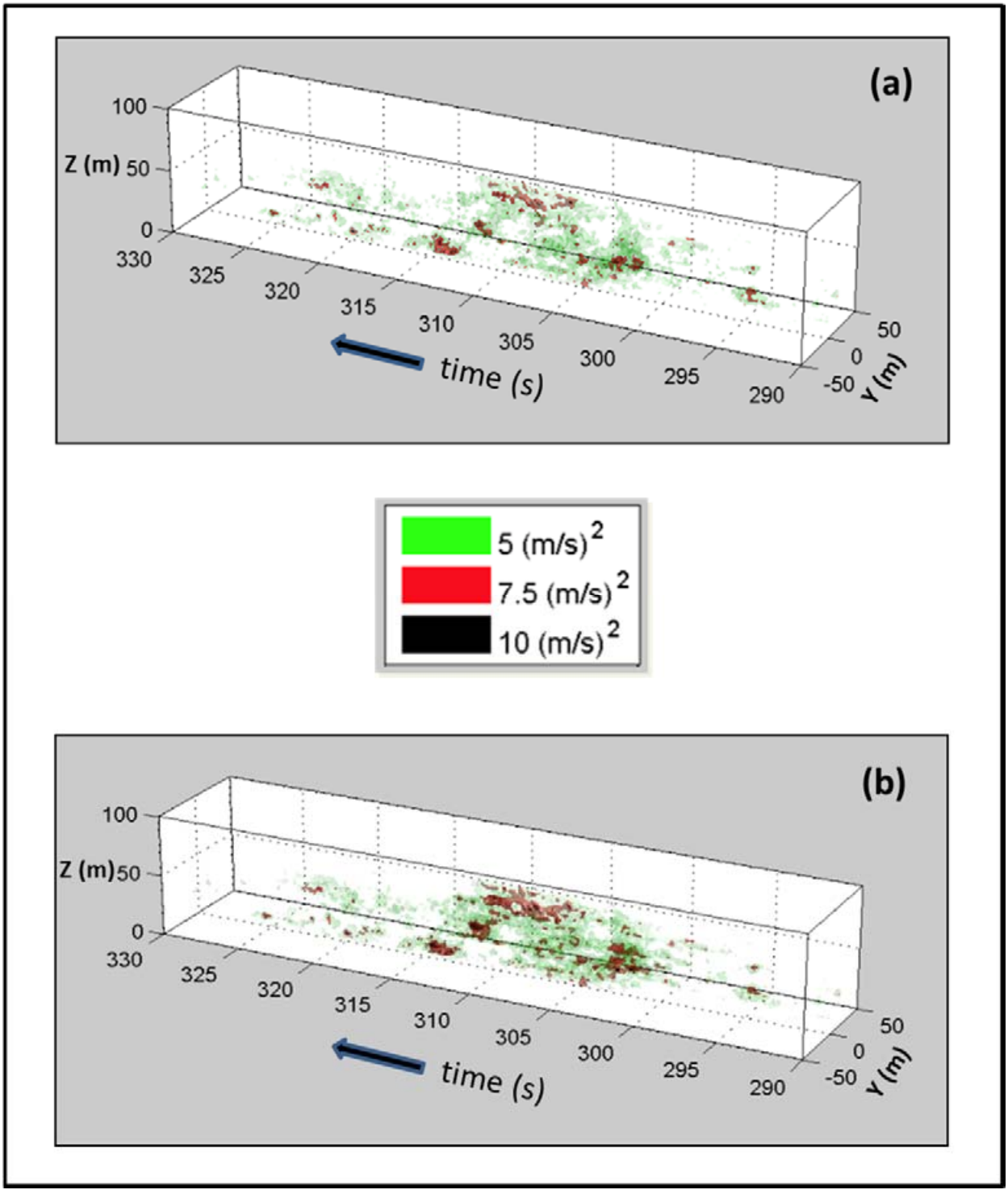

Figure 9-37. TurbSim simulation of NWTC LIST ART inflow observation of December 15, 2001, at 0736 MST. Isocontours of simulated E_{coh} (a) without coherent structures and (b) with coherent structures.

Figure 9-38 plots isocontours of the u, v, and w turbulence components and E_{coh} from a single TurbSim stochastic simulation realization for 550 to 600 seconds. The complex, 3-D turbulent structure is very evident. Values of E_{coh} reach more than 30 $m^2\ s^{-2}$ during the very intense and coherent turbulent period from about 580 to 588 seconds. Figure 9-38a does not include any superimposed coherent structures, but Figure 9-38b does. As with Figure 9-37, adding these structures increased the size and intensity of the coherent turbulent patches in the simulated background flow.

In Figure 9-39 we plot the isocontours of E_{coh} from a TurbSim GP_LLJ spectral model simulation of a much less turbulent situation. Here we simulate a typical Great Plains inflow to the NREL 5-MW Reference Turbine without the presence of a low-level jet and accompanying coherent structures. The mean hub-height wind speed is above rated wind speed at 13 $m\ s^{-1}$, the Ri_{TL} is +0.02, the disk-layer u_{*D} is 0.422 $m\ s^{-1}$, and the rotor disk shear exponent α is 0.139. Default values were used for the remaining boundary conditions. At the beginning of the simulated record in Figure 9-39a there is a small coherent structure with a small and more intense core that dies away rather quickly. For the period of 125 to 225 seconds in Figure 9-39b, larger patches of E_{coh} reappear but their intensity is at the turbine dynamic response threshold of 2 $m^2\ s^{-2}$ and most likely a low level of vibratory excitation is developing in the structure.

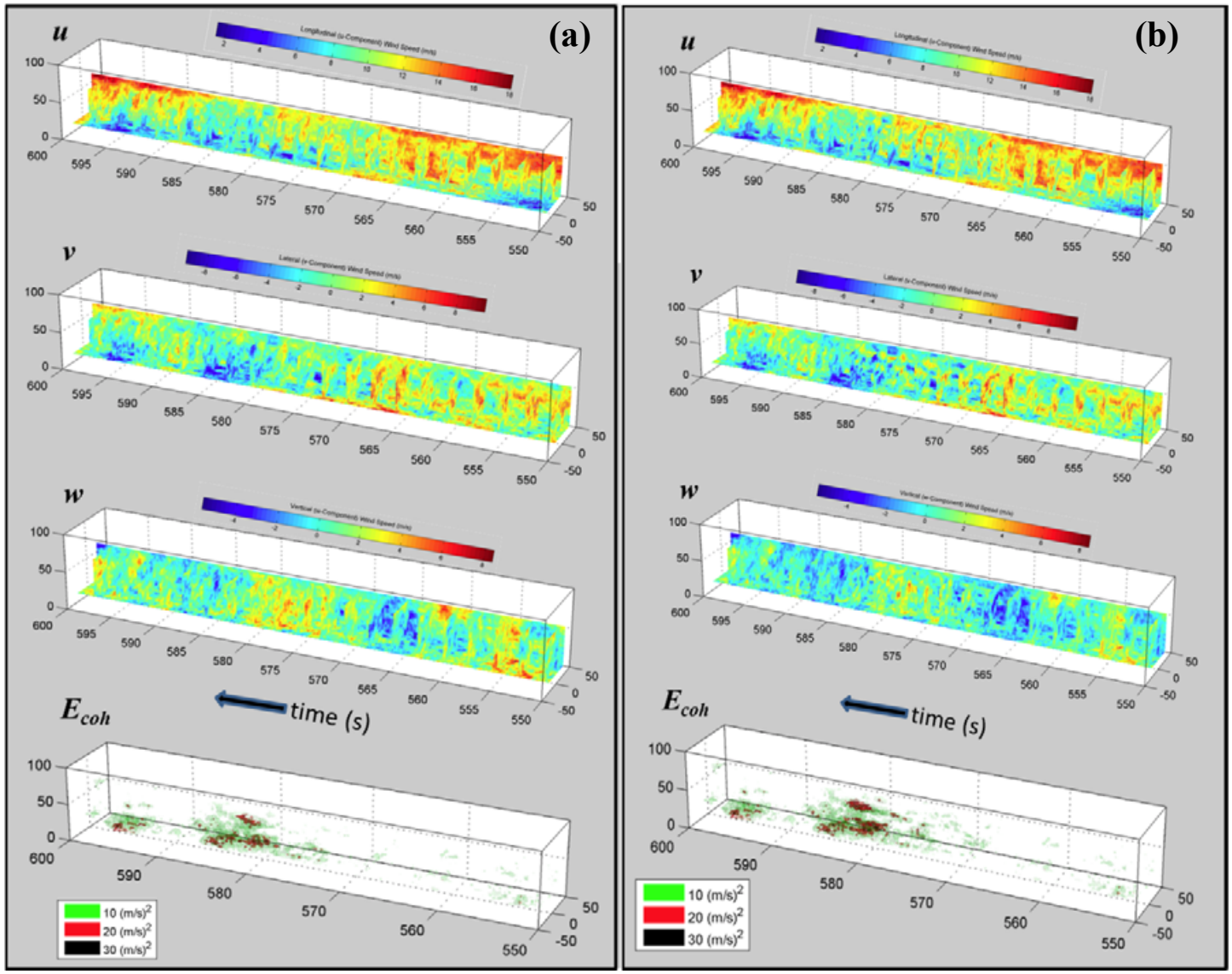

Figure 9-38. TurbSim simulation of intense LIST ART inflow turbulence observation, February 5, 2001, 0505 MST: (a) without coherent structures and (b) with coherent structures

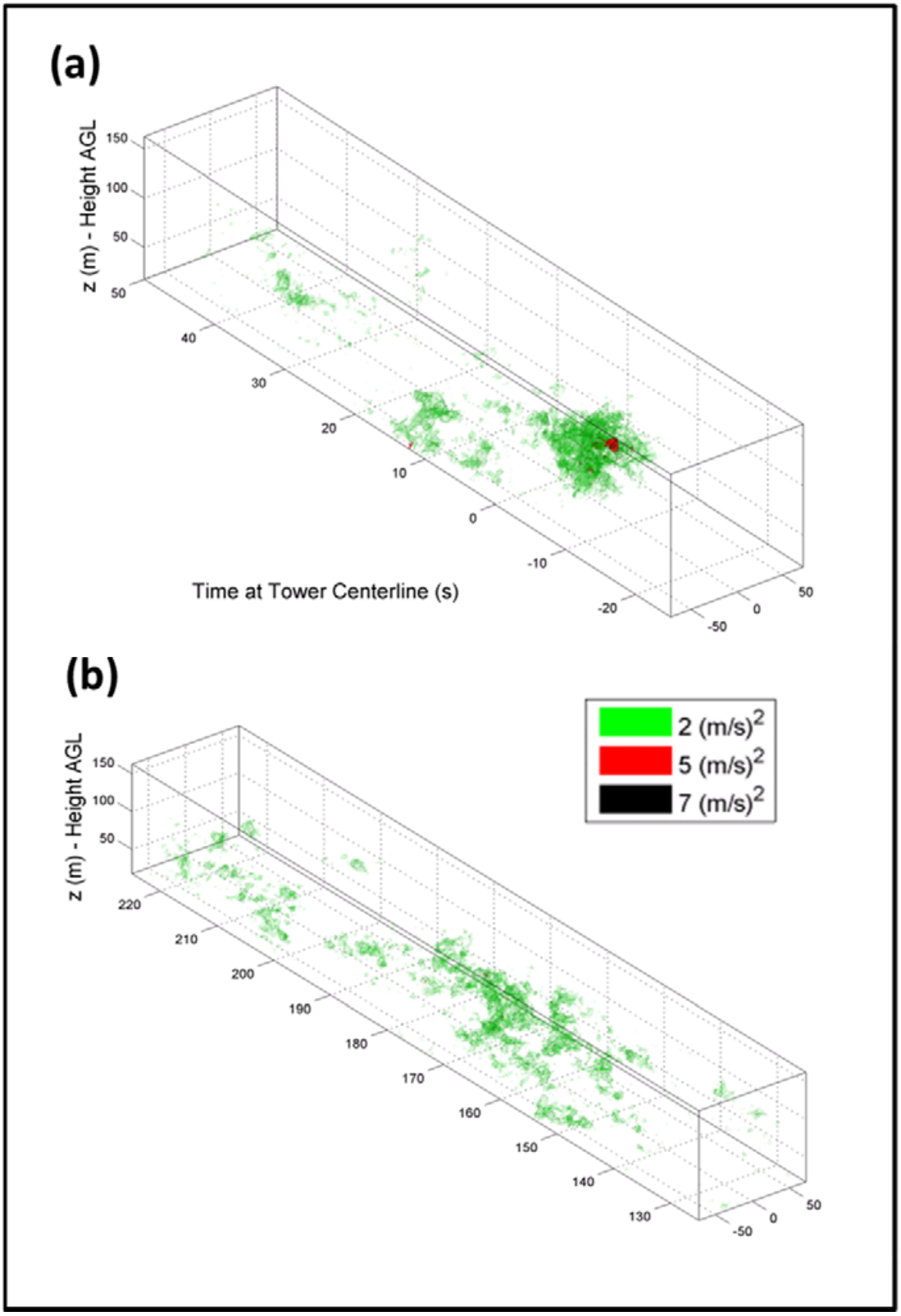

Figure 9-39. TurbSim GP_LLJ spectral model simulation of inflow E_{coh} to NREL 5-MW Reference turbine without LLJ and no coherent structures: (a) –5 to +50 seconds and (b) 125- to 225-second periods

9.5 Validation of TurbSim NWTCUP and GP_LLJ Spectral Models

We validated the TurbSim wind farm (WF_UPW, WF_07D, and, WF_14D), NWTCUP, and GP_LLJ site-specific spectral models. This was accomplished obtaining the median values of a range of turbulence parameters from the P05–P95 distributions from the observations taken in the wind farm, the NWTC upwind planar array, and the Lamar site 120-m met tower. We used 2 m s^{-1} wind speed bins over a range of 2 to 24 m $s^{-1}$and the previously defined stability classes (STC01, STC02, STC03, STC04, and STC05) to make the problem more tractable. Table 9-7 summarizes these wind speed bins. We applied the bin medians as the TurbSim boundary conditions to calculate an ensemble of 31 stochastic realizations for each site. In Figure 9-40 we present boxplot distributions from the NWTC and the Lamar site of the P05–P95 measured subpopulations and the aggregate distributions from the 31 simulation ensemble for the hub-height local u_* and peak or maximum value of E_{coh}. The distributions of observed u_* in Figure 9-40 reflect the variation in the actual flow, and the simulated results reflect the observed population median that was used for scaling. There is, however, no such constraint on the peak values of E_{coh}. In general, the simulated distributions of this important parameter track the observed ones very well.

In Figure 9-41 we compare the distributions of the measured hub-height turbulent component standard deviations σ_u, σ_v, and σ_w for the NWTC and Lamar sites with the aggregate distributions of the simulated ensembles. Our goal was to have the Q1–Q3 IQR (P25–P75) of simulated results to fall within at least the P10–P90 range of the observations. An examination of Figures 9-41a and b shows that in general simulated distributions fall close to the observed Q1–Q3 quartile range, but the NWTC σ_u and σ_w have a tendency to be negatively biased. Figure 9-42 compares distributions of the observed hub-height mean Reynolds stress components and the simulated ones. Again, because of the relationship between u_* and $\overline{u'w'}$ there is no variation in the former because it was a specified scaling parameter. There are generally reasonable agreements with the $\overline{u'v'}$ and $\overline{v'w'}$ components, though the NWTCUP model predicted values exhibit much wider distributions than those seen with the GP_LLJ model.

Table 9-7. Wind Speed Bin Classification

Bin Value	Speed Range (m s^{-1})
3	2–4
5	4–6
7	6–8
9	8–10
11	10–12
13	12–14
15	14–16
17	16–18
19	18–20
21	20–22
23	22–24

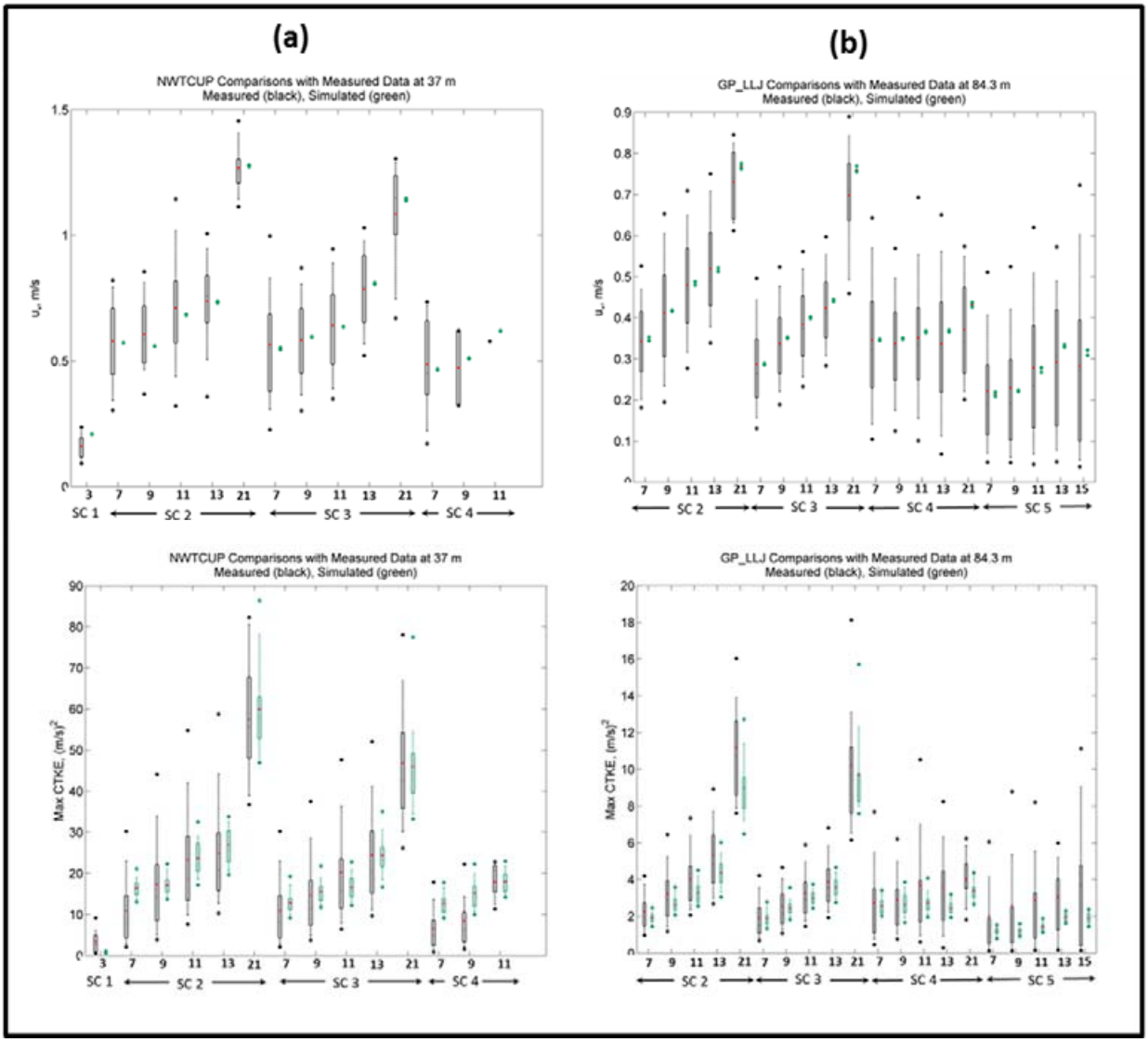

Figure 9-40. Statistical comparisons of observed probability distributions of P05–P95 range observed hub-height u_* and peak E_{coh} with stability and mean wind speed classes with NWTCUP and GP_LLJ TurbSim simulations using observed median values for boundary conditions: (a) NWTCUP and (b) GP_LLJ

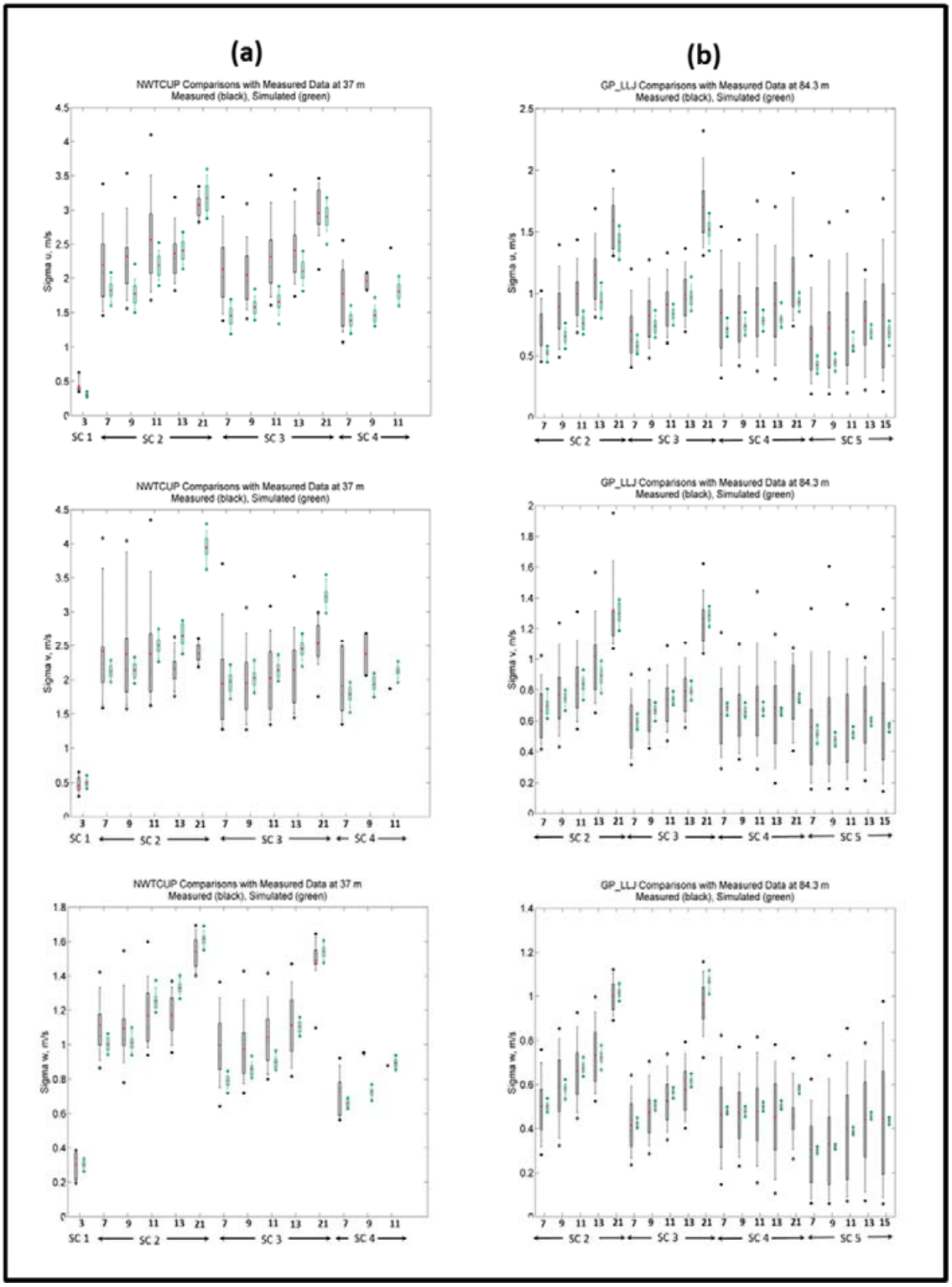

Figure 9-41. Same as Figure 9-40, but observed hub-height σ_u, σ_v, and σ_w with NWTCUP and GP_LLJ TurbSim simulations using observed median values for boundary conditions: (a) NWTCUP and (b) GP_LLJ

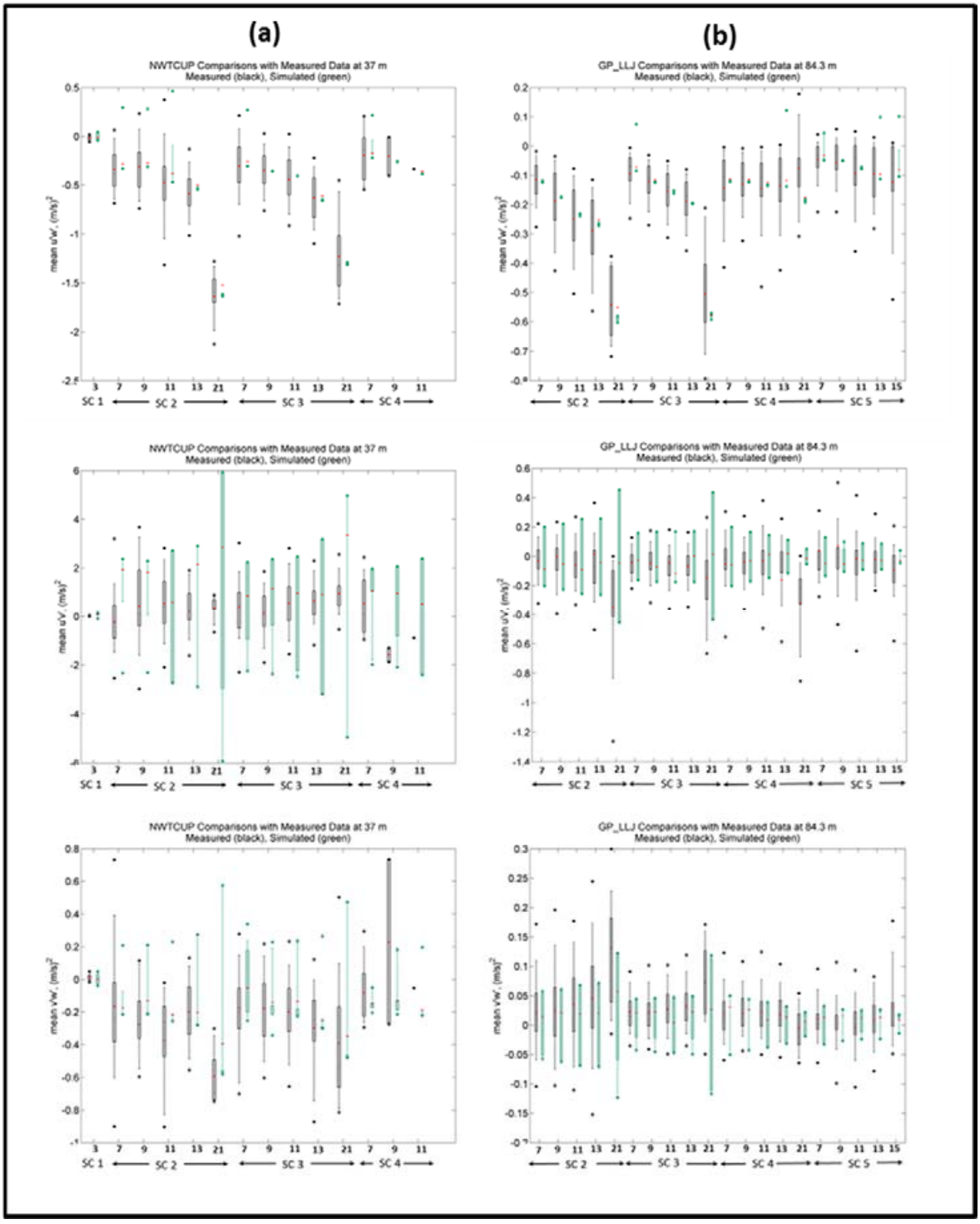

Figure 9-42. Same as Figure 9-40, but for observed hub-height mean *u'w'*, *u'v'*, and *v'w'* Reynolds stresses with NWTCUP and GP_LLJ TurbSim simulations using observed median values for nine boundary conditions: (a) NWTCUP and (b) GP_LLJ

10.0 Summary and Conclusions

Using simultaneous, time-synchronized measurements of the turbulent inflow microscale characteristics and the dynamic response of wind turbine structural components, we developed an understanding of the role of the physics of the inflow turbulence characteristics in creating excessive loads and fatigue damage in turbine structures. We used data collected from two adjacent 65-kW turbines deep within a 41-row wind farm in San Gorgonio, California; a 600-kW turbine operated in the rigorous flow at the National Wind Technology Center (NWTC) near Boulder, Colorado; and in atmospheric conditions at the site of a since installed wind farm on the high plains of southeastern Colorado. Analyzing these data allowed us to identify a narrow range of critical atmospheric conditions common to the sites. These atmospheric conditions are responsible for the majority if not all of the turbulence-induced fatigue damage seen on the two turbines in California and at the NWTC.

In this report we discussed the evolution of our understanding of the impact of atmospheric turbulence on wind turbines, along with the atmospheric conditions that create the specific turbulence characteristics that are so damaging. We also described how we developed a computer code that simulates these characteristics for use with the turbine models and design codes. We now summarize our conclusions in each of these areas.

10.1 The Impact of Turbulence on Turbine Dynamics

Our measurements and analysis enabled us to identify the role that organized or coherent turbulent patches in the background flow play in inducing large load excursions and fatigue damage. Using both numerical simulations and physical measurements, we showed that a resonant coupling of kinetic energy exists between these coherent turbulent patches and the natural vibrational modes of the turbine blades as the turbulence passes through the rotor. These organized turbulent patches frequently develop within the much more random turbulent and vertically sheared background flow of the stable, nocturnal boundary layer because of atmospheric Kelvin-Helmholtz Instability (KHI). KHI is a form of atmospheric resonance brought about by the influence of buoyancy on the intensification of turbulent perturbations moving through the background or mean flow. The fluctuating velocities of these resonant flows are spatially and temporally organized and can create a similar response characteristic induced by the unsteady aerodynamics of a turbine blade (i.e., the additive superposition of modal excursions into a large, phase-coherent load excursion). This process induces a flux or transport of turbulent energy into the blade structure, which is then propagated through the root attachments, the drivetrain, and the remainder of the structure.

Simply put, a coherent turbulent structure ingested by a turbine rotor blade induces a coherent aeroelastic response in the turbine structure. The turbine's design and the dynamic characteristics of its load paths—their modal frequencies and damping—determines how this energy is propagated through the turbine structure and where it is ultimately dissipated. As towers continued to be built taller, and turbine rotors become much larger and more flexible, the role of this process has likely become more influential in creating fatigue damage throughout the turbine structure.

10.2 Atmospheric Dynamics Associated with Turbine Dynamic Response

We showed that coherent turbulent kinetic energy—both locally generated and transported—is a major contributor to increased turbine fatigue damage. Kelvin-Helmholtz Instability (KHI) is often the most dominant process that creates these important turbine inflow turbulence characteristics. KHI is associated with stable, sheared flows that are the hallmark of the nocturnal atmospheric boundary layer. Often, the depth of the atmospheric boundary layer within which turbines reside exhibits stable characteristics approaching two-thirds of a diurnal period.

We found that the vertical dynamic stability of the atmospheric layer inhabited by a turbine is one of the most influential atmospheric parameters affecting loading and fatigue damage. More specifically, we discovered a very narrow range of weakly stable conditions that is most damaging to turbine structures. It is within this critical stability range that the development of KHI and the attendant coherent turbulence occurs. Such damaging conditions are more likely to occur within certain periods of the stable portion of a normal diurnal cycle (i.e., typically during the early evening hours after sunset and again in the early morning hours between midnight and sunrise). During both of these periods, significant vertical shears can develop from the rapid changes that take place at sunset when convective turbulence ceases, as well as later, when atmospheric inertial oscillations contribute to the maximum strength of low-level jet streams (LLJs). In both cases conditions are ripe for the development of KHI.

KHI creates organized or coherent turbulent perturbations, which propagate through the mean flow when the turbine layer stability falls within the critical range, that grow and intensify rapidly. We found that the greatest turbine dynamic response takes place when the fastest growing turbulent eddy size is near the equivalent diameter dimension of the turbine rotor. We also found that the vertical transport or flux of coherent turbulence into a turbine rotor disk layer is an important source of turbine dynamic response. This was true within the California wind farm and at the NWTC. Strong vertical fluxes exist in both locations, caused in California by the presence of the large wind farm itself combined with nearby mountainous terrain, and at the NWTC by the adjacent mountainous landscape. Our purpose in making turbulence measurements associated with an LLJ was to identify the presence, intensity, and frequency of the coherent turbulence conditions we found using the 65- and 600-kW turbines. The Great Plains hold the greatest wind resource in the United States, but they are also known to harbor strong, nocturnal LLJs and intense vertical shears beneath the jet maximum velocities. By combining direct measurements from a 120-m met tower and remotely sensed velocity measurements using an acoustic wind profiler (sodar)—and, for a short period, a scanning lidar—we found that such conditions do indeed exist, though often with less intensity than are observed in the California wind farm and at the NWTC. The diurnal occurrence was similar to what we found in the wind farm and at the NWTC, indicating that the responsible nocturnal boundary layer dynamics that are responsible for the observed excessive turbine dynamic responses are more ubiquitous and extend to a much greater range of wind energy sites. We also found that the presence of LLJs well above the maximum height of turbine rotors was often responsible for significant downward fluxes of coherent turbulent energy similar to those seen in lee flows downwind of mountainous terrain. These LLJs, then, are an important source of this turbine-sensitive turbulence characteristic.

10.3 Simulating Critical Turbulence Characteristics

The TurbSim stochastic inflow turbulence code was developed to produce numerical simulations of full-field flows that mimic the statistical characteristics of inflow turbulence over a wide range of turbine operating conditions. We extended Paul Veers' (Sandia National Laboratories) original SNLWIND simulator to include all three turbulent wind components in a diabatic as well as neutrally stable atmosphere. We used field measurements from the California wind farm and an upwind planar array at the NWTC, as well as from a 120-m met tower and acoustic wind profiler at the Lamar site, to develop individual site-specific spectral models to simulate the conditions in each location. Once we identified KHI as major contributor to the largest turbine dynamic loads, colleagues at the National Center for Atmospheric Research created a high-resolution simulation of the life cycle of a stationary Kelvin-Helmholtz (K-H) billow turbulent structure.

We incorporated several well-defined excerpts from this simulation in the TurbSim code along with similar ones derived from an even more highly resolved K-H billow simulation furnished by our colleagues at Colorado Research Associates. Adding the coherent structure elements derived from the high-resolution K-H billow simulations (and scaled based on actual measurements) allowed us to correct the under prediction of fatigue damage caused by a TurbSim predecessor. Including wind direction profiles in addition to velocity in the simulation of LLJs also revealed an important source of dynamic loads associated with wind direction shear across the rotor disk.

Statistical summaries of the TurbSim simulations compared well with observed summaries, particularly for the NWTC and Great Plains spectral models where larger data sets were available for analysis. Limited validations of the observed and simulated loads for the 600-kW turbine in the NWTC operating environment showed them to be in reasonable agreement. Similar validations for the wind farm and Great Plains spectral models have been hampered by the lack of a more complete dynamics model of the 65-kW turbines at the wind farm and by only virtual models of the simulated 1.5- and 5-MW turbines being available.

We believe the TurbSim site-specific spectral models give the turbine designer a range of realistic emulations of the full-field turbulent inflows seen in each environment, particularly within the critical stability range. Such conditions are not available in the current International Electrotechnical Commission (IEC) Normal Turbulence Models (NTMs). We highly recommend that designers use the TurbSim NWTC and Great Plains spectral models, particularly with added emphasis on the critical range stability boundary conditions to bracket a range of likely wind turbine operating conditions. Finally, we also encourage designers to employ one of the available multibody turbine dynamic codes that use the NREL AeroDyn code as the interface with TurbSim for such simulations.

11.0 Bibliography

Banta, R.M., Oliver, L.D.; Neff, W.D.; Levinson, D.H.; Ruffieux, D. (1995). "Influence of Canyon-Induced Flow on Flow and Dispersion over Adjacent Plains." *Theoretical and Applied Climatology* (52); pp. 27–42.

Banta, R.M.; Pichugina, Y.L.; Newsom, R.K. (2003). "Relationship between Low-Level Jet Properties and Turbulence Kinetic Energy in the Nocturnal Stable Boundary Layer." *Journal of the Atmospheric Sciences* (60); pp. 2549–2555.

Banta, R.M; Orr, B.W.; Grund, C.J.; Levinson, D.H.; Frish, A.S.; Mayor, S.D. (1997). "Estimation of TKE and Momentum Flux Profiles from Doppler Lidar Scans during LIFT." *12th Symposium on Boundary Layers and Turbulence*, Vancouver, B.C., Canada. Boston, MA: American Meteorological Society; pp. 11–12.

Bonner, W.D. (1968). "Climatology of the Low-Level Jet." *Monthly Weather Review* (96); pp. 833–850.

Businger, J.A.; Wyngaard, J.C.; Izumi, Y.; Bradley, E.F. (1971). "Flux-Profile Relationships in the Atmospheric Surface Layer." *Journal of the Atmospheric Sciences* (28); pp.181–189.

Cleveland, W.S.; Devlin, S.J. (1988). "Locally-Weighted Regression: An Approach to Regression Analysis by Local Fitting." *Journal of the American Statistical Association* (83:403); pp. 596–610.

Downing, S.D; Socie, D.F. (1982). "Simple Rainflow Counting Algorithms." *International Journal of Fatigue,* (4:1); pp. 31-40.

Dutton, J.A.; Panofsky, H.A.; Larko, D.; Shirer, H.N.; Stone, G.; Vilardo, M. (October 1979). *Statistics of Wind Fluctuations over Complex Terrain*. DOE/ET/20560-1. University Park, PA: Pennsylvania State University, Department of Meteorology.

ESDU. (April 1993). *Characteristics of Atmospheric Turbulence near the Ground. Part II: Single Point Data for Strong Winds (Neutral Atmosphere)*. Report No. 85020. London: Engineering Sciences Data Unit.

Frehlich, R.; Kelley, N. (March 2008). "Measurements of Wind and Turbulence Profiles with Scanning Doppler LIDAR for Wind Energy Applications." *IEEE Journal of Selected Topics in Applied Earth Observations and Remote Sensing* (1:1); pp. 42–47.

Grund, C.J.; Banta, R.M.; George, J.L.; Howell, J.N., Post, M.J.; Richter, R.A.; Weickmann, A.M. (2001). "High-Resolution Doppler Lidar for Boundary Layer and Cloud Research." *Journal of Atmospheric and Oceanic Technology* (18); pp. 376–393.

Gurley, K.; Kareem, A. (1999). "Applications of Wavelet Transforms in Wind, Earthquake, and Ocean Engineering." *Engineering Structures* (21:2); pp. 149–167.

Hogg, A.M.; Ivey, G.N. (2003). "The Kelvin-Helmholtz to Holmboe Instability Transition in Stratified Exchange Flows." *Journal of Fluid Mechanics* (477); pp. 339–362.

Højstrup, J. (October 1982). "Velocity Spectra in the Unstable Planetary Boundary Layer." *Journal of the Atmospheric Sciences* (39); pp. 2239–2248.

Holtslag, A.A.M.; Nieuwstadt, F.T.M. (1986). "Scaling the Atmospheric Boundary Layer." *Boundary-Layer Meteorology* (36:1-2); pp. 201-209.

Howard, L.N. (1961). "Note on a Paper of John W. Miles." *Journal of Fluid Mechanics* (10); pp. 509–512.

IEC. (1999). *Wind Turbines—Part 1: Design Requirements*, 2nd edition. IEC 61400-1. Geneva, Switzerland: International Electrotechnical Commission.

IEC. (August 2005). *Wind Turbines—Part 1: Design Requirements*, 3rd edition. IEC 61400-1. Geneva, Switzerland: International Electrotechnical Commission.

Jonkman, B.J. (2009). *TurbSim User's Guide* (Version 1.50). NREL/TP-500-46198. Golden, CO: National Renewable Energy Laboratory (NREL).

Jonkman, J.M.; Buhl, M.L. (August 2005). *FAST User's Guide.* NREL/EL-500-38230. Golden, CO: NREL.

Jonkman, J.; Butterfield, S.; Musial, W.; Scott, G. (February 2009). *Definition of 5-MW Reference Wind Turbine for Off Shore System Development.* NREL/TP-500-38060. Golden, CO: NREL.

Jonkman, J.; Cotrell, J. (2003). *Demonstration of the Ability of RCAS to Model Wind Turbines.* NREL/TP-500-34632. Golden, CO: NREL.

Kaimal, J.C; Finnigan, J.J. (1994). *Atmospheric Boundary Layer Flows.* New York: Oxford University Press.

Kaimal, J.C.; Wyngaard, J.C.; Izumi. Y.; Coté, O.R. (1972). "Spectral Characteristics of Surface Layer Turbulence." *Quarterly Journal of the Royal Meteorological Society* (98); pp. 563–589.

Kelley, N.D. (November 1992). *Full Vector (3-D) Inflow Simulation in Natural and Wind Environments Using An Expanded Version of the SNLWIND (Veers) Turbulence Code.* NREL/TP-442-5225. Golden, CO: NREL.

Kelley, N.D. (November 1993). *The Identification of Inflow Fluid Dynamics Parameters That Can Be Used to Scale Fatigue Loading Spectra of Wind Turbine Structural Components.* NREL/TP-442-6008. Golden, CO: NREL.

Kelley, N.D.; Osgood, R.M.; Bialasiewicz, J.T.; Jakubowski, A. (2000). "Using Wavelet Analysis to Assess Turbulence/Rotor Interactions." *Wind Energy* (3); pp. 121–134.

Kelley, N.D.; Sutherland, H.J. (1996). *Damage Estimates from Long-Term Structural Analysis of a Wind Turbine in a U.S. Wind Farm Environment.* NREL/ CP-440-21672. Golden, CO: NREL.

Kelley, N.D.; Wright, A.D.; Buhl, M.L.; Tangler, J.L. (October 1996). *Long-Term Simulation of Turbulence-Induced Loads Using the SNLWIND-3D, FAST, YawDyn, and ADAMS Numerical Codes.* NREL/CP-440-21673. Golden, CO: NREL.

Kelley, N.; Shirazi, M.; Jager, D.; Wilde, S.; Adams, J., Buhl, M.; Sullivan, P.; Patton, E. (2004). *Lamar Low-Level Jet Project—Interim Report.* NREL/TP-500-34593. Golden, CO: NREL.

Kundu, P.K. (1990). *Fluid Mechanics*. San Diego, CA: Academic Press, Inc.

Lindzen, R.S. (1974). "Stability of a Helmholtz Velocity Profile in Continuously Stratified, Infinite Boussinesq Fluid—Application to Clear Air Turbulence." *Journal of the Atmospheric Sciences* (31); pp. 1507–1514.

Mahrt, L. (1999). "Stratified Atmospheric Boundary Layers." *Boundary-Layer Meteorology* (90); pp. 375–396.

Malcolm, D.J.; Hansen, A.C. (August 2002). *WindPACT Turbine Rotor Design Study.* Work performed by Global Energy Concepts, Kirkland, WA, and Windward Engineering, Salt Lake City, UT. NREL/SR-500-32495. Golden, CO: NREL.

Mann, J. (1994). "The Spatial Structure of Neutral Atmospheric Turbulence." *Journal of Fluid Mechanics* (273); pp. 141–168.

Mann, J. (1998). "Wind Field Simulation." *Problems in Engineering Mechanics* (13:4); pp. 269–282.

Miles, J.W. (1961). "On the Stability of Heterogeneous Shear Flows." *Journal of Fluid Mechanics* (10); pp. 496–508.

Miles, J.W.; Howard, L.N. (1964). "Note on a Heterogeneous Shear Flow." *Journal of Fluid Mechanics* (20); pp. 331–336.

Mitchell, M.K.; Arritt, R.W.; Labas, K. (September 1995). "An Hourly Climatology of the Summertime Great Plains Low-Level Jet Using Wind Profiler Observations." *Weather Forecasting* (10); pp. 576–591.

Monin, A.S.; Obukhov, A.M. (1954). "Basic Laws of Turbulent Mixing in the Ground Layer of the Atmosphere." Translations of Geophysics. Inst. Akad. Nauk USSR (151); pp. 163–187, as referenced in Kaimal and Finnigan (1994).

Moriarty, P.J.; Hansen, A.C. (December 2005). *AeroDyn Theory Manual*. NREL/EL-500-36881. Golden, CO: NREL.

Nelson, L.D., Manuel, L.; Sutherland, H.J.; Veers, P.S. (November 2003). "Statistical Analysis of Inflow and Structural Response Data from the *LIST* Program." *Journal of Solar Energy Engineering* (125:4); pp. 541–549.

Olesen, H.R.; Larsen, S.E.; Højstrup, J. (July 1984). "Modeling Velocity Spectra in the Lower Part of the Planetary Boundary Layer." *Boundary-Layer Meteorology* (29); pp. 285–312.

Osgood, R.M. (June 3, 2004). *CART Natural Frequency Snap-back Test Report.* NREL Internal Draft Report. Golden, CO: NREL.

Osgood, R.M.; McFarland, H.G.; Johnson, G.L. (February 2002). *Full System Modal Survey Test Results of the Controls Advanced Research Turbine (CART) Located at NWTC Site 4.3*. NREL Internal Letter Report. Golden, CO: NREL.

Panofsky, H.A.; Dutton, J.A. (1984). *Atmospheric Turbulence: Models and Methods for Engineering Applications.* New York: Wiley-Interscience; 397 pp.

Pichugina, Y.L.; Banta, R.M.; Kelley, N.D.; Sandberg, S.P.; Machol, J.L.; Brewer, W.A. (2004). "Nocturnal Low-Level Jets Characteristics over Southeastern Colorado." Preprints, *16th Symposium on Boundary Layers and Turbulence,* Portland, ME. Boston, MA: American Meteorological Society; pp. 4–11.

Rosenthal, A.J.; Lindzen, R.S. (1983). "Instabilities in Stratified Fluid Having One Critical Level. Part I: Results." *Journal of the Atmospheric Sciences* (40:3); pp. 509–520.

Smyth, W.D. (2004). "Kelvin-Helmholtz Billow Evolution from a Localized Source." *Journal of the Royal Meteorological Society* Part B (130:603); pp. 2753–2766.

Smyth, W.D.; Moum, J.N.; Caldwell, D.R. (2001). "The Efficiency of Mixing in Turbulent Patches: Inferences from Direct Simulations and Microstructure Observations." *Journal of Physical Oceanography* (31:8); pp. 1969–1992.

Stull, R.B. (1988). *An Introduction to Boundary Layer Meteorology.* Dordrecht, The Netherlands: Kluwer Academic Publishers; 666 pp.

Sutherland, H. J. (April 1994). "Fatigue Case Study and Loading Spectra for Wind Turbines*." Proceedings of the IEA Third Symposium on Wind Turbine Fatigue.* IEA, Implementing Agreement for a Programme of Research and Development onWind Energy Conversion Systems – Annex XI, April 1994, pp. 77–87.

Sutherland, H.J. (June 1999). *On the Fatigue Analysis of Wind Turbines*. SAND99-0089. Albuquerque, NM: Sandia National Laboratories (SNL).

Sutherland, H.J. (2002). "Inflow and the Fatigue of the LIST Wind Turbine." *Proceedings of the 2002 ASME Wind Energy Symposium*. Reno, NV. New York, NY: ASME; pp. 427-437.

Sutherland, H.J.; Kelley, N.D. (1995). "Fatigue Damage Estimate Comparisons for Northern Europe and U.S. Wind Farm Loading Environments." *Proceedings of WindPower 95*, Washington, D.C. Washington: American Wind Energy Association; pp. 177-186.

Sutherland, H.J.; Mandell, J.F. (November 2004). "Effect of Mean Stress on the Damage of Wind Turbine Blades." *Journal of Solar Energy Engineering* (126:4); pp.1041–1049.

Tangler, J.; Smith, B.; Kelley, N.; Jager, D. (1991). *Measured and Predicted Rotor Performance for the SERI Advanced Wind Turbine Blades*. NREL/TP-253-4673. Golden, CO: NREL.

Tangler, J.L.; Somers, D.M. (January 1995). *NREL Airfoil Families for HAWTs.* NREL/TP-442-7109. Golden, CO: NREL.

Thresher, R.W.; Holley, W.E.; Smith, C.E.; Jafarey, N.; Lin, S.-R. (August 1981). *Modeling the Response of Wind Turbines to Atmospheric Turbulence.* RL0/227-81/2. Corvallis, OR: Oregon State University, Department of Mechanical Engineering.

Veers, P.S. (October 1983). *A General Method for Fatigue Analysis of Vertical Axis Wind Turbine Blades.* SAND82-2543. Albuquerque, NM: SNL.

Veers, P.S. (March 1988). *Three-Dimensional Wind Simulation.* SAND88-0152. Albuquerque, NM: SNL.

Werne, J.; Fritts, D.C. (February 15, 1999). "Stratified Shear Turbulence: Evolution and Statistics." *Geophysical Research Letters* (26:4); pp. 439–442.

Whiteman, C.D.; Bian, X.; Zhong, S. (October 1997). "Low-Level Jet Climatology from Enhanced Rawinsonde Observations at a Site in the Southern Great Plains." *Journal of Applied Meteorology* (36); pp. 1363–1376.

Wright, A.D. (2004). Personal Communication. Golden, CO: NREL.